

Yonghui Wang · Xudong Zhi ·  
Ximei Zhai · Jiachuan Yan · Rong Zhang

---

# Innovations in Impact and Blast Protections

Foam-Filled Energy Absorbers and  
Steel-Concrete-Steel Sandwich  
Structures

# Innovations in Impact and Blast Protections

@seismicisolation

Yonghui Wang · Xudong Zhi · Ximei Zhai ·  
Jiachuan Yan · Rong Zhang

# Innovations in Impact and Blast Protections

Foam-Filled Energy Absorbers  
and Steel-Concrete-Steel Sandwich Structures



Springer

@seismicisolation

Yonghui Wang  
School of Civil Engineering  
Harbin Institute of Technology  
Harbin, Heilongjiang, China

Ximei Zhai  
School of Civil Engineering  
Harbin Institute of Technology  
Harbin, Heilongjiang, China

Rong Zhang  
School of Civil Engineering  
Harbin Institute of Technology  
Harbin, Heilongjiang, China

Xudong Zhi  
School of Civil Engineering  
Harbin Institute of Technology  
Harbin, Heilongjiang, China

Jiachuan Yan  
School of Civil Engineering  
Harbin Institute of Technology  
Harbin, Heilongjiang, China

ISBN 978-981-19-4374-4                    ISBN 978-981-19-4375-1 (eBook)  
<https://doi.org/10.1007/978-981-19-4375-1>

© The Editor(s) (if applicable) and The Author(s), under exclusive license to Springer Nature Singapore Pte Ltd. 2023

This work is subject to copyright. All rights are solely and exclusively licensed by the Publisher, whether the whole or part of the material is concerned, specifically the rights of translation, reprinting, reuse of illustrations, recitation, broadcasting, reproduction on microfilms or in any other physical way, and transmission or information storage and retrieval, electronic adaptation, computer software, or by similar or dissimilar methodology now known or hereafter developed.

The use of general descriptive names, registered names, trademarks, service marks, etc. in this publication does not imply, even in the absence of a specific statement, that such names are exempt from the relevant protective laws and regulations and therefore free for general use.

The publisher, the authors, and the editors are safe to assume that the advice and information in this book are believed to be true and accurate at the date of publication. Neither the publisher nor the authors or the editors give a warranty, expressed or implied, with respect to the material contained herein or for any errors or omissions that may have been made. The publisher remains neutral with regard to jurisdictional claims in published maps and institutional affiliations.

This Springer imprint is published by the registered company Springer Nature Singapore Pte Ltd.  
The registered company address is: 152 Beach Road, #21-01/04 Gateway East, Singapore 189721,  
Singapore

# Preface

For recent decades, the extreme events or threats on buildings and infrastructures related to impact and blast loads have shown an increasing trend, which results in severe damage or even collapse of the structures. Hence, there is an urgent need to improve their resistances against impact and blast loads. Generally, the impact and blast protections can be categorized into two groups, including “soft” and “stiff” protections. “Soft” protection refers to the use of “soft” materials (e.g., foam) or structures (e.g., thin-walled tube) to dissipate impact and blast energy through plastic deformation. “Stiff” protection refers to the utilization of structures with high resistance and ductility to directly resist potential impact and blast loads. More recently, the combination of “soft” and “stiff” protection is more appealing in terms of lightweight, high energy absorption capacity, failure mode regulating, etc.

This book aims to present some new protective methods from three aspects, including “soft” protection, “stiff” protection, and the combination of the two. In the first part of this book, the aluminum foam- and polyurethane foam-filled structures have been developed for dissipating impact and blast energy. Experimental and numerical studies have been conducted to obtain their behaviors under impact loading. Moreover, analytical models have been proposed to assess their energy absorption performances and facilitate the impact and blast-resistant design when using the proposed foam-filled structures as energy absorbers. In the second part of this book, Steel-Concrete-Steel (SCS) sandwich structures with novel shear connectors have been developed, and their behaviors under impact and blast loads have been experimentally, numerically, and analytically studied. The analytical models for predicting the impact and blast responses of SCS sandwich structures have been developed. In the third part of this book, a new Steel-Polyurethane Foam-Steel-Concrete-Steel (SPUFSCS) panel (i.e., the combination of “soft” and “stiff” protection) has been developed to achieve a higher impact-resistant performance. Owing to the increasing impact and blast threats on buildings and infrastructures, the studies presented in this book are of significance for providing new solutions for impact and blast enhancements. The main contents of this book are as follows:

Chapter 1: Two types of novel aluminum foam-filled energy absorption connectors are presented, and their energy absorption performances under impact load are

reported. The analytical models considering transient strain rate effect of steel are presented to predict force–displacement of the aluminum foam-filled energy absorption connectors. A design method is presented for conducting the blast-resistant design of the structures employing the proposed energy absorption connectors as additional energy absorbers.

Chapter 2: Two types of Polyurethane (PU) foam-filled energy absorption connectors are developed, and their energy absorption performances are experimentally and numerically examined. Moreover, the analytical models for predicting the force–displacement responses of PU foam-filled energy absorption connectors are presented, and the transient strain rate effects of both steel and PU foam are incorporated into the analytical models.

Chapter 3: A novel Aluminum Foam-Filled Circular-Triangular Nested Tube (AFCTNT) energy absorber is presented to resist impact load, and its energy absorption performance, force–displacement response, and deformation mode are experimentally and numerically examined.

Chapter 4: Experimental and numerical studies on a cladding sandwich panel with Aluminum Foam-Filled Tubular Cores (AFTC panel) under local impact are presented. The impact force and displacement response, failure mode, and energy absorption performance of the AFTC panel are discussed.

Chapter 5: Aiming to enhance the impact resistance of the traditional SCS sandwich panel, a flat steel plate-concrete-corrugated steel plate sandwich panel is proposed, and its impact response is experimentally and numerically studied.

Chapter 6: A new Stiffener-Enhanced Steel-Concrete-Steel (SESCS) sandwich structure is proposed for resisting impact load. Drop-weight impact tests and numerical simulations on the SESCS sandwich beams and panels are presented. Failure mode, impact force, and displacement response of the SESCS sandwich beams and panels are discussed. An analytical model is presented for predicting displacement response of the SESCS sandwich beam under impact load.

Chapter 7: Curved SCS sandwich shells under impact load are experimentally and numerically studied, and their failure modes, impact force, and displacement responses are discussed. The effects of concrete thickness, steel plate thickness, and spacing of shear connectors on the impact performances of curved SCS sandwich shells are examined. An analytical model is presented for predicting displacement response of the curved SCS sandwich shell under impact load.

Chapter 8: The performances of non-composite SCS sandwich panels under simulated blast load are experimentally and numerically studied. The simulated blast load is applied by utilizing an inflated airbag to transmit the impact force from the dropped hammer onto the SCS sandwich panel in the form of uniform pressure loading. The deformation modes, applied pressures, displacement, and strain responses of the SCS sandwich panels are discussed.

Chapter 9: Two approaches for predicting displacement response of the axially restrained SCS sandwich panel under blast loading are reported. The tensile membrane action of steel faceplates of the SCS sandwich panel is considered in the two models. The resistance–deflection function of the SCS sandwich panel is

obtained by utilizing the energy balance principle. The transient strain rate effects of steel and concrete are also incorporated into the two analytical models.

Chapter 10: The blast responses of curved SCS sandwich shells are numerically studied, and their failure modes under close- and far-field blast loading are examined. An analytical model is developed for predicting displacement response of the curved SCS sandwich shell under blast load, and its dimensionless Pressure–Impulse (P–I) diagram is presented. Finally, the procedures are presented for conducting blast-resistant design of the curved SCS sandwich shell via employing the dimensionless P–I diagram.

Chapter 11: A new Steel-Polyurethane Foam-Steel-Concrete-Steel (SPUFSCS) panel, which consists of “soft” and “stiff” layers, is proposed, and its impact behavior is experimentally, numerically, and analytically studied. The failure mode, impact force, and displacement responses are discussed, and the benefits of employing “soft” layer on enhancing the impact resistance are demonstrated. An analytical model is developed for predicting displacement response of the SPUFSCS panel under impact load.

Professors Shizhao Shen and Feng Fan are our guides through the research of protective structures against impact and blast loads. Our sincere appreciation is dedicated to them for their continuous supports, encouragements, and generous guidance. Special thanks also go to Prof. J. Y. Richard Liew at National University of Singapore, who was the supervisor of the first author. The present work is the result of a cooperative effect of our team. The authors would like to thank our colleagues and postgraduates, including Jingyi Lu, Chen Yan, Suntao Liu, Bowen Xue, and Wenjian Ying. The long-term support from National Natural Science Foundation of China is also greatly appreciated.

Harbin, China

Yonghui Wang  
Xudong Zhi  
Ximei Zhai  
Jiachuan Yan  
Rong Zhang

# Contents

<b>1</b>	<b>Aluminum Foam-Filled Energy Absorption Connectors Under Impact .....</b>	<b>1</b>
1.1	Introduction .....	1
1.2	Experimental Study .....	3
1.2.1	Design of Specimens .....	3
1.2.2	Test Setup and Instrumentation .....	3
1.2.3	General Observations .....	6
1.2.4	Energy Absorption Performances of Type I Connectors .....	10
1.2.5	Energy Absorption Performances of Type II Connectors .....	15
1.3	Numerical and Analytical Models .....	17
1.3.1	Numerical Model .....	17
1.3.2	Analytical Model for Type I Connector .....	19
1.3.3	Analytical Model for Type II Connector .....	28
1.3.4	Comparisons and Discussions .....	30
1.4	Blast Resistant Design Using Energy Absorption Connectors .....	32
1.5	Summary .....	34
	References .....	35
<b>2</b>	<b>Polyurethane Foam-Filled Energy Absorption Connectors Under Impact .....</b>	<b>39</b>
2.1	Introduction .....	39
2.2	Methodologies .....	41
2.2.1	Experimental Approach .....	41
2.2.2	Finite Element Models .....	44
2.3	Results and Discussions .....	46
2.3.1	FE Model Validation .....	46
2.3.2	Deformation Mode .....	49
2.3.3	Force–Displacement Responses .....	52

2.3.4	Energy Absorption Performance of Type III Connector .....	53
2.3.5	Energy Absorption Performance of Type IV Connector .....	56
2.4	Analytical Model .....	57
2.4.1	Analytical Model for Type III Connector .....	58
2.4.2	Analytical Model for Type IV Connector .....	62
2.5	Summary .....	71
	References .....	72
<b>3</b>	<b>Aluminum Foam-Filled Circular-Triangular Nested Tubes Under Impact .....</b>	<b>75</b>
3.1	Introduction .....	75
3.2	Methodologies .....	78
3.2.1	Experimental Methodology .....	78
3.2.2	Numerical Methodology .....	79
3.3	Results and Discussions .....	82
3.3.1	Energy Absorption Parameters .....	82
3.3.2	FE Model Validation .....	83
3.3.3	Deformation Mode .....	86
3.3.4	Force and Energy Absorption Responses .....	87
3.3.5	Energy Absorption Performance .....	89
3.3.6	Further FE Analysis .....	90
3.4	Summary .....	92
	References .....	93
<b>4</b>	<b>Sandwich Panel with Aluminum Foam-Filled Tubular Cores Under Impact .....</b>	<b>95</b>
4.1	Introduction .....	95
4.2	Methodologies .....	98
4.2.1	Experimental Methodology .....	98
4.2.2	Numerical Methodology .....	99
4.3	Results and Discussions .....	104
4.3.1	Failure Modes .....	104
4.3.2	Impact Force, Displacement and Energy Absorption Responses .....	108
4.3.3	Parametric Studies .....	111
4.4	Summary .....	116
	References .....	117
<b>5</b>	<b>Flat Steel-Concrete-Corrugated Steel Sandwich Panel Under Impact .....</b>	<b>119</b>
5.1	Introduction .....	119
5.2	Methodologies .....	121
5.2.1	Experimental Methodology .....	121
5.2.2	Numerical Methodology .....	123

5.3	Results and Discussions .....	128
5.3.1	FE Model Validation .....	128
5.3.2	Failure Mode .....	130
5.3.3	Impact Force and Displacement Responses .....	133
5.3.4	Internal Energy Response .....	136
5.3.5	FE Parametric Studies .....	137
5.4	Summary .....	140
	References .....	141
<b>6</b>	<b>Stiffener-Enhanced Steel-Concrete-Steel Sandwich Beam and Panel Under Impact .....</b>	<b>143</b>
6.1	Introduction .....	143
6.2	SESCS Sandwich Beam Under Impact .....	146
6.2.1	Experimental Study .....	146
6.2.2	Numerical Study .....	156
6.2.3	Analytical Study .....	163
6.3	SESCS Sandwich Panel Under Impact .....	171
6.3.1	Experimental Study .....	171
6.3.2	Numerical Study .....	181
6.4	Summary .....	187
	References .....	188
<b>7</b>	<b>Curved Steel-Concrete-Steel Sandwich Shells Under Impact .....</b>	<b>191</b>
7.1	Introduction .....	191
7.2	Test Program .....	192
7.2.1	Specimens .....	192
7.2.2	Materials .....	193
7.2.3	Test Setup .....	194
7.3	Test Results and Discussions .....	195
7.3.1	Damage Analysis of CSCS Shells .....	195
7.3.2	Impact Force History .....	202
7.3.3	Displacement History and Permanent Deformation .....	204
7.4	Numerical Modeling .....	205
7.4.1	FE Model Establishment .....	205
7.4.2	FE Results and Discussions .....	208
7.5	Analytical Model .....	209
7.5.1	Force-Displacement Relationship .....	209
7.5.2	Displacement Response .....	216
7.6	Summary .....	220
	References .....	220
<b>8</b>	<b>Steel-Concrete-Steel Sandwich Panel Under Simulated Blast Loading .....</b>	<b>223</b>
8.1	Introduction .....	223
8.2	Experimental Study .....	225
8.2.1	Design of Specimens .....	225

8.2.2	Test Setup and Instrumentation .....	227
8.2.3	Test Results and Discussions .....	229
8.3	Numerical Study .....	233
8.3.1	Material Models .....	234
8.3.2	Model Description .....	237
8.3.3	Numerical Results and Discussions .....	239
8.3.4	Further Numerical Simulations and Discussions .....	240
8.4	Summary .....	243
	References .....	244
<b>9</b>	<b>Analytical Models for Axially-Restrained Steel–Concrete–Steel Sandwich Panel Under Blast .....</b>	<b>247</b>
9.1	Introduction .....	247
9.2	FE Model Calibration .....	249
9.2.1	Blast Loading Test on SCS Sandwich Panels .....	249
9.2.2	FE Model Establishment .....	249
9.2.3	FE Model Validation .....	250
9.3	SDOF Model .....	253
9.3.1	Resistance–Deflection Function Contributed by Concrete Core .....	254
9.3.2	DIF for SDOF Model .....	260
9.3.3	Equation of Motion for SDOF System .....	263
9.4	Lagrange Equation Model .....	264
9.4.1	Equation of Motion .....	264
9.4.2	DIF for Lagrange Equation Model .....	265
9.5	Results and Discussions .....	266
9.6	Summary .....	270
	References .....	270
<b>10</b>	<b>Curved Steel–Concrete–Steel Sandwich Shell Under Blast .....</b>	<b>273</b>
10.1	Introduction .....	273
10.2	FE Model Establishment and Verification .....	275
10.2.1	FE Model of Curved SCS Sandwich Shell .....	275
10.2.2	FE Model Verification .....	277
10.3	Curved SCS Sandwich Shell Without Shear Connectors .....	279
10.4	Curved SCS Sandwich Shell with Shear Connectors .....	279
10.4.1	Influence of Shear Connectors .....	282
10.4.2	Influence of Blast Loading .....	284
10.4.3	Influence of Rise Height .....	287
10.4.4	Influence of Rear to Front Plate Thickness Ratio .....	288
10.5	SDOF Model for Curved SCS Sandwich Shell .....	289
10.5.1	Deflection Shape Function .....	289
10.5.2	Strain–Displacement Relationship .....	292
10.5.3	Equation of Motion .....	296
10.6	P–I Diagram for Curved SCS Sandwich Shell .....	298
10.6.1	Internal Energy–Displacement Relationship .....	299

10.6.2	Dimensionless Pressure and Impulse .....	300
10.6.3	Dimensionless P-I Diagram Establishment .....	301
10.7	Blast Resistant Design Approach .....	302
10.8	Summary .....	304
	References .....	304
<b>11</b>	<b>Steel-PU Foam-Steel–Concrete-Steel Panel Under Impact .....</b>	<b>307</b>
11.1	Introduction .....	307
11.2	SPUFSCS Panel Under the Impact of a Hemispherical Hammer .....	308
11.2.1	Experimental Study .....	308
11.2.2	Numerical Study .....	322
11.3	SPUFSCS Panel Under the Impact of a Cylindrical Hammer .....	335
11.3.1	Experimental Study .....	335
11.3.2	Numerical Study .....	339
11.3.3	Analytical Study .....	345
11.4	Summary .....	356
	References .....	357

# Chapter 1

## Aluminum Foam-Filled Energy Absorption Connectors Under Impact



### 1.1 Introduction

In recent decades, lightweight structures (e.g., thin-walled or foam-filled structures) have been increasingly used as energy absorbers to protect structures from extreme loading, such as blast and impact. Lightweight energy absorbers have been successfully applied in aerospace, military, automotive engineering, civil structures, and other industries (Alghamdi 2001; Lu and Yu 2003). As shown in Fig. 1.1a, an energy absorber can be used to attach guardrails to bollards for dissipating impact energy during automobile accidents. Additionally, a lightweight energy absorber can be utilized as the energy absorption connector (Fig. 1.1b) to connect the blast resistant façade/wall and building to dissipate the blast energy. Aluminum foam is known to exhibit high energy absorption, and therefore it can be inserted into thin-walled structures to enhance their energy absorption performances. In this chapter, two types of novel aluminum foam-filled energy absorption connectors (Fig. 1.1b) were developed, and the energy absorption can be realized via compression of aluminum foam and plastic deformation of curved/pleated plates.

Owing to the advantages of easy fabrication and low cost, the metallic material was usually employed for fabricating energy absorbers which were designed to dissipate energy via plastic deformation, splitting of steel plate, friction and free inversion of circular tubes (Baroutaji et al. 2017). As the energy absorbers generally experienced dynamic crushing load when they were used for impact and blast load mitigation, extensively works have been done to study the dynamic crushing responses of the metallic energy absorbers, and the inertia and strain rate effect generally led to higher energy absorption performance as compared to the quasi-static loading case (Su et al. 1995a, b). Baroutaji et al. (2016) studied the response of the nested system under low-velocity impact loading, and its behavior was similar to that under quasi-static loading owing to the insignificant strain rate and inertia effect. However, the numerical results demonstrated that increasing impact velocity could lead to higher energy absorption capacity of the nested system. In addition, the optimized design of nested tubes under lateral impact loading was conducted by

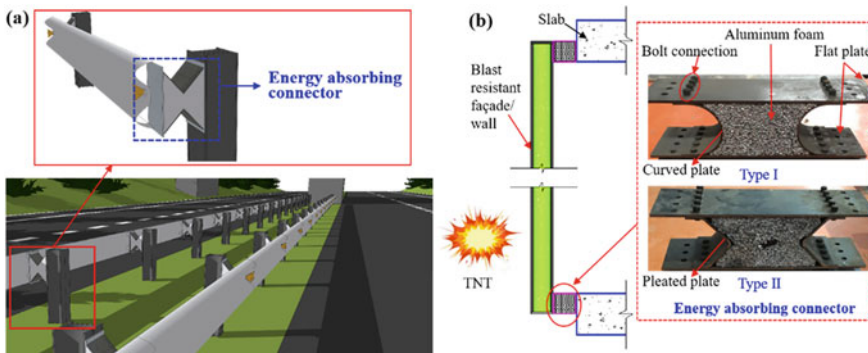


**Fig. 1.1** Applications of energy absorption connector in: **a** Guardrail; **b** Blast resistant façade/wall

Olabi et al. (2008a, b), and the optimized energy absorbers exhibited more desirable force–deflection responses than their standard counterparts.

Recently, metallic foams have been increasingly employed for energy absorbers owing to its lightweight and high energy absorption performance, thus attracting a considerable amount of interest. It was demonstrated that the energy absorption performance could be improved when filling the tubes with metallic foams (Reyes et al. 2004a, b; Hall et al. 2002; Shen et al. 2015). As compared to the crushing behaviors of the metal foam-filled columns/tubes under axial and oblique loading (Santosa et al. 2000; Reyes et al. 2004a, b), their behaviors under lateral crushing loading (Hall et al. 2002; Shen et al. 2015; Baroutaji et al. 2015) were more desirable in terms of fewer fluctuations of load and lower amplitude of peak load (Shen et al. 2015). As the energy absorbers underwent dynamic loading in most cases, the dynamic crushing behaviors of the metallic foam-filled energy absorbers were also extensively studied (Shahbeyk et al. 2007; Smith et al. 2016). The dynamic lateral crushing behaviors of sandwich circular tubes were investigated by Fan et al. (2013), and the energy absorption capacity over its quasi-static counterpart and the deformation profile showed some differences, which could be attributed to the inertia effect under dynamic loading. The responses of foam-filled conical tubes under axial impact loading were numerically investigated by Ahmad and Thambiratnam (2009), and the foam filler was found to be able to stabilize the crushing process and improve the energy absorption capacity. Kilicaslan (2015) studied the dynamic crushing responses of aluminum foam-filled corrugated single- and double-tubes. It was also noted that the tubes with corrugations experienced progressive and concertina type of deformation, and tubes with smaller corrugation length was more desirable in terms of smooth force–displacement curve and low initial peak load.

In this chapter, the dynamic crushing responses of the proposed aluminum foam-filled energy absorption connectors were experimentally studied. In addition, the effects of loading rate, aluminum foam filler and geometrical parameters of curved/pleated plates on the energy absorption performances of the connectors were also quantitatively evaluated. The numerical studies on the tested connectors were

also conducted by employing the explicit code in LS-DYNA. The analytical models considering the strain rate effect of mild steel were developed to predict the force–displacement responses of the aluminum foam-filled energy absorption connectors under impact loading.

## 1.2 Experimental Study

The drop-weight impact tests on the proposed aluminum foam-filled energy absorption connectors were conducted to obtain their deformation modes, force–displacement responses and energy absorption performances. In addition, four of the connectors were tested under quasi-static loading to reveal the effect of loading rate on their responses. The test specimens, setup and results are presented in the following sections.

### 1.2.1 Design of Specimens

There are two types of aluminum foam-filled energy absorption connectors being fabricated, i.e., one is with curved plates (Type I in Fig. 1.2a) and the other is with pleated plates (Type II in Fig. 1.2b). The energy absorption connectors were fabricated from mild steel as face plates and closed cell aluminum foam as core material. As shown in Fig. 1.2, two curved plates (for type I connectors) or pleated plates (for type II connectors) were connected to two flat plates on the top and bottom through bolts (M12 bolt with grade of 6.8) in order to form a four-side confined space where the aluminum foam could be subsequently filled in. There are totally 16 energy absorption connectors being fabricated for the tests with eight type I connectors and eight type II connectors. The detailed geometries of the specimens are given in Fig. 1.3 and summarized in Table 1.1. The studied parameters for type I connectors include loading rate, aluminum foam filler, curved plate thickness and radius. With regard to type II connectors, the effects of loading rate, aluminum foam filler, pleated plate thickness and angle  $\theta_0$  on their energy absorption performances were experimentally investigated. The material properties of mild steel and aluminum foam were obtained from uniaxial tensile coupon tests and uniaxial compression loading tests, respectively, and are given in Table 1.2.

### 1.2.2 Test Setup and Instrumentation

An instrumented drop-weight impact test machine was employed to apply the impact loading on the connectors. The photographs of the test setup are given in Fig. 1.4. The connector was inserted between a hammer and a piezoelectric force transducer,

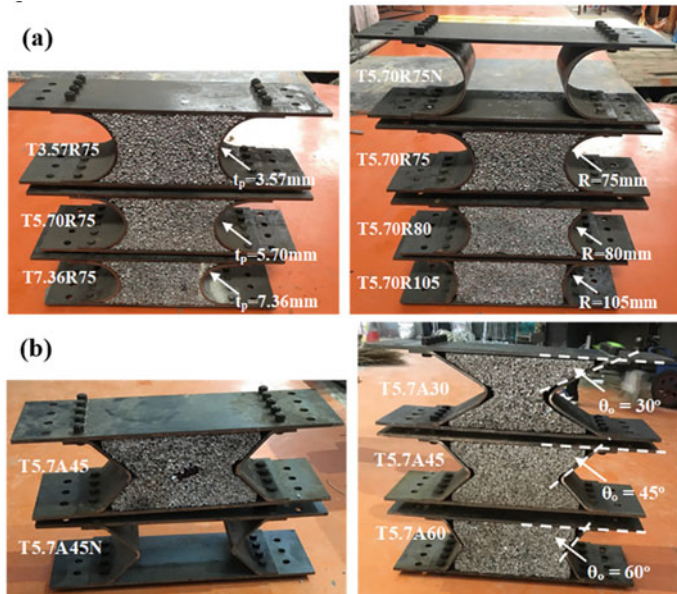


**Fig. 1.2** Photos of energy absorption connectors: **a** type I connector and **b** type II connector ( $t_p$ —plate thickness,  $R$ -curved plate radius), reprinted from Wang et al. (2018a, b), copyright 2022, with permission from Elsevier

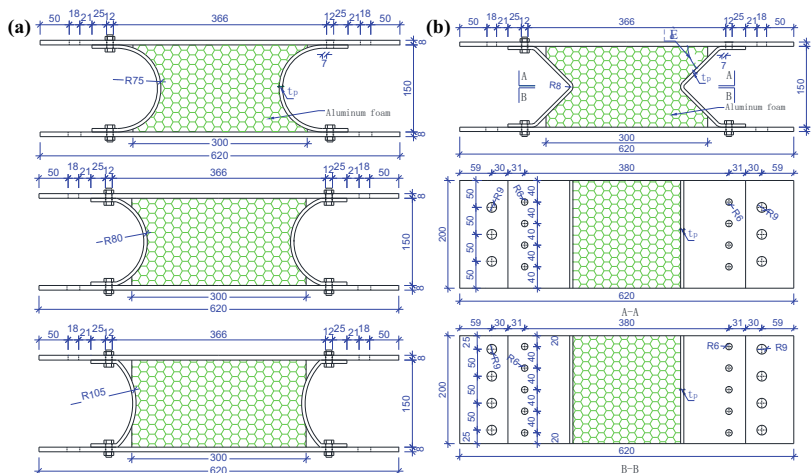


**Fig. 1.3** Dimensions of the energy absorption connectors (unit: mm): **a** type I connector and **b** type II connector, reprinted from Wang et al. (2018a, b), copyright 2022, with permission from Elsevier

**Table 1.1** Geometry of the energy absorption connectors

Type I connector	$R$ (mm)	$t_p$ (mm)	Aluminum Foam	$H_d$ (m)
T3.57R75	75	3.57	Yes	6.17
T5.70R75*	75	5.70	Yes	7.35
T5.70R75N*	75	5.70	No	4.23
T7.36R75	75	7.36	Yes	8.62
T5.70R80	80	5.70	Yes	7.97
T5.70R105	105	5.70	Yes	8.62
Type II connector	$\theta_o$ ( $^{\circ}$ )	$t_p$ (mm)	Aluminum Foam	$H_d$ (m)
T3.57A45	45	3.57	Yes	6.17
T5.70A45	45	5.70	Yes	7.35
T5.70A45N*	45	5.70	No	2.50
T7.36A45*	45	7.36	Yes	8.62
T5.70A30	30	5.70	Yes	5.63
T5.70A60	60	5.70	Yes	8.62

Note  $R$ —Curved plate radius;  $t_p$ —Curved/pleated plate thickness;  $\theta_o$ —Angle between flat plate and pleated plate;  $H_d$ —Drop height in the impact loading test. The specimens with star indicate that two same specimens were fabricated, with one for impact loading test and the other for quasi-static loading test

**Table 1.2** Material properties of mild steel and aluminum foam

Mild steel	$E_y$ (GPa)	$\sigma_y$ (MPa)	$\sigma_u$ (MPa)
$t_p = 3.57$ mm	200	333.5	562.3
$t_p = 5.70$ mm	200	275.6	528.3
$t_p = 7.36$ mm	200	289.7	538.3
Aluminum foam	$\rho_f$ (g/cm <sup>3</sup> )	$\sigma_p$ (MPa)	$E_f$ (MPa)
—	0.235	0.81	114.0

Note  $E_y$ ,  $E_f$ —Young's modulus of steel and aluminum foam;  $\sigma_y$ ,  $\sigma_u$ —Yield and ultimate stress of mild steel;  $\rho_f$ ,  $\sigma_p$ —Density and Plateau stress of aluminum foam

and they were subsequently supported on a rigid base. A cylindrical hammer with the diameter of 200 mm was used. Two 20-mm-thick steel plates were bolted to the connector on the top and bottom plates, respectively, to impede the bending deformation of these two flat plates during the test. Before the test, the hammer was raised to the predetermined drop height using a hydraulic controlled mechanical hosting system. As the maximum impact force that can be measured by the piezoelectric force transducer is 600 kN, the trail numerical analysis was conducted to determine the drop height of each connector (in Table 1.1) by ensuring the maximum impact force slightly below 600 kN. Once the electromagnet release mechanism is manually triggered, the hammer with the weight of 400 kg can slide freely along the vertical guide rails towards the specimen below it. The piezoelectric force transducer was installed

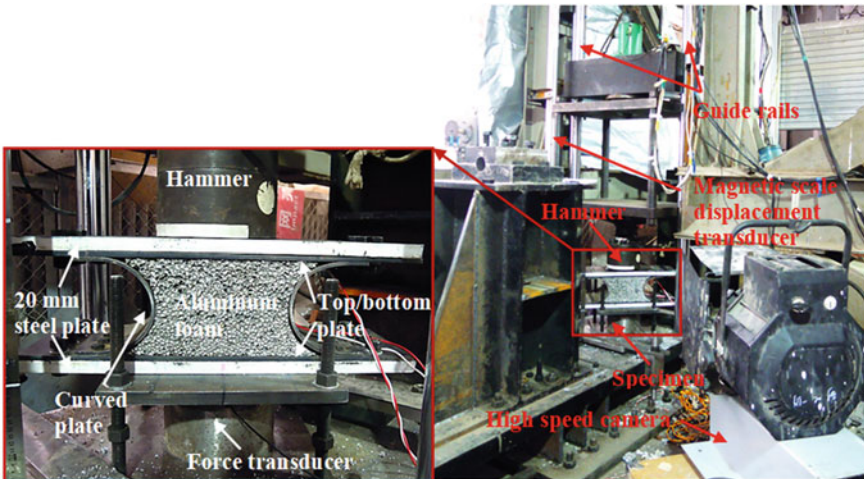


**Fig. 1.4** Drop-weight impact test setup and instrumentation, reprinted from Wang et al. (2018b), copyright 2022, with permission from Elsevier

at the bottom of connector to measure the pure crushing force excluding inertial force. Displacement of the hammer was measured by a magnetic scale displacement transducer with an accuracy of 0.05 mm. The magnetic sensor was mounted on one of the vertical guide rail, and its associated scales were mounted on the hammer to measure the crushing displacement of the connector. A high-speed camera was used to monitor the entire deformation process at a speed of 2000 frames per second.

The quasi-static loading tests were conducted using a material testing machine (MTS) with the loading capacity of 2500 kN. Figure 1.5 shows the test setup and instrumentation. The connector was inserted between the actuator and a fixed support. The force was applied by moving the actuator downwards with a speed of 2 mm/min to ensure a quasi-static loading rate. The same to the drop-weight impact tests, two 20-mm-thick steel plates were also bolted to the connector on the two flat plates. The crushing displacement and compressive force of the connector were measured by two Linear Variable Displacement Transducers (LVDTs) and a load cell, respectively. The readings from LVDTs and load cell were recorded using a data logger.

### 1.2.3 General Observations

The typical collapse processes of the type I connector (T5.70R75) under impact and quasi-static loading are presented in Fig. 1.6. The similar collapse process can be observed for the connector under both impact and quasi-static loading, i.e., the connector generally exhibits symmetric deformation about the middle horizontal plane. The observed similar collapse mode of the connector under both impact and

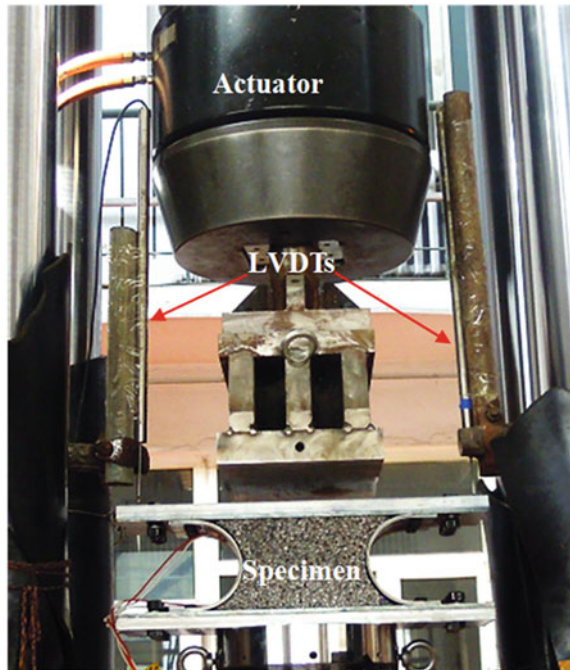


**Fig. 1.5** Quasi-static loading test setup and instrumentation, reprinted from Wang et al. (2018b), copyright 2022, with permission from Elsevier

quasi-static loading can be attributed to relatively low-impact velocity in the tests, i.e., the maximum impact velocity is around 13 m/s. The similar deformation mode of sandwich circular tubes under quasi-static and dynamic (crushing velocity = 10 m/s) loading was also observed by Fan et al. (2013). However, non-symmetric deformation pattern about the horizontal plane with the collapse initiating at the top was observed from FE analysis when the sandwich tubes were loaded with higher crushing velocity (>20 m/s). Hence, there was a critical crushing velocity to cause deformation mode change and energy absorption improvement of sandwich tubes (Fan et al. 2013). The similar observation was also noted by Baroutaji et al. (2016) via studying the internally nested tubes subjected to impact loading. The collapse processes in Fig. 1.6 indicate that both the compression of aluminum foam and plastic deformation of curved plates (via plastic hinge rotation and flattening of curved plates) contribute to the energy absorption. The permanent deformation of connector T5.70R75 after impact loading is given in Fig. 1.6c, which shows that two plastic hinges are formed at the middle plane and the original curved plates with radius of  $R$  gradually changes to flattened plates. As for the connector under impact loading, the flying debris of aluminum foam can be observed at the two surfaces (front and rear surfaces) without lateral confinement when crushing displacement exceeds 20 mm. The flying debris is found to initiate from the top where the connector experiences direct impact loading

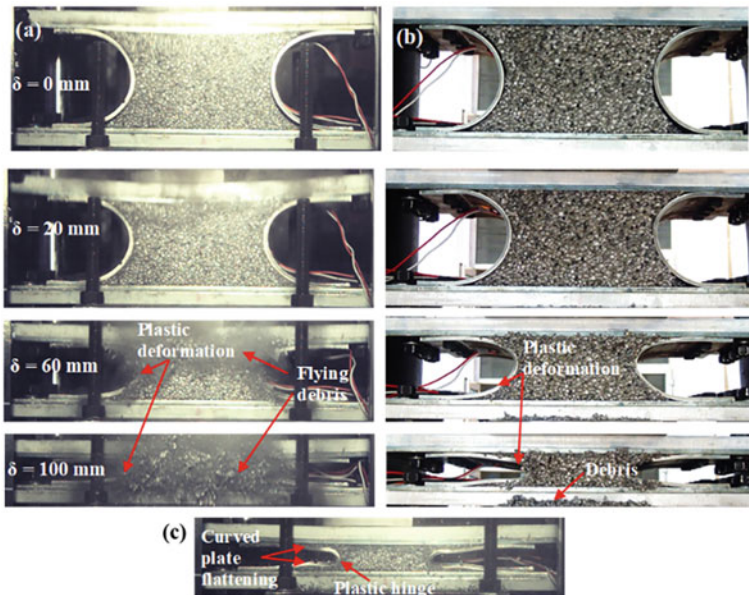


**Fig. 1.6** Typical collapse processes of the typical I connector: **a** impact loading, **b** static loading and **c** permanent deformation, reprinted from Wang et al. (2018b), copyright 2022, with permission from Elsevier

and gradually propagates to the bottom. Similarly, the debris was observed for the connector under quasi-static loading at the front and rear surfaces. However, the separation portion of aluminum foam as debris is not significant and only observed at front and rear surfaces, as shown in Fig. 1.6c. In the whole test, no fracture failure of curved plates was observed for all the tested connectors, which demonstrates that the curved plates can effectively absorb energy and provide confinements to aluminum foam.

The collapse processes of all the type II connectors are found to be similar under both impact and quasi-static loading. Hence, only the collapse processes of connector T5.70A45 and T5.70A45N, which can represent the typical collapse processes of the type II connectors with and without aluminum foam, are presented in Fig. 1.7. As illustrated in Fig. 1.7a, the type II connector without aluminum foam mainly relies on plastic hinge rotation of pleated plates to absorb energy. As for the type II connector with aluminum foam filler in Fig. 1.7b, both plastic deformation of pleated plates and compression of aluminum foam contribute to the energy absorption. In addition, the flying debris was also observed at the two surfaces of aluminum foam without lateral confinement during impact test, which is similar to the type I connectors.

Figure 1.8 presents the force–displacement curves of all the tested connectors. Relatively smoother force–displacement curves can be observed for the connectors under quasi-static loading, as shown in Fig. 1.8a, c. In terms of the connectors under impact loading, the force shows evident peak value at the beginning and followed by

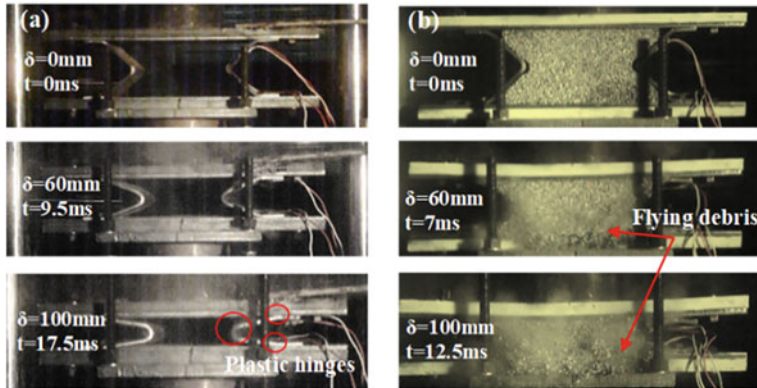


**Fig. 1.7** Typical collapse processes of the type II connector under impact loading: **a** without aluminum foam and **b** with aluminum foam, reprinted from Wang et al. (2018a), copyright 2022, with permission from Elsevier

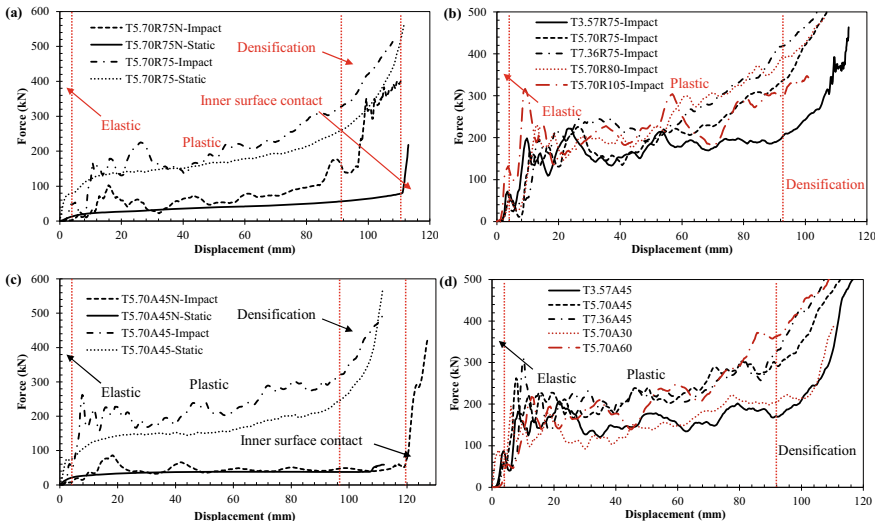


**Fig. 1.8** Force–displacement curves of energy absorption connectors: effects of **a** aluminum foam and loading rate and **b** curved plate thickness and radius for type I connectors; effects of **c** aluminum foam and loading rate and **d** pleated plate thickness and angle  $\theta_0$  for type II connectors, reprinted from Wang et al. (2018a, b), copyright 2022, with permission from Elsevier

a sudden drop as displacement increases. Then, the force shows continual fluctuation with further dynamic crushing. The fluctuation of the force in the dynamic loading case is mainly due to the inertial force that cannot be completely removed from the drop-weight impact tests. It is noted in Fig. 1.8a, c that the forces of the connectors under impact loading are higher as compared to those under quasi-static loading,

which is mainly due to the strain rate effect of mild steel. The aluminum foam filler is shown to significantly increase the forces of the connectors under both impact and quasi-static loading, as shown in Fig. 1.8a, c. Figure 1.8b shows that both increasing curved plate thickness and radius generally results in higher force and energy absorption capacity. With regard to type II connectors, Fig. 1.8d shows that both increasing pleated plate thickness and angle  $\theta_0$  generally leads to higher force and energy absorption capacity. The quantitative evaluations on the effects of loading rate, aluminum foam filler, curved plate thickness and radius as well as pleated plate thickness and angle  $\theta_0$  on the energy absorption performances of the proposed connectors are discussed in the following sections. The deformation processes of the tested connectors in Fig. 1.8 exhibit three stages, i.e., elastic deformation, plastic deformation and inner surface contact (for the connectors without aluminum foam) (Shen et al. 2015) or aluminum foam densification (for the aluminum foam filled connectors). However, the boundaries between elastic and plastic deformation stages are not clear for the connectors under impact loading. The crushing displacement in the plastic deformation stage is considerably larger than another two deformation stages and the force also shows insignificant variation in this stage, both of which are desirable for an energy absorber. After the densification of aluminum foam or contact of inner surfaces of curved/pleated plates, the force shows sudden increase and the connector reaches its ultimate energy absorption capacity.

#### 1.2.4 Energy Absorption Performances of Type I Connectors

The quantitative evaluations on the energy absorption performances of the tested connectors can be realized via comparing the following parameters, including mean crushing force (*MCF*), densification displacement ( $x_D$ ), energy absorption (*EA*), specific energy absorption (*SEA*) and crushing force efficiency (*CFE*). All the aforementioned energy absorption parameters can be calculated based on crushing force–displacement curve of the energy absorber. *EA* is given as

$$EA = \int_0^\delta F(x)dx \quad (1.1)$$

where  $F(x)$  and  $\delta$  are crushing force and displacement, respectively. *SEA* is energy absorption per unit mass and given as

$$SEA = EA/m \quad (1.2)$$

where  $m$  is total mass of aluminum foam and curved/pleated plates that contribute to the energy absorption. *CFE*, which can represent the fluctuation magnitude of crushing force–displacement curve, is defined as the ratio of *MCF* to peak crushing force (*PCF*)

$$CFE = MCF/PCF \quad (1.3)$$

where  $PCF$  is the maximum crushing force with displacement ranging from 0 to  $\delta$ , and  $MCF$  is calculated as

$$MCF = EA(\delta)/\delta \quad (1.4)$$

It is noted from Eqs. (1.1)–(1.4) that the values of  $EA$ ,  $SEA$ ,  $CFE$ , and  $MCF$  strongly depend on the value of  $\delta$ , and densification displacement is generally employed for determining these energy absorption parameters for an energy absorber. As the force–displacement curves of the tested energy absorption connectors are similar to the compressive stress–strain curve of aluminum foam in shape, the method used to determine onset strain of aluminum foam densification was adopted and modified to determine densification displacement of the connector. There were several methods for determining the onset strain of densification, i.e., the intersection of the tangents to the stress plateau regime and the densification regime (Nieh et al. 2000; Paul and Ramamurty 2000), the strain at the last local minimum before the stress rises steeply (Vural and Ravichandran 2003), the strain at which the slope of the tangent is equal to that of the elastic regime (Chan and Xie 2003). To bring down the uncertainties in abovementioned methods, an energy efficiency-based approach was proposed by Li et al. (2006) to determine the onset strain of densification. In this study, a new approach to determine the densification displacement of the connector is proposed considering both the maximization of energy absorption efficiency and peak crushing force. By replacing the stress and strain with force and displacement, the energy absorption efficiency of the connector can be defined as

$$\eta(x) = \frac{1}{F(x)H} \int_{x_y}^x F(x)dx \quad (1.5)$$

where  $F(x)$  is crushing force,  $H$  is height of aluminum foam and  $x_y$  is displacement at yield. The densification displacement,  $x_D'$ , can be determined as follows: (a) determining the displacement,  $x_D'$ , corresponding to the stationary point at the energy absorption efficiency–displacement curve where the efficiency reaches a maximum value, i.e.,

$$\left. \frac{d\eta(x)}{dx} \right|_{x=x_D'} = 0 \quad (1.6)$$

and (b) finding the maximum force,  $F_{max}$ , within the displacement from 0 to  $x_D'$ . Then, the densification displacement,  $x_D$ , is determined as the displacement corresponding to the first maximum force,  $F_{max}$ , after  $x_D'$ . Figure 1.9 illustrates the determination of densification displacement of the connector based on a given force–displacement curve. The calculated energy absorption parameters of the tested connectors under

**Fig. 1.9** Determination of densification displacement, reprinted from Wang et al. (2018b), copyright 2022, with permission from Elsevier

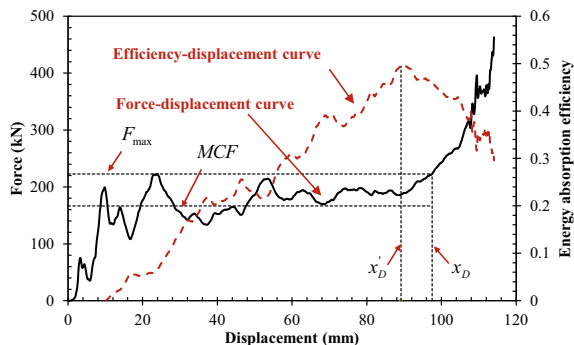


**Table 1.3** Energy absorption parameters of type I connectors under impact loading

Specimen	$x_D$ (mm)	MCF (kN)	EA (kJ)	SEA (kJ/kg)	CFE (%)
T3.57R75	97.5	166.4	16.2	3.16	74.7
T5.70R75	94.2	194.2	18.3	2.60	56.6
T5.70R75N	96.9	69.6	6.7	1.24	39.3
T7.36R75	103.2	252.0	26.0	2.98	51.3
T5.70R80	99.7	237.8	23.7	3.53	56.3
T5.70R105	99.7	224.1	22.3	3.47	66.6

Note  $x_D$ —Densification displacement; MCF—Mean crushing force, EA—Energy absorption, SEA—specific energy absorption, CFE—Crushing force efficiency

impact loading are given in Table 1.3, and the effects of loading rate, aluminum foam filler, curved plate thickness and radius on the energy absorption performances of type I connectors are presented in Fig. 1.10.

Figure 1.10a shows the effect of loading rate on the energy absorption performances of connector T5.70R75N (without aluminum foam) and T5.70R75 (with aluminum foam). It should be mentioned that the densification displacement of T5.70R75N under both static and impact loading in Fig. 1.10a is determined as the minimum value of the calculated densification displacements of T5.70R75N under static and impact loading, as the premature contact between top and bottom bolts were observed before the contact of inner surfaces of curved plates, which leads to smaller densification displacement. Comparing the connector T5.70R75N and T5.70R75 under quasi-static and impact loading reveals that higher loading rate (impact loading) can lead to higher energy absorption performance, i.e., the MCF and EA (or SEA) of connector T5.70R75N under impact loading are increased by 85.1% and 85.2%, respectively, as compared to those under static loading, and the corresponding increases for the connector T5.70R75 are 18.0% and 20.4%. More significant improvement in energy absorption performance of the type I connector without aluminum foam indicates that the strain rate effect of mild steel is the main

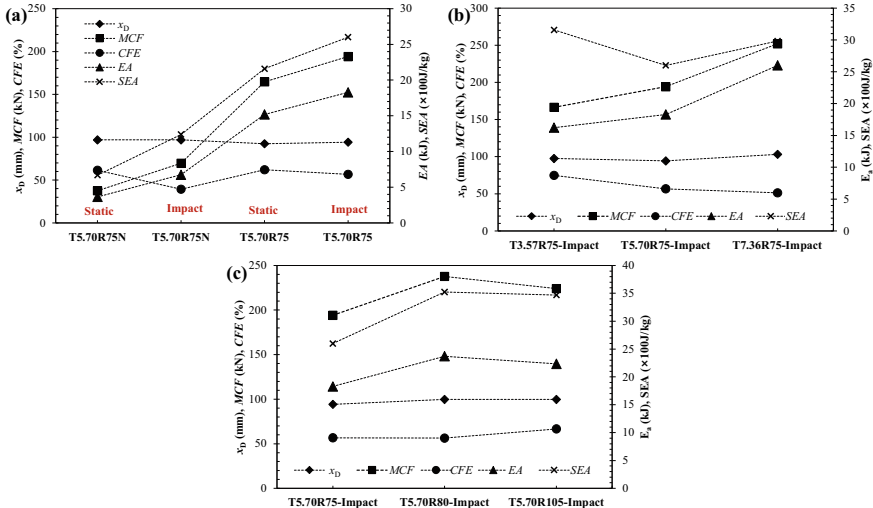


**Fig. 1.10** Comparison of energy absorption performances for type I connectors: effects of **a** loading rate and aluminum foam, **b** curved plate thickness and **c** radius, reprinted from Wang et al. (2018b), copyright 2022, with permission from Elsevier

contributor to the energy absorption improvement considering the consistent deformation mode of the connectors under both quasi-static and impact loading. It is also noted that the increased values of *MCF* for connector T5.70R75N and T5.70R75 under impact loading are similar. This also demonstrates the main contributor from strain rate effect of mild steel to the observed energy absorption improvement. The inertia effect can only induces fluctuation of the force–displacement curve under impact loading, but shows little effect on the *MCF* and *EA* owing to the relatively low-velocity impact loading. However, Fan et al. (2013) and Baroutaji et al. (2016) found that the inertia effect can lead to deformation mode change and improvement of *MCF* and *EA* when the impact velocity exceeds certain value. In terms of *CFE*, loading rate shows little effect on the connector T5.70R75 with aluminum foam. However, higher loading rate leads to 36.0% reduction of *CFE* for the connector T5.70R75N without aluminum foam.

The effect of aluminum foam filler on the energy absorption performances of type I connectors under both quasi-static and impact loading is also presented in Fig. 1.10a, which shows that the energy absorption performance can be significantly improved by filling the connector with aluminum foam. The *MCF*, *EA* and *SEA* of connector T5.70R75 under quasi-static loading are increased by 338.0%, 317.3% and 223.0%, respectively, as compared to connector T5.70R75N, and the corresponding increases of 179.2%, 171.4% and 110.0% are observed for the impact loading case. Both the plastic deformation of curved plates and compression of aluminum foam of connector T5.70R75 contribute to the energy absorption as compared to the connector T5.70R75N with only plastic deformation of curved plates to absorb energy. This leads to improved *EA* of the connector with aluminum foam. The less significant

improvement in the energy absorption performance of the connector under impact loading can be explained by the aforementioned finding that the strain rate effect of mild steel is the main contributor to the energy absorption improvement. However, the aluminum foam filler can still evidently improve the values of *EA* and *SEA* for the type I connector under impact loading. The increase of *SEA* by filling the connector with aluminum foam indicates that the energy absorption per unit mass of aluminum foam is higher as compared to curved plates. In terms of *CFE*, it is nearly unaffected by the aluminum foam filler for the quasi-static loading case, whereas 44.0% increase in *CFE* is observed for the impact loading case. This is because the aluminum foam filler can increase the crushing force, and thus reducing the fluctuation magnitude of crushing force (Fig. 1.8a), which results in higher *CFE*.

Figure 1.10b shows the effect of curved plate thickness on the energy absorption performances of type I connectors. Increasing curved plate thickness can lead to an increase in *MCF* and *EA*, i.e., they are increased by 16.7% and 12.8%, respectively, via increasing curved plate thickness from 3.57 mm to 5.70 mm, and further increasing curved plate thickness from 5.70 mm to 7.36 mm leads to 29.8% and 42.2% increase of *MCF* and *EA*. Thicker curved plate means higher plastic bending moment, and therefore leads to higher *MCF* and *EA*. As for *SEA*, it shows initial decrease and subsequent increase with the increase of curved plate thickness. This observation is owing to the fact that the calculated *SEA* is closely related to the densification displacement and clearly different densification displacements are observed for the connectors with curved plate thicknesses of 5.70 and 7.36 mm, i.e., the densification displacements of T5.70R75 and T7.36R75 are 94.2 and 103.2 mm. If the densification displacement of connector T7.36R75 is assumed to be same with that of connector T5.70R75, i.e.,  $x_D = 94.2$  mm, the *SEA* is decreased by 3.4% when increasing curved plate thickness from 5.70 mm to 7.36 mm. From above discussions, the *SEA* is believed to be decreasing with increasing curved plate thickness, as the energy absorption per unit mass of the curved plate is lower as compared to aluminum foam. In summary, increasing curved plate thickness generally leads to the increase in *MCF* and *EA*, but decrease in *SEA*. As for the *CFE*, it shows monotonic decrease with the increase of curved plate thickness.

Figure 1.10c shows the effect of curved plate radius on the energy absorption performances of type I connectors. The *MCF*, *EA* and *SEA* are increased by 22.5%, 29.7% and 35.6%, respectively, via increasing the curved plate radius from 75 to 80 mm. This may be owing to the increased volume of aluminum foam by increasing curved plate radius. However, further increasing curved plate radius shows little effect on the *MCF*, *EA* and *SEA* because the variation of curved plate radius from 80 to 105 mm results in a negligible increase in volume of aluminum foam. As for the densification displacement and *CFE*, they are nearly unaffected by the variance of curved plate radius.

### 1.2.5 Energy Absorption Performances of Type II Connectors

In order to evaluate the energy absorption performances of the type II connectors, the energy absorption parameters (i.e.,  $MCF$ ,  $x_D$ ,  $EA$  and  $CFE$ ) were calculated based on equations presented in Sect. 1.2.3. The calculated energy absorption parameters of type II connectors under impact loading are given in Table 1.4, and the effects of loading rate, aluminum foam filler, pleated plate thickness and angle  $\theta_o$  on the energy absorption performances of type II connectors are presented in Fig. 1.11 and discussed in the followings.

Figure 1.11a shows the effect of loading rate on the energy absorption performances of connector T5.70A45N (without aluminum foam) and T5.70A45 (with

**Table 1.4** Energy absorption parameters of type II connectors under impact loading

Specimen	$x_D$ (mm)	$MCF$ (kN)	$EA$ (kJ)	$CFE$ (%)
T5.70A30	102.82	155.14	15.95	69.59
T3.57A45	99.72	155.7	15.53	74.84
T5.70A45N	120.26	43.69	5.25	50.38
T5.70A45	92.63	214.68	19.89	70.86
T7.36A45	90.85	209.71	19.05	65.77
T5.70 A60	93.54	206.28	19.3	55.23

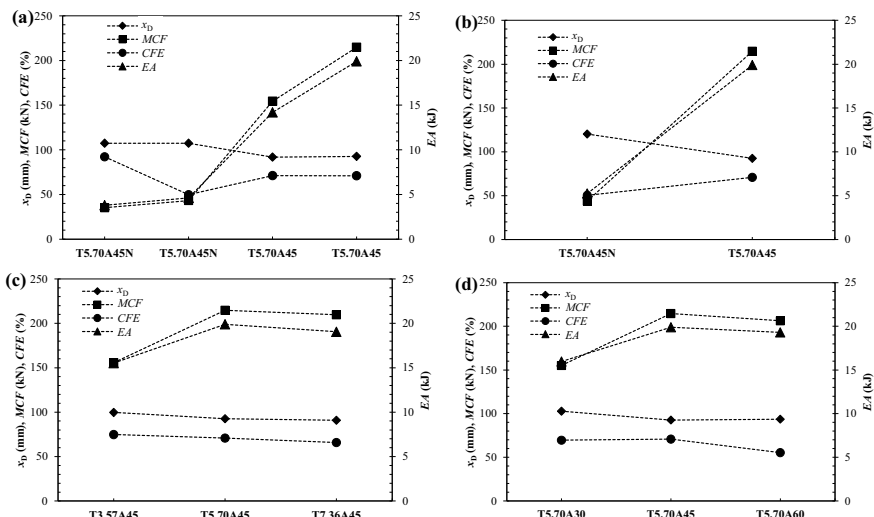


**Fig. 1.11** Comparison of energy absorption performances for type II connectors: effects of **a** loading rate, **b** aluminum foam, **c** pleated plate thickness and **d** angle  $\theta_o$ , reprinted from Wang et al. (2018a), copyright 2022, with permission from Elsevier

aluminum foam). Owing to strain rate effect, both the two connectors exhibit improved energy absorption performance under impact loading, i.e., the *MCF* and *EA* of connector T5.70A45N under impact loading are increased by 22.6% and 22.2%, respectively, as compared to those under static loading, and the corresponding increases for the connector T5.70A45 are 39.0% and 40.3%. As for the *CFE*, the loading rate shows little effect on the connector T5.70A45 with aluminum foam. However, higher loading rate results in 46.0% reduction of *CFE* for the connector T5.70A45N without aluminum foam. The densification displacement of the connector T5.70A45 is nearly unaffected by the loading rate owing to the similar deformation modes of the connectors under both quasi-static and impact loading.

Figure 1.11b exhibits the effect of aluminum foam filler on the energy absorption performances of type II connectors under impact loading, and significant improvement of energy absorption performance can be observed when filling the connector with aluminum foam. The *MCF* and *EA* of connector T5.70A45 are increased by 391.4% and 278.9%, respectively, as compared to connector T5.70A45N. The increase in *EA* is less significant as compared to *MCF*, which can be attributed to 23.0% reduction of densification displacement by filling the connector with aluminum foam. This is because the densification displacement of connector T5.70A45 is governed by the aluminum foam densification which occurs earlier than the inner surface contact observed for the connector T5.70A45N. In terms of *CFE*, it shows 40.7% increase by filling the connector with aluminum foam.

The effect of pleated plate thickness on the energy absorption performances of type II connectors is illustrated in Fig. 1.11c. The densification displacement and *CFE* only show slight variation by increasing the pleated plate thickness from 3.57 mm to 7.36 mm, i.e., the densification displacement and *CFE* for the three connectors are in the range of 90.9–99.7 mm and 65.8%–74.8%, respectively. However, the *MCF* and *EA* are increased by 37.9% and 28.1%, respectively, via increasing the pleated plate thickness from 3.57 mm to 5.70 mm. Further increasing pleated plate thickness from 5.70 mm to 7.36 mm results in slight decrease of *MCF* and *EA*. This counterintuitive observation may be attributed to inconsistent strengths of pleated plate and aluminum foam as well as different densification displacements for the two connectors.

Figure 1.11d shows the effect of angle  $\theta_o$  on the energy absorption performances of type II connectors, and improved energy absorption performances can be observed by increasing angle  $\theta_o$  from  $30^\circ$  to  $45^\circ$ , i.e., the *MCF* and *EA* are increased by 38.4% and 24.7%, respectively. Similar to the effect of pleated plate thickness, further increasing angle  $\theta_o$  from  $45^\circ$  to  $60^\circ$  leads to slight decrease of *MCF* and *EA*, which may be caused by inconsistent material strengths. Figure 1.11d shows that the variation of densification displacement is negligible by varying the angle  $\theta_o$ . As for the *CFE*, it is reduced by 22.1% by increasing angle  $\theta_o$  from  $45^\circ$  to  $60^\circ$ .

## 1.3 Numerical and Analytical Models

The numerical and analytical models are developed to predict the force–displacement responses of the aluminum foam-filled energy absorption connectors. The analytical model can be employed to quickly evaluate the energy absorption performance of the proposed connectors.

### 1.3.1 Numerical Model

The explicit code in LS-DYNA was adopted to conduct the numerical analysis, and the mild steel was modeled with Piecewise Linear Plasticity material model (Hallquist 2006). This elasto-plastic material model allows to defining arbitrary stress versus strain curve and strain rate dependency. The deviatoric stresses satisfy the follow yield function (Hallquist 2006).

$$\phi = \frac{1}{2} s_{ij} s_{ij} - \frac{1}{3} \sigma_y^2 \leq 0 \quad (1.7)$$

where  $s_{ij}$  is stress deviator tensor, and  $\sigma_y$  is given as

$$\sigma_y(\varepsilon_{eff}^p, \dot{\varepsilon}_{eff}^p) = \sigma_y(\varepsilon_{eff}^p) \left[ 1 + \left( \frac{\dot{\varepsilon}_{eff}^p}{C} \right)^{1/P} \right] \quad (1.8)$$

where  $\varepsilon_{eff}^p$  is effective plastic strain,  $\sigma_y(\varepsilon_{eff}^p)$  is yield stress without considering strain rate effect, and the input true stress–effective plastic strain curves of mild steels used in the connectors were obtained from the tensile coupon tests,  $\dot{\varepsilon}_{eff}^p$  is effective plastic strain rate,  $C$  and  $P$  are strain rate parameters in the Cowper-Symonds model. In this study, the strain rate parameters  $C$  and  $P$  were adopted as  $802 \text{ s}^{-1}$  and  $3.585$  for mild steel (Abramowicz and Jones 1986).

The aluminum foam was modeled by using a crushable foam material model (MAT\_63 in LS-DYNA), which is dedicated to model crushable foam with optional damping and tension cutoff. As for the yield of MAT\_63, it is governed by the largest principle stress, i.e., the three principle stresses ( $\sigma_1$ ,  $\sigma_2$  and  $\sigma_3$ ) are compared with the yield stress  $Y$  for compressive principle stress component and  $Y_t$  for tensile principle stress component.  $Y$  is a yield stress from a user-defined volumetric strain-hardening function, and  $Y_t$  is a user-defined constant tensile cutoff stress (Hanssen et al. 2002). Hence, the stress–strain curve in compression can be defined piecewisely, and tension is treated as elastic-perfectly-plastic (Yang and Qi 2013). The

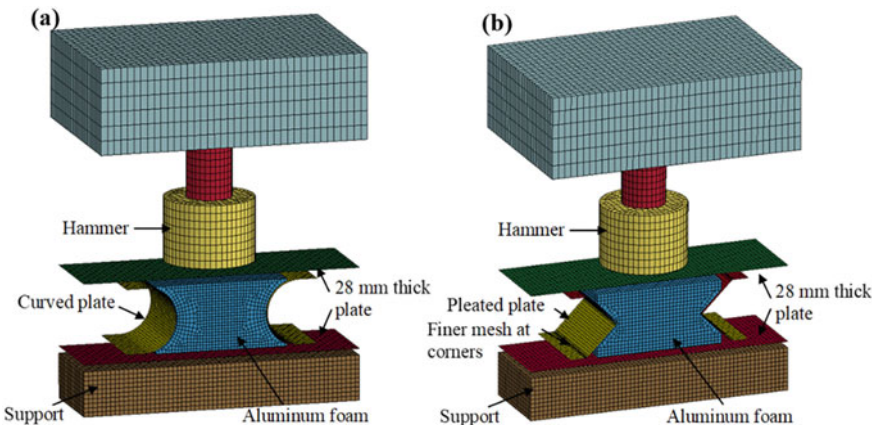


**Fig. 1.12** FE models of connectors under impact loading: **a** Type I connector and **b** type II connector, reprinted from Wang et al. (2018a, b), copyright 2022, with permission from Elsevier

input yield stress  $Y$  versus volumetric strain curve of aluminum foam was obtained from uniaxial compression loading tests. Song et al. (2005) noted that the aluminum foam almost showed no lateral expansion under uniaxial compression loading, and the some observations were also demonstrated by the authors via testing the samples of aluminum foam under uniaxial compression loading. Hence, the plastic Poisson's ratio of aluminum foam was set to be 0.01 (Yang and Qi 2013).

The FE models of the type I and II connectors under impact loading are shown in Fig. 1.12. The shell element with five integration points along the thickness was employed for steel plates, and eight-node brick element with reduced integration was used to model aluminum foam, support and hammer. The 8 mm and 20 mm thick steel plates were bolted together in the tests, and there was no separation being observed during the impact test. Hence, the single steel plate with 28 mm thickness was chosen as an alternative, as shown in Fig. 1.12. In the FE model, the contacts between two parts are captured through 'master–slave' contact interfaces, which are defined by using the surface to surface contact option in LS-DYNA. The penalty-based contact approach is a generally used method where the contact stiffness is determined by an algorithm according to the sizes and material properties of contact segments. Hence, it works more effectively when the material stiffness parameters between the contacting surfaces are of the same order-of-magnitude, such as that between steel plates. However, this contact may break down when materials with dissimilar stiffness come into contact, as the contact stiffness, which is roughly the minimum of the slave and master stiffness, may be too small. Therefore, the soft constraint-based contact approach, whose contact stiffness is independent of material parameters and well suited for treating contact between materials of different stiffness, was used to simulate the interaction between steel plates and aluminum foam. The dynamic and static friction coefficients between all the contact surfaces were assumed to be 0.2 (Zhang et al. 2010). During the impact test, there was no failure of bolts that were used

to connect curved/pleated plates and flat plates. Hence, the perfect bolt connection was applied in the FE model by connecting the selected nodes on curved/pleated plates to flat plates via \*CONTACT\_TIED\_SHELL\_EDGE\_TO\_SURFACE in LS-DYNA (Hallquist 2012).

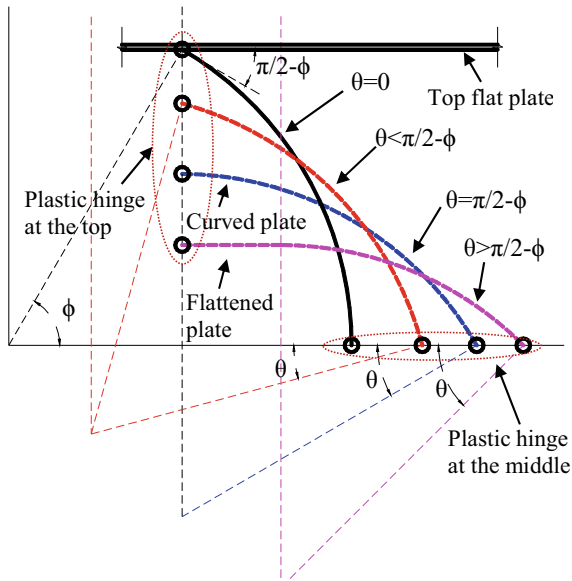
### 1.3.2 Analytical Model for Type I Connector

The crushing force of the type I connector under impact loading is mainly contributed by two parts, i.e., compression of aluminum foam and plastic deformation of curved plate, and they can be calculated separately. As for the force contributed by curved plate ( $F_{pd}$ ), the strain rate effect of mild steel should be incorporated into the analytical model. The following assumptions are employed to simplify the calculations:

- (1) The stress in the curved plate is a state of plane stress;
- (2) The nominal stress-strain relationship of mild steel conforms to rigid-linear strain-hardening behavior;
- (3) The presence of aluminum foam does not change the deformed shape of curved plates.

Figure 1.13 shows the deformation process of the type I connector without aluminum foam and the force is contributed by plastic deformation of the curved plate, including plastic hinge rotation and curvature change (i.e., from an initial

**Fig. 1.13** Deformation process of the type I connector without aluminum foam (quarter model), reprinted from Wang et al. (2018b), copyright 2022, with permission from Elsevier



curved plate to a flat plate). As illustrated in Fig. 1.13, two deformation patterns can be identified. When  $\theta < \pi/2 - \phi$ , the curved plate is not in contact with the top flat plate, and there are two plastic hinges being formed with one at the top and the other one at the middle. This is named as deformation pattern I. When  $\theta > \pi/2 - \phi$ , part of the curved plate at the top starts to contact with the top flat plate, and the plastic hinge at the top stops rotating. This is named as deformation pattern II, and the energy absorption is contributed by the plastic hinge rotation at the middle and plastic bending of the curved plate (from a curved plate to a flat plate).

### 1.3.2.1 Energy Absorption from Plastic Hinge at the Middle

If assuming the axial strain is linearly distributed along thickness of the curved plate and letting  $x$  represents the distance to neutral axis of the curved plate, the following relationships can be obtained

$$\varepsilon = \kappa x \text{ and } \dot{\varepsilon} = \dot{\kappa}x \quad (1.9)$$

where  $\varepsilon$  and  $\kappa$  are axial strain and curvature change of the curved plate, respectively, and the upper dot on the variable stands for its differential with respect to time. To include the strain rate effect of mild steel into the analytical model, the Cowper-Symonds model is used to establish the relationship between Dynamic Increase Factor (*DIF*) of mild steel and plastic strain rate ( $\dot{\varepsilon}$ ) as follow

$$DIF(\dot{\varepsilon}) = 1 + \left( \frac{\dot{\varepsilon}}{C} \right)^{1/P} \quad (1.10)$$

By utilizing the rigid-linear strain-hardening constitutive model to describe the stress-strain relationship of mild steel, the variation of internal energy per unit volume of the curved plate,  $du$ , can be formulated as

$$du = \sigma_D d\varepsilon = \left[ 1 + \left( \frac{\dot{\varepsilon}}{C} \right)^{1/P} \right] (\sigma_s + E' \varepsilon) d\varepsilon \quad (1.11)$$

where  $\sigma_D$  is flow stress of mild steel considering strain rate effect,  $\sigma_s$  is yield stress of mild steel without strain rate effect, and  $E'$  is strain hardening modulus. Substituting Eq. (1.9) to Eq. (1.11) leads to the function of  $du$  in terms of  $\kappa$  and  $\dot{\kappa}$  as follow

$$du = x \left[ 1 + \left( \frac{\dot{\kappa}x}{C} \right)^{1/P} \right] (\sigma_s + E' \kappa x) d\kappa \quad (1.12)$$

If assuming that the curvature change within the plastic hinge zone is uniform, the variation of internal energy of the curved plate at one plastic hinge,  $dU$ , can be

obtained by integrating  $du$  in Eq. (1.12) along the thickness and multiplying width,  $b$ , and plastic hinge length,  $t_{ph}$ , as follow

$$\begin{aligned} dU &= 2bt_{ph} \int_0^{t_p/2} du dx \\ &= bt_{ph} \left[ \frac{\sigma_s t_p^2}{4} + \frac{E' \kappa t_p^3}{12} + \frac{\sigma_s t_p^{1/P+2}}{2^{1/P+1}(1/P+2)} \left( \frac{\kappa}{C} \right)^{1/P} + \frac{E' \kappa t_p^{1/P+3}}{2^{1/P+2}(1/P+3)} \left( \frac{\kappa}{C} \right)^{1/P} \right] dk \end{aligned} \quad (1.13)$$

where  $t_p$  is curved plate thickness. There are totally two plastic hinges at the middle, the force contributed by these two plastic hinges,  $F_m$ , can be obtained as

$$\begin{aligned} F_m &= 2 \frac{dU_m}{d\delta} \\ &= 2bt_{ph} \left[ \frac{\sigma_s t_p^2}{4} + \frac{E' \kappa_m t_p^3}{12} + \frac{\sigma_s t_p^{1/P+2}}{2^{1/P+1}(1/P+2)} \left( \frac{\dot{\kappa}_m}{C} \right)^{1/P} + \frac{E' \kappa_m t_p^{1/P+3}}{2^{1/P+2}(1/P+3)} \left( \frac{\dot{\kappa}_m}{C} \right)^{1/P} \right] \frac{d\kappa_m}{d\delta} \end{aligned} \quad (1.14)$$

By referring to the geometric relationship in Fig. 1.13, the unknown parameters in Eq. (1.14) can be obtained as

$$\kappa_m = \frac{2\theta}{t_{ph}}, \quad \dot{\kappa}_m = \frac{2}{t_{ph}} \frac{d\theta}{d\delta} \dot{\delta} \quad \text{and} \quad \frac{d\kappa_m}{d\delta} = \frac{2}{t_{ph}} \frac{d\theta}{d\delta} \quad (1.15)$$

In order to establish  $F_m$  in terms of displacement,  $\delta$ , and velocity,  $\dot{\delta}$ , the relationship between  $\theta$  and  $\delta$  needs to be established. As their relationships for deformation pattern I and II are different, they are separately calculated and given as follows. For deformation pattern I (Fig. 1.14a), i.e.,  $\delta \leq 2R(\sin \phi - 2 \sin^2 \frac{\phi}{2})$ ,  $\theta$  and  $\frac{d\theta}{d\delta}$  can be obtained as

$$\theta = \arccos \left( \frac{\sin \phi - \delta/2R}{2 \sin(\phi/2)} \right) - \frac{\phi}{2} \quad \text{and} \quad \frac{d\theta}{d\delta} = \frac{1}{4R \sin(\frac{\phi}{2}) \sqrt{1 - \left( \frac{\sin \phi - \delta/2R}{2 \sin(\phi/2)} \right)^2}} \quad (1.16)$$

For deformation pattern II (Fig. 1.14b), i.e.,  $\delta > 2R(\sin \phi - 2 \sin^2 \frac{\phi}{2})$ ,  $\theta$  and  $\frac{d\theta}{d\delta}$  can be obtained as

$$\theta = \arcsin(1 + \delta/2R - \sin \phi) \quad \text{and} \quad \frac{d\theta}{d\delta} = \frac{1}{2R \sqrt{1 - (1 + \delta/2R - \sin \phi)^2}} \quad (1.17)$$

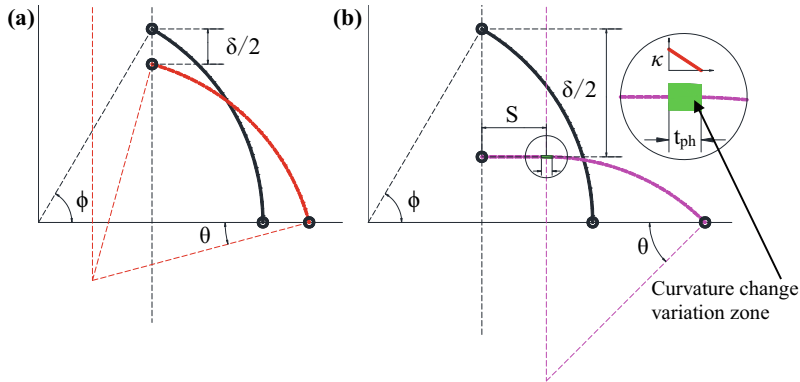


**Fig. 1.14** Deformation of the type I connector: **a** deformation pattern I and **b** deformation pattern II, reprinted from Wang et al. (2018b), copyright 2022, with permission from Elsevier

### 1.3.2.2 Energy Absorption from Plastic Hinge at the Top and Curvature Change

For deformation pattern I shown in Fig. 1.14a, the energy absorption from the top part of the curved plate is only contributed by the plastic hinge rotation at the top. There are totally four plastic hinges of the connector with two at the top and the other two at the bottom, and therefore the force contributed by these four plastic hinges,  $F_{t1}$ , can be obtained as

$$\begin{aligned} F_{t1} &= 4 \frac{dU_t}{d\delta} \\ &= 4bt_{ph} \left[ \frac{\sigma_s t_p^2}{4} + \frac{E' \kappa_t t_p^3}{12} + \frac{\sigma_s t_p^{1/P+2}}{2^{1/P+1}(1/P+2)} \left( \frac{\dot{\kappa}_t}{C} \right)^{1/P} + \frac{E' \kappa_t t_p^{1/P+3}}{2^{1/P+2}(1/P+3)} \left( \frac{\dot{\kappa}_t}{C} \right)^{1/P} \right] \frac{d\kappa_t}{d\delta} \end{aligned} \quad (1.18)$$

where  $\kappa_t = \frac{1}{t_{ph}} \arccos\left(\frac{\sin\phi - \delta/2R}{2\sin(\phi/2)}\right) - \frac{\phi}{2}$ ,  $\dot{\kappa}_t = \frac{\dot{\delta}}{4t_{ph} R \sin(\frac{\phi}{2}) \sqrt{1 - \left(\frac{\sin\phi - \delta/2R}{2\sin(\phi/2)}\right)^2}}$  and  $\frac{d\kappa_t}{d\delta} = \frac{1}{4t_{ph} R \sin(\frac{\phi}{2}) \sqrt{1 - \left(\frac{\sin\phi - \delta/2R}{2\sin(\phi/2)}\right)^2}}$ .

For deformation pattern II shown in Fig. 1.14b, the energy absorption is contributed by curvature change of the curved plate (from  $1/R$  to zero). According to geometric relationship, the length of flattened plate,  $S$ , can be obtained as

$$S = R\left(\phi + \theta - \frac{\pi}{2}\right) \quad (1.19)$$

As illustrated in Fig. 1.14b, certain distance is needed for the change of the original curved plate with curvature of  $1/R$  to the flat plate, which is called curvature change variation zone. It means that the curvature change at the left of curvature change

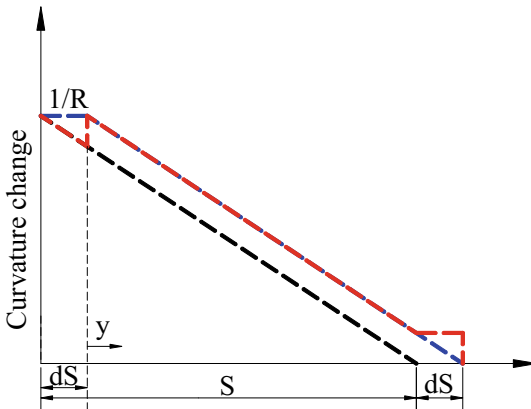


**Fig. 1.15** Curvature change distribution with increment of flattened plate length, reprinted from Wang et al. (2018b), copyright 2022, with permission from Elsevier

variation zone is  $1/R$ , and that at the right is zero. The curvature change variation zone can be treated as a plastic hinge zone, which moves with the continuous crushing of the connector. Hence, it is reasonable to assume that the length of curvature change variation zone equals to the length of plastic hinge zone,  $t_{ph}$ . We also assume that the curvature change,  $\kappa$ , linearly varies along the curvature change variation zone (see black dash line in Fig. 1.15) for the following calculation.

According to previous calculation, the variation of internal energy per unit length of the curved plate induced by curvature change is given as

$$d\tilde{u} = b(\bar{A} + \bar{B}\kappa)d\kappa \quad (1.20)$$

where  $\bar{A} = \frac{\sigma_s t_p^2}{4} + \frac{\sigma_s t_p^{1/P+2}}{2^{1/P+1}(1/P+2)}\left(\frac{\dot{\kappa}}{C}\right)^{1/P}$ ,  $\bar{B} = \frac{E' t_p^3}{12} + \frac{E' t_p^{1/P+3}}{2^{1/P+2}(1/P+3)}\left(\frac{\dot{\kappa}}{C}\right)^{1/P}$  and  $\dot{\kappa} = \frac{\delta}{2Rt_{ph}\sqrt{1-(1+\delta/2R-\sin\phi)^2}}$ .

As illustrated in Fig. 1.15 for curvature change distribution along the curvature change variation zone, the infinitesimal increment of flattened plate ( $dS$ ) leads to new curvature change distribution (blue dash line) and increase of internal energy ( $dU$ ). To simplify the calculation of the variation of internal energy, the red dash line in Fig. 1.15 is adopted to represent the new curvature change distribution.

As illustrated in Fig. 1.15, when  $0 < y < t_{ph}-dS$ , the curvature change,  $\kappa$ , varies from  $\kappa_0 - (dS+y)\bar{\kappa}$  to  $\kappa_0 - \bar{\kappa}y$  (where  $\kappa_0 = 1/R$  and  $\bar{\kappa} = 1/Rt_{ph}$ ). Hence, the increase of internal energy per unit length due to the increment of flattened plate,  $dS$ , for  $y = 0 \sim t_{ph}-dS$  is

$$d\bar{u}_{y1} = \int_{\kappa_0 - (dS+y)\bar{\kappa}}^{\kappa_0 - \bar{\kappa}y} d\tilde{u} \quad (1.21)$$

Then, substituting Eq. (1.20) into Eq. (1.21) and integrating Eq. (1.21) lead to Eq. (1.22). It should be mentioned that the second order of  $dS$  is neglected in the calculation.

$$d\bar{u}_{y1} = b\bar{\kappa}(\bar{A} + \bar{B}\kappa_0)dS - b\bar{B}\bar{\kappa}^2 dS \cdot y \quad (1.22)$$

When  $t_{ph}-dS < y < t_{ph}$ , the curvature change,  $\kappa$ , varies from 0 to  $\bar{\kappa}dS$ . Hence, the increase of internal energy per unit length due to the increment of the flattened plate,  $dS$ , for  $y = t_{ph}-dS \sim t_{ph}$  is

$$d\bar{u}_{y2} = \int_0^{\bar{\kappa}dS} d\tilde{u} \quad (1.23)$$

Then, integrating Eq. (1.23) and neglecting the second order of  $dS$  leads to the follow

$$d\bar{u}_{y2} = b\bar{A}\bar{\kappa}dS \quad (1.24)$$

Hence, the increase of internal energy,  $dU_t$ , due to the increment of flattened plate,  $dS$ , can be obtained as

$$dU_t = \int_0^{t_{ph}-dS} d\bar{u}_{y1} dy + \int_{t_{ph}-dS}^{t_{ph}} d\bar{u}_{y2} dy = b\bar{\kappa}t_{ph} \left( \bar{A} + \bar{B}\kappa_0 - \frac{\bar{B}\bar{\kappa}t_{ph}}{2} \right) dS \quad (1.25)$$

As there are totally four flattened plates, the force contributed by curvature change of the curved plate,  $F_{t2}$ , can be obtained as

$$F_{t2} = 4 \frac{dU_t}{d\delta} = 4 \frac{dU_t}{dS} \frac{dS}{d\delta} \quad (1.26)$$

where  $\frac{dU_t}{dS} = b\bar{\kappa}t_{ph} \left( \bar{A} + \bar{B}\kappa_0 - \frac{\bar{B}\bar{\kappa}t_{ph}}{2} \right)$  and  $\frac{dS}{d\delta} = \frac{1}{2\sqrt{1-(1+\delta/2R-\sin\phi)^2}}$ .

Hence, the total crushing force of the type I connector contributed by plastic deformation of curved plates,  $F_{pd}$ , can be summarized as follow

$$F_{pd} = F_m + \begin{cases} F_{t1}, & \delta \leq 2R(\sin\phi - 2\sin^2\frac{\phi}{2}) \\ F_{t2}, & \delta > 2R(\sin\phi - 2\sin^2\frac{\phi}{2}) \end{cases} \quad (1.27)$$

Equation (1.27) establishes the force contributed by curved plates,  $F_{pd}$ , in terms of displacement,  $\delta$ , and velocity,  $\dot{\delta}$ . It is noted that  $F_{pd}$  is the summation of static terms (the terms without  $\dot{\delta}$ ) and dynamic terms (the terms with  $\dot{\delta}$ ).

### 1.3.2.3 Energy Absorption from Aluminum Foam

The energy absorption of aluminum foam filled in the type I connector is realized through its compression (i.e., volumetric reduction) under impact loading, and the formulae for calculating the crushing force contributed by aluminum foam are presented as followings. The relationship between compressive stress and volumetric strain of aluminum foam can be given as (Reyes et al. 2003).

$$\sigma_f = \sigma_p + \gamma \frac{\varepsilon_V}{\varepsilon_D} + \alpha_2 \ln \left( \frac{1}{1 - (\varepsilon_V / \varepsilon_D)^\beta} \right) \quad (1.28)$$

where  $\varepsilon_V$  is volumetric strain, and  $\sigma_p$ ,  $\gamma$ ,  $\varepsilon_D$ ,  $\alpha_2$  and  $\beta$  are material properties which can be determined by fitting the material test data.

Owing to symmetry, only quarter model of the type I connector in Fig. 1.16 is analyzed. To simplify the calculation, the connector is assumed to be fully filled with aluminum foam when calculating the volume change of aluminum foam and the crushing force will be determined by multiplying the ratio of actual initial aluminum foam volume,  $V_f$ , to initial total enclosed volume,  $V_o$ , which can be calculated as follows:

$$V_f = 4b \left[ (L_o - L_1)H - 1/2\phi' R^2 + 1/4R^2 \sin 2\phi' \right] \quad (1.29)$$

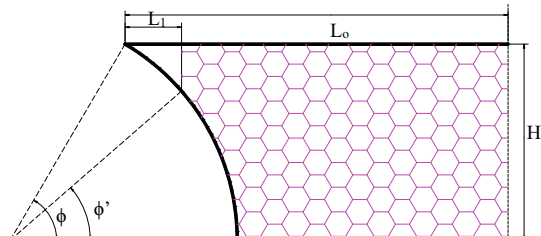
$$V_o = 4b(L_o H - 1/2\phi R^2 + 1/4R^2 \sin 2\phi) \quad (1.30)$$

where  $\phi' = \arccos(L_1/R + \cos \phi)$ ,  $b$  is width of the connector,  $L_o$ ,  $L_1$  and  $H$  are given in Fig. 1.16, and  $R$  is radius of the curved plate.

For deformation pattern I, i.e.,  $\delta \leq 2R(\sin \phi - 2 \sin^2 \frac{\phi}{2})$ , the relationship between current volume of aluminum foam,  $V_{cl}$ , and displacement,  $\delta$ , during crushing can be formulated as

$$V_{cl} = 2b \left[ 2L_o(H - \delta/2) - R^2 \sin \frac{\phi}{2} \sin(\phi + 2\theta) - \phi R^2 + R^2 \sin \phi \right] \quad (1.31)$$

**Fig. 1.16** Quarter model of the type I connector with aluminum foam, reprinted from Wang et al. (2017b), copyright 2022, with permission from Elsevier



where  $\theta = \arccos\left(\frac{\sin\phi - \delta/2R}{2\sin(\phi/2)}\right) - \frac{\phi}{2}$ , and the volumetric strain of aluminum foam can be determined as

$$\varepsilon_{VI} = 1 - \frac{V_{cI}}{V_o} = 1 - \frac{2L_o(H - \delta/2) - R^2 \sin \frac{\phi}{2} \sin(\phi + 2\theta) - \phi R^2 + R^2 \sin \phi}{2L_o H - \phi R^2 + 1/2R^2 \sin 2\phi} \quad (1.32)$$

It should be noted that the volumetric strain is taken as positive in compression. Then, the force contributed by aluminum foam for deformation pattern I can be obtained as

$$F_{fI} = \frac{dE_{pfI}}{d\delta} \frac{V_f}{V_o} = \frac{-\sigma_f dV_{cI}}{d\delta} \frac{V_f}{V_o} \quad (1.33)$$

where  $\sigma_f$  is a function of volumetric strain and given in Eq. (1.28), and the differential of current volume,  $V_{cI}$ , with respect to displacement,  $\delta$ , can be formulated as

$$\frac{dV_{cI}}{d\delta} = -b \left[ 2L_o + 4R^2 \sin \frac{\phi}{2} \cos(\phi + 2\theta) \frac{d\theta}{d\delta} \right] \quad (1.34)$$

where  $\frac{d\theta}{d\delta}$  can be obtained from Eq. (1.16).

For deformation pattern II, i.e.,  $\delta > 2R(\sin\phi - 2\sin^2 \frac{\phi}{2})$ , the relationship between current volume of aluminum foam,  $V_{cII}$ , and displacement,  $\delta$ , during crushing can be formulated as

$$V_{cII} = b \{ 4[L_o - R(\phi + \theta - \pi/2)](H - \delta/2) - 2R^2(\pi/2 - \theta) + R^2 \sin 2\theta \} \quad (1.35)$$

where  $\theta = \arcsin(1 + \delta/2R - \sin\phi)$ , and the volumetric strain of aluminum foam can be determined as

$$\varepsilon_{VII} = 1 - \frac{4[L_o - R(\phi + \theta - \pi/2)](H - \delta/2) - 2R^2(\pi/2 - \theta) + R^2 \sin 2\theta}{4L_o H - 2\phi R^2 + R^2 \sin 2\phi} \quad (1.36)$$

Then, the force contributed by aluminum foam for deformation pattern II can be obtained as

$$F_{fII} = \frac{dE_{pfII}}{d\delta} \frac{V_f}{V_o} = \frac{-\sigma_f dV_{cII}}{d\delta} \frac{V_f}{V_o} \quad (1.37)$$

where  $\sigma_f$  is given in Eq. (1.28), and the differential of current volume,  $V_{cII}$ , with respect to displacement,  $\delta$ , can be formulated as

$$\frac{dV_{cII}}{d\delta} = -2b \left\{ L_o - R \left( \phi + \theta - \frac{\pi}{2} \right) + \left[ 2R \left( H - \frac{\delta}{2} \right) - R^2 (1 + \cos 2\theta) \right] \frac{d\theta}{d\delta} \right\} \quad (1.38)$$

where  $\frac{d\theta}{d\delta}$  can be obtained from Eq. (1.17). The force–displacement relationship of the type I connector with aluminum foam can be obtained by summing the force contributed by curved plates and aluminum foam as

$$F = \begin{cases} F_m + F_{t1} + F_{fI}, & \delta \leq 2R(\sin \phi - 2 \sin^2 \frac{\phi}{2}) \\ F_m + F_{t2} + F_{fII}, & \delta > 2R(\sin \phi - 2 \sin^2 \frac{\phi}{2}) \end{cases} \quad (1.39)$$

It is noted that the calculated volume change of aluminum foam is smaller than the actual volume change, which is induced by nonzero curved plate thickness. The inner surfaces of the curved plate are fully contacted when displacement  $\delta_i = 2(H - t_p)$ , and the aluminum foam volume can be determined as

$$V_{ci}^T = 4t_p b(L_0 - R\phi) \quad (1.40)$$

whereas, the aluminum foam volume at displacement  $\delta_i$  given by Eq. (1.35) is

$$V_{cIIIi} = b \{ 4[L_o - R(\phi + \theta_i - \pi/2)](H - \delta_i/2) - 2R^2(\pi/2 - \theta_i) + R^2 \sin 2\theta_i \} \quad (1.41)$$

To ensure the correct volume change of aluminum foam at displacement  $\delta_i$ , a constant ratio,  $k$ , is introduced to modify the volume change of aluminum foam as

$$\Delta V_f^T = k \Delta V_f \quad (1.42)$$

where  $\Delta V_f^T$  and  $\Delta V_f$  are the volume change of aluminum foam after and before correcting, and  $k$  can be determined in Eq. (1.43) by ensuring that the volume change of aluminum foam at displacement  $\delta_i$  equals to the actual one.

$$k = \frac{V_o - V_{ci}^T}{V_o - V_{cIIIi}} \quad (1.43)$$

Then, the corrected volumetric strain of aluminum foam can be obtained as

$$\varepsilon_V^T = k \varepsilon_V \quad (1.44)$$

Similarly, the differential of current volume of aluminum foam with respect to displacement can be corrected as

$$\frac{dV_c^T}{d\delta} = k \frac{dV_c}{d\delta} \quad (1.45)$$

Hence, the corrected crushing force of the type I connector can be obtained by scaling the force contributed by aluminum foam and volume strain by a factor,  $k$ , as

$$F = \begin{cases} F_m + F_{t1} + k \frac{-\sigma_f(k\varepsilon_{V1})dV_{cI}}{d\delta} \frac{V_f}{V_o}, & \delta \leq 2R(\sin \phi - 2 \sin^2 \frac{\phi}{2}) \\ F_m + F_{t2} + k \frac{-\sigma_f(k\varepsilon_{VII})dV_{cII}}{d\delta} \frac{V_f}{V_o}, & \delta > 2R(\sin \phi - 2 \sin^2 \frac{\phi}{2}) \end{cases} \quad (1.46)$$

### 1.3.3 Analytical Model for Type II Connector

Similar to the type I connector, the crushing force of the type II connector is also contributed by two parts, i.e., plastic hinge rotation of pleated plates and compression of aluminum foam. In addition, the assumptions in Sect. 1.3.2 are also employed herein to simplify the calculations of crushing force of the type II connector.

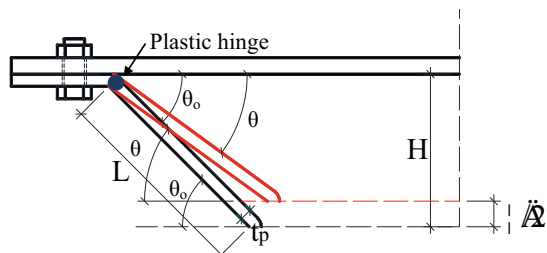
#### 1.3.3.1 Energy Absorption from Pleated Plates

As shown in Fig. 1.17 for the quarter model of the type II connector without aluminum foam, there are two plastic hinges with same angle change from  $\theta_0$  to  $\theta$ . By employing the variation of internal energy of the pleated plate at one plastic hinge in Eq. (1.13), the total force contributed by pleated plates,  $F_{pd}$ , via rotation of eight plastic hinges can be obtained as

$$F_{pd} = 8 \frac{dU}{d\delta} = 8bt_{ph} \left[ \frac{\sigma_y t_p^2}{4} + \frac{E' \kappa t_p^3}{12} + \frac{\sigma_y t_p^{1/P+2}}{2^{1/P+1}(1/P+2)} \left( \frac{\dot{\kappa}}{C} \right)^{1/P} + \frac{E' \kappa t_p^{1/P+3}}{2^{1/P+2}(1/P+3)} \left( \frac{\dot{\kappa}}{C} \right)^{1/P} \right] \frac{d\kappa}{d\delta} \quad (1.47)$$

In order to obtain the formula of  $F_{pd}$  in terms of displacement ( $\delta$ ) and velocity ( $\dot{\delta}$ ), the relationship between  $\kappa$  and  $\delta$  has to be established. As illustrated in Fig. 1.17, the rotation angle of plastic hinge is  $\theta_0 - \theta$  with displacement of  $\delta$ . According to the

**Fig. 1.17** Deformation of the type II connector without aluminum foam, reprinted from Wang et al. (2018a), copyright 2022, with permission from Elsevier



assumption that the curvature change within the plastic hinge zone is uniform, the curvature change,  $\kappa$ , and curvature change rate,  $\dot{\kappa}$ , within the plastic hinge zone can be obtained as

$$\kappa = \frac{\theta_0 - \theta}{t_{ph}} \text{ and } k = \frac{-\dot{\theta}}{t_{ph}} \quad (1.48)$$

According to Fig. 1.17, the current angle  $\theta$  can be given as

$$\theta = \arcsin\left(\frac{H - \delta/2}{L}\right) \quad (1.49)$$

Substituting Eq. (1.49) into Eq. (1.48) leads to following formulae

$$\begin{aligned} \kappa &= \frac{\theta_0 - \arcsin\left(\frac{H - \delta/2}{L}\right)}{t_{ph}}, \quad \dot{\kappa} = \frac{\dot{\delta}}{2t_{ph}L\sqrt{1 - \left(\frac{H - \delta/2}{L}\right)^2}}, \\ \frac{d\kappa}{d\delta} &= \frac{1}{2t_{ph}L\sqrt{1 - \left(\frac{H - \delta/2}{L}\right)^2}} \end{aligned} \quad (1.50)$$

Then, substituting Eq. (1.50) into Eq. (1.47) yields the force contributed by pleated plates,  $F_{pd}$ , in terms of displacement,  $\delta$ , and velocity,  $\dot{\delta}$ .

### 1.3.3.2 Energy Absorption from Aluminum Foam

As for the type II connector with aluminum foam, the crushing force,  $F$ , is determined as the summation of force contributed by pleated plates and aluminum foam, as given in Eq. (1.51).

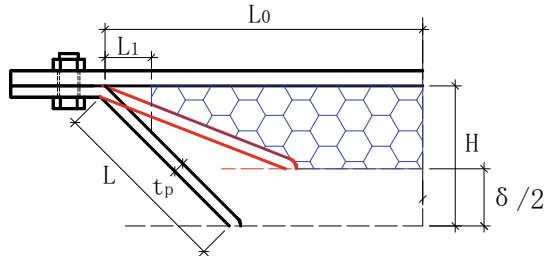
$$F = F_{pd} + F_f \quad (1.51)$$

where  $F_{pd}$  is given in Eq. (1.47), and  $F_f$  is the force contributed by compression of aluminum foam which can be determined as

$$F_f = -\sigma_f \frac{dV_c}{d\delta} \quad (1.52)$$

where  $\sigma_f$  and  $V_c$  are compressive stress and current volume of aluminum foam, respectively. The relationship between  $\sigma_f$  and volumetric strain of aluminum foam can be found in Eq. (1.28).

**Fig. 1.18** Deformation of the type II connector with aluminum foam, reprinted from Wang et al. (2017a), copyright 2022, with permission from Elsevier



According to Fig. 1.18, the relationship between volumetric strain,  $\varepsilon_V$ , and displacement,  $\delta$ , can be given as

$$\varepsilon_V = 1 - \frac{n_1 \left( 2L_0 - \frac{n_2 + L_1^2}{\sqrt{n_2}} \right) - \frac{(n_2 - L_1^2)t_p \delta}{2(H - t_p)\sqrt{n_2}}}{H \left( 2L_0 - \frac{L^2 - H^2 + L_1^2}{\sqrt{L^2 - H^2}} \right)} \quad (1.53)$$

where  $n_1 = H - \delta/2$  and  $n_2 = L^2 - (H - \delta/2)^2$ . The differential of current aluminum foam volume with respect to displacement can be given as

$$\frac{dV_c}{d\delta} = b \left( k_1 \sqrt{n_2} + k_2 \frac{1}{\sqrt{n_2}} + k_3 \frac{1}{n_2^{3/2}} - 2L_0 \right) \quad (1.54)$$

where  $k_1 = \frac{H - 2t_p}{H - t_p}$ ,  $k_2 = L_1^2 - n_1^2 - \frac{(n_1 \delta - 2L_1^2)t_p}{2(H - t_p)}$  and  $k_3 = n_1^2 L_1^2 - \frac{n_1 L_1^2 t_p \delta}{2(H - t_p)}$ .

It should be noted that the proposed analytical model is more applicable to the connectors under low-velocity impact, whose deformation mode is similar to the quasi-static loading case. In terms of higher impact velocity which may trigger the deformation mode change of the connector, the developed analytical model may underestimate the energy absorption capacity of the connector owing to the neglect of energy absorption enhancement induced by the deformation mode change.

### 1.3.4 Comparisons and Discussions

The force–displacement curves of type I connectors obtained from numerical and analytical predictions are compared with those from test results in Fig. 1.19, and good agreement between them can be observed. This demonstrates that the developed numerical and analytical models are accurate to predict the force–displacement responses of type I connectors. The observed fluctuations of force–displacement curves from tests and numerical predictions are caused by the inertia force, which cannot be completely excluded from the tests and numerical simulations. It is also noted that the predictions from numerical and analytical models are closer to each

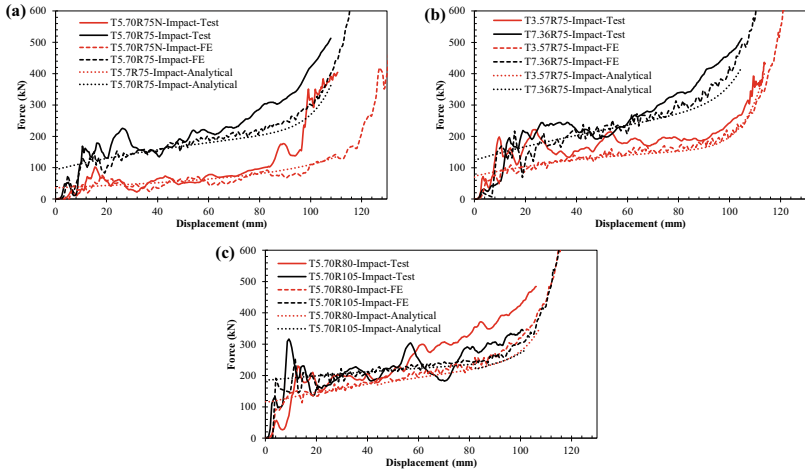


**Fig. 1.19** Comparison of numerical and analytical predictions with test results for type I connectors: **a** with and without aluminum foam, **b** variant curved plate thickness **c** variant radius, reprinted from Wang et al. (2018b), copyright 2022, with permission from Elsevier

other as compared to their comparisons with test results. In addition, both the numerical and analytical predictions show slightly later densification as compared to test results. This is because the numerical and analytical models are specified with same material properties (e.g., strain rate parameters of mild steel and uniformly distributed density of aluminum foam), which may slightly differ from those in the tests. Both the forces from numerical and analytical predictions are slightly lower than those from test results, which may be attributed to the assumed strain rate insensitivity of aluminum foam in these two models. As for the connector T5.70R75N without aluminum foam, the early contact between top and bottom bolts before the contact of inner surfaces of curved plates was observed during the test, which leads to smaller densification displacement from the test as compared to those from numerical and analytical predictions. The numerical and analytical predictions in Fig. 1.19b also demonstrate that increasing curved plate thickness results in the increase of force. Figure 1.19c indicates that increasing curved plate radius leads to the initial improvement of force, but shows little effect on final force and densification displacement.

Figure 1.20 presents the comparisons of force–displacement curves of type II connectors obtained from numerical and analytical predictions with those from impact tests, which also demonstrates the accuracies of developed numerical and analytical models for type II connectors. The fluctuations of force–displacement curves from tests and numerical predictions are also observed for type II connectors, which are consistent with type I connectors. Figure 1.20b shows that increasing pleated plate thickness leads to an increase in mean force, but decrease in densification displacement. It is also evident from Fig. 1.20c that the mean force can be improved by increasing angle  $\theta_0$ .

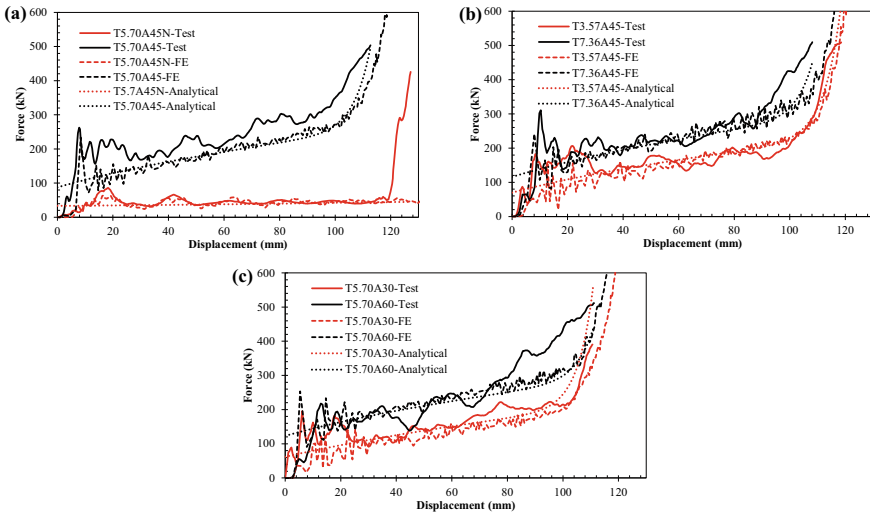


**Fig. 1.20** Comparison of numerical and analytical predictions with test results for type II connectors: **a** with and without aluminum foam, **b** variant pleated plate thickness **c** variant angle  $\theta_0$ , reprinted from Wang et al. (2018a), copyright 2022, with permission from Elsevier

## 1.4 Blast Resistant Design Using Energy Absorption Connectors

The proposed energy absorption connectors can be inserted between a blast resistant façade/panel and building for dissipating blast energy and reducing the blast load transmitted to the protected structure. The design approach of blast resistant façade/panel with energy absorption connectors as additional energy absorbers is presented in this section, which may assist the blast resistant design of such structural system. The single-degree-of-freedom (SDOF) method (Biggs 1964; Rigby et al. 2012) has been widely used to predict the dynamic response of a continuous member (e.g., blast resistant façade/panel) under blast loading. In terms of the blast resistant façade/panel with energy absorption connectors, the two-degrees-of-freedom (TDOF) method is applicable.

The equations of motion of the blast resistant façade/panel with energy absorption connectors can be formulated by applying Lagrange's equation, which are given as

$$\frac{d}{dt} \left( \frac{\partial K}{\partial \dot{y}_i} \right) + \frac{\partial (U + V)}{\partial y_i} = 0, \quad i = 1, 2 \quad (1.55)$$

where  $K$  is kinetic energy,  $U$  is strain energy,  $V$  is potential energy of blast loading, and  $y_i$  is generalized displacement. As shown in Fig. 1.21, the kinetic energy and strain energy (or internal energy) of connectors can be obtained in Eqs. (1.56) and (1.57), respectively.

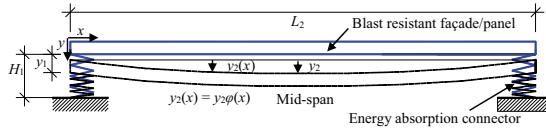


**Fig. 1.21** Blast resistant façade/panel with energy absorption connectors, reprinted from Wang et al. (2017a), copyright 2022, with permission from Elsevier

$$K_c = \frac{1}{2} \int_0^{H_1} m_c \frac{\dot{y}_1^2}{L_1^2} y^2 dy \quad (1.56)$$

where  $H_1$  is length of connector,  $m_c$  is mass per unit length of connectors, and  $\dot{y}_1$  is velocity of the connector at top layer.

$$U_c = \int_0^{y_1} R_c(y, \dot{y}) dy \quad (1.57)$$

where  $y_1$  is displacement of the connector at top layer, and  $R_c(y, \dot{y})$  is force–displacement curve of the connector obtained in this study.

For a blast resistant façade/panel, the kinetic energy and strain energy can be formulated in Eqs. (1.58) and (1.59), respectively.

$$K_f = \frac{1}{2} \int_0^{L_2} m_f [\dot{y}_1 + \dot{y}_2\varphi(x)]^2 dx \quad (1.58)$$

where  $L_2$  and  $m_f$  are span length and mass per unit span length of the blast resistant façade/panel,  $\dot{y}_2$  is relative velocity at mid-span, and  $\varphi(x)$  is deflection shape function of the blast resistant façade/panel.

$$U_f = \int_0^{L_2} \frac{\varphi(x)}{L_2} dx \int_0^{y_2} R_f(y) dy \quad (1.59)$$

where  $y_2$  is relative displacement at mid-span, and  $R_f(y)$  is force–displacement curve of the blast resistant façade/panel under uniformly distributed pressure loading. Hence, the kinetic energy and strain energy of the whole system can be obtained as

$$U = U_c + U_f \quad (1.60)$$

$$K = K_c + K_f \quad (1.61)$$

Then, the potential energy of blast loading can be obtained as

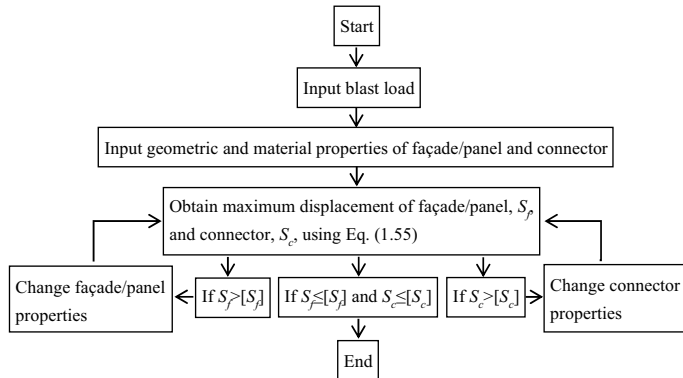


**Fig. 1.22** Flow chart of design procedure, reprinted from Wang et al. (2017a), copyright 2022, with permission from Elsevier

$$V = -B \int_0^{L_2} P(t)[y_1 + y_2\varphi(x)]dx \quad (1.62)$$

where  $B$  is width of the blast resistant façade/panel, and  $P(t)$  is pressure–time history of applied blast loading. The equations of motion of the blast resistant façade/panel with energy absorption connectors can be obtained by substituting Eqs. (1.60)–(1.62) into Eq. (1.55). The numerical method (e.g., fourth-order Runge–Kutta time stepping procedure) can be utilized to solve the equations of motion and obtain the displacement–time histories of the blast resistant façade/panel and connector.

The design procedure of the blast resistant façade/panel with energy absorption connectors is illustrated in Fig. 1.22. The blast load is first determined based on risk assessment. Then, the geometric and material properties of the blast resistant façade/panel and energy absorption connector are preliminarily selected, which can be used to yield the required parameters in equations of motion (in Eq. (1.55)). Once the maximum displacement of the blast resistant façade/panel,  $S_f$ , and connector,  $S_c$ , are obtained by solving the equations of motion, they are checked with the allowable maximum displacement of the blast resistant façade/panel,  $[S_f]$ , and connector,  $[S_c]$ . If  $S_f > [S_f]$  or  $S_c > [S_c]$ , it is needed to change the geometrical or material properties of the blast resistant façade/panel or connector and redo the calculation.

## 1.5 Summary

In this chapter, the drop-weight impact tests were conducted to study the energy absorption performances of the proposed connectors. In addition, the effects of loading rate, aluminum foam filler, curved plate thickness and radius (for type I

connectors) as well as pleated plate thickness and angle  $\theta_0$  (for type II connectors) on the energy absorption performances were experimentally investigated. Then, the numerical and analytical models were developed to predict the force–displacement responses of the connectors. Finally, the design approach of the blast resistant façade/panel with energy absorption connectors as additional energy absorbers was presented. The main findings from this work are summarized as follows:

- (1) Experimental results showed that the collapse processes of the proposed energy absorption connectors under impact loading were similar to those under quasi-static loading owing to the low impact velocity (less than 13 m/s). The collapse processes of the tested connectors under impact loading could be categorized into three stages, i.e., elastic deformation, plastic deformation and inner surface contact (for the connectors without aluminum foam) or aluminum foam densification stage (for the connectors with aluminum foam).
- (2) The mean crushing force and energy absorption capacity of the connector under impact loading were improved as compared to those under quasi-static loading, which could be attributed to the strain rate of mild steel. In addition, the mean crushing force and energy absorption capacity of the connector were also shown to be improved by filling the connector with aluminum foam as well as increasing curved plate thickness and radius (for type I connectors) and increasing pleated plate thickness and angle  $\theta_0$  (for type II connectors).
- (3) The developed numerical and analytical models were shown to be accurate by comparing the force–displacement responses from numerical and analytical predictions with those from drop-weight impact tests. The analytical model could be used to quickly evaluate the energy absorption performances of the proposed connectors.

## References

- Abramowicz W, Jones N (1986) Dynamic progressive buckling of circular and square tubes. *Int J Impact Eng* 4:243–270
- Ahmad Z, Thambiratnam DP (2009) Dynamic computer simulation and energy absorption of foam-filled conical tubes under axial impact loading. *Comput Struct* 87:186–197
- Alghamdi AAA (2001) Collapsible impact energy absorbers: an overview. *Thin-Walled Struct* 39(2):189–213
- Baroutaji A, Gilchrist MD, Smyth D et al (2015) Analysis and optimization of sandwich tubes energy absorbers under lateral loading. *Int J Impact Eng* 82:74–88
- Baroutaji A, Gilchrist MD, Olabi AG (2016) Quasi-static, impact and energy absorption of internally nested tubes subjected to lateral loading. *Thin-Walled Struct* 98:337–350
- Baroutaji A, Sajjia M, Olabi AG (2017) On the crashworthiness performance of thin-walled energy absorbers: Recent advances and future developments. *Thin-Walled Struct* 118:137–163
- Biggs JM (1964) Introduction to structural dynamics. McGraw-Hill, New York
- Chan KC, Xie LS (2003) Dependency of densification properties on cell topology of metal foams. *Scr Mater* 48(8):1147–1152
- Fan Z, Shen J, Lu G, Ruan D (2013) Dynamic lateral crushing of empty and sandwich tubes. *Int J Impact Eng* 53:3–16

- Hall IW, Guden M, Claar TD (2002) Transverse and longitudinal crushing of aluminum-foam filled tubes. *Scr Mater* 46:513–518
- Hallquist JO (2006) LS-DYNA theory manual. Livermore Software Technology Corporation (LSTC). Livermore, California
- Hallquist JO (2012) LS-DYNA keyword user's manual. Livermore Software Technology Corporation. Livermore, California
- Hanssen AG, Hopperstad OS, Langseth M et al (2002) Validation of constitutive models applicable to aluminium foams. *Int J Mech Sci* 44:359–406
- Kilicaslan C (2015) Numerical crushing analysis of aluminum foam-filled corrugated single- and double-circular tubes subjected to axial impact loading. *Thin-Walled Struct* 96:82–94
- Li QM, Magkiriadis I, Harrigan JJ (2006) Compressive strain at the onset of densification of cellular solids. *J Cell Plast* 42(5):371–392
- Lu GX, Yu TX (2003) Energy absorption of structures and materials. CRC Press, Boca Raton
- Nieh TG, Higashi K, Wadsworth J (2000) Effect of cell morphology on the compressive properties of open-cell aluminum foams. *Mater Sci Eng A* 283(1–2):105–110
- Olabi AG, Morris E, Hashmi MSJ et al (2008a) Optimised design of nested oblong tube energy absorbers under lateral impact loading. *Int J Impact Eng* 35:10–26
- Olabi AG, Morris E, Hashmi MSJ et al (2008b) Optimised design of nested circular tube energy absorbers under lateral impact loading. *Int J Mech Sci* 50:104–116
- Paul A, Ramamurty U (2000) Strain rate sensitivity of a closed-cell aluminium foam. *Mater Sci Eng A* 281(1):1–7
- Reyes A, Hopperstad OS, Berstad T et al (2003) Constitutive modeling of aluminum foam including fracture and statistical variation of density. *Eur J Mech A/Solids* 22:815–835
- Reyes A, Hopperstad OS, Hanssen AG et al (2004a) Modeling of material failure in foam-based components. *Int J Impact Eng* 30:805–834
- Reyes A, Hopperstad OS, Langseth M (2004b) Aluminum foam-filled extrusions subjected to oblique loading: experimental and numerical study. *Int J Solids Struct* 41:1645–1675
- Rigby SE, Tyas A, Bennett T (2012) Single-Degree-of-Freedom response of finite targets subjected to blast loading – The influence of clearing. *Eng Struct* 45:396–404
- Santosa SP, Wierzbicki T, Hanssen AG et al (2000) Experimental and numerical studies of foam-filled sections. *Int J Impact Eng* 24:509–534
- Shahbeyk S, Petrinic N, Vafai A (2007) Numerical modelling of dynamically loaded metal foam-filled square columns. *Int J Impact Eng* 34:573–586
- Shen J, Lu G, Ruan D, Seah CC (2015) Lateral plastic collapse of sandwich tubes with metal foam core. *Int J Mech Sci* 91:99–109
- Smith R, Altenhof W, Lapain M (2016) Transverse impact loading of aluminum foam filled braided stainless steel tubes. *Int J Impact Eng* 88:214–226
- Song HW, Fan ZJ, Yu G et al (2005) Partition energy absorption of axially crushed aluminum foam-filled hat sections. *Int J Solids Struct* 42(9):2575–2600
- Su XY, Yu TX, Reid SR (1995a) Inertia-sensitive impact energy-absorbing structures part I: effects of inertia and elasticity. *Int J Impact Eng* 16(4):651–672
- Su XY, Yu TX, Reid SR (1995b) Inertia-sensitive impact energy-absorbing structures part II: effects of strain rate. *Int J Impact Eng* 16(4):673–689
- Vural M, Ravichandran G (2003) Microstructural aspects and modelling of failure in naturally occurring porous composites. *Mech Mater* 35(3–6):523–536
- Wang Y, Liew JYR, Lee SC et al (2017a) Experimental and analytical studies of a novel aluminum foam filled energy absorption connector under quasi-static compression loading. *Eng Struct* 131:136–147
- Wang Y, Liew JYR, Lee SC et al (2017b) Crushing of a novel energy absorption connector with curved plate and aluminum foam as energy absorber. *Thin-Walled Struct* 111:145–154
- Wang Y, Zhai X, Yan J et al (2018a) Experimental, numerical and analytical studies on the alu-minum foam filled energy absorption connectors under impact loading. *Thin-Walled Struct* 131:566–576

- Wang Y, Zhai X, Ying W et al (2018b) Dynamic crushing response of an energy absorption connector with curved plate and aluminum foam as energy absorber. *Int J Impact Eng* 121:119–133.
- Yang S, Qi C (2013) Multiobjective optimization for empty and foam-filled square columns under oblique impact loading. *Int J Impact Eng* 54:177–191
- Zhang Z, Liu S, Tang Z (2010) Crashworthiness investigation of kagome honeycomb sandwich cylindrical column under axial crushing loads. *Thin-Walled Struct* 48:9–18

# Chapter 2

## Polyurethane Foam-Filled Energy Absorption Connectors Under Impact



### 2.1 Introduction

In this chapter, two types of polyurethane (PU) foam-filled energy absorption connectors were proposed, aiming to enhance the energy absorption performances of the aluminum foam-filled energy absorption connectors presented in Chap. 1. The PU foam, which generally exhibits higher specific energy absorption as compared to aluminum foam, was employed as the filler material. In addition, the multiple pleated (MP) plates and asymmetric pleated (AP) plates were employed for the PU foam-filled energy absorption connectors (with their names of type III and type IV connectors, as shown in Figs. 2.1 and 2.2, respectively), and the MP and AP plates could trigger more plastic hinges and achieve higher energy absorption as compared to type II connectors.

Recently, PU foam was increasingly employed for energy absorbers owing to its high energy absorption capacity and lightweight (Gilchrist and Mills 2001; Koohbor et al. 2016; Deb and Shivakumar 2009). Up to date, most of the studies on the PU foam-filled energy absorbers were focused on their behaviors under quasi-static crushing load. Lateral crushing on PU foam-filled tubes usually yielded smoother force–displacement responses (i.e., higher crushing force efficiency) as compared to axial crushing. It was also demonstrated that PU foam filler could enhance the energy absorption capacity as compared to the empty tubes (Niknejad et al. 2013, 2012; Yan et al. 2014; Elahi et al. 2017). Moreover, the PU foam filler could also bring more regular deformation mode as compared to empty ones, which could be attributed to the interaction effect between the foam filler and tube (Niknejad et al. 2013; Hanssen et al. 2000; Song et al. 2005). The absorbed energy of foam-filled circular tube under axial loading was generally higher as compared to that under lateral loading, thus attracting a lot of interest (Rezaei et al. 2015; Niknejad et al. 2015; Haorongbam et al. 2017). It was observed that PU foam filler could lead to deformation mode change of aluminum square tubes under axial crushing (Hussein et al. 2017). In terms of PU foam-filled circular composite tubes, the specific energy absorption was shown to increase with smaller diameter to thickness ratio

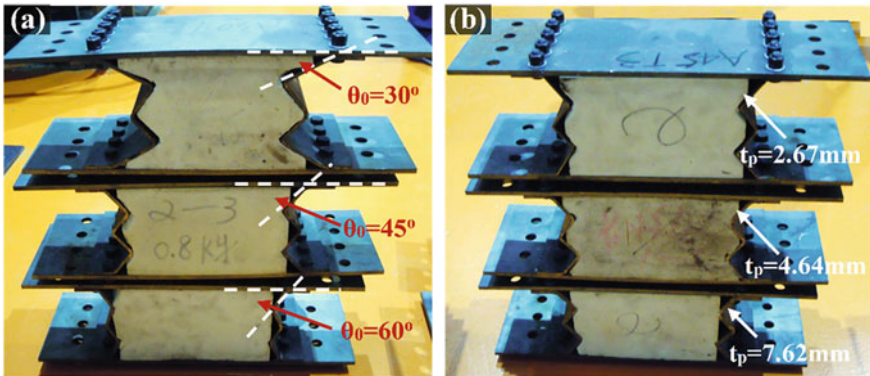


**Fig. 2.1** Type III energy absorption connectors with varying **a** angle  $\theta_0$  and **b** MP plate thickness, reprinted from Wang et al. (2019), copyright 2022, with permission from Elsevier

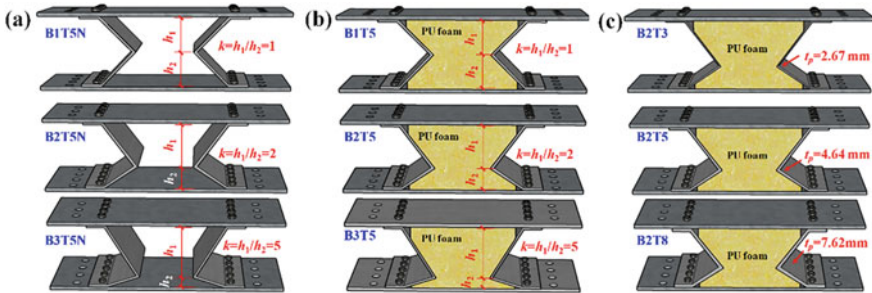


**Fig. 2.2** Type IV energy absorption connectors: **a** Without foam; **b** Variant parameter  $k$ ; **c** Variant plate thickness, reprinted from Wang et al. (2020), copyright 2022, with permission from Elsevier

(Zhang et al. 2018). The metallic tubes with grooves were generally employed to stabilize the deformation mode (Darvizeh et al. 2013; Daneshi and Hosseiniipour 2002), and the varying grooves distance could lead to the deformation mode change when studying grooved circular tubes with PU foam filler under axial crushing (Abedi et al. 2018). The foam-filled bi-tubular tubes were also developed to enhance the energy absorption capability of the foam-filled single tubes (Azarakhsh et al. 2015; Jafarian and Rezvani 2017). With regard to PU foam-filled energy absorbers under dynamic loading, fewer works were conducted. It was found by Onsalung et al. (2014) that the PU foam-filled circular aluminum tube exhibited the change of collapse modes as compared to the empty counterpart when subjected to impact loading. In addition, the foam filler could also reduce the force fluctuations owing to the smooth stress-strain curve of PU foam (Onsalung et al. 2014; Reid and Reddy 1986), and this effect was more pronounced under dynamic loading conditions (Reid and Reddy 1986). For the foam-filled connector under low-velocity impact loading that did not trigger the deformation mode change, the strain rate effect mainly contributed

to the improvement of energy absorption capability. Hence, the energy absorption capability of PU foam-filled absorbers was closely related to the strain rate effect (Zhou et al. 2016; Reid and Reddy 1986).

In this chapter, two types of PU foam-filled energy absorption connectors were developed, and their energy absorption performances were experimentally, numerically and analytical studied. Drop-weight impact tests on the PU foam-filled connectors were first conducted to obtain their deformation modes, force–displacement responses and energy absorption behaviors. Moreover, the main parameters that affect the energy absorption performances of the PU foam-filled connectors were also experimentally investigated. The analytical models incorporating strain rate effects of PU foam and steel were developed to predict the force–displacement responses of the proposed connectors.

## 2.2 Methodologies

### 2.2.1 *Experimental Approach*

The deformation modes and force–displacement responses of the proposed PU foam-filled connectors were obtained by conducting drop-weight impact tests. The details of specimens, test setup and instrumentation are described in this section.

#### 2.2.1.1 Test Specimens

Figures 2.1 and 2.2 present the type III and type IV energy absorption connectors designed for drop-weight impact tests. The connector consists of mild steel and PU foam as face plates and core material, respectively. Two MP plates (for type III connector) or AP plates (for type IV connector) were attached to the top and bottom flat plates, respectively, through bolt connection to form a four-sides enclosed space for the filling of PU foam. As shown in Table 2.1, Eight type III connectors were prepared for the impact loading tests, and the investigated parameters include angle  $\theta_0$  (the angle between MP plate and flat plate in Fig. 2.3), MP plate thickness and PU foam filler. The detailed geometry of the fabricated type III connector is illustrated in Fig. 2.3. It should be mentioned that the MP plate is designed with different lever arms (i.e., the lever arm of 1–2 is twice of that of 2–3) to ensure the successive development of plastic hinges at the corners and stabilize the deformation mode of the MP plate. This will be further discussed in Sect. 2.3, together with the deformation modes and force–displacement responses of type III connectors. With regard to type IV connectors, there are eight specimens being fabricated, and the investigated parameters include geometric parameter of AP plate  $k$ , AP plate thickness and PU foam filler, as shown in Table 2.1. The geometric parameter  $k$ , which is employed to describe the shape of the pleated plate, is illustrated in Figs. 2.2

**Table 2.1** Geometries of PU foam-filled energy absorption connectors

Type III connector	$\theta_0$ (°)	$t_p$ (mm)	PU foam	Drop height (m)
A30t5	30	4.64	Yes	5.3
A45t5	45	4.64	Yes	7.0
A60t5	60	4.64	Yes	8.1
A45t3	45	2.67	Yes	4.3
A45t8	45	7.62	Yes	10.0
A30t5N	30	4.64	No	1.9
A45t5N	45	4.64	No	4.4
A60t5N	60	4.64	No	5.6
Type IV connector	$k$	$t_p$ (mm)	PU foam	Drop height (m)
B1T5	1:1	4.64	Yes	5.1
B2T5	2:1	4.64	Yes	5.1
B3T5	5:1	4.64	Yes	6.3
B2T3	2:1	2.67	Yes	5.1
B2T8	2:1	7.62	Yes	7.3
B1T5N	1:1	4.64	No	1.7
B2T5N	2:1	4.64	No	2.6
B3T5N	5:1	4.64	No	4.2

Note  $\theta_0$ —Angle between MP plate and flat plate;  $t_p$ —MP/AP plate thickness;  $k$ —Geometric parameter of AP plate

**Fig. 2.3** Dimensions of type III connectors (unit: mm), reprinted from Wang et al. (2019), copyright 2022, with permission from Elsevier

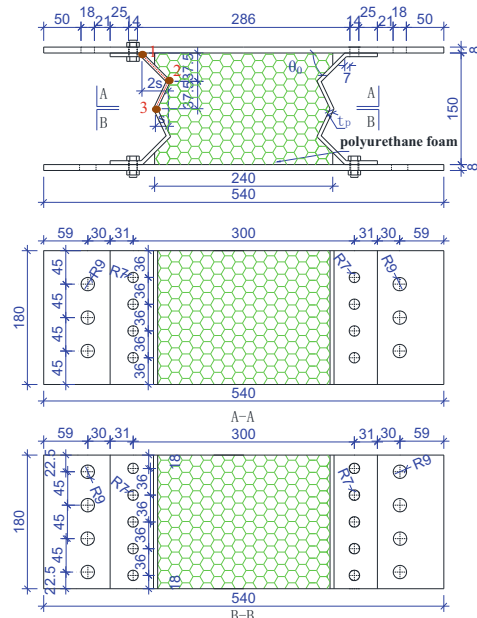


**Fig. 2.4** Dimensions of type IV connectors (unit: mm), reprinted from Wang et al. (2020), copyright 2022, with permission from Elsevier

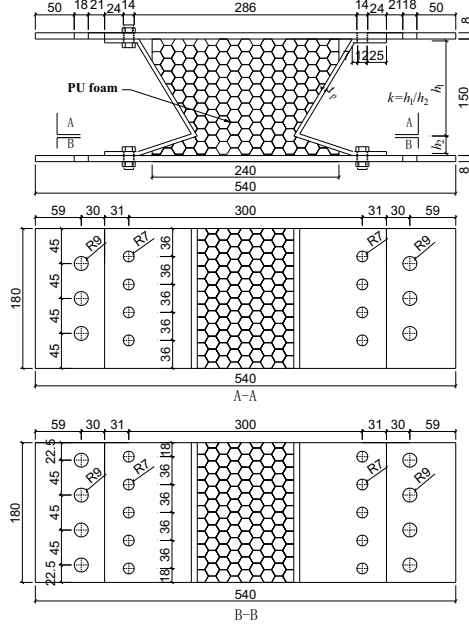


**Table 2.2** Material parameters of mild steel and PU foam

Mild steel	$E_y$ (GPa)	$\sigma_y$ (MPa)	$\sigma_u$ (MPa)
$t_p = 2.67$ mm	200	298.3	430.7
$t_p = 4.64$ mm	200	292.4	442.4
$t_p = 7.62$ mm	200	282.5	427.5
PU foam	$\rho_f$ (g/cm <sup>3</sup> )	$\sigma_p$ (MPa)	$E_f$ (MPa)
—	0.11	0.79	29.6

Note  $E_y$ ,  $E_f$ —Young's modulus of steel and PU foam;  $\sigma_y$ ,  $\sigma_u$ —Yield and ultimate stress of mild steel;  $\rho_f$ ,  $\sigma_p$ —Density and yield stress of PU foam

and 2.4. The material properties of PU foam and mild steel used to fabricate the connectors are given in Table 2.2, and they were determined via conducting uniaxial compression loading test and tensile coupon test, respectively.

### 2.2.1.2 Test Setup and Instrumentation

Figure 2.5 presents the test setup and instrumentations. The impact tests were conducted via employing a drop-weight impact test system. As illustrated in Fig. 2.5, the specimen was firstly bolted to a 30-mm-thick steel plate on the top and bottom in order to prevent bending of the top plate of the connector during impact. Then, the specimen was placed on a force transducer which was seated on the rigid support.

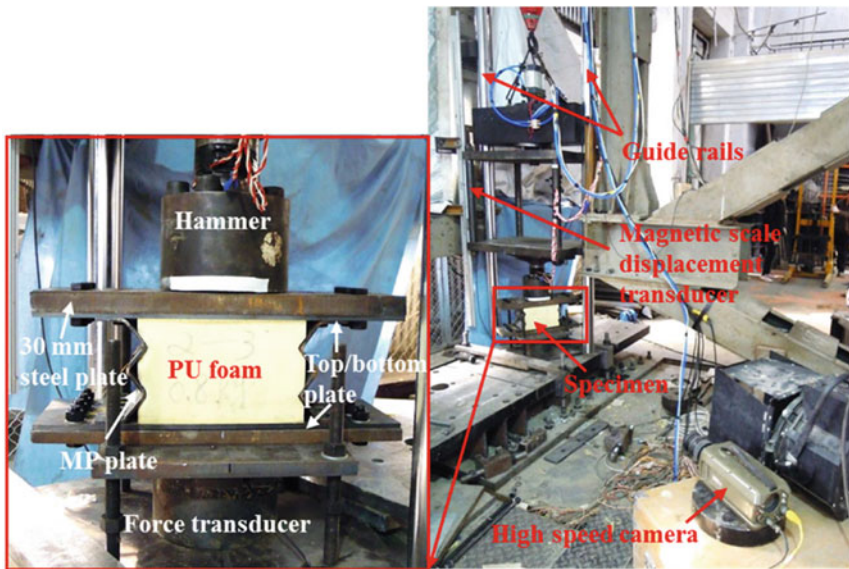


**Fig. 2.5** Drop-weight impact test setup and instrumentation, reprinted from Wang et al. (2019), copyright 2022, with permission from Elsevier

The 400 kg hammer was lifted up to the pre-determined height and dropped freely along the vertical guide rails to hit the connector. The piezoelectric force transducer with measuring range of 600 kN was placed below the connector to record the pure force. To ensure that all the tested connectors could reach densification and the maximum impact force was smaller than the allowable value of piezoelectric force transducer, the trial numerical analyses were carried out to obtain the drop height for each connector (as given in Table 2.1) via assuring the FE-calculated impact force within the range of 550–600 kN. The magnetic scale displacement transducer was utilized to measure displacement of the hammer. In addition, the high-speed camera was utilized to capture the deformation process during impact with a speed of 2000 frames per second.

### 2.2.2 Finite Element Models

The explicit code in LS-DYNA was used to reproduce the responses of the tested PU foam-filled connectors under impact loading, and the FE model of the typical PU foam-filled connector is given in Fig. 2.6. The PU foam, hammer and support were modeled with eight-node hexahedral element with reduced integration, and the MP plates and flat plates were modeled with shell element with five integration points

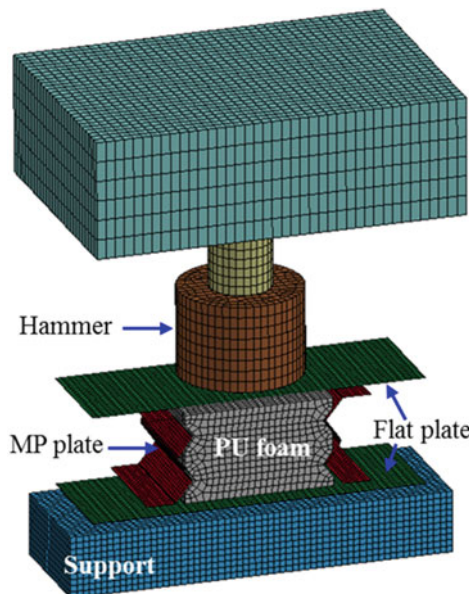


**Fig. 2.6** FE model of PU foam-filled connector under drop-weight impact loading, reprinted from Wang et al. (2019), copyright 2022, with permission from Elsevier

in the thickness direction. The contacts between two parts were treated via “master-slave” contact options, which could be defined in LS-DYNA with surface to surface contact option. The dynamic and static friction coefficients between all the contact surfaces were selected to be 0.2. The bolt connection in the specimens was simulated by utilizing the keyword \*CONTACT\_TIED\_SHELL\_EDGE\_TO\_SURFACE. To apply an impact loading, the hammer was defined with an initial velocity via the keyword \*INITIAL\_VELOCITY\_GENERATION.

The Piecewise Linear Plastic material model (MAT\_24) was chosen to model the mechanical behavior of mild steel, and the input true stress–effective plastic strain curves are given in Fig. 2.7a. The Cowper-Symonds model was chosen to enhance the yield stress (as defined in Eq. (1.8)), and the strain rate parameters  $C$  and  $P$  were defined as  $802\text{ s}^{-1}$  and 3.585 for mild steel (Abramowicz and Jones 1986). PU foam also exhibits strain rate dependency. Hence, the Modified Crushable Foam model (MAT\_163), which is allowed to define the yield stress to be a formula of volumetric strain as well as volumetric strain rate, was employed to model PU foam. To account for strain rate effect, the yield stress–volumetric strain curves corresponding to variant strain rates need to be defined. As given in Fig. 2.7b, the yield stress–volumetric strain curve of PU foam with strain rate of  $8\text{e}{-4}\text{ s}^{-1}$  was determined by conducting uniaxial compression loading tests, and the yield stress–volumetric strain curves for other strain rates could be determined by scaling reference yield stress–volumetric strain curve with a factor as (Jeong et al. 2012)

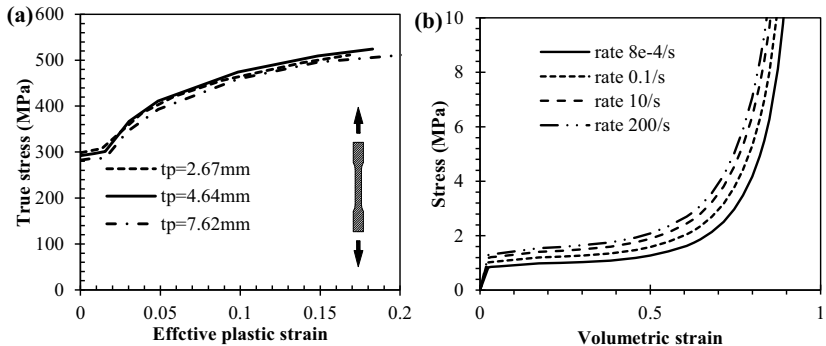


**Fig. 2.7** Input stress–strain curves of: **a** mild steels and **b** PU foam, reprinted from Wang et al. (2019), copyright 2022, with permission from Elsevier

$$1 + (a_0 + b_0 \varepsilon) \ln\left(\frac{\dot{\varepsilon}}{\dot{\varepsilon}_0}\right) \quad (2.1)$$

where the strain rate parameters  $a_0$  and  $b_0$  are 0.0430 and 0.0165, respectively, and the reference strain rate  $\dot{\varepsilon}_0$  is  $8e-4 \text{ s}^{-1}$ .

## 2.3 Results and Discussions

### 2.3.1 FE Model Validation

Figures 2.8 and 2.9 present the force–displacement responses of the tested connectors obtained from FE analyses and impact tests, and generally well matches between them can be observed. However, there are still slight differences between the numerical and experimental results. This may be caused by the geometric imperfections of the fabricated connectors. Generally, the PU foam-filled connectors show better agreement as compared to empty connectors, as shown in Figs. 2.8 and 2.9. This is because the PU foam-filled connectors are less sensitive to the geometric imperfections of MP/AP plates owing to the presence of PU foam. In addition, the material parameters defined in the FE model (e.g., strain rate parameters of mild steel and PU foam) may slightly differ from those in the experiments, which can also result in the differences between the numerical and experimental results. The deformation processes of the two type III connectors (one with PU foam and the other without PU foam) obtained from FE predictions are also validated against the test observations in Fig. 2.10, and the FE model is able to accurately capture the deformation shapes of type III connectors. The FE-predicted deformation processes of type IV connectors are presented in Fig. 2.11, which are close to the test results in Fig. 2.15. In addition, Fig. 2.12 exhibits the plastic strain contours of the AP plate of type IV

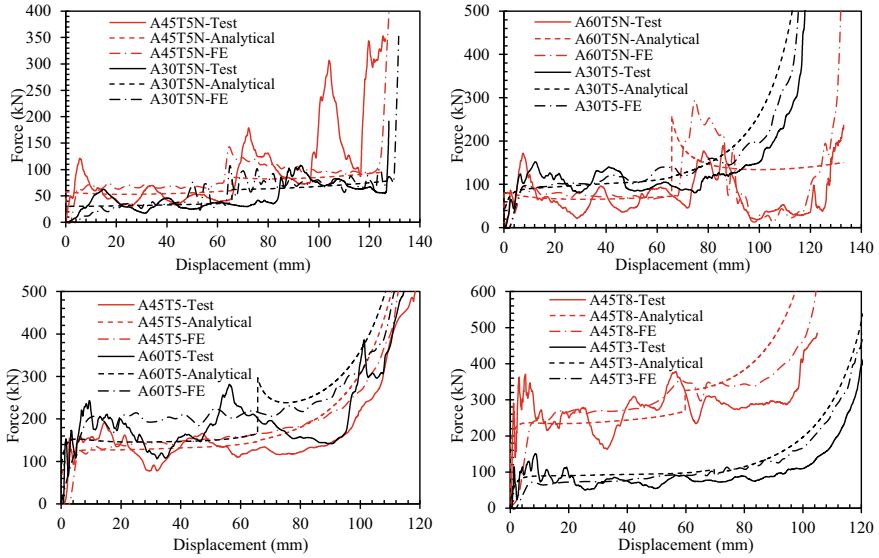


**Fig. 2.8** Comparison of force–displacement curves of type III connectors obtained from test, FE and analytical models, reprinted from Wang et al. (2019), copyright 2022, with permission from Elsevier

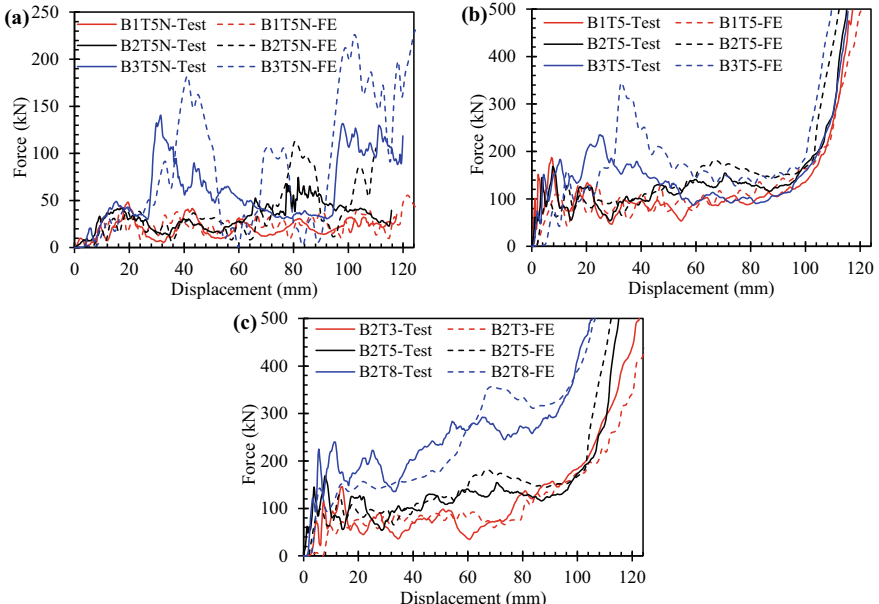


**Fig. 2.9** Comparison of force–displacement curves of type IV connectors obtained from test and FE model: **a** Variant pleated plate parameter  $k$  without foam; **b** Variant pleated plate parameter  $k$  with foam; **c** Variant pleated plate thickness with foam, reprinted from Wang et al. (2020), copyright 2022, with permission from Elsevier

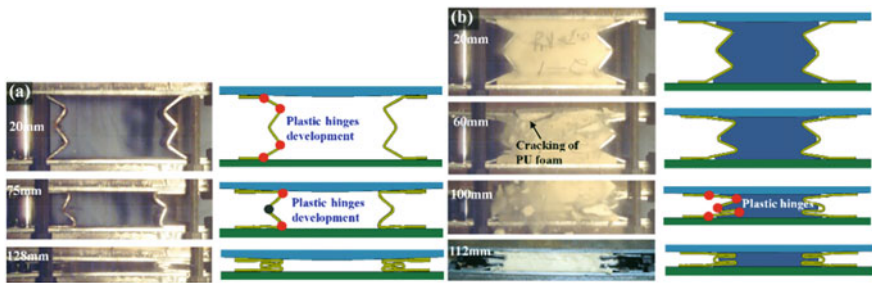


**Fig. 2.10** Comparison of deformation processes of type III connectors between test and FE: **a** without PU foam; **b** with PU foam, reprinted from Wang et al. (2019), copyright 2022, with permission from Elsevier

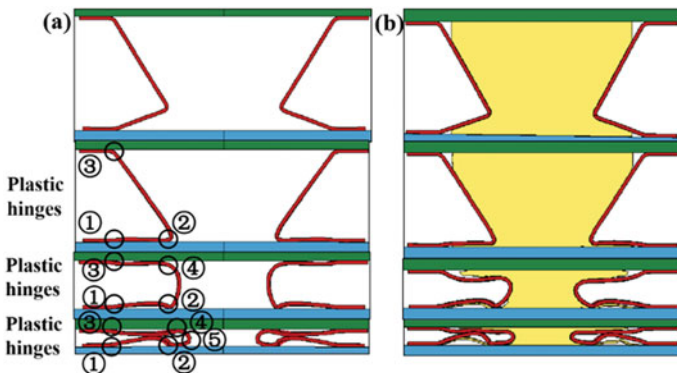


**Fig. 2.11** Deformation processes of type IV connectors from FE analyses: **a** without PU foam; **b** with PU foam, reprinted from Wang et al. (2020), copyright 2022, with permission from Elsevier

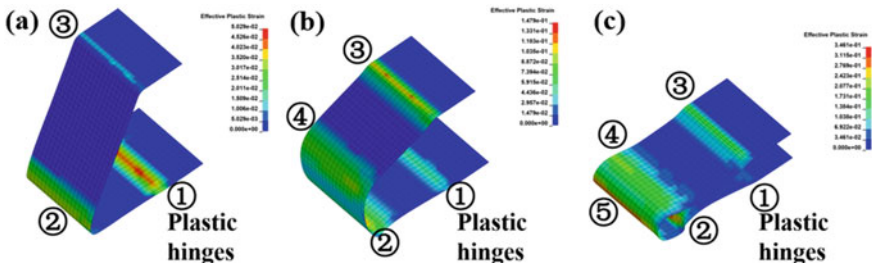


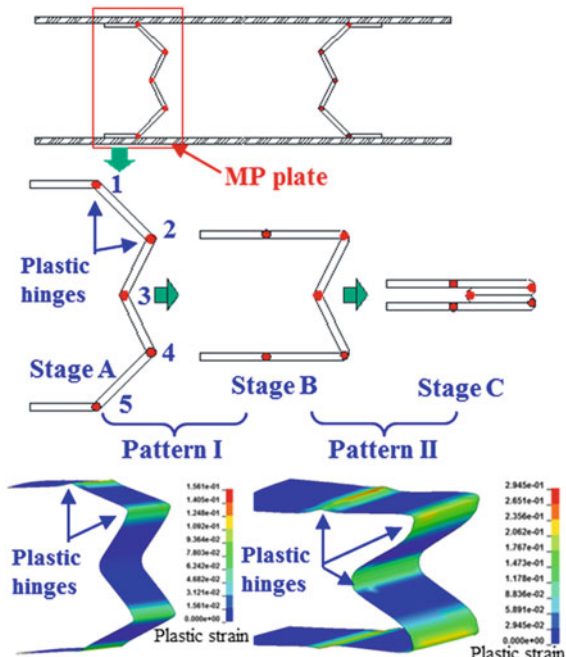
**Fig. 2.12** Plastic strain contours of the AP plate of type IV connector: **a** Deformation stage I; **b** Deformation stage II; **c** Deformation stage III, reprinted from Wang et al. (2020), copyright 2022, with permission from Elsevier

connector. The formation and rotation process of plastic hinges are consistent with the experimental observations. From above comparisons, the established FE models of the tested connectors are deemed to be reasonable and can be used for the further calculation and in-depth analysis.

### 2.3.2 Deformation Mode

Figure 2.10a illustrates the typical deformation modes of the type III connector without PU foam, and continuous plastic deformation of the MP plate in way of plastic hinge rotation at the corners can be observed. Generally, two evidently different deformation patterns can be identified during impact, which are more clearly illustrated in Fig. 2.13. Since the lever arm of 1–2 is longer than that of 2–3, the plastic hinges are firstly formed at point 1, 2, 4 and 5, and the plastic hinges keep rotating with continuous compression. This is called deformation pattern I (from stage A to B in Fig. 2.13). When the MP plate touches the top and bottom plate, the plastic hinge at point 3 is developed and rotates together with plastic hinges at point 2 and 4. However, the plastic hinges at point 1 and 5 stop rotating. This is called deformation pattern II (from stage B to C in Fig. 2.13). Figure 2.10a shows that the deformation patterns of the type III connector without PU foam are consistent to the designed deformation patterns, showing two deformation patterns with boundary displacement

**Fig. 2.13** Deformation patterns of MP plate under impact loading, reprinted from Wang et al. (2019), copyright 2022, with permission from Elsevier



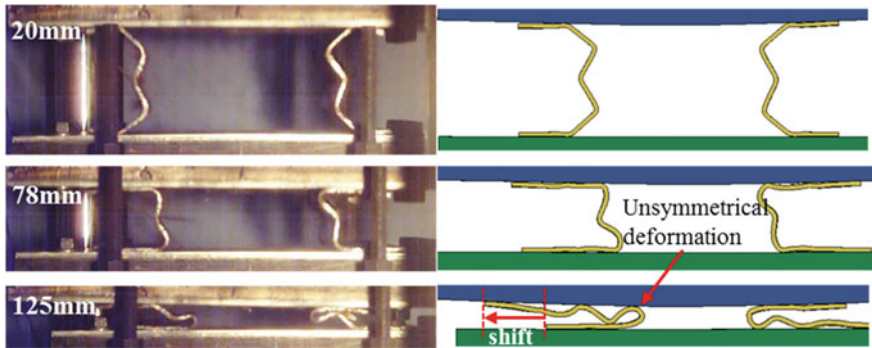


**Fig. 2.14** Deformation mode of connector A60T5N, reprinted from Wang et al. (2019), copyright 2022, with permission from Elsevier

of 75 mm. The typical deformation mode of the type III energy connector with PU foam is illustrated in Fig. 2.10b. Besides the plastic deformation of MP plates, the PU foam compression also helps to absorb impact energy. Comparing the deformation patterns of MP plates of type III connectors with and without PU foam reveals that the presence of PU foam does not change the plastic hinge locations (at the corners); whereas it slightly changes the plastic hinge rotation angle for each point. Generally, the total plastic hinge rotation angles of MP plates for type III connectors with and without PU foam are almost identical, which can be observed from their permanent deformations, as shown in Fig. 2.10.

All the tested type III connectors show designed deformation mode except for the connector A60T5N which experiences unsymmetrical deformation with shifting between top plate and bottom plate, as illustrated in Fig. 2.14. In fact, A60T5N nearly follows the designed deformation mode with plastic hinges developed at point 1, 2, 4 and 5 (refer to Fig. 2.13 for the locations of plastic hinges) within deformation pattern I when the displacement is less 78 mm. However, the plastic hinge at point 3 is not developed with further compression due to the evident shifting between the top and bottom plate. This also leads to the sudden drop of impact force, as shown in Fig. 2.8. The unsymmetrical deformation of A60T5N can be induced by geometric imperfection of the fabricated specimen. In fact, the connector A60T5N with highest angle  $\theta_0$  (or shortest level arm) among the tested type III connectors is more sensitive to the geometric imperfection and prone to behave unstable deformation mode during impact. However, the presence of PU foam seems to stabilize the deformation mode, as the connector A60T5 with same angle  $\theta_0$  does not experience unsymmetrical deformation shape.

The typical deformation modes and distributions of plastic hinges of the type IV connectors with and without PU foam observed from drop-weight impact tests are shown in Fig. 2.15. Because of the asymmetry of pleated plates, the deformation mode of the type IV connector without PU foam can be divided into three stages,

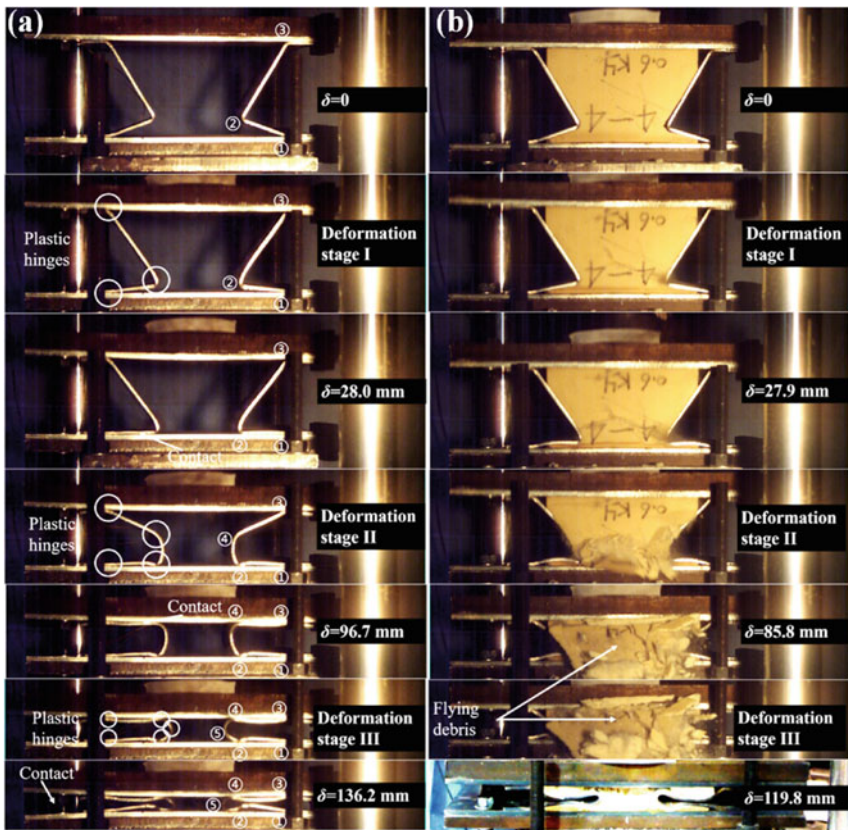


**Fig. 2.15** Deformation processes of type IV connectors: **a** without PU foam; **b** with PU foam, reprinted from Wang et al. (2020), copyright 2022, with permission from Elsevier

as illustrated in Fig. 2.15a. At the first stage, three pairs of plastic hinges occur at point 1, 2 and 3. When the plastic hinge at point 2 and flat plate come into contact, the deformation mode enters the second stage, and the critical displacement between stage I and II is defined as  $D_1$ . At this stage, the long arms of AP plates start to buckle, and subsequently the forth pair of plastic hinges occur at point 4. Meanwhile, plastic hinges at point 3 continue rotating, plastic hinges at 2 rotate reversely, and plastic hinges at point 1 stop rotating. When plastic hinges at point 4 and flat plate come into contact, the deformation mode enters the third stage, and the critical displacement between stage II and III is defined as  $D_2$ . At this stage, the AP plates buckle again, and subsequently the fifth pair of plastic hinges occurs at point 5. Meanwhile, plastic hinges at point 2 continue rotating, plastic hinges at point 4 rotate reversely, and plastic hinges at point 3 stop rotating.

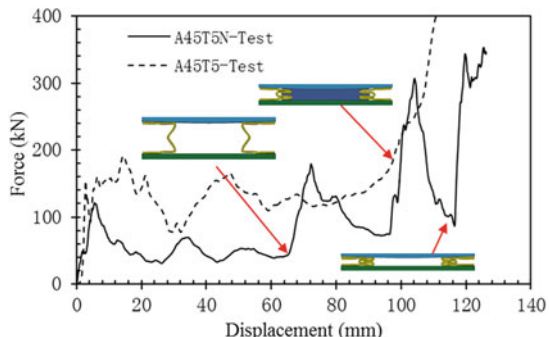
As for the deformation mode of the type IV connector with PU foam shown in Fig. 2.15b, it is similar to the deformation mode of the type IV connector without PU

foam in Fig. 2.15a, which may be owing to the significant difference of the Young's modulus between PU foam and steel. Hence, the deformation mode of the type IV connectors with PU foam can also be divided into three stages on the basis of the sequence of plastic hinge development. However, the PU foam filler can reduce the critical displacements of  $D_1$  and  $D_2$ , i.e., the plastic hinges at point 4 and 5 of type IV connectors with PU foam form earlier as compared to the counterparts without PU foam, since the AP plates cannot completely contact with flat plates.

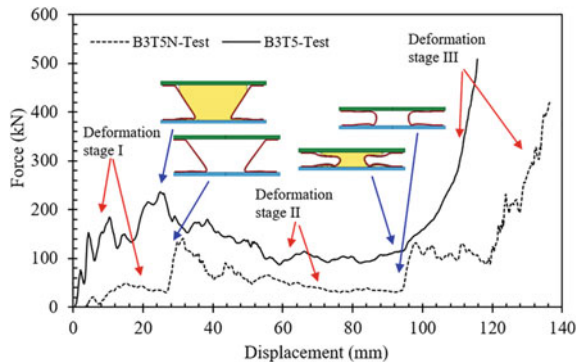
### 2.3.3 Force–Displacement Responses

Figure 2.16 presents the typical force–displacement curves of type III connectors with and without PU foam. The PU foam filler is found to significantly increase the crushing force, but leads to slight decrease of densification displacement. Both the two curves show initial peak force and followed by sudden drops with increase of displacement. The observed fluctuations of the force–displacement curves are mainly induced by the inertial force. Without considering the inertial force, the analytical model can provide smooth curves, as given in Fig. 2.8. For the type III connector without PU foam, the force shows sudden rise with displacement of 65 mm when the MP plate start to touch the top/bottom plate and the deformation pattern shift from I to II. This is because the lever arm of 2–3 is smaller than that of 1–2 (shown in Fig. 2.13) and the force is mainly governed by the lever arm of 2–3 at this moment. Relatively smoother curve can be observed for the PU foam-filled connector owing to the smooth stress–strain curve of PU foam, as given in Fig. 2.7b. Figure 2.8 shows that all the tested type III connectors have three deformation processes, including initial elastic deformation, following plastic deformation and final inner surface contact (without PU foam) or PU foam densification (with PU foam) (Wang et al. 2018). The displacement range at plastic deformation stage is significantly higher than the other two deformation stages. In addition, the varying magnitude of crushing force is not significant at this stage, especially for the type III connectors with PU foam. Both of them are of benefit to an energy absorber. Figure 2.8 also shows that the force

**Fig. 2.16** Typical force–displacement curves of type III connectors with and without PU foam, reprinted from Wang et al. (2019), copyright 2022, with permission from Elsevier



**Fig. 2.17** Typical force–displacement curves of type IV connectors with and without PU foam, reprinted from Wang et al. (2020), copyright 2022, with permission from Elsevier



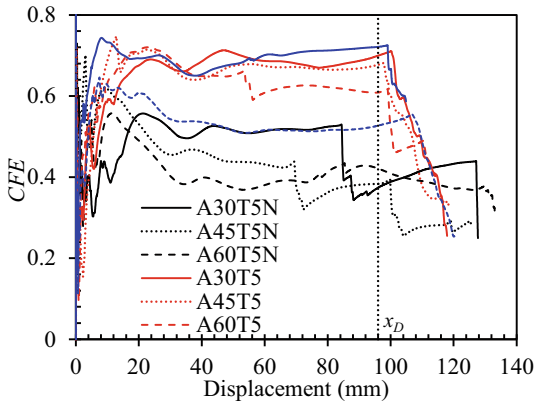
and energy absorption capability can be generally increased by increasing angle  $\theta_0$  and MP plate thickness as well as filling the connector with PU foam.

The typical force–displacement curves of type IV connectors with and without PU foam are presented in Fig. 2.17. For the connector B3T5N without PU foam, when the displacement of connector,  $\delta$ , reaches 26.9 and 94.2 mm, the force–displacement curve shows sudden changes because the AP plates are in contact with flat plates. Meanwhile, AP plates start buckling, and the connector enters the next deformation stage. The curve also exhibits that the force tends to decrease during the deformation stage II and III, which may be induced by the continuous increase of arm length. For the connector B3T5 with PU foam, there is no significant sudden change in the force versus displacement curve because of the presence of PU foam which shows smooth stress–strain response. When displacement,  $\delta$ , reaches 25.2 mm, a peak value of the force appears, and the critical point corresponding to the boundary of stage I and II ( $D_1$ ) is near the peak point. However, the critical displacement corresponding to the boundary of stage II and III ( $D_2$ ) is not evident, owing to the presence of PU foam. For the deformation stage I, the PU foam is in the elastic region at first, and the force increases rapidly. When the PU foam enters the plateau region, the increasing rate of the force slows down. For the deformation stage II, the force shows decrease with increasing displacement. This is because the force contributed by the plastic deformation of AP plates decreases, and the force contributed by PU foam, which is still within the plateau region, increases slowly. For the deformation stage III, the force shows continuously rising because of the densification of PU foam.

### 2.3.4 Energy Absorption Performance of Type III Connector

Several energy absorption parameters, including energy absorption (*EA*), specific energy absorption (*SEA*) and crushing force efficiency (*CFE*) were employed to quantitatively evaluate the energy absorption performances of type III connectors and reveal the corresponding influential parameters. *EA*, *SEA* and *CFE* can be obtained

**Fig. 2.18** *CFE* versus displacement curves of type III connectors, reprinted from Wang et al. (2019), copyright 2022, with permission from Elsevier



from Eqs. (1.1)–(1.3). To fairly assess the effect of PU foam filler on *EA*, *SEA* and *CFE*, the identical densification displacement should be determined for all the eight type III connectors. It can be observed from *CFE*–displacement curves in Fig. 2.18 that the *CFE* value decreases when the peak crushing force (*PCF*) shows monotonic increase with increasing displacement. Hence, the *CFE* value will show sudden drop after densification of the connector when the force increase suddenly and monotonically. By carefully examine all the tested type III connectors, the densification displacement is chosen to be 96 mm, which can ensure all the densification displacements of the tested connectors appearing after this value, as illustrated in Fig. 2.18.

#### 2.3.4.1 Effect of PU Foam Filler

Table 2.3 summarizes the values of *EA*, *SEA* and *CFE* corresponding to densification displacement of 96 mm for all the tested type III connectors. The foam filler is found to evidently improve the energy absorption performance via increasing *EA*, *SEA* and *CFE*. The average increasing percentages of *EA*, *SEA* and *CFE* for the three type III connectors without PU foam (i.e., A30T5N, A45T5 and A60T5N) are 122.5%, 93.1% and 69.4%, respectively, by filling PU foam. The 122.5% increase of *EA* indicates that PU foam filler contributes more than half of the absorbed energy. The increase of *SEA* by filling PU foam is mainly owing to the higher *SEA* of PU foam than that of MP plate. The FE-calculated *SEA* values of PU foam and MP plate are 12.62 kJ/kg and 1.12 kJ/kg, 12.44 kJ/kg and 2.15 kJ/kg, and 15.40 kJ/kg and 3.09 kJ/kg for A30T5, A45T5 and A60T5, respectively. The averaged *SEA* of PU foam is 6.36 times of *SEA* of MP plate. The *CFE* is also improved with the presence of PU foam, as the PU foam filler can smooth the force–displacement curves, as shown in Fig. 2.8.

**Table 2.3** Energy absorption parameters of PU foam-filled energy absorption connectors

Specimen	EA (kJ)	SEA (kJ/kg)	CFE
A30T5N	3.87	0.88	0.37
A45T5N	6.59	1.80	0.38
A60T5N	7.64	2.30	0.42
A30T5	10.21	2.08	0.70
A45T5	12.45	2.93	0.68
A60T5	16.43	4.15	0.61
A45T3	7.64	2.68	0.53
A45T8	26.20	4.13	0.72
B1T5	8.01	1.82	0.48
B2T5	9.76	2.18	0.66
B3T5	11.55	2.52	0.56
B2T3	6.557	2.34	0.50
B2T8	19.026	2.76	0.74
B1T5N	1.679	0.44	0.40
B2T5N	2.641	0.68	0.40
B3T5N	4.357	1.09	0.35

Note EA—Energy absorption; SEA—Specific energy absorption;  
CFE—Crushing force efficiency

#### 2.3.4.2 Effect of MP Plate Thickness

Table 2.3 shows that both *EA* and *SEA* of type III connectors can be improved by increasing MP plate thickness, whereas the variation of *CFE* by changing MP plate thickness is insignificant. The *EA* and *SEA* are improved by 243.1% and 53.9%, respectively, by increasing the thickness of MP plate from 2.67 to 7.62 mm. thicker MP plate means higher plastic bending moment (or accumulated plastic strain energy), which leads to the improvement of *EA*. In addition, the increasing rate of plastic bending moment is higher than that of mass via increasing MP plate thickness, which results in the improved *SEA* of the connector.

#### 2.3.4.3 Effect of Angle $\theta_0$

As for the influence of angle  $\theta_0$  on energy absorption performances of type III connectors, increasing angle  $\theta_0$  is found to result in higher *EA* and *SEA*, as shown in Table 2.3. The values of *EA* and *SEA* of the type III connector without PU foam are increased by 97.5% and 161.3%, respectively, by increasing angle  $\theta_0$  from 30° to 60°. This is because increasing angle  $\theta_0$  leads to higher total plastic hinge rotation angles, and thus resulting in improved *EA*. In addition, the total length (or mass) of the MP plate is reduced with increasing angle  $\theta_0$ , which results in more significant increase of *SEA*.

as compared to *EA*. In terms of the type III connector with PU foam, less significant improvement of *EA* and *SEA* is observed, i.e., 60.9 and 99.6% increase of *EA* and *SEA* via increasing angle  $\theta_0$  from 30° to 60°. This is because the improved *EA* of the MP plate via increasing total plastic hinge rotation angle is more significant as compare to the improved *EA* of PU foam through increased volume of PU foam. Although the improved energy absorption performance of the type III connector without PU foam is more significant than that of the connector with PU foam, the angle  $\theta_0$  should be limited to an acceptable value to prevent the unsymmetrical deformation mode. Moreover, the PU foam filler can also help to stabilize the deformation mode.

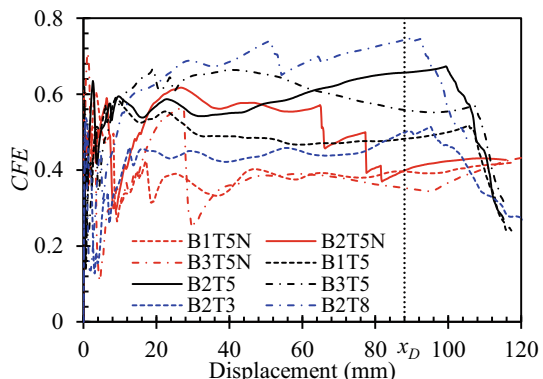
### 2.3.5 Energy Absorption Performance of Type IV Connector

The energy absorption parameters, *EA*, *SEA* and *CFE*, were employed to evaluate the energy absorption performances of type IV connectors, and *CFE*-displacement curves were also referred to determine densification displacement of the connectors. As shown in Fig. 2.19, the densification displacement of all the type IV connectors can be determined as 88 mm.

#### 2.3.5.1 Effect of PU Foam Filler

Table 2.3 gives the values of energy absorption parameters with  $x_D$  of 88 mm for all the type IV connectors. Because of the good energy absorption capability of PU foam, the increasing percentages of *EA* for the three connectors (B1T5N, B2T5N and B3T5N) are 376.8%, 269.4% and 165.0%, respectively, by filling them with PU foam, as shown in Table 2.3. In addition, the corresponding increasing percentages of *SEA* are 314%, 222% and 132%, respectively, owing to the low density of PU foam. Moreover, the *CFE* is also improved because the force fluctuation of the connectors

**Fig. 2.19** *CFE* versus displacement curves of type IV connectors, reprinted from Wang et al. (2020), copyright 2022, with permission from Elsevier



with PU foam is less significant as compared to the connectors without PU foam, i.e., the force–displacement curve of the connector becomes smoother with the presence of PU foam.

### 2.3.5.2 Effect of Geometric Parameter $k$

For the type IV connectors without PU foam, Table 2.3 shows that  $EA$  and  $SEA$  increase by 57.3% and 53.5%, respectively, by changing symmetric pleated plates (B1T5N) into AP plates (B2T5N) owing to the increase in the number of plastic hinges as well as the total plastic hinge rotation angle. In addition, higher parameter  $k$  can also lead to 65% and 61% increase of  $EA$  and  $SEA$ , respectively, by comparing the specimen B3T5N and B2T5N, as higher parameter  $k$  leads to higher total plastic hinge rotation angle with the same crushing displacement. However, the  $CFE$  shows decrease when the parameter  $k$  is increased, since the force–displacement curve of the connector with higher parameter  $k$  shows higher peak crushing force. For the type IV connectors with PU foam, the energy absorption parameters ( $EA$  and  $SEA$ ) of specimen B2T5 are 21.9% and 19.6% higher than those of B1T5, and these energy absorption parameters of specimen B3T5 are 18.3% and 15.8% higher than those of B2T5. The improvement of energy absorption parameters for the connectors with PU foam is less significant as compared to the connectors without PU foam. This indicates that the improvement of energy absorption performance by increasing geometric parameter  $k$  is mainly contributed by pleated plates.

### 2.3.5.3 Effect of AP Plate Thickness

Table 2.3 shows that  $EA$  of the type IV connector is significantly improved by increasing AP plate thickness, owing to the increased energy absorption from plastic hinge rotation of the AP plate with higher plastic moment capacity. For the same reason, the  $SEA$  of specimen B2T8 is 26.5% higher than that of specimen B2T5. However, the  $SEA$  of specimen B2T5 is lower than specimen B2T3 because of the lower mass of specimen B2T3. Moreover, increasing AP plate thickness also leads to higher  $CFE$ , since the fluctuation of force is not significant as compared to its increased mean crushing force.

## 2.4 Analytical Model

The force–displacement curves of PU foam-filled connectors are necessary to evaluate their energy absorption performances and conduct the blast resistant design when employing the proposed connectors as blast energy absorber in Fig. 1.1b. The following assumptions are employed to facilitate the calculations: (a) nominal stress–strain relation of steel employed for the connectors pertains to rigid-linear

strain-hardening behavior, (b) stress state of the MP/AP plate is plane stress and (c) PU foam is uniformly compressed and its influence on the deformation pattern of the MP/AP plate is negligible.

### 2.4.1 Analytical Model for Type III Connector

#### 2.4.1.1 Energy Absorption from MP Plate

As observed from the experimental and numerical results, the energy absorption from MP plates is through plastic hinge rotation, and two different deformation patterns during impact is determined, as shown in Fig. 2.20. Based on the observed deformation patterns,  $EA$  of the type III connector without PU foam is first formulated with respect to displacement. Then, the force–displacement relation can be obtained by differentiating  $EA$  with respect to displacement. In addition, the varying Dynamic Increase Factor (DIF) with respect to transient strain rate is included into the analytical model to accurately consider the strain rate effect of MP plates.

The variation of internal energy for one plastic hinge of the MP plate considering strain rate effect is presented in Eq. (1.13). It is noted that the energy absorption rate of each plastic hinge may vary with different deformation patterns, and therefore the formulae for describing the force–displacement relationships of the type III connector without PU foam in different deformation patterns are calculated separately and given as below.

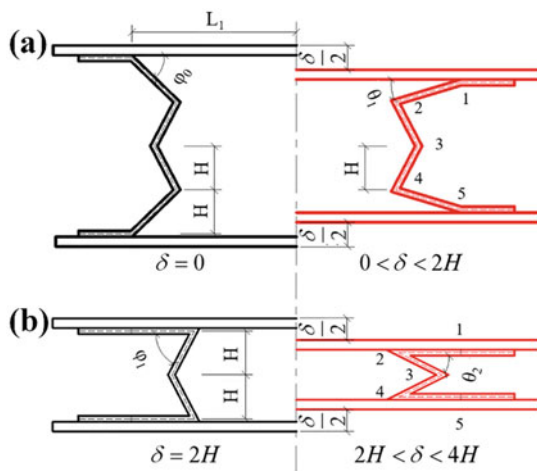


**Fig. 2.20** Deformation patterns of the type III connector: **a** Deformation pattern I; **b** Deformation pattern II, reprinted from Wang et al. (2019), copyright 2022, with permission from Elsevier

In the stage of deformation pattern I (refer to Fig. 2.20a), namely,  $0 \leq \delta \leq 2H$ , the two MP plates totally have eight plastic hinges (point 1, 2, 4 and 5) rotating during crushing, and the rotation rates of all the plastic hinges are identical. Hence, the total force contributed by two MP plates within deformation pattern I ( $F_{p1}$ ) can be obtained as

$$\begin{aligned} F_{p1} &= 8 \frac{dU}{d\delta} \\ &= 8bt_{ph} \left[ \frac{\sigma_y t_p^2}{4} + \frac{E' \kappa_1 t_p^3}{12} + \frac{\sigma_y t_p^{1/P+2}}{2^{1/P+1}(1/P+2)} \left( \frac{\dot{\kappa}_1}{C} \right)^{1/P} \right. \\ &\quad \left. + \frac{E' \kappa_1 t_p^{1/P+3}}{2^{1/P+2}(1/P+3)} \left( \frac{\dot{\kappa}_1}{C} \right)^{1/P} \right] \frac{d\kappa_1}{d\delta} \end{aligned} \quad (2.2)$$

where  $\kappa_1$  and  $\dot{\kappa}_1$  are curvature change and its rate at the plastic hinge point 1 within deformation pattern I, and they can be formulated with respect to displacement ( $\delta$ ) and velocity ( $\dot{\delta}$ ) by referring to the geometric relation in Fig. 2.20a as follows:

$$\kappa_1 = (\varphi_0 - \theta_1)/t_{ph} \quad (2.3)$$

$$\theta_1 = \arcsin \frac{(H - \delta/2) \sin \varphi_0}{H} \quad (2.4)$$

$$\frac{d\kappa_1}{d\delta} = \left[ 2t_{ph} \sqrt{\left( \frac{H}{\sin \varphi_0} \right)^2 - \left( H - \frac{\delta}{2} \right)^2} \right]^{-1} \quad (2.5)$$

$$\dot{\kappa}_1 = -\frac{\dot{\theta}_1}{t_{ph}} = \dot{\delta} \left[ 2t_{ph} \sqrt{\left( \frac{H}{\sin \varphi_0} \right)^2 - \left( H - \frac{\delta}{2} \right)^2} \right]^{-1} \quad (2.6)$$

When the end of deformation pattern I is reached, i.e.,  $\delta_{Ie} = 2H$ , let  $\bar{\kappa}_1 = \kappa_1(\delta_{Ie})$ .

In the stage of deformation pattern II (refer to Fig. 2.20b), namely,  $2H < \delta < 4H$ , the plastic hinges at point 2, 3 and 4 rotate during crushing. It is noted that the rotation rates of plastic hinges at point 2 and 4 are identical, and the rotation rate at point 3 is double of point 2 and 4. Therefore, the force contributed by MP plates within deformation pattern II can be divided into two groups according to the plastic hinge rotation rates. They are given as

$$\begin{aligned} F_{p21} &= bt_{ph} \left[ \frac{\sigma_y t_p^2}{4} + \frac{E'(\kappa_2 + \bar{\kappa}_1)t_p^3}{12} + \frac{\sigma_y t_p^{1/P+2}}{2^{1/P+1}(1/P+2)} \left( \frac{\dot{\kappa}_2}{C} \right)^{1/P} \right. \\ &\quad \left. + \frac{E'(\kappa_2 + \bar{\kappa}_1)t_p^{1/P+3}}{2^{1/P+2}(1/P+3)} \left( \frac{\dot{\kappa}_2}{C} \right)^{1/P} \right] \frac{d\kappa_2}{d\delta} \end{aligned} \quad (2.7)$$

$$F_{p22} = 2bt_{ph} \left[ \frac{\sigma_y t_p^2}{4} + \frac{E' \kappa_2 t_p^3}{6} + \frac{\sigma_y t_p^{1/P+2}}{2(1/P+2)} \left( \frac{\dot{\kappa}_2}{C} \right)^{1/P} + \frac{E' \kappa_2 t_p^{1/P+3}}{2(1/P+3)} \left( \frac{\dot{\kappa}_2}{C} \right)^{1/P} \right] \frac{d\kappa_2}{d\delta} \quad (2.8)$$

where  $F_{p21}$  and  $F_{p22}$  are forces contributed by the rotation of plastic hinge at point 2 (or 4) and point 3, respectively. The unknown parameters in Eqs. (2.7) and (2.8) are given in Eqs. (2.9)–(2.11) according to the geometric relation in Fig. 2.20b.

$$\kappa_2 = \left[ \arcsin \left( \frac{H}{L} \right) - \arcsin \frac{2H - \delta/2}{L} \right] / t_{ph} \quad (2.9)$$

$$\frac{d\kappa_2}{d\delta} = \left[ 2t_{ph} \sqrt{L^2 - \left( 2H - \frac{\delta}{2} \right)^2} \right]^{-1} \quad (2.10)$$

$$\dot{\kappa}_2 = \dot{\delta} \left[ 2t_{ph} \sqrt{L^2 - \left( 2H - \frac{\delta}{2} \right)^2} \right]^{-1} \quad (2.11)$$

where  $L = H \sqrt{1 + \frac{1}{4\tan^2\varphi_0}}$ . Then, the total force contributed by two MP plates within deformation pattern II can be obtained as

$$F_{p2} = 4F_{p21} + 2F_{p22} \quad (2.12)$$

Hence, the force–displacement relation of the type III connector without PU foam ( $F_p$ ) can be summarized as

$$F_p = \begin{cases} F_{p1} & \delta \leq 2H \\ F_{p2} & 2H < \delta \leq 4H \end{cases} \quad (2.13)$$

#### 2.4.1.2 Energy Absorption from PU Foam

The experimental results showed that both PU foam compression and plastic deformation of MP plates contributed to the absorbed energy of the type III connector with PU foam. Hence, its total crushing force can be obtained by summing the forces contributed by MP plates and PU foam. Assuming the uniform compression of PU foam leads to the force contributed by PU foam ( $F_f$ ) as

$$F_f = -\sigma_f \frac{dV_c}{d\delta} \quad (2.14)$$

**Table 2.4** Material parameters of PU foam

$A$	$B$	$E$	$m$	$n$
0.7934	0.7469	43.29	5.122	1.209

where  $V_c$  and  $\sigma_f$  are current volume and compressive stress of PU foam, and  $\sigma_f$  can be formulated in Eq. (2.15) with the strain rate effect being considered (Jeong et al. 2012).

$$\sigma_f = \left[ 1 + (a_0 + b_0 \varepsilon) \ln\left(\frac{\dot{\varepsilon}_V}{\dot{\varepsilon}_0}\right) \right] \left[ A \left(1 - e^{-(E/A)\varepsilon_V(1-\varepsilon_V)^m}\right) + B \left(\frac{\varepsilon_V}{1-\varepsilon_V}\right)^n \right] \quad (2.15)$$

where  $A$ ,  $B$ ,  $E$ ,  $m$  and  $n$  are material parameters of PU foam and given in Table 2.4 via fitting the material test data. The reference strain rate  $\dot{\varepsilon}_0$  as well as strain rate parameters  $a_0$  and  $b_0$  are given in Sect. 2.2.2. The volumetric strain and strain rate can be given as follows:

$$\varepsilon = 1 - V_c/V_0 \quad (2.16)$$

$$\dot{\varepsilon} = -\frac{\dot{\delta}}{V_0} \frac{dV_c}{d\delta} \quad (2.17)$$

where  $\dot{\delta}$  is velocity, and  $V_0$  is initial volume of PU foam and can be obtained as

$$V_0 = \left( 8HL_1 - \frac{5H^2}{\tan \varphi_0} \right) b \quad (2.18)$$

The geometric properties in Eq. (2.12) can be found in Fig. 2.20, and the formulae of  $V_c$  and  $dV_c/d\delta$  in deformation pattern I and II are summarized as below.

In the stage of deformation pattern I, namely,  $0 \leq \delta \leq 2H$ , the current volume of PU foam and its differential with respect to displacement can be obtained as

$$V_c = \left[ 8HL_1 - 2\delta L_1 + \frac{H^2}{\tan \varphi_0} - (6H - \delta) \sqrt{\left(\frac{H}{\sin \varphi_0}\right)^2 - \left(H - \frac{\delta}{2}\right)^2} \right] b \quad (2.19)$$

$$\frac{dV_c}{d\delta} = \left[ -2L_1 + \sqrt{\left(\frac{H}{\sin \varphi_0}\right)^2 - \left(H - \frac{\delta}{2}\right)^2} + \frac{(\delta - 6H)(2H - \delta)}{4\sqrt{\left(\frac{H}{\sin \varphi_0}\right)^2 - \left(H - \frac{\delta}{2}\right)^2}} \right] b \quad (2.20)$$

In the stage of deformation pattern II, i.e.,  $2H < \delta < 4H$ , the current volume of PU foam and its differential with respect to displacement can be obtained as

$$V_c = \left[ 2L_1 - \frac{2H}{\sin \varphi_0} + \sqrt{\left(1 + \frac{1}{4 \tan^2 \varphi_0}\right) H^2 - \left(2H - \frac{\delta}{2}\right)^2} \right] (4H - \delta)b \quad (2.21)$$

$$\begin{aligned} \frac{dV_c}{d\delta} = & \frac{2Hb}{\sin \varphi_0} - 2L_1b - b \sqrt{\left(1 + \frac{1}{4 \tan^2 \varphi_0}\right) H^2 - \left(2H - \frac{\delta}{2}\right)^2} \\ & + \frac{(\delta - 4H)^2 b}{4 \sqrt{\left(1 + \frac{1}{4 \tan^2 \varphi_0}\right) H^2 - \left(2H - \frac{\delta}{2}\right)^2}} \end{aligned} \quad (2.22)$$

Then, substituting Eqs. (2.15)–(2.22) into Eq. (2.14) leads to the force contributed by PU foam. Finally, the total force of the type III connector with PU foam ( $F_u$ ) can be obtained as

$$F_u = F_p + F_f \quad (2.23)$$

#### 2.4.1.3 Validation with Experimental and Numerical Results

The force–displacement curves obtained from the analytical model are compared with those obtained from experiments and FE analyses in Fig. 2.8. Consistent results among them can be seen. The sudden change of force induced by deformation mode change can be reasonably captured by the analytical model. However, the fluctuations of the force–displacement curves induced by inertial effect are not captured by the analytical model. However, these differences are not significant and will not affect the energy absorption evaluation of the connectors. From above discussions, the developed analytical model is proven to be accurate in predicting the force–displacement responses and energy absorptions of the type III connectors.

#### 2.4.2 Analytical Model for Type IV Connector

##### 2.4.2.1 Energy Absorption from AP Plate

As analyzed in Sect. 2.3.2, EA of the type IV connector without PU foam is generally concentrated at the plastic hinge zones, and its deformation mode is divided into three stages. Hence, an analytical model to calculate EA of the connector contributed by

plastic hinge rotation is proposed, and its geometric parameters are presented in Fig. 2.21. According to geometric relation, the critical displacement  $D_1$  and  $D_2$  can be calculated as:

$$D_1 = (k + 1)H - H_0 \quad \text{and} \quad D_2 = (k + 1)H - \sqrt{H_0^2 + L^2} + L \quad (2.24)$$

where  $H_0 = \sqrt{k^2 - 1}H$ . Similar to the type III connector, the energy absorption rate of each plastic hinge for the type IV connector also varies with different deformation stages. Hence, the force–displacement relationship of the type IV connector at different deformation stages should be calculated separately, and  $EA$  can be subsequently calculated by numerically integrating the force to displacement.

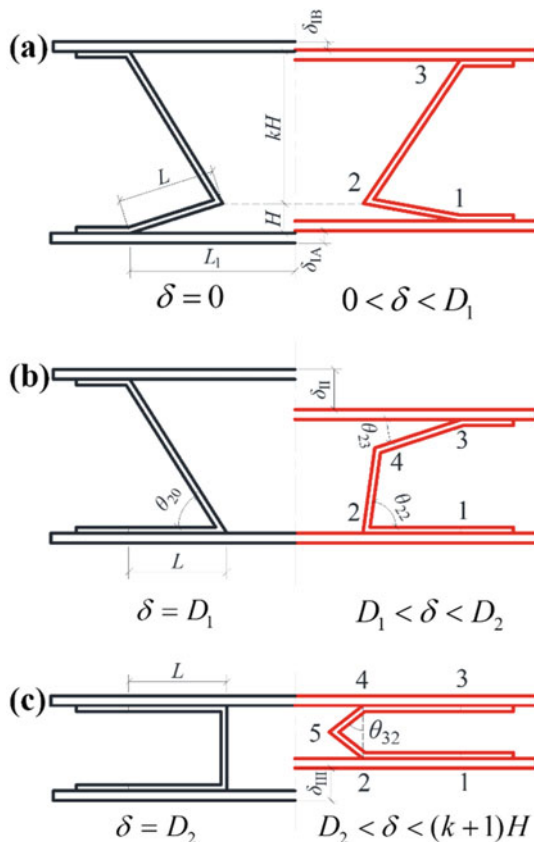


**Fig. 2.21** Deformation patterns of the type IV connector: **a** Deformation stage I; **b** Deformation stage II; **c** Deformation stage III, reprinted from Wang et al. (2020), copyright 2022, with permission from Elsevier

In deformation stage I (Fig. 2.21a), i.e.,  $0 \leq \delta \leq D_1$ , the total force contributed by AP plates,  $F_{p1}$ , is determined by summing the forces contributed by the six plastic hinges at point 1, 2 and 3, i.e.,

$$F_{p1} = 2(F_{11} + F_{12} + F_{13}) \quad (2.25)$$

and the forces contributed by the plastic hinges at point 1, 2 and 3 in deformation stage I (i.e.,  $F_{11}$ ,  $F_{12}$  and  $F_{13}$ ) can be obtained as

$$F_{11} = \frac{dU_{11}}{d\delta} = bt_{ph} \left[ \frac{\sigma_y t_p^2}{4} + \frac{E' \kappa_{11} t_p^3}{12} + \frac{\sigma_y t_p^{1/P+2}}{2^{1/P+1}(1/P+2)} \left( \frac{\dot{\delta}}{C} \cdot \frac{d\kappa_{11}}{d\delta} \right)^{1/P} \right. \\ \left. + \frac{E' \kappa_{11} t_p^{1/P+3}}{2^{1/P+2}(1/P+3)} \left( \frac{\dot{\delta}}{C} \cdot \frac{d\kappa_{11}}{d\delta} \right)^{1/P} \right] \frac{d\kappa_{11}}{d\delta} \quad (2.26)$$

$$F_{12} = \frac{dU_{12}}{d\delta} = bt_{ph} \left[ \frac{\sigma_y t_p^2}{4} + \frac{E' (\kappa_{11} + \kappa_{13}) t_p^3}{12} + \frac{\sigma_y t_p^{1/P+2}}{2^{1/P+1}(1/P+2)} \left( \frac{\dot{\delta}}{C} \cdot \frac{d\kappa_{11} + d\kappa_{13}}{d\delta} \right)^{1/P} \right. \\ \left. + \frac{E' (\kappa_{11} + \kappa_{13}) t_p^{1/P+3}}{2^{1/P+2}(1/P+3)} \left( \frac{\dot{\delta}}{C} \cdot \frac{d\kappa_{11} + d\kappa_{13}}{d\delta} \right)^{1/P} \right] \frac{d(\kappa_{11} + \kappa_{13})}{d\delta} \quad (2.27)$$

$$F_{13} = \frac{dU_{13}}{d\delta} = bt_{ph} \left[ \frac{\sigma_y t_p^2}{4} + \frac{E' \kappa_{13} t_p^3}{12} + \frac{\sigma_y t_p^{1/P+2}}{2^{1/P+1}(1/P+2)} \left( \frac{\dot{\delta}}{C} \cdot \frac{d\kappa_{13}}{d\delta} \right)^{1/P} \right. \\ \left. + \frac{E' \kappa_{13} t_p^{1/P+3}}{2^{1/P+2}(1/P+3)} \left( \frac{\dot{\delta}}{C} \cdot \frac{d\kappa_{13}}{d\delta} \right)^{1/P} \right] \frac{d\kappa_{13}}{d\delta} \quad (2.28)$$

where

$$\kappa_{11} = \frac{1}{t_{ph}} \left( \arcsin \frac{H}{L} - \arcsin \frac{H - \delta_{IA}}{L} \right) \quad (2.29)$$

$$\kappa_{13} = \frac{1}{t_{ph}} \left( \arcsin \frac{kH}{\sqrt{H_0^2 + L^2}} - \arcsin \frac{kH - \delta_{IB}}{\sqrt{H_0^2 + L^2}} \right) \quad (2.30)$$

$$\frac{d\kappa_{11}}{d\delta} = \frac{4(kH - \delta)(kH + H - \delta) + 2\delta(2kH - \delta)}{t_{ph}[2H(k + 1) - 2\delta]^2 \sqrt{L^2 - (H - \delta_{IA})^2}} \quad (2.31)$$

$$\frac{d\kappa_{13}}{d\delta} = \frac{4(H - \delta)(kH + H - \delta) + 2\delta(2H - \delta)}{t_{ph}[2H(k + 1) - 2\delta]^2 \sqrt{(H_0^2 + L^2) - (kH - \delta_{IB})^2}} \quad (2.32)$$

$$\delta_{IA} = \frac{(2kH - \delta)\delta}{2H(k + 1) - 2\delta} \quad (2.33)$$

$$\delta_{IB} = \frac{(2H - \delta)\delta}{2H(k + 1) - 2\delta} \quad (2.34)$$

In Eqs. (2.29)–(2.34),  $\kappa_{11}$  and  $\kappa_{13}$  are the changes of curvature at point 1 and 3,  $\delta_{IA}$  and  $\delta_{IB}$  are the displacements of bottom plate and top plate relative to point 2 (refer to Fig. 2.21a), and  $\delta = \delta_{IA} + \delta_{IB}$  is the total displacement. When  $\delta = D_1$ , let  $\bar{\kappa}_{13} = \kappa_{13}(D_1)$ .

In deformation stage II (Fig. 2.21b), i.e.,  $D_1 \leq \delta \leq D_2$ , as analyzed in Sect. 2.3.2, the forth pair of plastic hinges occur at point 4, and plastic hinge 1 stops rotating. Meanwhile, plastic hinge 3 continues rotating, and plastic hinge 2 starts to rotate reversely. Hence, the total force in deformation stage II,  $F_{p2}$ , is obtained by summing the forces contributed by the six plastic hinges at point 2, 3 and 4, i.e.,

$$F_{p2} = 2(F_{22} + F_{23} + F_{24}) \quad (2.35)$$

and the forces contributed by the plastic hinges at point 2, 3 and 4 in deformation stage II (i.e.,  $F_{22}$ ,  $F_{23}$  and  $F_{24}$ ) can be obtained as

$$F_{22} = \frac{dU_{22}}{d\delta} = bt_{ph} \left[ \frac{\sigma_y t_p^2}{4} + \frac{E' \kappa_{22} t_p^3}{12} + \frac{\sigma_y t_p^{1/P+2}}{2^{1/P+1}(1/P+2)} \left( \frac{\dot{\delta}}{C} \cdot \frac{d\kappa_{22}}{d\delta} \right)^{1/P} \right. \\ \left. + \frac{E' \kappa_{22} t_p^{1/P+3}}{2^{1/P+2}(1/P+3)} \left( \frac{\dot{\delta}}{C} \cdot \frac{d\kappa_{22}}{d\delta} \right)^{1/P} \right] \frac{d\kappa_{22}}{d\delta} \quad (2.36)$$

$$F_{23} = \frac{dU_{23}}{d\delta} = bt_{ph} \left[ \frac{\sigma_y t_p^2}{4} + \frac{E'(\kappa_{23} + \bar{\kappa}_{13}) t_p^3}{12} + \frac{\sigma_y t_p^{1/P+2}}{2^{1/P+1}(1/P+2)} \left( \frac{\dot{\delta}}{C} \cdot \frac{d\kappa_{23}}{d\delta} \right)^{1/P} \right. \\ \left. + \frac{E'(\kappa_{23} + \bar{\kappa}_{13}) t_p^{1/P+3}}{2^{1/P+2}(1/P+3)} \left( \frac{\dot{\delta}}{C} \cdot \frac{d\kappa_{23}}{d\delta} \right)^{1/P} \right] \frac{d\kappa_{23}}{d\delta} \quad (2.37)$$

$$F_{24} = \frac{dU_{24}}{d\delta} = bt_{ph} \left[ \frac{\sigma_y t_p^2}{4} + \frac{E'(\kappa_{22} + \kappa_{23}) t_p^3}{12} + \frac{\sigma_y t_p^{1/P+2}}{2^{1/P+1}(1/P+2)} \left( \frac{\dot{\delta}}{C} \cdot \frac{d\kappa_{22} + d\kappa_{23}}{d\delta} \right)^{1/P} \right. \\ \left. + \frac{E'(\kappa_{22} + \kappa_{23}) t_p^{1/P+3}}{2^{1/P+2}(1/P+3)} \left( \frac{\dot{\delta}}{C} \cdot \frac{d\kappa_{22} + d\kappa_{23}}{d\delta} \right)^{1/P} \right] \frac{d\kappa_{22} + d\kappa_{23}}{d\delta} \quad (2.38)$$

where

$$\kappa_{22} = \frac{\theta_{22} - \theta_{20}}{t_{ph}} \quad (2.39)$$

$$\kappa_{23} = \frac{\theta_{20} - \theta_{23}}{t_{ph}} \quad (2.40)$$

$$\frac{d\kappa_{22}}{d\delta} = \frac{(H_0 - \delta_{II}) \left( 2L\sqrt{H_0^2 + L^2} - 2H_0\delta_{II} + \delta_{II}^2 \right)}{t_{ph}[(H_0 - \delta_{II})^2 + L^2] \sqrt{4L^2 \left( \sqrt{H_0^2 + L^2} - L \right)^2 - \left[ (H_0 - \delta_{II})^2 - \left( \sqrt{H_0^2 + L^2} - L \right)^2 \right]^2}} - \frac{L}{t_{ph}[(H_0 - \delta_{II})^2 + L^2]} \quad (2.41)$$

$$\frac{d\kappa_{23}}{d\delta} = \frac{(H_0 - \delta_{II}) \left[ (H_0 - \delta_{II})^2 + 2L^2 + H_0^2 - 2L\sqrt{H_0^2 + L^2} \right]}{t_{ph}[(H_0 - \delta_{II})^2 + L^2] \sqrt{4L^2[(H_0 - \delta_{II})^2 + L^2] - \left[ (H_0 - \delta_{II})^2 + 2L\sqrt{H_0^2 + L^2} - H_0^2 \right]^2}} + \frac{L}{t_{ph}[(H_0 - \delta_{II})^2 + L^2]} \quad (2.42)$$

$$\theta_{20} = \arctan \frac{H_0}{L} \quad (2.43)$$

$$\theta_{22} = \pi - \arcsin \frac{(H_0 - \delta_{II})^2 + \left( \sqrt{H_0^2 + L^2} - L \right)^2}{2 \left( \sqrt{H_0^2 + L^2} - L \right) \sqrt{(H_0 - \delta_{II})^2 + L^2}} - \arctan \frac{L}{H_0 - \delta_{II}} \quad (2.44)$$

$$\theta_{23} = \arcsin \frac{\delta_{II}^2 - 2H_0\delta_{II} + 2L\sqrt{H_0^2 + L^2}}{2L\sqrt{(H_0 - \delta_{II})^2 + L^2}} - \arctan \frac{L}{H_0 - \delta_{II}} \quad (2.45)$$

$$\delta_{II} = \delta - \left( k + 1 - \sqrt{k^2 - 1} \right) H \quad (2.46)$$

In Eqs. (2.39)–(2.46),  $\kappa_{22}$  and  $\kappa_{23}$  are the changes of curvature at point 2 and 3,  $\theta_{20}$  is the initial angle at point 2, and  $\theta_{22}$  and  $\theta_{23}$  are the angle changes at point 2 and 3 (refer to Fig. 2.21b), and  $\delta_{II}$  is the displacement increment during deformation stage II. When  $\delta = D_2$ , let  $\bar{\kappa}_{22} = \kappa_{22}(D_2)$ .

In deformation stage III (Fig. 2.21c), i.e.,  $D_2 \leq \delta \leq (k + 1)H$ , the fifth pair of plastic hinges occur at point 5, and plastic hinge 3 stops rotating. Meanwhile, plastic hinge 2 continues rotating, and plastic hinge 4 starts to rotate reversely. Hence, the total force in deformation stage III,  $F_{p3}$ , is obtained by summing the forces contributed by the six plastic hinges at point 2, 4 and 5, i.e.,

$$F_{p3} = 2(F_{32} + F_{34} + F_{35}) \quad (2.47)$$

and the forces contributed by the plastic hinges at point 2, 4 and 5 in deformation stage III (i.e.,  $F_{32}$ ,  $F_{34}$  and  $F_{35}$ ) can be obtained as

$$F_{32} = \frac{dU_{32}}{d\delta} = bt_{ph} \left[ \frac{\sigma_y t_p^2}{4} + \frac{E'(\kappa_{32} + \bar{\kappa}_{22})t_p^3}{12} + \frac{\sigma_y t_p^{1/P+2}}{2^{1/P+1}(1/P+2)} \left( \frac{\dot{\delta}}{C} \cdot \frac{d\kappa_{32}}{d\delta} \right)^{1/P} \right. \\ \left. + \frac{E'(\kappa_{32} + \bar{\kappa}_{22})t_p^{1/P+3}}{2^{1/P+2}(1/P+3)} \left( \frac{\dot{\delta}}{C} \cdot \frac{d\kappa_{32}}{d\delta} \right)^{1/P} \right] \frac{d\kappa_{32}}{d\delta} \quad (2.48)$$

$$F_{34} = \frac{dU_{34}}{d\delta} = bt_{ph} \left[ \frac{\sigma_y t_p^2}{4} + \frac{E' \kappa_{32} t_p^3}{12} + \frac{\sigma_y t_p^{1/P+2}}{2^{1/P+1}(1/P+2)} \left( \frac{\dot{\delta}}{C} \cdot \frac{d\kappa_{32}}{d\delta} \right)^{1/P} \right. \\ \left. + \frac{E' \kappa_{32} t_p^{1/P+3}}{2^{1/P+2}(1/P+3)} \left( \frac{\dot{\delta}}{C} \cdot \frac{d\kappa_{32}}{d\delta} \right)^{1/P} \right] \frac{d\kappa_{32}}{d\delta} \quad (2.49)$$

$$F_{35} = \frac{dU_{35}}{d\delta} = 2bt_{ph} \left[ \frac{\sigma_y t_p^2}{4} + \frac{E' \kappa_{32} t_p^3}{6} + \frac{\sigma_y t_p^{1/P+2}}{2(1/P+2)} \left( \frac{\dot{\delta}}{C} \cdot \frac{d\kappa_{32}}{d\delta} \right)^{1/P} \right. \\ \left. + \frac{E' \kappa_{32} t_p^{1/P+3}}{2(1/P+3)} \left( \frac{\dot{\delta}}{C} \cdot \frac{d\kappa_{32}}{d\delta} \right)^{1/P} \right] \frac{d\kappa_{32}}{d\delta} \quad (2.50)$$

where

$$\kappa_{32} = \frac{1}{t_{ph}} \theta_{32} \quad (2.51)$$

$$\frac{d\kappa_{32}}{d\delta} = \frac{1}{t_{ph} \sqrt{2\delta_{III} \left( \sqrt{H_0^2 + L^2} - L \right) - \delta_{III}^2}} \quad (2.52)$$

$$\theta_{32} = \arccos \frac{\sqrt{H_0^2 + L^2} - L - \delta_{III}}{\sqrt{H_0^2 + L^2} - L} \quad (2.53)$$

$$\delta_{III} = \delta - (k+1)H + \sqrt{H_0^2 + L^2} - L \quad (2.54)$$

In Eqs. (2.51)–(2.53),  $\kappa_{32}$  and  $\theta_{32}$  are curvature change and angle change at point 2, and  $\delta_{III}$  is the displacement increment during deformation stage III, as illustrated in Fig. 2.21c.

In summary, the EA of the type IV connector without PU foam can be formulated as

$$EA_p(\delta) = \begin{cases} \int_0^\delta F_{p1}(\delta)d\delta & 0 \leq \delta \leq D_1 \\ \int_0^{D_1} F_{p1}(\delta)d\delta + \int_{D_1}^\delta F_{p2}(\delta)d\delta & D_1 \leq \delta \leq D_2 \\ \int_0^{D_1} F_{p1}(\delta)d\delta + \int_{D_1}^{D_2} F_{p2}(\delta)d\delta + \int_{D_2}^\delta F_{p3}(\delta)d\delta & D_2 \leq \delta \leq D_3 \end{cases} \quad (2.55)$$

#### 2.4.2.2 Energy Absorption from PU Foam

The some method presented in Sect. 2.4.1.2 (i.e., Eqs. (2.14)–(2.17)) can be employed herein to calculate the force–displacement response of the type IV connector contributed by PU foam. According to the geometric relationship shown in Fig. 2.21a, the initial volume of PU foam filled in the type IV connector,  $V_0$ , can be formulated as

$$V_0 = (k + 1) \left( 2L_1 - \sqrt{L^2 - H^2} \right) bH \quad (2.56)$$

To obtained the volumetric strain  $\varepsilon$  and strain rate  $\dot{\varepsilon}$ , the current volume,  $V_c$ , and its derivative of current volume of PU foam with respective to displacement ( $dV / d\delta$ ) in three deformation stages should be calculated and presented as follows.

In deformation stage I, i.e.,  $0 \leq \delta \leq D_1$ , the current volume of PU foam,  $V_{c1}$ , is calculated as

$$V_{c1} = [(k + 1)H - \delta_{IA} - \delta_{IB}] \left[ 2L_1 - \sqrt{L^2 - (H - \delta_{IA})^2} \right] b \quad (2.57)$$

and  $dV_{c1} / d\delta$  is calculated as

$$\begin{aligned} \frac{dV_{c1}}{d\delta} &= b \left( -\frac{d\delta_{IA}}{d\delta} - \frac{d\delta_{IB}}{d\delta} \right) \left( 2L_1 - \sqrt{L^2 - (H - \delta_{IA})^2} \right) \\ &+ b[(k + 1)H - \delta_{IA} - \delta_{IB}] \frac{\delta_{IA} - H}{\sqrt{L^2 - (H - \delta_{IA})^2}} \cdot \frac{d\delta_{IA}}{d\delta} \end{aligned} \quad (2.58)$$

where

$$\frac{d\delta_{IA}}{d\delta} = \frac{2H(k + 1)(kH - \delta) + \delta^2}{2[H(k + 1) - \delta]^2} \quad (2.59)$$

$$\frac{d\delta_{IB}}{d\delta} = \frac{2H(k + 1)(H - \delta) + \delta^2}{2[H(k + 1) - \delta]^2} \quad (2.60)$$

In deformation stage II, i.e.,  $D_1 < \delta < D_2$ , the current volume of PU foam,  $V_{c2}$ , is calculated as

$$V_{c2} = [(2L_1 - L - L \cos \theta_{23})(H_0 - \delta_{II}) + L^2 \sin \theta_{23}]b \quad (2.61)$$

and  $dV_{c2}/d\delta$  is calculated as

$$\frac{dV_{c2}}{d\delta} = bL(H_0 - \delta_{II}) \sin \theta_{23} \frac{d\theta_{23}}{d\delta} - b(2L_1 - L - L \cos \theta_{23}) + bL^2 \cos \theta_{23} \frac{d\theta_{23}}{d\delta} \quad (2.62)$$

where

$$\begin{aligned} \frac{d\theta_{23}}{d\delta} = & \frac{(\delta_{II} - H_0) \left[ (H_0 - \delta_{II})^2 + 2L^2 + H_0^2 - 2L\sqrt{H_0^2 + L^2} \right]}{\left[ (H_0 - \delta_{II})^2 + L^2 \right] \sqrt{4L^2[(H_0 - \delta_{II})^2 + L^2] - \left[ (H_0 - \delta_{II})^2 + 2L\sqrt{H_0^2 + L^2} - H_0^2 \right]^2}} \\ & - \frac{L}{(H_0 - \delta_{II})^2 + L^2} \end{aligned} \quad (2.63)$$

In deformation stage III, i.e.,  $D_2 \leq \delta \leq (k+1)H$ , the current volume of PU foam,  $V_{c3}$ , is calculated as

$$V_{c3} = b \left( 2L_1 - 2L - \frac{\sqrt{H_0^2 + L^2} - L}{2} \sin \theta_{32} \right) \left( \sqrt{H_0^2 + L^2} - L \right) \cos \theta_{32} \quad (2.64)$$

and  $dV_{c3}/d\delta$  is calculated as

$$\begin{aligned} \frac{dV_{c3}}{d\delta} = & -b \left( \sqrt{H_0^2 + L^2} - L \right)^2 \cdot \frac{\cos^2 \theta_{32}}{2} \cdot \frac{d\theta_{32}}{d\delta} \\ & - b \left( 2L_1 - 2L - \frac{\sqrt{H_0^2 + L^2} - L}{2} \sin \theta_{32} \right) \cdot \sin \theta_{32} \cdot \frac{d\theta_{32}}{d\delta} \end{aligned} \quad (2.65)$$

where

$$\frac{d\theta_{32}}{d\delta} = \frac{1}{\sqrt{2\delta_{III} \left( \sqrt{H_0^2 + L^2} - L \right) - \delta_{III}^2}} \quad (2.66)$$

In summary, the EA of the type IV connector contributed by PU foam can be obtained as

$$EA_f(\delta) = \int_0^\delta F_f(\delta)d\delta \quad (2.67)$$

and the total  $EA$  of the type IV connector with PU foam,  $EA_u$ , is obtained as

$$EA_u(\delta) = EA_p(\delta) + EA_f(\delta) \quad (2.68)$$

#### 2.4.2.3 Validation with Experimental Results

Figure 2.22 shows the  $EA$ -displacement curves of type IV connectors obtained from experiments and analytical predictions, and the analytical-predicted results are found to be generally consistent with test results. However, the analytical predictions are still slightly different from experimental results. This is mainly because the analytical model does not consider the initial bending of AP plates corresponding to the critical displacements  $D_1$  and  $D_2$ , which leads to the sudden changes of  $EA$ -displacement curves from the analytical model. Another reason is that the influence of PU

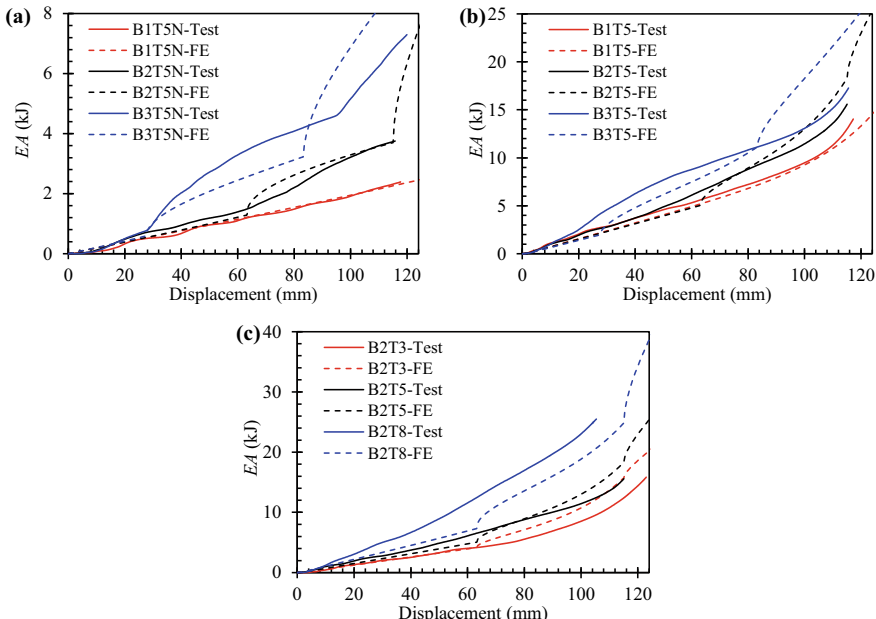


**Fig. 2.22** Comparison of  $EA$ -displacement curves of type IV connectors between tests and analytical predictions: **a** Variant pleated plate parameter  $k$  without foam; **b** Variant pleated plate parameter  $k$  with foam; **c** Variant pleated plate thickness with foam, reprinted from Wang et al. (2020), copyright 2022, with permission from Elsevier

foam on the deformation shape of AP plates becomes increasingly significant after densification, especially in the deformation stage III (as shown in Fig. 2.22b, c). Moreover, geometric imperfection as well as cracking and peeling of PU foam can also cause the difference between the analytical and experimental results. However, the differences are not significant and will not affect the rationality of the analytical results, especially for the deformation stage I and II. Hence, the proposed analytical model can be employed to predict the *EA* (or force) of the type IV connector under impact loading.

## 2.5 Summary

Two types of PU foam-filled energy absorption connectors were proposed in this chapter, and their energy absorption performances were experimentally, numerically and analytically studied. The deformation modes, force–displacement responses of the PU foam-filled connectors with varying geometries were investigated via conducting drop-weight impact tests. Finally, the analytical models were developed for predicting force–displacement responses of the proposed connectors. The main findings from this chapter could be summarized as follows:

- (1) The deformation process of type III connectors could be divided into two patterns according to the different distributions of plastic hinge zones, and three patterns could be observed for the type IV connectors.
- (2) PU foam filler could evidently improve the energy absorption performances of both type III and IV connectors in terms of the improvement of *EA*, *SEA* and *CFE*, which could be attributed to the higher energy absorption, lightweight and smooth stress–strain curve of PU foam.
- (3) Increasing MP plate thickness and angle  $\theta_0$  resulted in significant increase of *EA* and *SEA* for type III connectors. In addition, the type III connector without PU foam was found to be more sensitive to the variation of angle  $\theta_0$ . With regard to type IV connectors, increasing the geometric parameter *k* could increase *EA* and *SEA*. In addition, increasing AP thickness could increase *EA*, whereas the *SEA* was not necessarily increased owing to the increase in mass.
- (4) The developed analytical models could provide acceptable predictions on the force–displacement relations of the PU foam-filled connectors via comparing with the experimental and numerical results. Hence, they could be utilized to evaluate the energy absorption performances of proposed connectors.

## References

- Abedi MM, Niknejad A, Liaghat GH et al (2018) Foam-filled grooved tubes with circular cross section under axial compression: An experimental study. *Iran J Sci Technol-Trans Mech Eng* 42:401–413
- Abramowicz W, Jones N (1986) Dynamic progressive buckling of circular and square tubes. *Int J Impact Eng* 4:243–270
- Azarakhsh S, Rahi A, Ghamarian A et al (2015) Axial crushing analysis of empty and foam-filled brass bitubular cylinder tubes. *Thin-Walled Struct* 95:60–72
- Daneshi GH, Hosseiniipour SJ (2002) Grooves effect on crashworthiness characteristics of thin-walled tubes under axial compression. *Mater Des* 23:611–617
- Darvizeh A, Darvizeh M, Ansari R et al (2013) Effect of low density, low strength polyurethane foam on the energy absorption characteristics of circumferentially grooved thick-walled circular tubes. *Thin-Walled Struct* 71:81–90
- Deb A, Shivakumar ND (2009) An experimental study on energy absorption behavior of polyurethane foams. *J Reinf Plas Compos* 28:3021–3026
- Elahi SA, Rouzegar J, Niknejad A et al (2017) Theoretical study of absorbed energy by empty and foam-filled composite tubes under lateral compression. *Thin-Walled Struct* 114:1–10
- Gilchrist A, Mills NJ (2001) Impact deformation of rigid polymeric foams: experiments and FEA modeling. *Int J Impact Eng* 25:767–786
- Haorongbam B, Deb A, Gupta NK (2017) Behavior of polyurethane foam-filled steel hat sections under axial loading: Testing and simulation. *Procedia Eng* 173:1349–1356
- Hanssen AG, Langseth M, Hopperstad OS (2000) Static and dynamic crushing of circular aluminium extrusions with aluminium foam filler. *Int J Impact Eng* 24:475–507
- Hussein RD, Ruan D, Lu G et al (2017) Crushing response of square aluminium tubes filled with polyurethane foam and aluminium honeycomb. *Thin-Walled Struct* 110:140–154
- Jafarian B, Rezvani MJ (2017) An experimental investigation on energy absorption of thin-walled bitubular structures by inversion and axial collapse. *Int J Mech Sci* 126:270–280
- Jeong KY, Cheon SS, Munshi MB (2012) A constitutive model for polyurethane foam with strain rate sensitivity. *J Mech Sci Technol* 26:2033–2038
- Koohbor B, Kidane A, Lu WY et al (2016) Investigation of the dynamic stress-strain response of compressible polymeric foam using a non-parametric analysis. *Int J Impact Eng* 91:170–182
- Niknejad A, Elahi SA, Liaghat GH (2012) Experimental investigation on the lateral compression in the foam-filled circular tubes. *Mater Des* 36:24–34
- Niknejad A, Assaee H, Elahi SA et al (2013) Flattening process of empty and polyurethane foam-filled E-glass/vinylester composite tubes – An experimental study. *Compos Struct* 100:479–492
- Niknejad A, Abedi MM, Liaghat GH et al (2015) Absorbed energy by foam-filled quadrangle tubes during the crushing process by considering the interaction effects. *Arch Civ Mech Eng* 15:376–391
- Onsalung N, Thinvongpituk C, Pianthong K (2014) Impact response of circular aluminum tube filled with polyurethane foam. *Mater Trans* 55:207–215
- Reid SR, Reddy TY (1986) Axial crushing of foam-filled tapered sheet metal tubes. *Int J Mech Sci* 28:643–656
- Rezaei B, Niknejad A, Assaee H et al (2015) Axial splitting of empty and foam-filled circular composite tubes – An experimental study. *Arch Civ Mech Eng* 15:650–662
- Song H, Fan Z, Yu G et al (2005) Partition energy absorption of axially crushed aluminum foam-filled hat sections. *Int J Solids Struct* 42:2575–2600
- Wang Y, Zhai X, Ying W et al (2018) Dynamic crushing response of an energy absorption connector with curved plate and aluminum foam as energy absorber. *Int J Impact Eng* 121:119–133
- Wang Y, Lu J, Zhai X et al (2019) Response of energy absorbing connector with polyurethane foam and multiple pleated plates under impact loading. *Int J Impact Eng* 133:103356
- Wang Y, Lu J, Zhai X et al (2020) Crushing of energy absorption connectors with polyurethane foam and asymmetric pleated plates. *J Constr Steel Res* 166:105902

- Yan L, Chouw N, Jayaraman K (2014) Lateral crushing of empty and polyurethane-foam filled natural flax fabric reinforced epoxy composite tubes. Compos Part B: Eng 63:15–26
- Zhang Z, Sun W, Zhao Y et al (2018) Crashworthiness of different composite tubes by experiments and simulations Compos Part B: Eng 143:86–95
- Zhou P, Beeh E, Kriescher M et al (2016) Experimental comparison of energy absorption characteristics of polyurethane foam-filled magnesium and steel beams in bending. Int J Impact Eng 93:76–87

# Chapter 3

## Aluminum Foam-Filled Circular-Triangular Nested Tubes Under Impact



### 3.1 Introduction

Thin-walled empty or foam-filled metallic tubes were widely employed as energy absorbers to dissipate impact energy owing to their easy fabrication and desirable energy absorption performance. The axial crushing performances of empty or foam-filled metallic tubes generally outperformed the laterally loaded counterparts in terms of enhanced energy absorption capacity (Baroutaji et al. 2017). However, fewer fluctuation of crushing force and more stable deformation mode were observed for the “tube-type” energy absorbers under lateral loading (Tran 2017) or with windowed shaped cuttings (Tran et al. 2021). The laterally loaded empty or foam-filled metallic tubes could be the desirable energy absorbers if their energy absorptions could be enhanced. Hence, the nested tubes and the tubes with constraints or functionally graded thickness were generally proposed for improving energy absorption capacity (Nikkhah et al. 2020; Baroutaji et al. 2021). Recently, a new circular-triangular nested tube (CTNT) energy absorber was proposed by the authors (Wang et al. 2020a), and the constraints between circular and triangular tubes were found to evidently enhance its energy absorption capacity. In this study, the CTNT energy absorber was filled with aluminum foam to further improve its energy absorption performance, as shown in Fig. 3.1. With the aim of using the proposed aluminum foam-filled circular-triangular nested tube (AFCTNT) energy absorber to further improve the energy absorption performance of the CTNT energy absorber, this work is of significance for revealing the energy absorption behavior of the AFCTNT energy absorber under impact loading and facilitating its application in impact energy dissipation.

The responses of circular tubes under lateral crushing have been extensively studied as they generally exhibited stable energy dissipation (Gupta et al. 2005). The formulae for calculating the force–displacement responses of the laterally loaded circular tubes were also developed (Wang 1987; McDevitt and Simmonds 2003), which could be used to assess their energy absorption performances. The dynamic lateral crushing behavior of circular tubes was also studied by Fan et al. (2013) as the energy absorbers were generally employed for dissipating impact or blast energy.

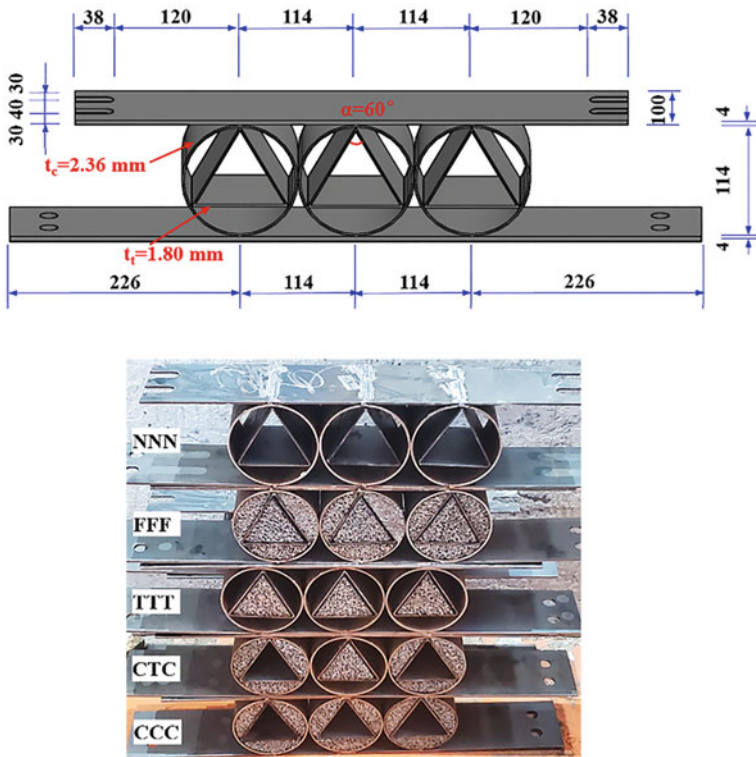


**Fig. 3.1** Geometry of the AFCTNT energy absorbers (mm), reprinted from Wang et al. (2021), copyright 2022, with permission from Elsevier

It was found that the inertial effect induced by dynamic loading could result in the change of deformation modes of the circular tubes, which together with strain rate effect could enhance their energy absorption capacities (Su et al. 1995a, b). In addition, rectangular, triangular and elliptical tubes could also be employed for dissipating impact or blast energy and its response under lateral crushing was also extensively studied (Gupta et al. 2001; Wu and Carney 1997; Tran and Ton 2016; Fan et al. 2015). The laterally loaded triangular tubes generally exhibited improved energy absorption capacity comparing with circular tubes, and three deformation modes and a unified energy dissipation mechanism were observed by Wang et al. (2015). However, larger initial peak force was observed for the triangular tube, which could reduce its energy absorption efficiency. External constraints or nested tubes were widely adopted to enhance the energy absorption performance of the single tube. It was found that the energy absorption of a circular tube subjected to lateral loading was improved with the presence of external constraints owing to more severe plastic deformation as compared to the counterparts without external constraints (Reid et al. 1983; Reddy and Reid 1979). With regard to the nested tubes which consist of at least two tubes, significant improvement in energy absorption performance could also be observed

(Morris et al. 2006). The behavior of nested tubes under lateral dynamic loading was studied (Baroutaji et al. 2016; Olabi et al. 2008), and the improved energy absorption performance of the nested tubes could be observed through optimized design.

Recently, aluminum foam was increasingly employed as the filler of a metallic tube to enhance its energy absorption performance owing to the light weight, high specific energy absorption and stable energy dissipation of aluminum foam. Till date, a considerable amount of studies have been conducted to reveal the behavior of aluminum foam-filled energy absorbers under axial (Duarte et al. 2015; Shahbeyk et al. 2007) or oblique (Reyes et al. 2004) crushing. It was found that the energy absorption performance could be evidently improved by filling tubes with aluminum foam (Santosa et al. 2000). In addition, the foam filler was found to stabilize the deformation mode and enhance the energy absorption capacity through investigating the axially loaded foam-filled conical tubes (Ahmad and Thambiratnam 2009). To smooth the crushing force–displacement curve and reduce the initial peak force, the aluminum foam-filled corrugated tubes were proposed, and its behavior under dynamic crushing was also studied (Kilicaslan 2015). The results indicated that aluminum foam-filled corrugated tubes experienced progressive and concertina type of deformation mode. A new dual functionally graded structure with variation of both foam density and tube wall thickness was proposed by Fang et al. (2016), and the improved energy absorption performance was demonstrated by comparing with the uniform counterparts. The multi-objective optimisation design (MOD) of foam-filled tubes under oblique impact loading was conducted to enhance their crashworthiness (Yang and Qi 2013; Qi and Yang 2014). It was found that more robust designs could be achieved by incorporating multiple load angles into the MOD process (Yang and Qi 2013). With regard to the lateral crushing behavior of foam-filled tubes, smoother crushing force–displacement responses could be observed as compared to the axially loaded counterparts (Shen et al. 2015). The energy absorption performances of sandwich tubes under dynamic lateral crushing were studied by Fan et al. (2013), and different deformation modes of the sandwich tubes between the dynamic and quasi-static loading cases could be observed owing to the inertial effect. Further, MOD was employed for finding the optimal configuration of laterally loaded sandwich tubes, and the tube with a minimum diameter of inner layer and a maximum foam thickness was found to be more desirable (Baroutaji et al. 2015). Up to date, no study has been performed on the new aluminum foam-filled nested system presented in this chapter, which is composed of circular tubes, triangular tubes, and aluminum foam.

A new AFCTNT energy absorber was proposed for improving the energy absorption performance of the recently developed CTNT energy absorber. Drop-weight impact tests on the AFCTNT energy absorbers with different volumes of aluminum foam filler were first conducted to reveal their energy absorption performances. In addition, numerical simulations on the AFCTNT energy absorbers under impact loading were also carried out by employing the explicit code in LS-DYNA, and more in-depth discussions on the impact behavior of the AFCTNT energy absorbers were presented based on the numerical results.

## 3.2 Methodologies

### 3.2.1 Experimental Methodology

#### 3.2.1.1 Specimens

The AFCTNT energy absorber specimens prepared for the drop-weight impact tests are presented in Fig. 3.1. Five types of AFCTNT energy absorbers are designed with the variation of aluminum foam volume, and the notations of the specimens are illustrated in Fig. 3.1. Two identical energy absorbers of each type of specimens were fabricated for validating the repeatability of the experimental results. The CTNT energy absorber includes two flat plates, three circular tubes, and three triangular tubes, as shown in Fig. 3.1. The fabrication process of the CTNT energy absorber includes: (a) welding three steel plates with equal lengths together to form the inner triangular tube with cross-section to be an equilateral triangle, (2) filling three triangular tubes into three circular tubes, and (3) fixing the circular tubes to the top and bottom flat plates through welding. Finally, the CTNT energy absorbers were filled with aluminum foam, and different volumes of aluminum foam filler were chosen for revealing its influence on the behavior of the AFCTNT energy absorber. The geometries of the specimens are presented in Fig. 3.1. All the specimens share the same geometries of the CTNT energy absorber with width and outer diameter of circular tubes to be 100 and 114 mm, respectively. The measured thicknesses of circular and triangular tubes are 2.36 and 1.80 mm, respectively. The material properties of mild steel and aluminum foam employed for the specimens are given in Table 3.1.

#### 3.2.1.2 Experimental Setup and Instrumentation

The impact tests on the AFCTNT energy absorbers were carried out via employing a drop-weight impact test system, and Fig. 3.2 presents the test setup and instrumentation. The drop-weight impact test system mainly includes a hammer with adjustable weight from 400 to 1000 kg, a hydraulic-controlled mechanical hosting system, two guide rails, a dynamic load cell, a high-speed camera, and two lights. The hammer

**Table 3.1** Material parameters of mild steel and aluminum foam

Mild steel	$E_y$ (GPa)	$\sigma_y$ (MPa)	$\sigma_u$ (MPa)
$t_p = 1.80$ mm	200	292	433
$t_p = 2.36$ mm	200	294	393
Aluminum foam	$\rho_f$ (g/cm <sup>3</sup> )	$\sigma_p$ (MPa)	$E_f$ (MPa)
–	0.28	2.87	207.8

Note  $E_y$ ,  $E_f$  –Young's modulus of steel and aluminum foam;  $\sigma_y$ ,  $\sigma_u$  –Yield and ultimate stress of steel;  $\rho_f$ ,  $\sigma_p$  –Density and plateau stress of aluminum foam

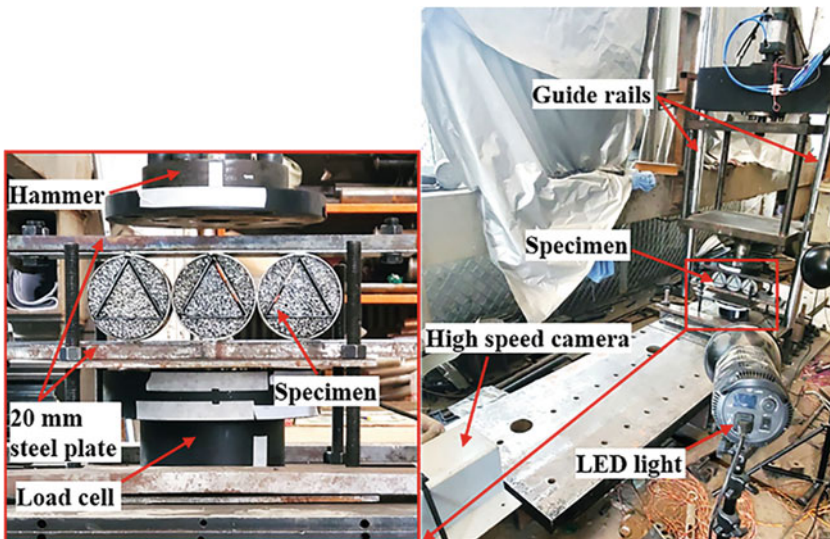


**Fig. 3.2** Test setup of AFCTNT energy absorber, reprinted from Wang et al. (2021), copyright 2022, with permission from Elsevier

can be lift up to 20 m using the hosting system. It drops freely along the guide rails and strikes the specimens once the electromagnet release mechanism is triggered. The dynamic load cell is installed below the specimen to measure the pure impact force and remove the inertial force from the measurement. The top and bottom plates of the AFCTNT energy absorbers are enhanced with two steel plates with thickness of 20 mm through bolting connection for preventing plastic deformation of these two plates and assuring the impact energy only dissipated through circular tubes, triangular tubes, and aluminum foam. The total drop weight was 400 kg, and the drop heights of the specimens presented in Table 3.2 were determined based on trial numerical simulations, assuring the specimens reaching densification and maximum impact force being smaller than 2000 kN (the maximum measurement range of the dynamic load cell). The high-speed camera was employed to capture the crushing process of the specimen and movement of the hammer at a speed of 3000 frames per second.

### 3.2.2 Numerical Methodology

The numerical simulations on the AFCTNT energy absorbers under impact loading were performed by employing the explicit code in LS-DYNA (Hallquist 2006). Figure 3.3 presents the FE model of the specimen FFF with fully-filled aluminum foam under impact loading. The aluminum foam and hammer were meshed with

**Table 3.2** Energy absorption parameters of the energy absorbers ( $\delta = 63$  mm)

Specimen	$H_d$ (m)	EA (kJ)	SEA (kJ/kg)	MCF (kN)	CFE
NNN-1	3	5.87	1.90	93.17	0.46
NNN-2	3	6.49	2.09	102.92	0.42
NNN-mean	—	6.18	2.00	98.04	0.44
TTT-1	4	9.18	2.74	145.63	0.58
TTT-2	4	9.90	2.96	157.11	0.49
TTT-mean	—	9.54	2.85	151.37	0.53
CCC-1	4	10.40	2.94	165.01	0.67
CCC-2	4	10.12	2.86	160.52	0.60
CCC-mean	—	10.26	2.90	162.76	0.64
CTC-1	4	8.74	2.52	138.74	0.66
CTC-2	4	8.88	2.56	140.78	0.61
CTC-mean	—	8.81	2.54	139.76	0.63
FFF-1	4.3	15.04	3.97	238.69	0.56
FFF-2	5	14.76	3.90	233.96	0.67
FFF-mean	—	14.90	3.93	236.32	0.62

Note  $H_d$ —Drop height; EA—Energy absorption; SEA—Specific energy absorption; MCF—Mean crushing force; CFE—Crushing force efficiency

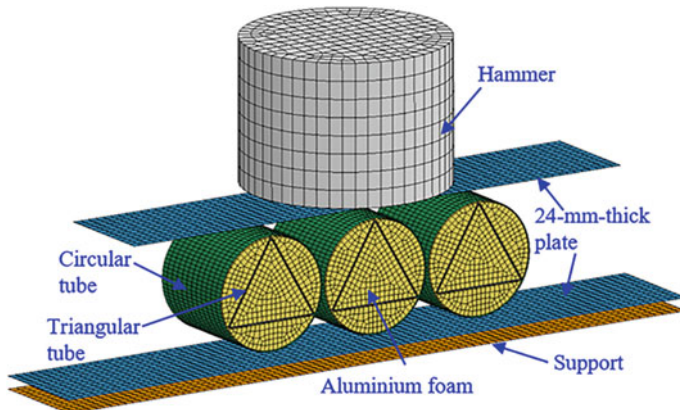
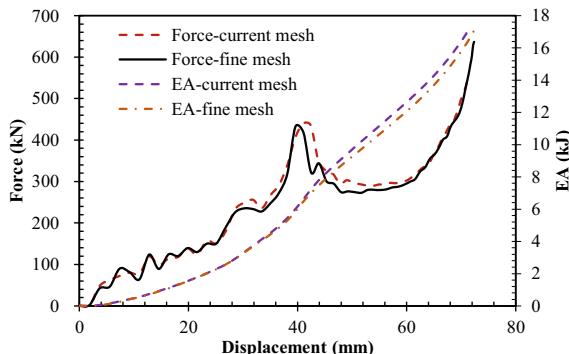


**Fig. 3.3** FE model of the specimen FFF under impact loading, reprinted from Wang et al. (2021), copyright 2022, with permission from Elsevier

8-node solid elements, and reduced integration of the solid element was employed to reduce computation time. The Belytschko-Tsay shell element was employed for meshing circular and triangular tubes, flat plates and support, and five integration points were specified along thickness of the shell element. The stiffness-based hour-glass control was employed for prohibiting the zero-energy deformation modes of

the elements with reduced integration. The mesh size of 4 mm was chosen for the circular tubes, triangular tubes and aluminum foam which experienced severe plastic deformation during impact, and 8 mm mesh size was adopted for the support and flat plates. The current mesh sizes in the FE modeling were chosen based on the mesh sensitivity analysis. The FE model of the specimen FFF with fine mesh sizes (by halving the current mesh sizes) was also established, and the FE-predicted energy absorption and force versus displacement curves were found to be close on employing the two mesh sizes, as presented in Fig. 3.4. Therefore, the current mesh sizes were adopted for the following numerical simulations in this study, which could assure both the accuracies of the FE results and reasonable computation time. The contacts between two parts of the FE model were simulated utilizing the “automatic surface to surface” option in LS-DYNA. The penalty-based contact approach was employed for the contact pairs with steel material (i.e., hammer, flat plate, circular tube, triangular tube and support), since its contact stiffness is determined by an algorithm based on the sizes and material properties of contact segments and it works more effectively when the material stiffness parameters between the contacting surfaces are of the same order-of-magnitude. The contact between aluminum foam and metallic tubes was modeled through the soft constraint-based contact approach, whose contact stiffness is independent of material parameters and suited for treating the contact between materials of different stiffness parameters (i.e., aluminum foam and steel plate). The fixed boundary condition was applied to the support, and all the degrees of freedom of the nodes on the hammer were constrained except for the vertical direction. The initial impact velocity of the hammer was specified via the keyword “\*Initial\_Velocity\_Generation”. The welding connections between the circular tubes and flat plates were modeled through tying the nodes on the welding zone of circular tubes to flat plates, since welding connection failure was not observed from the drop-weight impact tests. The 4-mm-thick top and bottom steel plates were bolted to the two 20-mm-thick steel plates in the test setup, and no bolting connection failure was observed from the tests. Hence, the 24-mm-thick steel plates were adopted in the FE model to replace the two flat plates (with thickness of 4 and 20 mm, respectively) connected by bolts (Fig. 3.3).

**Fig. 3.4** Mesh sensitivity analysis of AFCTNT energy absorber, reprinted from Wang et al. (2021), copyright 2022, with permission from Elsevier



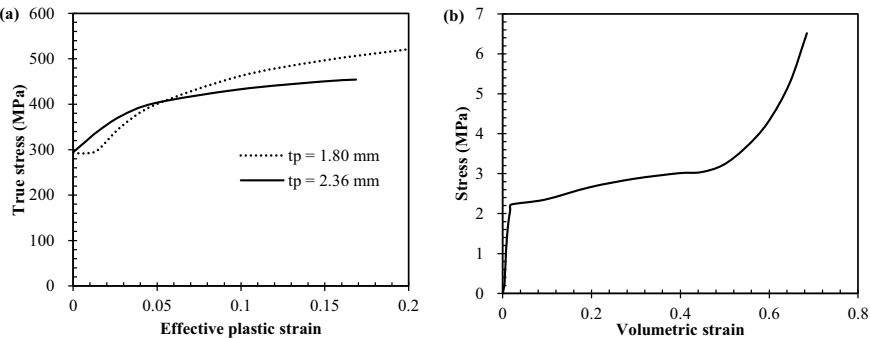


**Fig. 3.5** Stress–strain curves defined in the FE model: **a** mild steels and **b** aluminum foam, reprinted from Wang et al. (2021), copyright 2022, with permission from Elsevier

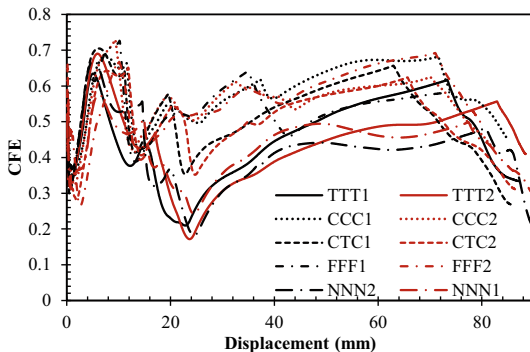
The Piecewise Linear Plasticity model (MAT\_24 in LS-DYNA) was employed in the FE model to simulate steel materials of the AFCTNT energy absorber. The strain rate effect was considered in this model via employing the Cowper-Symonds model, and the strain rate parameters  $C$  and  $P$  are defined as  $40.4\text{ s}^{-1}$  and 5 for mild steel (Jones 1988). The material properties of circular and triangular tubes defined in the FE model were obtained from tensile coupon tests and presented in Table 3.1, and the true stress–effective plastic strain curves are presented in Fig. 3.5a. The Crushable Foam material model (MAT\_63), which showed desirable performance and high computational efficiency (Hanssen et al. 2002), was adopted for simulating aluminum foam. The input stress–volumetric strain curve for aluminum foam was obtained from the uniaxial compressive loading tests and given in Fig. 3.5b. The plastic Poisson’s ratio of aluminum foam was defined to be 0.01 (Qi et al. 2018; Yang and Qi 2013) as the lateral expansion of aluminum foam under uniaxial compressive loading was found to be minimal (Song et al. 2005).

### 3.3 Results and Discussions

#### 3.3.1 Energy Absorption Parameters

The energy absorption parameters, e.g., energy absorption ( $EA$ ), specific energy absorption ( $SEA$ ), mean crushing force ( $MCF$ ), and crushing force efficiency ( $CFE$ ), were generally employed for quantitatively assessing the energy absorption performances of energy absorbers. All the aforementioned energy absorption parameters can be calculated based on crushing force–displacement curve of the energy absorber and are given in Eqs. (1.1)–(1.4). The  $CFE$ –displacement curve is employed herein to determine the densification displacement of the AFCTNT energy absorber, and

**Fig. 3.6** CFE–displacement curves of all the specimens, reprinted from Wang et al. (2021), copyright 2022, with permission from Elsevier

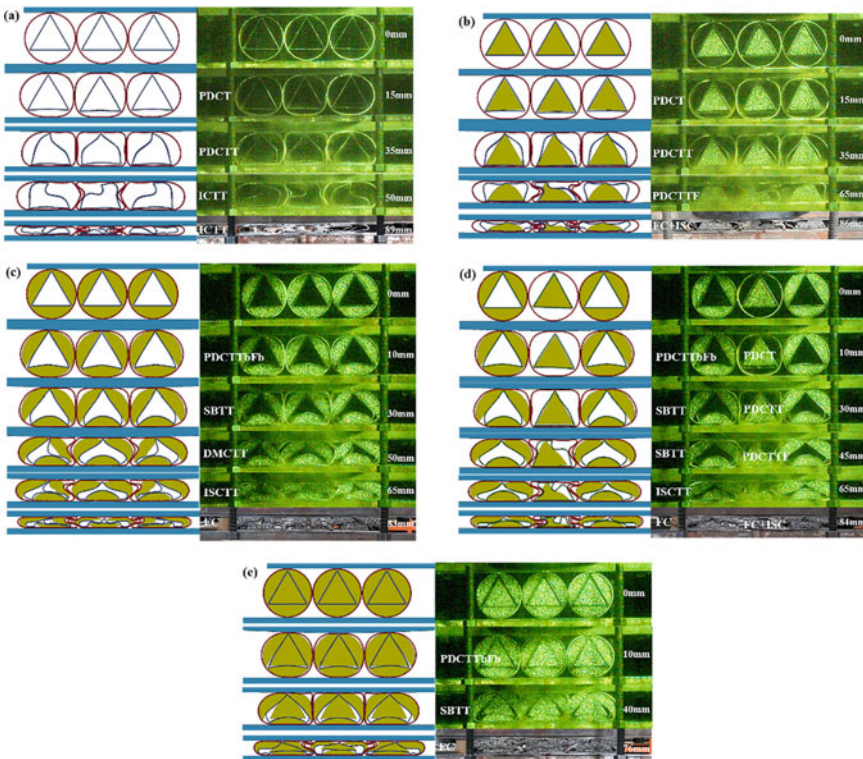


its densification is reached when *CFE* exhibits continuous and sudden drop (Wang et al. 2019). In addition, an identical densification displacement should be chosen for all the specimens to assure a faire comparison of their energy absorption performances. As illustrated in Fig. 3.6, the minimum densification displacement of all the ten specimens (63 mm) was chosen to assure all the specimens reaching densification after this value. Table 3.2 presents the energy absorption parameters of all the tested energy absorbers corresponding to crushing displacement of 63 mm.

### 3.3.2 FE Model Validation

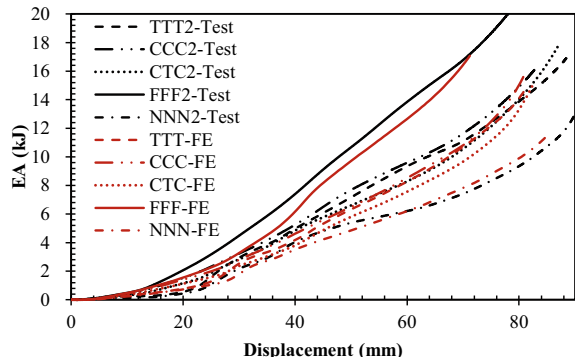
Figure 3.7 provides a comparison of deformation modes of the AFCTNT energy absorbers obtained from FE simulations and drop-weight impact tests, and the FE-predicted deformation modes are found to be consistent with those from the tests. Plastic deformations of the circular and triangular tubes as well as crushing of the aluminum foam can be reasonably captured by the established FE models, including plastic hinge lines and curvature change of nested tubes, buckling modes of triangular tubes, inner surface contacts of nested tubes, and aluminum foam densification. However, There are slightly different deformation modes of the specimen NNN between the test and FE prediction being observed, i.e., the buckling direction of the triangular tube from the FE simulation is not consistent with that from the test. This may be caused by the geometrical imperfection of the fabricated specimen (Wang et al. 2020a), and the buckling direction of the triangular tube is random. The buckling direction of triangular tube has little effect on the energy absorption as the unsymmetrical deformation mode of the triangular tube is observed from both the test and FE prediction. The detailed discussions on the crushing processes of the energy absorbers are given in Sect. 3.3.3.

Figure 3.8 presents a comparison of *EA*–displacement curves obtained from the tests and FE analyses, and good agreement between them can be observed. Generally, the FE-predicted *EA* is found to be slightly smaller than that from tests. In addition, a comparison of force–displacement curves obtained from the tests and FE analyses



**Fig. 3.7** Crushing processes of AFCTNT energy absorbers under impact load: **a** NNN, **b** TTT, **c** CCC, **d** CTC and **e** FFF (PDCT—plastic deformation of only circular tubes; PDCIT—plastic deformation of both circular and triangular tubes; ICTT—interaction between circular and triangular tubes; ISC—inner surface contact; PDCTTF—plastic deformation of circular and triangular tubes and aluminum foam; FC + ISC—aluminum foam compaction and inner surface contact; PDCT-TbFb—plastic deformation of circular tubes, bottom sides of triangular tubes and aluminum foam at bottom; SBTT—symmetrical buckling of triangular tubes; DMCTT—deformation mode change of outer triangular tubes; ISCTT—inner surface contacts of triangular tubes; FC—aluminum foam compaction), reprinted from Wang et al. (2021), copyright 2022, with permission from Elsevier

**Fig. 3.8** Comparison of EA-displacement curves obtained from tests and FE simulations, reprinted from Wang et al. (2021), copyright 2022, with permission from Elsevier



is also presented in Fig. 3.9, which further confirms the reasonable predictions from FE models. The slight differences of force–displacement curves between the tests and FE predictions may be caused by geometric imperfections of the fabricated specimens. The aforementioned comparisons of deformation modes as well as force and energy absorption versus displacement curves between the tests and FE simulations demonstrate that the FE modeling of the AFCTNT energy absorber under impact loading is acceptable and can be employed for further analysis.

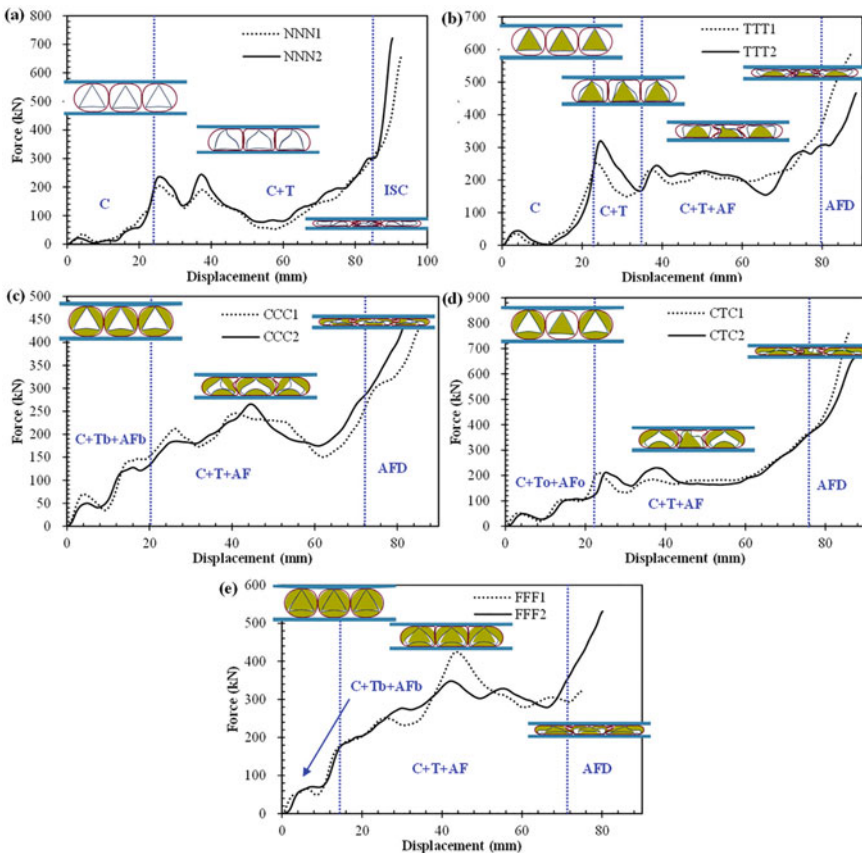


**Fig. 3.9** Force–displacement curves of the AFCTNT energy absorbers: **a** NNN, **b** TTT, **c** CCC, **d** CTC and **e** FFF. (C—Energy dissipation by circular tubes; C + T—Energy dissipation by circular and triangular tubes; C + T + AF—Energy dissipation by circular and triangular tubes as well as aluminum foam; AFD—Aluminum foam densification; C + To + AFo—Energy dissipation by circular tubes as well as triangular tubes and AF of two outer units; C + Tb + AFb—Energy dissipation by circular tubes as well as bottom side of triangular tubes and AF at the bottom; ISC—Inner surface contact), reprinted from Wang et al. (2021), copyright 2022, with permission from Elsevier

### 3.3.3 Deformation Mode

Figure 3.7 presents the crushing processes of the tested AFCTNT energy absorbers subjected to impact loading. For the specimen NNN without aluminum foam, the impact energy is dissipated through plastic deformation of circular and triangular tubes, and four crushing stages are identified (Wang et al. 2020a). Only circular tubes exhibit plastic deformation at initial crushing stage ( $\delta = 15$  mm in Fig. 3.7a), and the interaction between adjacent circular tubes is achieved via assembling the circular tubes to be contacted with each other, and meanwhile welding the circular tubes to the top and bottom flat plates. This results in higher energy absorption than that of circular tubes without constraints. The inclined sides of triangular tubes start to buckle and absorb impact energy via plastic deformation with further crushing, and both symmetrical and asymmetrical deformation modes of the three triangular tubes are observed after buckling ( $\delta = 35$  mm in Fig. 3.7a). When  $\delta = 50$  mm, the triangular tubes contact with circular tubes, and the interaction between triangular and circular tubes can be observed, which leads to the deformation mode change of the middle triangular tube (from a symmetrical mode to an asymmetrical one). Finally, the inner surface contacts of triangular tubes occurs, which leads to densification of the specimen ( $\delta = 89$  mm in Fig. 3.7a).

As for the specimen TTT with aluminum foam only being filled in three triangular tubes, four different crushing stages can also be found. The deformation modes of the specimen TTT at the first and second crushing stages are similar to those of specimen NNN without aluminum foam filler, i.e., plastic deformation of only circular tubes and plastic deformation of both circular and triangular tubes for the first and second crushing stage, respectively ( $\delta = 15$  and 35 mm, respectively, in Fig. 3.7b). Herein, all the triangular tubes exhibit asymmetrical deformation mode after buckling. With further crushing of the specimen TTT, aluminum foam starts to experience evident compaction and dissipate impact energy ( $\delta = 65$  mm in Fig. 3.7b). Moreover, the interactions between the triangular tubes and aluminum foam as well as between the triangular and circular tubes are also observed, which can improve the energy absorption capacity of the specimen. The densification of specimen TTT is reached after complete compaction of aluminum foam and inner surface contacts of nested tubes ( $\delta = 86$  mm in Fig. 3.7b).

Figure 3.7c presents the crushing processes of the specimen CCC with aluminum foam only being filled in the gaps between the circular and triangular tubes, and five crushing stages can be observed. At initial crushing stage ( $\delta = 10$  mm in Fig. 3.7c), plastic deformation of the circular tubes and bottom sides of the triangular tubes can be observed, and meanwhile aluminum foam below the bottom sides of triangular tubes also exhibits evident compaction. All the triangular tubes then experience symmetrical deformation mode after buckling, and the plastic deformation occurs at the inclined sides of triangular tubes with further crushing of the specimen ( $\delta = 30$  mm in Fig. 3.7c). The determined symmetrical deformation mode of triangular tubes at this crushing stage is believed to be triggered by upward bending of the bottom sides of triangular tubes. When crushing displacement is 50 mm, concavity

of the two outer circular tubes at the contacted surfaces is developed, which results in the change of deformation mode of the two outer triangular tubes, i.e., from a symmetrical mode to an asymmetrical one. With continuous crushing, inner surface contacts of triangular tubes occur when crushing displacement is 65 mm. After that, aluminum foam exhibits more rapid crushing, and densification of the specimen is reached with complete compaction of aluminum foam ( $\delta = 83$  mm in Fig. 3.7c).

The crushing processes of the specimen CTC under impact loading is presented in Fig. 3.7d. Aluminum foam is filled in the middle triangular tube as well as in the gaps between the circular and triangular tubes of the two outer nested tubes. With regard to the deformation modes of the specimen CTC, the two outer nested tubes with aluminum foam filled in the gaps between the circular and triangular tubes exhibit similar deformation modes to those of specimen CCC, while the deformation modes of the middle nested tubes with aluminum foam filled in the triangular tube is consistent with those of specimen TTT. Figure 3.7e presents the crushing processes of the specimen FFF with fully-filled aluminum foam, and three crushing stages can be identified. Similar to the deformation mode of the specimen CCC at initial crushing stage, the specimen FFF also exhibits plastic deformations of circular tubes, bottom sides of triangular tubes, and aluminum foam below the bottom sides of triangular tubes at initial crushing stage ( $\delta = 10$  mm in Fig. 3.7e). Subsequently, symmetrical deformation mode of all three triangular tubes after buckling is observed with further crushing, similar to the deformation mode of specimen CCC at the second crushing stage. Meanwhile, all the aluminum foam fillers exhibit evident compaction at  $\delta = 40$  mm. Finally, densification of the specimen FFF is reached after complete compaction of aluminum foam.

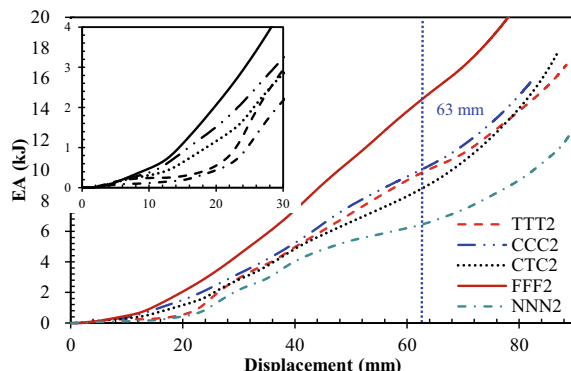
### 3.3.4 Force and Energy Absorption Responses

The force–displacement responses of the AFCTNT energy absorbers under impact loading are presented in Fig. 3.9, and the repeatability of the experimental data can be confirmed. Figure 3.9a presents the force–displacement curves of the specimen NNN without aluminum foam, and three stages can be identified based on its energy absorption characteristic. The specimen NNN exhibits low crushing force and energy absorption at initial stage, since only plastic deformation of circular tubes contributes to the energy absorption. The crushing force exhibits rapid increase with displacement exceeding 20 mm, which indicates that the inclined sides of the triangular tubes start to resist impact force and buckle after the first peak force. Subsequently, plastic deformation of both circular and triangular tubes contributes to the energy dissipation, which leads to larger crushing force as compared to the initial stage. Finally, rapid and continuous increase of crushing force is observed when inner surface contacts of the tubes occur, and densification of the specimen NNN is reached. With regard to the specimen TTT, the first two stages of the force–displacement response are similar to those of specimen NNN, i.e., only plastic deformation of circular tubes contributing to energy dissipation at the first stage and the following energy

dissipation via plastic deformation of both circular and triangular tubes at the second stage. The aluminum foam starts to undergo evident compaction and dissipate impact energy when displacement exceeds 35 mm. It enters the third stage, and energy dissipation is contributed by circular and triangular tubes as well as aluminum foam. The crushing force also exhibits sudden increase after densification of the specimen when complete compaction of aluminum foam occurs. For the specimens CCC, CTC and FFF which exhibit similar force–displacement response, three stages can be identified from their force–displacement curves. At the initial stage, the force–displacement curves of the specimens CCC and FFF are similar owing to their similar energy dissipation manners, i.e., plastic deformations of circular tubes, bottom sides of triangular tubes, and aluminum foam below the bottom sides of triangular tubes. With regard to the specimen CTC at the initial stage, lower crushing force as compared to specimens CCC and FFF can be observed because the triangular tubes and aluminum foam filled in the middle triangular tube of the specimen CTC have not contributed to energy dissipation at the initial stage. The three specimens (CCC, CTC and FFF) share similar energy dissipation at the second and third stages, i.e., energy dissipation from the circular and triangular tubes, and aluminum foam at the second stage, followed by densification of the specimen induced by aluminum foam compaction at the third stage. It is also noted in Fig. 3.9 that filling aluminum foam in the gaps between the circular and triangular tubes can reduce the peak buckling force, i.e., the specimens CCC, CTC and FFF exhibit smaller peak buckling forces and smoother force–displacement curves as compared to specimens NNN and TTT.

Figure 3.10 presents a comparison of  $EA$ –displacement curves of the AFCTNT energy absorbers with variation in aluminum foam volume. All the specimens initially exhibit low energy dissipation rate because the triangular tubes and aluminum foam fillers have not undergone plastic deformation and dissipated impact energy at the initial stage, as discussed in Sect. 3.3.3. Generally, the AFCTNT energy absorber with larger volume of aluminum foam exhibits higher  $EA$ , except for specimens CTC and TTT.  $EA$  of the specimen TTT with smaller volume of aluminum foam is higher than that of specimen CTC with displacement ranging from 37 to 78 mm. However, the specimen CTC exhibits higher  $EA$  than that of specimen TTT at the

**Fig. 3.10** Comparison of  $EA$ –displacement curves from the five types of energy absorbers, reprinted from Wang et al. (2021), copyright 2022, with permission from Elsevier



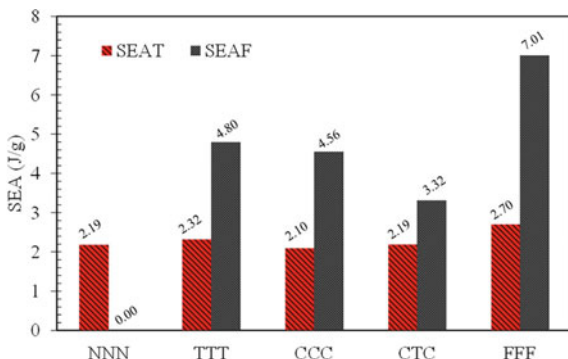
initial and final crushing stages. It can be concluded that filling the energy absorber with aluminum foam is an effectively way to improve its energy absorption performance. The comparison of *EA*-displacement curves between the specimen NNN and TTT in Fig. 3.10 reveals that energy absorptions of the two specimens are similar at the initial crushing stage and the specimen TTT exhibits higher *EA* when displacement exceeds 20 mm. This is because the aluminum foam filled in triangular tubes only experiences evident compaction and start to dissipate energy with displacement exceeding 20 mm. This also leads to similar *EA* of specimen FFF and CCC at the initial crushing stage when displacement is smaller than 15 mm, as can be seen in Fig. 3.10. With further crushing, the specimen FFF with fully-filled aluminum foam exhibits higher *EA* as compared to the specimen CCC when the aluminum foam filled in triangular tubes initiates energy dissipation. Hence, it can be concluded that the aluminum foam filled in the gaps between circular and triangular tubes experiences earlier compaction as compared to that filled in the triangular tubes. In addition, *EA* of aluminum foam filled in the gaps between circular and triangular tubes is found to be higher as compared to that filled in triangular tubes owing to its larger volume of aluminum foam.

### 3.3.5 Energy Absorption Performance

The energy absorption parameters of the tested specimens, including *EA*, *SEA*, *MCF* and *CFE*, are presented in Table 3.2, and the energy absorption parameters of the two identical specimens are found to be close, which confirms the repeatability of the experimental data. The comparison of specimens with and without aluminum foam filler reveals that the aluminum foam filler can significantly improve the energy absorption performance in terms of the increase in *EA*, *SEA*, *MCF* and *CFE*. Further, *EA*, *SEA* and *MCF* generally exhibit increase as the volume of aluminum foam increases. The aluminum foam-filled specimens TTT, CCC, CTC and FFF exhibit 54.4%, 66.0%, 42.5% and 141.0% increase in *EA* (or *MCF*) as compared to the specimen without aluminum foam (NNN). The corresponding increase percentages of *SEA* are 42.7%, 45.5%, 27.2% and 97.2%, and the improvement in *SEA* by filling aluminum foam is due to higher *SEA* of aluminum foam as compared to nested tubes (as presented in Fig. 3.11). In addition, *CFE* of the energy absorber is also improved with the presence of aluminum foam filler, i.e., the specimens TTT, CCC, CTC and FFF exhibits 21.6, 45.3, 44.4 and 40.7% increase in *CFE* as compared to the specimen NNN. This indicates that the aluminum foam filler can effectively smooth the force-displacement curve and improve the energy absorption efficiency of the energy absorber.

Figure 3.11 presents the FE-predicted *SEA* values of nested tubes and aluminum foams of the specimens corresponding to crushing displacement of 63 mm. The *SEA* of nested tubes of the specimen FFF with fully-filled aluminum foam is found to be improved by 23.3% as compared to the specimen NNN. In addition, filling aluminum foam in triangular tubes (specimen TTT) also results in 5.9% increase of

**Fig. 3.11** SEAs of nested tubes (SEAT) and aluminum foam (SEAF) from FE analyses, reprinted from Wang et al. (2021), copyright 2022, with permission from Elsevier

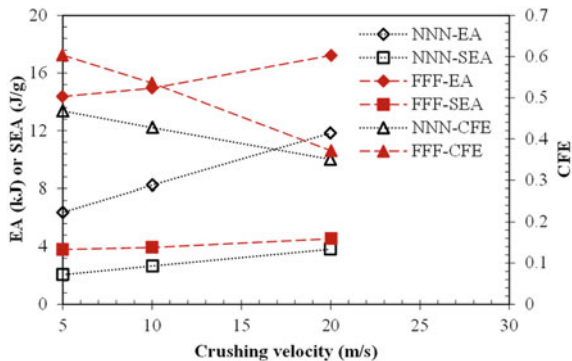


SEA of nested tubes. This indicates that the interaction effect between nested tubes and aluminum foam can enhance energy absorption performance of nested tubes for specimens FFF and TTT. Further, the specimen FFF with fully-filled aluminum foam exhibits highest SEA of nested tubes, indicating its more significant interaction effect between nested tubes and aluminum foam as compared to the other energy absorbers. With regard to SEA of aluminum foam, the highest value is observed for the specimen FFF (7.01 J/g), followed by specimens TTT and CCC (4.80 and 4.56 J/g, respectively). The specimen CTC exhibits lowest SEA of aluminum foam (3.32 J/g). Hence, it can be concluded that the AFCTNT energy absorber with fully-filled aluminum foam is superior to the other energy absorbers with partially-filled aluminum foam or without aluminum foam in terms of higher SEA of nested tubes and aluminum foam. This can be attributed to its more significant interaction effect between nested tubes and aluminum foam.

### 3.3.6 Further FE Analysis

During the drop-weight impact tests, different drop heights (or initial impact velocities) were chosen for different specimens in order to assure all the specimens reaching densification and the maximum impact force being smaller than 2000 kN. Herein, the FE simulations on the specimens FFF and NNN under the same crushing velocity are conducted in order to more fairly compare the performances of energy absorbers with and without aluminum foam filler. Moreover, three different crushing velocities are also adopted for the specimens FFF and NNN, including 5, 10 and 20 m/s, and the effect of crushing velocity on the energy absorption performance can be revealed. Figure 3.12 presents a comparison of energy absorption parameters of FFF and NNN under variant crushing velocity. Increasing crushing velocity is found to result in the evident increase in EA and SEA, but decrease in CFE. In addition, an almost linear variation of these energy absorption parameters to crushing velocity can be observed. The EA (or SEA) of FFF and NNN are increased by 19.8% and 85.7%, respectively, on increasing crushing velocity from 5 m/s to 20 m/s. This can

**Fig. 3.12** Effect of crushing velocity on energy absorption performance, reprinted from Wang et al. (2021), copyright 2022, with permission from Elsevier



be attributed to the significant strain rate sensitivity of mild steel. It is also noted that the increase percentage of FFF with fully-filled aluminum foam is smaller than that of NNN without aluminum foam filler. This is because the aluminum foam generally exhibits strain rate insensitivity. Moreover, the inertial effect may also result in the increase in *EA* (or *SEA*) of FFF and NNN via changing deformation mode. Figure 3.12 also shows that the *CFE* of FFF and NNN is decreased by 38.5% and 17.2%, respectively, on increasing crushing velocity from 5 m/s to 15 m/s, which can be attributed to the increased peak buckling forces of the two energy absorbers. The comparison of energy absorption parameters of FFF and NNN indicates that the aluminum foam filled energy absorber (FFF) outperforms the one without aluminum foam (NNN) in terms of higher *EA*, *SEA* and *CFE*, which is mainly owing to the high *SEA* and smooth stress-strain relationship of aluminum foam.

To further confirm the superior performance of the AFCTNT energy absorber with aluminum foam filler, the FE simulations are conducted on two additional CTNT energy absorbers which have identical weight to the AFCTNT energy absorber via increasing the thickness of circular tube (NNN-C) and triangular tube (NNN-T), respectively. Figure 3.13 presents a comparison of energy absorption parameters of the three specimens with identical weight (i.e., FFF, NNN-C and NNN-T) under crushing velocity of 10 m/s. The specimen FFF is found to outperform the other two specimens without aluminum foam filler (NNN-C and NNN-T). With regard to *EA* (or *SEA*) of the three specimens, the highest value is observed for FFF, followed by NNN-T and NNN-C, owing to higher *SEA* of aluminum foam as compared to triangular and circular tubes. The laterally loaded triangular tube generally exhibits higher *EA* and *SEA* as compared to circular tube (Wang et al. 2020a), which results in higher *EA* and *SEA* of NNN-T with increased thickness of triangular tube as compared to NNN-C with increased thickness of circular tube. However, the crushing force-displacement curve of laterally loaded triangular tube is less smooth than that of circular tube, which generally yields a smaller *CFE*. Hence, the specimen NNN-T exhibits lowest *CFE* among the three specimens. It is known that increasing the thickness of laterally loaded tube can generally increase its *SEA* as the increase in *EA* of the tube is more significant as compared to the increase in weight via increasing

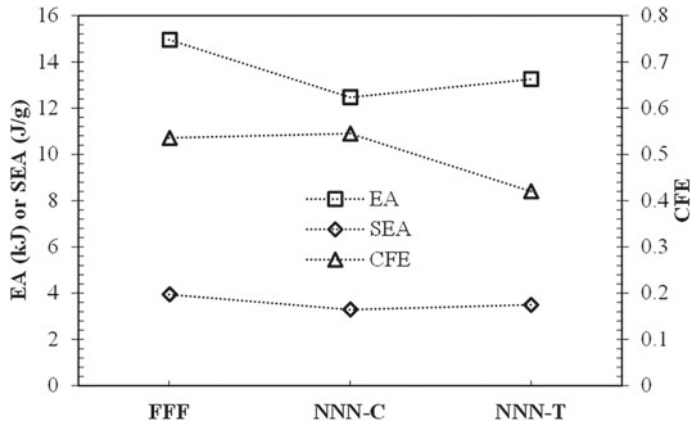


**Fig. 3.13** Energy absorption parameters of FFF, NNN-C and NNN-T, reprinted from Wang et al. (2021), copyright 2022, with permission from Elsevier

thickness of the tube (Wang et al. 2020b). However, thicker tube may be more prone to fracture failure under severe crushing. With regard to aluminum foam, it exhibits both high *SEA* and smooth stress–strain relationship, which can be employed for improving the performance of “tube-type” energy absorbers.

### 3.4 Summary

In this chapter, a new AFCTNT energy absorber was proposed, and its energy absorption performance under impact loading was experimentally and numerically studied. The energy absorption parameters, deformation modes, and force–displacement responses of the AFCTNT energy absorbers were obtained by employing an instrumented drop-weight impact test system. In addition, numerical studies on the AFCTNT energy absorbers under impact loading were also performed to further reveal their impact responses and energy absorption performances. The main findings from the experimental and numerical studies were summarized as follows:

1. The variation in aluminum foam volume exhibited evident influence on the deformation modes and impact energy dissipation manners of AFCTNT energy absorbers. The aluminum foam filled in the gaps between circular and triangular tubes exhibited earlier impact energy dissipation as compared to that filled in triangular tubes.
2. Experimental results showed that the variation in aluminum foam volume also affected the force–displacement responses of the AFCTNT energy absorbers. The aluminum foam filled in the gaps between circular and triangular tubes was found to smooth the force–displacement curve of the energy absorber, thus resulting in higher energy absorption efficiency.

3. The energy absorption parameters of AFCTNT energy absorbers (*EA*, *SEA*, *MCF* and *CFE*) were found to be significantly improved by filling aluminum foam, and the AFCTNT energy absorbers filled with larger volume of aluminum foam generally exhibited higher energy absorption capacity.
4. The AFCTNT energy absorber with fully-filled aluminum foam was found to outperform the other AFCTNT energy absorbers with partially-filled aluminum foam or without aluminum foam in terms of higher *EA* and *SEA*, which could be attributed to more significant interaction effect between nested tubes and aluminum foam.
5. Numerical results showed that increasing crushing velocity could result in evident increase in *EA* and *SEA*, but decrease in *CFE*. In addition, the aluminum foam could be a desirable energy absorbing material to be filled in the CTNT energy absorber for enhancing its energy absorption performance.

## References

- Ahmad Z, Thambiratnam DP (2009) Dynamic computer simulation and energy absorption of foam-filled conical tubes under axial impact loading. *Comput Struct* 87:186–197
- Baroutaji A, Arjunan A, Stanford M et al (2021) Deformation and energy absorption of additively manufactured functionally graded thickness thin-walled circular tubes under lateral crushing. *Eng Struct* 226:111324
- Baroutaji A, Gilchrist MD, Olabi AG (2016) Quasi-static, impact and energy absorption of internally nested tubes subjected to lateral loading. *Thin-Walled Struct* 98:337–350
- Baroutaji A, Gilchrist MD, Smyth D et al (2015) Analysis and optimization of sandwich tubes energy absorbers under lateral loading. *Int J Impact Eng* 82:74–88
- Baroutaji A, Sajjia M, Olabi AG (2017) On the crashworthiness performance of thin-walled energy absorbers: Recent advances and future developments. *Thin-Walled Struct* 118:137–163
- Duarte I, Vesenjak M, Krstulović-Opara L et al (2015) Static and dynamic axial crush performance of in-situ foam-filled tubes. *Compos Struct* 124:128–139
- Fan H, Hong W, Sun F et al (2015) Lateral compression behaviors of thin-walled equilateral triangular tubes. *International Journal of Steel Structures Int J Steel Struct* 15(4):85–795
- Fan Z, Shen J, Lu G et al (2013) Dynamic lateral crushing of empty and sandwich tubes, *Int J Impact Eng* 53:3–16
- Fang J, Gao Y, An X et al (2016) Design of transversely-graded foam and wall thickness structures for crashworthiness criteria. *Compos Part B: Eng* 92:338–349
- Gupta NK, Sekhon GS, Gupta PK (2001) A study of lateral collapse of square and rectangular metallic tubes, *Thin-Walled Struct* 39(9):745–772
- Gupta NK, Sekhon GS, Gupta PK (2005) Study of lateral compression of round metallic tubes. *Thin-Walled Struct* 43:895–992
- Hallquist JO (2006) LS-DYNA theory manual. Livermore Software Technology Corporation (LSTC). Livermore, California
- Hanssen AG, Hopperstad OS, Langseth M et al (2002) Validation of constitutive models applicable to aluminium foams, *Int J Mech Sci* 44:359–406
- Jones N (1988) Structural Impact. Cambridge University Press, Cambridge/New York
- Kilicaslan C (2015) Numerical crushing analysis of aluminum foam-filled corrugated single- and double-circular tubes subjected to axial impact loading. *Thin-Walled Struct* 96:82–94

- McDevitt TJ, Simmonds JG (2003) Crushing of an elastic-plastic ring between rigid plates with and without unloading. *J Appl Mech* 70:799–808
- Nikkhah H, Baroutaji A, Kazancı Z et al (2020) Evaluation of crushing and energy absorption characteristics of bio-inspired nested structures. *Thin-Walled Struct* 148:106615
- Morris E, Olabi AG, Hashmi MSJ (2006) Analysis of nested tube type energy absorbers with different indenters and exterior constraints. *Thin-Walled Struct* 44:872–885
- Olabi AG, Morris E, Hashmi MSJ et al (2008) Optimised design of nested oblong tube energy absorbers under lateral impact loading. *Int J Impact Eng* 35(1):10–26
- Qi C, Sun Y, Yang S (2018) A comparative study on empty and foam-filled hybrid material double-hat beams under lateral impact. *Thin-Walled Struct* 129:327–341
- Qi C, Yang S (2014) Crashworthiness and lightweight optimisation of thin-walled conical tubes subjected to an oblique impact. *Int J Crashworthiness* 19(4):334–351
- Santosa SP, Wierzbicki T, Hanssen AG et al (2000) Experimental and numerical studies of foam-filled sections. *Int J Impact Eng* 24:509–534
- Reddy TY, Reid SR (1979) Lateral compression of tubes and tube-systems with side constraints. *Int J Mech Sci* 21 (3):187–199
- Reid SR, Drew SLK, Carney JF (1983) Energy absorbing capacities of braced metal tubes, *Int J Mech Sci* 25(9–10):649–667
- Reyes A, Hopperstad OS, Langseth M (2004) Aluminum foam-filled extrusions subjected to oblique loading: experimental and numerical study. *Int J Solids Struct* 41:1645–1675
- Shahbeyk S, Petrinic N, Vafai A (2007) Numerical modelling of dynamically loaded metal foam-filled square columns. *Int J Impact Eng* 34:573–586
- Shen J, Lu G, Ruan D, Seah CC (2015) Lateral plastic collapse of sandwich tubes with metal foam core. *Int J Mech Sci* 91:99–109
- Song HW, Fang ZJ, Yu G et al (2005) Partition energy absorption of axially crushed aluminium foam-filled hat sections. *Int J Solids Struct* 42(9):2575–2600
- Su XY, Yu TX, Reid SR (1995a) Inertia-sensitive impact energy-absorbing structures part I: effects of inertia and elasticity. *Int J Impact Eng* 16(4):651–672
- Su XY, Yu TX, Reid SR (1995b) Inertia-sensitive impact energy-absorbing structures part II: effects of strain rate. *Int J Impact Eng* 16(4):673–689
- Tran T (2017) Crushing analysis of multi-cell thin-walled rectangular and square tubes under lateral loading. *Compos Struct* 160:734–747
- Tran T, Ton TNT (2016) Lateral crushing behaviour and theoretical prediction of thin-walled rectangular and square tubes, *Compos Struct* 154:374–384
- Tran TN, Baroutaji A, Estrada Q et al (2021) Crashworthiness analysis and optimization of standard and windowed multi-cell hexagonal tubes. *Struct Multidisc Optim* 63:2191–2209
- Wang CY (1987) Crushing of an elastic-perfectly plastic ring or tube between two planes. *J Appl Mech* 54:159–164
- Wang P, Zheng Q, Fan H et al (2015) Quasi-static crushing behaviors and plastic analysis of thin-walled triangular tubes. *J Constr Steel Res* 106:35–43
- Wang Y, Lu J, Zhai X et al (2019) Response of energy absorbing connector with polyurethane foam and multiple pleated plates under impact loading. *Int J Impact Eng* 133:103356
- Wang Y, Zhai X, Liu S et al (2020a) Energy absorption performance of a new circular-triangular nested tube and its application as sacrificial cladding. *Thin-Walled Struct* 106:992
- Wang Y, Zhang B, Lu J et al (2020b) Quasi-static crushing behaviour of the energy absorbing connector with polyurethane foam and multiple pleated plates. *Eng Struct* 211:110404
- Wang Y, Zhang R, Liu S et al (2021) Energy absorption behaviour of an aluminium foam-filled circular-triangular nested tube energy absorber under impact loading. *Structures* 34:95–104
- Wu L, Carney JF (1997) Initial collapse of braced elliptical tubes under lateral compression. *Int J Mech Sci* 39(9):1023–1036
- Yang S, Qi C (2013) Multiobjective optimization for empty and foam-filled square columns under oblique impact loading. *Int J Impact Eng* 54:177–191

# Chapter 4

## Sandwich Panel with Aluminum Foam-Filled Tubular Cores Under Impact



### 4.1 Introduction

In recent years, excessive devastations of civil structures caused by vehicle impacts, terrorist attacks and rockfall accidents have shown an increasing trend (Roy and Matsagar 2021; Yu et al. 2021). Hence, it is of significance to assure the high impact resistance of critical infrastructures (Iqbal et al. 2019; Soltani et al. 2020). In order to further enhance the impact resistances of structures, an energy absorbing layer can be employed as the sacrificial cladding to dissipate impact energy, as exhibited in Fig. 4.1. Therefore, it is of necessity to develop novel energy absorbing panels and study their impact responses and energy absorption performances.

The metallic tubes have been widely employed as energy absorbers owing to their good energy absorption performances (Baroutaji et al. 2021; Xu et al. 2018). The dynamic behaviors of metallic tubes under lateral loading were extensively studied. The metallic tube could effectively dissipate energy through plastic deformation (Baroutaji et al. 2014), and its energy absorption could be further increased via constraining its lateral movements (Reddy and Reid 1979). The metallic tube subjected to impact loading was also found to dissipate more energy as compared to that under quasi-static loading owing to strain rate effect and inertial effect (Baroutaji et al. 2016). Recently, metallic foam was extensively employed as energy absorption components, and its mechanical behaviors were extensively studied. The deformation process of the foam under compressive loading could be divided into three stages: elastic, plateau and densification (Fang et al. 2017). During the plateau stage, the metallic foam exhibited large compressive deformation at a nearly constant compressive stress, and thus could dissipate energy effectively (Wang et al. 2021). To further improve the energy absorption performances of the metallic tubes, the aluminum foam-filled metallic tubes were developed (Baroutaji et al. 2017; Kılıçaslan 2015; Song et al. 2020), and its specific energy absorption was found to be greatly improved as compared to the empty tubes (Hall et al. 2002). Moreover, the quasi-static and dynamic bending responses of aluminum foam-filled metallic tubes were studied

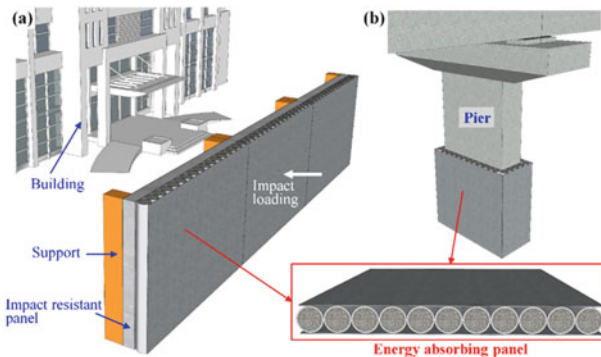


**Fig. 4.1** Application of the energy absorbing panel for impact resisting: **a** impact resistant panel and **b** pier, reprinted from Lu et al. (2021), copyright 2022, with permission from Elsevier

through quasi-static three-point bending tests and drop-weight impact tests, respectively (Guo and Yu 2011a, b; Zhang et al. 2020a). The deformation mode of the foam-filled tube under impact loading was found to be different from that under quasi-static loading, and the impact behaviors of the metallic foam-filled circular tube could be predicted via employing analytical methodology (Zhang et al. 2020a). Moreover, a novel energy absorption connector with aluminum foam filler and pleated steel plates was recently proposed, which could be inserted between the blast resistant panel and the building to dissipate blast or impact energy (Wang et al. 2017; Wang et al. 2018a, b; Wang and Zhai 2019). The quasi-static and dynamic behaviors of the connectors were experimentally and numerically studied, and their energy absorption performances could be evaluated by employing a developed analytical model.

Previous studies demonstrated that the civil structures could be effectively protected from extreme events via employing the energy absorbing layer to dissipate impact and blast energy (Schenker et al. 2005; Xu et al. 2021). Hence, several energy absorbing panels have been developed (Li et al. 2020; Ouadai et al. 2018; Xie et al. 2020; Zhang et al. 2020b). An enormous amount of studies were performed on the impact behaviors of foam-core sandwich panels (Huo et al. 2020; Mocian et al. 2017, 2018; Zhu and Sun 2020). The impact responses of the foam-core sandwich panel were found to be significantly affected by the impactor shape (Huo et al. 2020). Zhu and Sun (2020) developed an analytical model to predict the impact responses of foam-core sandwich panels. In addition, extensive studies have been conducted on the dynamic responses of energy absorbing sandwich panels with thin-walled structures as core (Liu et al. 2019; Qi et al. 2017; Qin et al. 2020; Zhang et al. 2017). Qin et al. (2020) reported that the impact position had significant influence on the impact responses of honeycomb sandwich plates, and the impact resistance of the sandwich plate decreased as the impact was shifted from the central position to the non-central positions. Zhang et al. (2017) studied the effect of impact energy on the dynamic responses of the honeycomb sandwich panels, and the results indicated that

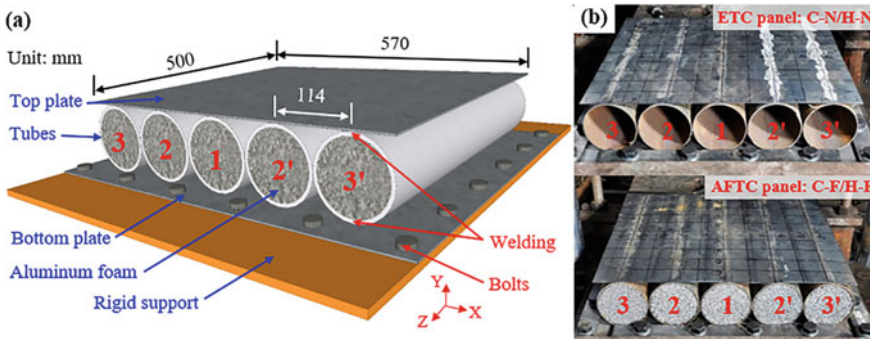


**Fig. 4.2** Details of the proposed sandwich panels: **a** 3D view and **b** photographs, reprinted from Lu et al. (2021), copyright 2022, with permission from Elsevier

increasing impact energy resulted in the linear increase of energy absorption under a low-energy drop-weight impact. Moreover, varying impact energy via altering impact velocity or impactor mass also led to different deformation modes of the sandwich panels. Recently, the energy absorption behaviors of cladding sandwich panels with tubular cores under blast loading were studied (Wang et al. 2019, 2020; Xia et al. 2016; Yuen et al. 2017). The results showed that the foam filler could add extra energy absorbing capacity of the cladding sandwich panels (Yuen et al. 2017). In addition, Wang et al. (2019) reported that the interaction between the tubular cores led to the increase of the number of plastic hinges. However, the impact behaviors of cladding sandwich panels with aluminum foam-filled tubular cores have not yet been reported in open literature.

In this chapter, a novel cladding sandwich panel with aluminum foam-filled tubular cores (AFTC panel) was proposed for absorbing impact energy, as presented in Fig. 4.2, and the cladding sandwich panel with empty tubular cores (ETC panel), as the counterpart, was also studied. The deformation mode, impact force and displacement responses of the AFTC and ETC panels under impact loading were obtained via conducting drop-weight impact tests. In addition, Finite Element (FE) models of the sandwich panels under impact loading were also established to further reveal their failure modes and energy absorption performances. The effects of impactor shape, impact position, aluminum foam filler and thickness ratio of flat steel plate to tubes ( $t_f/t_t$ ) on energy absorption performances of the sandwich panels were analyzed. This study is of significance for understanding the energy absorption behavior of the novel AFTC and ETC panels and facilitating their applications in dissipating impact energy.

## 4.2 Methodologies

### 4.2.1 Experimental Methodology

#### 4.2.1.1 Test Specimens

Figure 4.2 presents the AFTC and ETC panels employed for the drop-weight impact tests, and their dimensions are given in Fig. 4.2a. Five identical circular steel tubes with outer diameter of 114 mm were welded to two flat steel plates first. The cylindrical aluminum foam filler with the diameter of 108 mm was subsequently filled in the tubular cores. The thicknesses of the flat steel plates and circular steel tubes were measured to be 1.82 mm and 2.36 mm, respectively. The top steel plate, aluminum foam filler and circular steel tubes shared the same length of 500 mm. The bottom steel plate of the sandwich panel was bolted to a rigid support. The numbering of the aluminum foam-filled tubes or empty tubes is shown in Fig. 4.2.

Table 4.1 presents the four sandwich panels fabricated for the drop-weight impact tests, including two AFTC panels and two ETC panels. The two ETC panels were designed as the counterparts to study the effect of aluminum foam filler on the dynamic responses of sandwich panels. In addition, two types of the impactors (i.e., drop hammer with cylindrical head and hemispherical head) were employed to study the effect of impactor shape on the impact responses of sandwich panels.

#### 4.2.1.2 Setup of Drop-Weight Impact Test

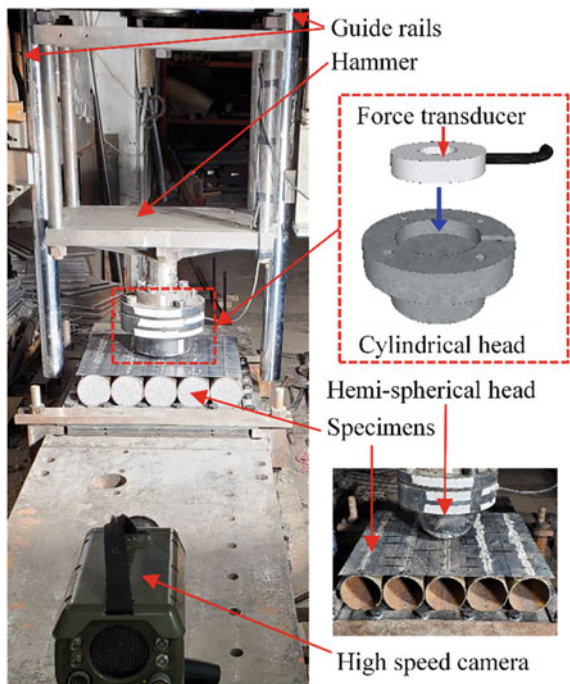
The impact tests on proposed sandwich panels were conducted via employing an instrumented drop-weight impact test machine. Figure 4.3 exhibits the setup and instrumentation of the drop-weight impact test. The impact load was applied to the specimens at their centers via dropping a hammer with a mass of 450 kg. The head of the hammer was replaceable. A 200-mm-diameter cylindrical head was employed for the specimen C-N and C-F, and the specimen H-N and H-F was subjected to the impact of a 200-mm-diameter hemispherical head, as shown in Fig. 4.3 and Table 4.1. The drop height was chosen as 4.0 m. With regard to the measurement system, a dynamic force transducer with the measurement range of 2000 kN was embedded in the hammer head

**Table 4.1** Parameters of test specimens

Specimen	Hammer head	Aluminum foam	V (m/s)	$E_I$ (kJ)
C-F	Cylindrical head	Yes	8.420	16.0
C-N	Cylindrical head	No	8.365	15.7
H-F	Hemispherical head	Yes	8.507	16.3
H-N	Hemispherical head	No	8.455	16.1

Note  $V$ -Initial impact velocity of hammer;  $E_I$ -Impact energy

**Fig. 4.3** Test setup and instrumentation, reprinted from Lu et al. (2021), copyright 2022, with permission from Elsevier



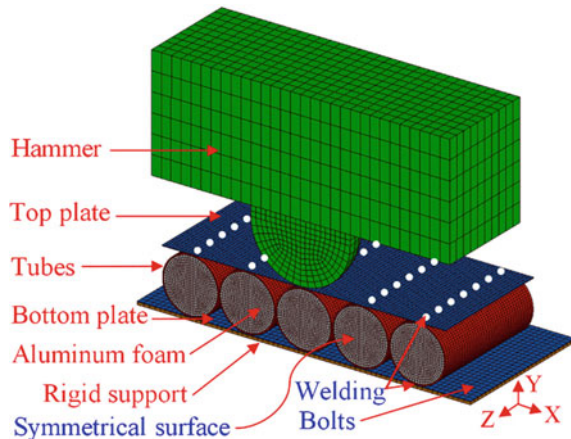
for the measurement of impact force during the impact tests, as illustrated in Fig. 4.3. Moreover, the impact process was recorded via employing a high-speed camera with speed of 3000 frames per second. The vertical displacement and velocity histories of the drop hammer could also be obtained through analyzing the high-speed camera data. The obtained initial impact velocities of the drop hammers and corresponding impact energies are presented in Table 4.1.

#### 4.2.2 Numerical Methodology

##### 4.2.2.1 Numerical Model Description

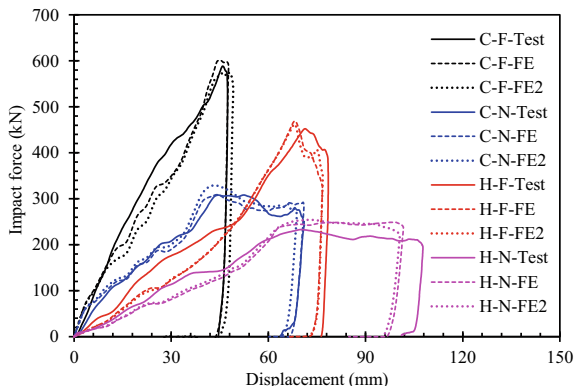
The numerical simulation was conducted via employing the explicit code in LS-DYNA (Hallquist 2013) to further study the energy absorption performances of the AFTC and ETC panels. The established FE model of the sandwich panel subjected to impact loading is exhibited in Fig. 4.4. The half-symmetric FE model was established owing to the symmetry of the specimen and loading condition. The hammer and aluminum foam cores were meshed with eight-node solid elements. Shell elements comprising five integration points in the thickness direction were employed for the meshing of steel plates, circular tubes and support. The mesh

**Fig. 4.4** Details of half-symmetric FE model of sandwich panel, reprinted from Lu et al. (2021), copyright 2022, with permission from Elsevier



sizes of the top steel plates, tubes and foam fillers were about  $7 \times 7 \text{ mm}^2$ ,  $7 \times 4 \text{ mm}^2$ , and  $7 \times 4 \times 4 \text{ mm}^3$ , respectively. The mesh sensitivity analysis was conducted via halving the aforementioned elements, and the impact force–displacement curves obtained from the FE models with current mesh size and smaller element size are compared in Fig. 4.5. Similar results were obtained, and the differences of maximum impact forces and displacements for the two meshing approaches were less than 6% and 3%, respectively. Therefore, the current element size was employed in the following analysis, considering both the accuracy and computation time. The contacts between hammer and top steel plate, flat steel plates and tubes, tubes and foam filler as well as bottom steel plate and support were modeled via employing the keyword “\*CONTACT\_AUTOMATIC\_SURFACE\_TO\_SURFACE” in LS-DYNA, and the penalty-based contact approach was adopted. The self-contact was defined for tubular cores through adopting the keyword “\*CONTACT\_AUTOMATIC\_SINGLE\_SURFACE” since the self-contact of the

**Fig. 4.5** Comparison of impact force–displacement curves of sandwich panels from impact tests and FE simulations, reprinted from Lu et al. (2021), copyright 2022, with permission from Elsevier



tubes could be observed during the drop-weight impact tests. In addition, the nodes of the tubes at the welding zone were tied to the flat steel plates to simulate the welding connection via employing the keyword “\*CONTACT\_TIED\_NODES\_TO\_SURFACE”, as there was no welding failure between tubular cores and flat steel plates being observed during the impact tests. The nodes of the bottom steel plate with the same coordinates as bolts were tied to the support to model the bolt connection between the bottom plate and rigid support. With regard to the boundary conditions, the nodes of the support were constrained in three translational directions. The nodes at the symmetrical plane of the half-symmetric FE model were restrained in the translational direction along Z axis and rotational direction around X and Y axis via employing the keyword “\*BOUNDARY\_SPC\_SET”. The initial velocity of the hammer was applied through adopting the keyword “\*INITIAL\_VELOCITY\_GENERATION”. The initial velocities specified in the FE models were consistent with those measured in the impact tests, which are given in Table 4.1. Since the densification of the AFTC panels and compaction of ETC panels were not observed during the drop-weight impact tests owing to the insufficient applied impact energy, the FE models of sandwich panel C-N, C-F, H-N and H-F under higher impact energy (i.e., higher hammer weight) were also established to study the energy absorption performances of the sandwich panels until compaction or densification of the specimens being reached, and the corresponding applied impact energies of these four specimens were 31.5, 63.8, 32.2 and 32.6 kJ, respectively.

#### 4.2.2.2 Material Models

The Piecewise Linear Plasticity model (\*MAT\_24 in LS-DYNA) was employed to simulate the mechanical behavior of circular steel tubes and flat steel plates. The strain rate effect of steel was considered via employing the Cowper-Symonds model, as defined in Eq. (1.8), and strain rate parameters  $C$  and  $P$  were adopted as  $802\text{ s}^{-1}$  and 3.585, respectively (Abramowicz and Jones 1986). The tensile coupon tests were conducted to obtain the material parameters of steels. The input true stress–effective plastic strain curves of mild steels corresponding to flat steel plates and tubes are exhibited in Fig. 4.6a. The material parameters of mild steels are shown in Table 4.2. Moreover, the failure strain of the steel material was defined as 0.2 (Yan et al. 2020), and the elements of steel tubes and flat steel plates were removed from the FE calculation when their effective plastic strain values exceeded 0.2.

The aluminum foam material was simulated via using the Crushable Foam material model (\*MAT\_63 in LS-DYNA). The material parameters of the aluminum foam were obtained through uniaxial compressive loading tests. The obtained compressive stress–volumetric strain curve is presented in Fig. 4.6b, and the material parameters of aluminum foam are shown in Table 4.2.

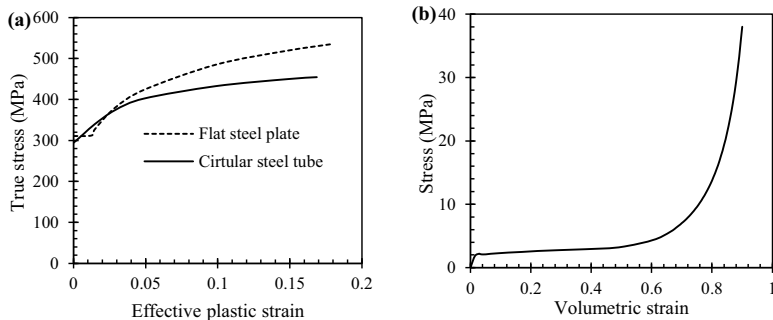


**Fig. 4.6** Input stress–strain curves in FE model: **a** True stress–effective plastic strain curves for mild steels, **b** Stress–volumetric strain curve for aluminum foam, reprinted from Lu et al. (2021), copyright 2022, with permission from Elsevier

**Table 4.2** Material parameters of mild steel and aluminum foam

Mild steel	$E_y$ (GPa)	$\sigma_y$ (MPa)	$\sigma_u$ (MPa)
Flat plate	217	311	534
Tube	211	295	454
Aluminum foam	$E_f$ (MPa)	$\sigma_f$ (MPa)	$\rho_f$ (g/cm <sup>3</sup> )
	120	2.69	0.286

Note  $E_y$ —Young's modulus of steel;  $\sigma_y$ —Yield stress of steel;  $\sigma_u$ —Ultimate stress of steel;  $E_f$ —Young's modulus of aluminum foam;  $\sigma_f$ —Plateau stress of aluminum foam;  $\rho_f$ —Density of aluminum foam

#### 4.2.2.3 Numerical Model Validation

The comparisons of deformation modes of the sandwich panels obtained from drop-weight impact tests and FE simulations are presented in Fig. 4.7. The established FE models are found to reasonably capture the local indentation at the impact zone of the sandwich panel, and the shape of the local indentation is consistent with the test observation. The permanent deformation shapes of top steel plates, tubular cores and aluminum foam filler obtained from FE simulations exhibit good agreement with those from impact tests. The asymmetrical deformation mode of the tubular cores observed for specimen C-N is caused by its geometric imperfection during the fabrication, which is not captured in the FE model, as shown in Fig. 4.7. Nevertheless, this slight difference of the deformation modes has little effect on the impact force and displacement responses as well as energy absorption performances of the sandwich panels, since the length, number and rotation angle of the plastic hinges of the symmetrical and asymmetrical deformed tubular cores are consistent. The fractures of the top steel plates observed for specimen H-F can also be predicted by the FE model, as exhibited in Fig. 4.7.

Figure 4.5 presents the comparisons of the FE-simulated impact force versus displacement curves with those from tests, and good agreement between them can

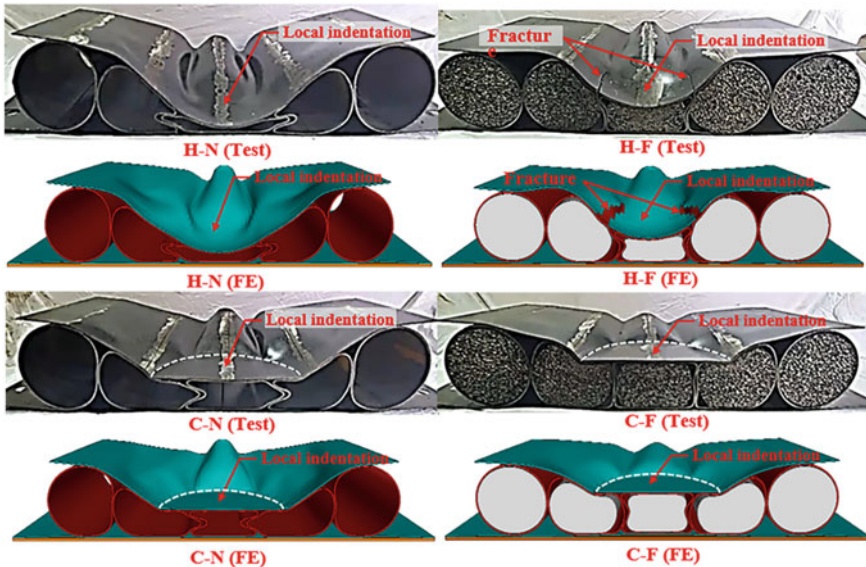


**Fig. 4.7** Comparison of the permanent deformation of sandwich panels from impact tests and FE simulations, reprinted from Lu et al. (2021) copyright 2022, with permission from Elsevier

be observed. Table 4.3 compares the maximum impact force ( $F_{\max}$ ) and displacement ( $D_{\max}$ ) of the four specimens obtained from experimental and numerical methods. The results show that the differences of  $F_{\max}$  and  $D_{\max}$  between tests and FE simulations are less than 7% and 6%, respectively. There are still slight differences between numerical and experimental results, which may be caused by the geometric imperfection of the sandwich panels during the fabrication, which were ignored in the established FE models. The above validations indicate that the developed FE models offer reasonable estimations on the impact responses of the proposed sandwich panels and can be employed to further study their energy absorption performances.

**Table 4.3** Summary of experimental and numerical results

Specimen	$D_{\max\text{Test}}$ (mm)	$D_{\max\text{FE}}$ (mm)	$D_{\max\text{Test}}/D_{\max\text{FE}}$	$F_{\max\text{Test}}$ (kN)	$F_{\max\text{FE}}$ (kN)	$F_{\max\text{Test}}/F_{\max\text{FE}}$	$EA_{\text{FE}}$ (kJ)
C-N	71.09	70.97	1.00	308.03	308.78	1.00	21.68
C-F	47.40	47.73	0.99	588.26	600.65	0.98	45.86
H-N	107.73	101.67	1.06	232.92	248.91	0.94	17.71
H-F	78.50	76.69	1.02	452.26	469.04	0.96	25.48

Note  $D_{\max}$ —Maximum center displacement obtained from test;  $D_{\max\text{FE}}$ —Maximum center displacement obtained from FE simulation;  $F_{\max}$ —Maximum impact force obtained from test;  $F_{\max\text{FE}}$ —Maximum impact force obtained from FE simulation;  $EA_{\text{FE}}$ —Energy absorption obtained from FE simulation

## 4.3 Results and Discussions

### 4.3.1 Failure Modes

The deformation processes of the sandwich panels under the impact of cylindrical head and hemispherical head were successfully recorded by the high-speed camera during the drop-weight impact tests. However, the high-speed camera could not capture the deformation processes of the sandwich panels at local indentation region below the hammer head. In addition, the tested specimens also did not reach compaction or densification. Hence, the deformation processes of the sandwich panel C-N, C-F, H-N and H-F under higher impact energy (with corresponding applied impact energies of 31.5, 63.8, 32.2 and 32.6 kJ, respectively) were obtained from FE simulations to further reveal the failure modes of the sandwich panels until compaction or densification of the specimens being reached.

Figure 4.8a presents the deformation process of the ETC panel subjected to the impact of cylindrical head (i.e., specimen C-N), together with the effective plastic strain contours of the tubes and top steel plate. The plastic deformation of the tubes and top steel plate can be revealed in the effective plastic strain contours in Fig. 4.8a, including curvature change of tubes and the occurrence and evolution of plastic hinges. The numbering of the plastic hinges is shown in Fig. 4.8a. The first and second number donates the numbering of tubes (as shown in Fig. 4.2) and the numbering of plastic hinges of the tube, respectively. The impact process can be divided into three stages according to the occurrence and evolution of plastic hinges of the tubes. During the Stage I, a circular local indentation zone with a diameter of 200 mm can be observed, and the shape and size of the indentation zone is governed by the shape of cylindrical hammer head. Meanwhile, the plastic hinge 14 and 25 for tubes and the plastic hinge 41 for the top plate appear at the indentation zone along the edge of the hammer head. In addition, the membrane stretching of the top plate can also be observed outside the indentation zone. Since the tubes were welded to the two flat steel plates and were initially contacted with each other, the interaction between the tubes can be observed, i.e., the curvatures decrease of tubular cores can be observed at the contact zones between tube 1 and 2 as well as tubular cores and flat steel plates ( $\delta = 19.8$  mm in Fig. 4.8a), and plastic hinges 11, 13, 21, 23 appear. Subsequently, the local buckling of tube 1 and 2 can be observed, and the plastic hinge 12 and 22 appear successively ( $\delta = 41.3$  mm in Fig. 4.8a). The bucking directions of the tubes are random and may be affected by the geometric imperfection of the specimen during the fabrication, which may result in the different bucking direction observed in the drop-weight impact test, as mentioned in Sect. 4.2.2.3. When the local buckling occurs to tube 1 and tube 2, the deformation process enters the Stage II, and the corresponding critical displacement is defined as  $x_1$ . During the Stage II, the local indentation deformation exhibits continuous increase, and tube 1, 2 and 2' are further crushed with continuously increased rotation angles of plastic hinges. The rotation angles of plastic hinges of tubes at local indentation region below the cylindrical hammer head are uniformly distributed. However, the rotation angles

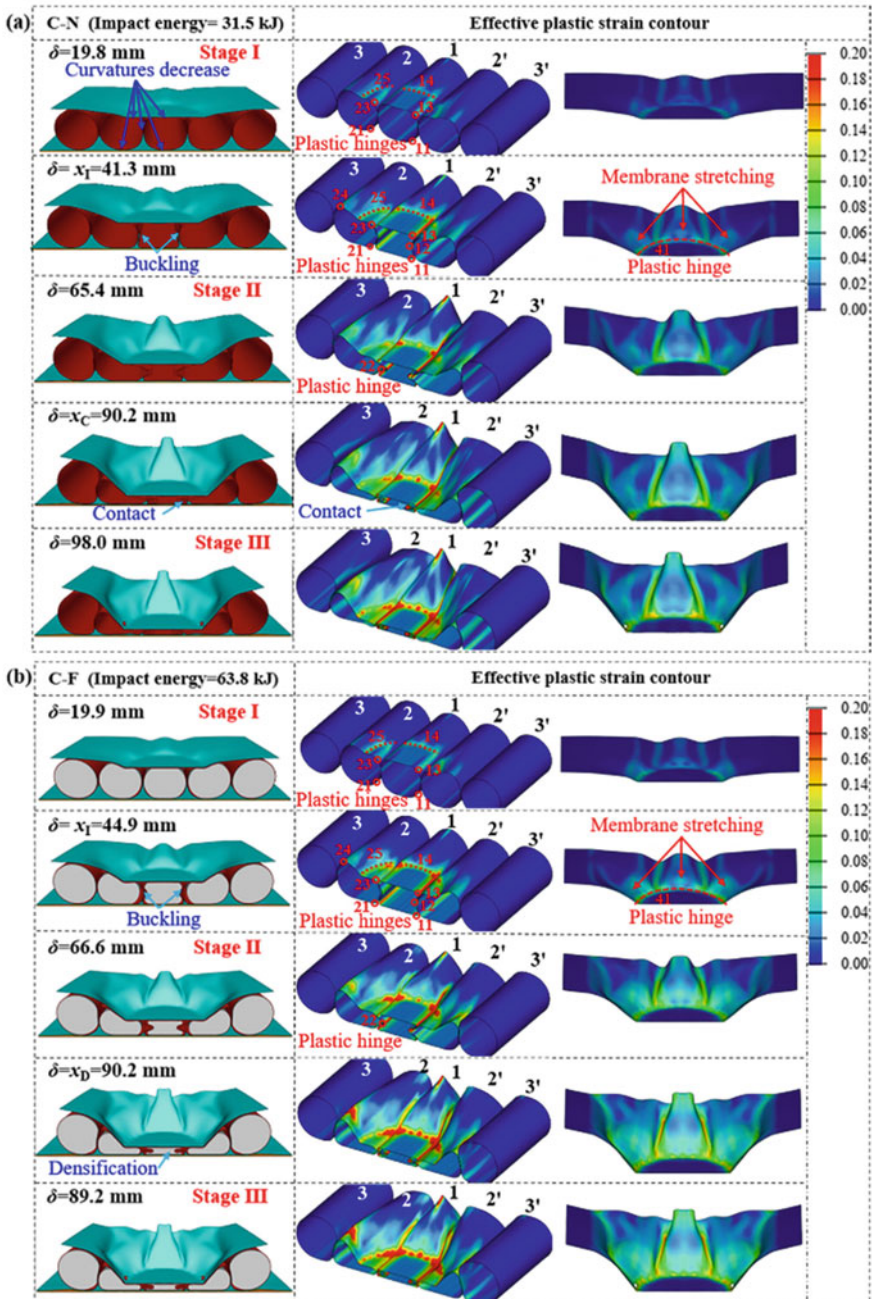


**Fig. 4.8** Deformation process of the sandwich panels from FE predictions: **a** ETC panel C-N, **b** AFTC panel C-F, **c** ETC panel H-N, **d** AFTC panel H-F, reprinted from Lu et al. (2021), copyright 2022, with permission from Elsevier

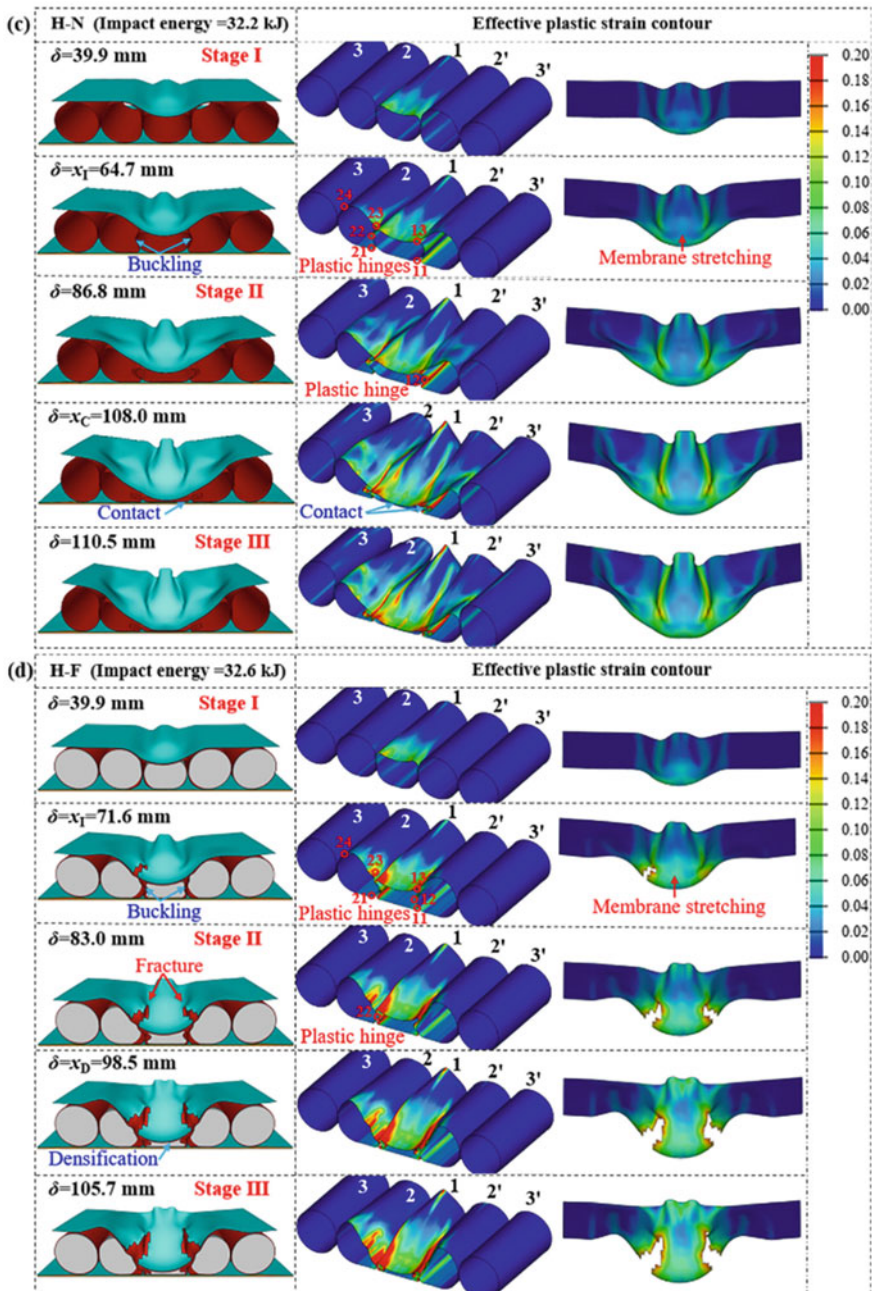


Fig. 4.8 (continued)

of plastic hinges (or plastic deformation magnitude) of the tubes exhibit variation outside the region contacted with hammer head, i.e., it shows decrease when shifting to the periphery of the ETC panel. When the displacement reaches 90.2 mm, the inner surface contact of the tube 1 and 2 can be observed, which indicates that the ETC panel approaches the compaction stage and reaches its ultimate energy absorption capacity. The corresponding displacement is defined as  $x_C$ . Subsequently, the deformation process enters the Stage III. In addition, it can be observed that there is no significant plastic deformation for the tube 3 and 3' since they are away from the impact position.

Figure 4.8b exhibits the failure mode of the AFTC panel under the impact of cylindrical head (i.e., specimen C-F) obtained through the FE simulation. Similar deformation modes of the top steel plate and tubular cores can be observed as compared to those of ETC panel. The occurrence and evolution of plastic hinges of the AFTC panel are also consistent with that of the ETC panel. This is owing to the significant lower Young's modulus of the aluminum foam as compared to the steel, and the foam filler has little effect on the deformation mode of the sandwich panel. Hence, the impact process of specimen C-F can also be divided into three stages. The aluminum foam fillers in tube 1, 2 and 2' are compressed continuously during the impact process, while there is no significant deformation being observed for the aluminum foam-filled tube 3 and 3'. The aluminum foam filled in tube 1 reaches densification when the displacement is 89.2 mm, and the ultimate energy absorption capacity of the AFTC panel is reached.

The deformation mode of the ETC panel subjected to the impact of hemispherical head (i.e., specimen H-N) is presented in Fig. 4.8c. The occurrence and evolution of plastic hinge 11, 12, 13, 21, 22 and 23 for specimen H-N is similar to that for specimen C-N. Hence, the impact process of specimen H-N can also be divided into three stages. During the Stage I, the hemispherical local indentation can be observed at the impact zone. The evident membrane stretching can be observed for the top steel plate at the impact zone, and the area of the membrane stretching zone is larger than that of specimen C-N. The crushing of tube 1 is more significant as compared to tube 2 and 2' under the impact of hemispherical head, and the local bucking direction of tube 1 and tube 2 of specimen H-N is different from that of specimen C-N owing to the different hammer heads employed for the two specimens. Moreover, the evident plastic deformation can also be observed in tube 2 and 2' during the Stage II. When the displacement reaches 108.0 mm, the inner surface contact of tube 1 can be observed at the center point of impact zone and the specimen approaches the ultimate energy absorption capacity.

The failure mode of the AFTC panel under the impact of hemispherical head (i.e., specimen H-F) is shown in Fig. 4.8d. Specimen H-F with aluminum foam filler exhibit similar deformation mode to the specimen H-N without aluminum foam filler, and the deformation process of the specimen H-F can also be divided into three stages. In addition, the fracture of the top steel plate can be capture from both the drop-weight impact test and FE simulation. This may be caused by the more significant membrane stretching of the top steel plate of the specimen H-F. FE simulation shows that filling aluminum foam results in the smaller deformations of tubes 2, 2', 3 and

$3'$ , and smaller area of local indentation zone, which leads to stiffer constraint to the top steel plate and higher radial tensile strain of the top steel plate at the impact zone as compared to the ETC panel (H-N) corresponding to the same displacement, as shown in Fig. 4.8c, d. Moreover, the local buckling direction of tube 1 and tube 2 of specimen H-F with aluminum foam filler is also different from that of specimen H-N without aluminum foam filler. This is also attributed to the stiffer constraint from tube 2 with the presence of aluminum foam filler.

#### 4.3.2 Impact Force, Displacement and Energy Absorption Responses

The impact force–displacement curves of the four sandwich panels under impact loads with variant impact energies via changing hammer weight are shown in Fig. 4.9. Moreover, to evaluate the energy absorption performances of the sandwich panels quantitatively, their energy absorptions (EA) are compared in Table 4.3. The method for determining EA presented Sect. 1.2.3 is employed, and EA can be expressed as (Wang et al. 2018a):

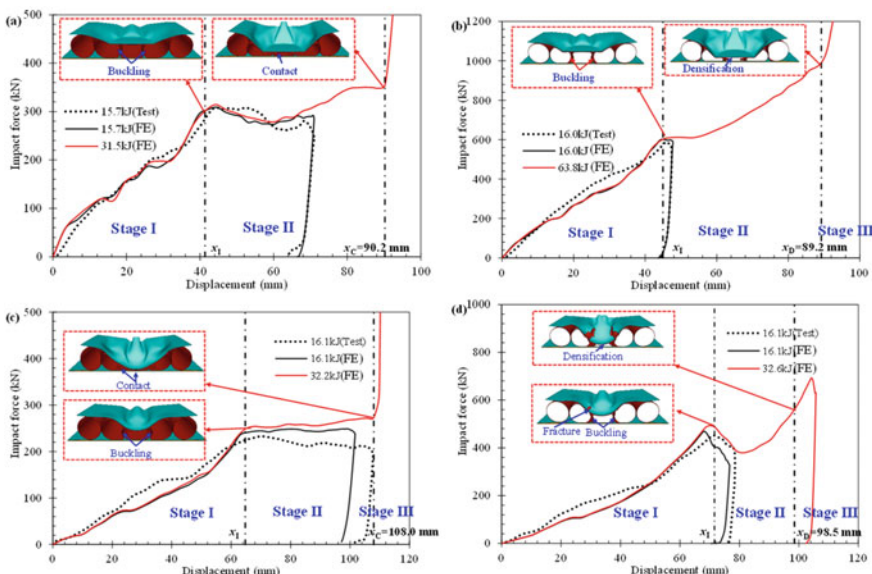


**Fig. 4.9** Impact force–displacement curves of the sandwich panels under variant impact energy: **a** ETC panel C-N, **b** AFTC panel C-F, **c** ETC panel H-N, **d** AFTC panel H-F, reprinted from Lu et al. (2021), copyright 2022, with permission from Elsevier

$$EA = \int_0^{x_{II}} F(\delta) d\delta \quad (4.1)$$

where  $F(\delta)$  and  $\delta$  denote the impact force and displacement, respectively,  $x_{II}$  donates the compaction displacement  $x_C$  (for ETC panel) or densification displacement  $x_D$  (for AFTC panel), which is determined based on the energy absorption efficiency method (Li et al. 2006; Wang et al. 2018a). First, the energy absorption efficiency ( $\eta$ ) of the sandwich panel is obtained as:

$$\eta(\delta) = \frac{1}{F(\delta)D_T} \int_0^{\delta} F(x) dx \quad (4.2)$$

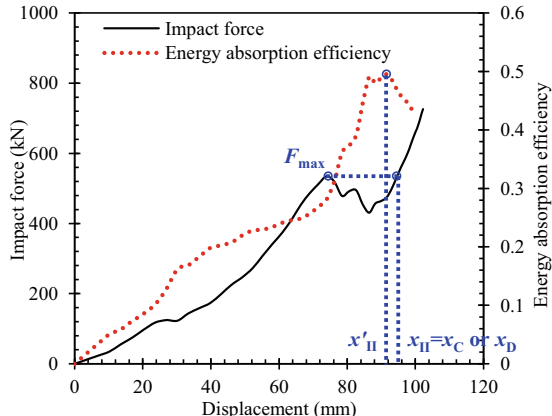
where  $D_T$  is the inner diameter of the tube. Displacement  $x'_{II}$  is defined as the stationary point at the  $\eta - \delta$  curve where  $\eta$  reaches the maximum value, i.e.,

$$\left. \frac{d\eta(\delta)}{d\delta} \right|_{\delta=x'_{II}} = 0 \quad (4.3)$$

Then, the maximum force within the displacement ranging of 0 to  $x'_{II}$  is defined as  $F_{max1}$ , and  $x_{II}$  can be determined as the displacement corresponding to the first maximum force ( $F_{max1}$ ) after  $x'_{II}$  (Wang et al. 2018a). The calculation of  $x_{II}$  is illustrated in Fig. 4.10.

The impact force–displacement curves of the ETC panels subjected to the impact of cylindrical head and hemispherical head are exhibited in Fig. 4.9a, c, respectively. The impact force shows continuous increase during the Stage I. This is due to the increasing number and length of plastic hinges as well as curvature change of tubes,

**Fig. 4.10** Determination of compaction displacement  $x_C$  or densification displacement  $x_D$ , reprinted from Lu et al. (2021), copyright 2022, with permission from Elsevier



which can lead to the continuous improvement of energy dissipation rate. However, the impact force tends to a constant value during the Stage II since all the plastic hinges have appeared after the local buckling of tubular cores and the plastic hinge lengths approach constant values with further crushing. This results in the constant energy dissipation rate of the ETC panel. In addition, the impact force exhibits a sharp increase when the displacement reaches  $x_C$  owing to the compaction of tubular cores. With regard to the impact force–displacement curves of AFTC panels, the impact force also exhibits continuous increase during the Stage I, as shown in Fig. 4.9b, d. However, the increasing rate of the impact force is higher than that of ETC panel owing to the compression of aluminum foam filler which also contribute to the impact energy dissipation. The impact force of specimen C-F also tends to a constant value at the beginning of Stage II. However, the impact force of specimen H-F shows sudden decrease at the beginning of Stage II due to the occurrence of fractures on the top plate, which results in the reduction of the loading capacity contributed by the top steel plate. Nevertheless, the impact force of the AFTC panel shows continuous increase subsequently owing to the densification of the aluminum foam filler. Moreover, the impact force exhibits increase with a higher rate during the Stage III. However, the increasing rate of impact force of AFTC panel in Stage III is lower than that of ETC panel owing to the buffering effect of the aluminum foam filler.

The energy dissipation of variant parts of the sandwich panels corresponding to  $x_C$  or  $x_D$  are summarized in Fig. 4.11. The results indicate that the tubular cores of the ETC panel absorb the majority of the impact energy through plastic deformation (i.e., plastic hinge rotation and curvature change) under impact loading, i.e., the energy dissipation proportions of the tubes of specimen C-N and H-N are 84.5% and 75.0%, respectively. The top steel plate can also absorb impact energy through plastic deformation, while its energy dissipation is smaller as compared to the tubular cores owing to its fewer plastic hinges and lower rotation angle of plastic hinges. Nevertheless, the energy dissipation of the top steel plate can be improved under the impact of hemispherical head as compared to that under the impact of cylindrical head. This is attributed to the larger membrane stretching zone of the top steel plate, as shown in Fig. 4.8. With regard to the AFTC panels, it can be observed that the energy dissipation proportions of the aluminum foam filler for specimen C-F and H-F are 41.2% and 31.5%, respectively, which indicates that filling the aluminum

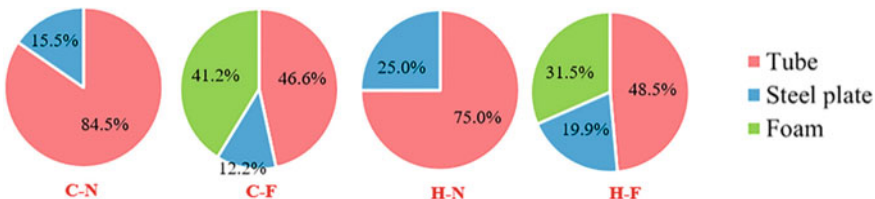


**Fig. 4.11** Energy dissipation of variant parts of sandwich panels, reprinted from Lu et al. (2021), copyright 2022, with permission from Elsevier

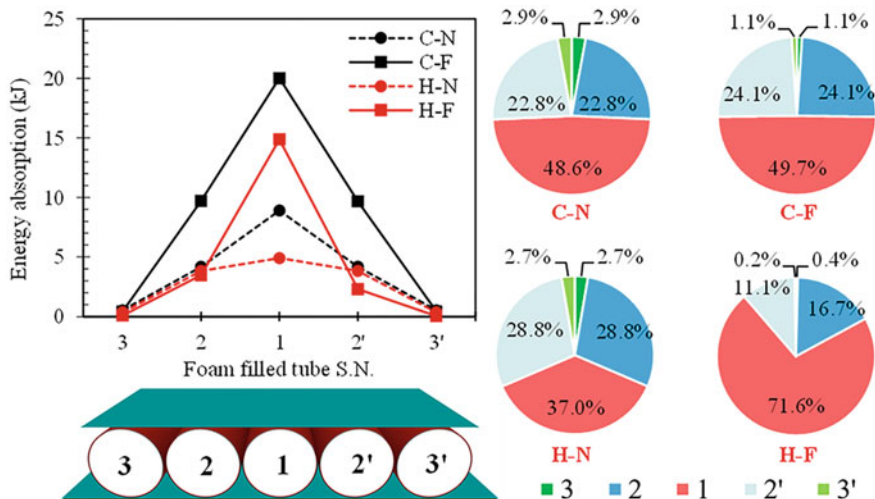


**Fig. 4.12** Energy dissipation of variant empty tubes and foam-filled tubes, reprinted from Lu et al. (2021), copyright 2022, with permission from Elsevier

foam can effectively improve the energy absorption performances of the sandwich panel. Moreover, the top steel plate of the AFTC panel also exhibits slight energy dissipation, and its energy dissipation proportions for specimen C-F and H-F are only 12.2% and 19.9%, respectively.

Figure 4.12 presents the comparison of the energy dissipation of five empty tubes and aluminum foam-filled tubes corresponding to  $x_C$  and  $x_D$ , respectively. Moreover, their energy dissipation proportions are also provided. The results reveal that the tube 1, which is at the center of the impact zone, dissipates more impact energy as compared to other tubes owing to more severe plastic deformation of the tubular core and compression of the aluminum foam filler. The tube 2 and 2' can also effectively dissipate impact energy through plastic deformation of tubular cores and compression of aluminum foam fillers. However, the energy dissipation proportions of tube 3 and 3' are less than 3% since these tubes are away from the impact zone, and the plastic deformation of these tubes and compression of aluminum foam fillers are minimal.

### 4.3.3 Parametric Studies

#### 4.3.3.1 Effect of Impactor Shape

Table 4.3 summaries the maximum impact force ( $F_{\max}$ ) and displacement ( $D_{\max}$ ) of sandwich panels under impact loading with variant shapes of hammer head. The drop-weight impact test results reveal that the  $F_{\max}$  of the ETC panel and the AFTC

panel under the impact of cylindrical head are increased by 32.2% and 30.1%, respectively, as compared to that under the impact of hemispherical head, and the corresponding  $D_{\max}$  are reduced by 34.0% and 39.6%, respectively. This is owing to the larger contact area between the cylindrical head and specimens, which results in the larger local indentation zone and higher energy absorption capacity of the sandwich panel under the impact of cylindrical head. The  $EA$  of specimen C-N and C-F under the impact of cylindrical head is improved by 22.4% and 80.0%, respectively, as compared to specimen H-N and H-F under the impact of hemispherical head, as shown in Table 4.3. The above results indicate that the sandwich panel exhibits better energy absorption performance if the impactor has larger contact area with the sandwich panel.

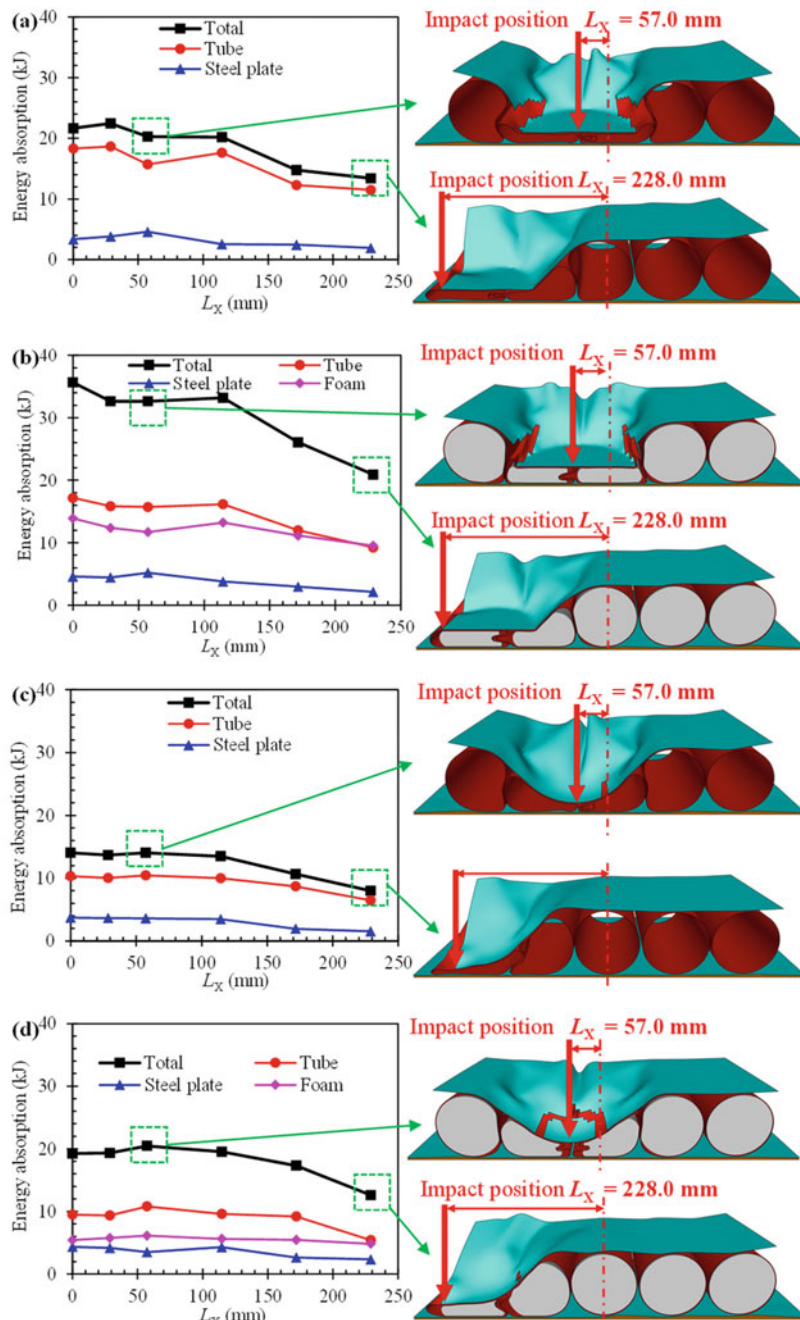
#### 4.3.3.2 Effect of Aluminum Foam Core

$F_{\max}$  and  $D_{\max}$  of ETC and AFTC panels obtained through drop-weight impact tests are presented in Table 4.3. Filling aluminum foam results in the increase of  $F_{\max}$  by 91.0% and 94.2%, respectively, for the sandwich panel under the impact of cylindrical and hemispherical head, but the corresponding decrease of  $D_{\max}$  by 33.3% and 27.1% is observed with the filling of aluminum foam. In addition, Table 4.3 presents the  $EAs$  of ETC and AFTC panels. The results reveal that filling aluminum foam can significantly improve the energy absorption capacity of the sandwich panel, i.e., the  $EA$  of the AFTC panel C-F and H-F are found to be improved by 111.5% and 43.9%, respectively, as compared to the ETC panel C-N and H-N. This is attributed to the high energy absorption capacity of the aluminum foam.

#### 4.3.3.3 Effect of Impact Position

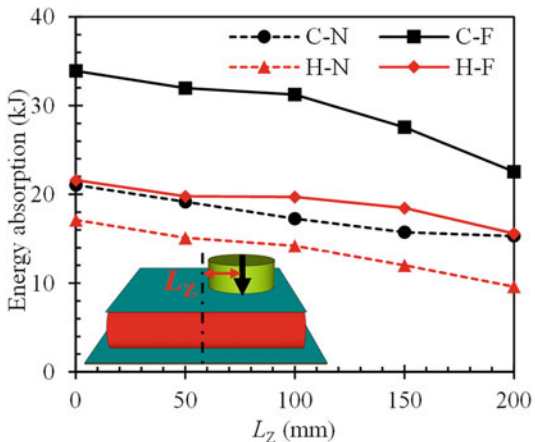
Since the variation of impact position may affect the deformation mode and energy absorption performances of the proposed sandwich panels, the impact responses of sandwich panels under variant impact positions (i.e.,  $L_X = 0, 28.5, 57.0, 114.0, 171.0$  and  $228.0$  mm;  $L_Z = 0, 50.0, 100.0, 150.0$  and  $200.0$  mm) were studied via employing FE simulation.  $L_X$  and  $L_Z$  denotes the distance between the impact position and the center point of the panel along the X-axis direction and Z-axis direction, as presented in Figs. 4.13 and 4.14.

Figure 4.13 exhibits the deformation modes and  $EAs$  of the four sandwich panels under variant impact positions along the X-axis direction ( $L_X$ ). Different deformation modes of the sandwich panels can be observed when the impact position is between the tube 1 and 2 (i.e.,  $L_X = 57.0$  in Fig. 4.13). However, the impact position has little effect on the energy dissipation of top steel plate, tubular cores and aluminum foam filler for the  $L_X$  ranging from 0 to 114.0 mm (i.e.,  $L_X \leq 0.5nD - 1.5D$ , where  $D$  and  $n$  denotes outer diameter and numbering of the tubes), and thus has insignificant effect on the  $EA$  of the four sandwich panels. However, the  $EA$  exhibits significant decrease when the  $L_X$  ranges from 171.0 mm to 228.0 mm (i.e.,  $L_X \geq 0.5nD - D$ ).



**Fig. 4.13** Impact responses of sandwich panels under variant impact position  $L_x$ : **a** ETC panel C-N, **b** AFTC panel C-F, **c** ETC panel H-N, **d** AFTC panel H-F, reprinted from Lu et al. (2021), copyright 2022, with permission from Elsevier

**Fig. 4.14** Impact responses of sandwich panels under variant impact position  $L_Z$ , reprinted from Lu et al. (2021), copyright 2022, with permission from Elsevier



This is attributed to the reduction of the local indentation zone when the hammer impacts the edge of the sandwich panel (as shown in Fig. 4.13), which leads to less significant plastic deformation of the top steel plate and tubular cores as well as compression of the aluminum foam. In addition, tube 3 is only constrained on side by tube 2, which also results in less significant plastic deformation of tube 3 than that of tube 1 and 2 under the same crushing displacement, thus leading to the decrease of EA. Figure 4.14 presents the EAs of the four sandwich panels under variant impact positions along the Z-axis direction ( $L_Z$ ). The impact position also has insignificant effect on the EA of the sandwich panels for the  $L_Z$  ranging from 0 to 100.0 mm, i.e., the difference of the EA is less than 20%. However, the EA of the sandwich panel also exhibits significant decrease when the  $L_Z$  is larger than 150.0 mm owing to the decrease of the plastic hinge length and compression of the aluminum foam. The above results indicate that the impact position will not significantly affect the energy absorption performances of the proposed sandwich panel when it is away from the edge of the sandwich panel.

#### 4.3.3.4 Effect of Thickness Ratio of Flat Plate to Tube

Since the thickness ratio of flat steel plate to tube ( $t_f/t_t$ ) may affect the deformation mode and energy absorption performance of the sandwich panel, the impact responses of sandwich panels with variant  $t_f/t_t$  of 0.18, 0.77, 0.87, 1.00, 2.43 and 6.07 were studied via employing FE simulations. All the specimens shared the same total mass of the top steel plate and tubes.

The EAs of sandwich panels with variant  $t_f/t_t$  are compared in Fig. 4.15. The typical deformation modes of the sandwich panels with the  $t_f/t_t$  of 0.18 and 6.07 are also compared in Fig. 4.15. With regard to the specimen H-N in Fig. 4.15a, the EA exhibits initial increase and subsequent decrease with the increase of  $t_f/t_t$ , and the maximum EA is reached when  $t_f/t_t$  is 0.77. The thinner top plate may result in

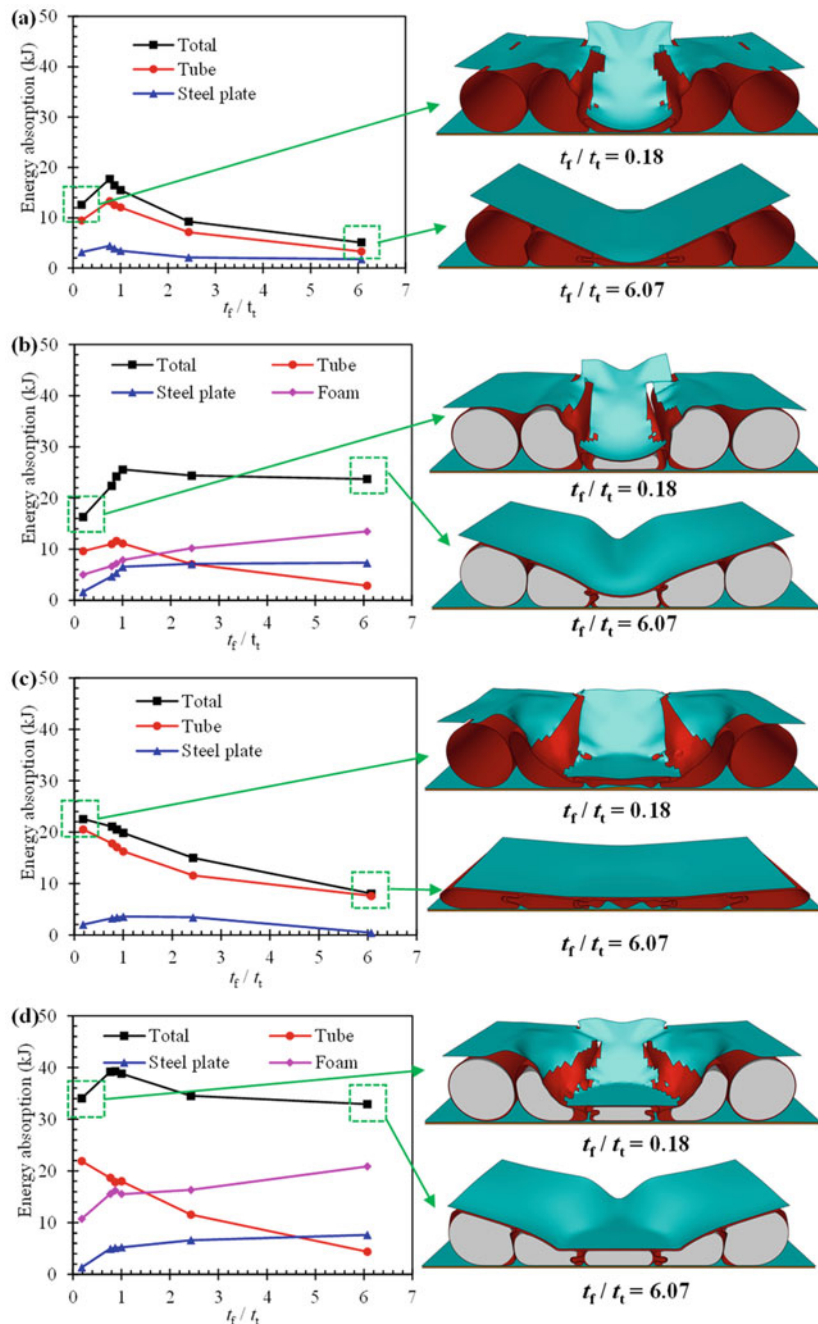


**Fig. 4.15** Energy absorptions and deformation modes of sandwich panels with variant  $t_f/t_t$ : **a** ETC panels H-N, **b** AFTC panels H-F, **c** ETC panels C-N, **d** AFTC panels C-F, reprinted from Lu et al. (2021), copyright 2022, with permission from Elsevier

premature fracture of the top plate and smaller local indentation zone, as shown in Fig. 4.15a, which leads to 28.9% reduction of *EA* as the  $t_f/t_t$  is decreased from 0.77 to 0.18. However, increasing the  $t_f/t_t$  from 0.77 to 6.07 results in the reduction of *EA* by 69.1%. This is because the decrease of the thickness of tubes results in the reduction of energy dissipation through plastic deformation of tubes which contributes the majority of the total *EA*. With regard to the specimen H-F in Fig. 4.15b, increasing  $t_f/t_t$  from 1.00 to 6.07 exhibits little effect on the total *EA* although energy dissipation of tubular cores is observed to be reduced. This is because increasing the top plate thickness results in the larger local indentation zone of the sandwich panel, which leads to higher energy dissipation of aluminum foam, as shown in Fig. 4.15b. Similar results can also be observed for the specimen C-N and C-F. However, Fig. 4.15c, d reveal that the decrease of  $t_f/t_t$  from 0.77 to 0.18 results in the improvement of energy dissipation of tubular cores for the specimens under the impact of cylindrical head, which is different from the specimen H-N and H-F under the impact of hemispherical head. The reason is that the contact area between the cylindrical head and sandwich panel as well as local indentation zone is not significantly affected by fracture of the top plate when the thinner top plate is employed (i.e.,  $t_f/t_t = 0.18$ ). The above results indicate that designing the tubes and flat steel plate to be of similar thickness may result in better energy absorption performance of the proposed sandwich panels.

## 4.4 Summary

Novel AFTC and ETC sandwich panels were proposed for dissipating impact energy. The dynamic responses of the sandwich panels were studied via employing drop-weight impact tests and FE simulations. These experimental and numerical studies support the following conclusions:

- (1) The impact process of the sandwich panel can be divided into three stages based on the occurrence and evolution process of plastic hinges of tubular cores as well as the characteristics of impact force–displacement curves.
- (2) The tubular cores dissipate more impact energy as compared to other parts of the sandwich panel via plastic hinge rotation and curvature change. The compression of aluminum foam filler can also effectively dissipate impact energy. In addition, the tubular core which is closer to the impact position tends to dissipate more impact energy.
- (3) The sandwich panel exhibits higher energy absorption and maximum impact force as well as lower maximum displacement under the impact of cylindrical head as compared to that under the impact of hemispherical head. However, the impact position exhibits insignificant effect on the energy absorption of the sandwich panels when it is away from the edge of the sandwich panel.
- (4) Filling aluminum foam is found to result in the reduction of maximum displacement as well as improvement of impact force and energy absorption of the sandwich panel. In addition, filling aluminum foam can also avoid the sharp increase

of impact force when the sandwich panel reaches densification. Moreover, the sandwich panel exhibits higher energy absorption capability by specifying the flat steel plate and tubular cores to be of similar thickness.

## References

- Abramowicz W, Jones N (1986) Dynamic progressive buckling of circular and square tubes. *Int J Impact Eng* 4:243–270
- Baroutaji A, Arjunan A, Stanford M et al (2021) Deformation and energy absorption of additively manufactured functionally graded thickness thin-walled circular tubes under lateral crushing. *Eng Struct* 226:111324
- Baroutaji A, Gilchrist MD, Olabi AG (2016) Quasi-static, impact and energy absorption of internally nested tubes subjected to lateral loading. *Thin-Walled Struct* 98:337–350
- Baroutaji A, Morris E, Olabi AG (2014) Quasi-static response and multi-objective crashworthiness optimization of oblong tube under lateral loading. *Thin-Walled Struct* 82:262–277
- Baroutaji A, Sajja M, Olabi AG (2017) On the crashworthiness performance of thin-walled energy absorbers: Recent advances and future developments. *Thin-Walled Struct* 118:137–163
- Fang H, Bi J, Zhang C et al (2017) A constitutive model of aluminum foam for crash simulations. *Int J Nonlin Mech* 90:124–136
- Guo LW, Yu JL (2011a) Bending behavior of aluminum foam-filled double cylindrical tubes. *Acta Mech* 222(3):233–244
- Guo L, Yu J (2011b) Dynamic bending response of double cylindrical tubes filled with aluminum foam. *Int J Impact Eng* 38(2):85–94
- Hall IW, Guden M, Claar TD (2002) Transverse and longitudinal crushing of aluminum-foam filled tubes. *Scr Mater* 46(7):513–518
- Hallquist JO (2013) LS-DYNA keyword user's manual. Livermore Software Technology Corporation (LSTC). Livermore, California
- Huo X, Liu H, Luo Q et al (2020) On low-velocity impact response of foam-core sandwich panels. *Int J Mech Sci* 181:105681
- Iqbal MA, Kumar V, Mittal AK (2019) Experimental and numerical studies on the drop impact resistance of prestressed concrete plates. *Int J Impact Eng* 123:98–117
- Kılıçaslan C (2015) Numerical crushing analysis of aluminum foam-filled corrugated single- and double-circular tubes subjected to axial impact loading. *Thin-Walled Struct* 96:82–94
- Li QM, Magkiriadis I, Harrigan JJ (2006) Compressive strain at the onset of densification of cellular solids. *J Cell Plast* 42(5):371–392
- Li Y, Lv Z, Wang Y (2020) Blast response of aluminum foam sandwich panel with double V-shaped face plate. *Int J Impact Eng* 144:103666
- Liu J, Chen W, Hao H et al (2019) Numerical study of low-speed impact response of sandwich panel with tube filled honeycomb core. *Compos Struct* 220:736–748
- Lu J, Wang Y, Zhai X et al (2021) Impact behavior of a cladding sandwich panel with aluminum foam-filled tubular cores. *Thin-Walled Struct* 169:108459
- Mocian O, Constantinescu DM, Sandu M et al (2018) Experimental and numerical analyses of the impact response of lightweight sandwich panels. *Mater Today: Proc* 5(13):26634–26641
- Mocian O, Constantinescu DM, Sandu M et al (2017) Impact response of polyurethane and polystyrene sandwich panels. *Procedia Struct Integr* 5:653–658
- Ouadday R, Marouene A, Morada G et al (2018) Experimental and numerical investigation on the impact behavior of dual-core composite sandwich panels designed for hydraulic turbine applications. *Compos Struct* 185:254–263

- Qi C, Remennikov A, Pei L et al (2017) Impact and close-in blast response of auxetic honeycomb-cored sandwich panels: Experimental tests and numerical simulations. *Compos Struct* 180:161–178
- Qin Q, Chen S, Li K et al (2020) Structural impact damage of metal honeycomb sandwich plates. *Compos Struct* 252:112719
- Reddy TY, Reid SR (1979) Lateral compression of tubes and tube-systems with side constraints. *Int J Mech Sci* 21(3):187–199
- Roy T, Matsagar V (2021) Probabilistic framework for failure investigation of reinforced concrete wall panel under dynamic blast loads. *Eng Failure Anal* 125:105368
- Schenker A, Anteby I, Nizri E et al (2005) Foam-protected reinforced concrete structures under impact: Experimental and Numerical Studies. *J Struct Eng* 131(8):1233–1242
- Soltani H, Khaloo A, Sadraie H (2020) Dynamic performance enhancement of RC slabs by steel fibers vs. Externally bonded GFRP sheets under impact loading. *Eng Struct* 213:110539
- Song J, Xu S, Xu L et al (2020) Experimental study on the crashworthiness of bio-inspired aluminum foam-filled tubes under axial compression loading. *Thin-Walled Struct* 155:106937
- Wang C, Xu B, Yuen SCK (2019) Numerical analysis of cladding sandwich panels with tubular cores subjected to uniform blast load. *Int J Impact Eng* 133:103345
- Wang E, Sun G, Zheng G et al (2021) On multiaxial failure behavior of closed-cell aluminum foams under medium strain rates. *Thin-Walled Struct* 160:107278
- Wang Y, Liew JYR, Lee SC et al (2017) Crushing of a novel energy absorption connector with curved plate and aluminum foam as energy absorber. *Thin-Walled Struct* 111:145–154
- Wang Y, Zhai X (2019) Dynamic crushing behaviors of aluminum foam filled energy absorption connectors. *Int J Steel Struct* 19(1):241–254
- Wang Y, Zhai X, Liu S et al (2020) Energy absorption performance of a new circular-triangular nested tube and its application as sacrificial cladding. *Thin-Walled Struct* 157:106992
- Wang Y, Zhai X, Yan J et al (2018a) Experimental, numerical and analytical studies on the aluminum foam filled energy absorption connectors under impact loading. *Thin-Walled Struct* 131:566–576
- Wang Y, Zhai X, Ying W et al (2018b) Dynamic crushing response of an energy absorption connector with curved plate and aluminum foam as energy absorber. *Int J Impact Eng* 121:119–133
- Xia Z, Wang X, Fan H et al (2016) Blast resistance of metallic tube-core sandwich panels. *Int J Impact Eng* 97:10–28
- Xie S, Jing K, Zhou H et al (2020) Mechanical properties of nomex honeycomb sandwich panels under dynamic impact. *Compos Struct* 235:111814
- Xu F, Zhang X, Zhang H (2018) A review on functionally graded structures and materials for energy absorption. *Eng Struct* 171:309–325
- Xu S, Liu Z, Li J et al (2021) Dynamic behaviors of reinforced NSC and UHPC columns protected by aluminum foam layer against low-velocity impact. *J Build Eng* 34:101910
- Yan C, Wang Y, Zhai X (2020) Low velocity impact performance of curved steel-concrete-steel sandwich shells with bolt connectors. *Thin-Walled Struct* 150:106672
- Yu Y, Lee S, Cho J (2021) Deflection of reinforced concrete beam under low-velocity impact loads. *Int J Impact Eng* 154:103878
- Yuen SCK, Cunliffe G, Du Plessis MC (2017) Blast response of cladding sandwich panels with tubular cores. *Int J Impact Eng* 110:266–278
- Zhang D, Fei Q, Zhang P (2017) Drop-weight impact behavior of honeycomb sandwich panels under a spherical impactor. *Compos Struct* 168:633–645
- Zhang J, Ye Y, Yuan H et al (2020a) A theoretical study of low-velocity impact of metal foam-filled circular tubes. *Thin-Walled Struct* 148:106525
- Zhang X, Xu F, Zang Y et al (2020b) Experimental and numerical investigation on damage behavior of honeycomb sandwich panel subjected to low-velocity impact. *Compos Struct* 236:111882
- Zhu Y, Sun Y (2020) Dynamic response of foam core sandwich panel with composite facesheets during low-velocity impact and penetration. *Int J Impact Eng* 139:103508

# Chapter 5

## Flat Steel–Concrete–Corrugated Steel Sandwich Panel Under Impact



### 5.1 Introduction

In recent years, the events of terrorist attack and vehicle impact on civil structures have shown an increasing trend (Do et al. 2019; Li et al. 2019; Mehreganian et al. 2019; Micallef et al. 2012; Sohel et al. 2020; Zhu and Khanna 2016), which might cause severe damage of the structures. Therefore, it is of significance to develop a new-type sandwich panel to enhance the impact resistance of traditional sandwich panels and mitigate the impact-induced damage to the structures.

Reinforced concrete panel was widely employed for impact resisting owing to low cost and easy fabrication (Lee et al. 2021; Ning et al. 2020; Oucif et al. 2020; Xu et al. 2019). An enormous number of studies have been performed on the impact resistant performances of reinforced concrete panels. The dynamic responses of reinforced concrete panels with variant steel reinforcement ratios were studied via employing the low-velocity impact tests, and the results indicated that the crack patterns and failure modes were found to be more dependent on the reinforcement arrangement (Othman and Marzouk 2016; Zineddin and Krauthammer 2007). Comparing with the traditional reinforced concrete panel, the pre-stressed concrete panel showed superior impact resistance and energy absorption performance under the impact of a falling hammer (Kumar et al. 2017). In addition, the dynamic responses of reinforced concrete panels under the impacts of projectile and aircraft were studied by Oucif and Mauludin (2019) and Sadiq et al. (2014), respectively, via employing the Finite Element (FE) method. The numerical results were shown to be accurate by comparing with the experimental results. Owing to the massive weight and volume as well as the limited impact resistance of the traditional reinforced concrete panel, it is necessary to propose a new impact resistant panel to achieve superior impact resistant performance.

Steel–concrete–steel (SCS) sandwich structure can be employed for impact resisting because of its desirable impact resistance, energy absorption performance and light weight. Thus, extensively studies have been conducted on the impact response behaviors of SCS sandwich structures (Liew et al. 2009; Sohel et al. 2015;

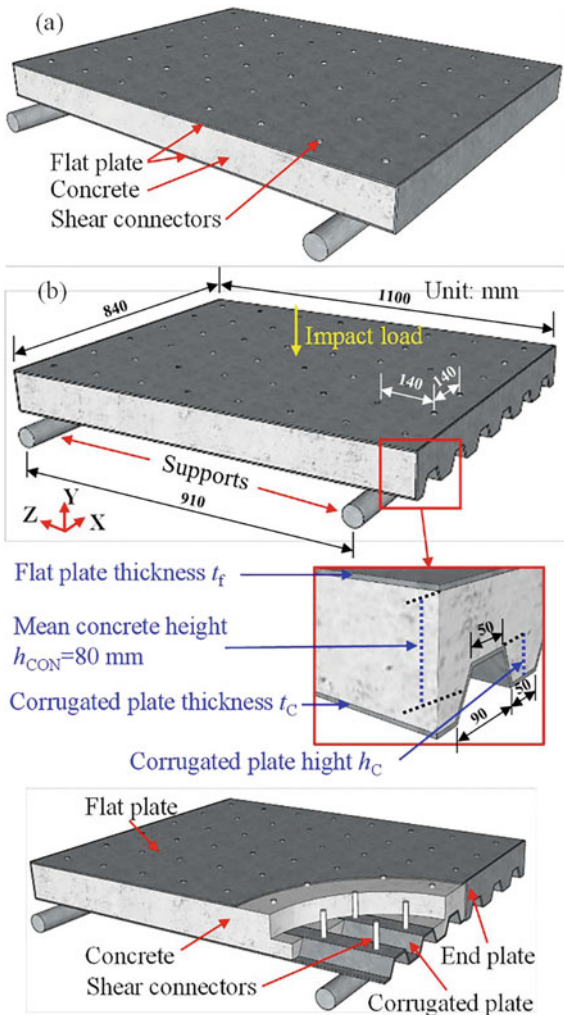
Yan and Liew 2016; Yan et al. 2016a, b, c) The dynamic responses of SCS panels under static and impact loads were studied, and the analytical models were developed for predicting the static and dynamic responses of SCS panels (Sohel and Liew 2011, 2014; Sohel et al. 2012). Further, an equivalent single-degree-of-freedom (SDOF) model for predicting the displacement responses of SCS panels under impact loading was proposed, and its rationality was verified by comparing with the test results (Guo and Zhao 2019). Moreover, Remennikov and Kong (2012) studied the dynamic responses of axially-restrained SCS panels through impact tests and FE simulations, and the strain rate effects of materials were found to significantly affect the numerically-predicted bending resistance of the SCS panel.

The responses of the SCS panel under specific dynamic loading scenarios, including vehicle and projectile impacts as well as blast loading, were also studied (Feng et al. 2020; Remennikov et al. 2013; Wang et al. 2015a, b). Remennikov et al. (2013) experimentally and numerically studied the responses of the axially-restrained non-composite SCS panel under vehicle impact. The results showed that the proposed SCS panel could resist large impact energy and terminate the fast-moving vehicle. Wang et al. (2015a, b) studied the dynamic responses of simply-supported SCS panels under blast loading by employing the experimental and numerical methods. In addition, the equivalent SDOF model and Lagrange Equation approach were found to provide accurate predictions on the blast-induced displacement responses of the SCS panel.

Recently, curved SCS shells were proposed to resist variant loading scenarios, e.g., static, impact and blast loads Huang and Liew (2015, 2016), Wang et al. (2016b), Yan et al. 2019, 2020a, b). Huang and Liew (2015, 2016) studied failure mechanisms of the curved SCS shell filled with ultra-lightweight cement composite through quasi-static loading tests and FE simulation, and the formulae for predicting shear capacity of the curved SCS shell was provided. The blast response of the curved SCS shell was numerically studied by Wang et al. (2016b), and the shear connectors was found to be effective in bonding the faceplates to concrete core, and thus significantly improving the blast resistance of the curved SCS shell. Yan et al. (2019, 2020a, b) investigated the responses of the curved SCS shell under static and impact loads by employing the experimental method. Three failure modes were summarized and three impact stages were identified from the experiments, including inertial stage, loading stage and unloading stage.

With the aim of improving the impact resistance of the traditional SCS sandwich panel, a new flat steel plate-concrete-corrugated steel plate (FS–C–CS) sandwich panel was proposed in this chapter (as shown in Fig. 5.1). By employing the corrugated steel plate in tension side, the bending resistance and stiffness of the one-way supported FS–C–CS panel along span direction (around X-axis as shown in Fig. 5.1) could be improved as compared to the traditional SCS panel with two flat faceplates, owing to the increased moment of inertia. This also results in the improved impact resistance of the FS–C–CS panel. The dynamic responses of the FS–C–CS panels under impact loading were studied through drop-weight impact tests and FE simulations to reveal the failure mode, impact force and deformation responses as well as impact energy dissipation mechanism of the FS–C–CS panel.

**Fig. 5.1** 3D schematic view of **a** SCS sandwich panel and **b** FS–C–CS sandwich panel, reprinted from Lu et al. (2021), copyright 2022, with permission from Elsevier



## 5.2 Methodologies

### 5.2.1 Experimental Methodology

#### 5.2.1.1 Specimen Design

As shown in Fig. 5.1, the FS–C–CS panel proposed in this study was assembled by a flat steel plate, a corrugated steel plate and concrete core. In order to assure structural integrity of the FS–C–CS panel, high-strength bolts were adopted as shear connectors to bond the flat plate and corrugated plate to concrete as well as provide longitudinal

**Table 5.1** Geometries of test specimens

Specimen	$h_c$ (Design value/measured value)/mm	$t_f$ (Design value/measured value)/mm	$t_c$ (Design value/measured value)/mm	$V_0$ (Measured value)/(m/s)
H444	40.0/40.35	4.0/3.49	4.0/3.49	7.963
H435	40.0/42.72	3.0/2.79	5.0/4.35	8.028
H453	40.0/41.82	5.0/4.35	3.0/2.79	8.036
H244	20.0/20.52	4.0/3.49	4.0/3.49	8.006
H044	0 (Flat plate)	4.0/3.49	4.0/3.49	8.028

Note  $h_c$ —Corrugated plate height;  $t_f$ —Flat plate thickness;  $t_c$ —Corrugated plate thickness;  $V_0$ —Impact velocity of the hammer

and transverse shear resistance. Moreover, two end plates were also welded to the flat plate and corrugated plate to further improve the composite action of the FS–C–CS panel, since the full composite action of the SCS sandwich structure with the presence of end plates was demonstrated even though insufficient shear connectors were provided (Kang 2012; Wang et al. 2016a).

Five specimens were designed for the drop-weight impact tests, and their geometric parameters are given in Fig. 5.1 and Table 5.1. The dimension of the specimens was 1100 mm × 840 mm (length × width). Specimen H444, H435 and H453 were FS–C–CS panels designed with nominal steel plate thickness of 3, 4 and 5 mm and the measured steel plate thickness is presented in Table 5.1. Specimen H444, H244 and H044 were sandwich panels with variant corrugated plate heights, among which specimen H044 was the traditional SCS panel with two flat faceplates. All the specimens shared the same concrete volume with mean concrete height ( $h_{CON}$ ) to be 80 mm, as shown in Fig. 5.1. The diameter of the shear connectors was 12 mm.

### 5.2.1.2 Test Setup and Instrumentation

The drop-weight impact tests on the FS–C–CS panels were conducted to obtain the impact force and displacement responses, and the test setup and instrumentation are presented in Fig. 5.2. The specimen was simply supported on the two rigid round bars with clear span of 910 mm. The impact loading was applied on the specimen through dropping a 620 kg hammer with a hemispherical head. The diameter of the hemispherical hammer head was 200 mm.

With regard to the measurement system, three displacement transducers were adopted to measure the displacements of the FS–C–CS panel. The measurement points of the specimen included the center point of corrugated plate (corresponding to displacement transducer A in Fig. 5.2b), quarter-span point of corrugated plate (corresponding to displacement transducer B in Fig. 5.2b) and edge point of corrugated plate at mid-span (corresponding to displacement transducer C in Fig. 5.2b). A dynamic force transducer with a measurement range of 2000 kN was embedded in

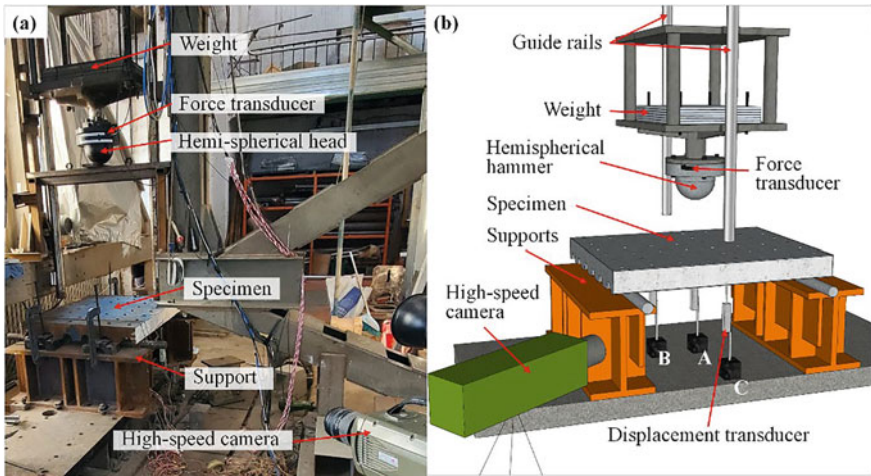


**Fig. 5.2** Drop-weight impact test setup and instrumentation: **a** photograph and **b** 3D schematic view, reprinted from Lu et al. (2021), copyright 2022, with permission from Elsevier

the hammer head to record the impact force–time history during impact. Moreover, a high-speed camera was employed to record the impact process. The initial impact velocities of the hammer for the five specimens were obtained via analyzing the high-speed camera data, and they are presented in Table 5.1. The sampling frequency of displacement transducers, force transducer and high-speed camera were  $10^5$ ,  $10^5$  and 3000 Hz, respectively.

### 5.2.2 Numerical Methodology

To further reveal the impact responses of FS–C–CS panels subjected to impact loading, the numerical studies were conducted via employing the explicit program in LS-DYNA.

#### 5.2.2.1 Material Models

The material parameters of mild steel employed for fabricating the specimens were obtained through tensile coupon tests, and the obtained nominal stress–strain curves of mild steel with different thicknesses are given in Fig. 5.3. The material parameters of mild steel are presented in Table 5.2. The Piecewise Linear Plasticity material model (MAT\_24 in LS-DYNA) was employed to simulate steel plates of the FS–C–CS panel. In addition, material behaviors of the bolt shear connectors were simulated by employing the Plastic Kinematic material model (MAT\_12 in LS-DYNA). The

**Fig. 5.3** Nominal Stress-strain curves of mild steels, reprinted from Lu et al. (2021), copyright 2022, with permission from Elsevier

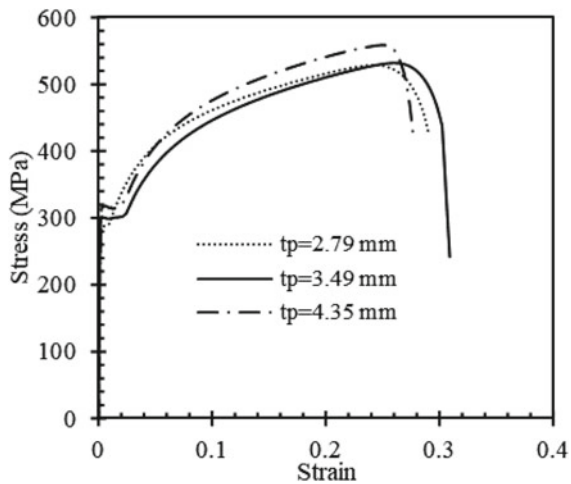


**Table 5.2** Material properties of mild steel and shear connector

Mild steel	$E_y$ (GPa)	$\sigma_y$ (MPa)	$\sigma_u$ (MPa)
$t_p = 2.79$ mm	195	294	529
$t_p = 3.49$ mm	193	304	532
$t_p = 4.35$ mm	197	307	559
Shear connector	207	640	800

Note  $E_y$ —Young's modulus of steel;  $\sigma_y$ —Yield stress of steel;  $\sigma_u$ —Ultimate stress of steel

material parameters of the bolts are shown in Table 5.2. The strain rate effects of mild steel and bolts were considered by adopting the Cowper-Symonds model, and strain rate parameter  $C$  and  $P$  were defined to be  $802 \text{ s}^{-1}$  and 3.585, respectively (Abramowicz and Jones 1986).

The Continuous Surface Cap (CSC) model, i.e., MAT\_159 in LS-DYNA, was adopted to simulate the behaviors of concrete. It is a cap model which has a smooth intersection between the failure surface and hardening cap (Yan et al. 2020a). The yield surface of CSC model is formulated in terms of three stress invariants, including the first invariant of the stress tensor ( $J_1$ ), the second invariant of the deviatoric stress tensor ( $J'_2$ ) and the third invariant of the deviatoric stress tensor ( $J'_3$ ), which can be given as

$$\begin{cases} J_1 = 3P \\ J'_2 = \frac{1}{2} S_{ij} S_{ij} \\ J'_3 = \frac{1}{3} S_{ij} S_{jk} S_{ki} \end{cases} \quad (5.1)$$

where  $P$  and  $S_{ij}$  are pressure and deviatoric stress tensor. The shear failure surface is defined as

$$F_f(J_1) = \alpha - \lambda \exp^{-\beta J_1} + \theta J_1 \quad (5.2)$$

where  $\alpha$ ,  $\beta$ ,  $\lambda$  and  $\theta$  are material parameters obtained via conducting tri-axial compressive tests on concrete cylinders. A damage formulation is adopted to model the softening behavior of concrete. Both strain softening and modulus reduction of concrete can be modeled by the damage formulation. The damage formulation is given as follow (Simo and Ju 1987):

$$\sigma_{ij}^d = (1 - d)\sigma_{ij}^{vp} \quad (5.3)$$

where  $d$  is scalar damage parameter;  $\sigma_{ij}^d$  and  $\sigma_{ij}^{vp}$  are stress tensors with and without damage, respectively. Moreover, rate effect formulations are adopted to model the enhancement of concrete induced by strain rate effect, and they are applied to the plasticity surface, damage surface and fracture energy. The viscoplastic algorithm is employed for the yield surface. The viscoplastic algorithm interpolates between the elastic trial stress,  $\sigma_{ij}^T$ , and the inviscid stress (without rate effects),  $\sigma_{ij}^P$ , at each time step to obtain the viscoplastic stress (with rate effects),  $\sigma_{ij}^{vp}$  as follow:

$$\sigma_{ij}^{vp} = (1 - \gamma)\sigma_{ij}^T + \gamma\sigma_{ij}^P \quad \gamma = \frac{\Delta t/\eta}{1 + \Delta t/\eta} \quad (5.4)$$

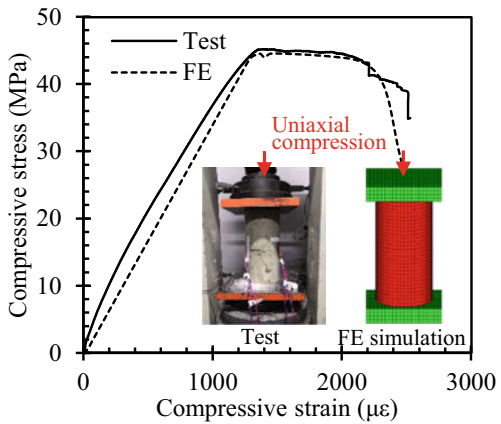
where  $\eta$  and  $\Delta t$  are fluidity coefficient and time step, respectively. The uniaxial tensile and compressive strengths can be obtained as:

$$\begin{aligned} f_T^{'dynamic} &= f'_T + E\dot{\varepsilon}\eta \\ f_C^{'dynamic} &= f'_C + E\dot{\varepsilon}\eta \end{aligned} \quad (5.5)$$

where  $\dot{\varepsilon}$  is the effective strain rate calculated based on the six strain components.

The input material parameters of concrete were obtained through uniaxial compressive tests conducted on the concrete cylinders. The stress-strain curve of concrete obtained through uniaxial compressive tests on concrete cylinder is given in Fig. 5.4. The elastic modulus, compressive strength and Poisson's ratio of the concrete are 34 GPa, 45 MPa and 0.21, respectively, based on the uniaxial compressive tests. In addition, a FE model of concrete cylinder under uniaxial compression was also established. The stress-strain curves of concrete obtained from uniaxial compressive tests and FE simulation are compared in Fig. 5.4, and the two curves are found to be well matched, which validates the accuracy of the material model of concrete core.

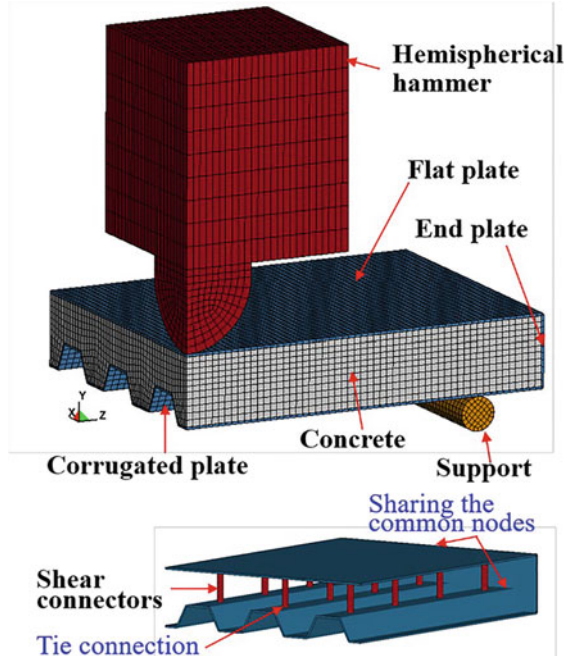
**Fig. 5.4** Comparison of stress–strain curve of concrete obtained from uniaxial compressive tests and FE simulation, reprinted from Lu et al. (2021), copyright 2022, with permission from Elsevier



### 5.2.2.2 Model Description

The FE model of the FS–C–CS panel under drop-weight impact loading is presented in Fig. 5.5. The quarter model was established to reduce the computation time. The eight-node solid elements were adopted to simulate the drop hammer, supports and concrete. The shell elements comprising five integration points along the thickness of the shell were used to simulate steel plates. The beam elements were used to

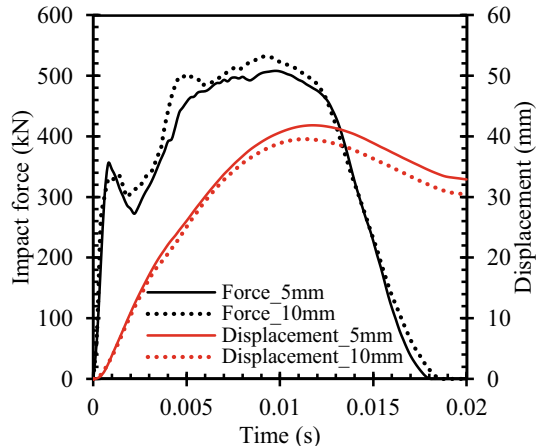
**Fig. 5.5** FE model of the FS–C–CS panel under impact loading, reprinted from Lu et al. (2021), copyright 2022, with permission from Elsevier



simulate shear connectors. The perfect bond behavior between the concrete and shear connectors was assumed, which was achieved in the FE modeling by sharing the common nodes of the shear connector elements and concrete elements. The two end nodes of each shear connectors were tied to the flat plate and corrugated plate, respectively, via employing the keyword \*CONTACT\_TIED\_NODES\_TO\_SURFACE in LS-DYNA (Hallquist 2013), since there was no connection failure between bolts and steel plates during the drop-weight impact test. The keyword \*CONTACT\_AUTOMATIC\_SURFACE\_TO\_SURFACE was adopted to model the contacts between two parts in the FE model, including concrete and steel plates, hammer and flat plates as well as support and corrugated plate. Moreover, the nodes at the bottom of the support was constrained in three translational directions via employing the keyword \*BOUNDARY\_SPC\_SET. Since the quarter FE model was established, the symmetrical restraints were applied to the XY plane at mid-span of the FS-C-CS panel via restraining the translation along Z direction and rotations along X and Y axis. Moreover, the translation along X direction and rotations along Y and Z axis in the YZ plane at middle of the specimen were also restrained. The mass and initial velocities of the hammer were defined as the measured values from the drop-weight impact tests, and the keyword \*INITIAL\_VELOCITY\_GENERATION was adopted to specify initial velocity of the hammer.

The mesh size of concrete core and steel plates were about  $10 \times 10 \times 10 \text{ mm}^3$  and  $10 \times 10 \text{ mm}^2$ , respectively. The current mesh size was determined based on mesh sensitivity analysis. The FE model of specimen H444 with smaller mesh size (about 5 mm) was established. Figure 5.6 presents the impact force- and center displacement-time histories obtained from the FE models with current element size (about 10 mm) and smaller element size (about 5 mm). The differences of FE predictions with variant mesh sizes are limited. Hence, the current element size (about 10 mm) was employed in this study, considering both the accuracy and computation time.

**Fig. 5.6** Effect of different mesh sizes on FE simulation results, reprinted from Lu et al. (2021), copyright 2022, with permission from Elsevier



### 5.3 Results and Discussions

#### 5.3.1 FE Model Validation

Figure 5.7 presents the comparison of failure modes of the specimen H444 obtained from the drop-weight impact test and FE simulation. The FE model is found to reasonably predict the global flexural deformation and local indentation of the FS–C–CS panel under impact load. Moreover, the vertical cracks of concrete near the mid-span observed from the impact test can also be captured by the established FE model, as shown in Fig. 5.7a. The comparisons of center displacement and impact force responses obtained from impact tests and FE analyses are presented in Figs. 5.8 and 5.9, respectively. The FE results showed good agreement with the experimental results. Table 5.3 presents the comparisons of maximum impact forces and maximum center displacements obtained from impact tests and FE analyses, and their differences are found to be less than 9% and 11% for the maximum impact force and center displacement, respectively, except for the specimen H244 owing to its geometric imperfection during the fabrication. The comparisons of FE-predictions and test results in terms of failure mode, impact force and displacement response can verify the rationality of the established FE models.

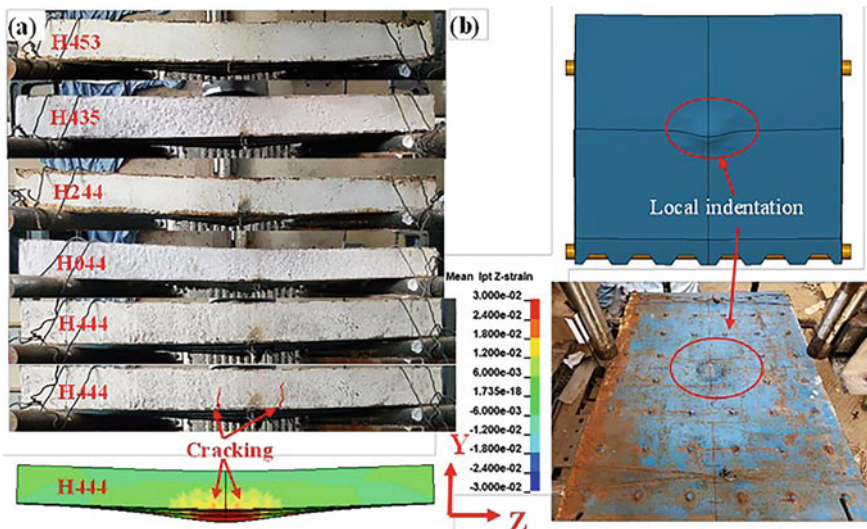


**Fig. 5.7** Failure modes of tested specimens: **a** global flexural deformation and **b** local indentation, reprinted from Lu et al. (2021), copyright 2022, with permission from Elsevier

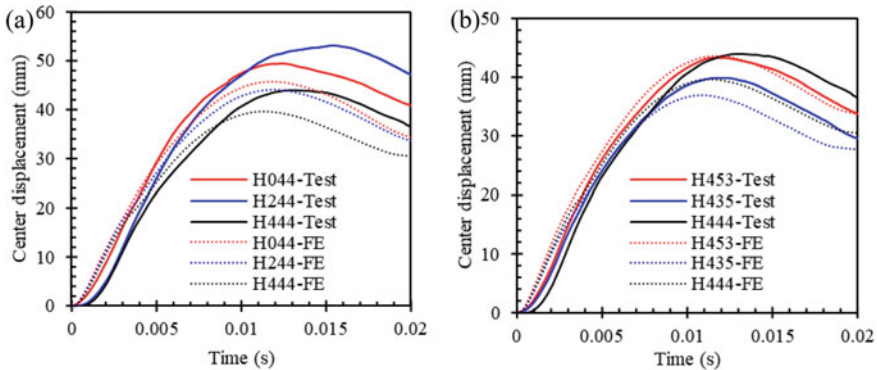


**Fig. 5.8** Center displacement–time histories of tested specimens: **a** Variant corrugated plate height, **b** Variant steel plate thickness, reprinted from Lu et al. (2021), copyright 2022, with permission from Elsevier

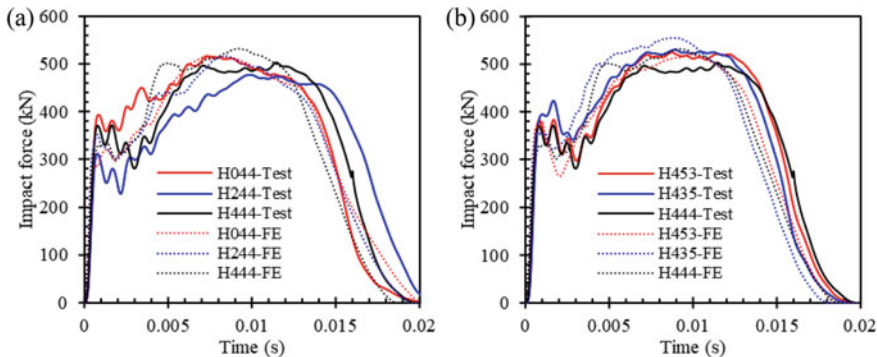


**Fig. 5.9** Impact force–time histories of tested specimens: **a** Variant corrugated plate height, **b** Variant steel plate thickness, reprinted from Lu et al. (2021), copyright 2022, with permission from Elsevier

**Table 5.3** Comparison of maximum impact force and center displacement from test and FE simulations

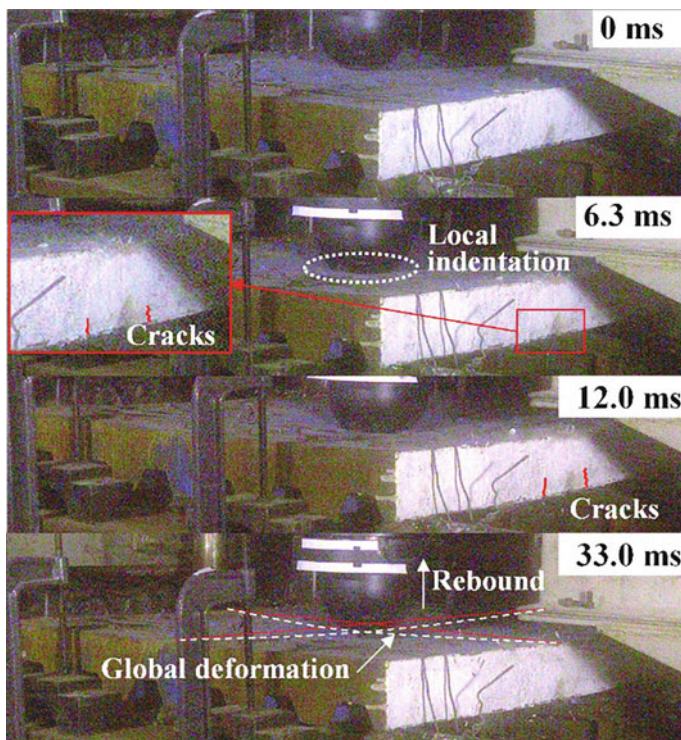
Specimen	$F_{\max}$ (kN)	$F_{\max\text{FE}}$ (kN)	$F_{\max}/F_{\max\text{FE}}$	$D_{\max\text{A}}$ (mm)	$D_{\max\text{FE}}$ (mm)	$D_{\max\text{A}}/D_{\max\text{FE}}$
H453	524.82	520.81	1.01	43.33	43.62	0.99
H435	530.58	554.94	0.96	39.87	36.94	1.08
H244	477.33	516.98	0.92	53.13	44.08	1.21
H044	516.87	514.11	1.01	49.44	45.73	1.08
H444	503.02	532.30	0.95	43.96	39.63	1.11

Note  $F_{\max}$ —Maximum impact force obtained from test;  $F_{\max\text{FE}}$ —Maximum impact force obtained from FE simulation;  $D_{\max\text{A}}$ —Maximum center displacement obtained from test;  $D_{\max\text{FE}}$ —Maximum center displacement obtained from FE simulation

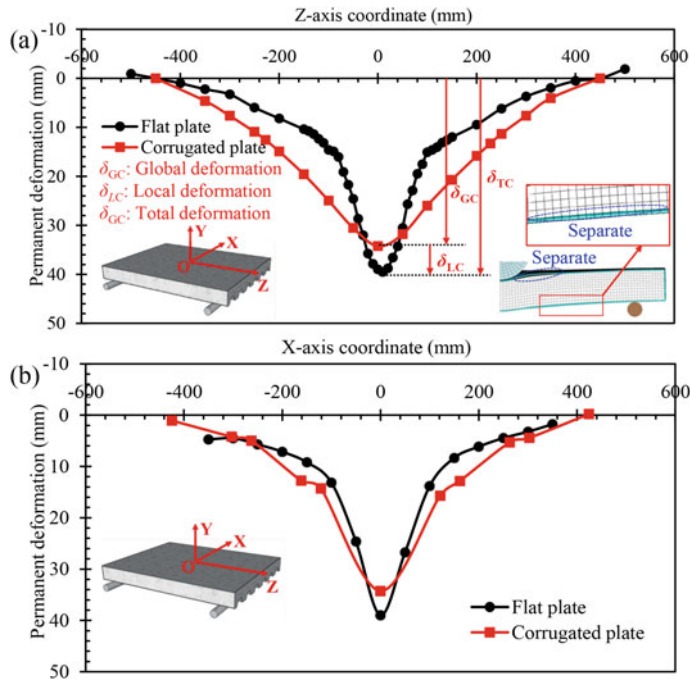
### 5.3.2 Failure Mode

Figure 5.7 presents the failure mode of the tested specimens, which exhibit local indentation at the impact zone and global flexural deformation with plastic hinge at mid-span. The vertical cracks near the mid-span of the panel are also observed owing to the large sagging moment. Figure 5.10 presents the impact process of FS-C-CS panel H444 recorded by the high-speed camera, from which the combination of local indentation and global flexural deformation along both span and width directions can be observed. The deformation of the FS-C-CS panel exhibits continuous increase at 0–12.0 ms under the impact of a hemi-spherical head. The vertical cracks of the concrete core near the mid-span occur at 6.3 ms owing to the sagging moment, and the length of the vertical cracks shows continuous increase with further collision. The deformation of the FS-C-CS panel and the length of the cracks reach their maximum values at 12.0 ms. The hemispherical head and FS-C-CS panel rebounded subsequently, as shown in Fig. 5.10.

Figure 5.11a presents the permanent deformation profile of the specimen H444 in span direction. The bi-linear shape of the permanent deformation of the corrugated



**Fig. 5.10** Impact process of FS-C-CS panel H444, reprinted from Lu et al. (2021), copyright 2022, with permission from Elsevier



**Fig. 5.11** Permanent deformation of specimen H444: **a** Permanent deformation in Z-axis direction, **b** Permanent deformation in X-axis direction, reprinted from Lu et al. (2021), copyright 2022, with permission from Elsevier

plate further confirms the global flexural deformation, and local indentation can be observed from the permanent deformation of the flat plate. Figure 5.12 presents the axial strain contours of the concrete. It is noted that the concrete at mid-span experiences compression and tension at its top and bottom surfaces, respectively, caused by the sagging moment which also results in the vertical cracks of concrete at

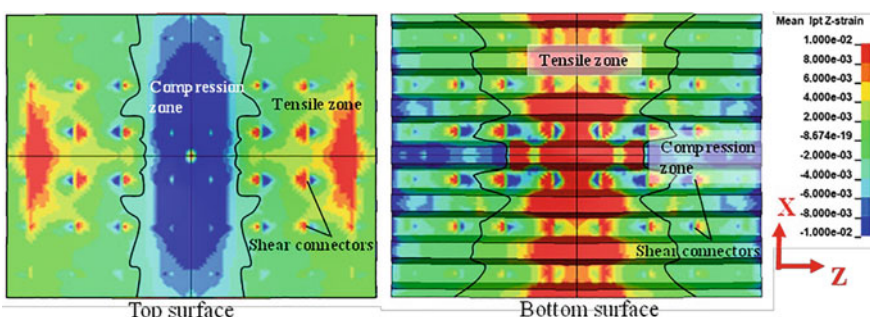


**Fig. 5.12** Axial strain contours of concrete of specimen H444

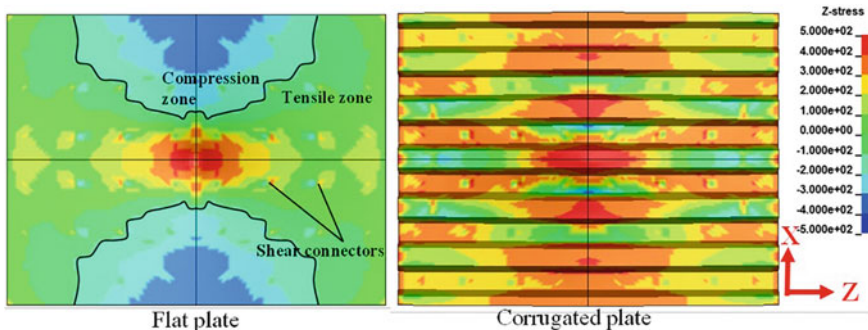


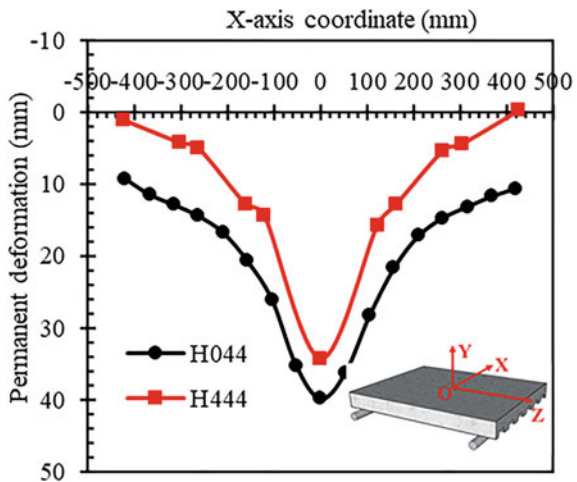
**Fig. 5.13** Axial stress contours of steel plates of specimen H444, reprinted from Lu et al. (2021), copyright 2022, with permission from Elsevier

mid-span. The axial stress contours of the steel plates are presented in Fig. 5.13, and the flat and corrugated plates are generally in compression and tension, respectively, at the zone near mid-span. With regard to the stress state at the zone near the support, the bottom surface of concrete experiences compressive force applied by the end plate, as shown in Fig. 5.12, since the bending-induced expansion of concrete at the bottom surface is restrained by the end plate. Meanwhile, the end plate also applies tensile force on the flat plate to balance the compressive force of concrete, which results in tension of the flat plate near the support, as shown in Fig. 5.13. This also causes the top surface of concrete experiencing tension near the support, as shown in Fig. 5.12, since the full composite action of the panel can be assured with the presence of shear connectors and end plates.

As illustrated in Fig. 5.11a, the permanent deformations at the center points of flat and corrugated plate are defined as total deformation ( $\delta_{TC}$ ) and global deformation ( $\delta_{GC}$ ), respectively. It can be observed in Fig. 5.11a that the total deformation ( $\delta_{TC}$ ) was 13.8% higher than global deformation ( $\delta_{GC}$ ) owing to the presence of local indentation induced by the hemispherical hammer head. Moreover, flat plate also exhibits large membrane stretching under local impact load, which leads to local tension of flat plate at impact zone, as shown in Fig. 5.13. However, the permanent deformation of flat plate was found to be smaller than that of corrugated plate except for the local impact zone, as shown in Fig. 5.8a. This is owing to the separation between the steel plates and concrete core of the FS–C–CS panel after the rebounding of hemispherical head since there is no shear connector at the valley of the corrugated plate.

With regard to deformation of the FS–C–CS panel in width direction, the combination of local indentation and global flexural deformation can be observed, as shown in Fig. 5.11b. Figure 5.14 presents the comparison of permanent deformations of the FS–C–CS panel and traditional SCS panel in width direction. The results showed that the global deformation of the FS–C–CS panel (H444) was 16.3% lower than that of SCS panel (H044) owing to the increased bending resistance and stiffness of the FS–C–CS panel with corrugated plate. However, the deformation difference between

**Fig. 5.14** Permanent deformation of the FS–C–CS panel and SCS panel in width direction, reprinted from Lu et al. (2021), copyright 2022, with permission from Elsevier



center point and edge point of the specimen H444 was 13.1% higher than that of specimen H044, as the presence of corrugated plate reduces the bending resistance and stiffness of the FS–C–CS panel in width direction.

### 5.3.3 Impact Force and Displacement Responses

The typical impact force– and displacement–time curves of the specimen H444 under impact load are presented in Fig. 5.15. The impact process can be divided into three stages based on the characteristics of the impact force and displacement response histories, including inertial stage, loading stage and unloading stage. The inertial stage occurs from 0 to 0.003 s for the specimen H444. The impact zone of the specimen was forced to move downwards with the same velocity of the hammer, and thus the velocity of the impact zone increased rapidly once the hammer struck the specimen. The impact force exhibits continuous increase to its first peak value, and this peak impact force is induced by inertial effect. Further, the impact force experiences continuous fluctuation after the first peak value. The hammer displacement is found to increase faster than that of center displacement due to the presence of local indentation. The difference between the hammer and center displacement can present the local indentation depth which approaches a constant value at the end of initial stage. This indicates that the local indentation appears at the initial stage. Moreover, the edge displacement (point C in Fig. 5.2) exhibits initial decrease due to the inertial effect, as shown in Fig. 5.15. The loading stage occurs from 0.003 to 0.012 s for the specimen H444, and the hammer and center displacements show continuous increase to their maximum values at the end of loading stage. The impact force–hammer displacement curve is presented in Fig. 5.16. The impact force exhibits increase with the increase of displacement during loading stage owing to

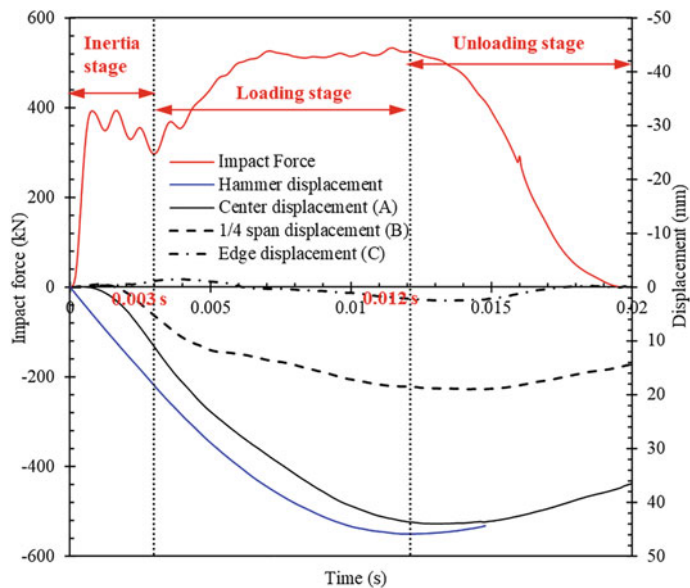
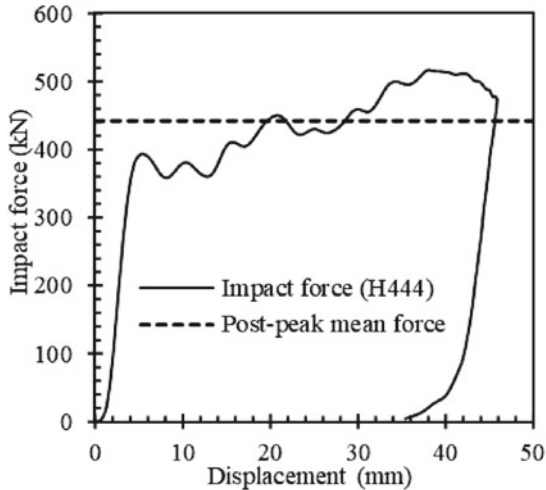


**Fig. 5.15** Impact force and displacement versus time curves of specimen H444, reprinted from Lu et al. (2021), copyright 2022, with permission from Elsevier

**Fig. 5.16** Impact force–center displacement curves of specimen H444, reprinted from Lu et al. (2021), copyright 2022, with permission from Elsevier



the membrane stretching of the flat plate under large deformation, and the impact force reaches its maximum value at the end of loading stage. Owing to the negligible inertial force as compared to resistance of the FS–C–CS panel at loading stage, the impact force can generally represent the resistance of the panel. The unloading stage

occurs from 0.012 to 0.0196 s. The hammer and panel start to rebound, and therefore the center and hammer displacements exhibit continuous decrease. As shown in Fig. 5.15, the rebound velocity of the hammer is higher than the panel, which results in decreasing contact area between the hammer and panel. Hence, the impact force shows continuous decrease and reduces to zero when the hammer is completely separated from the panel.

Figure 5.8 presents the comparison of the center displacement–time histories of the specimens with variant corrugated plate heights and steel plate thicknesses, and the maximum center displacement values are summarized in Table 5.3. The results reveal that maximum center displacement of the FS–C–CS panel H444 is reduced by 11.1% comparing with the SCS panel H044 with the same concrete volume and steel plate thickness, owing to higher bending resistance and stiffness of the FS–C–CS panel with corrugated plate. However, the maximum center displacement of specimen H244 obtained from impact test is larger than that of specimen H044, which may be attributed to geometric imperfection of the specimen H244. It is confirmed by the FE modeling without geometric imperfection that the maximum center displacement of specimen H244 obtained from FE simulation is reduced by 3.6% comparing with specimen H044, as presented in Table 5.3. It can be concluded that the maximum deformation of the FS–C–CS panel can be reduced by increasing corrugated plate height. The effect of steel plate thickness on impact response of the F–C–CS panel is also presented in Table 5.3 and Fig. 5.8b. The maximum center displacement of the FS–C–CS panel is found to be reduced by increasing corrugated plate thickness and reducing flat plate thickness, which can be attributed to the improved tension strength of the corrugated plate and bending resistance of the FS–C–CS panel. The maximum center displacement is reduced by 9.3% on increasing corrugated plate thickness from 3.49 mm to 4.35 mm. However, the maximum center displacement exhibits increase with the increase of corrugated plate thickness from 2.79 mm to 3.49 mm owing to the geometric imperfection of the specimen H453 and H444. Moreover, FE results indicate that the maximum center displacement of the specimen H444 is reduced by 9.2% comparing with the specimen H453, as shown in Table 5.3.

Figure 5.9 presents the comparison of the impact force–time histories of tested specimens, and their maximum impact forces ( $F_{\max}$ ) and post-peak mean forces ( $F_m$ ) are summarized in Tables 5.3 and 5.4, respectively. The post-peak mean force ( $F_m$ ) can be determined as

$$F_m = \frac{\int_{D_0}^{D_{\max}} F(D)dD}{D_{\max} - D_0} \quad (5.6)$$

**Table 5.4** Post-peak mean forces obtained from impact tests

Specimen	H453	H435	H244	H044	H444
$F_m$ (kN)	414.57	436.67	358.03	438.67	441.96

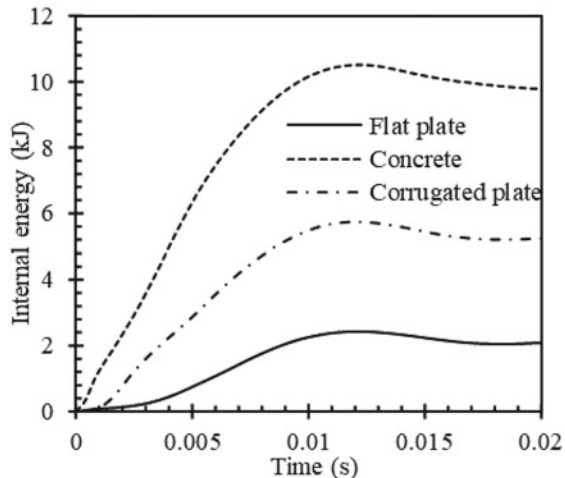
Note  $F_m$ —Post-peak mean force

where  $F$  is impact force,  $D$  is displacement at center point of the flat plate,  $D_{\max}$  is the maximum displacement, and  $D_0$  is displacement corresponding to first peak impact force. As shown in Table 5.4, the post-peak mean force of the FS–C–CS panel H444 is increased by 0.8% comparing with the SCS panel H044, which indicates the improvement in bending resistance of the FS–C–CS panel with corrugated plate. However, the maximum impact force of the specimen H044 obtained from impact test is larger than that of specimen H444. With regard to the FE results presented in Table 5.3, the maximum impact force of the specimen H444 is increased by 2.8% comparing with the specimen H044. Generally, the maximum impact force and post-peak mean force of the FS–C–CS panel are found to increase with the increase of corrugated plate thickness owing to the improved bending resistance of the panel, as shown in Tables 5.3 and 5.4. The maximum impact force is found to be increased by 5.5% on increasing corrugated plate thickness from 3.49 mm to 4.35. However, the maximum impact force exhibits decrease on increasing corrugated plate thickness from 2.79 mm to 3.49 mm owing to geometric imperfections of the fabricated specimens. As shown in Table 5.3, the maximum impact force of the specimen H444 obtained from FE simulation is increased by 2.2% comparing with the specimen H453.

### 5.3.4 Internal Energy Response

Figure 5.17 shows the internal energy–time histories of the flat plate, concrete and corrugated plate of the specimen H444 obtained from FE simulation. The internal energy of steel plates and concrete exhibits continuous increase in inertial

**Fig. 5.17** Internal energy–time histories of the specimen H444, reprinted from Lu et al. (2021), copyright 2022, with permission from Elsevier



stage and loading stage, since the deformation of the specimen increases continuously. However, the internal energy of steel plates and concrete exhibits decrease in unloading stage due to the elastic recovery of the specimen. It is noted in Fig. 5.17 that the concrete dissipates the majority of impact energy, accounting for 53.5% of the total impact energy, which can be attributed to the significantly larger volume of concrete as compared to steel plates. 12.4% of impact energy is dissipated by the flat plate with smallest volume, and the evident membrane stretching of the flat plate at local indentation zone is believed to contribute to the majority of impact energy dissipated by the flat plate. With regard to the corrugated plate, it exhibits higher impact energy dissipation (29.2%) as compared to the flat plate, since the yielding zone of the corrugated plate is larger than that of flat plate, as shown in Fig. 5.13. Hence, the corrugated plate can dissipate more impact energy via plastic deformation.

### 5.3.5 FE Parametric Studies

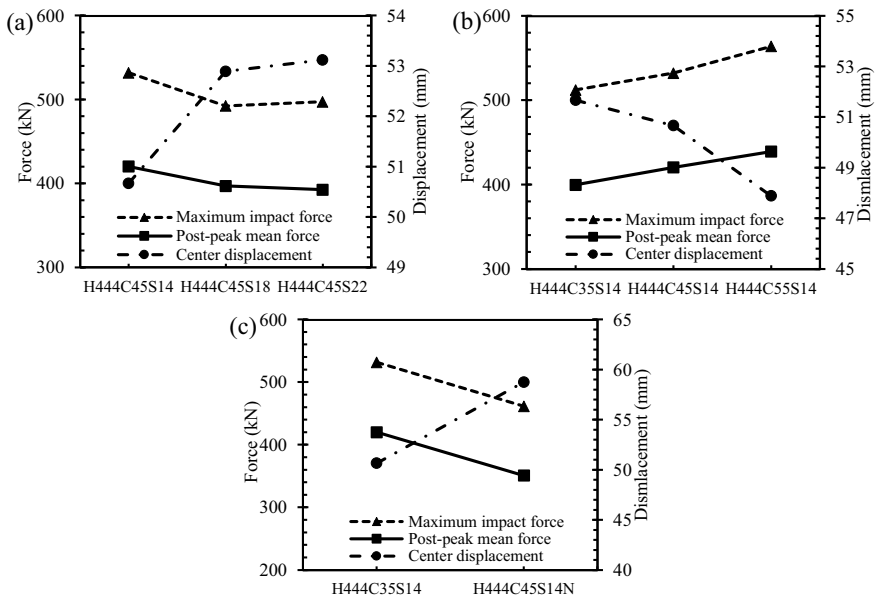
With the validated FE model, parametric studies were conducted to investigate the effects of variant parameters on impact responses of the FS–C–CS panel. The varying parameters included the compressive strength of concrete ( $f_c$ ), spacing of shear connectors along span direction ( $S$ ) as well as end steel plates, as presented in Table 5.5. All the specimens shared the same steel plate thickness (4 mm) and corrugated plate height (40 mm).

Figure 5.18a presents the comparison of the maximum center displacement of flat steel plate ( $D_{\max\text{FE}}$ ), maximum impact force ( $F_{\max\text{FE}}$ ) and post-peak mean force ( $F_{\text{mFE}}$ ) of FS–C–CS panels with variant spacing of shear connectors along span direction. Increasing  $S$  from 140 to 180 mm results in the increase of  $D_{\max\text{FE}}$  by 4.4%, and the decrease of  $F_{\max\text{FE}}$  and  $F_{\text{mFE}}$  by 7.4% and 5.5%, respectively. This is because of the weakened composite action between the steel plates and concrete core, which results in the reduction of bending resistance and stiffness of the FS–C–CS panel. However, further increasing  $S$  has little effect on the impact responses, since the longitudinal shear force between the steel plates and concrete core is mainly

**Table 5.5** Details and results of FS–C–CS panel in FE parametric studies

Specimen	$f_c/\text{MPa}$	$S/\text{mm}$	End plate
H444C45S14	45.0	140	Yes
H444C45S18	45.0	180	Yes
H444C45S22	45.0	220	Yes
H444C35S14	35.0	140	Yes
H444C55S14	55.0	140	Yes
H444C45S14N	45.0	140	No

Note  $f_c$ —Compressive strength of concrete;  $S$ —Spacing of shear connectors along span direction



**Fig. 5.18** Center displacement, maximum impact force and post-peak mean force of FS–C–CS panels obtained through FE simulations: **a** Variant spacings of shear connectors, **b** Variant compressive strength of concrete, **c** With and without end plates, reprinted from Lu et al. (2021), copyright 2022, with permission from Elsevier

transmitted by the end steel plates when the number of shear connector is too few. In addition, Fig. 5.19a exhibits the comparison of maximum internal energies of steel plates and concrete core of FS–C–CS panels with variant spacing of shear connectors. With an increase in the shear connector spacing, there is an increase in the impact energy dissipation of steel plates induced by more severe plastic deformation of steel plates. This also results in the decrease of internal energy of concrete core since all the specimens share the same initial impact energy from the drop hammer.

Figure 5.18b shows the effect of compressive strength of concrete ( $f_c$ ) on impact responses of FS–C–CS panels, and the impact resistance is found to be improved by increasing the concrete strength. The  $D_{\max\text{FE}}$  is reduced by 1.9%, and  $F_{\max\text{FE}}$  and  $F_{m\text{FE}}$  are increased by 3.9% and 5.2%, respectively, via increasing  $f_c$  from 35 to 45 MPa. In addition, further increasing  $f_c$  from 45 to 55 MPa results in the reduction of  $D_{\max\text{FE}}$  by 5.5%, and the corresponding increases of  $F_{\max\text{FE}}$  and  $F_{m\text{FE}}$  are 6.0% and 4.5%, respectively. This is due to the increase of bending resistance and stiffness of the FS–C–CS panel by increasing  $f_c$ . Figure 5.19b compares the maximum internal energies of variant parts of FS–C–CS panels with different  $f_c$ . The internal energy of concrete core is found to be improved by increasing  $f_c$  from 35 to 45 MPa since the concrete with higher concrete strength could dissipate more impact energy. However, further increasing  $f_c$  may result in the reduction of internal energy of concrete core

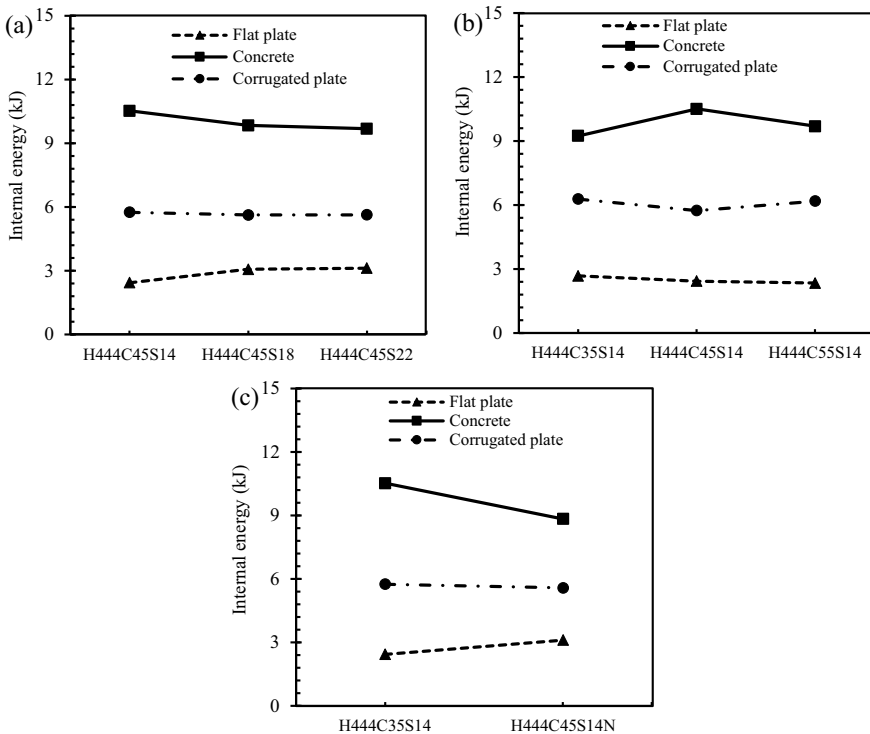


**Fig. 5.19** Internal energy of variant parts of FS–C–CS panels obtained through FE simulations: **a** Variant spacing of shear connectors, **b** Variant compressive strength of concrete, **c** With and without end plates, reprinted from Lu et al. (2021), copyright 2022, with permission from Elsevier

owing to the reduced deformation of the FS–C–CS panel, and thus leading to lower plastic deformation and damage of the concrete core.

The effect of employing end plates on the impact responses of the FS–C–CS panel is presented in Fig. 5.18c, which shows that the  $D_{\max\text{FE}}$  of the FS–C–CS panel end plates is reduced by 16.0% as compared to the FS–C–CS panel without end plates. Moreover, the  $F_{\max\text{FE}}$  and  $F_{m\text{FE}}$  are increased by 13.2% and 16.5%, respectively. This indicates that employing the end plates can significantly improve the composite action between steel plates and concrete core, and thus improving the bending resistance and stiffness of FS–C–CS panel. In addition, the significant slippage (with maximum slippage value of 7.9 mm) between the corrugated plate and concrete core of specimen H444C45S14N without end plates can be observed in Fig. 5.20, which indicates that specimen H444C45S14N is not a fully-composited sandwich panel, and employing the end plates can prevent the slippage between steel plates and concrete core and improve the impact resistance of the FS–C–CS panel. Moreover, the steel plates of the FS–C–CS panel without end plates are found to dissipate more impact energy via plastic deformation, as shown in Fig. 5.19c, owing

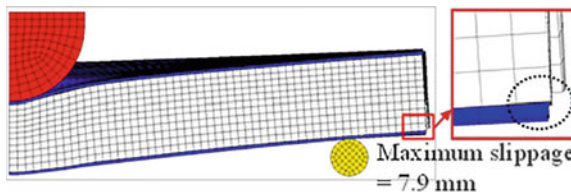


**Fig. 5.20** Slippage between the corrugated plate and concrete core of specimen H444C45S14N, reprinted from Lu et al. (2021), copyright 2022, with permission from Elsevier

to the significant increased deformation of the FS–C–CS panel. Meanwhile, there is also a reduction in the impact energy dissipation of concrete core for the FS–C–CS panel without end plates owing to the weakened composite action.

## 5.4 Summary

The impact responses of FS–C–CS panels were studied through drop-weight impact tests and FE simulation. Moreover, the effects of corrugated steel plate height and steel plate thickness on the impact behaviors of FS–C–CS panels were analyzed. The conclusions from this study were summarized as below:

- (1) The global flexural deformation was observed for the FS–C–CS panel subjected to impact load. Meanwhile, the panel also exhibited local indentation at the impact zone.
- (2) Based on the impact force and displacement responses of the FS–C–CS panel subjected to impact load, the impact process could be divided into three stages, including inertial stage, loading stage and unloading stage.
- (3) The deformation of the FS–C–CS panel under impact load was found to be reduced as compared to the traditional SCS panel with two flat faceplates. In addition, the FS–C–CS panel also exhibited an increase in maximum impact force and post-peak mean force. The maximum deformation of the FS–C–CS panel under impact load was found to be reduced by increasing corrugated plate height and thickness.
- (4) Decreasing the spacing of shear connectors, increasing the compressive strength of concrete and employing end plates could enhance impact resistance of the FS–C–CS panel in terms of smaller maximum deformation as well as higher maximum impact force and post-peak mean force.
- (5) The FE models of FS–C–CS panels under impact load were established and validated against the impact test results. The FE results revealed that concrete core of the FS–C–CS panel absorbed the majority of impact energy, followed by the corrugated plate and flat plate. The end plates were found to be effective in restraining the expansion of concrete and enhancing the composite action of the panel.

## References

- Abramowicz W, Jones N (1986) Dynamic progressive buckling of circular and square tubes. *Int J Impact Eng* 4:243–270
- Do TV, Pham TM, Hao H (2019) Impact force profile and failure classification of reinforced concrete bridge columns against vehicle impact. *Eng Struct* 183:443–458
- Feng J, Li W, Ding C et al (2020) Numerical and analytical investigations on projectile perforation on steel-concrete-steel sandwich panels. *Results Eng* 8:100164
- Guo Q, Zhao W (2019) Displacement response analysis of steel-concrete composite panels subjected to impact loadings. *Int J Impact Eng* 131:272–281
- Hallquist JO (2013) LS-DYNA keyword user's manual. Livermore Software Technology Corporation (LSTC). Livermore, California
- Huang Z, Liew JYR (2015) Nonlinear finite element modelling and parametric study of curved steel-concrete-steel double skin composite panels infilled with ultra-lightweight cement composite. *Constr Build Mater* 95:922–938
- Huang Z, Liew JYR (2016) Experimental and analytical studies of curved steel-concrete-steel sandwich panels under patch loads. *Mater Des* 93:104–117
- Kang KW (2012) Blast resistance of steel-concrete composite structures. Dissertation, National University of Singapore
- Kumar V, Iqbal MA, Mittal AK (2017) Energy absorption capacity of prestressed and reinforced concrete slabs subjected to multiple impacts. *Procedia Struct Integr* 6:11–18
- Lee S, Kim C, Yu Y et al (2021) Effect of reinforcing steel on the impact resistance of reinforced concrete panel subjected to hard-projectile impact. *Int J Impact Eng* 148:103762
- Li Z, Chen L, Fang Q et al (2019) Experimental and numerical study on CFRP strip strengthened clay brick masonry walls subjected to vented gas explosions. *Int J Impact Eng* 129:66–79
- Liew JYR, Sohel KMA, Koh CG (2009) Impact tests on steel-concrete-steel sandwich beams with lightweight concrete core. *Eng Struct* 31(9):2045–2059
- Lu J, Wang Y, Zhai X (2021) Response of flat steel-concrete-corrugated steel sandwich panel under drop-weight impact load by a hemi-spherical head. *J Build Eng* 44:102890
- Mehreganian N, Fallah AS, Louca LA (2019) Plastic dynamic response of simply supported thick square plates subject to localised blast loading. *Int J Impact Eng* 126:85–100
- Micallef K, Fallah AS, Pope DJ et al (2012) The dynamic performance of simply-supported rigid-plastic circular steel plates subjected to localised blast loading. *Int J Mech Sci* 65:177–191
- Ning J, Meng F, Ma T et al (2020) Failure analysis of reinforced concrete slab under impact loading using a novel numerical method. *Int J Impact Eng* 144:103647
- Oucif C, Kalyana Rama JS, Shankar Ram K et al (2020) Damage modeling of ballistic penetration and impact behavior of concrete panel under low and high velocities. *Def Technol* 17:202–211
- Oucif C, Mauludin LM (2019) Numerical modeling of high velocity impact applied to reinforced concrete panel. *Undergr Space* 4(1):1–9
- Othman H, Marzouk H (2016) An experimental investigation on the effect of steel reinforcement on impact response of reinforced concrete plates. *Int J Impact Eng* 88:12–21
- Remennikov AM, Kong SY (2012) Numerical simulation and validation of impact response of axially-restrained steel-concrete-steel sandwich panels. *Compos Struct* 94(12):3546–3555
- Remennikov AM, Kong SY, Uy B (2013) The response of axially restrained non-composite steel-concrete-steel sandwich panels due to large impact loading. *Eng Struct* 49:806–818
- Sadiq M, Xiu Yun Z, Rong P (2014) Simulation analysis of impact tests of steel plate reinforced concrete and reinforced concrete slabs against aircraft impact and its validation with experimental results. *Nucl Eng Des* 273:653–667
- Simo JC, Ju JW (1987) Strain- and stress-based continuum damage models—I. Formulation. *Int J Solids Struct* 23(7):821–840
- Sohel KMA, Al-Jabri K, Al Abri AHS (2020) Behavior and design of reinforced concrete building columns subjected to low-velocity car impact. *Structures* 26:601–616

- Sohel KMA, Liew JYR (2011) Steel–Concrete–Steel sandwich slabs with lightweight core — Static performance. Eng Struct 33(3):981–992
- Sohel KMA, Liew JYR (2014) Behavior of steel–concrete–steel sandwich slabs subject to impact load. J Constr Steel Res 100:163–175
- Sohel KMA, Liew JYR, Koh CG (2015) Numerical modelling of lightweight Steel-Concrete-Steel sandwich composite beams subjected to impact. Thin-Walled Struct 94:135–146
- Sohel KMA, Liew JYR, Yan JB et al (2012) Behavior of Steel–Concrete–Steel sandwich structures with lightweight cement composite and novel shear connectors. Compos Struct 94(12):3500–3509
- Wang Y, Liew JYR, Lee SC (2015a) Experimental and numerical studies of non-composite Steel–Concrete–Steel sandwich panels under impulsive loading. Mater Des 81:104–112
- Wang Y, Liew JYR, Lee SC (2015b) Theoretical models for axially restrained steel-concrete-steel sandwich panels under blast loading. Int J Impact Eng 76:221–231
- Wang Y, Liew JYR, Lee SC (2016a) Ultimate strength of steel-concrete-steel sandwich panels under lateral pressure loading. Eng Struct 115:96–106
- Wang Y, Zhai X, Lee SC et al (2016b) Responses of curved steel-concrete-steel sandwich shells subjected to blast loading. Thin-Walled Struct 108:185–192
- Xu X, Ma T, Ning J (2019) Failure analytical model of reinforced concrete slab under impact loading. Constr Build Mater 223:679–691
- Yan JB, Liew JYR (2016) Design and behavior of steel–concrete–steel sandwich plates subject to concentrated loads. Compos Struct 150:139–152
- Yan JB, Qian X, Liew JYR et al (2016a) Damage plasticity based numerical analysis on steel–concrete–steel sandwich shells used in the Arctic offshore structure. Eng Struct 117:542–559
- Yan JB, Wang J, Liew JYR et al (2016b) Ultimate strength behaviour of steel–concrete–steel sandwich plate under concentrated loads. Ocean Eng 118:41–57
- Yan JB, Zhang W, Liew JYR et al (2016c) Numerical studies on shear resistance of headed stud connectors in different concretes under Arctic low temperature. Mater Des 112:184–196
- Yan C, Wang Y, Zhai X et al (2019) Experimental study on curved steel-concrete-steel sandwich shells under concentrated load by a hemi-spherical head. Thin-Walled Struct 137:117–128
- Yan C, Wang Y, Zhai X (2020a) Low velocity impact performance of curved steel-concrete-steel sandwich shells with bolt connectors. Thin-Walled Struct 150:106672
- Yan C, Wang Y, Zhai X et al (2020b) Strength assessment of curved steel-concrete-steel sandwich shells with bolt connectors under concentrated load. Eng Struct 212:110465
- Zineddin M, Krauthammer T (2007) Dynamic response and behavior of reinforced concrete slabs under impact loading. Int J Impact Eng 34(9):1517–1534
- Zhu H, Khanna SK (2016) Dynamic response of a novel laminated glass panel using a transparent glass fiber-reinforced composite interlayer under blast loading. Int J Impact Eng 89:14–24

# Chapter 6

## Stiffener-Enhanced Steel-Concrete-Steel Sandwich Beam and Panel Under Impact



### 6.1 Introduction

Steel-concrete-steel (SCS) sandwich structure is composed of two external steel plates and a concrete core. The mechanical shear connectors are usually employed to bond the steel plates to concrete core and provide longitudinal and transverse shear resistance as well as prevent separation between the external steel plates and concrete core. The SCS sandwich structures were found to outperform traditional reinforced concrete structures in terms of superior strength, ductility and spalling protection (Wang et al. 2016), which promoted its application in resisting potential impact load. The mechanical shear connector was proven to be of significance in ensuring structural integrity and improving impact resistance of the SCS sandwich structure (Liew et al. 2009). Hence, several types of shear connectors have been developed in recent decades, including headed shear stud (Oduyemi and Wright 1989), Bi-steel (Foundoukos 2005), angle shear connector (Guo et al. 2020), interlocked J-hook connector (Liew and Sohel 2009), bolt connector (Yan et al. 2020a) and enhanced C-channel connector (Yan et al. 2020c, d). As illustrated in Fig. 6.1, a new SCS sandwich structure enhanced with stiffeners in the tension plate, namely stiffener-enhanced SCS (SESCS) sandwich structure, was proposed to improve the impact resistance of the SCS sandwich structure with traditional bolt connectors, and its impact behavior was studied and presented in this chapter.

Owing to the desirable ductility and strength of the SCS sandwich structure, it was widely employed to resist variant loads, including static, impact and blast loads (Wang et al. 2016; Nie et al. 2014; Sohel and Liew 2014; Liew et al. 2015). The interfacial bonding strength, which is usually achieved via shear connectors and cohesive material, is of significance for bonding the concrete core to faceplates and assuring the composite action of SCS sandwich structures. In the past, headed studs were usually employed to be welded to the two faceplates for preventing separation and longitudinal slip between faceplates and concrete core (Thang et al. 2016; Dogan and Roberts 2012; Subedi and Coyle 2002) owing to its low costing and easy fabrication. However, the headed studs were found to be weak in preventing tensile

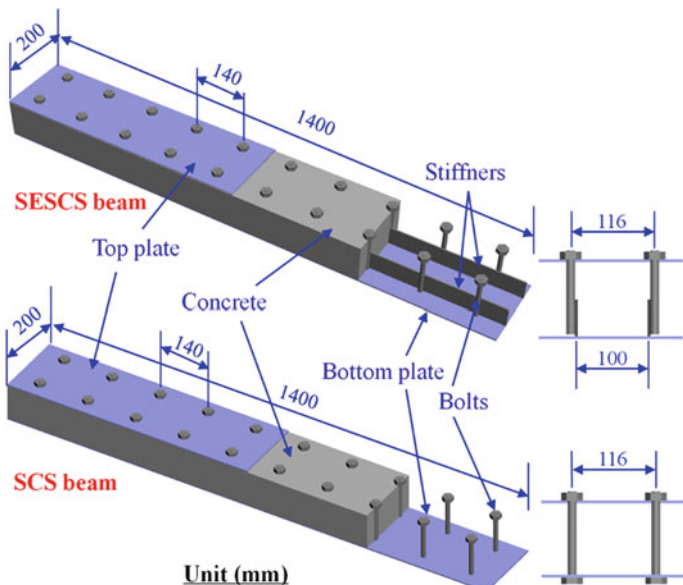


**Fig. 6.1** General illustration of SESCS and SCS sandwich beams, reprinted from Wang et al. (2021), copyright 2022, with permission from Elsevier

separation of faceplates (Liew et al. 2009), since they were embedded into the concrete core separately, and the tensile force was transferred through the concrete core. In addition, steel angles could also be welded to the two faceplates of SCS sandwich structures to provide longitudinal and transverse shear resistance (Shariati et al. 2012, 2013, 2016). Similar to the headed shear studs, the separation between faceplates and concrete core could be observed owing to the shallowly embedding depth of steel angles (Yan et al. 2015). In order to improve the structural integrity of the SCS sandwich structure and prevent separation of faceplates, several “through-through” types of shear connectors have been proposed. Xie et al. (2007) developed a friction-welded shear connector, which allowed straight steel bar connectors being connected to the two faceplates via friction welding (Xie et al. 2007; Clubley et al. 2003). Hence, the tensile separation of faceplates could be resisted via developing tensile force in the steel bar connectors. Bolts could be another type of shear connectors with desirable bonding strength and easy fabrication (Yan et al. 2020b). Recently, the interlocked J-hook connectors were developed by Liew and Sohel (2009), and they were found to be an effective bonding method for SCS sandwich structures. The combination of headed shear studs and tie bars were also employed for SCS sandwich slabs to yield desirable longitudinal and transverse shear resistance (Wang et al. 2020). More recently, an enhanced C-channel connector was developed by Yan et al. (2020a, b, c, d), and the strong tension separation resistance of faceplates from concrete core and faceplate-concrete interfacial shear resistance could be achieved when using the novel enhanced C-channel connectors (Yan et al. 2020c).

Most of the previous studies have been focused on the behaviors of SCS sandwich structures subjected to static or quasi-static loading. Few studies have been focused on the impact responses of SCS sandwich structures. Experimental studies were conducted by Sohel et al. (2003) to investigate the impact behaviors of SCS sandwich beams with angle connectors, and tension separation of faceplates were observed for most of the test specimens owing to the weak tension separation resistance of angle connectors. The J-hook connectors were proposed for enhancing the tension separation resistance of faceplates, and the improved impact resistant performance of SCS sandwich structures with J-hook connectors could be observed (Liew et al. 2009, 2015; Sohel and Liew 2014). It was also found by Liew et al. (2009) that the composite action of SCS sandwich beams could be enhanced when fiber reinforced concrete was employed for the core material. By employing the experimental, numerical and analytical approaches, the dynamic response behaviors of SCS sandwich beams with J-hook connectors were studied (Liew et al. 2009, 2015), and the developed analytical model was found to be accurate in predicting the impact force and displacement responses of the SCS sandwich beams (Liew et al. 2009). With regard to the impact behaviors of axially-restrained SCS sandwich panels without shear connectors, the highly ductile response could be observed with initial flexural response and following tensile membrane stretching of faceplates (Remennikov and Kong 2012; Remennikov et al. 2013). The enhanced blast resistant performance of axially-restrained non-composite SCS sandwich panels via developing tensile membrane stretching were also demonstrated by Wang et al. (2015a). The SCS sandwich structures could be subjected to the combination of axial compressive pre-load and lateral impact load when they were employed as walls and meanwhile experienced an accidental collision. Experimental studies were conducted on the impact responses of SCS sandwich panels with axial compressive pre-load. The combination of local indentation and global flexure was observed (Zhao and Guo 2018; Zhao et al. 2018). In addition, an analytical model was also developed for predicting the impact-induced displacement response of the SCS sandwich panel (Guo and Zhao 2019a, b). On employing bolt connectors, the impact responses of curved SCS sandwich shells were studied by Yan et al. (2020a, b, c, d). The local deformation was found to be dominated, and the bolt connectors have shown a high tension separation resistance of faceplates.

In this chapter, a new SESCS sandwich structure was proposed to resist impact loading. Drop-weight impact tests on SESCS sandwich beams and panels were conducted to reveal their behaviors under low-velocity impact loading. In addition, the numerical studies were also conducted to further reveal the impact responses of SESCS sandwich structures. An analytical model was developed for predicting the displacement response of the SESCS sandwich beam under impact loading.

## 6.2 SESCS Sandwich Beam Under Impact

### 6.2.1 Experimental Study

#### 6.2.1.1 Specimens

The SESCS sandwich beams designed for the drop-weight impact tests are shown in Fig. 6.1. The two stiffeners were welded to the tension plate (bottom plate) of the SCS sandwich beam first (Fig. 6.2b). Subsequently, one end of the bolt was welded to the stiffener (Fig. 6.2b) with the other being fastened to the compression plate (top plate) through nuts, as shown in Fig. 6.2c. Finally, concrete casting was implemented (Fig. 6.2d), and the specimens were curing for at least 28 days before test. There were seven SCS sandwich beams being fabricated for the impact tests, and all the specimens shared the same length and width of 1400 and 200 mm, respectively. The 12 mm-diameter bolts were employed for all the specimens with spacing of 140 mm. The stiffeners of all the SESCS sandwich beams shared the same dimension of  $1400 \times 50 \times 3.52$  mm. There were six SESCS sandwich beams being designed, and the variant parameters included faceplate thickness, concrete core thickness and impact velocity. In addition, one SCS sandwich beam with traditional bolt connectors was also fabricated for comparison and confirming the enhanced impact resistance of the SESCS sandwich beam. As shown in Fig. 6.1, the two

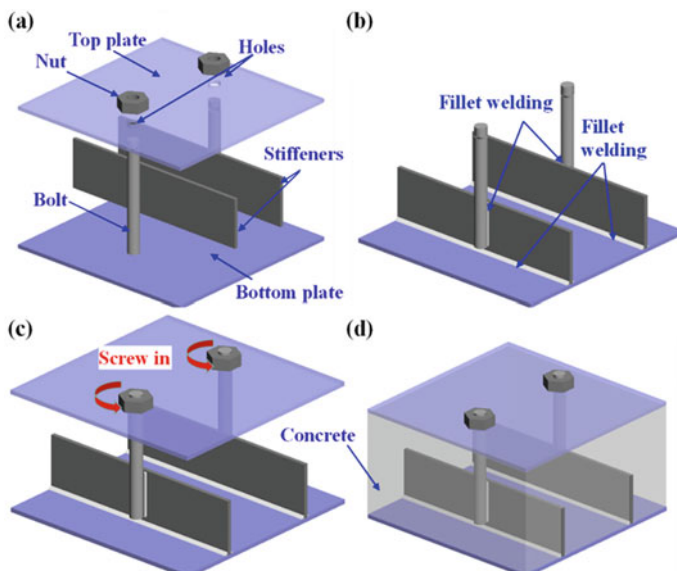


**Fig. 6.2** Fabrication process of the SESCS sandwich beam: **a** Components, **b** Welding stiffener and bolt, **c** Assembling two plates by bolt, **d** Concrete casting, reprinted from Wang et al. (2021), copyright 2022, with permission from Elsevier

**Table 6.1** Summary of test specimens for SESCS sandwich beam (unit: mm)

Specimen	$t_c$	$h_c$	$t_b$	$H$	$V$ (m/s)
Bs4-100	3.52	100	3.52	1200	4.62
Bs3-100	2.84	100	2.84	1200	4.68
Bs5-100	4.46	100	4.46	1200	4.72
Bs4-120	3.52	120	3.52	1200	4.66
Bs4-150	3.52	150	3.52	1200	4.65
Bb4-100	3.52	100	3.52	1200	4.68
Bs4-100 V	3.52	100	3.52	1400	5.09

Note  $t_c$ ,  $h_c$ , and  $t_b$ —Thicknesses of top plate, concrete core and bottom plate;  $H$ ,  $V$ —Drop height and velocity of the hammer; Bs and Bb stand for the SCS sandwich beam with stiffeners in tension plate and bolt connectors, respectively

**Table 6.2** Material parameters of mild steel, bolt and concrete

Mild steel	$E_s$ (GPa)	$f_y$ (MPa)	$f_u$ (MPa)
$t_p = 2.84$ mm	202	323	455
$t_p = 3.52$ mm	205	286	404
$t_p = 4.46$ mm	210	274	377
Bolt	200	640	800
Concrete	$E_c$ (GPa)	$f_c$ (MPa)	$\mu$
—	29	45	0.211

Note  $E_s$ ,  $f_y$ ,  $f_u$ —Young's modulus, yield stress and ultimate stress of steel;  $t_p$ —steel plate thickness;  $E_c$ ,  $f_c$ ,  $\mu$ —Elastic modulus, compressive stress and Poisson's ratio of concrete

faceplates were punched with holes for the bolts being through the faceplates, and the nuts were employed for fastening the two faceplates. Finally, concrete casting was implemented. The bolt employed for the SCS sandwich beam shared the same diameter and strength with the SESCS sandwich beam. The information of the test specimens are given in Table 6.1. The mild steel was employed for the faceplates and stiffeners. The concrete core was normal weight concrete with compressive strength of 45 MPa. The material properties of mild steel, bolts and concrete employed for fabricating the sandwich beams are presented in Table 6.2.

### 6.2.1.2 Test Setup and Instrumentation

An instrumented drop-weight impact test machine was employed to conduct the impact tests on the SCS sandwich beams, and Fig. 6.3 presents the test setup and instrumentation. As illustrated in Fig. 6.3b, the SCS sandwich beam was simply supported on the two round bars with clear span to be 1200 mm. The drop weight of all the test specimens is 400 kg, and the drop heights and measured impact velocities

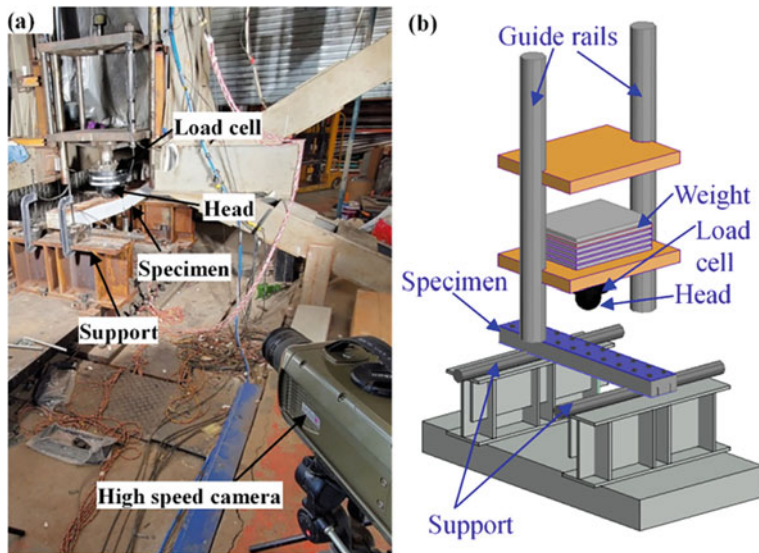


**Fig. 6.3** Test setup and instrumentation: **a** photograph and **b** schematic view, reprinted from Wang et al. (2021), copyright 2022, with permission from Elsevier

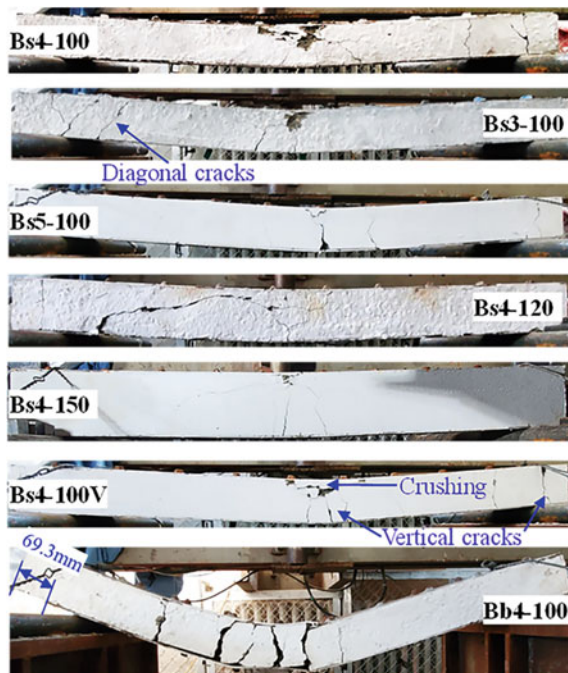
are given in Table 6.1. The hemispherical hammer head with the diameter of 200 mm was employed for all the test specimens. To measure the impact force, a dynamic load cell with 2000-kN-loading capacity was embedded in the hammer head. Three potentiometers were placed below the specimen to record the deflections, with one at the mid-span and the other two at the quarter-spans. All the readings from the load cell and potentiometers were recorded by a data logger with the sampling rate of 100 kHz. In addition to the measurements of force and displacement, a high-speed camera was utilized for capturing movement of the hammer and deformation of the specimen with the speed of 3000 frames per second.

### 6.2.1.3 Test Results and Discussions

#### Failure Modes

The failure modes of the test specimens are presented in Fig. 6.4, and typical flexural failure mode is observed for all the seven SCS sandwich beams with plastic hinges at their mid-spans. The large impact-induced sagging moment at the mid-span results in the appearance of vertical cracks whose widths exhibit largest value near the bottom surface and gradually reduces when they approaches the neutral axis. In addition, sagging moment also causes concrete crushing at compression zone for the six SESCS sandwich beams. The observed cracking patterns of the SESCS sandwich beam are consistent with those of an under-reinforced concrete beam with typical

**Fig. 6.4** Failure modes of SESCS sandwich beams, reprinted from Wang et al. (2021), copyright 2022, with permission from Elsevier



flexural failure. There is no buckling and separation of the top plate being observed for the six SESCS sandwich beams, which demonstrates the effectiveness of employing bolts for fastening the top plate to concrete core. Besides the concrete crushing and cracking observed near the mid-span of the beam, the vertical and diagonal cracks are also observed for the test beams near only one end of the beam, which results in the slippage between the bottom plate and concrete core occurred at these ends with cracks. It is observed after the impact test that all the beams (except for Bs4-150) exhibit some slippages between the bottom plate and concrete core at only one end of the beam, and the values of slippage are presented in Table 6.3. It is noted that increasing bottom plate thickness and reducing concrete core thickness results in larger value of slippage. In addition, the comparison of slippages of Bs4-100 and Bs4-100 V reveals that larger deformation also causes larger value of slippage. One SCS sandwich beam with bolt connectors (Bb4-100) was also tested under the same impact load as the SESCS sandwich beam. However, it failed to resist the impact load and experienced very large deformation (i.e., the mid-span displacement is greater than 135.7 mm). All the bolts in the left half-span of Bb4-100 exhibited shear failure after impact test, which resulted in large slippage between the bottom plate and concrete core in the left half-span with slippage value exceeding 69.3 mm. The comparison of Bs4-100 and Bb4-100 reveals that the impact resistance of the SCS sandwich beam can be significantly improved by employing stiffeners in the tension plate. It should be mentioned that a temporary rigid support was placed below the beam before the test to prevent falling of the beam from the two round bar supports and protect the

**Table 6.3** Summary of test results for SESCS sandwich beam

Specimen	$F_{\max}$ (kN)	$F_m$ (kN)	$D_{mm}$ (mm)	$D_{qm1}$ (mm)	$D_{qm2}$ (mm)	$S_s$ (mm)
Bs4-100	181.12	103.63	38.53	23.89	20.03	5.29
Bs3-100	178.36	96.12	42.68	22.37	23.81	5.15
Bs5-100	175.31	103.92	38.92	26.49	19.59	9.23
Bs4-120	204.91	131.49	29.99	15.25	17.27	4.17
Bs4-150	262.14	206.34	18.27	9.69	9.42	0
Bs4-100 V	182.00	102.14	44.69	26.93	24.04	7.00
Bb4-100	–	–	> 135.73	–	–	> 69.3

Note  $F_{\max}$ ,  $F_m$ —Peak impact force and post-peak mean force;  $D_{mm}$ ,  $D_{qm1}$ ,  $D_{qm2}$ —Maximum values of mid-span and quarter-span displacement;  $S_s$ —Value of slippage

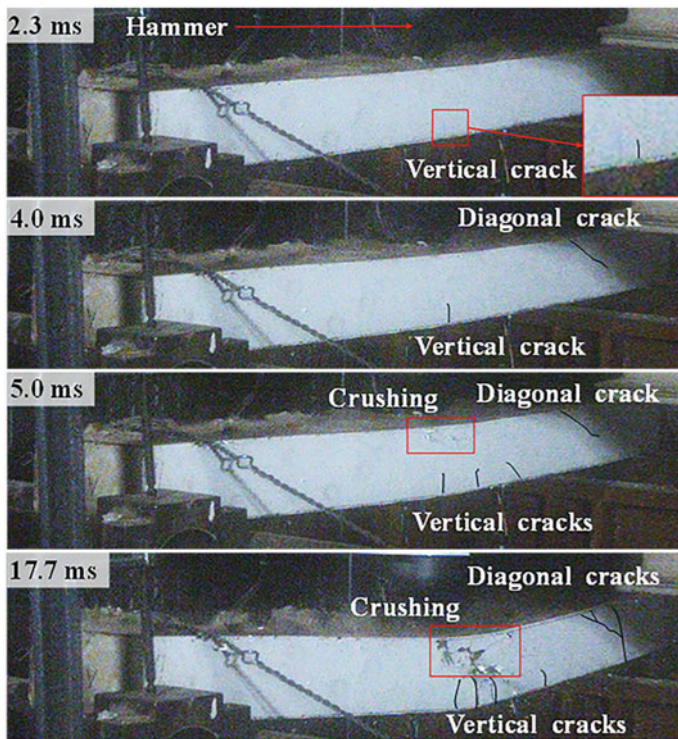
instrumentations. The specimen Bb4-100 was found to touch the temporary rigid support during the impact test. Hence, the measurements for Bb4-100 are not the real values, and the real ones should be larger than the measurements.

Figure 6.5 presents the impact process of the specimen Bs4-100 V obtained from the high-speed camera, and the failure mode and cracking evolution of the SESCS sandwich beam can be observed. The first vertical crack of the concrete core occurs at 2.3 ms near the mid-span. With continuous impact of the hammer, the shear force-induced diagonal crack near the support occurs at 4.0 ms. Subsequently, the crushing of concrete at compression zone occurs at 5.0 ms. The sequential occurrence of vertical crack at tension zone and concrete crushing at compression zone is consistent with the cracking patterns of an under-reinforced concrete beam with typical flexural failure. This also indicates that the crushing of concrete at compression zone is mainly caused by the sagging moment. With further impact of the hammer, the concrete crushing zone exhibits continuous increase in area, and the vertical and diagonal cracks also exhibit increase in their widths and numbers before the beam reaching its maximum deflection at 17.7 ms.

The normalized deformed shapes of the SESCS sandwich beams are presented in Fig. 6.6a, b, in which the ratios of  $\delta/\delta_{\max}$  were measured from the top plate and bottom plate, respectively, after the impact test. Herein,  $\delta$  is the measured vertical distance between the measured point and the point of the top (or bottom) plate at the support after the impact tests, and  $\delta_{\max}$  is the maximum value of  $\delta$  along the span direction of the beam. The normalized deformed profiles of all the test SESCS sandwich beams exhibit bi-linear shapes with peak values of  $\delta/\delta_{\max}$  at their mid-spans, which further confirms the flexural deformation modes of the SESCS sandwich beams.

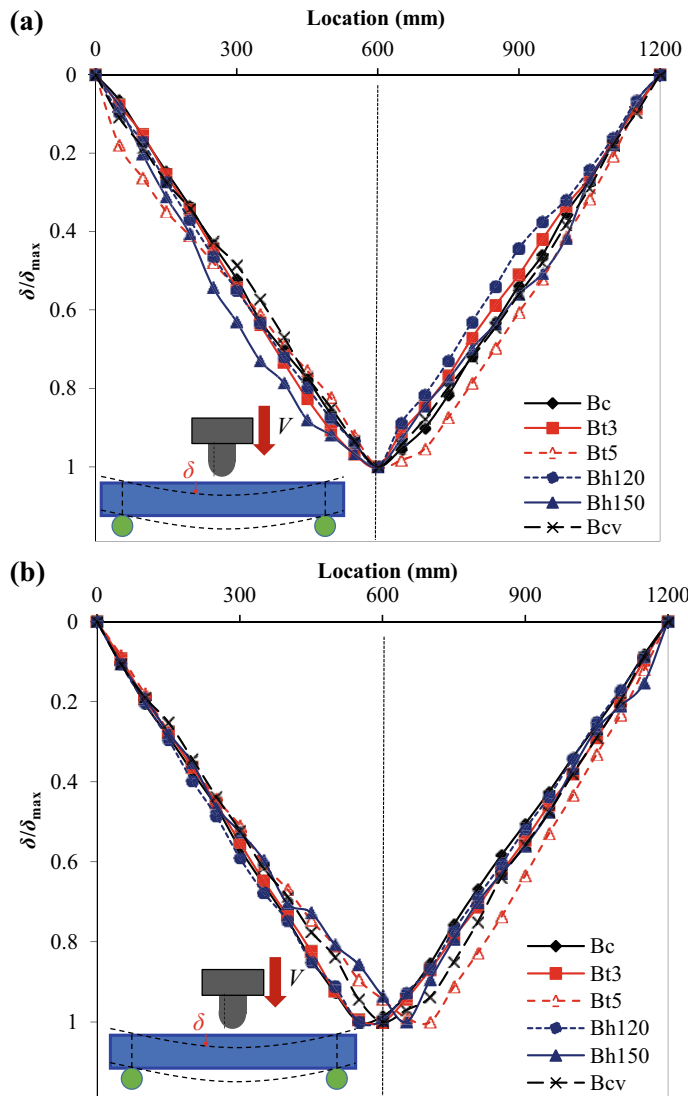
### Load and Displacement Response

Figure 6.7 presents the typical impact force–time curve of the SESCS sandwich beam (Bs4-100), together with its mid-span and hammer displacements versus time curves. Three stages of the SESCS sandwich beam under impact load can be identified based



**Fig. 6.5** Impact process of the specimen Bs4-100 V, reprinted from Wang et al. (2021), copyright 2022, with permission from Elsevier

on the impact force and displacement response histories in Fig. 6.7, including inertial, loading and unloading stages, as observed by other researchers (Zhao and Guo 2018; Yan et al. 2020a, b, c, d). The impact force exhibits rapid and continuous increase to the peak value once the hammer strikes the beam. The first peak impact force, which is generally larger than the resistance of the beam, is induced by inertial effect at the initial impact stage. This peak impact force cannot represent the real load carried by the beam, and its value is governed by many factors, e.g., local contact stiffness, beam mass, drop weight and height (or impact velocity), etc. In addition, the maximum local indentation depth occurs at the inertial stage owing to the large first peak impact force. At inertial stage, the hammer displacement increase faster as compared to mid-span displacement of the beam, and the displacement difference between the two, which can generally represent the local indentation depth, reaches a constant value at the end of inertial stage. This also indicates that the maximum local indentation depth occurs at the inertial stage. In the loading stage, the beam continuously moves downwards, sharing the identical velocity to the drop hammer. Hence, the inertial effect is insignificant, and the impact force can generally represent the real load carried by the beam. The impact force nearly exhibits a constant value with fluctuation



**Fig. 6.6** Normalized deformed shapes of SESCS sandwich beams: **a** Top surface, **b** Bottom surface, reprinted from Wang et al. (2021), copyright 2022, with permission from Elsevier

of the curve in the loading stage. When the beam reaches its maximum displacement, the hammer and beam start to rebound together. It enters unloading stage, and both the hammer and mid-span displacements exhibit continuous decrease. In addition, the impact force also decreases, which can be attributed to reduced contact area between the hammer and beam caused by higher rebound speed of the hammer as compared to the beam. The impact force drops to zero when the hammer completely separates

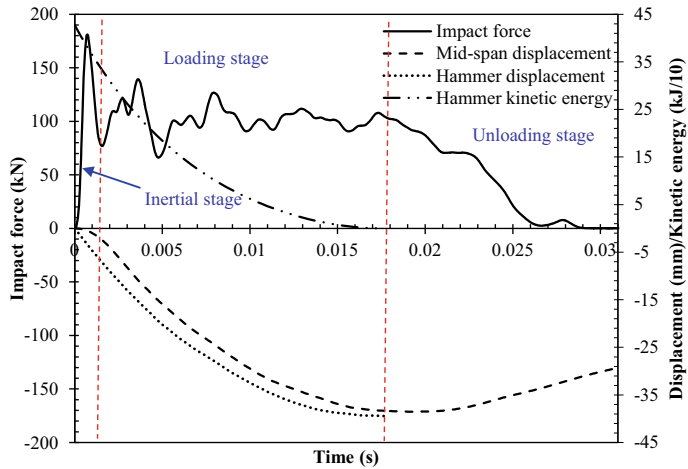
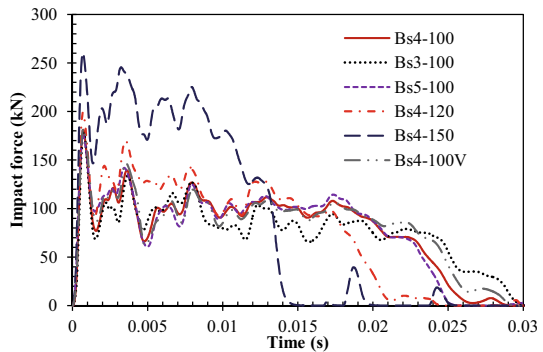


**Fig. 6.7** Typical impact force, kinetic energy and displacement–time histories of SESCS beam, reprinted from Wang et al. (2021), copyright 2022, with permission from Elsevier

**Fig. 6.8** Impact force–time histories of test specimens, reprinted from Wang et al. (2021), copyright 2022, with permission from Elsevier



from the beam. The kinetic energy of the hammer is also presented in Fig. 6.7, and it exhibits continuous decrease once the hammer strikes the beam. Moreover, the monotonic increases of the hammer and mid-span displacements are also observed. The impact energy of the hammer is completely absorbed by the SESCS sandwich beam when the hammer and mid-span displacements reach their maximum values. Moreover, the kinetic energy of the hammer also reduces to zero. It is also noted in Fig. 6.7 that the impact energy absorbed through local indentation of the beam is minimal and only occurs at inertial stage. Hence, the majority of the impact energy is dissipated via global deformation of the SESCS sandwich beam.

Figure 6.8 presents the comparison of impact force–time histories of the SESCS sandwich beams, and all the curves initially exhibit rapid increase to their peak values, followed by the post-peak stable phase and decreasing phase. The load–mid-span displacement curves of the SESCS sandwich beams are plotted in Fig. 6.9, and the

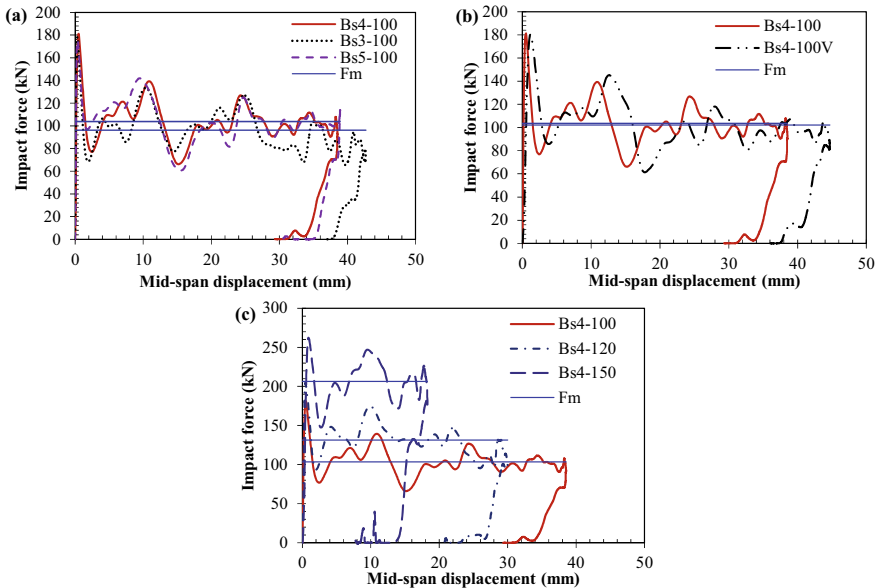


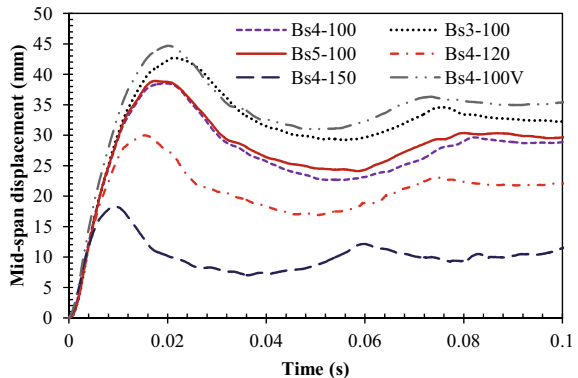
**Fig. 6.9** Impact force–mid-span displacement curves of test specimens: effects of **a** faceplate thickness, **b** impact velocity and **c** concrete thickness, reprinted from Wang et al. (2021), copyright 2022, with permission from Elsevier

effects of faceplate thickness, impact velocity and concrete core thickness on the load–mid-span displacement curves can also be revealed from Fig. 6.9. Further, the post-peak mean force ( $F_m$ ), which is defined in Eq. (6.1) (Wang et al. 2014), is plotted in Fig. 6.9 for comparison.

$$F_m = \frac{\int_{D_o}^{D_{mm}} F dD}{D_{mm} - D_o} \quad (6.1)$$

where  $D_{mm}$  is the maximum mid-span displacement,  $D_o$  is the mid-span displacement corresponding to first peak impact force, and  $F$  is the impact force. Figure 6.9a shows that faceplate thickness has negligible effect on the peak impact force, i.e., the differences of peak impact forces between Bs4-100, Bs3-100 and Bs5-100 are less than 3.3%, as presented in Table 6.3. The similar peak impact forces of these three specimens can be attributed to the fact that these three specimens share similar local contact stiffness, beam mass, drop weight and velocity. With regard to the post-peak mean force which can represent the resistance of the beam, it is increased by 7.8% on increasing faceplate thickness from 2.84 to 3.52 mm, and further increasing faceplate thickness to 4.46 mm has negligible effect on the post-peak mean force owing to lower strength of faceplate and larger slippage being observed for Bs5-100. Figure 6.9b presents the comparison of load–mid-span displacement curves of the

**Fig. 6.10** Mid-span displacement–time histories of test specimens, reprinted from Wang et al. (2021), copyright 2022, with permission from Elsevier



SESCS sandwich beams with different drop heights, and increasing drop height from 1.2 to 1.4 m exhibits little effect on the peak impact force and post-peak mean force. The effect of concrete core thickness on the load–mid-span displacement curves of the SESCS sandwich beams is illustrated in Fig. 6.9c. The peak impact force is increased by 13.1 and 44.7%, respectively, on increasing concrete core thickness from 100 mm to 120 and 150 mm, owing to the increased beam mass and local contact stiffness. In addition, increasing concrete core thickness also results in the corresponding increase of post-peak mean force by 26.9 and 99.1%, respectively, owing to the improved resistance of the beam.

Figure 6.10 presents the mid-span displacement–time curves of the six SESCS sandwich beams. The beams exhibit continuous and rapid increase of deflection to their peak values after struck by the hammer. Subsequently, the mid-span displacements decrease when the hammer and beam start to rebound and move upwards. The following constant value of mid-span displacement (i.e., permanent displacement) can be observed. The comparison of maximum displacements of the beams is presented in Table 6.3. Generally, the maximum deflection of the SESCS sandwich beam is found to decrease with the increase of faceplate thickness. The maximum mid-span displacement of the SESCS sandwich beam is decreased by 9.7% on increasing the faceplate thickness from 2.84 to 3.52 mm owing to the improved resistance of the beam, and further increasing faceplate thickness to 4.46 mm exhibits negligible influence on the maximum displacement. It is also noted in Table 6.3 that increasing concrete core thickness results in evident reduction of maximum deflection of the SESCS sandwich beam owing to the improved resistance, i.e., the maximum mid-span displacement is decreased by 22.2 and 52.6%, respectively, on increasing the concrete core thickness from 100 mm to 120 and 150 mm.

## 6.2.2 Numerical Study

### 6.2.2.1 FE Model Establishment

FE modeling of the SESCS sandwich beam under drop-weight impact loading was conducted by employing the explicit code in LS-DYNA (Hallquist 2006). Figure 6.11 presents a typical half-symmetric FE model of the SESCS sandwich beam. As the measured deformed shapes of the SESCS sandwich beams after the drop-weight impact tests were not exactly symmetrical about their mid-spans, a shift of impact point by 10 mm away from the mid-span was employed in the FE model. The concrete, support and hammer were meshed with eight-node hexahedral elements with reduced integration, and a stiffness-based hourglass control was employed for preventing zero energy modes of the hexahedral element. The top and bottom plates were meshed with Belytschko-Tsay shell elements, and five integration points were chosen along the thickness of the shell element. The stiffeners were meshed with eight-node thick-shell elements, which was convenient for the contact treatment between the stiffeners and concrete. The bolts were meshed with Hughes-Liu beam elements. The element size was determined as 10 mm based on the mesh sensitivity analysis. As illustrated in Fig. 6.12, the impact force and mid-span displacement over time curves obtained from the FE models with current element size (10 mm) and smaller element size (5 mm) are found to be well matched. Hence, the current element size was employed in the following analyses to reduce the computation time. The contacts between two parts in the FE model were simulated via employing the keyword “\*Contact\_Automatic\_Surface\_to\_Surface” in LS-DYNA (Hallquist 2013). The soft constraint-based contact approach was employed for the contacts between the concrete and steel which had different material stiffness parameters. The stiffness-based contact approach was utilized to model the other contacts between two

**Fig. 6.11** Half-symmetric FE model of SESCS sandwich beam, reprinted from Wang et al. (2021), copyright 2022, with permission from Elsevier

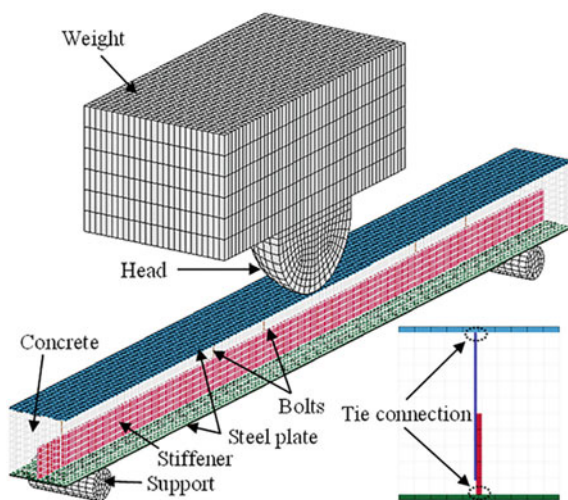
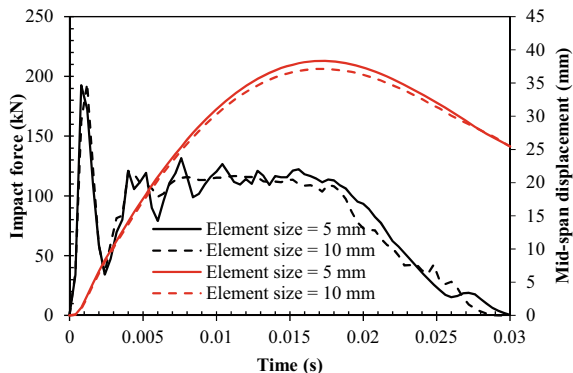


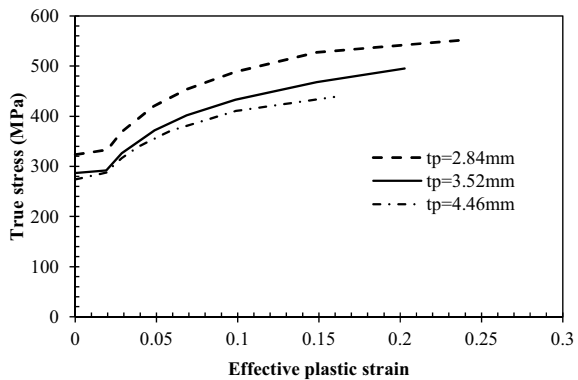
**Fig. 6.12** Mesh sensitivity study of the FE model, reprinted from Wang et al. (2021), copyright 2022, with permission from Elsevier



steel parts. There was no connection failure between the bolts and top plate as well as between the stiffeners and bottom plate being observed during the test. The selected nodes of the bolts and stiffeners were tied to the top and bottom plate, respectively, via keyword “\*Contact\_Tied\_Nodes\_to\_Surface”, as illustrated in Fig. 6.11. The perfect bond behavior between the concrete and bolts was assumed in the FE model, and this approach has been applicable to modeling the SCS sandwich panels and reinforced concrete structures under dynamic loading (Wang et al. 2016; Li et al. 2015; Chen et al. 2015). The nodes at the bottom of the round bar supports were constrained in the translational and rotational directions. The keyword “\*Initial\_Velocity\_Generation” in LS-DYNA was employed to specify an initial impact velocity of the drop hammer which was consistent with the measured impact velocity from the drop-weight impact test. The damping was not considered in the FE model, as it has negligible effect on the maximum displacement of the sandwich structure under impact loading (Liew et al. 2015; Yan et al. 2020a, b, c, d).

Steel material of the SESCS sandwich beam was modeled with the Piecewise Linear Plasticity model with the strain rate effect being considered via employing the Cowper-Symonds model. Figure 6.13 presents the input true stress–effective plastic

**Fig. 6.13** True stress–effective strain curves for FE analyses, reprinted from Wang et al. (2021), copyright 2022, with permission from Elsevier



strain curves of the mild steels obtained from the tensile coupon tests. The flow stress of the mild steel is enhanced by multiplying a factor of  $1 + (\dot{\varepsilon}_{eff}^p/C)^{1/P}$  with the strain rate parameters  $C$  and  $P$  to be defined as  $802\text{ s}^{-1}$  and  $3.585$ , respectively (Abramowicz and Jones 1986). With regard to the modeling of concrete, the Continuous Surface Cap (CSC) model (FHWA 2007a, b) was employed, as it had successful application in modeling concrete material under impact and blast loading (Wang et al. 2016; Yan et al. 2020a). The failure surface, flow rule, damage formulation and strain rate effect treatment of the CSC model were presented by FHWA (2007b). This model is user-friendly, since the default parameters of the CSC model can be generated by inputting mass density and unconfined compressive strength of the concrete.

### 6.2.2.2 FE Results and Discussions

The comparison of failure modes of the SESCS sandwich beam (Bs4-100) obtained from the FE analysis and drop-weight impact test is presented in Fig. 6.14. The flexural failure mode of the SESCS sandwich beam with plastic hinge at the mid-span can be reasonably captured by the established FE model. It can be seen from the damage contour in Fig. 6.14 that the concrete exhibits more severe damage at the mid-span and support where the cracking and crushing of concrete are observed from the test.

Figure 6.15 presents the comparison of impact force-time curves obtained from the impact tests and FE analyses, and the FE models are shown to provide accurate predictions on the impact force responses of the SESCS sandwich beams. The peak impact forces and post-peak mean forces of the SESCS sandwich beams obtained from the FE analyses are compared with those from impact tests, and the comparison is given in Table 6.4. The differences of peak impact forces between the FE-predictions and test results are found to be less than 10%, and the differences of post-peak mean forces are less than 12%. The average FE to test ratios of peak impact force and post-peak mean force are 1.07 and 1.08, respectively, and their

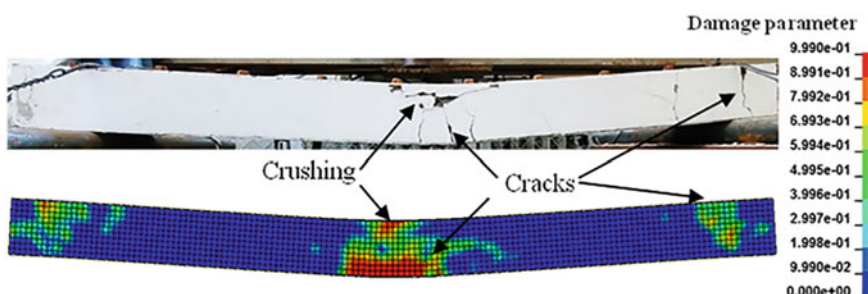


**Fig. 6.14** Comparison of failure modes between FE and test, reprinted from Wang et al. (2021), copyright 2022, with permission from Elsevier

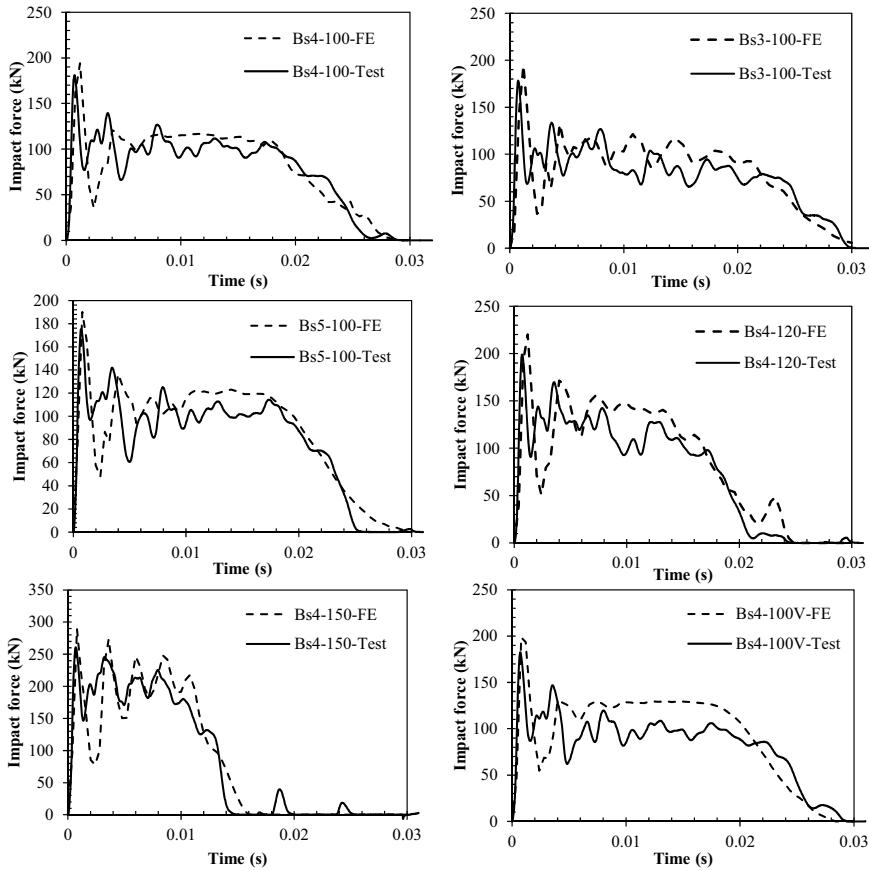


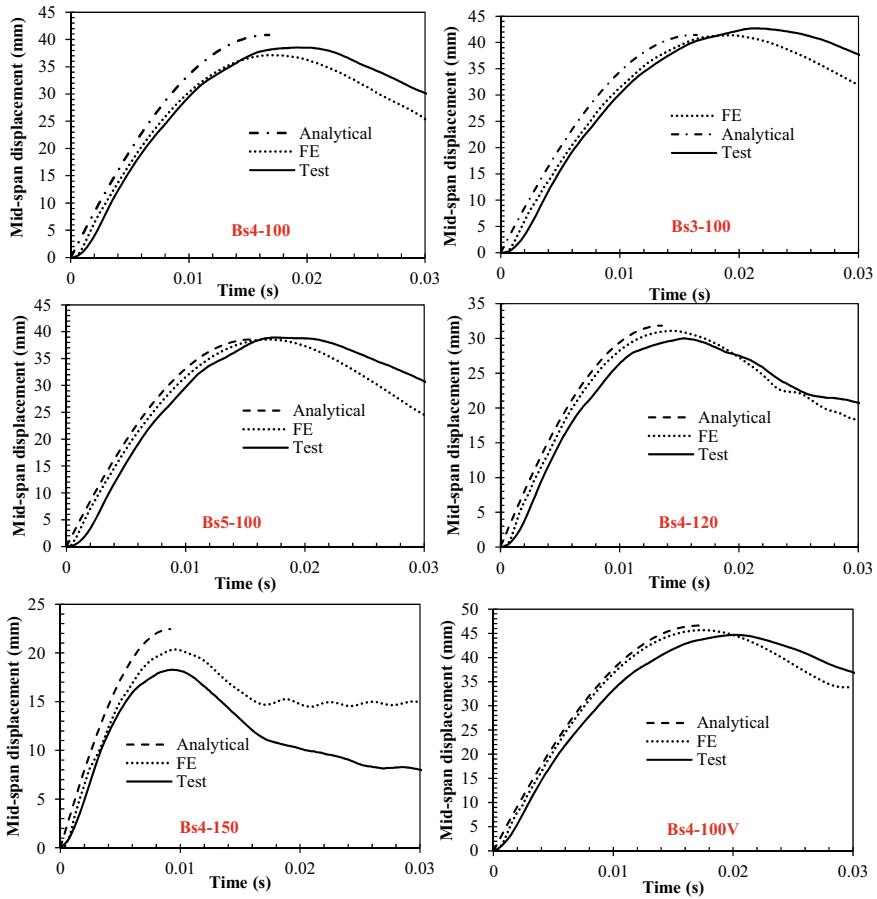
**Fig. 6.15** Comparison of impact force–time histories, reprinted from Wang et al. (2021), copyright 2022, with permission from Elsevier

corresponding coefficients of variation are 0.028 and 0.056, respectively. Figure 6.16 presents the comparison of displacement responses of the SESCS sandwich beams obtained from the FE analyses and impact tests, and good agreement between them can also be observed. Table 6.4 indicates that the differences of maximum mid-span displacements of the SESCS sandwich beams obtained from the FE analyses and impact tests are within 4%, except for the specimen Bs4-150 whose maximum mid-span displacement is over-predicted by 11%. This may be attributed to the absence of adhesive bonding between the concrete and steel plates in the FE model as well as the geometric imperfection of the fabricated specimen. The average FE to test ratio of maximum mid-span displacement is 1.02 with coefficient of variation to be 0.055. The comparisons of FE-predictions and test results in terms of failure mode, impact force and displacement response can demonstrate the accurate predictions provided by the established FE models of the SESCS sandwich beams.

**Table 6.4** Comparison of FE and analytical predictions with test results

Specimen	$F_{maxFE}$ (kN)	$F_{maxFE}/F_{max}$	$F_{mFE}$ (kN)	$F_{mFE}/F_m$	$D_{mmFE}$ (mm)	$D_{mmFE}/D_{mm}$	$D_{mmaA}$ (mm)	$D_{mmaA}/D_{mm}$
Bs4-100	194.09	1.07	113.32	1.09	37.14	0.96	40.81	1.06
Bs3-100	194.88	1.09	107.68	1.12	41.38	0.97	41.45	0.97
Bs5-100	190.00	1.08	113.04	1.09	38.54	0.99	38.56	0.99
Bs4-120	220.00	1.07	146.72	1.12	31.08	1.04	31.83	1.06
Bs4-150	289.25	1.10	198.03	0.96	20.35	1.11	22.44	1.23
Bs4-100 V	185.00	1.02	112.84	1.10	45.64	1.02	46.59	1.04
Average	—	1.07	—	1.08	—	1.02	—	1.06
COV	—	0.028	—	0.056	—	0.055	—	0.086

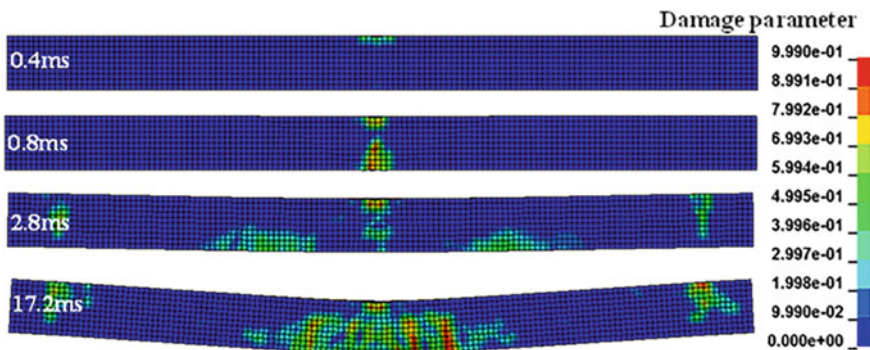
Note The parameters with  $FE$  and  $A$  as the subscript stand for the FE and analytical predictions, respectively



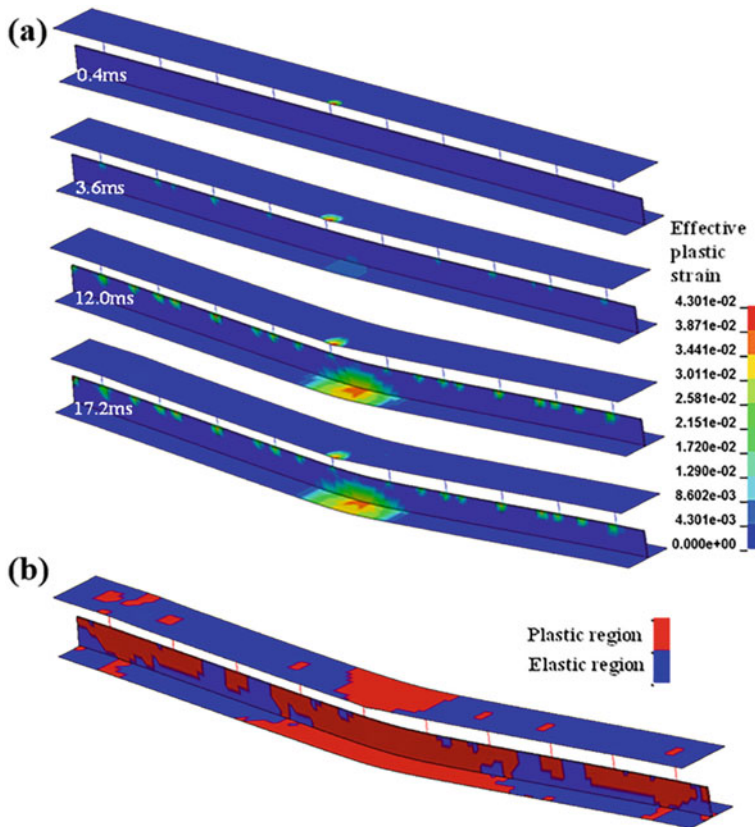
**Fig. 6.16** Comparison of displacement–time histories, reprinted from Wang et al. (2021), copyright 2022, with permission from Elsevier

Figure 6.17 presents the concrete damage evolution of the specimen Bs4-100 during impact. The upper layer of the concrete at the mid-span exhibits immediate local damage once struck by the hammer (see concrete damage contour at 0.4 ms in Fig. 6.17). Subsequently, the lower part of the concrete core at the mid-span also experiences evident damage at 0.8 ms, which is caused by the tensile stress. With further impact by the hammer, the vertical cracking near the support occurs at 2.8 ms after the impact. The concrete damage contour of Bs4-100 at 17.2 ms when its maximum deflection occurs is also presented in Fig. 6.17. The severe damage of concrete is observed at the mid-span with more severe damage located at the bottom surface, which confirms the flexural failure mode of the beam.

Figure 6.18a presents the plastic strain evolutions of the top plate, stiffener and bottom plate. The top plate below the hammer immediately experiences local plastic



**Fig. 6.17** Damage evolution of concrete of Bs4-100 during impact, reprinted from Wang et al. (2021), copyright 2022, with permission from Elsevier



**Fig. 6.18** Plastic strain distributions of steels of Bs4-100: **a** Plastic strain evolution of steel components, **b** Plastic strain distributions of steel components at 17.2 ms, reprinted from Wang et al. (2021), copyright 2022, with permission from Elsevier

deformation at 0.4 ms once the hammer strikes the beam. The local plastic deformation region of the top plate continuously grows with further impact of the hammer (see effective plastic strain contour of the top plate at 3.6 ms in Fig. 6.18a). Subsequently, the plastic deformation also occurs to the bottom plate (at the mid-span) and stiffener (at the mid-span and regions welded with bolts). The plastic deformations of the top plate, stiffener and bottom plate exhibit continuous growing with increasing deflection of the beam (i.e., larger plastic strain values and plastic deformation regions), as can be seen in Fig. 6.18a at time of 12.0 and 17.2 ms. The regions of the top plate, stiffener and bottom plate that experience plastic deformations are clearly presented in Fig. 6.18b. The whole cross-sections of the top plate, stiffener and bottom plate yield at the mid-span of the beam, which indicates the effective enhancement of the stiffener to the bending resistance of the beam. In addition, the plastic deformations of the stiffener are observed at the regions welded with bolts, which is caused by the longitudinal shear forces from the bolts. The effective bonding behavior between the stiffener and bolts plays essential roles on preventing the shear failure of bolts which was observed for the SCS sandwich beam without stiffeners after the drop-weight impact test.

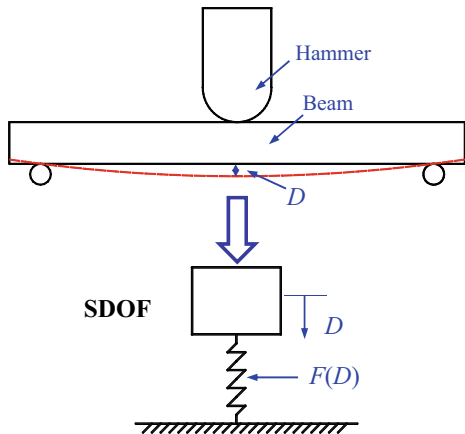
### 6.2.3 Analytical Study

The analytical model for predicting the global displacement–time history of the SESCS sandwich beam is presented in this section. Generally, both local and global deformation of a structural member determines its impact-induced damage level (Wang et al. 2015b). Owing to the insignificant local damage of the SESCS sandwich beam observed from the drop-weight impact test, the damage level of the SESCS sandwich beam can be dominated by its global deformation. Hence, the maximum global deflection of the SESCS sandwich beam can be employed for evaluating its impact-induced damage level, similar to the damage level evaluation of the structural member under blast loading (ASCE 2011). The analytical model presented in this section can be a simple alternative for predicting the damage level of the SESCS sandwich beam under impact loading.

#### 6.2.3.1 Analytical Formulation

It is assumed that the SESCS sandwich beam immediately moves downwards with the velocity being identical to the hammer once it is struck by the hammer. Hence, an equivalent Single-Degree-of-Freedom (SDOF) system can be employed for representing the displacement response of the SESCS sandwich beam under impact loading, as illustrated in Fig. 6.19. This approach has also been successfully applied in predicting the displacement responses of the SCS sandwich beams and panels under low-velocity impact loading (Liew et al. 2009; Guo and Zhao 2019b). The equation of motion of the SDOF system can be written as

**Fig. 6.19** Equivalent SDOF system for SESCS sandwich beam under impact loading, reprinted from Wang et al. (2021), copyright 2022, with permission from Elsevier



$$(m_e + m_h)\ddot{D} + F(D) = 0 \quad (6.2)$$

where  $m_e$  is the equivalent mass of the beam,  $m_h$  is the hammer mass, and  $F(D)$  is the resistance versus displacement relationship of the beam. The equivalent mass of the beam can be given as

$$m_e = k_m m_b \quad (6.3)$$

where  $k_m$  and  $m_b$  are the mass factor and beam mass, respectively. The mass factor is calculated as (Biggs 1964)

$$k_m = \frac{\int_0^L \varphi^2(x) dx}{L} \quad (6.4)$$

where  $L$  is the clear span of the beam, and  $\varphi(x)$  is the shape function and given in Eq. (6.5) for the left half-span ( $x < L/2$ ) (Biggs 1964).

$$\varphi(x) = \begin{cases} \frac{x}{L^3}(3L^2 - 4x^2) & \text{elastic} \\ \frac{2x}{L} & \text{plastic} \end{cases} \quad (6.5)$$

With regard to the resistance–displacement function of the beam under concentrated load at the mid-span,  $F(D)$ , the flexural resistance and deflection are calculated, since they govern the resistance and deflection of the beam with flexural failure mode. The following assumptions are employed for simplifying the calculation of yielding and ultimate bending moment of the SESCS sandwich beam: (a) the steel faceplates abide by the elastic-perfectly plastic behavior, (b) plane section assumption still works in the SESCS sandwich beam and (c) tension strength of concrete is negligible. In the

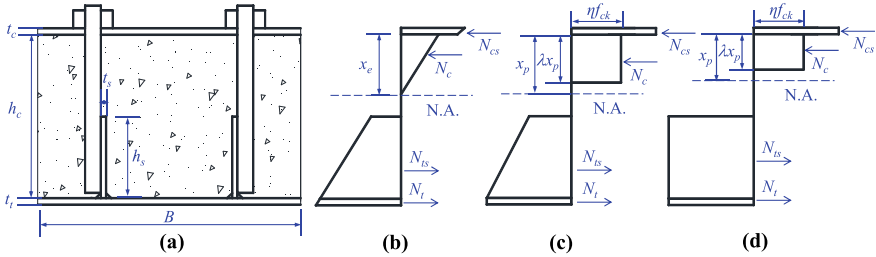


**Fig. 6.20** Stress diagram for bending resistance calculation of SESCS sandwich beam: **a** cross-section, **b** stress for yielding bending resistance **c** stress for ultimate bending resistance (yielding of partial cross-section of stiffener) and **d** stress for ultimate bending resistance (yielding of whole cross-section of stiffener), reprinted from Wang et al. (2021), copyright 2022, with permission from Elsevier

elastic range, both the strain and stress are linearly distributed along the depth of the SESCS sandwich beam, as illustrated in Fig. 6.20. Employing the force equilibrium gives

$$N_t + N_{ts} - N_c - N_{cs} = 0 \quad (6.6)$$

Based on the linear relationship of stress and strain in the elastic range, the resultant forces in Eq. (6.6) can be obtained as

$$\begin{aligned} N_t &= \frac{h_c - x_e + t_t/2}{x_e} E_s \varepsilon_e t_t B \\ N_{ts} &= \frac{2h_c - 2x_e - h_s}{x_e} E_s \varepsilon_e h_s t_s \\ N_c &= \frac{1}{2} x_e B E_c \varepsilon_e \\ N_{cs} &= \min\left(\frac{x_e + t_c/2}{x_e} E_s \varepsilon_e t_c B, n P_{Rd}\right) \\ P_{Rd} &= \min\left(0.2 f_u \pi d^2 / \gamma_v, 0.29 \alpha d^2 \sqrt{f_{ck} E_c} / \gamma_v\right) \end{aligned} \quad (6.7)$$

As illustrated in Fig. 6.20,  $N_t$ ,  $N_{ts}$ ,  $N_c$ ,  $N_{cs}$  are the resultant forces of the bottom plate, stiffener, concrete and top plate, respectively;  $x_e$  denotes the neutral axis position;  $h_c$ ,  $t_t$ ,  $h_s$ ,  $t_c$  and  $B$  are the geometric parameters of the SESCS sandwich beam in Fig. 6.20;  $E_s$  and  $E_c$  are the Young's modulus of steel and concrete, respectively;  $\varepsilon_e$  is the strain at the top compression fiber of the concrete corresponding to the end of elastic range;  $P_{Rd}$ ,  $n$  and  $d$  are the shear strength of single bolt connector as specified in Eurocode 4 (2004a), number of bolt connectors provided between maximum moment and zero moment, and diameter of bolt connector, respectively;

$f_u$  and  $f_{ck}$  are the ultimate strength of bolt connector and compressive strength of concrete;  $\gamma_v$  is the partial factor (Eurocode 2004b).

If  $N_{cs} = \frac{x_e+t_c/2}{x_e} E_s \varepsilon_e t_c B$ , substituting Eqs. (6.7) into (6.6) leads to the neutral axis position,  $x_e$ , as

$$x_e = \frac{-I_1 + \sqrt{I_1^2 + 2BK I_2}}{BK} \quad (6.8)$$

where  $K = E_c/E_s$ ,  $I_1 = (t_t + t_c)B + 2h_s t_s$ ,  $I_2 = (t_t h_c + t_t^2/2 - t_c^2/2)B + (2h_c - h_s)h_s t_s$ . If  $N_{cs} = n P_{Rd}$ , the neutral axis position,  $x_e$ , is calculated as

$$x_e = \frac{-I_3 + \sqrt{I_3^2 + 2BK I_4}}{BK} \quad (6.9)$$

where  $I_3 = t_t B + 2h_s t_s + n P_{Rd}/E_s \varepsilon_e$ ,  $I_4 = t_t B(h_c + t_t/2) + (2h_c - h_s)h_s t_s$ . The yielding bending moment,  $M_y$ , can be obtained by taking moment about the acting point of  $N_{cs}$  as

$$\begin{aligned} M_y = & \frac{\varepsilon_e(h_c - x_e + t_t/2)}{x_e} E_s B t_t (h_c + t_t/2 + t_c/2) \\ & + \frac{2\varepsilon_e(h_c - x_e - h_s)}{x_e} E_s h_s t_s (h_c - h_s/2 + t_c/2) \\ & + \frac{\varepsilon_e(h_c - x_e)}{x_e} E_s h_s t_s (h_c - h_s/3 + t_c/2) - \frac{1}{2} \varepsilon_e E_c x_e B (x_e/3 + t_c/2) \end{aligned} \quad (6.10)$$

where  $\varepsilon_e = \min(\varepsilon_1, \varepsilon_2, \varepsilon_3)$ .  $\varepsilon_1$ ,  $\varepsilon_2$  and  $\varepsilon_3$  are the strains at the top compression fiber of the concrete corresponding to three cases of the end of elastic range, and they are given as follows:

Case 1: the yielding of bottom plate, i.e.,  $\sigma_t = f_y$ , which leads to

$$\varepsilon_1 = \frac{x_e f_y}{(h_c - x_e + t_t) E_s} \quad (6.11)$$

Case 2: the strain of concrete reaches the limit of elastic strain, i.e.,  $\sigma_c = 0.4 f_{cu}$  (Eurocode 2004b), which gives

$$\varepsilon_2 = \frac{0.4 f_{cu}}{E_c} \quad (6.12)$$

Case 3: the shear strength of bolt connector is reached and  $N_{cs} = n P_{Rd}$ , we have

$$\varepsilon_3 = \frac{n P_{Rd}}{B t_c E_s} \quad (6.13)$$

With regard to the ultimate bending moment calculation for the SESCS sandwich beam, the force equilibrium in Eq. (6.6) is also applied, and the resultant forces can be given as

$$\begin{aligned} N_t &= f_y B t_t \\ N_{cs} &= \min(f_y B t_c, n P_{Rd}) \\ N_c &= \lambda x_p \eta f_{ck} B \end{aligned} \quad (6.14)$$

where  $\lambda$  and  $\eta$  are the factors defining the effective height of compression zone and effective strength of concrete, respectively. They are given as (Eurocode 2004b)

$$\begin{aligned} \lambda &= \begin{cases} 0.8 & f_{ck} \leq 50 \text{ MPa} \\ 0.8 - (f_{ck} - 50)/400 & 50 \text{ MPa} \leq f_{ck} \leq 90 \text{ MPa} \end{cases} \\ \eta &= \begin{cases} 1.0 & f_{ck} \leq 50 \text{ MPa} \\ 1.0 - (f_{ck} - 50)/200 & 50 \text{ MPa} \leq f_{ck} \leq 90 \text{ MPa} \end{cases} \end{aligned} \quad (6.15)$$

The ultimate bending moment of the SESCS sandwich beam is reached when the top compression fiber of the concrete reaches ultimate compressive strain,  $\varepsilon_{cu}$ . They are two different stress distributions of the stiffeners when the ultimate bending moment is achieved, i.e., partial or whole cross-section of the stiffener yields, as illustrated in Figs. 6.20c, d, respectively. When the strain at the top layer of the stiffener exceeds yield strain,  $\varepsilon_{sy}$ , whole cross-section of the stiffener yields, which leads to

$$\frac{h_c - x_p - h_s}{x_p} \varepsilon_{cu} \geq \varepsilon_{sy} \quad (6.16)$$

Then, we have

$$x_p \leq \frac{\varepsilon_{cu}(h_c - h_s)}{\varepsilon_{cu} + \varepsilon_{sy}} \quad (6.17)$$

In this case, the resultant force of the stiffener,  $N_{ts}$ , is given as

$$N_{ts} = 2h_s t_s f_y \quad (6.18)$$

Substituting Eqs. (6.14) and (6.18) into Eq. (6.6) yields

$$N_{cs} + \lambda \eta x_p B f_c - 2h_s t_s f_y - B t_t f_y = 0 \quad (6.19)$$

Then, we have

$$x_p = \frac{2h_s t_s f_y + Bt_t f_y - N_{cs}}{\lambda \eta B f_c} \quad (6.20)$$

Hence, if  $\frac{2h_s t_s f_y + Bt_t f_y - N_{cs}}{\lambda \eta B f_c} \leq \frac{\varepsilon_{cu}(h_c - h_s)}{\varepsilon_{cu} + \varepsilon_{sy}}$ , the whole cross-section of the stiffener yields, and Eqs. (6.19) and (6.20) are applicable. Taking moment about the acting point of  $N_c$  gives the ultimate bending moment of the SESCS sandwich beam as

$$M_u = f_y B t_t \left( \frac{2h_c + t_t - \lambda x_p}{2} \right) + N_{cs} \left( \frac{t_c + \lambda x_p}{2} \right) + f_y t_s h_s (2h_c - \lambda x_p - h_s) \quad (6.21)$$

If  $\frac{2h_s t_s f_y + Bt_t f_y - N_{cs}}{\lambda \eta B f_c} > \frac{\varepsilon_{cu}(h_c - h_s)}{\varepsilon_{cu} + \varepsilon_{sy}}$ , the partial cross-section of the stiffener yields. The force equilibrium gives

$$N_{cs} + \lambda \eta x_p B f_c - 2t_s \left\{ h_s f_y - \frac{\left[ f_y - \frac{h_c - x_p - h_s}{x_p} \varepsilon_{cu} E_s \right] \left[ h_s - h_c + \frac{(\varepsilon_{cu} + \varepsilon_{sy}) x_p}{\varepsilon_{cu}} \right]}{2} \right\} - B t_t f_y = 0 \quad (6.22)$$

Then,  $x_p$  can be calculated as

$$x_p = \frac{-I_5 + \sqrt{I_5^2 + 4I_6 I_7}}{I_6 t_s} \quad (6.23)$$

where  $I_5 = (h_s - h_c)(f_y - \varepsilon_{cu} E_s + (\varepsilon_{cu} + \varepsilon_{sy})/\varepsilon_{cu})$ ,  $I_6 = (f_y - \varepsilon_{cu} E_s)(\varepsilon_{cu} + \varepsilon_{sy})/\varepsilon_{cu} t_s$ ,  $I_7 = t_s(h_s - h_c)^2 - 2h_s t_s f_y - B f_y t_t + N_{cs}$ . Then, the ultimate bending moment of the SESCS sandwich beam can be given in Eq. (6.24) by taking moment about the acting point of  $N_c$ .

$$\begin{aligned} M_u = & f_y B t_t (h_c + t_t/2 - \lambda x_p/2) + N_{cs} (t_c/2 + \lambda x_p/2) + 2f_y t_s h_s (h_c - \lambda x_p/2 - h_s/2) \\ & - t_s \left( f_y - \frac{h_c - x - h_s}{x} \varepsilon_{cu} E_s \right) \left[ h_s - h_c + \frac{(\varepsilon_{cu} + \varepsilon_{sy}) x p}{\varepsilon_{cu}} \right] \\ & \left[ h_c - x_p/2 - h_s + h_c/3 - \frac{(\varepsilon_{cu} + \varepsilon_{sy}) x_p}{3\varepsilon_{cu}} \right] \end{aligned} \quad (6.24)$$

The curvatures corresponding to the yielding and ultimate bending moment of the SESCS sandwich beam ( $\phi_y$  and  $\phi_p$ ) can be given as

$$\phi_y = \frac{\varepsilon_e}{x_e}; \quad \phi_p = \frac{\varepsilon_{cu}}{x_p} \quad (6.25)$$

Then, the corresponding mid-span displacements can be calculated as

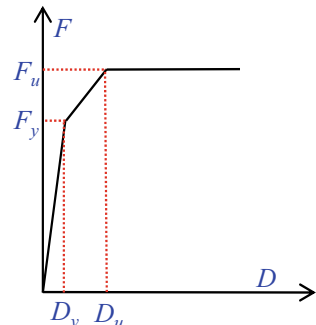
$$D_y = \frac{\phi_e L^2}{12}; \quad D_u = \frac{\phi_p L^2}{12} \quad (6.26)$$

Herein, the calculation of  $D_u$  is based on the “minimum stiffness principle” (Gu et al. 2015), which assumes that the bending stiffness along the whole span of the beam is the same, and the bending stiffness at the position with maximum bending moment (or minimum bending stiffness) is chosen for the deflection calculation. This method leads to larger curvature and flexure-induced deflection of the beam as compared to the actual one. However, the shear deformation of the beam which is not considered in this method may offset the calculation deviance due to using the “minimum stiffness principle”. The resistances of the beam corresponding to the yielding and ultimate bending moment ( $F_y$  and  $F_u$ ) are given as

$$F_y = \frac{4M_y}{L}; \quad F_u = \frac{4M_u}{L} \quad (6.27)$$

The tri-linear curve is employed herein to describe the resistance–displacement relationship of the SESCS sandwich beam under concentrated load at the mid-span, as illustrated in Fig. 6.21. It is known that the mild steel exhibits evident strain rate effect, and its strength increases with the increase of strain rate. The Dynamic Increase Factor (DIF) is usually employed to represent the strength enhancement. Owing to the variation of strain rate during impact, the strength enhancement or DIF also varies. The average strain rate was employed herein to simplify the treatment of strain rate effect on the strength enhancement. The maximum strain rate of the beam occurs at initial impact stage when the beam exhibits maximum velocity. Subsequently, the strain rate of the top and bottom plate at initial impact stage can be calculated in Eq. (6.28) by assuming the neutral axis is located at middle layer of the beam.

**Fig. 6.21** Tri-linear force–displacement curve employed for analytical model, reprinted from Wang et al. (2021), copyright 2022, with permission from Elsevier



$$\dot{\varepsilon}_s = \left( \frac{h_c + t_c}{2} \right) \dot{\phi} \quad (6.28)$$

where  $\dot{\phi}$  is the curvature rate of the beam at the mid-span and given in Eq. (6.29) by employing the elastic deflection shape function in Eq. (6.5).

$$\dot{\phi} = \frac{12V_0}{L^2} \quad (6.29)$$

where  $V_0$  is the initial velocity of the beam and can be obtained in Eq. (6.30) by applying the conservation of momentum.

$$V_0 = \frac{m_h V}{m_e + m_h} \quad (6.30)$$

where  $V$  is the impact velocity of the hammer. Since the strain rate drops to zero when the maximum displacement is reached, the average strain rate can be taken as the half of the maximum strain rate as

$$\dot{\varepsilon}_{\bar{s}} = \dot{\varepsilon}_s / 2 \quad (6.31)$$

Then, DIF of the faceplate can be obtained by employing the Cowper-Symonds model as

$$DIF_s = 1 + (\dot{\varepsilon}_{\bar{s}}/C)^{1/P} \quad (6.32)$$

To include the strain rate effect of mild steel into the analytical model, yield stress of the faceplate,  $f_y$ , in the equations for calculating the resistances is enhanced via multiplying a factor of  $DIF_s$  in Eq. (6.32). For the established SDOF system with the equation of motion being presented in Eq. (6.2), the initial displacement and velocity are zero and  $V_0$ , respectively. The numerical method can be employed to solve the equation of motion in Eq. (6.2) and obtain the displacement-time response of the SESCS sandwich beam. Herein, the fourth-order Runge–Kutta time stepping procedure was employed.

### 6.2.3.2 Analytical Validation

Figure 6.16 presents the comparison of mid-span displacement–time histories of the SESCS sandwich beams obtained from the analytical models with those obtained from the tests and FE analyses, and reasonable agreements among them can be observed. Table 6.4 lists the maximum mid-span displacements and their comparisons with test data. The differences of the maximum mid-span displacements

between the analytical predictions and tests are less than 6%, except for the specimen Bs4-150 with analytical-predicted maximum mid-span displacement being 23% larger than test data. The over-predicted displacement response of the specimen Bs4-150 from the analytical model may be caused by the underestimation of the stiffness of the beam after yielding due to using the “minimum stiffness principle” (Gu et al. 2015). The underestimation of the stiffness of the beam has more significant effect on the displacement response of the beam with smaller deformation. Hence, the bigger difference of the maximum mid-span displacement between the test and analytical-prediction is observed for the specimen Bs4-150 with smallest maximum mid-span displacement (18.27 mm). The average analytical-prediction to test ratio of the maximum mid-span displacement is 1.06 with coefficient of variation to be 0.086. The aforementioned comparisons demonstrate that the proposed analytical model is reasonable and can be employed as a simple alternative to predict displacement response of the SESCS sandwich beam under impact loading.

## 6.3 SESCS Sandwich Panel Under Impact

### 6.3.1 Experimental Study

#### 6.3.1.1 Specimens

Figure 6.22 presents the SESCS sandwich panel designed for the drop-weight impact test. The fabrication process of the SESCS sandwich panel is similar to that of

**Fig. 6.22** General illustration of the SESCS sandwich panel, reprinted from Wang et al. (2022), copyright 2022, with permission from Elsevier

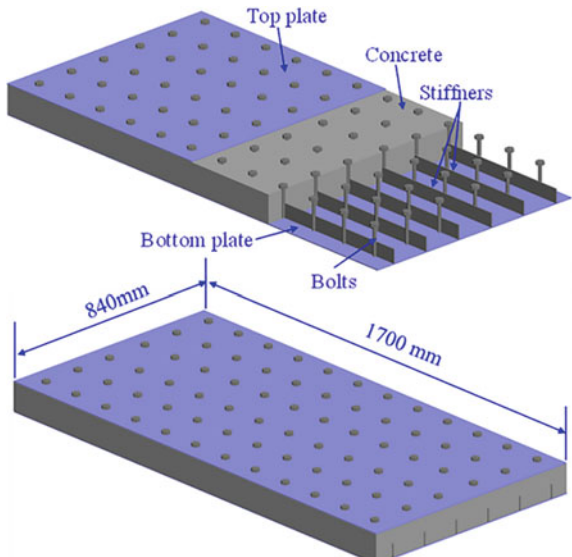


**Table 6.5** Summary of specimens for SESCS sandwich panel (unit: mm)

Specimen	$t_c$	$h_c$	$t_t$	$H$
Ps4-70	3.52	70	3.52	1800
Ps3-70	2.84	70	2.84	1800
Ps5-70	4.46	70	4.46	1800
Ps4-80	3.52	80	3.52	1800
Ps4-90	3.52	90	3.52	1800
Pb4-70	3.52	70	3.52	1800
Ps4-70 V	3.52	70	3.52	1400

Note  $t_c$ ,  $h_c$ , and  $t_t$ —Thicknesses of top plate, concrete core and bottom plate;  $H$ —Drop height; Ps and Pb stand for the SESCS sandwich panel and SCS sandwich panel, respectively

SESCS sandwich beam, which includes four steps, as illustrated in Fig. 6.2. Seven specimens were prepared for the drop-weight impact tests to study the effects of various parameters on the impact responses of SESCS sandwich panels. Table 6.5 presents the varying parameters for all the specimens. One specimen (Ps4-70) was designed as a control specimen with 3.52 mm thick steel plates and 70 mm thick concrete core. To study the effects of the steel plate and concrete core thicknesses, two specimens were designed with 2.84 and 4.46 mm thick steel plates, and two specimens were designed with concrete core thickness of 80 and 90 mm. Furthermore, one specimen with all the parameters same as the control specimen was prepared to study the influence of drop height, and one specimen was designed as a traditional SCS sandwich panel without stiffeners to compare the impact resistance with the newly developed SESCS sandwich panel. The length and width of all the specimens were same (i.e., 1700 and 840 mm for length and width, respectively). The diameter and spacing of bolts for all the specimens were 12 and 140 mm, respectively. The stiffeners of SESCS sandwich panels had the same dimension of  $1700 \times 40 \times 3.52$  mm<sup>3</sup>, and the spacing of stiffeners in width direction was 140 mm. Q235 mild steel was employed for the steel plates of the SESCS sandwich panels, and normal weight concrete was employed for the concrete core. Their material properties were obtained from the tensile coupon tests and uniaxial unconfined compressive tests for steel and concrete, respectively. Table 6.2 presents the material properties of mild steel plates, bolts and concrete.

### 6.3.1.2 Test Setup and Instrumentation

The drop-weight impact test method has been widely adopted by researchers to evaluate the impact resistance of the SCS sandwich structures (Lu et al. 2021; Zhao et al. 2018). Hence, in this study, the impact tests on SESCS sandwich panels were performed using a drop-weight impact test system, as shown in Fig. 6.23 for the impact test setup and instrumentation. The preliminary FE simulations on the SESCS sandwich panels were conducted to obtain the suitable mass and drop height of the

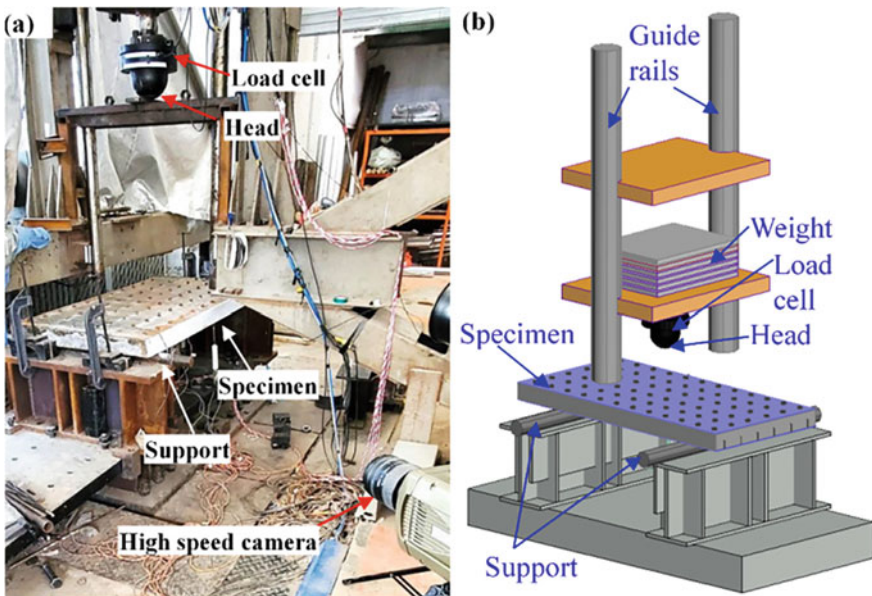


**Fig. 6.23** Test setup and instrumentation: **a** Photograph and **b** schematic view, reprinted from Wang et al. (2022), copyright 2022, with permission from Elsevier

hammer. The mass of the hammer for all the specimens was 590 kg, and the hammer was dropped freely from the height of 1.8 m for all the specimens except for one specimen which was subjected to a drop height of 1.4 m (refer to Table 6.5). The SESCS sandwich panels were simply supported on two circular bar supports with a clear span of 1500 mm, as presented in Fig. 6.23. It should be mentioned that the specimens were tied to the support using steel wires to prevent the uplift of the specimens during their rebounds. A dynamic load cell was embedded in the hammer head to measure the impact force, and three potentiometers (one at the center of the panel, one at the free side of the panel in mid-span, and one at quarter-span) were used to measure the displacements of the specimens. A data logger with a sampling frequency of 100 kHz was employed for recording the impact force–and displacement–time histories. The impact process and deformation of the SESCS sandwich panels were captured using a high-speed camera with a sampling frequency of 3000 frames/sec.

### 6.3.1.3 Test Results and Discussions

There were seven specimens subjected to impact load at their centers using the hemispherical drop hammer. The test results are summarized in Table 6.6, including peak impact forces and maximum displacements recorded by the dynamic load cell and three potentiometers, respectively.

**Table 6.6** Summary of test results for SESCS sandwich panel

Specimen	$F_{\max}$ (kN)	$F_m$ (kN)	$D_{mm}$ (mm)	$D_{mms}$ (mm)	$D_{qm}$ (mm)
Ps4-70	323.91	243.92	40.87	35.95	21.48
Ps3-70	306.35	217.70	42.26	37.10	22.60
Ps5-70	387.82	274.89	36.43	29.70	17.26
Ps4-80	371.90	270.44	33.63	28.20	17.56
Ps4-90	438.52	300.91	28.85	24.59	15.96
Pb4-70	228.81	185.20	54.03	37.04	27.97
Ps4-70 V	330.86	242.64	31.15	27.02	17.05

Note  $F_{\max}$ ,  $F_m$ —Peak impact force and post-peak mean force;  $D_{mm}$ ,  $D_{mms}$ ,  $D_{qm}$ —Maximum values of the displacements at mid-spans (center and free side) and quarter-spans of the panels

### Damage Analysis of SESCS Sandwich Panels

Figure 6.24 presents the seven specimens after drop-weight impact tests, and all of them exhibit global flexural deformation mode with plastic hinges being observed at their mid-spans. The flexural deformation mode also results in vertical cracks occurred at the mid-spans of specimens, and the vertical crack width exhibits the largest value near the bottom surface and gradually decrease as the crack approaches the neutral axis. Besides the flexure-induced vertical cracks at the mid-span, the shear force-induced diagonal cracks near the support are observed for the specimens

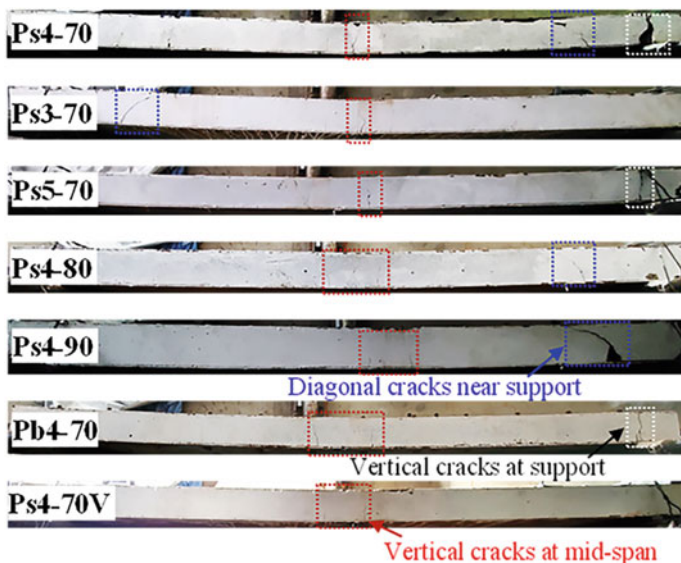


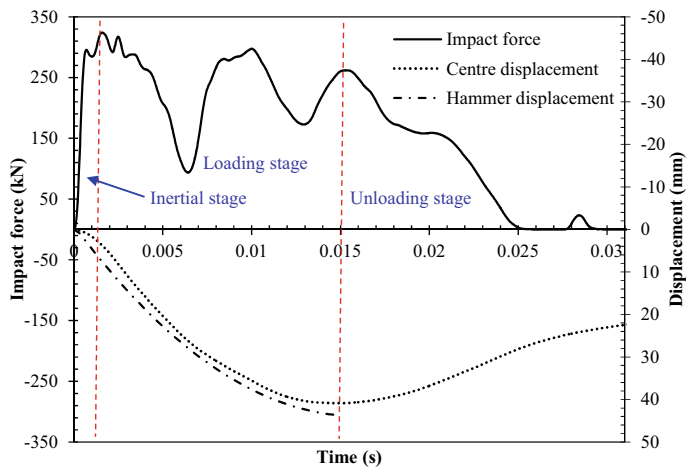
**Fig. 6.24** Failure modes of SESCS sandwich panels, reprinted from Wang et al. (2022), copyright 2022, with permission from Elsevier

Ps3-70, Ps4-70, Ps4-80, and Ps4-90. Moreover, some of the specimens (Ps4-70, Ps5-70, and Ps4-70) exhibit vertical cracks of concrete above the support, which is caused by the larger reaction force. There is no fracture, buckling, or separation of the steel plates being observed for any of the tested specimens, which indicates that the structural integrity of the SESCS sandwich panels is maintained. Moreover, no slip between the concrete core and steel plates is observed, which reveals that the proposed SESCS sandwich panels exhibit desirable resistance to interfacial shear.

The comparison of cracking patterns of the specimens with variant steel plate thicknesses reveals that increasing steel plate thickness tends to reduce the occurrence of diagonal crack near the support, i.e., the diagonal crack is not observed for the specimen Ps5-70 with the thickest steel plate, while both the specimens Ps3-70 and Ps4-70 exhibit diagonal cracks. However, increasing steel plate thickness of the SESCS sandwich panel can result in the increased possibility of occurrence of vertical crack above the support, i.e., the specimens Ps4-70 and Ps5-70 with higher steel plate thickness exhibit vertical crack above the support. This is because increasing steel plate thickness leads to larger bending resistance of the SESCS sandwich panel, and thus larger reaction force from the support. It is also noted in Fig. 6.24 that increasing concrete thickness results in reduced width and length of vertical cracks at mid-span owing to the decreased impact-induced deformation of the SESCS sandwich panel. Moreover, the possibility of occurrence of vertical crack above the support is found to be reduced by increasing the thickness of concrete core, which can be attributed to the improved local bearing resistance for the panel with a thicker concrete core. The presence of stiffeners in tension plate is found to reduce the vertical crack width owing to the smaller deformation of the specimen Ps4-70 as compared to Pb4-70 without stiffeners. The drop height also exhibits a noticeable influence on the cracking patterns of the SESCS sandwich panel. Only vertical crack of concrete at mid-span is observed for the specimen Ps4-70 V with a lower drop height of 1.4 m. However, increasing drop height from 1.4 to 1.8 m causes the increase of vertical crack width at mid-span as well as the occurrence of diagonal crack near the support and vertical crack above the support.

### Impact Force Response

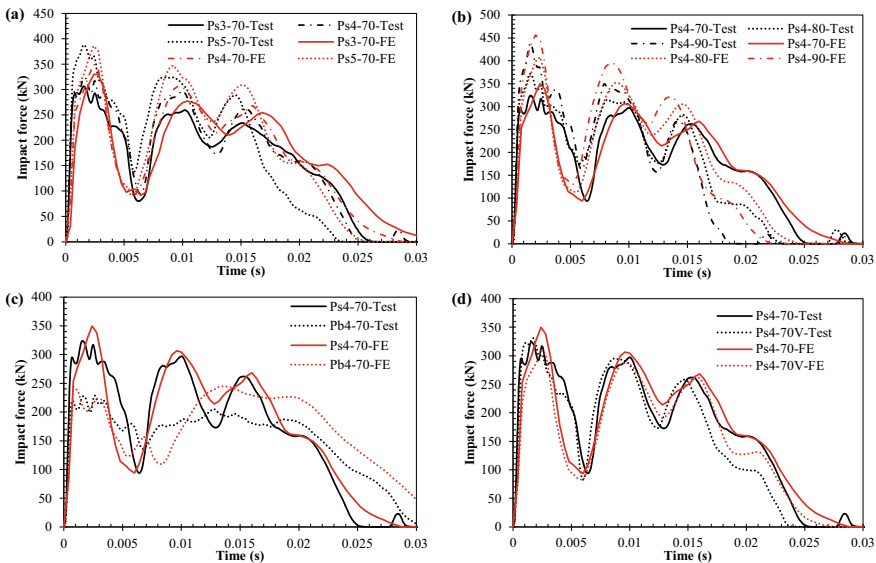
The impact force and displacement over time responses of all the tested specimens exhibit similar behavior. Figure 6.25 presents the typical impact force–time curve as well as center and hammer displacement versus time curves to reveal the impact response of the SESCS sandwich panel. Three impact response stages can be identified based on Fig. 6.25, including inertial, loading, and unloading stages, similar to the observations by other researchers (Yan et al. 2020a, b, c, d; Zhao and Guo 2018). In the inertial stage, there is a sudden increase in the impact force within 2 ms, which is due to the inertial effect. During this stage, a contact is developed between the drop hammer and panel, initiating local indentation on the top surface. Meanwhile, the local indentation zone of the panel is forced to move downwards with the same velocity as that of drop hammer. The hammer displacement exhibits



**Fig. 6.25** Typical impact force and displacement–time histories of the SESCS sandwich panel, reprinted from Wang et al. (2022), copyright 2022, with permission from Elsevier

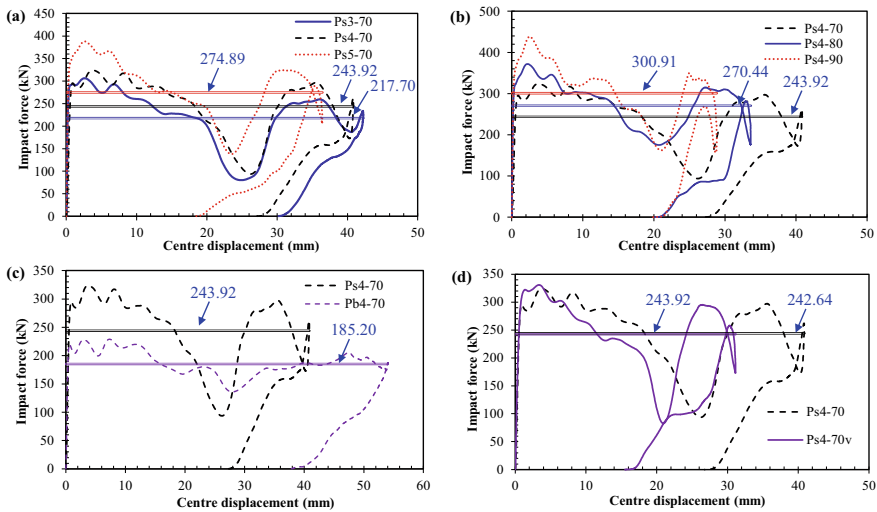
faster increase as compared to center displacement, and the displacement difference between the two increases in the inertial stage and approaches a constant value at the end of inertial stage. The loading stage occurs from 2 to 15 ms, during which the drop hammer and panel move downwards together. The impact force exhibits evident fluctuation in the loading stage, which can be attributed to the relative motion of the drop hammer and panel. With regard to center and hammer displacements in the loading stage, both of them exhibit continuous increase up to their maximum values, and the displacement difference is nearly constant. At the end of loading stage, the maximum deformation of the panel occurs, and the hammer velocity reduces to zero. The unloading stage is observed from 15 to 25 ms with the rebound of the panel. The impact force and displacement exhibit monotonic decrease in the unloading stage. The impact force drops to zero when the hammer is completely separated from the panel. Partial impact energy stored in the panel transforms to kinetic energy owing to elastic recovery of the panel.

Figure 6.26 shows the impact force–time histories of all the tested specimens, and the peak impact forces are also listed in Table 6.6. The effect of steel plate thickness on the impact force response is illustrated in Fig. 6.26a, and higher impact force in loading stage is observed for the SESCS sandwich panel with thicker steel plate owing to the improved resistance of the panel. This effect was also observed in a study conducted by Zhao et al. (2018). With regard to the peak impact force presented in Table 6.6, it also exhibits increase with the rise in steel plate thickness owing to the enhanced contact stiffness and resistance of the panel. The peak impact force is increased from 306.35 kN to 323.91 and 387.82 kN (by 5.73% and 26.59%), respectively, on increasing the thickness of steel plate from 2.84 mm to 3.52 and 4.46 mm. There is a noticeable improvement in the impact resistance of the SESCS sandwich panel with the increase of concrete core thickness, as presented in Fig. 6.26b



**Fig. 6.26** Impact force–time histories of test specimens: effects of **a** steel plate thickness, **b** concrete core thickness, **c** presence of stiffener, and **d** drop height, reprinted from Wang et al. (2022), copyright 2022, with permission from Elsevier

and Table 6.6. The peak impact force of the SESCS sandwich panel with a 70 mm thick concrete core (Ps4-70) is 323.91 kN which is increased to 371.90 kN and 438.52 kN (by 14.81 and 35.38%), respectively, when concrete core thickness is raised to 80 and 90 mm. The increase in concrete core thickness can improve contact stiffness and resistance of the panels, which results in higher peak impact force, as demonstrated in Fig. 6.23b. Sohel and Liew (2014) also revealed that the concrete thickness influenced the impact resistance of the SCS sandwich panel. A comparison of impact force–time histories of specimens Ps4-70 and Pb4-70 are presented in Fig. 6.26c to reveal the effect of stiffeners on the impact force response of the panels. Specimen Ps4-70 is the proposed SESCS sandwich panel, whereas specimen Pb4-70 is the traditional SCS sandwich panel without stiffeners. Figure 6.26c shows that the peak impact force of the panel is increased by 41.56% on employing stiffeners in the tension plate. This demonstrates that the impact resistance of the sandwich panel is significantly improved with the presence of stiffeners. Figure 6.26d presents the effect of drop height on the impact force response of the SESCS sandwich panels, and the reduction in drop height from 1.8 m to 1.4 m exhibits negligible effect on the peak impact force (330.86 kN and 323.91 kN). However, there is a reduction in damage and deformation of the panel owing to less applied impact energy. Zhao et al. (2018) noted that there was a limited influence on the maximum impact force in the loading stage for the SCS sandwich panel subjected to different impact velocities, and this study presented the similar observation.



**Fig. 6.27** Impact force–center displacement curve of test specimens: effects of **a** steel plate thickness, **b** concrete core thickness, **c** presence of stiffener, and **d** drop height, reprinted from Wang et al. (2022), copyright 2022, with permission from Elsevier

The peak impact force at the inertial stage cannot represent the actual resistance of the specimen because it is mainly caused by the inertial effect and strongly depends on the contact stiffness of the specimen. Nevertheless, the post-peak mean force (defined in Eq. (6.1)) could provide a better evaluation of the actual resistance of the specimen subjected to impact loading. The impact force versus center displacement curves for all the tested specimens are plotted in Fig. 6.27. There is a sharp rise in the impact force upon the impact by the hammer due to inertial effect and large contact stiffness, whereas the displacement remains below 2 mm. However, after the development of contact between the hammer and panel, the hammer forces the panel to move downwards, showing continuous increase in the displacement of the panel. Though there is continuous increase in the displacement, there are some fluctuations and drop in the impact force owing to the impact-induced vibration and crushing of the concrete at the impact point, respectively. It can be noticed from Figs. 6.27a, b that the post-peak mean force of the SESCS sandwich panel is evidently increased with the increase in the thickness of concrete core and steel plates, i.e., the post-peak mean force is increased by 23.4 and 26.3%, respectively, on increasing the concrete core thickness from 70 to 90 mm and steel plate thickness from 2.84 to 4.46 mm. The significant improved post-peak mean force (by 31.7%) of the SESCS sandwich panel can be observed in Fig. 6.27c as compared to the traditional SCS sandwich panel without stiffeners, which indicates the improved impact resistance of the SESCS sandwich panel owing to the presence of stiffeners in the tension plate. Figure 6.27d indicates that the impact velocity has negligible effect on the post-peak mean force and resistance of the specimen.

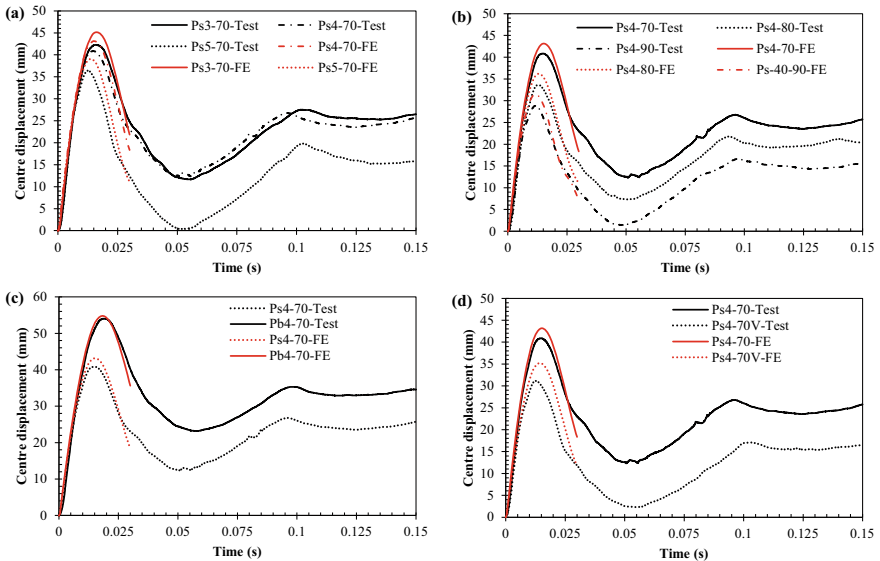


**Fig. 6.28** Center displacement–time histories of test specimens: effects of **a** steel plate thickness, **b** concrete core thickness, **c** presence of stiffener, and **d** drop height, reprinted from Wang et al. (2022), copyright 2022, with permission from Elsevier

### Displacement Response

The center displacement–time histories of the seven specimens are given in Fig. 6.28, and the corresponding maximum displacements are summarized in Table 6.6. During the experiments, when the drop hammer impact was applied on the panels, no detachment between panels and supports were observed during the loading process (i.e., up to the maximum displacement). However, the panels uplifted from the support during the unloading process due to the rebound, which can also be noticed in Fig. 6.28. After the rebound, the displacement of the panels became stable. The effect of steel plate thickness on the displacement–time histories are shown in Fig. 6.28a, and both the maximum and permanent displacements exhibit decrease with the increase of steel plate thickness, owing to the enhanced impact resistance of the panel. Table 6.6 indicates that the maximum center displacement of the panel is reduced by 3.40 and 16.00%, respectively, on increasing the thickness of steel plate from 2.84 mm to 3.52 and 4.46 mm. Moreover, the deflection of the SESCS sandwich panel is found to be reduced as the concrete core thickness is increased owing to the improved stiffness and resistance of the panel, as illustrated in Fig. 6.28b. Table 6.6 reveals that the maximum center displacement is reduced from 40.87 mm to 33.63 and 28.85 mm (by 21.52 and 41.66%), respectively, on increasing concrete core thickness from 70 mm to 80 and 90 mm. Figure 6.28c indicates that the SESCS sandwich panel with the presence of stiffeners evidently outperforms the traditional SCS sandwich panel in resisting impact load. The maximum center displacement of Ps4-70 is reduced by

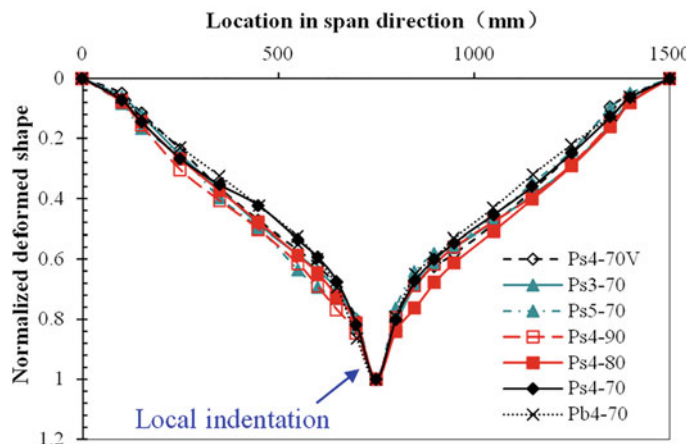


**Fig. 6.29** Normalized deformed shapes of SESCS sandwich panels, reprinted from Wang et al. (2022), copyright 2022, with permission from Elsevier

24.36% compared to that of Pb4-70. Figure 6.28d exhibits a reduction in the deflection of the panel due to decrease in drop height and impact energy, i.e., the maximum center displacement is reduced by 31.20% on decreasing drop height from 1.8 m to 1.4 m.

After the tests, the permanent deformed shapes of all the specimens were measured manually using a laser ranging device. Figure 6.29 presents the normalized deformed shapes of the tested specimens in span direction, which further demonstrates that the global flexural deformations of the panels are formed, along with local indentation in the impact zone.

#### Energy Absorption Response

Among the seven tested specimens, six of them were subjected to the same impact energy with mass of hammer and drop height of 590 kg and 1.8 m. But, one specimen (PS4-70v) was tested with lesser impact energy (i.e., 590 kg mass of hammer and 1.4 m drop height). Energy–displacement curve is considered to evaluate and compare the energy absorption behavior of the proposed SESCS sandwich panel and traditional SCS sandwich panel under impact load. Also, the effects of concrete thickness, steel plate thickness and drop height on the energy absorption response of the SESCS panel are studied. Figure 6.30 presents the energy versus hammer displacement curves of the seven tested specimens, which are obtained by integrating the impact force with hammer displacement. It is noted that the energy absorbed by the panel almost exhibits a linear increase with the hammer displacement and reaches the peak value when the displacement of the hammer is maximum. A small fraction of the impact energy absorbed by the panel is released owing to the elastic recovery

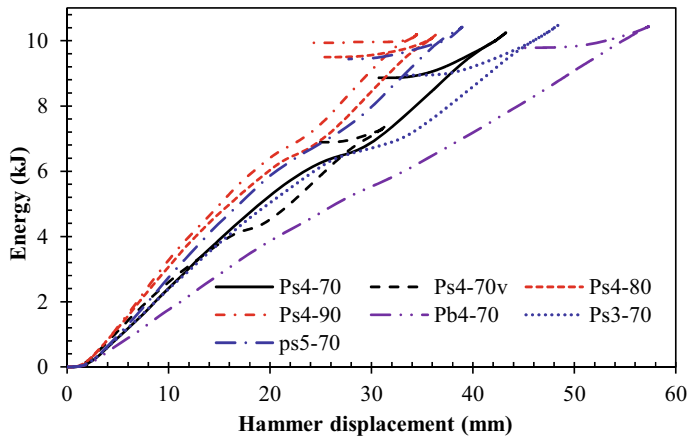


**Fig. 6.30** Energy versus hammer displacement curve, reprinted from Wang et al. (2022), copyright 2022, with permission from Elsevier

of the steel and concrete material. It is also noted in Fig. 6.30 that the maximum energy absorbed by the panel subjected to the same impact energy is approximately the same. Moreover, the energy absorbing rate of the panel is found to be increased by increasing the thickness of concrete core and steel plate as well as employing the stiffeners, which also indicates an improved impact resistant performance.

### 6.3.2 Numerical Study

#### 6.3.2.1 FE Model Establishment

The LS-DYNA software was used to carry out the numerical studies on the SESCS sandwich panels under impact loading. The half-symmetric FE model (shown in Fig. 6.31) was established owing to the symmetry of the specimen and loading condition. The element formulations, material models and properties, contact treatments and mesh sizes are consistent with those of SCS sandwich beams presented in Sect. 6.2.2.1.

#### 6.3.2.2 Numerical Results and Discussions

The comparisons of impact force and displacement–time histories obtained from the tests and FE predictions are presented in Figs. 6.26 and 6.28, respectively. Figure 6.26 shows that the FE-predicted impact force–time histories match well with the test results for all the SESCS sandwich panels. The impact force–time histories from the FE simulations also experience three impact stages (i.e., inertial, loading,

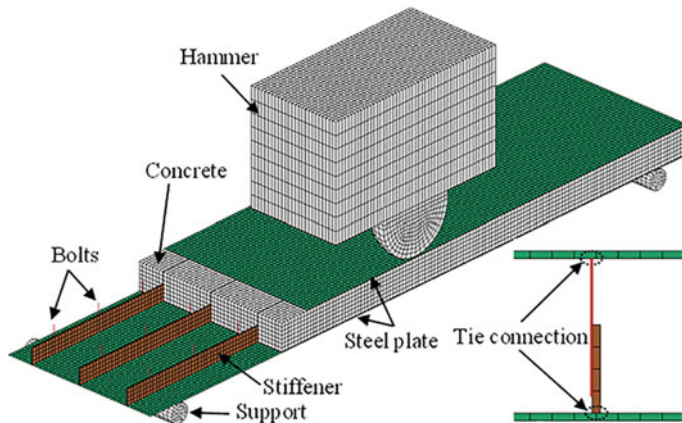


**Fig. 6.31** Half-symmetric FE model of the SESCS sandwich panel, reprinted from Wang et al. (2022), copyright 2022, with permission from Elsevier

and unloading stages), similar to the test results. Likewise, the FE-predicted center displacement-time histories of the panels are also well matched with the test data, as shown in Fig. 6.28. Table 6.7 presents the comparison of FE predictions and test results in terms of peak impact force and maximum center displacement. The difference between the FE predictions and test results for peak impact force is found to be less than 7%, and the average ratio of FE to test for peak impact force is 0.96 with a coefficient of variation (COV) of 0.059. With regard to the maximum center displacement, its difference between the FE predictions and test results is less than 13%, and the average ratio of FE to test for maximum center displacement is 1.07 with a COV of 0.033. From the above comparisons of impact force and displacement responses between the FE predictions and test results, the accuracies of the established FE models can be validated.

**Table 6.7** Comparison of FE predictions with test results

Specimen	$F_{\max\text{FE}}$ (kN)	$F_{\max\text{FE}}/F_{\max}$	$D_{\text{mm}\text{FE}}$ (mm)	$D_{\text{mm}\text{FE}}/D_{\text{mm}}$
Ps4-70	349.82	0.93	43.14	1.06
Ps3-70	330.22	0.93	45.18	1.07
Ps5-70	386.03	1.00	39.06	1.07
Ps4-80	408.30	0.91	36.18	1.08
Ps4-90	456.48	0.96	31.51	1.09
Pb4-70	245.15	0.93	54.77	1.01
Ps4-70 V	309.64	1.07	35.20	1.13
Average	—	0.96	—	1.07
COV	—	0.059	—	0.033

Note The parameters with  $FE$  as the subscript stand for the FE predictions

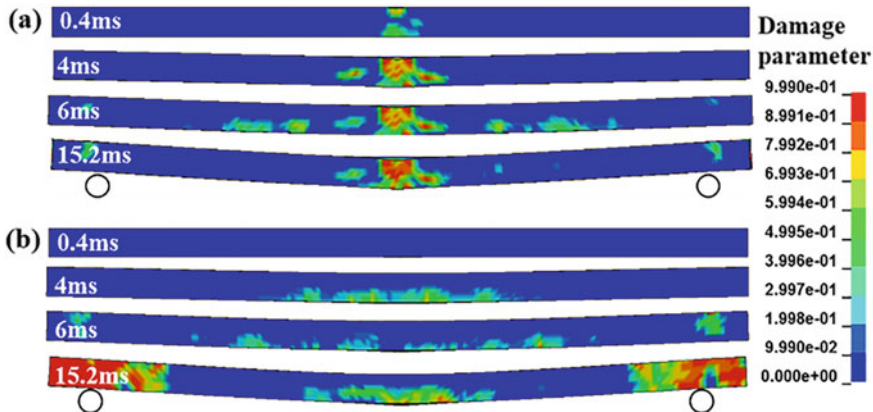


**Fig. 6.32** Damage evolution of concrete core during impact: **a** Cross-section at impact point, **b** Cross-section at free side, reprinted from Wang et al. (2022), copyright 2022, with permission from Elsevier

The validated FE model was employed to reveal the damage evolution of concrete core during impact, and Fig. 6.32 presents the damage contours of concrete core at different times. The concrete core at impact zone immediately experiences local damage once being struck by the drop hammer, as it can be seen in Fig. 6.32a at 0.4 ms. At this moment, the damage of concrete is not observed at the free side of the panel (see Fig. 6.32b at 0.4 ms). Subsequently, local punching shear failure of the concrete core at impact zone can be observed at 4 ms, whereas flexure-induced damage of concrete at the free side of the panel can be observed with damage of concrete only appearing at the bottom surface (refer to Fig. 6.32b at 4 ms). The damage of concrete above the support occurs at 6 ms, and the concrete core exhibits increasingly severe damage with further collision. The maximum deflection of the panel is reached at 15.2 ms, and corresponding damage contours of the concrete core are also presented in Fig. 6.32. Punching shear failure of the concrete core at impact zone is evident, and the severe damage of concrete core at the free side of the panel occurs at mid-span and support owing to the large sagging moment at mid-span and reaction force at the support, respectively.

### 6.3.2.3 Parametric Studies

The influences of limited parameters on the impact resistance of the SESCS sandwich panels were explored experimentally. However, the design of panels may include several parameters to be considered for its use as an impact-resistant structural member. Hence, by employing the validated FE model, parametric studies were conducted to investigate the influence of various parameters on the impact responses of SESCS sandwich panels. The examined parameters were the impact velocity, hammer mass, impact energy (or initial kinetic energy), and momentum of the

hammer. One specimen (Psc) was selected as the reference specimen with same geometry and material properties to the specimen Ps4-70; two specimens (Psv5 and Psv7) were employed to study the effect of impact velocity; Psm3 and Psm9 were considered to investigate the influence of mass of hammer; the effect of impact energy was studied using Psk81 and Psk135 (while the identical momentum of the hammer was kept by selecting different combinations of impact velocity and hammer mass); the influence of momentum of the hammer was explored through Psp18 and Psp54 (while keeping the identical kinetic energy of the hammer by selecting different combinations of impact velocity and hammer mass). The details of the specimens for parametric studies and results are listed in Table 6.8.

The effects of impact velocity on the peak impact force, post-peak mean force and maximum center displacement of the SESCS sandwich panel are depicted in Fig. 6.33a. With the increase in impact velocity from 5 m/s to 6 and 7 m/s, the peak impact force is increased by 14.69 and 24.49%, respectively. Likewise, the corresponding increase of post-peak mean force is 16.16 and 24.77%, as listed in Table 6.8. This is because of the increase in kinetic energy associated with the higher impact velocity applied on the panels. Moreover, the increased impact velocity also increases the maximum center displacement, which can also be attributed to the improved impact energy. The maximum center displacement of the SESCS sandwich panel is increased by 26.00 and 58.32%, respectively, on increasing the impact velocity from 5 m/s to 6 and 7 m/s (or increasing the impact energy by 44 and 96%). It is noted that the increase in percentage of maximum center displacement is smaller than that of impact energy, which can be attributed to the improved post-peak mean force with the increase in the impact velocity. The energy–hammer displacement curves in Fig. 6.34a exhibit a noticeable rise in the maximum energy absorption and hammer displacement with the increase in the impact velocity. Moreover, evidently higher energy absorbing rate (i.e., the slope of energy versus hammer displacement curve) can be observed for the SESCS sandwich panel subjected to higher impact velocity when the hammer displacement exceeds around 10 mm.

**Table 6.8** Summaries of numerical results

Specimen	$v$ (m/s)	$m$ (kg)	$k$ (kJ)	$p$ (kg·m/s)	$F_{\max}$ (kN)	$F_m$ (kN)	$D_{mm}$ (mm)
Psc	6.0	600	10.8	3600	367.00	219.84	43.98
Psv5	5.0	600	7.5	3000	319.98	189.25	34.90
Psv7	7.0	600	14.7	4200	398.35	236.14	55.26
Psm3	6.0	300	5.4	1800	327.35	145.36	26.04
Psm9	6.0	900	16.2	5400	368.21	245.61	58.90
Psk81	4.5	800	8.1	3600	289.30	198.68	37.58
Psk135	7.5	480	13.5	3600	403.77	229.30	51.12
Psp18	12	150	10.8	1800	438.71	255.23	38.42
Psp54	4.0	1350	10.8	5400	313.35	213.70	45.54

Note  $v$ ,  $m$ ,  $k$ ,  $p$ —Impact velocity, hammer mass, kinetic energy and momentum of the hammer

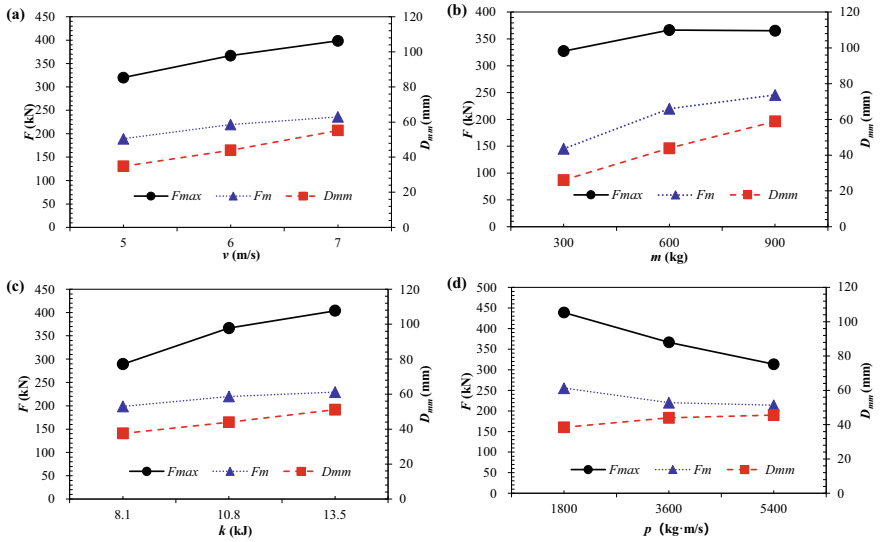


**Fig. 6.33** Effects of **a** impact velocity, **b** hammer mass, **c** kinetic energy and **d** momentum of the hammer on the peak impact force, post-peak mean force and maximum center displacement, reprinted from Wang et al. (2022), copyright 2022, with permission from Elsevier

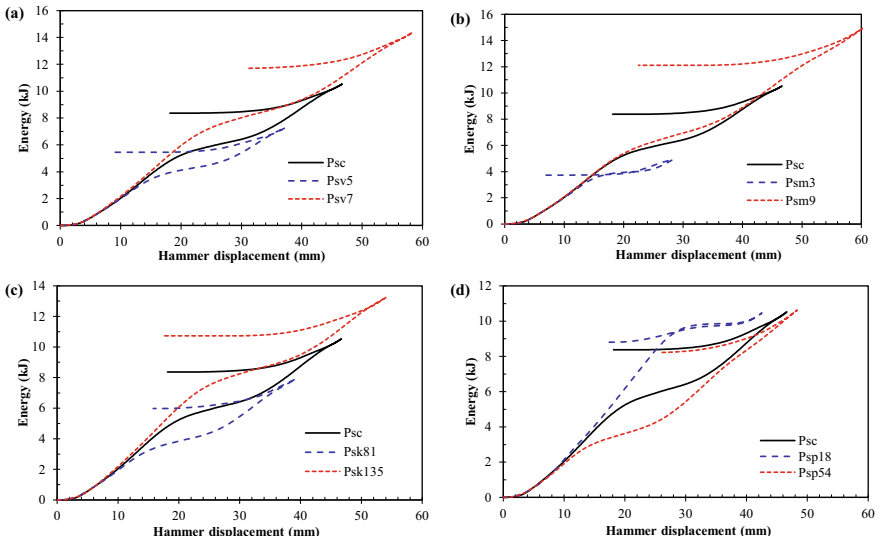


**Fig. 6.34** Effects of **a** impact velocity, **b** hammer mass, **c** kinetic energy, and **d** momentum of the hammer on the energy–hammer displacement curves, reprinted from Wang et al. (2022), copyright 2022, with permission from Elsevier

Figure 6.33b presents the influence of mass of hammer on the peak impact force, post-peak mean force and maximum center displacement of the SESCS sandwich panel. The increase in the hammer mass from 300 kg to 600 and 900 kg shows a limited influence on the peak impact force of the SESCS sandwich panel (i.e., increase by 12.11 and 12.48%, respectively). However, a noticeable increase of post-peak mean force by 51.24 and 68.97% is observed owing to the higher impact energy applied on the panel. Moreover, increasing hammer mass from 300 kg to 600 and 900 kg also leads to 68.89% and 126.19% increase in the maximum center displacement, which is also due to the significantly increased impact energy (by 100% and 200%). Likewise, the increase in magnitude of maximum center displacement is less significant as compared to the improvement of impact energy. The influence of increase in hammer mass on the energy absorption behavior of the SESCS sandwich panel is found to be similar to the influence of increasing impact velocity, as presented in Fig. 6.34b.

Figure 6.33c presents the effect of impact energy on the impact response of the SESCS sandwich panel. Herein, the same momentum of the hammer is kept by varying both the impact velocity and hammer mass, as presented in Table 6.8. It is noted in Fig. 6.33c that the peak impact force, post-peak mean force and maximum center displacement exhibit increase with the increase of impact energy, which is consistent with the effects of impact velocity and hammer mass on the impact response of the SESCS sandwich panel. The peak impact force, post-peak mean force and maximum center displacement are increased by 39.56%, 15.41% and 36.03%, respectively, on increasing the impact energy from 8.1 to 13.5 kJ (by 66.67%). Energy–hammer displacement curves plotted in Fig. 6.34c also demonstrates that the energy absorbed by the SESCS sandwich panel increases with the increase in the applied impact energy (or initial kinetic energy). Higher applied impact energy results in higher peak impact force and post-peak mean force, which also leads to an increased energy absorbing rate of the SESCS sandwich panel.

The influence of momentum of the hammer on the impact response of the SESCS sandwich panel is presented in Fig. 6.33d. Herein, the same impact energy of the hammer is kept by varying both the impact velocity and hammer mass, as listed in Table 6.8. The peak impact force in Fig. 6.33d exhibits an evident decrease (by 16.34 and 28.57%, respectively) by increasing the momentum of the hammer from 1800 kg·m/s to 3600 and 5400 kg·m/s. This is mainly caused by the reduced impact velocity, i.e., the impact velocity is reduced from 12 m/s to 6 and 4 m/s. This indicates that the peak impact force is more sensitive to the impact velocity, which is consistent with the observation from Fig. 6.33a. Figure 6.33d also indicates that the increase of momentum leads to the reduction of post-peak mean force, but the increase of maximum center displacement. Although the same impact energy is applied on the SESCS sandwich panel, the reduced impact velocity may result in a smaller strain rate and resistance of the panel. Hence, lower post-peak mean force and higher maximum center displacement are observed for the panel subjected to the impact with a higher momentum (or smaller impact velocity). The energy versus hammer displacement curves in Fig. 6.34d also shows that the energy absorbed by the panels is approximately the same owing to the identical applied impact energy. In addition,

the energy absorbing rate is found to be reduced by increasing momentum of the hammer owing to the reduced post-peak mean force.

## 6.4 Summary

A new SCS sandwich structure enhanced with stiffeners in the tension plate (i.e., SESCS sandwich structure) was proposed for impact resisting. The impact responses of SESCS sandwich beams and panels were studied and presented in this chapter. The main findings are summarized as follows:

- (1) All the SESCS sandwich beams exhibited flexural failure modes with evident plastic hinges located at their mid-spans, which resulted in vertical cracks and crushing of concrete in the tension and compression zone, respectively. Some slippages between the bottom plate and concrete core were observed, which could be caused by the vertical and diagonal cracks near the support. Experimental results revealed that the impact resistance of the SESCS sandwich beam was significantly improved as compared to the SCS sandwich beam with bolt connectors.
- (2) The impact resistance of the SESCS sandwich beam was found to be improved by increasing concrete core and faceplate thickness in terms of larger post-peak mean force and smaller deflection.
- (3) Numerical studies on the SESCS sandwich beam under impact loading were conducted, and the damage evolution of the concrete core during impact was revealed. Moreover, the whole cross-section of the stiffener at the mid-span was found to yield, which demonstrated the effective enhancement of the stiffener to the bending resistance of the beam. An analytical model based on the equivalent SDOF system was proposed for predicting the displacement response of the SESCS sandwich beam under impact loading, and reasonable predictions from the analytical model was demonstrated.
- (4) All the SESCS sandwich panels exhibited the combined deformation mode of global flexure and location indentation, and three types of concrete cracks were observed, including vertical cracks at mid-span, diagonal cracks near the support, and vertical cracks above the support.
- (5) The proposed SESCS sandwich panels with stiffeners in tension plate exhibited superior impact resistance compared to the traditional SCS sandwich panel in terms of higher peak impact force and post-peak impact force as well as smaller deformation. The maximum displacement of the SESCS sandwich panel was reduced by 36.90% on increasing the thickness concrete core by 20 mm, and there was a reduction of 15.67% by increasing the steel plate thickness from 2.84 to 4.46 mm.
- (6) The damage evolution of concrete core of the SESCS sandwich panel during impact was revealed. Punching shear failure of concrete core was observed at

- the impact zone, whereas flexure-induced damage of concrete at the free side of the panel was observed.
- (7) Parametric studies indicated that the peak impact force was more sensitive to the impact velocity. The post-peak mean force was found to be increased by increasing the impact velocity and mass of hammer. The maximum displacement of the SESCS sandwich panel was slightly increased by increasing the momentum of the hammer even though the same impact energy was applied on the panel.

## References

- Abramowicz W, Jones N (1986) Dynamic progressive buckling of circular and square tubes. *Int J Impact Eng* 4:243–270
- ASCE/SEI 59-11 (2011) Blast protection of buildings. American Society of Civil Engineers, Reston, Virginia
- Biggs JM (1964) Introduction to structural dynamics. McGraw-Hill, New York
- Chen W, Hao H, Chen S (2015) Numerical analysis of prestressed reinforced concrete beam subjected to blast loading. *Mater Des* 65:662–674
- Clubley S K, Moy SSJ, Xiao RY (2003) Shear strength of steel-concrete-steel composite panels. Part I—testing and numerical modelling. *J Constr Steel Res* 59:781–794
- Dogan O, Roberts TM (2012) Fatigue performance and stiffness variation of stud connectors in steel-concrete-steel sandwich systems. *J Constr Steel Res* 70:86–92
- Eurocode 4 (2004a) Design of composite steel and concrete Structures—Part 1.1: General rules and rules for buildings, BS EN 1994–1–1, London
- Eurocode 2 (2004b) Design of concrete structures—Part 1–1: General rules and rules for buildings, BS EN 1992–1–1, London
- Federal Highway Administration (2007a) Evaluation of LS-DYNA concrete material model 159
- Federal Highway Administration (2007b) Users manual for LS-DYNA concrete material model 159
- Foundoukou N (2005) Behavior and design of steel-concrete-steel sandwich construction. Dissertation, University of London
- Gu X, Jin X, Zhou Y (2015) Basic principles of concrete structures. Tongji University Press, Shanghai
- Guo YT, Chen J, Nie X et al (2020) Investigation of the shear resistance of steel-concrete-steel composite structures with bidirectional webs. *J Constr Steel Res* 164:105846
- Guo Q, Zhao W (2019a) Design of steel-concrete composite walls subjected to low-velocity impact. *J Constr Steel Res* 154:190–196
- Guo Q, Zhao W (2019b) Displacement response analysis of steel-concrete composite panels subjected to impact loadings. *Int J Impact Eng* 131:272–281
- Hallquist JO (2013) LS-DYNA keyword user's manual. Livermore Software Technology Corporation (LSTC). Livermore, California
- Hallquist JO (2006) LS-DYNA theory manual. Livermore Software Technology Corporation (LSTC). Livermore, California
- Li X, Chen JF, Lu Y et al (2015) Modelling static and dynamic FRP-concrete bond behavior using a local concrete damage model. *Adv Struct Eng* 18(1):45–58
- Liew JYR, Sohel KMA (2009) Lightweight steel-concrete-steel sandwich system with J-hook connectors. *Eng Struct* 31:1166–1178

- Liew JYR, Sohel KMA, Koh CG (2009) Impact tests on steel-concrete-steel sandwich beams with lightweight concrete core. *Eng Struct* 31(9):2045–2059
- Liew JYR, Sohel KMA, Koh CG (2015) Numerical modeling of lightweight steel-concrete-steel sandwich composite beams subjected to impact. *Thin-Walled Struct* 94:135–146
- Lu J, Wang Y, Zhai X (2021) Response of flat steel-concrete-corrugated steel sandwich panel under drop-weight impact load by a hemi-spherical head. *J Build Eng* 44:102890
- Nie JG, Ma XW, Tao MX et al (2014) Effective stiffness of composite shear wall with double plates and filled concrete. *J Constr Steel Res* 99:140–148
- Oduyemi TOS, Wright HD (1989) An experimental investigation into the behavior of double skin sandwich beams. *J Constr Steel Res* 14(3):197–220
- Remennikov AM, Kong SY (2012) Numerical simulation and validation of impact response of axially-restrained steel-concrete-steel sandwich panels. *Compos Struct* 94(12):3546–3555
- Remennikov AM, Kong SY, Uy B (2013) The response of axially restrained non-composite steel-concrete-steel sandwich panels due to large impact loading. *Eng Struct* 49:806–818
- Shariati M, Ramli Sulong NH, Arabnejad Khanouki MM (2012) Experimental assessment of channel shear connectors under monotonic and fully reversed cyclic loading in high strength concrete. *Mater Des* 34:325–331
- Shariati M, Ramli Sulong NH, Shariat A et al (2013) Comparison of behaviour between channel and angle shear connectors under monotonic and fully reversed cyclic loading. *Constr Build Mater* 38:582–593
- Shariati M, Ramli Sulong NH, Shariat A et al (2016) Comparative performance of channel and angle shear connectors in high strength concrete composites: an experimental study. *Constr Build Mater* 120:382–392
- Sohel KMA, Liew JYR (2014) Behavior of steel-concrete-steel sandwich slabs subject to impact load. *J Constr Steel Res* 100:163–175
- Sohel KMA, Liew JYR, Alwis WAM et al (2003) Experimental investigation of low-velocity impact characteristics of steel-concrete-steel sandwich beams. *Steel Compos Struct* 3(4):289–306
- Subedi NK, Coyle NR (2002) Improving the strength of fully composite steel-concrete-steel beam elements by increased surface roughness—an experimental study. *Eng Struc* 24:1349–1355
- Thang V, Marshall P, Brake NA et al (2016) Studded bond enhancement for steel-concrete-steel sandwich shells. *Ocean Eng* 124:32–41
- Wang Y, Liew JYR, Lee SC (2015a) Theoretical models for axially restrained steel-concrete-steel sandwich panels under blast loading. *Int J Impact Eng* 76:221–231
- Wang Y, Lu J, Liu S et al (2021) Behaviour of a novel stiffener-enhanced steel-concrete-steel sandwich beam subjected to impact loading. *Thin-Walled Struct* 165:107989
- Wang Y, Qian X, Liew JYR et al (2014) Experimental behavior of cement filled pipe-in-pipe composite structures under transverse impact. *Int J Impact Eng* 72:1–16
- Wang Y, Qian X, Liew JYR et al (2015b) Impact of cement composite filled steel tubes: An experimental, numerical and theoretical treatise. *Thin-Walled Struct* 87:76–88
- Wang Y, Sah TP, Liu S et al (2022) Experimental and numerical studies on novel stiffener-enhanced steel-concrete-steel sandwich panels subjected to impact loading. *J Build Eng* 45:103479
- Wang Y, Zhai, X, Lee SC et al (2016) Response of curved steel-concrete-steel sandwich shells subjected blast loading. *Thin-Walled Struct* 108:185–192
- Wang Z, Yan J, Liu Y et al (2020) Mechanical properties of steel-UHPC-steel slabs under concentrated load considering composite action. *Eng Struct* 222:111095
- Xie M, Foundoukos N, Chapman J.C (2007) Static tests on steel-concrete-steel sandwich beams. *J Constr Steel Res* 63(6):735–750
- Yan C, Wang Y, Zhai X (2020a) Low velocity impact performance of curved steel-concrete-steel sandwich shells with bolt connectors. *Thin-Walled Struct* 150:106672
- Yan C, Wang Y, Zhai X et al (2020b) Strength assessment of curved steel-concrete-steel sandwich shells with bolt connectors under concentrated load. *Eng Struct* 212:110465
- Yan JB, Guan H, Wang T (2020c) Steel-UHPC-steel sandwich composite beams with novel enhanced C-channel connectors: Tests and analysis. *J Constr Steel Res* 170:106077

- Yan JB, Hu H, Wang T (2020d) Shear behavior of novel enhanced C-channel connectors in steel-concrete-steel sandwich composite structures. *J Constr Steel Res* 166:105903
- Yan JB, Liew JYR, Zhang MH et al (2015) Experimental and analytical study on ultimate strength behaviour of steel-concrete-steel sandwich composite beam structures. *Mater Struct* 48(5):1523–1544
- Zhao W, Guo Q (2018) Experimental study on impact and post-impact behavior of steel-concrete composite panels. *Thin-Walled Struct* 130:405–413
- Zhao W, Guo Q, Dou X et al (2018) Impact response of steel-concrete composite panels: Experiments and FE analyses. *Steel Compos Struct* 26(3):255–263

# Chapter 7

## Curved Steel–Concrete–Steel Sandwich Shells Under Impact



### 7.1 Introduction

A curved steel–concrete–steel (CSCS) sandwich shell is composed of two curved steel plates, concrete core and shear connectors. It is developed to be mainly used in nuclear plants, offshore platforms, arctic caissons and protective structures (Ali et al. 2013; Hoff 1998; Huang and Liew 2016d; Huang et al. 2015b; Montague 1975) owing to its good mechanical performance. Meanwhile, the concrete debris will not spall outside when subjected to impact load owing to confinement provided by steel plates, which is suitable for protective structures (Mizuno et al. 2005).

Most of the existing studies were concentrated on the performances of SCS sandwich structures subjected to static load. To name a few, Yan et al. (2019a) conducted static experiments on CSCS sandwich shells under concentrated load. Lin et al. (2018 and 2019) explored the failure mechanisms of SCS beams through static tests, and their failure types were also identified. The extensive studies on the static performances of CSCS sandwich shells were also conducted (Yan et al. 2016a, b, c, 2019b; Yan and Zhang 2017). Huang and Liew (2016a, c) proposed the SCS wall and established an analytical model to calculate its resistance. Huang and Liew (2015a; 2016b) also carried out experimental, numerical and analytical studies on SCS panels with novel ultra-lightweight cement as core material. The flexure and shear performances of SCS slabs were also experimentally studied (Leng et al. 2015; Leng and Song 2017), and an analytical model was developed to predict their resistances.

However, the studies on impact behaviors of SCS sandwich structures (especially CSCS sandwich shells) are still limited. Liew et al. (2009) and Sohel et al. (2015) carried out experimental studies on SCS beams subjected to impact loading, and an analytical model was developed to predict their force–indentation relationships. In addition, Sohel and Liew (2014) also studied the impact behaviors of SCS sandwich slabs by employing experimental and analytical methods. Remennikov and Kong (2012) and Remennikov et al. (2013) conducted low-velocity impact tests on the axially-restrained SCS sandwich panels, and the corresponding Finite Element (FE) models were also established and validated against the test data. The responses of

SCS sandwich panels under drop-weight impact loading were experimentally and numerically studied (Zhao and Guo 2018; Zhao et al. 2018). Moreover, an analytical model was developed by Guo and Zhao (2019) for predicting displacement responses of the SCS sandwich panels under impact loading. With regard to the SCS sandwich panel under blast loading, its analytical model was developed and validated with the FE results (Wang et al. 2015, 2016b). Wang et al. (2016a) also experimentally studied the SCS sandwich panels under lateral pressure load, and the uniform pressure loading was achieved by employing an inflated airbag. However, all previous studies were focused on impact performances of SCS sandwich beams or panels, while limited works were carried out on impact performances of CSCS sandwich shells which had been proven to have superior performance under static loading (Huang et al. 2015b; Yan et al. 2016a, 2019a). Therefore, the impact performances of CSCS sandwich shells need to be studied to promote the application of such structure in resisting impact loading.

In this chapter, impact tests on nine CSCS sandwich shells were conducted by dropping a hammer with hemispherical head to obtain the impact force, displacement histories and failure modes. The effects of concrete thickness, steel plate thickness and spacing of shear connectors on the impact performances of CSCS sandwich shells were discussed. The FE models of CSCS sandwich shells were established and validated by comparing the FE-predicted impact force histories, displacement histories and failure modes with experimental results. In addition, an analytical model based on the equivalent single-degree-of-freedom (SDOF) method was proposed for predicting displacement responses of the CSCS sandwich shells under impact loading.

## 7.2 Test Program

### 7.2.1 Specimens

Nine CSCS sandwich shells were tested under drop-weight impact loading. Figure 7.1 illustrates the geometries of the specimens. The width ( $W$ ), span ( $L$ ), radius ( $R$ ) and rise height ( $H$ ) of all the nine specimens are 1200, 1200, 750 and 300 mm, respectively. High strength bolts with grade 8.8 were used as shear connectors in order to achieve strong composite action. The diameter of bolt was 12 mm. Four parameters were experimentally studied based on nine test specimens, including concrete thickness (70, 80 and 90 mm), steel plate thickness (2.87, 3.57 and 4.54 mm), thickness ratio of top to bottom steel plate (2.87–4.54 and 4.54–2.87 mm-mm) and spacing of shear connector (140, 200 and 260 mm), as shown in Table 7.1. The fabrication process of CSCS sandwich shells are given in Fig. 7.2. The steel plates were rolled into curved shape in the factory and welded to the end plates for forming the skeletons of CSCS shells. The bolts were installed through the holes reserved on the steel plates. Subsequently, the skeletons of CSCS shells were erected on the

**Fig. 7.1** General illustration of the CSCS sandwich shell, reprinted from Yan et al. (2020a), copyright 2022, with permission from Elsevier

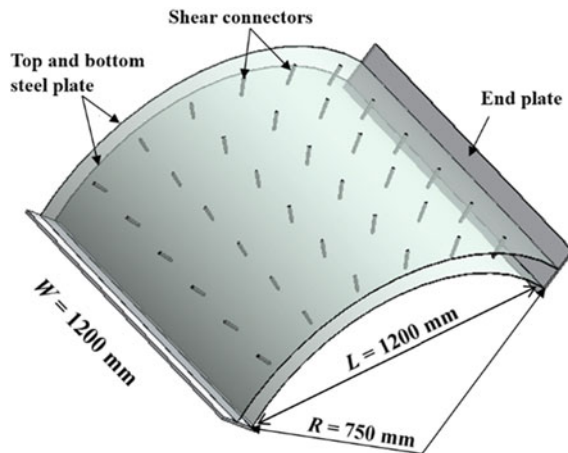


**Table 7.1** Parameters of CSCS sandwich shells

Specimen	$t_c$ (mm)	$f_c$ (MPa)	$t_{ts}$ (mm)	$t_{bs}$ (mm)	$f_y$ (MPa)	$E_s$ (GPa)	$S$ (mm)
CSCS3-70-3-200	70	32.73	2.87	2.87	350.32	209.27	200
CSCS3-80-3-200	80	32.73	2.87	2.87	350.32	209.27	200
CSCS3-90-3-200	90	32.73	2.87	2.87	350.32	209.27	200
CSCS4-70-4-200	70	32.73	3.57	3.57	307.28	206.70	200
CSCS5-70-5-200	70	32.73	4.54	4.54	332.70	215.61	200
CSCS3-70-5-200	70	32.73	2.87	4.54	350.32/332.70	209.27/215.61	200
CSCS5-70-3-200	70	32.73	4.54	2.87	332.70/350.32	215.61/209.27	200
CSCS3-70-3-140	70	32.73	2.87	2.87	350.32	209.27	140
CSCS3-70-3-260	70	32.73	2.87	2.87	350.32	209.27	260

Note  $t_c$  is concrete core thickness,  $t_{ts}$  is top steel plate thickness,  $t_{bs}$  is bottom steel plate thickness,  $f_c$  is compressive strength of concrete,  $f_y$  is yield strength of steel plate,  $E_s$  is elastic modulus of steel plate, and  $S$  is spacing of shear connector

ground, and concrete casting was implemented. After 28 days curing of the concrete, the fabrication of specimens was completed.

### 7.2.2 Materials

Q235 mild steel was employed for the skeletons of CSCS sandwich shells, including top and bottom steel plates as well as end plates (in Fig. 7.1). The material properties of mild steel were obtained through conducting tensile coupon tests. Table 7.1 shows the yield stress ( $f_y$ ) and elastic modulus ( $E_s$ ) of steel plates with different thicknesses. The unconfined compressive strength of concrete was 32.73 MPa, and its elastic



**Fig. 7.2** Fabrication process: **a** rolling steel plates into curved shape, **b** erecting CSCS sandwich shells and **c** casting concrete, reprinted from Yan et al. (2020a), copyright 2022, with permission from Elsevier

modulus was 27.13 GPa. The yield and ultimate stress of bolt were 640 and 800 MPa, respectively.

### 7.2.3 Test Setup

The impact tests were carried out by utilizing a drop-weight impact test device, as shown in Fig. 7.3. The drop-weight impact test device is composed of a hammer with 100-mm-diameter hemispherical head, alterable counterweights (from 400 to 1000 kg) as well as a 600-kN force sensor which is installed between the hammer head and counterweights. The hammer weight ( $M$ ) was 800 kg, and the drop height was 3 and 5 m, as given in Table 7.2.

CSCS sandwich shells were fixed to the triangular supports (refer to Fig. 7.3) via 18 bolts with diameter of 20 mm. The triangular supports were settled on the supporting beam (refer to Fig. 7.3) by 32 high strength bolts with diameter of 30 mm. All movements and rotations of the end plates of the CSCS sandwich shells are restrained by bolts to realize the fixed boundary condition. The high-speed camera was employed to capture the drop hammer with 2000 frames per second. In order to obtain the displacement histories of the bottom steel plate, two displacement transducers were used, and their layouts are shown in Fig. 7.4. The data logger TST5912 was used to record the impact forces and displacements.

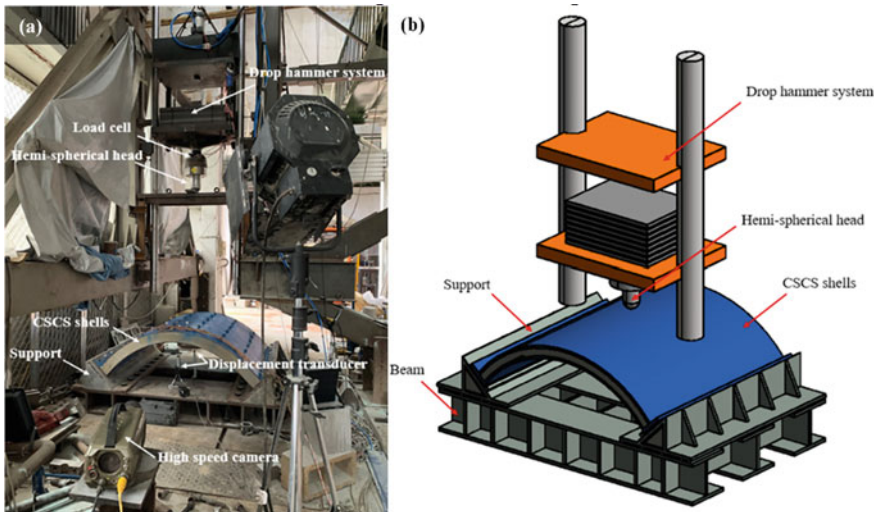


**Fig. 7.3** Drop-weight impact test setup **a** photo and **b** 3D view, reprinted from Yan et al. (2020a), copyright 2022, with permission from Elsevier

## 7.3 Test Results and Discussions

Nine CSCS sandwich shells were tested against low-velocity impact loading. Eight specimens were subjected to the impact loading by dropping the hammer with drop height of 3 m. One specimen (CSCS3-70-3-260) was tested under the impact loading with drop height of 5 m to obtain the severe damage of the CSCS sandwich shell. Therefore, the effects of different parameters on impact performances of the CSCS sandwich shells were analyzed based on the former eight specimens with the same impact loading.

### 7.3.1 Damage Analysis of CSCS Shells

All specimens exhibited a deformation mode combined by local and global deformation. The central displacement of the bottom steel plate ( $D_b$ ) was obtained by the displacement transducer WB2 (refer to Fig. 7.4). The displacement of the hammer ( $D_h$ ) was measured by the high-speed camera.

The failure modes of all nine CSCS shells are dominated by local indentation and can be categorized into three types (refers to Fig. 7.5). Failure type I (plastic deformation of steel plate without fracture) occurred to specimen CSCS5-70-5-200, CSCS5-70-3-200 and CSCS3-70-3-140. Failure type II (fracture of top steel plate) occurred to specimen CSCS3-70-3-200, CSCS4-70-4-200 and CSCS3-70-5-200. Failure type

**Table 7.2** Test parameters and results

Specimen	Drop height $H$ (m)	Drop hammer weight $M$ (kg)	Initial energy $E_0$ (kJ)	Inertial peak force $F_I$ (kN)	Peak impact force $F_p$ (kN)	$D_{bmax}$ (mm)	$D_{hmax}$ (mm)	Failure type
CSCS3-70-3-200	3	800	23.54	202.34	304.86	57.00	72.47	II
CSCS3-80-3-200	3	800	23.54	224.80	316.40	49.68	70.87	III
CSCS3-90-3-200	3	800	23.54	282.45	331.71	41.75	65.04	III
CSCS4-70-4-200	3	800	23.54	208.35	339.73	54.04	68.99	II
CSCS5-70-5-200	3	800	23.54	238.19	389.93	49.31	51.35	I
CSCS3-70-5-200	3	800	23.54	206.44	361.72	49.83	54.84	II
CSCS5-70-3-200	3	800	23.54	226.73	369.71	48.68	50.44	I
CSCS3-70-3-140	3	800	23.54	218.15	360.21	52.45	55.21	I
CSCS3-70-3-260	5	800	39.23	264.13	292.79	-	154.10	III

Note Failure type I means plastic deformation of steel plate without fracture, type II means fracture of top steel plate, and type III means penetration of top steel plate

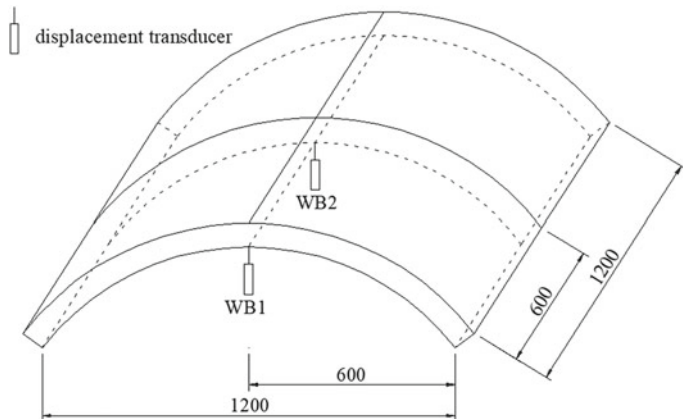


**Fig. 7.4** Layout of displacement transducers, reprinted from Yan et al. (2020a), copyright 2022, with permission from Elsevier

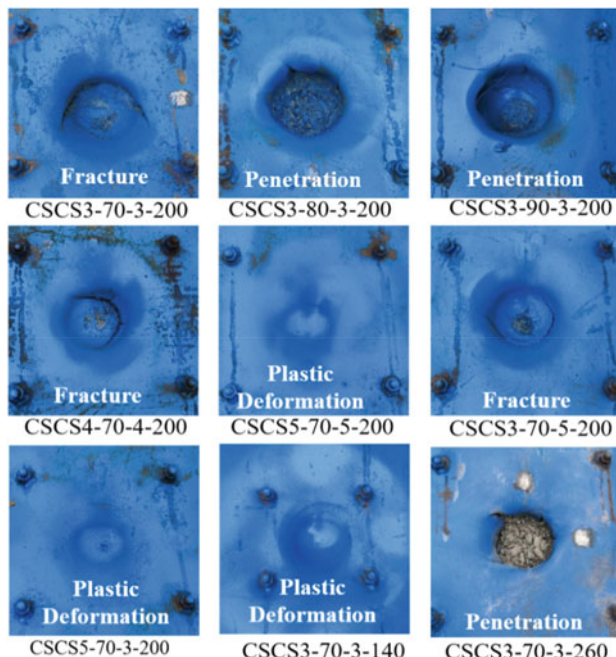


**Fig. 7.5** Local deformation of top steel plate, reprinted from Yan et al. (2020a), copyright 2022, with permission from Elsevier

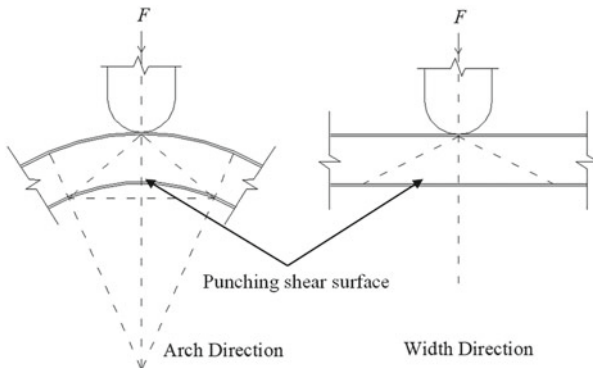
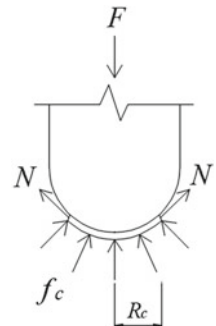


**Fig. 7.6** Concrete punching shear failure, reprinted from Yan et al. (2020a), copyright 2022, with permission from Elsevier

III (penetration of steel plate) was observed for specimen CSCS3-80-3-200, CSCS3-90-3-200 and CSCS3-70-3-260. With thicker top steel plate and smaller spacing of shear connectors, the impact resistance and composition action of specimens were improved, which resulted in minor damage of the CSCS shell (Failure type I). This is because the thicker steel plate improved the punching shear resistance of the CSCS sandwich shell, which has been proved in former studies (Yan et al. 2019a, 2016a). The failure mode of the CSCS sandwich shell subjected to low-velocity impact load is similar to that under static concentrated load, i.e., initial punching shear failure and subsequent membrane stretching of steel plates (Yan et al. 2019a). When the deformation was small, the steel plate and concrete core resisted impact force together, as illustrated in Fig. 7.6. In this stage, concrete core was the main contributor to the impact resistance. After the concrete core was punched, the membrane stretching of the top steel plate mainly contributed to the impact resistance. The concrete could still offer some impact resistance, as the bottom steel plate provided confinement to the concrete core (refers to Fig. 7.7). Thus, the thicker steel plate resulted in higher impact resistance of the CSCS shell. The impact resistance of the CSCS shell would be decreased as the decease of top steel plate thickness. Thus, the failure damage

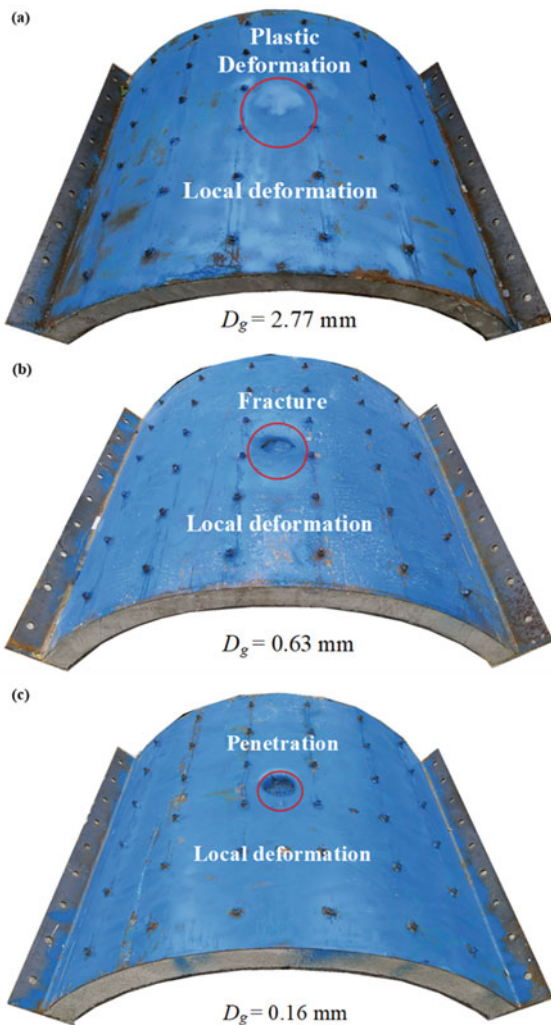
**Fig. 7.7** Membrane stretching of steel plate, reprinted from Yan et al. (2020a), copyright 2022, with permission from Elsevier



became more serious, which was fracture of the top steel plate in this test. However, if the spacing of shear connectors was too large, the composition action of the CSCS shell would be weakened, leading to the most serious failure type (penetration of top steel plate). Meanwhile, the thicker concrete core could enhance the impact resistance of the CSCS shell (i.e., higher impact force and smaller displacements of both bottom steel plate and hammer), but could result in the most serious failure type owing to reduced local deformation zone. The reason is that thicker concrete core resulted in higher stiffness of the CSCS shell, which could reduce the indentation of concrete core near the periphery of drop hammer and lead to smaller area of local deformation. Moreover, thicker concrete core resulted in smaller deformation of steel plates, which can be seen from Table 7.2 that both  $D_h$  and  $D_b$  decreased with increasing thickness of concrete core. Figure 7.8 shows the global deformation of the CSCS shells with typical three failure types after impact tests. The permanent global deformation ( $D_g$ ) was measured by the displacement transducer WB1 (refers to Fig. 7.4). It shows that the  $D_g$  of the specimens with three failure types were small (i.e., the ratio of global deformation to local deformation is less than 9.9% for all the tested specimens). The specimen with more serious failure type had smaller area of local deformation and global deformation. For thicker concrete core and thinner steel plates, the impact energy was mainly absorbed by the shear failure of concrete and fracture of top steel plate. While for thicker steel plates, the fracture of top steel plate was prevented, and thus the impact energy dissipated by global deformation was relatively higher.

Figure 7.9a shows the impact force and displacement histories of specimen CSCS5-70-5-200 with failure type I. The impact process is composed of three stages, i.e., inertial stage, loading stage and unloading stage (Zhao and Guo 2018). The inertial stage occurred in the first 2 ms. The drop hammer and the CSCS sandwich shell contacted during inertial stage, resulting in the local impact zone of the shell being forced to move downwards with the same velocity of the drop hammer. Thus, the impact force increased rapidly to a peak value. However, the significant change of impact force at this stage was induced by inertial effect and could not represent the actual load carrying capacity of the CSCS shell (Zhao and Guo 2018). The impact force vibrated after the inertial peak. Meanwhile, the central displacement of the bottom steel plate ( $D_b$ ) and hammer displacement ( $D_h$ ) increased rapidly. The loading stage occurred from 2 to 13 ms for specimen CSCS5-70-5-200. The drop hammer and CSCS sandwich shell moved together with the impact force increasing in this stage owing to the increasing resistance of the CSCS shell via membrane stretching of the top steel plate. When the specimen reached its maximum displacement, the impact force also achieved to its maximum value which was called peak impact force ( $F_p$ ). The impact force in this stage could generally represent the load carried by the CSCS shell. The local deformation zone was continuously expanding to achieve an increasing membrane resistance of the shell. The concrete core was also crushed, and partial impact force was transferred to the bottom steel plate through the concrete core and shear connectors. The loading stage finished as the velocity of the hammer reduced to zero. The unloading stage occurred from 13 to 23 ms for CSCS5-70-5-200. In this stage, the energy stored in the CSCS shell started to decrease. The impact

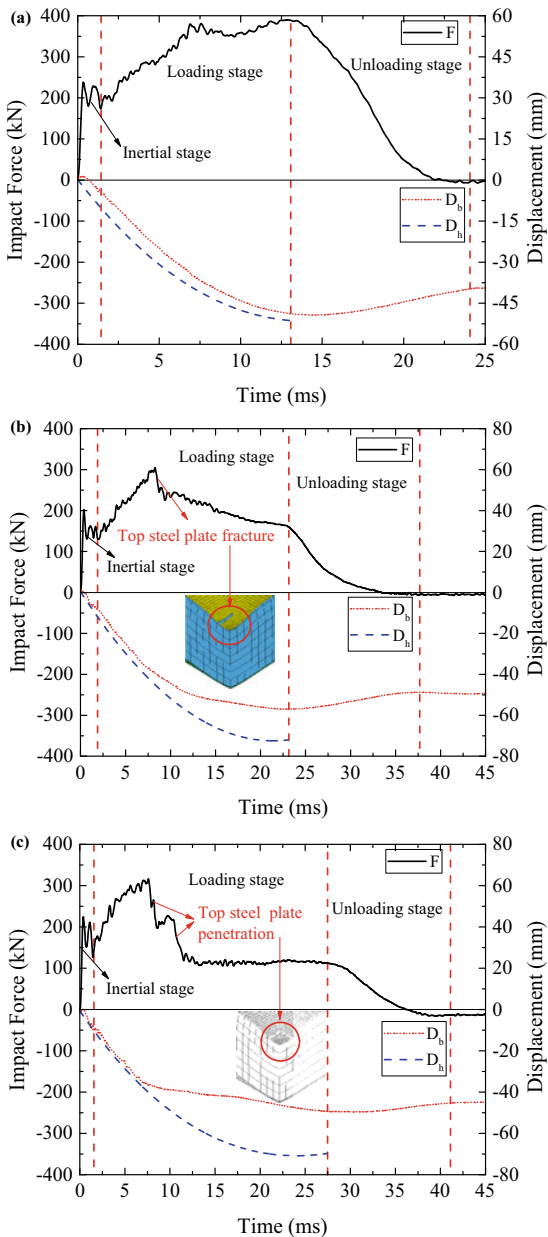
**Fig. 7.8** Global deformation of three failure types ( $D_g$  is global deformation): **a** CSCS5-70-5-200, **b** CSCS3-70-3-200, **c** CSCS3-80-3-20, reprinted from Yan et al. (2020a), copyright 2022, with permission from Elsevier



force would drop down to zero after the hammer rebounded, and the  $D_b$  recovered to a stable value. The two steel plates deformed together to resist impact load, and therefore the values of  $D_h$  and  $D_b$  showed same trend. However, almost constant difference between  $D_h$  and  $D_b$  during impact process observed in Fig. 7.9a was due to the local indentation.

As for the impact force and displacement histories of specimen CSCS3-70-3-200 with failure type II in Fig. 7.9b, three stages during impact process can also be observed, similar to the specimens with failure type I. However, the steel plate started to fracture at 6 ms during loading stage, which led to a sudden drop of impact force (refer to Fig. 7.9b). At this moment, the hammer still went downwards, while the

**Fig. 7.9** Impact force and central displacement histories for specimens with different failure types: **a** CSCS5-70-5-200, **b** CSCS3-70-3-200, **c** CSCS3-80-3-200, reprinted from Yan et al. (2020a), copyright 2022, with permission from Elsevier



impact force monotonically decreased because of the continuous fracture of the top steel plate. When the displacement reached to the maximum value, the velocity of the hammer reduced to zero, and the loading stage finished. The difference between  $D_h$  and  $D_b$  was stable before fracture of the top steel plate. After that, slower increase of  $D_b$  as compared to  $D_h$  was observed, which could be attributed to the reduced impact energy transferred to the bottom steel plate after fracture of the top steel plate, i.e., partial impact energy originally dissipated by the bottom steel plate before fracture was dissipated by concrete and top steel plate.

Figure 7.9c shows the impact force and displacement histories of specimen CSCS3-80-3-200 with failure type III, and similar three stages during impact process can also be observed. However, the top steel plate was penetrated by the hammer (6–12 ms in Fig. 7.9c), which led to the drop of impact force from the peak value to a stable value. At this moment, the hammer continuously moved downwards, while the impact force remained a stable value. This stable impact resistance was provided by the concrete core below the hammer head, which was confined by surrounding concrete and bottom steel plate. The difference between  $D_h$  and  $D_b$  remained stable before penetration of the top steel plate. After that, slower increase of  $D_b$  was seen, and the difference between  $D_h$  and  $D_b$  after penetration was more significant as compared to failure type II, which was due to more portion of impact energy dissipated by penetration of the top steel plate and subsequent crushing of concrete.

### 7.3.2 Impact Force History

Figure 7.10 depicts impact force–time histories of eight specimens under the same impact loading, and the influences of concrete core thickness, steel plate thickness, thickness ratio of top to bottom steel plate and spacing of shear connectors were discussed as follows.

Figure 7.10a shows the influences of concrete core thickness (70, 80, and 90 mm) on impact force histories. The variation of concrete core thickness showed little effect on peak impact force (increased from 304.86 to 316.40 kN and 331.71 kN). However, by increasing the thickness of concrete core, the failure type was shifted from fracture of the top steel plate to penetration, resulting in more serious damage. The reason is that thicker concrete core resulted in smaller area of local deformation and more serious damage of the top steel plate. Yan et al. (2019a) have observed the similar behaviors in the former studies on CSCS shells under concentrated load applied in a quasi-static manner. Generally, the inertial peak force is affected by impact velocity, mass and contact stiffness. The impact velocity and mass were same for the eight specimens, and therefore only contact stiffness affects the inertial peak force in this test. Figure 7.10a shows that thicker concrete core can enhance the contact stiffness, leading to the higher inertial peak force from 202.34 kN to 224.80 and 282.45 kN (improved by 11.1% and 39.6%).

Figure 7.10b shows the effect of steel plate thickness (2.87, 3.57 and 4.54 mm) on impact force histories. By increasing steel plate thickness from 2.87 to 3.57 and

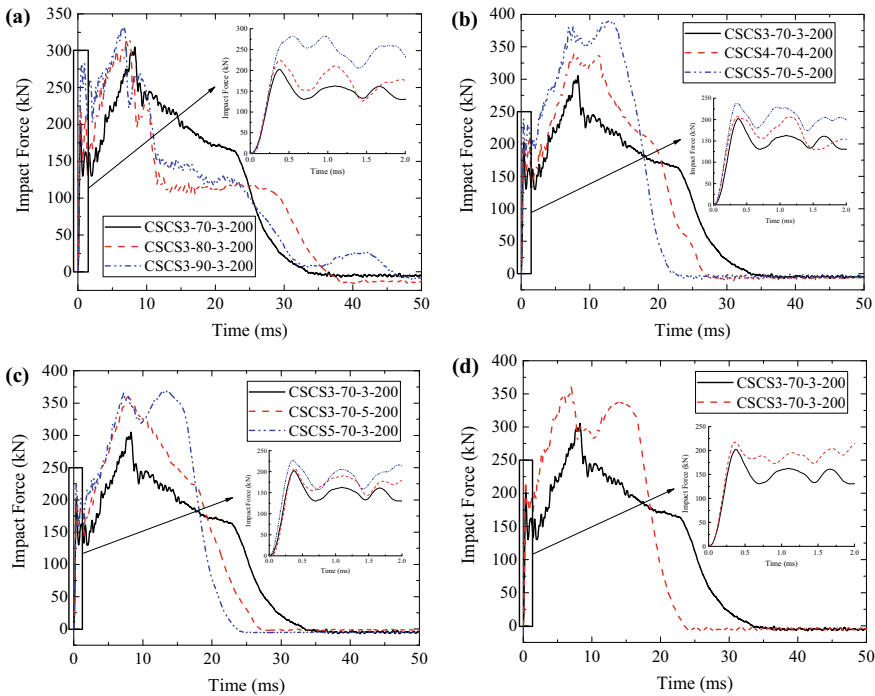


**Fig. 7.10** Comparison of impact force histories for specimens: **a** concrete core thickness, **b** steel plate thickness, **c** top to bottom steel plate thickness ratio and **d** spacing of shear connectors, reprinted from Yan et al. (2020a), copyright 2022, with permission from Elsevier

4.54 mm, the peak impact force was improved from 304.86 to 339.73 and 389.93 kN, respectively (improved by 10.2% and 27.9%). Meanwhile, the damage of CSCS shell could be mitigated, as “plastic deformation of steel plate without fracture” occurred to CSCS5-70-5-200 with thickest steel plate. The thicker steel plate means higher strength, which resulted in higher impact force of the CSCS shell during loading stage. Moreover, the thicker steel plate could dissipate more impact energy and resulted in less damage of the CSCS shell. Increasing thickness of steel plate also enhanced contact stiffness, leading to higher inertial peak force from 202.34 to 208.35 kN and 238.19 kN (improved by 3.0 and 17.7%).

Figure 7.10c depicts the influence of thickness ratio of top-to-bottom steel plate on impact force. Both CSCS3-70-5-200 and CSCS5-70-3-200 (with same total thickness of top and bottom steel plates, but different thickness ratio) exhibited the similar peak impact force, but the failure types of them were different. No fracture was observed for specimen CSCS5-70-3-200 with thicker top steel plate. However, fracture of the top steel plate occurred to specimen CSCS3-70-5-200. The inertial peak force showed in Fig. 7.10c indicates that increasing top steel plate thickness could enhance the contact stiffness, and therefore the higher inertial peak force was observed for specimen CSCS5-70-3-200 as compared to CSCS3-70-5-200. Increasing bottom steel plate

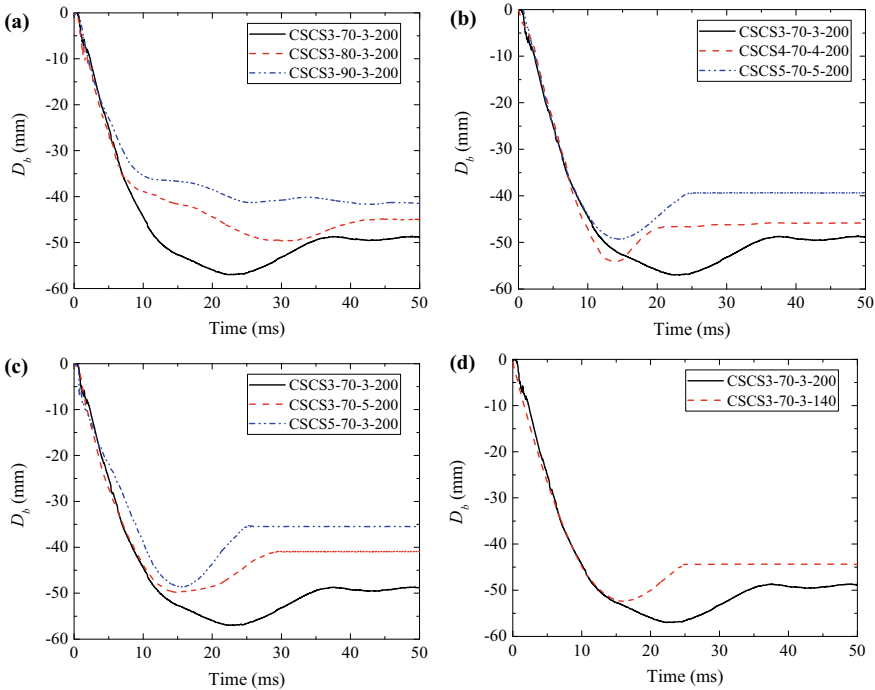
thickness could also enhance the contact stiffness, but showed less enhancement as compared to increasing top steel plate.

Figure 7.10d presents the effect of spacing of shear connectors on impact force. The decrease of spacing from 200 to 140 mm resulted in the increase of peak impact force from 304.86 to 360.21 kN (increased by 18.2%) owing to the enhanced composition action of the CSCS shell. The top and bottom steel plates as well as shear connectors worked together to resist the impact force during the loading stage, and smaller spacing of shear connectors could improve the contribution of the bottom steel plate to impact resistance of the CSCS shell. Figure 7.10d also shows that decreasing spacing of shear connectors can increase the inertial peak force from 202.34 to 218.15 kN (improved by 7.8%). This is mainly because the contact stiffness can be enhanced with higher composition action.

### 7.3.3 Displacement History and Permanent Deformation

The central displacement histories of the bottom steel plate ( $D_b$ ) of eight specimens are shown in Fig. 7.11. Increasing the concrete core thickness is found to reduce the maximum displacement of the bottom steel plate, as shown in Fig. 7.11a, i.e., the maximum displacement is reduced from 57.00 mm to 49.68 and 41.75 mm, respectively (decreased by 12.8 and 26.75%). This is mainly because both the stiffness and resistance of the specimen are enhanced by increasing thickness of concrete core. The influence of steel plate thickness on  $D_b$  is plotted in Fig. 7.11b. By increasing steel plate thickness from 2.87 mm to 3.57 and 4.54 mm, the maximum displacement decreases from 57.00 mm to 54.04 and 49.31 mm (decreased by 5.2% and 13.5%). The increased steel plate thickness can also improve the resistance and stiffness of the CSCS shell, which led to the reduction of maximum displacement. This phenomenon could also be observed from Fig. 7.11c. The summed thickness of top and bottom steel plates for specimen CSCS3-70-5-200 and CSCS5-70-3-200 were the same, and thus the maximum displacement of them were similar and higher than that of CSCS3-70-3-200 with smaller summed thickness. However, the thicker top steel plate showed higher resistance and stiffness, which resulted in slightly lower maximum displacement (48.68 mm for CSCS5-70-3-200 and 49.83 mm for CSCS3-70-5-200). Figure 7.11d depicts the effect of spacing of shear connectors on  $D_b$ . By decreasing the spacing of shear connectors, the maximum displacement was reduced from 57.00 mm to 52.45 mm (decreased by 8.7%) owing to the higher composition action of the CSCS shell.

Figure 7.12 plots the permanent deformations of the CSCS shells along arch and width directions. The deformations of top steel plates were obtained by using a laser ranging device after impact tests. The intervals were 10 mm within the impact area (a 200-mm-diameter circle) and 50 mm out of the impact area. The local deformation of the CSCS shell was more obvious while the global deformation occupied only a little part of the whole deformation. For the tested CSCS sandwich shells with thicker concrete core and thinner steel plates, the impact energy was mainly absorbed by



**Fig. 7.11** Comparison of central displacement history of bottom steel plate for specimens: **a** concrete core thickness, **b** steel plate thickness, **c** top to bottom steel plate thickness ratio and **d** spacing of shear connectors, reprinted from Yan et al. (2020a), copyright 2022, with permission from Elsevier

fracture of the top steel plate as well as shear failure of concrete. While for the CSCS sandwich shells with thicker steel plates, the fracture of the top steel plate was prevented, and thus relatively more impact energy was dissipated through global deformation.

## 7.4 Numerical Modeling

### 7.4.1 FE Model Establishment

The FE analysis was conducted based on LS-DYNA, and quarter FE model of the CSCS shell under drop-weight impact loading was established, as shown in Fig. 7.13. The concrete core and drop hammer were modeled with an eight-node brick element, combined with reduced integration. In order to simulate steel plates, Belytschko-Tsay shell element was employed. Hughes-Liu beam element was employed for modeling shear connectors. Yan et al. (2019a) have obtained the optimal mesh sizes for the

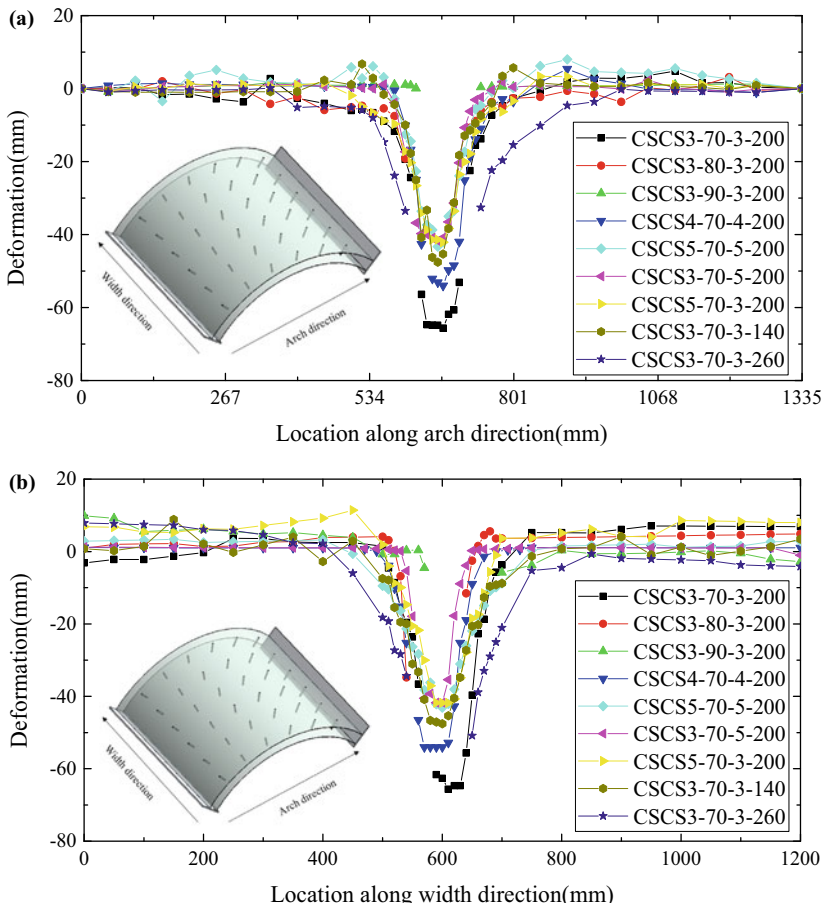


**Fig. 7.12** Permanent deformation of the top steel plate along **a** arch direction and **b** width direction, reprinted from Yan et al. (2020a), copyright 2022, with permission from Elsevier

CSCS shell in order to achieve both accurate FE-predictions and less computing time as follows:  $2 \times 2 \text{ mm}^2$  mesh size for steel plates in the impact zone and  $30 \times 30 \text{ mm}^2$  at the edge of the shell;  $10 \times 10 \times 10 \text{ mm}^3$  for concrete core; 10 mm for shear connectors.

In order to simulate concrete core under impact load with both accuracy and efficiency, the Continuous Surface Cap (CSC) material model in LS-DYNA (Hallquist 2006) was adopted. This model was developed by US Federal Highway Administration (FHWA 2007) and widely used in recent years to model concrete under dynamic loading. Meanwhile, the users can obtain the default parameters for ordinary concrete by inputting basic parameters, including unconfined compressive strength, density and maximum aggregate size. Piecewise Linear Plasticity (PLP) material model was

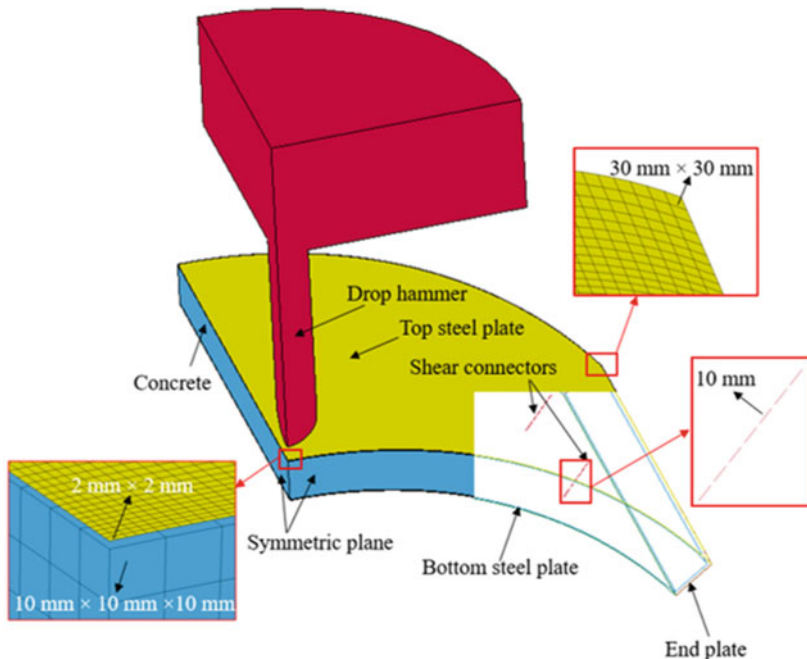
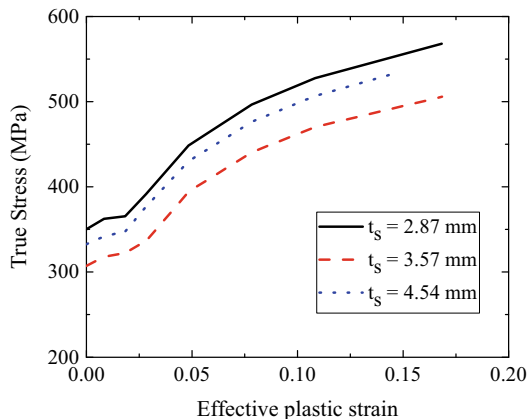


**Fig. 7.13** Quarter FE model, reprinted from Yan et al. (2020a), copyright 2022, with permission from Elsevier

employed to model steel plates and shear connectors. The users can define the stress–strain relationship and failure strain according to their tensile coupon test data. In this study, the true stress–effective plastic strain relationships for the steel plates with different thicknesses were given in Fig. 7.14. The failure strain was defined as 0.2 for failure type II and III, i.e., the element with effective plastic strain exceeding

**Fig. 7.14** True stress–effective plastic strain curves for steel plates, reprinted from Yan et al. (2020a), copyright 2022, with permission from Elsevier



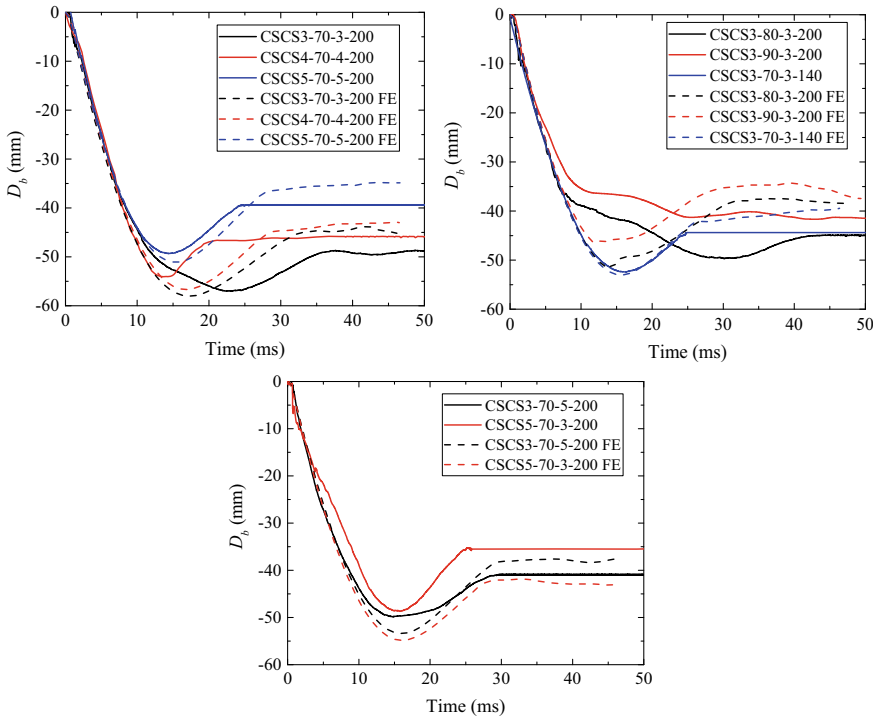
0.2 will be removed from the FE calculation. The strain rate effect was taken into consideration by using the Cowper-Symonds model, and the strain rate parameters  $C$  and  $P$  were  $802\text{ s}^{-1}$  and 3.585 (Abramowicz and Jones 1986). The Plastic Kinematic (PK) material model was applied for simulating the hammer.

By constraining the displacements and rotations of nodes on the end plate, the fixed boundary can be achieved in the FE model. In order to simulate the contacts between two parts, automatic surface to surface contact algorithm was adopted. Both static and dynamic coefficient of friction applied in the contact pairs were 0.2. \*Contact\_Tiebreak\_Nodes\_to\_Surface in LS-DYNA was adopted to simulate the connections between bolts and steel plates. The input strength was the ultimate strength of one bolt. Yan et al. (2019a) have confirmed its applicability in the former study.

#### 7.4.2 FE Results and Discussions

The comparisons of central displacement of the bottom steel plate ( $D_b$ ) and impact force histories between FE simulations and tests are shown in Figs. 7.15 and 7.16. Table 7.3 gives the results between FE-predictions and tests. Figure 7.15 shows that the value of  $D_b$  reached to a maximum value and then recovered to a stable value, which was matched with the test results. Meanwhile, the FE model can also provide accurate predictions on the hammer displacement ( $D_h$ ), as shown in Table 7.3. The impact force predicted by the FE model are also composed of three stages (i.e., inertial, loading and unloading stage), which can be seen from Fig. 7.16. The impact force histories show good agreement with the test results. Figure 7.17 depicts the different failure types of the specimens between tests and FE simulations. The FE model can accurately predict three failure types observed from the tests. The average FE-to-test ratio for impact force is 1.143 with a coefficient of variation of 0.065. The FE model overestimates the maximum value of  $D_b$  by 5.7% with a coefficient of variation of 0.040. While the maximum value of  $D_h$  is underestimated by the FE model by 5.2% with a coefficient of variation of 0.145. Based on the comparisons between the FE-predictions and tests in terms of impact force histories, central displacement of the bottom steel plate histories, hammer displacement histories and failure types, the accuracy of the FE model can be validated. The slight differences between the FE-predictions and test results may be attributed to the geometric imperfections of the fabricated specimens. Another possible reason is that the impact velocity inputted in the FE model may be slightly different from the actual impact velocity in the test owing to the existence of friction between the drop-weight system and guid rails.

Figure 7.18 shows the internal energies of the top steel plate, concrete core, and bottom steel plate of the specimens with typical three failure types (CSCS5-70-5-200, CSCS3-70-3-200 and CSCS3-80-3-200). The majority of the impact energy was dissipated by concrete core (72.9–75.6%), followed by top steel plate (18.0–19.9%) and bottom steel plate (6.4–7.4%). This also proved that concrete core was the main part to dissipate impact energy because of the shear failure of concrete (refers to



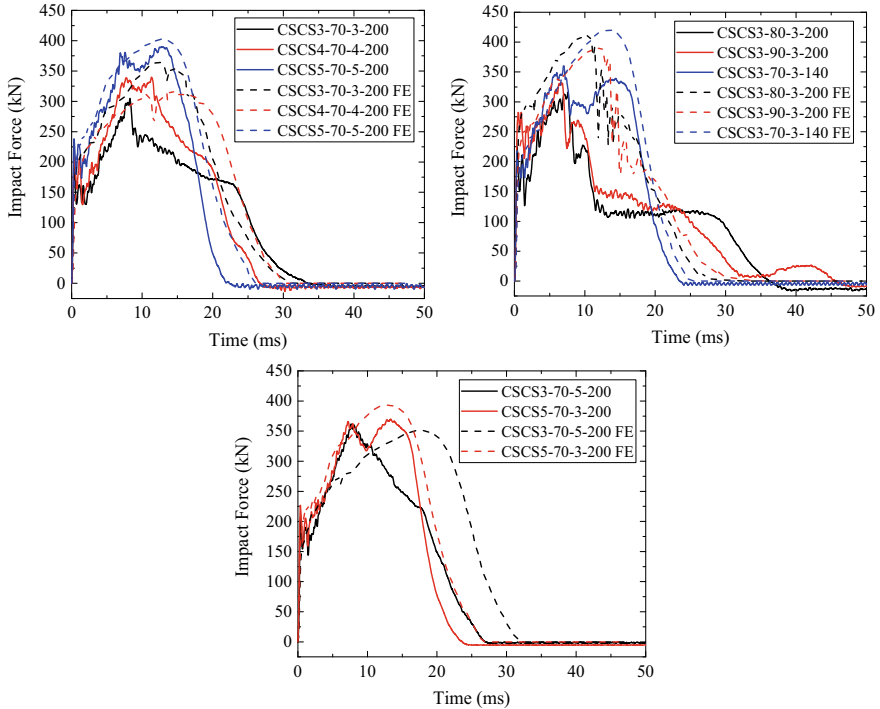
**Fig. 7.15** Comparison of central displacement of bottom steel plate histories between FE and experiments, reprinted from Yan et al. (2020a), copyright 2022, with permission from Elsevier

Fig. 7.6). After shear failure of concrete, the steel plate was the main part to resist impact force. However, the concrete core can still absorb the majority of the impact energy owing to the confinement provided by the bottom steel plate.

## 7.5 Analytical Model

### 7.5.1 Force–Displacement Relationship

Figure 7.19 presents the impact force–displacement curves of three CSCS sandwich shells obtained from the impact tests, and they can be approximately divided into two stages, i.e., elastic and plastic stage, as shown in Fig. 7.20. Therefore, a bilinear curve can be used to represent the impact force–displacement relationship of the CSCS sandwich shell.



**Fig. 7.16** Comparison of impact force between FE and experiments, reprinted from Yan et al. (2020a), copyright 2022, with permission from Elsevier

### 7.5.1.1 Elastic Stage

The calculation of the force–displacement relationship in elastic stage is based on the principle of minimum potential energy. The strain energy of the steel plate induced by membrane stretching was given in the theory of plates and shells (Timoshenko and Woinowsky-Krieger 1959):

$$V_s = \frac{E_s t_s}{1 - \nu^2} \int_0^{2\pi} \int_0^a (\varepsilon_r^2 + \varepsilon_\theta^2 + 2\nu \varepsilon_r \varepsilon_\theta) r dr d\theta \quad (7.1)$$

where  $\nu$  is Poisson's ratio,  $E_s$  is elastic modulus of the steel plate,  $t_s$  is thickness of the steel plate,  $\varepsilon_r$  is the radial strain, and  $\varepsilon_\theta$  is the circumferential strain.

Sohel and Liew (2014) gave the equations for the radial displacement as well as the values of  $C_1$  and  $C_2$ ,

$$u(r) = r(a - r)(C_1 + C_2 r) \quad (7.2)$$

**Table 7.3** Comparison of experiments and FE-predictions

Specimen	Peak impact force $F_p$ (kN)	Peak impact force $F_{pFE}$ (kN)	$\frac{F_{pFE}}{F_p}$	$D_{bm\max}$ (mm)	$D_{bm\max FE}$ (mm)	$\frac{D_{bm\max FE}}{D_{bm\max}}$	$D_{h\max}$ (mm)	$D_{h\max FE}$ (mm)	$\frac{D_{h\max FE}}{D_{h\max}}$
CSCS3-70-3-200	304.86	365.10	1.198	57.00	57.99	1.017	72.47	61.20	0.844
CSCS3-80-3-200	316.40	391.23	1.237	49.68	51.57	1.038	70.87	55.88	0.788
CSCS3-90-3-200	331.71	411.75	1.241	41.75	46.42	1.112	65.04	51.79	0.796
CSCS4-70-4-200	339.73	378.10	1.113	54.04	56.67	1.049	68.99	60.01	0.870
CSCS5-70-5-200	389.93	402.38	1.032	49.31	51.07	1.036	51.35	54.84	1.068
CSCS3-70-5-200	361.72	393.64	1.088	49.83	53.36	1.071	54.84	57.56	1.050
CSCS5-70-3-200	369.71	393.09	1.063	48.68	54.83	1.126	50.44	57.38	1.138
CSCS3-70-3-140	360.21	420.87	1.168	52.45	53.01	1.011	55.21	56.69	1.027
CSCS3-70-3-260	292.79	335.88	1.147	—	—	—	—	—	—
Average			1.143			1.057		0.948	
Cov			0.065			0.040		0.145	

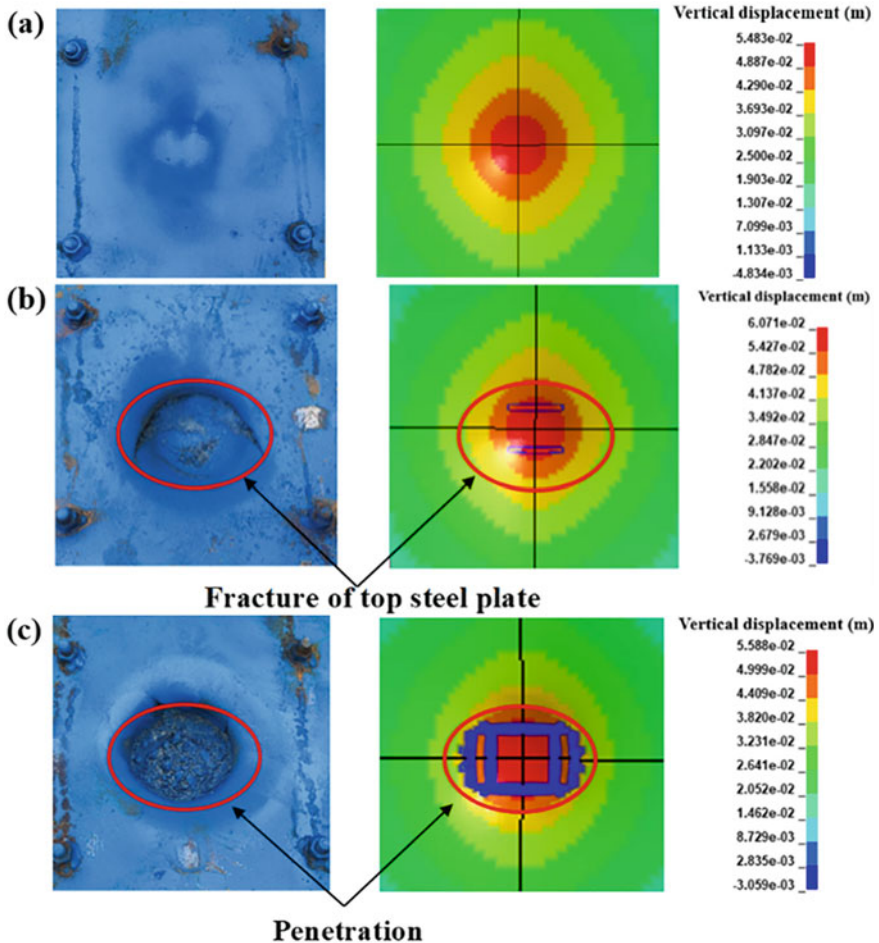


**Fig. 7.17** Comparison of failure types between FE and experiments: **a** no fracture, **b** fracture of top steel plate and **c** penetration, reprinted from Yan et al. (2020a), copyright 2022, with permission from Elsevier

$$C_1 = 0.596084 \frac{\delta^2}{a^3}; C_2 = -1.50127 \frac{\delta^2}{a^4} \quad (7.3)$$

Thus, the strain energy of the steel plate can be expressed as:

$$V_s = \frac{3.5014\pi E_s t_s \delta^4}{12(1-v^2)a^2} \quad (7.4)$$

The work done by concrete can be expressed as:

**Fig. 7.18** Internal energy of different parts s: **a** CSCS5-70-5-200, **b** CSCS3-70-3-200, **c** CSCS3-80-3-200, reprinted from Yan et al. (2020a), copyright 2022, with permission from Elsevier

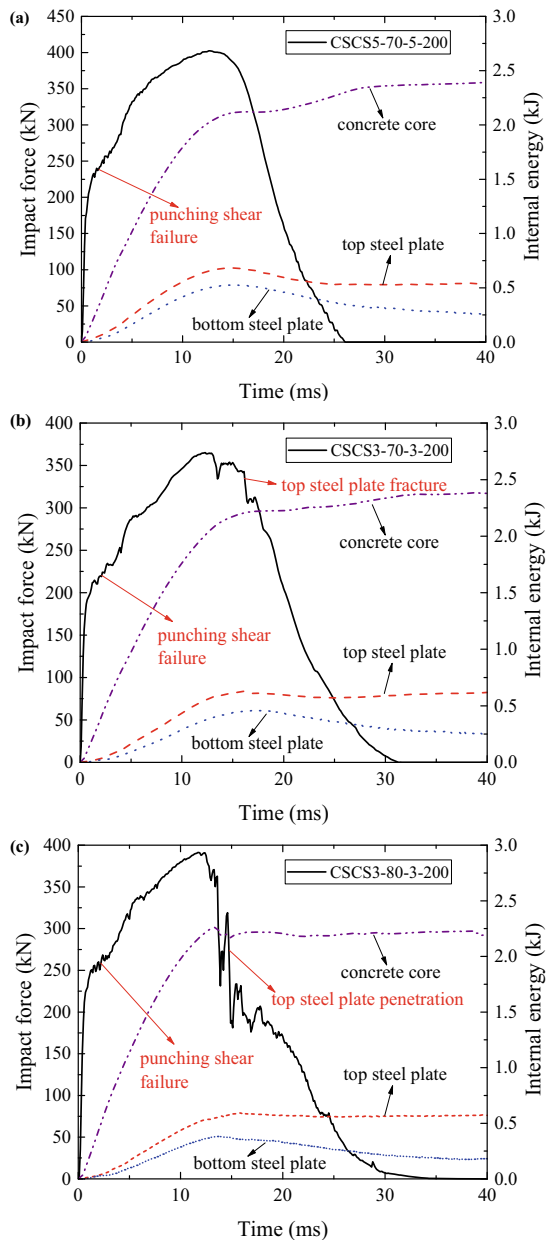


**Fig. 7.19** Impact force–displacement curves of CSCS shells under impact loading

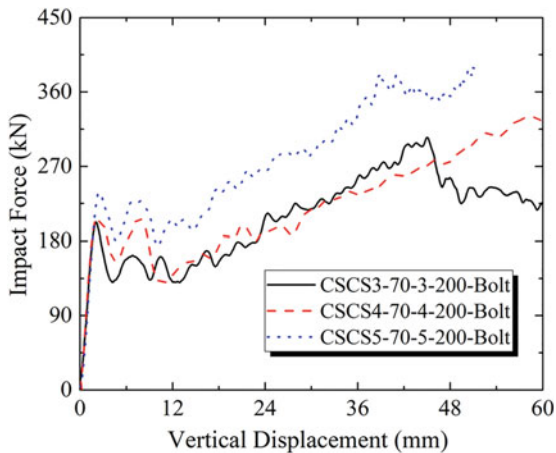
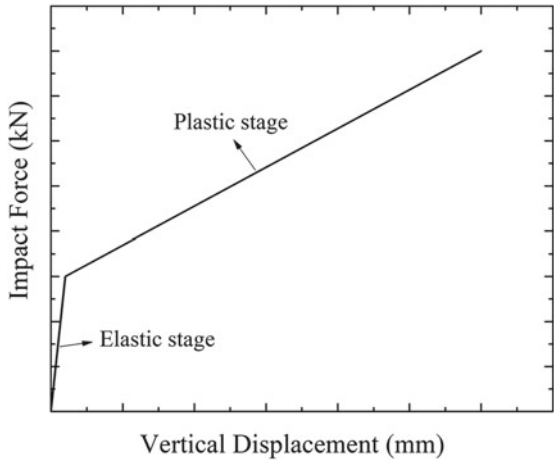


**Fig. 7.20** Simplified curve for impact force–displacement relation of the CSCS shell



$$V_{con} = \int_0^{\delta} F_{con} d\delta = \frac{\pi a^2 E_c \delta^2}{10 t_c} \quad (7.5)$$

where  $t_c$  and  $E_c$  are the thickness and elastic modulus of the concrete core, respectively. On the basis of the principle of minimum potential energy, the partial derivative of the total potential energy with respect to the vertical displacement ( $\delta$ ) is obtained, i.e., the relationship between the impact force, vertical displacement, and the size of local deformation ( $a$ ) is obtained as follows:

$$F = \frac{1.28\pi E_s t_s \delta^3}{a^2} + \frac{\pi a^2 \delta E_c}{5 t_c} \quad (7.6)$$

Minimalizing  $F$  with respect to  $a$  leads to the following equation:

$$a^2 = 2.53 \sqrt{\frac{E_s t_s t_c}{E_c}} \delta \quad (7.7)$$

Substituting Eq. (7.7) into Eq. (7.6), the relationship between the impact force and vertical displacement is obtained as follows:

$$F = 3.18 \sqrt{\frac{E_s t_s E_c}{t_c}} \delta^2; k_e = \frac{F_y}{\delta_y} \quad (7.8)$$

Equation (7.8) also defines the elastic stiffness, which is the ratio of the nominal yield strength ( $F_y$ ) to the corresponding vertical displacement ( $\delta_y$ ). The  $F_y$  can be calculated according to the formulae developed by Yan et al. (2020b), and the  $\delta_y$  can be calculated based on the relationship between the force and vertical displacement obtained in Eq. (7.8).

### 7.5.1.2 Plastic Stage

Table 7.4 summarizes the elastic stiffness and plastic stiffness of the three CSCS shells tested by Yan et al. (2020b). It can be found that the average ratio of plastic stiffness to elastic stiffness was 0.109. The impact force–displacement curve of the specimen under impact loading is similar to the load–displacement curve under quasi-static loading (Yan et al. 2020a). Therefore, it is assumed that the ratio of plastic stiffness to elastic stiffness is 0.11, as given in Eq. (7.9).

$$k_p = 0.11 k_e \quad (7.9)$$

**Table 7.4** Stiffness in elastic and plastic stage obtained from static tests

Specimen	$k_e$ (kN/mm)	$k_p$ (kN/mm)	$k_p / k_e$
CSCS3-70-3-200-Bolt	19.55	2.207	0.113
CSCS4-70-4-200-Bolt	29.96	2.914	0.097
CSCS5-70-5-200-Bolt	30.68	3.628	0.118

### 7.5.2 Displacement Response

#### 7.5.2.1 Equation of Motion

The calculation of the displacement response of the CSCS shell under impact loading is based on SDOF method. As shown in Fig. 7.21, the CSCS shell under drop-weight impact can be equivalent to a SDOF model, and its equation of motion is expressed as:

$$(m_e + m_h)\ddot{\delta} + c\dot{\delta} + R(\delta) = 0 \quad (7.10)$$

where  $m_e$  and  $c$  are the effective mass and damping of the CSCS shell, respectively, and  $m_h$  is the mass of the hammer.

The CSCS shell is a structural member with continuous mass distribution. To convert the continuously distributed mass into an equivalent concentrated mass, two assumptions are employed as follows: (1) The displacement of the mass in the SDOF model is same to vertical displacement of the CSCS shell; (2) The kinetic energy of the mass in the SDOF model is same to kinetic energy of the CSCS shell. Figure 7.21a presents the shape function  $\varphi(x, y)$  of the CSCS shell. The deformation of the CSCS shell at any point can be obtained based on the shape function when the central displacement of the shell is known. The effective mass ( $m_e$ ) can be obtained in Eq. (7.11) based on the second assumption:

$$\frac{1}{2}m_e\dot{\delta}^2 = \iint \frac{1}{2}m(x, y)[\dot{\delta}\varphi(x, y)]^2 dx dy \quad (7.11)$$

The permanent deformation shape of the CSCS shell was measured after the impact test, based on which the shape function is given as:

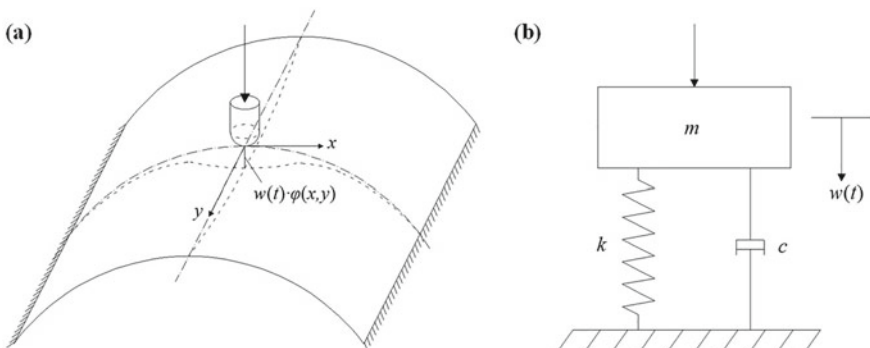


**Fig. 7.21** Analytical model: **a** CSCS shell and **b** SDOF system

$$\varphi(x, y) = \left(1 - \frac{x^2}{2.53\sqrt{\frac{f_y E_s t_s t_c}{f_c E_c}} \delta}\right)^4 \left(1 - \frac{y^2}{6.48\sqrt{\frac{f_y E_s t_s t_c}{f_c E_c}} \delta}\right)^4$$

$$|x| \leq \sqrt{2.53\sqrt{\frac{f_y E_s t_s t_c}{f_c E_c}} \delta}, |y| \leq \sqrt{6.48\sqrt{\frac{f_y E_s t_s t_c}{f_c E_c}} \delta} \quad (7.12)$$

where  $f_y$  is the yield stress of the steel plate,  $f_c$  is the cylindrical compressive strength of the concrete. The effective mass of the CSCS shell can be written as:

$$m_e = \iint m(x, y) [\varphi(x, y)]^2 dx dy \quad (7.13)$$

The damping has little effect on the impact response of the CSCS shell during the loading stage. Hence, the damping can be ignored, and the damping coefficient ( $c$ ) is adopted as 0 during the loading stage. However, the damping should be considered during the unloading stage as the free vibration amplitude decreases rapidly. The damping coefficient ( $c$ ) is adopted as  $2\sqrt{m_e k}$  during the unloading stage.

The equation of motion (Eq. 7.10) can be calculated based on finite difference method. The initial conditions of the equation of motion can be expressed as:

$$\begin{aligned} \delta(0) &= 0 \\ \dot{\delta}(0) &= \frac{m_h}{m_e + m_h} v_0 \end{aligned} \quad (7.14)$$

The displacement, velocity and acceleration of the SDOF system at time  $t_i$  can be given as:

$$\begin{aligned} \delta(t_i) &= \delta_i \\ \dot{\delta}(t_i) &= \dot{\delta}_i = \frac{\delta_{i+1} - \delta_i}{\Delta t} \\ \ddot{\delta}(t_i) &= \ddot{\delta}_i = \frac{\delta_{i+2} - 2\delta_{i+1} + \delta_i}{(\Delta t)^2} \end{aligned} \quad (7.15)$$

where  $\Delta t$  is the time step, and Eq. (7.10) can be written as:

$$(m_e + m_h) \frac{\delta_{i+2} - 2\delta_{i+1} + \delta_i}{(\Delta t)^2} + c \frac{\delta_{i+1} - \delta_i}{\Delta t} + R(\delta_i) = 0 \quad (7.16)$$

The displacement of the SDOF system at time  $t_{i+2}$  can be obtained as:

$$\delta_{i+2} = 2\delta_{i+1} - \delta_i - \frac{c \Delta t}{m_e + m_h} (\delta_{i+1} - \delta_i) - \frac{(\Delta t)^2}{m_e + m_h} R(\delta_i) \quad (7.17)$$

when  $i = 0$  and  $1$  (i.e.,  $t = 0$  and  $\Delta t$ ), the displacement of the SDOF system can be given as:

$$\begin{aligned}\delta(0) &= 0 \\ \delta(\Delta t) &= \delta(0) + \dot{\delta}(0)\Delta t = \frac{m_h}{m_e + m_h}v_0\Delta t\end{aligned}\quad (7.18)$$

Based on Eqs. (7.17) and (7.18), the displacement–time history of the CSCS shell can be obtained through iterative calculations.

### 7.5.2.2 Validation with Experimental Results

Figure 7.22 shows the comparison of the impact force–displacement curves obtained from tests and analytical-predictions, and good agreement between them can be observed. The observed differences in the elastic stages can be attributed to the inertial effect which is not considered in the analytical model and also exhibits little effect on the displacement response of the CSCS shell. Figure 7.23 shows the comparison of the displacement–time histories obtained from tests and analytical-predictions.

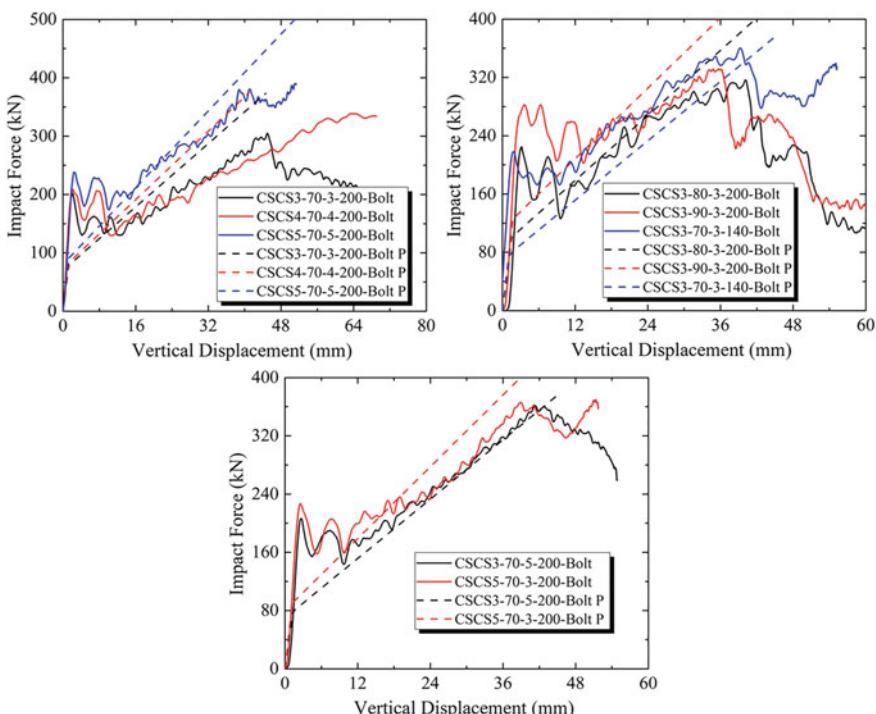


**Fig. 7.22** Comparison of impact force–vertical displacement curves between tests and predictions

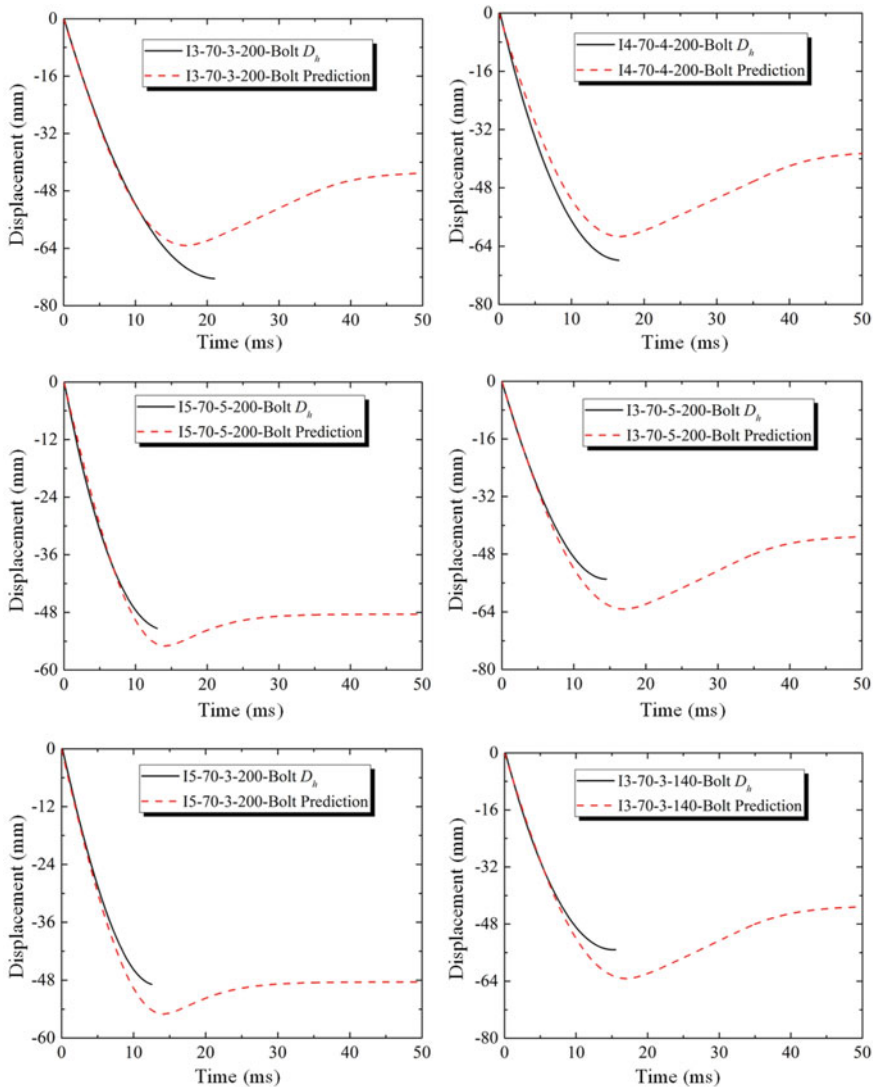


**Fig. 7.23** Comparison of displacement–time histories between tests and analytical predictions

The analytical model is found to reasonably predict the displacement response of the CSCS shell. The differences of maximum displacements between analytical predictions and impact tests are less than 15%. Hence, the proposed analytical model is proven to be acceptable and can be employed as a simple alternative to predict displacement response of the CSCS shell under impact loading.

## 7.6 Summary

Nine CSCS sandwich shells were tested to investigate their performances under drop-weight impact loading. The FE model of the CSCS shell was also established and verified against the experimental data. The main findings are summarized as follows:

- (1) Three failure types of the CSCS sandwich shells under impact load were observed, i.e., Failure type I (plastic deformation of steel plate without fracture), Failure type II (fracture of steel plate) and Failure type III (penetration of steel plate). The thicker concrete core led to more serious failure type (sifting from failure type II to type III). Increasing thickness of steel plates and decreasing spacing of shear connectors could mitigate damage of the CSCS sandwich shell.
- (2) Three stages of the impact process were summarized, i.e., inertial stage, loading stage and unloading stage. Both the three failure types showed similar phenomena in the inertial stage and unloading stage. While there were some differences in the loading stage, i.e., the impact force dropped down for the specimens with fracture or penetration of the steel plate.
- (3) The impact performances of CSCS sandwich shells with different parameters were analyzed. For the specimens with thicker concrete core, higher inertial peak force and impact resistance, and more serious failure type were observed. By increasing the thickness of steel plate or decreasing the spacing of shear connectors, the specimen showed higher inertial peak force and impact resistance as well as less damage.
- (4) The FE model of the CSCS shell was established and verified by comparing the impact force history, displacement history and failure type between the FE-predictions and experimental results. Concrete core was proven to be the main part to dissipate impact energy, followed by the top steel plate and bottom steel plate.
- (5) An analytical model based on the equivalent SDOF system was proposed for predicting displacement response of the CSCS sandwich shell under impact loading. The established analytical model was proven to be accurate by comparing the analytical-predictions with test data.

## References

- Abramowicz W, Jones N (1986) Dynamic progressive buckling of circular and square tubes. *Int J Impact Eng* 4:243–270
- Ali A, Kim D, Cho S G (2013) Modeling of nonlinear cyclic load behavior of I-shaped composite steel-concrete shear walls of nuclear power plants. *Nucl Eng Technol* 45(1):89–98
- Guo Q, Zhao W (2019) Displacement response of steel-concrete composite panels subjected to impact loadings. *Int J Impact Eng* 131:272–281
- Hoff GC (1998) A major research program on steel-concrete-steel sandwich elements. *Construction* 174:37–88

- Huang Z, Liew JYR (2016a) Compressive resistance of steel-concrete-steel sandwich composite walls with J-hook connectors. *J Constr Steel Res* 124:142–162
- Huang Z, Liew JYR (2016b) Experimental and analytical studies of curved steel-concrete-steel sandwich panels under patch loads. *Mater Des* 93:104–117
- Huang Z, Liew JYR (2015a) Nonlinear finite element modelling and parametric study of curved steel-concrete-steel double skin composite panels infilled with ultra-lightweight cement composite. *Const Build Mater* 95:922–938
- Huang Z, Liew JYR (2016c) Structural behaviour of steel-concrete-steel sandwich composite wall subjected to compression and end moment. *Thin-Walled Struct* 98:592–606
- Huang ZY, Liew JYR (2016d) Steel-concrete-steel sandwich composite structures subjected to extreme loads. *Inter J Steel Struct* 16(4):1009–1028
- Huang ZY, Wang JY, Liew JYR et al (2015b) Lightweight steel-concrete-steel sandwich composite shell subject to punching shear. *Ocean Eng* 102:146–161
- Hallquist JO (2006) LS-DYNA theory manual. Livermore Software Technology Corporation (LSTC). Livermore, California
- Leng YB, Song XB, Chu M et al (2015) Experimental study and theoretical analysis on resistance of steel-concrete-steel sandwich beams. *J Struct Eng* 141(2):04014113
- Leng YB, Song XB (2017) Flexural and shear performance of steel-concrete-steel sandwich slabs under concentrate loads. *J Constr Steel Res* 134:38–52
- Liew JYR, Sohel KMA, Koh CG (2009) Impact tests on steel-concrete-steel sandwich beams with lightweight concrete core. *Eng Struct* 31(9):2045–2059
- Lin Y, Yan J, Cao Z et al (2018) Ultimate strength behaviour of S-UHPC-S and SCS sandwich beams under shear loads. *J Constr Steel Res* 14a9:195–206
- Lin Y, Yan J, Wang Y et al (2019) Shear failure mechanisms of SCS sandwich beams considering bond-slip between steel plates and concrete. *Eng Struct* 181:458–475
- Mizuno J, Koshika N, Sawamoto Y et al (2005) Investigation on impact resistance of steel plate reinforced concrete barriers against aircraft impact Part 1: Test program and results. In: the 18th International Conference on Structural Mechanics in Reactor Technology, Beijing, China, 7–12 August 2005
- Montague P (1975) A simple composite construction for cylindrical shells subjected to external pressure. *J Mech Eng Sci* 17(2):105–113
- Remennikov AM, Kong SY (2012) Numerical simulation and validation of impact response of axially-restrained steel-concrete-steel sandwich panel. *Compos Struct* 94(12):3546–3555
- Remennikov AM, Kong SY, Uy B (2013) The response of axially restrained non-composite steel-concrete-steel sandwich panels due to large impact loading. *Eng Struct* 49:806–818
- Sohel KMA, Liew JYR (2014) Behavior of steel-concrete-steel sandwich slabs subject to impact load. *J Constr Steel Res* 100:163–175
- Sohel KMA, Liew JYR, Koh CG (2015) Numerical modelling of lightweight Steel-Concrete-Steel sandwich composite beams subjected to impact. *Thin-Walled Struct* 94:135–146
- Timoshenko SP, Woinowsky-Krieger S (1959) Theory of plates and shells. McGraw-Hill, New York
- Wang Y, Liew JYR, Lee SC (2015) Theoretical models for axially restrained steel-concrete-steel sandwich panels under blast loading. *Int J Impact Eng* 76:221–231
- Wang Y, Liew JYR, Lee SC (2016a) Ultimate strength of steel-concrete-steel sandwich panels under lateral pressure loading. *Eng Struct* 115:96–106
- Wang Y, Zhai X, Lee SC (2016b) Responses of curved steel-concrete-steel sandwich shells subjected to blast loading. *Thin-Walled Struct* 108:185–192
- Yan C, Wang Y, Zhai X et al (2019a) Experimental study on curved steel-concrete-steel sandwich shells under concentrated load by a hemi-spherical head. *Thin-Walled Struct* 137:117–128
- Yan C, Wang Y, Zhai X (2020a) Low velocity impact performance of curved steel-concrete-steel sandwich shells with bolt connectors. *Thin-Walled Struct* 150:106672
- Yan C, Wang Y, Zhai X et al (2020b) Strength assessment of curved steel-concrete-steel sandwich shells with bolt connectors under concentrated load. *Eng Struct* 212:110465

- Yan J, Zhou W, Zhang X et al (2019b) Interface monitoring of steel-concrete-steel sandwich structures using piezoelectric transducers. *Nucl Eng Technol* 51:1132–1141
- Yan JB, Liew JYR, Zhang MH et al (2016a) Punching shear resistance of steel-concrete-steel sandwich composite shell structure. *Eng Struct* 117:470–485
- Yan JB, Qian X, Liew JYR et al (2016b) Damage plasticity based numerical analysis on steel-concrete-steel sandwich shells used in the Arctic offshore structure. *Eng Struct* 117:542–559
- Yan JB, Xiong MX, Qian X et al (2016c) Numerical and parametric study of curved steel-concrete-steel sandwich composite beams under concentrated loading. *Mater Struct* 49(10):3981–4001
- Yan JB, Zhang W (2017) Numerical analysis on steel-concrete-steel sandwich plates by damage plasticity model: From materials to structures. *Constr Build Mater* 149:801–815
- Zhao W, Guo Q (2018) Experimental study on impact and post-impact behavior of steel-concrete composite panels. *Thin-Walled Struct* 130:405–413
- Zhao W, Guo Q, Dou X (2018) Impact response of steel-concrete composite panels: experiments and FE analyses. *Steel Compos Struct* 26(3):255–263

# Chapter 8

## Steel–Concrete–Steel Sandwich Panel Under Simulated Blast Loading



### 8.1 Introduction

Steel–concrete–steel (SCS) sandwich structure, which consists of a concrete core connected to two external steel faceplates using mechanic shear connectors, exhibited superior ductility and strength as compared to conventional reinforced concrete structures. The potential applications of SCS structures in resisting static, impact and blast loads have been demonstrated in previous studies (Liew and Sohel 2009; Sohel and Liew 2011; Liew et al. 2009; Remennikov and Kong 2012; Anandavalli et al. 2012; Wang et al. 2015b; Crawford and Lan 2006; Liew and Wang 2011; Lan et al. 2005). In the past, the SCS sandwich structure was applied to sustain static and impact loads, while the application has been extended to protective layer against blast loading owing to its high energy absorption capacity and scabbing protection (Anandavalli et al. 2012; Wang et al. 2015b; Crawford and Lan 2006; Liew and Wang 2011; Lan et al. 2005). Most reported works on SCS sandwich structures involved the use of mechanical shear connectors, whereas there was a lack of study on the performance of non-composite SCS sandwich panel under blast loading (Liew and Wang 2011), and its energy absorption performance was also not fully understood. Hence, the laboratory tests (by using a drop-weight impact test system and inflated airbag) were carried out to investigate the response of the non-composite SCS sandwich panel under simulated blast loading. Moreover, its energy absorption performance was further revealed by conducting numerical simulations using LS-DYNA which has been widely employed for simulating blast and impact responses of civil infrastructures, including concrete (Tabatabaei et al. 2013; Wu and Chew 2014; Lin et al. 2014; Mao et al. 2014; Chen et al. 2015; Jiang et al. 2012), steel (Zhai et al. 2013; Zhai and Wang 2013) and sandwich structures (Jing et al. 2013; Hou et al. 2013; Kilicaslan et al. 2013).

A blast is characterized by a rapid expansion of gas, generating a pressure wave propagating from the source of the explosion (Smith et al. 2009). The effect of a blast is in the form of a shock wave composed of a high-intensity shock front which expands outward from the surface of the explosive into the surrounding air. As the

wave expands, it decays in strength, lengthens in duration, and decreases in velocity (UFC 2008). The shape of the blast wave depends on the nature of the energy release. When the explosive is located on or near to the ground, the blast is considered to be a surface burst. The incident blast wave is reflected and amplified by the ground, and the reflected wave then merges with the incident wave to form a hemispherical blast wave. When the explosive is far from any reflecting surface, the blast is considered to be an air burst and is a spherical blast wave (Smith and Hetherington 1994).

The typical pressure–time profile for the blast wave in free air is shown in Fig. 8.1, which includes positive and negative phase. In the positive phase, the incident pressure ( $P_s$ ) decays to the ambient pressure ( $P_o$ ) within the time duration  $t_d$  (i.e., positive phase duration). For the following negative phase, the peak negative pressure is typically small as compared to the peak pressure in positive phase. Hence, the negative phase is usually ignored in the blast resistant design (UFC 2008; ASCE 2010, 2011). The positive phase of surface blast can be described by the modified Friedlander Equation (Baker 1973) as:

$$P(t) = P_r \left( 1 - \frac{t}{t_d} \right) \exp\left(-\frac{\bar{\theta}t}{t_d}\right) \quad (8.1)$$

where  $\bar{\theta}$  is the coefficient that describes the rate of decay of the pressure–time curve. The parameters  $P_r$ ,  $t_d$  and  $\bar{\theta}$  can be obtained using blast loading predictive tool CONWEP (Hyde 1991) by given TNT charge and standoff distance. Herein the reflected pressure  $P_r$  is used, as the blast wave is reflected and magnified with higher reflected pressure when it impinges onto the face of a target. In the blast resistant design, the pressure–time profile in positive phase can be further simplified as a bi-linear or triangular shape (UFC 2008; ASCE 2011).

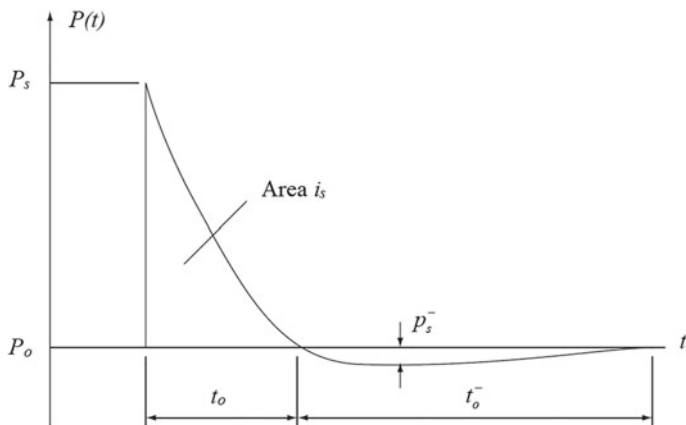


**Fig. 8.1** Typical pressure–time profile for blast wave in free air (Smith and Hetherington 1994)

Field blast test is a method to directly apply blast loading on structures (Clubley 2014; Foglar and Kovar 2013; Arora et al. 2011). This method is able to replicate the actual condition of the detonation of high explosives and can be used to test several specimens simultaneously. However, field blast test is generally expensive and requires remote testing site. Besides, the test data may be easy to lose due to the damage of transducers, cables or data acquisition equipment. Therefore, other methods such as shock tube and non-explosive test method have been devised to simulate the high pressure and short duration of a blast loading. In the shock tube test method, which is generally less expensive than the field blast test, the generated impulse loading can be well controlled. However, the specimen size is limited by the size of the shock tube, and the load duration is relatively longer compared with the field blast test (Lacroix et al. 2014; Schleyer et al. 2007). In the absence of field blast test and shock tube facilities, Mostaghel (2003) developed a simple non-explosive test method for generating impulsive loading by using a membrane formed inflated airtight chamber mounted to a frame system. A plate was dropped onto the membrane from various heights to achieve the required impulse magnitude and duration. Even though the load duration is longer than that generated by the field blast detonation, this method is simple and can be easily conducted in the laboratory, and therefore was adopted by some researchers to generate blast-type pressure loading (Chen and Hao 2014; Remennikov et al. 2009). Remennikov et al. (2009) adapted this method with an inflated airbag acting as the airtight chamber to test columns under impulse loading. The similar method was also employed by Chen and Hao (2014) to investigate the response of multi-arch double-layered panels under impulse loading. As the use of airbag to generate pressure loading in the laboratory appeared to be an easy and economical way, a similar concept was employed in this study by using high pressure airbag to test the SCS sandwich panels under impact-induced impulsive loading. The airbag was charged with initial pressure of 100 kPa before impact to reduce the loading duration to 0.042–0.049 s, which was shorter than those reported by Chen and Hao (2014) and Remennikov et al. (2009).

## 8.2 Experimental Study

### 8.2.1 Design of Specimens

Two SCS sandwich panels with different concrete core depths of 50 (SCS50) and 75 mm (SCS75) were fabricated from mild steel plates that were fillet welded together to form the outer skin, as shown in Fig. 8.2. A 32 mm (1¼ inch) inlet pipe with stopper ball valve and a 32 mm (1¼ inch) outlet pipe with threaded cap were provided at the side and end plates of the panels for pumping of cement grout into the core during casting. The schematic drawing of the panel is shown in Fig. 8.3, and the details are summarized in Table 8.1.

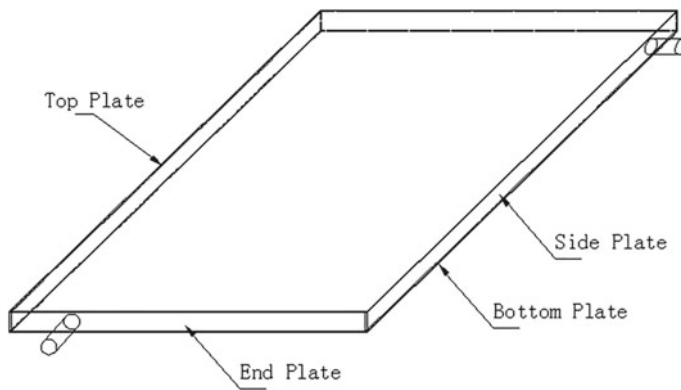


**Fig. 8.2** Notation for SCS sandwich panel, reprinted from Wang et al. (2015a), copyright 2022, with permission from Elsevier

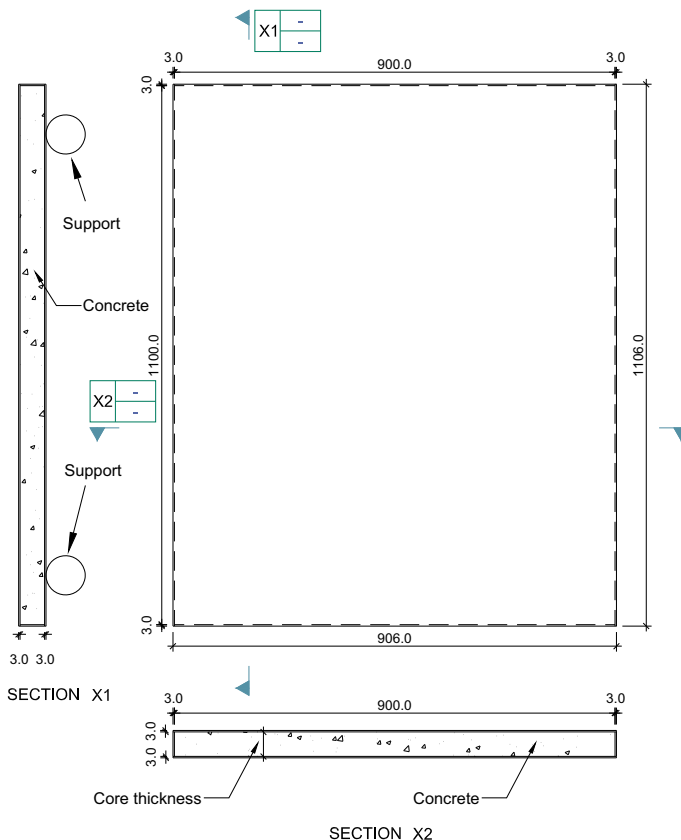


**Fig. 8.3** Schematic drawing of SCS sandwich panel, reprinted from Wang et al. (2015a), copyright 2022, with permission from Elsevier

**Table 8.1** Details of SCS sandwich panels

Label	Length × width (mm)	$t_s-t_c-t_s$ (mm)	Material strength	
			Mild steel	Grout
SCS50	1100 × 900	3–50–3	$f_y$ (MPa) 309	$f_u$ (MPa) 50
SCS75		3–75–3		

Note  $t_s$ ,  $t_c$ —face plate thickness and core depth;  $f_y$ ,  $f_u$ —yield stress and ultimate stress of steel

### 8.2.2 Test Setup and Instrumentation

The instrumented drop-weight impact test machine that was used to apply the impact-induced impulsive loading in the laboratory is shown in Fig. 8.4. A hydraulic controlled mechanical hoisting system is utilized to raise the projectile up to 4 m height. Once the winch brake is released, the projectile, which has an adjustable weight of 500–1200 kg, will slide down freely along the vertical guide rails. The SCS panel was placed below the projectile and simply supported on two 80-mm-diameter bars support with clear span of 900 mm, as shown in Fig. 8.5. The inflated height of the airbag between the impact plate (with size of 1000×1000×30 mm) and SCS panel was kept at 160 mm by using two wood beams that were inserted between the frame and impact plate. The airbag was charged with initial pressure of 100 kPa before impact. Even though the change in contact area between the airbag and SCS panel during impact test was expected to be less significant if higher initial pressure

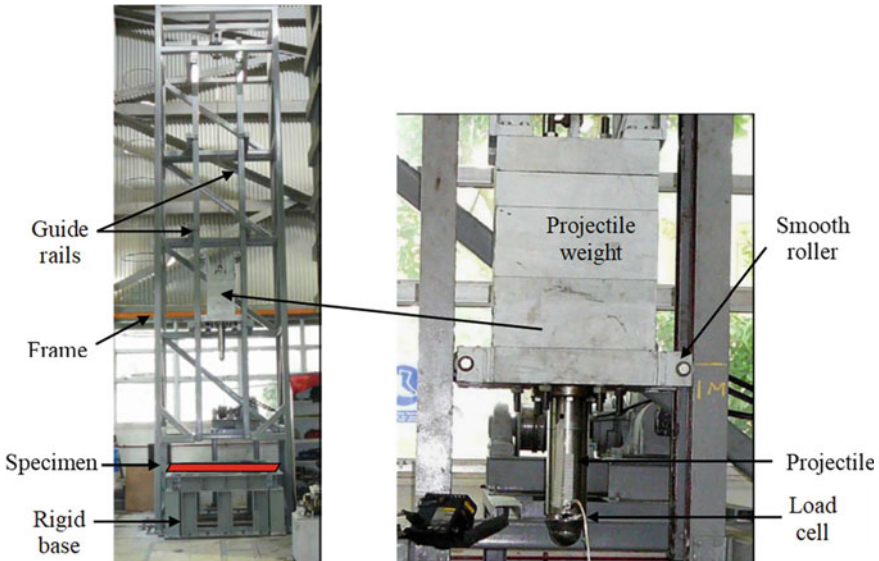


**Fig. 8.4** Drop-weight impact test machine, reprinted from Wang et al. (2015a), copyright 2022, with permission from Elsevier

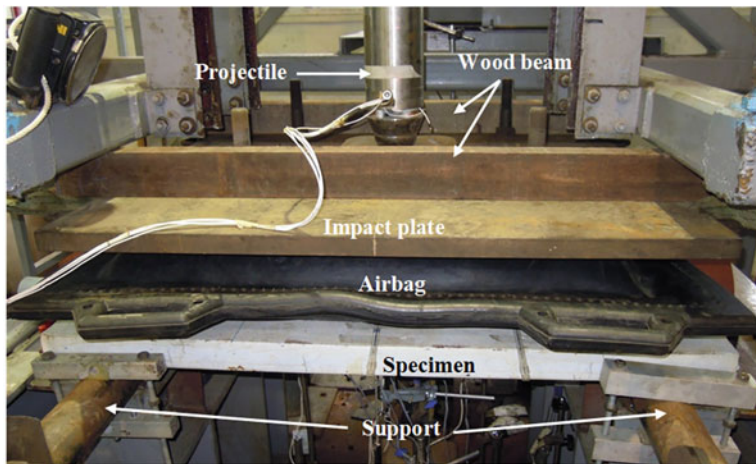


**Fig. 8.5** Test setup, reprinted from Wang et al. (2015a), copyright 2022, with permission from Elsevier

of airbag was applied, the current initial pressure (100 kPa) was selected such that the midpoint displacement of specimen was minimal (less than 2 mm) and within the elastic range. Wet paint was applied to the bottom surface of the inflated airbag which was not in contact with the SCS panel before test. As the wet paint would leave a marking on the SCS panel after impact test, the maximum contact area during impact could be determined. The inflated height of 160 mm was selected based on trial tests and kept as small as possible, since an inflated airbag with lower compressibility, which can be defined as the ratio of compression distance of airbag,  $\Delta H$ , to change of air pressure,  $\Delta P$ , will generate impulsive loading with shorter duration.

A digital circuit in combination with laser emitters and photodiodes was used to measure impact velocity of the projectile just before the impact and also to trigger the data acquisition system of the 16-channel Oscilloscope 1 with sampling rate of 1 MHz, as shown in Fig. 8.6. The Dytran high frequency 2300 V Low Impedance Voltage Mode (LIVM) pressure sensor was connected to the inlet pipe of the airbag to capture the air pressure, and three quartz force rings on the same plane with total capacity of 1050 kN were attached to the projectile to record the impact force. The displacement and strain responses of the specimen were respectively measured by using potentiometers and strain gauges at the positions shown in Fig. 8.7. The signals from the photodiodes, pressure sensor, quartz force rings and potentiometers were captured using Oscilloscope 1 while the strain gauge readings were recorded by the 16-channel Oscilloscope 2 with the sampling rate of 1 MHz. Oscilloscope 2 was triggered by the strain gauge S0 at the mid-span.

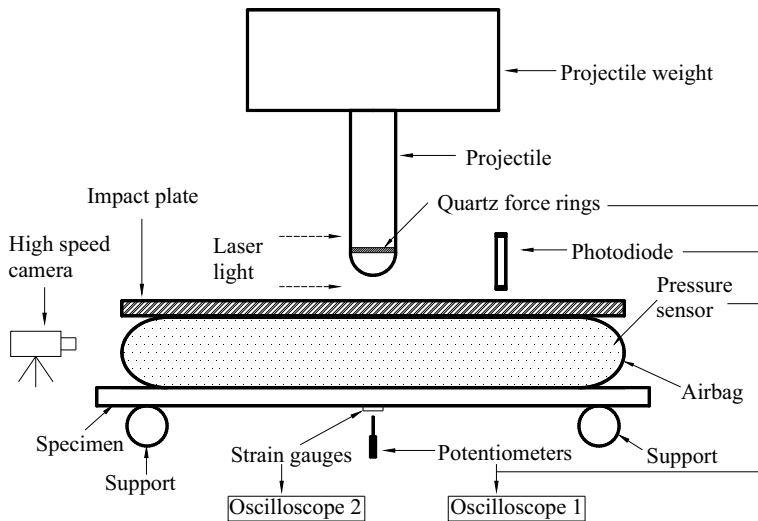


**Fig. 8.6** Overview of data acquisition system, reprinted from Wang et al. (2015a), copyright 2022, with permission from Elsevier

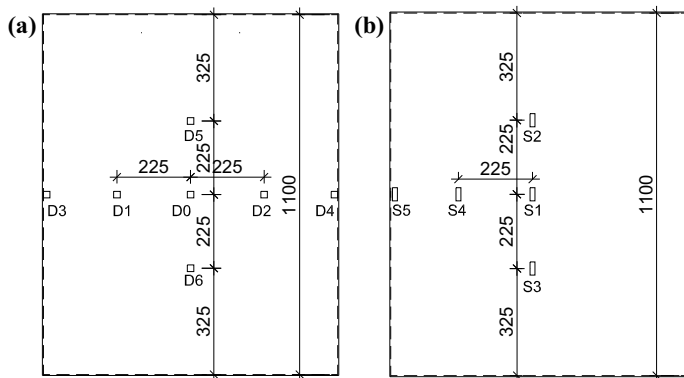


**Fig. 8.7** Instrumentation layout (bottom view): **a** potentiometers and **b** strain gauges, reprinted from Wang et al. (2015a), copyright 2022, with permission from Elsevier

### 8.2.3 Test Results and Discussions

The SCS50 and SCS75 sandwich panels were subjected to impact by an 800 kg projectile that was dropped from the height of 3.7 m. The impact force, air pressure, deformation and strain responses were measured in the test and are discussed as follows.

### 8.2.3.1 Impact Force and Air Pressure

The recorded impact force–time histories between the projectile and impact plate are plotted in Fig. 8.8. Multiple contacts between the two can be seen from the plots, since the heavier projectile continued to move downwards and hit the impact plate again multiple times after the first contact. The air pressure–time histories, which represent the impulsive loading acting on the SCS panel, are plotted in Fig. 8.9. The measured loading durations for the SCS50 and SCS75 panels are 0.049 and 0.042 s, respectively, which are shorter than those reported by Chen and Hao (2014) and Remennikov et al. (2009). The shorter duration can be attributed to the higher initial pressure and drop weight used in the current test. The recorded impact velocity ( $V$ ), maximum impact force ( $F_{max}$ ), impact impulse ( $I$ ) and maximum air pressure ( $P$ ) are summarized in Table 8.2. The impact impulse was obtained by integrating the impact force–time curve shown in Fig. 8.8. From Table 8.2, it appears that the SCS75 panel with higher resistance and mass absorbed higher impact impulse under the same impact condition.

**Fig. 8.8** Impact force–time history of SCS sandwich panels, reprinted from Wang et al. (2015a), copyright 2022, with permission from Elsevier

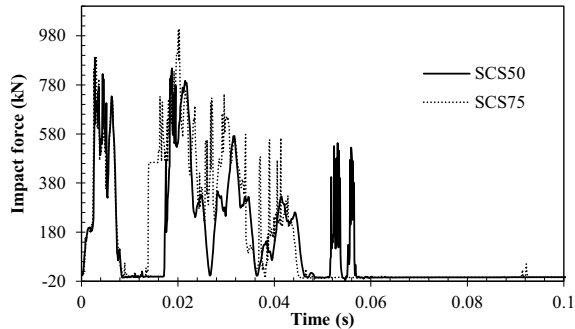


**Fig. 8.9** Pressure–time history of SCS sandwich panels, reprinted from Wang et al. (2015a), copyright 2022, with permission from Elsevier

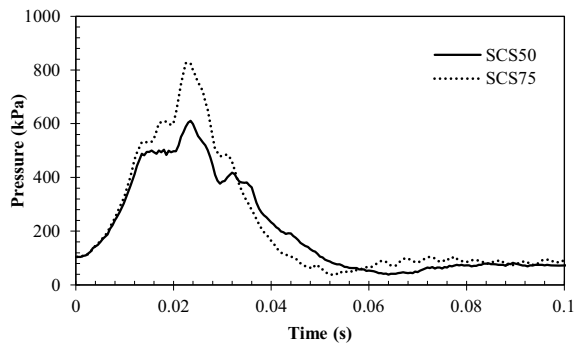


**Table 8.2** Summary of test results

Specimen	$V$ (mm/s)	$F_{\max}$ (kN)	$I$ (Ns)	$P$ (kPa)	$D_{\max}$ (mm)	$D_{\text{perm}}$ (mm)
SCS50	8147	895	12,837	617	34.7	20.4
SCS75	8070	1012	15,703	829	9.8	3.9

Note  $V$ —Impact velocity;  $F_{\max}$ —Maximum impact force;  $I$ —Impact impulse;  $P$ —Maximum pressure;  $D_{\max}$ ,  $D_{\text{perm}}$ —maximum and permanent displacement

### 8.2.3.2 Deformation Response

The deformation mode of the SCS50 panel under the impact-induced impulsive loading was a combination of flexure and shear, as shown in Fig. 8.10. Bulging near the support line was visible, which could be due to the expansion of grout after cracking under shear deformation. Comparison of the permanent deformation of SCS50 and SCS75 sandwich panels in Fig. 8.11 shows that the deformation was considerably reduced by increasing the concrete core depth owing to the increase in resistance and mass. However, the possibility of brittle shear failure may be increased

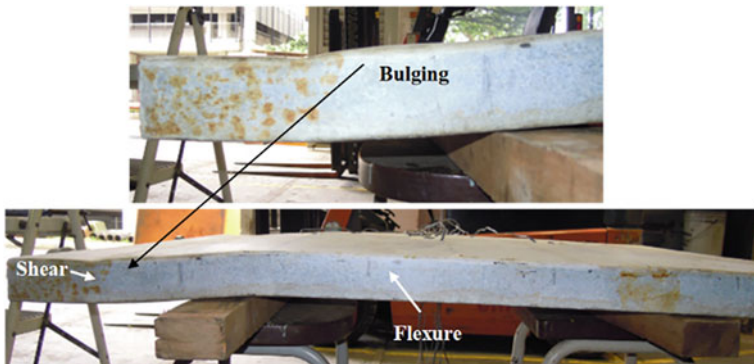


**Fig. 8.10** Deformed shape of SCS50 sandwich panel after test, reprinted from Wang et al. (2015a), copyright 2022, with permission from Elsevier



**Fig. 8.11** Comparison of permanent deformation of SCS50 and SCS75 sandwich panels after test, reprinted from Wang et al. (2015a), copyright 2022, with permission from Elsevier

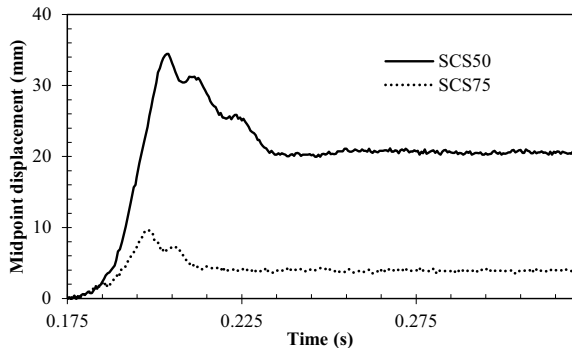


**Fig. 8.12** Displacement–time histories of SCS50 and SCS75 sandwich panels, reprinted from Wang et al. (2015a), copyright 2022, with permission from Elsevier

with increasing core depth. Therefore, it is important to ensure that the SCS sandwich panel with thicker concrete core has sufficient shear resistance to avoid shear failure.

Figure 8.12 compares the midpoint displacement–time histories of the SCS50 and SCS75 sandwich panels, and the maximum displacement of the SCS50 sandwich panel is about 3.5 times higher than that of SCS75 sandwich panel. The maximum displacements occurred at their first peaks in the curves, which are consistent with the recorded pressure–time histories. As shown in Table 8.2, the permanent midpoint displacement of the SCS75 sandwich panel was significantly less than that of SCS50 sandwich panel.

### 8.2.3.3 Strain Response

Figure 8.13 presents the longitudinal strain distribution (S1, S4 and S5) across the width of the SCS50 panel. The three strain readings were initially similar at the beginning of loading. As the load increases, the strain reading of S5 near the side plate continued to increase while there were no significant changes to the S1 and S4 readings after a sudden drop in strain at 0.187 s. This observed difference in the strain development and the sudden drop of strain value were likely due to the weakened composite action of the SCS panel without shear connectors after debonding of the grout core from the bottom plate. Another sudden drop was observed at 0.190 s, which indicates the progressive debonding between the grout and bottom plate with continuous impact. Similarly for the SCS75 panel, the strain reading of S5 near side plate continued to rise at higher rate than those of S1 and S4 after the sudden drop caused by debonding, as shown in Fig. 8.14. In the span direction (S1, S2 and S3), the mid-span strain reading S1 was higher than the quarter-span strains S2 and S3 for both the SCS50 and SCS75 panels before the debonding. However, higher strain readings were observed at the quarter-spans after debonding. This indicates that the debonding between grout core and bottom plate affected the strain development at the bottom plate of the SCS panels.

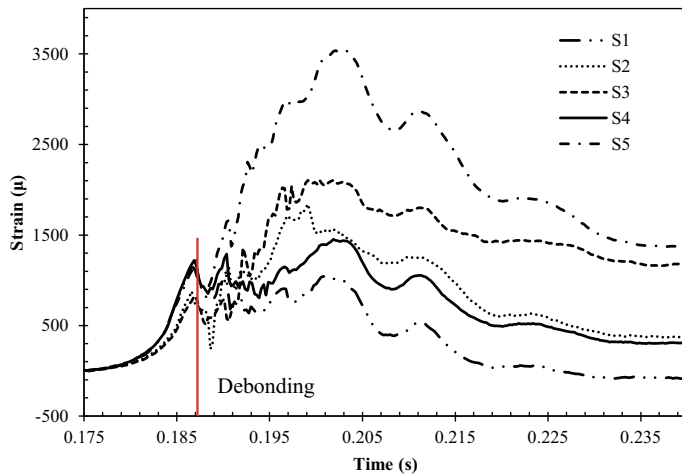


**Fig. 8.13** Longitudinal strain–time history of SCS50 sandwich panel, reprinted from Wang et al. (2015a), copyright 2022, with permission from Elsevier

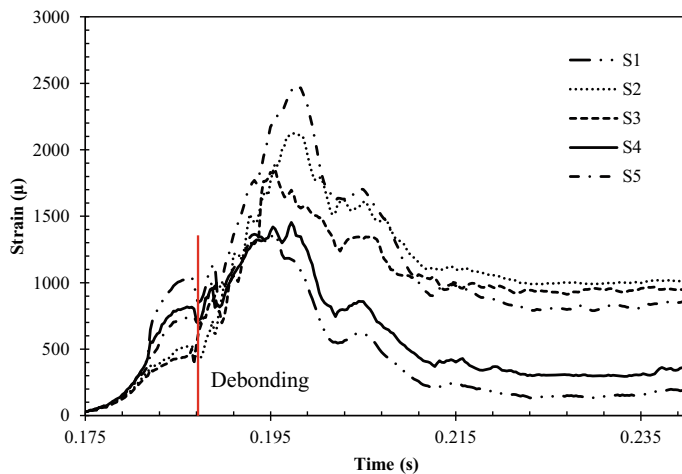


**Fig. 8.14** Longitudinal strain–time history of SCS75 sandwich panel, reprinted from Wang et al. (2015a), copyright 2022, with permission from Elsevier

### 8.3 Numerical Study

Following the laboratory test, the explicit code in LS-DYNA (Hallquist 2012) was employed to simulate the SCS sandwich panels under both impulsive loading and actual blast loading.

### 8.3.1 Material Models

#### 8.3.1.1 Grout Material

Concrete and other cement-based material (like grout) are heterogeneous materials that exhibit nonlinear inelastic behavior under multi-axial stress states. To accurately predict the material responses and failure modes under various loading scenarios, the key material characteristics have to be captured in the constitutive model, including the influence of confinement on strength and energy absorption capacity, compression hardening and softening behaviors, volumetric expansion upon cracking, tensile fracture and softening, biaxial response and strain rate effects under dynamic load (Crawford et al. 2012). In the current study, the Karagozian & Case concrete model (MAT\_72R3) in LS-DYNA, which was developed by Malvar et al. (1997), was adopted to model the grout.

The deviatoric strength of MAT\_72R3 is defined by three independent failure surfaces, including the initial yield surface, maximum failure surface and residual surface, which are written as follow (Magallanes et al. 2010):

$$\nabla \sigma_i(p) = a_{0i} + \frac{p}{a_{1i} + a_{2i} p} \quad (8.2)$$

where  $p$  is hydrostatic pressure, and  $a_{0i}$ ,  $a_{1i}$  and  $a_{2i}$  are parameters that define the failure surfaces.

For hardening, the current failure surface is linearly interpolated between the yield and maximum surfaces based on the value of damage parameter  $\eta$ , as given in Eq. (8.3). A similar interpolation is performed between the maximum and residual surfaces for softening in Eq. (8.4).

$$\Delta\sigma = \eta(\Delta\sigma_m - \Delta\sigma_y) + \Delta\sigma_y \quad (8.3)$$

$$\Delta\sigma = \eta(\Delta\sigma_m - \Delta\sigma_r) + \Delta\sigma_r \quad (8.4)$$

In above equations,  $\Delta\sigma_y$ ,  $\Delta\sigma_m$  and  $\Delta\sigma_r$  are the yield, maximum and residual surfaces, and  $\eta$  varies between 0 and 1 depending on the accumulated effective plastic strain parameter  $\lambda$ , which is defined as

$$\lambda = \int_0^{\varepsilon_p} \frac{d\varepsilon_p}{r_f(1 + p/r_f f_t)^{b_1}} \text{ for } p \geq 0 \quad (8.5)$$

$$\lambda = \int_0^{\varepsilon_p} \frac{d\varepsilon_p}{r_f(1 + p/r_f f_t)^{b_2}} \text{ for } p < 0 \quad (8.6)$$

where  $r_f$  is the strain rate enhancement factor,  $b_1$  and  $b_2$  are the damage scaling exponents, and  $d\varepsilon_p = \sqrt{(2/3)\varepsilon_{ij}^p\varepsilon_{ij}^p}$  is the effective plastic strain increment. The damage scaling exponents  $b_1$  and  $b_2$  govern the softening of unconfined uniaxial stress-strain curve in compression and tension, respectively (Malvar et al. 1997). To ensure constant fracture energy dissipation,  $b_2$  is determined by iterative calculation until the area under the stress-strain curve for a uniaxial unconfined tensile test coincides with  $G_f/h$ , where  $G_f$  and  $h$  are the fracture energy and element size, respectively. Similarly,  $b_1$  is determined using uniaxial unconfined compressive test. In this study, the fracture energy from uniaxial unconfined compressive test on the grout was used to determine  $b_1$ . The fracture energy of grout in tension-softening given by Ishiguro (2007) in Eq. (8.7) was used to determine  $b_2$ .

$$G_f = 0.0251 f_c^{0.105} \quad (8.7)$$

where  $f_c$  is the compressive strength of grout in MPa.

The volumetric response of the grout material is defined using the tabulated Equation of State (EOS), numbered as EOS\_8 in LS-DYNA. The EOS relates the hydrostatic pressure,  $p$ , the relative volume,  $V$ , and the internal energy,  $e_i$ . In the loading (compression) phase, the pressure is defined as

$$p = C(\varepsilon_v) + \gamma T(\varepsilon_v) e_i \quad (8.8)$$

where  $\varepsilon_v$  is the natural logarithm of the relative volume,  $C$  and  $T$  are coefficients given as function of  $\varepsilon_v$ , and  $e_i$  is the internal energy. Unloading occurs at the slope corresponding to the bulk modulus at the peak (most compressive) volumetric strain. Reloading follows the unloading path to the point where unloading begins and continues on the loading path (Hallquist 2006). In this study, the thermal state of grout  $\gamma T(\varepsilon_v) e_i$  in Eq. (8.8) was not considered, and the values of  $C$  and  $\varepsilon_v$  can be generated by using the automated generation option in MAT\_72R3, which is based on uniaxial strain test on normal concrete (Malvar et al. 1997). The bulk modulus of the grout (13.83 GPa) was determined from uniaxial unconfined compressive test and was applied in the parameters in the EOS\_8. Other material properties of the grout are also tabulated in Table 8.3.

The strain rate effect was captured in MAT\_72R3 by modifying the failure surface and damage function  $\lambda$  through the modified damage function in Eqs. (8.5) and (8.6).

**Table 8.3** Material properties of grout and mild steel

Material	$\rho$ (kg/m <sup>3</sup> )	$f_c/f_y$ (MPa)	$E$ (GPa)	$\mu$
Grout	2150	50.3	24.9	0.2
Steel	7850	309.2	205.2	0.28

Note  $\rho$ —Density;  $f_c/f_y$ —Compressive stress of grout/yield stress of mild steel;  $E$ —Young's modulus;  $\mu$ —Poisson's ratio

A radial rate enhancement on the concrete failure surface was implemented, and the enhanced strength  $\Delta\sigma_e$  corresponding to pressure  $p$  is determined as follow (Malvar et al. 1997):

$$\Delta\sigma_e = \gamma_f \Delta\sigma(p/\gamma_f) \quad (8.9)$$

where  $\gamma_f$  is the strain rate enhancement factor or Dynamic Increase Factor (DIF). The DIF-strain rate in Eq. (8.10) (Grote et al. 2001) was adopted in the current study for the grout in compression

$$DIF = \begin{cases} 0.0235 \log \dot{\epsilon} + 1.07 & (\dot{\epsilon} < 250) \\ 0.882(\log \dot{\epsilon})^3 - 4.48(\log \dot{\epsilon})^2 + 7.22 \log \dot{\epsilon} - 2.64 & (\dot{\epsilon} \geq 250) \end{cases} \quad (8.10)$$

For tension, the DIF-strain rate in Eq. (8.11) was obtained for the grout by fitting the experimental data from Ross et al. (1989).

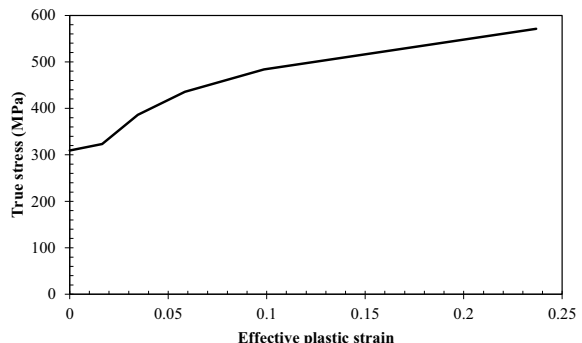
$$DIF = \exp\left\{0.0513[\log(\dot{\epsilon}/\dot{\epsilon}_s)]^{1.35}\right\} \quad (8.11)$$

where  $\dot{\epsilon}_s = 1E-7$ .

### 8.3.1.2 Steel Material

The Piecewise Linear Plasticity material model was adopted to simulate the mild steel material. The material properties given in Table 8.3 were determined from the tensile coupon tests, and the input true stress-effective plastic strain curve is given in Fig. 8.15. The strain rate effect of mild steel was considered by using the Cowper-Symonds model, as defined in Eq. (1.8). Jones (1988) obtained the values of  $C = 40.4 \text{ s}^{-1}$  and  $p = 5$  for the mild steel by fitting the experimental data assembled by

**Fig. 8.15** The input true stress-effective plastic strain curve of mild steel, reprinted from Wang et al. (2015a), copyright 2022, with permission from Elsevier



Symonds (1967). There is however, a considerable scatter to the data, which may be related to the different mild steels used in the experiments. As such, using these values may overestimate the strain rate effects of some kinds of mild steels. More recently, the values of  $C = 802 \text{ s}^{-1}$  and  $p = 3.585$  were determined by Abramowicz and Jones (1986) from dynamic uniaxial tensile tests. These values were employed for the mild steel in the current study to reduce the possibility of overestimating the strain rate effects owing to the lack of dynamic test data for the current mild steel.

### 8.3.2 Model Description

Since the applied impulsive pressure loading on the SCS panel can be represented by the measured air pressure–time history, only the parts shown in Fig. 8.16 were included in the FE model. Owing to symmetry, a quarter FE model of the SCS sandwich panel with round bars as support was modeled, as shown in Fig. 8.17. The nodes along the bottom of the round bars support were restricted from translation and rotation in the model to simulate the fixed round bar support. Since the airbag was flexible and has negligible contribution to the resistance of the SCS sandwich panel, it was not explicitly modeled. However, the mass of the bottom airbag skin that was in contact with the SCS panel was included in the FE model, because it moved together with the SCS panel and would increase the total mass, and thus affecting the

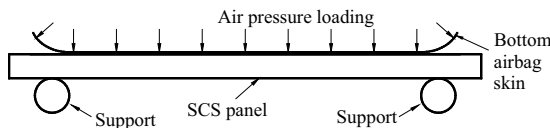


**Fig. 8.16** Simplification of FE simulation, reprinted from Wang et al. (2015a), copyright 2022, with permission from Elsevier

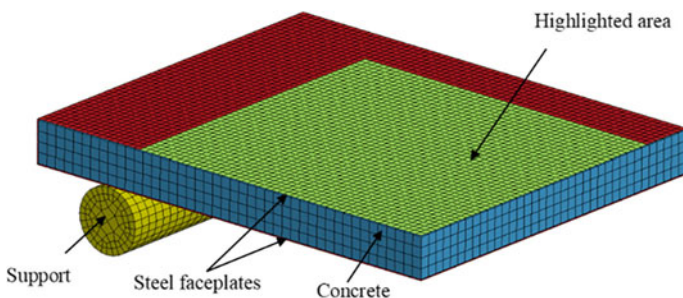


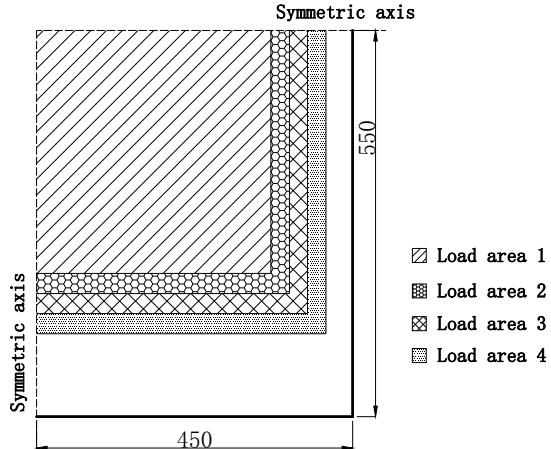
**Fig. 8.17** FE model of SCS sandwich panel, reprinted from Wang et al. (2015a), copyright 2022, with permission from Elsevier

structural response under impulsive loading. This was done by increasing the density of the highlighted elements of the top plate in Fig. 8.17 with additional mass.

Since the contact area between the airbag and specimen varied continuously during the test and only the contact areas corresponding to initial pressure and maximum pressure were recorded, a linear relationship between the contact area and pressure was assumed to obtain the contact area–time history during the test. The applied force–time history was then determined by multiplying the pressure with the contact area. Four contact areas were selected in the FE model to represent the variation of contact area, as illustrated in Fig. 8.18 for the SCS50 panel. The applied pressure–time histories on each load area were increased from zero. The total applied force–time history in the FE model was checked against the recorded applied force–time history, and they were kept to be identical. Dynamic relaxation approach was utilized to treat the initial static pressure that applied on the SCS sandwich panels before impact test.

The steel plates of the SCS sandwich panel were meshed using S/R Hughes-Liu shell element, and eight-node brick element with reduced integration was employed for the grout core and bar support (Hallquist 2012). The penalty-based contact approach, which is suitable for modeling contact between bodies of similar materials, was adopted for the contact between faceplates and support. The soft constraint-based contact approach, which is suitable for treating contact between bodies of dissimilar materials, was employed for the contact between faceplates and grout core. Since no shear connectors were used in the SCS panel, the bonding strength between the grout core and faceplates was only contributed by the adhesive strength of grout. This weak bonding strength was ignored in the analysis as it has little effect on the displacement response of the SCS panel under impulsive loading owing to the relatively longer loading duration as compared to the natural period of the SCS panel.

**Fig. 8.18** Varying load area in the FE model of SCS50 sandwich panel (quarter model), reprinted from Wang et al. (2015a), copyright 2022, with permission from Elsevier



### 8.3.3 Numerical Results and Discussions

The FE-predicted midpoint displacement–time histories of the SCS50 and SCS75 panels are compared with test results in Fig. 8.19. Reasonably well prediction of the displacement–time history of SCS50 panel can be seen in the comparison. Although the FE model overestimates the maximum displacement of SCS75 panel by 26.7%, the simulated permanent displacement matches closely with test result. The over-predictions by FE analyses may be due to the adopted strain rate parameters for the mild steel and geometric imperfection of the SCS panel. The midpoint displacements of both SCS50 and SCS75 sandwich panels in the tests continuously increase to their maximum values, whereas the displacement–time histories given by FE analyses show some fluctuating before reaching their maximum values. The reason is that the damping, which may eliminate the fluctuating of specimen in the test, is not incorporated into the FE model. This can also explain the higher magnitude of fluctuating of FE-predicted curves as compared to tests after the maximum displacement.

The FE-calculated internal energies of steel and grout materials in the SCS50 panel and their ratios are presented in Fig. 8.20. The internal energy of steel was higher than grout at the beginning, which may be attributed to the sudden applied impulsive loading on the top plate of the SCS panel. Subsequently, both the steel plates and grout core produced comparable internal energies with increasing deformation of the SCS panel. Finally, more internal energy was dissipated by the steel plates, and the

**Fig. 8.19** Comparison of FE predicted displacement–time histories with test results: **a** SCS50, **b** SCS75, reprinted from Wang et al. (2015a), copyright 2022, with permission from Elsevier

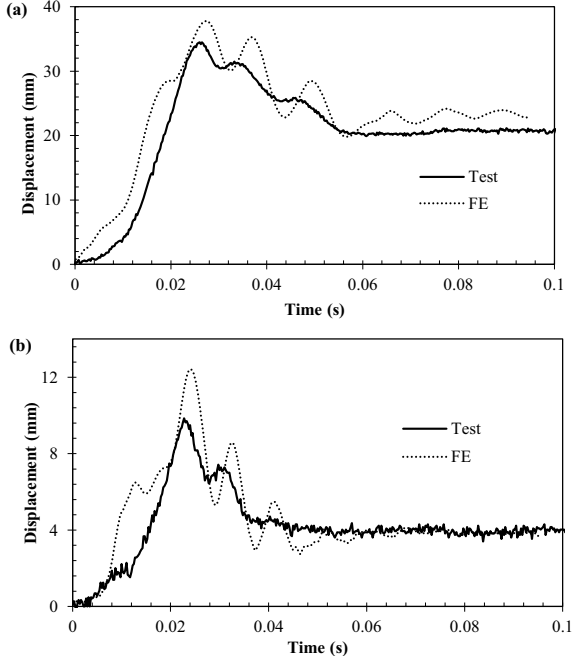
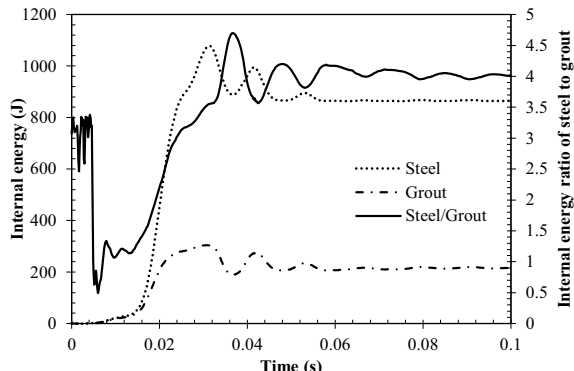


**Fig. 8.20** Internal energy of steel and grout material of SCS50 sandwich panel, reprinted from Wang et al. (2015a), copyright 2022, with permission from Elsevier



internal energy ratio of steel to grout was almost constant at 4.0. This was expected as the steel plate has higher strength and ductility as compared to the grout core. Although the energy absorption capacity of the grout is lower than steel plate, it helped to resist the buckling of faceplates and increase the total mass of the SCS panel.

### 8.3.4 Further Numerical Simulations and Discussions

The measured loading durations in the test ranged from 0.042 to 0.049 s for the two SCS sandwich panels. This loading duration is longer compared with the typical blast loading. For instance, the loading duration of 100-kg TNT charge detonated at 10 m away is 0.0097 s. The experimentally-verified FE models were utilized herein to investigate the performance of the SCS sandwich panel under blast loading. The same quarter FE model presented in Sect. 8.3 were used in the following analysis. The loading was changed to blast pressure loading which was applied on the whole top face of the SCS sandwich panel. The adopted blast pressure-time history has an exponential decay from peak pressure  $P_r$  to ambient pressure at time  $t_d$ . Negative pressure was omitted as it has little effect on the structural response and is normally neglected in the blast resistant design (UFC 2008; ASCE 2010, 2011). The positive phase can be described by the modified Friedlander equation (Baker 1973) as given in Eq. (8.1). In this analysis, 100-kg TNT charge detonated at 10 m away was adopted, and the peak pressure  $P_r$ , load duration  $t_d$  and decay coefficient  $\bar{\theta}$  were obtained as 845.5 kPa, 9.7 ms and 2.4, respectively, by using CONWEP (Hyde 1991).

In the impact tests, the simply supported boundary condition for SCS sandwich panels were employed, as the axially-restrained boundary conduction is generally difficult to be achieved. However, the axially-restrained boundary condition is preferred in actual applications owing to the enhanced blast resistance of SCS sandwich panels via tensile membrane effect of faceplates. Hence, the FE simulations

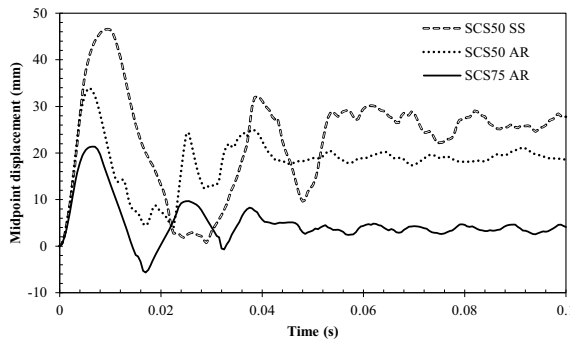


**Fig. 8.21** Midpoint displacement–time histories of SCS sandwich panels under blast loading (SS—Simply support; AR—Axially restrained)

were conducted to investigate the response of axially-restrained SCS sandwich panels under blast loading. The midpoint displacement–time histories of the SCS50 sandwich panel with simply supported and axially-restrained boundaries as well as the SCS75 sandwich panel with axially-restrained boundary are presented in Fig. 8.21. It can be seen that the maximum displacement of the axially-restrained SCS50 sandwich panel is reduced by 27% as compared to the simply supported panel. This can be attributed to the increase in resistance and ductility when the axially-restrained boundary is adopted. The FE simulations were also conducted to obtain the load (or resistance) versus displacement curve of the SCS sandwich panel under quasi-static uniform pressure loading. As demonstrated in Fig. 8.22, the maximum resistance and corresponding displacement of the axially-restrained SCS50 sandwich panel increase 268.0 and 93.9%, respectively, as compared to the simply supported panel. By comparing the SCS50 and SCS75 sandwich panels with axially-restrained boundary in Fig. 8.21, it is observed that the maximum displacement of the SCS75

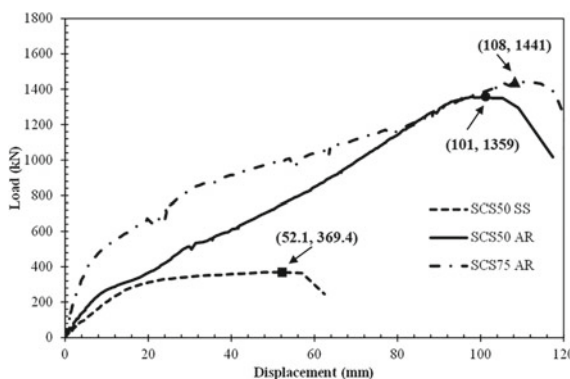


**Fig. 8.22** Load–displacement curves of SCS sandwich panels under quasi-static uniform pressure loading

sandwich panel can be reduced by 37% through increasing the grout core depth owing to the enhanced load–displacement response (as shown in Fig. 8.22) and increased total mass.

Further analyzing the load–displacement curves of the SCS50 sandwich panel with simply supported and axially-restrained boundaries in Fig. 8.22 reveals that both of them are similar at initial stage. This indicates that the SCS50 sandwich panel mainly relies on the bending action to resist the load at initial stage. After the failure of grout core, the load was taken over by the tensile membrane of the steel plates that were axially restrained, while the simply supported panel behaved shear failure. By comparing the load–displacement curves of the axially-restrained SCS50 and SCS75 sandwich panels, the increase in grout core depth improved the resistance at initial stage, but shows little effect on the final resistance and ductility. This is because the grout core has minimal contribution to the resistance after severe cracking of grout.

Figure 8.23 presents the scaled damage measure contours of the SCS50 sandwich panel with simply supported and axially-restrained boundaries. The scaled damage measure, which is a function of accumulated effective plastic strain parameter  $\lambda$ , is defined in MAT\_72R3 to evaluate the damage level of concrete. When it ranges from

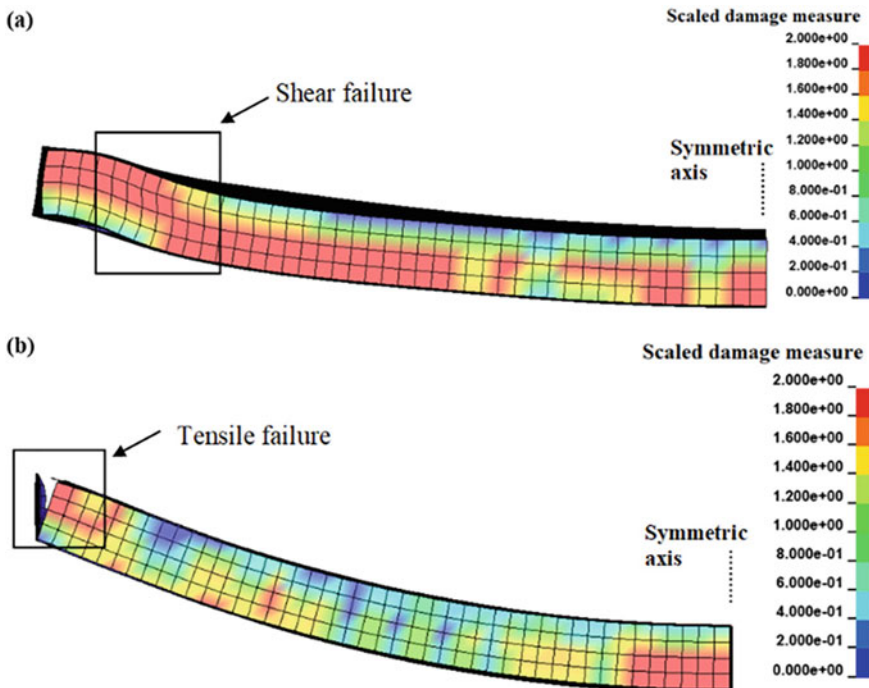


**Fig. 8.23** Failure modes of SCS50 under quasi-static uniform pressure loading: **a** simply supported, **b** axially restrained

0 to 1, the material transitions from the yield failure surface to the maximum failure surface. When it ranges from 1 to 2, the material transitions from the maximum failure surface to the residual failure surface. The grout core of both the two panels underwent severe damage after failure. Shear failure mode can be seen from the plot for the simply supported SCS50 sandwich panel, while the tensile membrane failure is shown in the plot for the axially-restrained panel. Owing to the different failure modes, the resistance of the simply supported SCS sandwich panel is mainly governed by the shear strength of grout, while the failure strain of mild steel governs the resistance of the axially-restrained SCS sandwich panel.

## 8.4 Summary

The performances of SCS sandwich panels under impulsive loading were experimentally studied in this chapter. The impulsive loading was achieved in the laboratory by utilizing an inflated high pressure airbag to transfer the applied load from dropped projectile onto the panels. In addition, FE simulations on SCS sandwich panels under blast loading were also conducted. The main findings from the experimental and numerical studies are summarized as follows:

- (1) A combination of flexure and shear deformation mode was observed for the SCS sandwich panel under impulsive loading.
- (2) The maximum and permanent deformations of the SCS75 panel with thicker core were significantly smaller as compared to the SCS50 panel owing to the higher resistance and mass. The SCS75 panel also absorbed higher impact impulse under the same impact condition.
- (3) The debonding between the grout core and bottom plate during impact was observed from the strain–time histories of both the two tested SCS sandwich panels.
- (4) The established FE models of SCS sandwich panels were shown to be reasonable by comparing with the test results. The majority of energy was absorbed by steel plates owing to the higher strength and ductility as compared to the grout core.
- (5) The blast resistance of axially-restrained SCS sandwich panel could be significantly improved as compared to the simply supported counterpart owing to the enhanced resistance and ductility via developing tensile membrane of steel plates.

## References

- Abramowicz W, Jones N (1986) Dynamic progressive buckling of circular and square tubes. *Int J Impact Eng* 4:243–270
- Anandavalli N, Lakshmanan N, Rajasankar J et al (2012) Numerical studies on blast loaded steel–concrete composite panels. *JCES* 1(3):102–108
- Arora H, Hooper PA, Dear JP (2011) Dynamic response of full-scale sandwich composite structures subject to air-blast loading. *Compos: Part A* 42:1651–1662
- ASCE (2010) Design of blast-resistant buildings in petrochemical facilities. American Society of Civil Engineers, Reston, Virginia
- ASCE (2011) Blast protection of buildings. American Society of Civil Engineers, Reston, Virginia
- Baker WE (1973) Explosions in air. University of Texas Press, Austin
- Chen W, Hao H (2014) Experimental investigations and numerical simulations of multi-arch double-layered panels under uniform impulsive loadings. *Int J Impact Eng* 63:140–157
- Chen W, Hao H, Chen S (2015) Numerical analysis of prestressed reinforced concrete beam subjected to blast loading. *Mater Des* 65:662–674
- Clubley SK (2014) Non-linear long duration blast loading of cylindrical shell structures. *Eng Struct* 59:113–126
- Crawford JE, Lan S (2006) Blast barrier design and testing. In: Proceedings of the ASCE Structures Congress, St. Louis, Missouri
- Crawford JE, Wu Y, Magallanes JM et al (2012) Modeling of concrete materials under extreme loads. Advances in Protective Structures Research, Taylor & Francis Group, London
- Foglar M, Kovar M (2013) Conclusions from experimental testing of blast resistance of FRC and RC bridge decks. *Int J Impact Eng* 59:18–28
- Grote DL, Park SW, Zhou M (2001) Dynamic behavior of concrete at high strain rate and pressure: I. experimental characterization. *Int J Impact Eng* 25:869–886
- Hallquist JO (2006) LS-DYNA theory manual. Livermore Software Technology Corporation (LSTC). Livermore, California
- Hallquist JO (2012) LS-DYNA keyword user's manual. Livermore, California: Livermore Software Technology Corporation. Livermore, California
- Hou S, Zhao S, Ren L et al (2013) Crashworthiness optimization of corrugated sandwich panels. *Mater Des* 51:1071–1084
- Hyde D (1991) Conventional Weapons programm (ConWep). US Army Waterways Experimental Station, Vicksburg
- Ishiguro S (2007) Experiments and analyses of fracture properties of grouting mortars. In: Proceedings of the 6th international conference on fracture mechanics of concrete and concrete structures
- Jiang H, Wang X, He S (2012) Numerical simulation of impact tests on reinforced concrete beams. *Mater Des*: 39:11–120
- Jing L, Xi C, Wang Z et al (2013) Energy absorption and failure mechanism of metallic cylindrical sandwich shells under impact loading. *Mater Des* 52: 470–480
- Jones N (1988) Structural impact. Cambridge University Press, New York
- Kilicaslan C, Guden M, Odaci IK et al (2012), The impact responses and the finite element modeling of layered trapezoidal corrugated aluminum core and aluminum sheet interlayer sandwich structures. *Mater Des* 46:121–133
- Lacroix DN, Doudak G, EI-Domiaty K (2014) Retrofit options for light-frame wood stud walls subjected to blast loading. *J Struct Eng* 140(4):04013104
- Lan S, Lok TS, Heng L (2005) Composite structural panels subjected to explosive loading. *Constr Build Mater* 19:387–395
- Liew JYR, Sohel KMA (2009) Lightweight steel-concrete-steel sandwich system with J-hook connectors. *Eng Struct* 31(5):1166–1178
- Liew JYR, Wang TY (2011) Novel steel-concrete-steel sandwich composite plates subjected to impact and blast load. *Adv Struct En* 14(4):673–686

- Liew JYR, Sohel KMA, Koh CG (2009) Impact tests on steel–concrete–steel sandwich beams with lightweight concrete core. *Eng Struct* 31(9):2045–2059
- Lin X, Zhang YX, Hazell PJ (2014) Modelling the response of reinforced concrete panels under blast loading. *Mater Des* 56:620–628
- Magallanes JM, Wu Y, Malvar LJ et al (2010) Recent improvements to release III of the K&C concrete model. In: the 11th international LS–DYNA users conference
- Malvar LJ, Crawford JE, Wesevich JW et al (1997) A plasticity concrete material model for DYNA3D. *Int J Impact Eng* 19:847–873
- Mao L, Barnett S, Begg D et al (2014) Numerical simulation of ultra high performance of fibre reinforced concrete panel subjected to blast loading. *Int J Impact Eng.* 64:91–100
- Mostaghel N (2003) Blast load simulation system. US Patent US06536258B1, 25 Mar 2003
- Remennikov AM, Liew JYR, Kong SY et al (2009) Simulation of impulsive loading on columns using an inflatable airbag technique. In: Proceedings of the 8th International Conference on Shock & Impact Loads on Structures, Adelaide, Australia
- Remennikov AM, Kong SY (2012) Numerical simulation and validation of impact response of axially-restrained steel–concrete–steel sandwich panels. *Compo Struct* 94:3546–3555
- Ross CA, Thompson PY, Tedesco JW (1989) Split–Hopkinson pressure–bar tests on concrete and mortar in tension and compression. *ACI Mater J* 86(5):475–481
- Schleyer GK, Lowak MJ, Polcyn MA et al (2007) Experimental investigation of blast wall panels under shock pressure loading. *Int J Impact Eng* 34:1095–1118
- Smith SJ, McCann DM, Kamara ME (2009) Blast resistant design guide for reinforced concrete structures. Portland Cement Association, Skokie
- Smith PD, Hetherington JG (1994) Blast and ballistic loading of structures. Butterworth–Heinemann, Oxford
- Sohel KMA, Liew JYR (2011) Steel–concrete–steel sandwich slabs with lightweight core–static performance. *Eng Struct* 33(3):981–992
- Symonds PS (1967) Survey of methods of analysis for plastic deformation of structures under dynamic loading. Division of Engineering Report BU/NSRDC/1–67, Brown University
- Tabatabaei ZS, Volz JS, Baird J et al (2013) Experimental and numerical analyses of long carbon fiber reinforced concrete panels exposed to blast loading. *Int J Impact Eng* 57:70–80
- UFC 3–340–02 (2008) Structures to resist the effects of accidental explosions. US Department of Army, Navy and the Air Force, Washington, DC
- Wang Y, Liew JYR, Lee SC (2015a) Experimental and numerical studies of non-composite Steel–Concrete–Steel sandwich panels under impulsive loading. *Mater Des* 81:104–112
- Wang Y, Liew JYR, Lee SC (2015b) Theoretical models for axi-ally restrained steel–concrete–steel sandwich panels under blast loading. *Int J Impact Eng* 6:221–231
- Wu J, Chew SH (2014) Field performance and numerical modeling of multi-layer pavement system subject to blast load. *Constr Build Mater* 52:177–188
- Zhai X, Wang Y (2013) Modelling and dynamic response of steel reticulated shell under blast loading. *Shock Vib* 20(1):19–28
- Zhai X, Wang Y, Huang M (2013) Performance and protection approach of single-layer reticulated dome subjected to blast loading. *Thin-Walled Struct* 73:57–67

# Chapter 9

## Analytical Models for Axially-Restrained Steel–Concrete–Steel Sandwich Panel Under Blast



### 9.1 Introduction

Steel–Concrete–Steel (SCS) sandwich panels were demonstrated to have good blast resistant performances through field blast tests (Liew and Wang 2011; Lan et al. 2005), and therefore they could be employed as protective structures against impact and blast loads. Previous studies showed that the SCS sandwich panel with axially-restrained boundary had significantly higher blast resistance as compared to its counterpart with simply supported boundary. Hence, the aim of this study is to develop the analytical models for predicting axially-restrained SCS sandwich panels under blast loading.

For a simply supported SCS sandwich panel, its failure mode includes flexure and shear. Therefore, the mechanical shear connectors are of significance to assure the composite action of SCS sandwich panels. Liew and Sohel (2009) proposed J-hooks and studied the impact performances of SCS sandwich beams with J-hook connectors (Liew et al. 2009). Moreover, field blast tests were also conducted to obtain the blast responses of SCS sandwich panels with J-hook connectors (Liew and Wang 2011). For the axially-restrained SCS sandwich panels, it mainly relies on the tensile membrane action to resist lateral pressure load, and therefore the shear connectors are relatively unimportant. Remennikov and Kong (2012) carried out the impact tests on the axially-restrained non-composite SCS sandwich panels. The tensile membrane resistance was found to be significantly higher than the bending resistance, and the ductility of the SCS sandwich panel was also improved (Remennikov and Kong 2012; Remennikov et al. 2013). The membrane action of Reinforced Concrete (RC) panels has already been considered in fire resistance design when the RC panels undergo large deformation after fire (Li et al. 2007; Bailey 2001). The formula used to predict resistance of RC panels considering membrane action was generally derived based on force equilibrium. The resistance–deflection function is necessary to predict the structural response under dynamic loading. In this study, the resistance–deflection function of the SCS sandwich panel contributed by concrete core is derived based

on the energy balance principle, since the force distribution on the concrete core is complex and it is nearly impossible to establish the force equilibrium equations.

The Single-Degree-Of-Freedom (SDOF) method is commonly adopted to predict the structural response under blast loading (UFC 2008; Biggs 1964; ASCE 2011), as it is a relatively simpler alternative as compared to the Finite Element (FE) method and the calculations are reasonable in most cases. A structural member can be equivalent to a SDOF system through transformation factor  $K_{LM}$ , which is a function of its deflection shape (Biggs 1964). Normally, the shape function is obtained by analyzing the member under uniformly distributed static load. In reality, the deflection shape changes during motion owing to the existence of inertia force which, together with the uniform pressure load, changes the load distribution on the member. It is accepted that shape function has little effect on the structural response if the adopted deflection shapes are in accordance with the actual boundary condition. However, the difference in maximum displacement obtained using different assumed shape functions may be over 10% in the elastic range (Baker et al. 1983) and may be even larger when the member enters plastic range. A constant value of Dynamic Increase Factor (DIF) was generally included in the SDOF model to represent the average strain rate effect on material strength (UFC 2008; ASCE 2011). Since the DIF is a function of strain rate, it also varies during motion. Hence, adopting a constant value of DIF may not accurately capture the strain rate effect. To overcome this limitation, Nassr et al. (2012) proposed a strain rate model that defines the maximum strain rate in terms of scaled distance for beam column. Different DIF values can be generated under different blast loads, but the model is still unable to capture the varying DIF with strain rate during motion. The varying DIF in terms of strain rate was recently included in the continuous beam model (Carta and Stochino 2013; Jones et al. 2009) and SDOF model (Carta and Stochino 2013) to analyze the simply supported RC panels under blast loading. The DIF was introduced by updating the resistance at each time step according to the strain rate at the corresponding time step, and the predictions with varying DIF were more accurate than those with constant DIF by comparing with test results.

In this chapter, the resistance–deflection function of the axially-restrained SCS sandwich panel was derived and then included into the SDOF model. The varying DIF in terms of strain rate was also considered in the SDOF model. Since only one deflection shape function can be included in the SDOF model, the Lagrange Equation model (Donaldson 2006; Schleyer and Hsu 2000; Langdon and Schleyer 2005) with combined shape functions and varying DIF was introduced to better predict the blast responses of axially-restrained SCS sandwich panels.

## 9.2 FE Model Calibration

### 9.2.1 Blast Loading Test on SCS Sandwich Panels

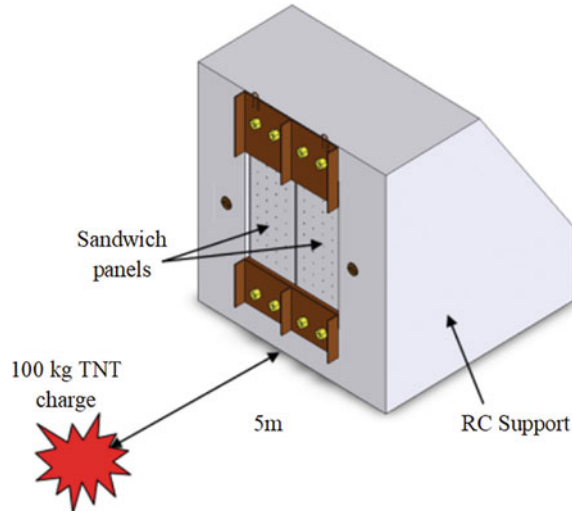
The field blast tests on SCS sandwich panels conducted by Kang et al. (2013) were employed for the FE model validation. There were six specimens being fabricated for three blast tests, and two specimens were tested in each blast test. The 100 kg TNT military cratering ordnance was detonated at a standoff distance of 5 m (Liew and Wang 2011; Kang et al. 2013). The setup of field blast test is shown in Fig. 9.1. Although six specimens were tested, only one specimen with normal concrete and without shear connectors was selected for validating the established FE model in the following section. The configuration of the non-composite SCS sandwich panel with normal concrete is shown in Fig. 9.2.

### 9.2.2 FE Model Establishment

The FE model of the SCS sandwich panel is shown in Fig. 9.3. Thick-shell and solid elements are used to mesh the steel plates and concrete core, respectively. The front, back, side and end steel plates were fillet welded together to form the outer skins of the panel during fabrication. Since no weld failure was observed after the blast test, the perfect weld condition is employed in the FE model by merging the coincident nodes of steel plates.

The Continuous Surface Cap (CSC) model in LS-DYNA (Hallquist 2006) was adopted to simulate the behavior of concrete. The CSC model was developed by US

**Fig. 9.1** Blast test setup with 100 kg TNT charge (Kang et al. 2013)



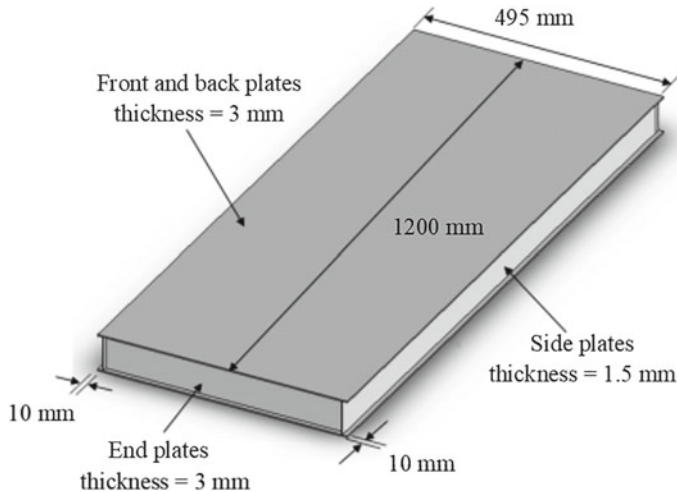


**Fig. 9.2** Details of SCS sandwich panel (Kang et al. 2013)

Federal Highway Administration for simulating the concrete-like material subjected to impact and blast loads (FHWA 2007a, b). This model has been proven to be a robust constitutive model for both implicit and explicit analysis. The detailed introduction of failure surface, flow rule, damage formulation and strain rate treatment for the CSC model can be found from FHWA (2007b). This FHWA material model is easy to use, since it can generate the default parameters for the normal concrete by only inputting the unconfined compressive strength. The main material parameters of concrete used in this analysis are given in Table 9.1.

Piecewise Linear Plasticity (PLP) model in LS-DYNA was adopted for the steel material. The input true stress–effective plastic strain curve was obtained from the tensile coupon test results. Cowper-Symonds equation (Cowper and Symonds 1958) is included in this material model to consider the strain rate effect, as shown in Eq. (9.1).

$$DIF_s = 1 + (\dot{\varepsilon} / c)^{1/p} \quad (9.1)$$

where  $c$  and  $p$  are strain rate parameters. For mild steel, the values of  $c$  and  $p$  are taken as  $40.4 \text{ s}^{-1}$  and 5, respectively (Jones 1988).

### 9.2.3 FE Model Validation

The blast pressure–time history recorded in the test is plotted in Fig. 9.4, together with the integrated impulse. The equivalent triangular blast load with similar peak

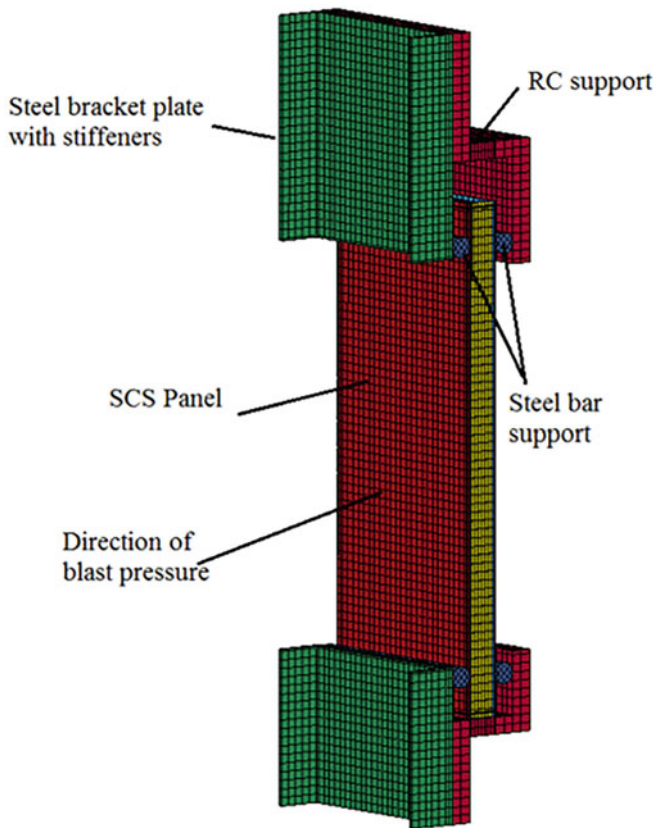


**Fig. 9.3** FE model of SCS sandwich panel and support, reprinted from Wang et al. (2015), copyright 2022, with permission from Elsevier

**Table 9.1** Material properties of concrete in FE analysis

Density (kg/m <sup>3</sup> )	Compressive strength (MPa)	Shear modulus (GPa)	Bulk modulus (GPa)
2310	35	12.06	13.21

impulse and pressure is applied in the FE model, as shown in Fig. 9.4. The mid-span permanent displacement of the SCS sandwich panel from blast test is compared with the FE-prediction, as shown in Fig. 9.5. Since the potentiometers failed to capture the data during the field blast test, the displacement–time history was not compared. Figure 9.5 shows that the measured permanent displacement from the blast test agrees well with the FE-prediction. Moreover, the FE-predicted failure mode of the SCS sandwich panel is also compared with test observations in Fig. 9.6. Both FE and test results exhibit the flexural failure mode at mid-span, with sign of shear deformation at

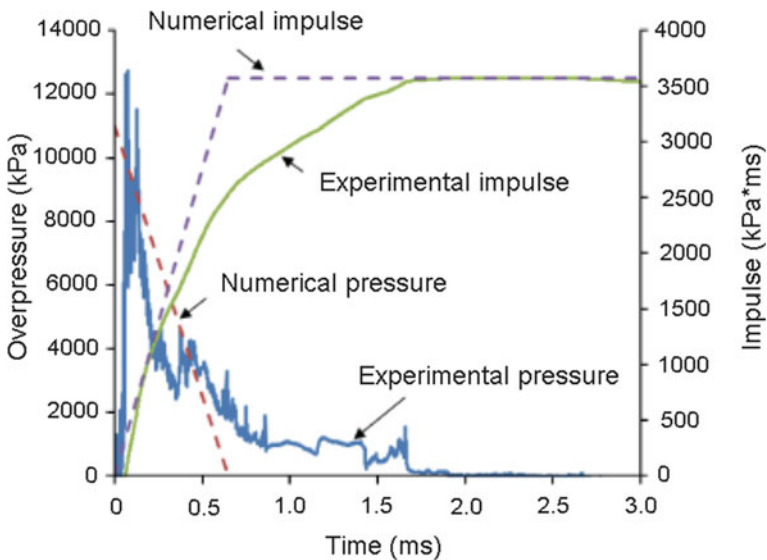
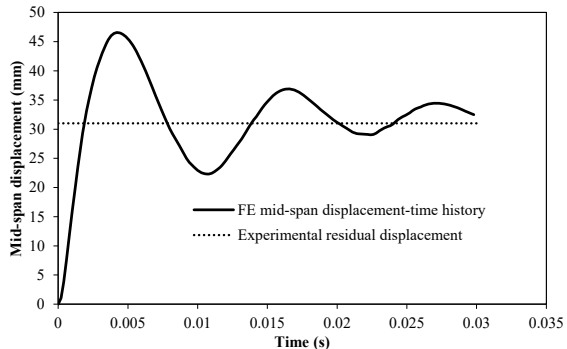


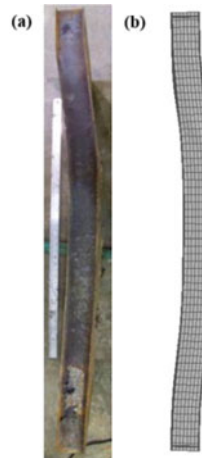
**Fig. 9.4** Experimental and numerical blast loading profiles (Kang et al. 2013)

**Fig. 9.5** Comparison of experimental and numerical results, reprinted from Wang et al. (2015), copyright 2022, with permission from Elsevier



the top end. Therefore, the established FE model can produce reasonable predictions on the responses of SCS sandwich panels subjected to blast loading. The established FE model will be used to verify the analytical models in the following sections by removing the side plates and support as well as imposing the axially-restrained boundary.

**Fig. 9.6** Comparison of failure modes from **a** blast test and **b** numerical simulation, reprinted from Wang et al. (2015), copyright 2022, with permission from Elsevier



### 9.3 SDOF Model

The SCS sandwich panel can be equivalent to a SDOF system, and the deflection shape function and resistance–deflection function of the SCS sandwich panel are necessary to establish the equation of motion as

$$K_{LM}m\ddot{y} + R(y) = F(t) \quad (9.2)$$

where  $K_{LM}$  is the load-mass factor and can be calculated based on the given deflection shape function;  $R(y)$  is the resistance–deflection function.

The deflection shape function and resistance–deflection function are generally derived by solving the differential equations established according to the force equilibrium. However, it is hard to establish the force equilibrium equations for the SCS sandwich panel owing to the undetermined composite action between steel plates and concrete core as well as the complex stress–strain relationship of concrete. In this study, the resistance–deflection function of the SCS sandwich panel is divided into two parts, i.e., the resistance contributed by steel plates and concrete core. The resistance–deflection function of the axially-restrained steel plate considering tensile membrane action has been obtained by utilizing force equilibrium equation (Wang and Xiong 2015), which is given as

$$R_s(Y) = \begin{cases} \frac{21.104Et_sY^3}{L^4} & \varepsilon \leq \varepsilon_y \\ \frac{8Et_s\varepsilon_y(1-\alpha)Y}{L^2} + \frac{21.104\alpha Et_sY^3}{L^4} & \varepsilon > \varepsilon_y \end{cases} \quad (9.3)$$

where  $E$  is the Young's modulus,  $t_s$  is the steel plate thickness,  $Y$  is the mid-span displacement,  $L$  is the span length,  $\varepsilon_y$  is the yield strain, and  $\alpha$  is the steel hardening coefficient. The deflection shape function has been obtained as (Wang and Xiong 2015)

$$\phi(x) = \frac{4}{L^2}(Lx - x^2) \quad (9.4)$$

The deflection shape function of the steel plate in Eq. (9.4) is also adopted as the deflection shape function for the SCS sandwich panel. This is because the deflection shape function has little effect on the structural response (Baker et al. 1983), and the steel plates of the SCS sandwich panel absorb the majority of blast energy. Another reason is that the constant curvature along the span of the SCS sandwich panel can be obtained according to the shape function in Eq. (9.4), which will significantly simplify the calculation.

The energy balance principle is adopted to derive the resistance-deflection function of the SCS sandwich panel contributed by concrete core. The procedure is that: (a) obtaining the strain distribution of concrete core and establish the relationship between strain and mid-span displacement; (b) deriving the relationship between the internal energy of concrete core and mid-span displacement; (c) differentiating the internal energy with respect to mid-span displacement and divided by load factor  $K_L$  to obtain the resistance-deflection function of the SCS sandwich panel contributed by concrete core.

### 9.3.1 Resistance-Deflection Function Contributed by Concrete Core

To simplify the calculation of resistance-deflection function of the SCS sandwich panel contributed by concrete core, the following influences are ignored, i.e., the tensile strength of concrete, the confinement effect on compressive strength of concrete, and the bonding and friction between steel plates and concrete core. Then, the force distribution on the concrete core and the compression strut along the span can be given in Fig. 9.7, together with the neutral axis along the span. According to the force equilibrium in horizontal direction, the compressive force from the end plate equals to the compressive force in concrete, i.e.,  $F_e = F_c$ . Therefore, it is reasonable to assume that the neutral depth (the distance between the outmost compression layer and neutral axis) at the end and mid-span is the same. Hence, according to Fig. 9.8,  $t_1$  equals to  $t_2$ , which leads to the following relationship.

$$\frac{\Delta L_S}{t_n - t_1} = \frac{\Delta L_C}{t_2} \quad (9.5)$$

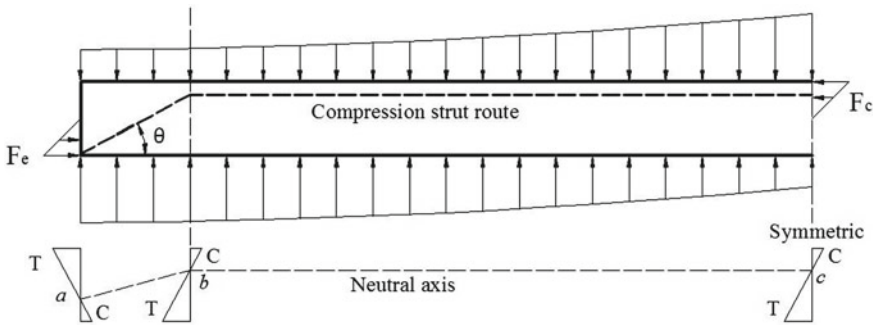
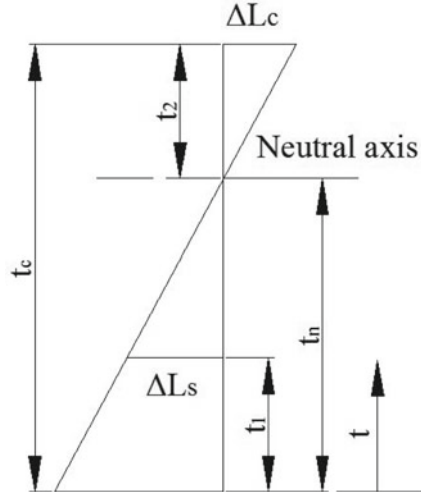


**Fig. 9.7** Force distribution and neutral axis on the concrete core, reprinted from Wang et al. (2015), copyright 2022, with permission from Elsevier

**Fig. 9.8** Deformation profile across the concrete depth, reprinted from Wang et al. (2015), copyright 2022, with permission from Elsevier



where  $\Delta L_s$  is the difference between developed length and original length of the steel plate, and  $\Delta L_C$  is the difference between compressed length and original length of concrete at the top layer. By adopting the deflection shape function in Eq. (9.4), the curvature of concrete core can be obtained in Eq. (9.6).

$$K = \frac{|y'|}{(1 + y'^2)^{3/2}} \approx 8Y/L^2 \quad (9.6)$$

Therefore,  $\Delta L_C$  and  $\Delta L_s$  can be obtained as

$$\Delta L_C = K(L - 2t_c/\tan\theta)t_2; \Delta L_s = \frac{1}{2} \int_0^L \left(\frac{dy}{dx}\right)^2 dx = \frac{8Y^2}{3L} \quad (9.7)$$

From above equations, the neutral axis is determined as

$$t_n = \frac{t_c}{2} + \frac{Y\xi}{6} \quad (9.8)$$

where  $\xi = L / (L - 2t_c / \tan \theta)$ . The value of  $\theta$  normally ranges from  $26.6^\circ$  to  $45^\circ$ . In this study,  $\theta$  is taken as  $26.6^\circ$  in accordance with Eurocode 2 (2004). Therefore, the axial strain above the neutral axis is obtained as

$$\varepsilon = \frac{8}{L^2} \left[ \left( t - \frac{t_c}{2} \right) Y - \frac{Y^2 \xi}{6} \right] \quad (9.9)$$

Figure 9.9 presents the comparison of the normal strain–mid-span displacement curves obtained from FE analysis and Eq. (9.9). The details of the FE model are listed in Table 9.2. It can be seen that the analytical-predicted strain agrees well with the FE-prediction. Hence, the established strain formula in Eq. (9.9) is reasonable and can be used for calculating the internal energy of concrete core.

Since it is complex to obtain the internal energy of concrete core based on current neutral axis which varies with the mid-span displacement, a constant neutral axis is proposed, based on which the equivalent curvature is then derived. If the internal energy of concrete core keeps increasing with the mid-span displacement rising from 0 to  $Y_n$ , the neutral axis  $t_n$  in Eq. (9.8) ranges from  $t_c/2$  to  $t_c/2 + Y_n \xi / 6$ . Therefore, it is rational to take the average neutral axis  $t_c/2 + Y_n \xi / 12$  as the constant neutral axis.  $Y_n$  is the minimum value of the maximum mid-span displacement ( $Y_{max}$ ) and

**Fig. 9.9** Comparison of axial strain–displacement curves between analytical and FE prediction, reprinted from Wang et al. (2015), copyright 2022, with permission from Elsevier

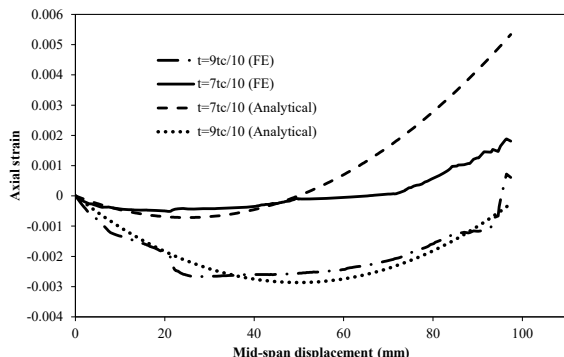


**Table 9.2** Details of FE model for implicit analysis on SCS sandwich panel

Front/back/end plate thickness (mm)	Concrete core thickness (mm)	Span (mm)	Steel yield stress (MPa)	Steel hardening coefficient (%)	Concrete compressive strength (MPa)
3	50	1180	320	0.5	35

$Y_m$ .  $Y_m$  is a value of the mid-span displacement. When the mid-span displacement exceeds  $Y_m$ , the equivalent curvature starts to decrease with the increasing of mid-span displacement.  $Y_m$  will be given later after establishing the equivalent curvature.

The equivalent curvature ( $K_e$ ) is derived based on the criteria that the internal energy of concrete core calculated by using original and equivalent strain expression is the same in the elastic range. The internal energy of concrete core per unit area is given as

$$\bar{u} = \int_0^{\eta_m} \frac{1}{2} E \varepsilon^2 d\eta = \frac{1}{6} E K^2 \eta_m^3 \quad (9.10)$$

where  $\eta$  is the distance between the compressive layer and neutral axis, and  $\eta_m = T/2 - Y_n \xi / 12$ . Then, the equivalent curvature is obtained as

$$K_e = \frac{8Y}{L^2} \left( \frac{1 - Y\xi / 3t_c}{1 - Y_n \xi / 6t_c} \right)^{3/2} \quad (9.11)$$

and the strain can be expressed as

$$\varepsilon = K_e \eta = \frac{8Y\eta}{L^2} \left( \frac{1 - Y\xi / 3t_c}{1 - Y_n \xi / 6t_c} \right)^{3/2} \left( 0 \leq \eta \leq \frac{t_c}{2} - \frac{Y_n \xi}{12} \right) \quad (9.12)$$

Differentiating the equivalent curvature  $K_e$  with respect to mid-span displacement  $Y$  and setting it to zero leads to the solution of  $Y_m$  to be  $6t_c / 5\xi$ . It indicates that when the mid-span displacement exceeds  $Y_m$ , the equivalent curvature  $K_e$  starts to decrease with increasing mid-span displacement.

The stress-strain curve of concrete under uniaxial compression is given by Eurocode 2 (2004) as

$$\frac{\sigma_c}{f_{cm}} = \frac{k\varepsilon/\varepsilon_o - (\varepsilon/\varepsilon_o)^2}{1 + (k-2)\varepsilon/\varepsilon_o} \text{ for } |\varepsilon| < |\varepsilon_c| \quad (9.13)$$

where  $k, f_{cm}, \varepsilon_o$  and  $\varepsilon_c$  can be found in Eurocode 2 (2004).

When all the compressive strains above the neutral axis are smaller than the crush strain of concrete  $\varepsilon_c$ , the stress-strain relationship given in Eq. (9.13) can be used for all the compressive concrete above the neutral axis. Hence, the internal energy of concrete core per unit volume can be calculated as

$$u_c(\varepsilon) = \int_0^{\varepsilon} \sigma_c d\varepsilon' = \int_0^{\varepsilon} f_{cm} \frac{k\varepsilon/\varepsilon_o - (\varepsilon/\varepsilon_o)^2}{1 + (k-2)\varepsilon/\varepsilon_o} d\varepsilon' = \varepsilon_0 f_{cm} g_1 \left( \frac{\varepsilon}{\varepsilon_o} \right) \quad (9.14)$$

$$\text{where } g_1\left(\frac{\varepsilon}{\varepsilon_o}\right) = \left[ \frac{(k-1)^2\varepsilon/\varepsilon_o}{(k-2)^2} - \frac{(\varepsilon/\varepsilon_o)^2}{2(k-2)} - \frac{(k-1)^2 \ln((k-2)\varepsilon/\varepsilon_o + 1)}{(k-2)^3} \right].$$

Provided that the internal energy density of concrete core along the compression strut is the same, the internal energy of concrete core in SCS sandwich panel can be calculated as

$$U_c^u = L_e B \int_0^{\eta_m} u_c(K_e \eta) d\eta \quad (9.15)$$

where  $B$  is the width of concrete core,  $L_e$  is the length of compression strut and can be calculated as  $L_e = L + 2t_c(1/\sin \theta - 1/\tan \theta)$ ,  $g_2\left(\frac{K_e \eta_m}{\varepsilon_o}\right) = \bar{A}\left(\frac{K_e \eta_m}{\varepsilon_o}\right)^2 - \bar{B}\left(\frac{K_e \eta_m}{\varepsilon_o}\right)^3 - \bar{C}\frac{K_e \eta_m}{\varepsilon_o} \left\{ \ln\left[(k-2)\frac{K_e \eta_m}{\varepsilon_o} + 1\right] - 1 \right\} - \bar{D} \ln\left[(k-2)\frac{K_e \eta_m}{\varepsilon_o} + 1\right]$ , where  $\bar{A} = \frac{(k-1)^2}{2(k-2)^2}$ ,  $\bar{B} = \frac{1}{6(k-2)}$ ,  $\bar{C} = \frac{(k-1)^2}{(k-2)^3}$ ,  $\bar{D} = \frac{(k-1)^2}{(k-2)^4}$ .

Thus, differentiating the internal energy of concrete core with respect to mid-span displacement leads to

$$\begin{aligned} \frac{dU_c^u}{dY} &= \frac{L_e B \varepsilon_o^2 f_{cm}}{K_e} K'_e \left\{ -g_2\left(\frac{K_e \eta_m}{\varepsilon_o}\right) \frac{1}{K_e} + 2\bar{A}\left(\frac{\eta_m}{\varepsilon_o}\right)^2 K_e \right. \\ &\quad - 3\bar{B}\left(\frac{\eta_m}{\varepsilon_o}\right)^3 K_e^2 - \bar{C}\frac{\eta_m}{\varepsilon_o} \left[ \ln\left[(k-2)\frac{K_e \eta_m}{\varepsilon_o} + 1\right] - 1 \right] \\ &\quad \left. - \bar{C}\frac{k-2}{(k-2)K_e \eta_m / \varepsilon_o + 1} \frac{K_e \eta_m^2}{\varepsilon_o^2} - \bar{D}\frac{k-2}{(k-2)K_e \eta_m / \varepsilon_o + 1} \frac{\eta_m}{\varepsilon_o} \right\} \end{aligned} \quad (9.16)$$

where  $K'_e = \frac{dK_e}{dY}$ . Then, the resistance-deflection function contributed by concrete core without crushing can be obtained as

$$R_{c1}(Y) = \frac{dU_c^u}{dY} \frac{1}{BLK_L} \quad (9.17)$$

where  $K_L$  is the load factor and can be calculated based on the given deflection shape function in Eq. (9.4).

When the maximum compressive strain in the concrete core exceeds crush strain of concrete  $\varepsilon_c$ , the internal energy of concrete core can be divided into two parts, i.e., the one with crushing and the rest without crushing. The internal energy of concrete core without crushing can be calculated as

$$U_{c,1} = L_e B \int_0^{\eta_0} u_c(K_e \eta) d\eta = \frac{L_e B \varepsilon_o^2 f_{cm}}{K_e} g_2\left(\frac{K_e \eta_0}{\varepsilon_o}\right) \quad (9.18)$$

where  $\eta_0 = \frac{\varepsilon_c L^2}{8Y} \left( \frac{1 - Y_n \xi / 6t_c}{1 - Y \xi / 3t_c} \right)$ , which is calculated by setting the strain expression in Eq. (9.12) to crushing strain  $\varepsilon_c$ . The internal energy of concrete core with crushing can be calculated as

$$U_{c,2} = L_e B (\eta_m - \eta_0) \varepsilon_o f_{cm} g_1 \left( \frac{\varepsilon_c}{\varepsilon_o} \right) \quad (9.19)$$

Hence, the total internal energy of concrete core after crushing is given as

$$U_c^c = U_{c,1} + U_{c,2} \quad (9.20)$$

Similarly, differentiating the internal energy of concrete core with respect to mid-span displacement leads to

$$\frac{dU_c^c}{dY} = -\frac{L_e B \varepsilon_o^2 f_{cm}}{K_e^2} K'_e g_2 \left( \frac{\varepsilon_c}{\varepsilon_o} \right) - L_e B \varepsilon_o f_{cm} g_1 \left( \frac{\varepsilon_c}{\varepsilon_o} \right) \eta'_0 \quad (9.21)$$

where  $\eta'_0 = \frac{\varepsilon_c L^2}{8} \left( 1 - \frac{Y_n \xi}{6t_c} \right)^{3/2} \left[ -\frac{1}{Y^2 (1 - Y \xi / 3t_c)^{3/2}} + \frac{\xi}{2t_c Y (1 - Y \xi / 3t_c)^{5/2}} \right]$ .

In the same way, the resistance-deflection function contributed by concrete core after crushing can be obtained as

$$R_{c2}(Y) = \frac{dU_c^c}{dY} \frac{1}{BLK_L} \quad (9.22)$$

The procedure for calculating the resistance-deflection function of the SCS sandwich panel contributed by concrete core can be summarized as follow.

Calculating the maximum strain of concrete core by Eq. (9.23).

$$\varepsilon_{\max} = \frac{8Y_m}{L^2} \left( \frac{1 - Y_m \xi / 3t_c}{1 - Y_n \xi / 6t_c} \right)^{3/2} \left( \frac{t_c}{2} - \frac{Y_n \xi}{12} \right) \quad (9.23)$$

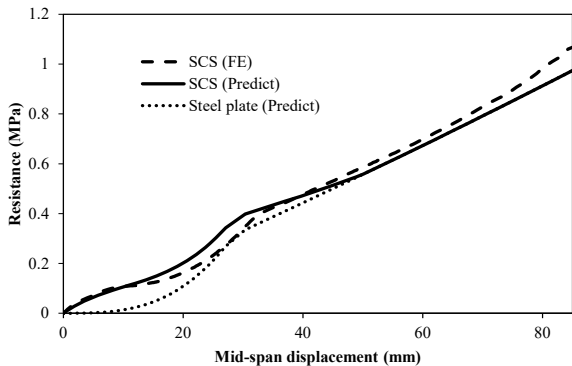
For  $\varepsilon_{\max} \leq \varepsilon_c$ , there is no concrete crushing. Then, the resistance-deflection function is given as

$$R_c = \begin{cases} R_{c1} & (Y \leq Y_m) \\ 0 & (Y > Y_m) \end{cases} \quad (9.24)$$

For  $\varepsilon_{\max} > \varepsilon_c$ , calculating  $Y_0$  by solving the Eq. (9.25).

$$\frac{8Y}{L^2} \left( \frac{1 - Y \xi / 3t_c}{1 - Y_n \xi / 6t_c} \right)^{3/2} \left( \frac{t_c}{2} - \frac{Y_n \xi}{12} \right) = \varepsilon_c \quad (9.25)$$

**Fig. 9.10** Comparison of resistance–deflection curves between analytical and FE models, reprinted from Wang et al. (2015), copyright 2022, with permission from Elsevier



Then, the resistance–deflection function is given as

$$R_c = \begin{cases} R_{c1} & (Y \leq Y_0) \\ R_{c2} & (Y_0 < Y \leq Y_m) \\ 0 & (Y > Y_m) \end{cases} \quad (9.26)$$

The total resistance of the SCS sandwich panel is obtained by summing the resistances contributed by steel plates and concrete core. Figure 9.10 presents the comparison of the analytical-predicted resistance–deflection of the SCS sandwich panel with that obtained by FE analysis, and good agreement between them can be observed. The resistance of steel plates is also plotted in Fig. 9.10, and it is lower than the resistance of the SCS sandwich panel obtained from FE analysis, especially for small displacement. This indicates that the concrete core helps in improving the initial stiffness of axially-restrained SCS sandwich panel, whereas the steel plates absorb the majority of blast energy when the SCS sandwich panel experiences large deformation.

### 9.3.2 DIF for SDOF Model

The strain rate effect is generally included in the analytical model by means of DIF which can be defined as a function of strain rate. In the FE method, the DIF–strain rate relationship can be directly specified in the constitutive model, and the varying value of DIF depending on strain rate can be applied in the FE calculation (Hallquist 2006). For the SDOF method, a constant DIF value is generally adopted to scale either the yield strength, ultimate strength or both of them depending on the deformation mode (UFC 2008; ASCE 2011). It has been argued that a single DIF value might not accurately capture the strain rate effect for highly varying strain rate, and it could be too conservative for large plastic deformation cases. Therefore, varying DIF in terms of strain rate is introduced into the SDOF and Lagrange Equation models to

accurately capture the strain rate effect. Since the strain rate has little effect on the Young's modulus of steel, it can be kept unchanged during calculation, while both yield stress and yield strain vary with the strain rate.

### 9.3.2.1 DIF for Steel Plate

The varying DIF can be taken into consideration during transformation of actual structural member to its equivalent SDOF system through energy balance principle. The variation for the internal energy of steel plates and its equivalent SDOF system is given by Eqs. (9.27) and (9.28), respectively.

$$dU_a = \int_0^L f(\dot{\varepsilon}_p)\sigma(Y)Ad\varepsilon dx \quad (9.27)$$

$$dU_e = DIF_s * K_R * R(Y)dY = DIF_s * \int_0^L \sigma(Y)Ad\varepsilon dx \quad (9.28)$$

where  $K_R$  is the resistance factor. By assuming that the internal energy along the span is constant and equating the above two equations leads to

$$DIF_s = \frac{\int_0^L f(\dot{\varepsilon}_p)dx}{L} \quad (9.29)$$

The configuration of infinitesimal element ( $dx$ ) is shown in Fig. 9.11 at  $t$  and  $t + \Delta t$ , based on which the plastic strain rate can be obtained as

$$\dot{\varepsilon}_p = \frac{[\phi(x)]^2 Y \dot{Y}}{1 + [\phi(x)Y]^2} \quad (9.30)$$

Equation (9.30) defines the strain rate in terms of shape function, displacement and velocity. For steel material, Eq. (9.31) can be obtained by using the Cowper-Symonds model to define the DIF as a function of strain rate.

$$f(\dot{\varepsilon}_p) = 1 + \left( \frac{[\phi(x)]^2 \dot{Y} Y}{c + c[\phi(x)Y]^2} \right)^{1/p} \quad (9.31)$$

Substituting Eq. (9.31) and shape function in Eq. (9.4) into Eq. (9.29), the  $DIF_s$  can be calculated as

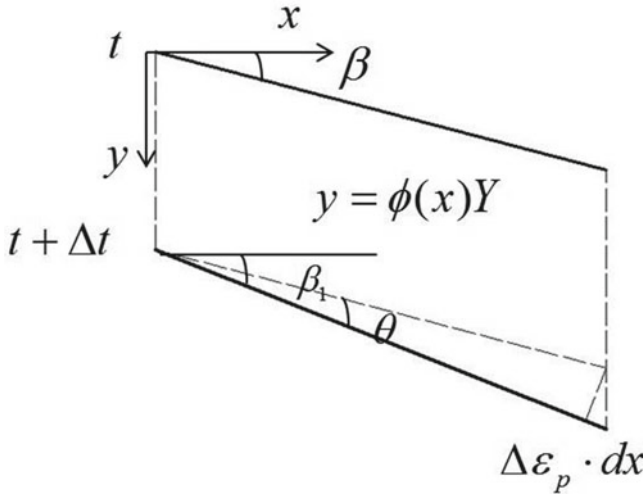


**Fig. 9.11** Configuration of infinitesimal element along span, reprinted from Wang et al. (2015), copyright 2022, with permission from Elsevier

$$DIF_s = 1 + \frac{\int_0^L \left( \frac{\chi \dot{\chi}}{c\chi^2 + c/16(1-2\chi/L)^2} \right)^{1/p} dx}{L} \quad (9.32)$$

where  $\chi = Y/L$  is the mid-span displacement to span ratio.

### 9.3.2.2 DIF for Concrete Core

The energy balance principle is also adopted to obtain the DIF for concrete core. The variation for the internal energy of concrete core without considering strain rate effect is given as

$$dU_c = BL_e f_{cm} \int_0^{\eta_m} \frac{k K_e \eta / \varepsilon_0 - (K_e \eta / \varepsilon_0)^2}{1 + (k - 2) K_e \eta / \varepsilon_0} \eta d\eta dK_e \quad (9.33)$$

Then, we have

$$\frac{dU_c}{dY} = BL_e f_{cm} \int_0^{\eta_m} \frac{k K_e \eta / \varepsilon_0 - (K_e \eta / \varepsilon_0)^2}{1 + (k - 2) K_e \eta / \varepsilon_0} \eta d\eta \frac{dK_e}{dY} \quad (9.34)$$

In the same way, the following equation can be obtained by considering the strain rate effect.

$$\frac{dU_{cD}}{dY} = BL_e f_{cm} \int_0^{\eta_m} D_c(\eta \dot{K}_e) \frac{k K_e \eta / \varepsilon_0 - (K_e \eta / \varepsilon_0)^2}{1 + (k-2) K_e \eta / \varepsilon_0} \eta d\eta \frac{dK_e}{dY} \quad (9.35)$$

Therefore, the DIF for concrete core is obtained as

$$DIF_{c1} = \frac{\int_0^{\eta_m} D_c(\eta \dot{K}_e) \frac{k K_e \eta / \varepsilon_0 - (K_e \eta / \varepsilon_0)^2}{1 + (k-2) K_e \eta / \varepsilon_0} \eta d\eta}{\int_0^{\eta_m} \frac{k K_e \eta / \varepsilon_0 - (K_e \eta / \varepsilon_0)^2}{1 + (k-2) K_e \eta / \varepsilon_0} \eta d\eta} \quad (9.36)$$

Equation (9.36) is only used to scale up the  $R_{c1}$ , and the DIF for scaling up  $R_{c2}$  is given in Eq. (9.37).

$$DIF_{c2} = \frac{\int_0^{\eta_0} D_c(\eta \dot{K}_e) \frac{k K_e \eta / \varepsilon_0 - (K_e \eta / \varepsilon_0)^2}{1 + (k-2) K_e \eta / \varepsilon_0} \eta d\eta}{\int_0^{\eta_0} \frac{k K_e \eta / \varepsilon_0 - (K_e \eta / \varepsilon_0)^2}{1 + (k-2) K_e \eta / \varepsilon_0} \eta d\eta} \quad (9.37)$$

In above equations,  $D_c(\dot{\varepsilon})$  defines the relationship between DIF and strain rate of concrete core and is given by CEB-FIP (1993).

$$D_c(\dot{\varepsilon}) = \begin{cases} (\dot{\varepsilon} / \dot{\varepsilon}_s)^{1.026\delta_s} & (\dot{\varepsilon} \leq 30s^{-1}) \\ \beta_s (\dot{\varepsilon} / \dot{\varepsilon}_s)^{1/3} & (\dot{\varepsilon} > 30s^{-1}) \end{cases} \quad (9.38)$$

where  $\delta_s = 1 / (5 + 9 f_{cm} / 10)$ ,  $\beta_s = 10^{(6.156\delta_s - 2.0)}$  and the static strain rate  $\dot{\varepsilon}_s = 30 \times 10^{-6}$ .

### 9.3.3 Equation of Motion for SDOF System

The equation of motion for the SDOF system can be established as

$$K_{LM}[\rho_s(t_{s1} + t_{s2}) + \rho_c t_c] \ddot{Y} + R_{s1} + R_{s2} + R_c = P(t) \quad (9.39)$$

where  $\rho_s$  and  $\rho_c$  are densities of steel and concrete;  $t_{s1}$ ,  $t_{s2}$  and  $t_c$  are thicknesses of front steel plate, back steel plate and concrete core;  $R_{s1}$ ,  $R_{s2}$  and  $R_c$  are the resistances of the SCS sandwich panel contributed by the front steel plate, back steel plate and concrete core;  $P(t)$  is pressure-time history of blast loading.

It should be noted that the equation of motion in Eq. (9.39) is only valid before the separation of front steel plate. The SCS sandwich panel can be divided into two parts, i.e., front steel plate and concrete core + back steel plate. Since the resistance intensity (i.e.,  $R_i / \rho_i t_i$ ) of the steel plate is higher than that of concrete core for large deformation, the front steel plate may separate from concrete core when the velocity reduction rate of the front steel plate is higher than that of concrete core and back steel plate. Therefore, the front steel plate starts to separate from concrete core when  $[R_{s1} - P(t)] / \rho_s t_{s1} > (R_{s2} + R_c) / (\rho_s t_{s2} + \rho_c t_c)$  and the equation of motion changes to

$$K_{LM}(\rho_s t_{s2} + \rho_c t_c)\ddot{Y} + R_{s2} + R_c = 0 \quad (9.40)$$

The fourth-order Runge–Kutta time stepping procedure is utilized to solve the equations of motion in Eqs. (9.39) and (9.40).

## 9.4 Lagrange Equation Model

### 9.4.1 Equation of Motion

According to the Lagrange Equation model, the equations of motion can be formulated as

$$\frac{d}{dt} \left( \frac{\partial T}{\partial \dot{C}_i} \right) + \frac{\partial(U + V)}{\partial C_i} = 0, \quad i = 1, 2, \dots, n. \quad (9.41)$$

where  $T$  is the kinetic energy,  $U$  is the internal energy,  $V$  is the potential energy of loading and  $C_i$  is the generalized displacement.

For the front and back steel plate in the SCS sandwich panel, only the tensile membrane force is considered to resist blast loading,  $T$ ,  $U$  and  $V$  in Eq. (9.41) can be formulated in Eqs. (9.42), (9.44) and (9.45), respectively.

$$T = \frac{1}{2} \int_0^L \rho A \dot{w}^2 dx \quad (9.42)$$

where  $L$  is the span,  $\rho$  is the density,  $A$  is the cross-section area, and  $\dot{w}$  is the velocity of the steel plate. The deflection of the steel plate,  $w$ , with  $n$  generalized displacements and deflection shape functions are given as

$$w(x, t) = \sum_{i=1}^n C_i(t) \phi_i(x) \quad (9.43)$$

The internal energy of steel plate  $U_s$  is calculated as

$$U_s = \begin{cases} \frac{1}{2}EA\frac{\Delta L^2}{L}, & \Delta L \leq \Delta L_y \\ \frac{EA}{2L}[\alpha\Delta L^2 + 2(1-\alpha)\Delta L_y\Delta L + (\alpha-1)\Delta L_y^2], & \Delta L > \Delta L_y \end{cases} \quad (9.44)$$

where  $\Delta L$  is the difference between the developed length and original length of the steel plate. For potential energy,

$$V = - \int_0^L P(t)w(x, t)dx \quad (9.45)$$

It should be noted that front steel plate must be removed after it separating from concrete core during calculation, similar to the SDOF model.

For the concrete core in the SCS sandwich panel, the calculation of kinetic energy  $T$  and potential energy  $V$  is same with the front and back steel plates. However, the derivation of the internal energy of concrete core  $U_c$  and its differential with generalized displacements in Eq. (9.41) are complex. To avoid recalculating the internal energy of concrete core, it is assumed that the combined deflection shape function in the Lagrange Equation model is same with that in the SDOF model. This assumption is reasonable for the axially-restrained SCS sandwich panel under blast loading, since the deflection shape function has little effect on the structural response, and the internal energy of concrete core is relatively small compared with steel plates, especially for the large deflection.

The mid-span displacement of the SCS sandwich panel is expressed as

$$Y = \sum_{i=1}^n C_i(t)\phi_i(L/2) \quad (9.46)$$

Hence, the differential of the internal energy of concrete core  $U_c$  with respect to generalized displacement  $C_i$  can be obtained as

$$\frac{\partial U_c}{\partial C_i} = \frac{\partial U_c}{\partial Y} \frac{\partial Y}{\partial C_i} \quad (9.47)$$

#### 9.4.2 DIF for Lagrange Equation Model

The DIF for concrete core in the Lagrange Equation model is same with that in the SDOF method, since the same deflection shape function is assumed when calculating

the internal energy of concrete core. However, the DIF for steel plates should be recalculated, as the different combined deflection shape function is employed for the Lagrange Equation model. The energy balance principle is utilized to introduce the varying DIF into the Lagrange Equation model. By applying the differential operator on the internal energy with and without consideration of strain rate effect (i.e.,  $U_s$  and  $U_{sD}$ ) for the front and back steel plates, the following equations are obtained

$$dU_s = \tilde{V}\sigma d\varepsilon \quad (9.48)$$

$$dU_{sD} = \tilde{V}f(\dot{\varepsilon}_p)\sigma d\varepsilon = f(\dot{\varepsilon}_p)dU_s \quad (9.49)$$

where  $\tilde{V}$  is the volume of the steel plate. Equation (9.49) can be rewritten as

$$\sum_{i=1}^n \left( \frac{\partial U_{sD}}{\partial C_i} - f(\dot{\varepsilon}_p) \frac{\partial U_s}{\partial C_i} \right) dC_i = 0 \quad (9.50)$$

Setting  $\frac{\partial U_{sD}}{\partial C_i} = f(\dot{\varepsilon}_p) \frac{\partial U_s}{\partial C_i}$  ( $i = 1, 2, \dots, n$ ) satisfies Eq. (9.50) and substituting them into Eq. (9.41) gives the equations of motion with varying DIF being considered.

Since the elongation of the steel plate  $\Delta L$  is a function of  $C_1, C_2, \dots, C_n$ , i.e.,  $\Delta L = g(C_1, C_2, \dots, C_n)$ , the strain rate can be derived as

$$\dot{\varepsilon} = \frac{\Delta \dot{L}}{L} = \frac{1}{L} \left( \frac{\partial g}{\partial C_1} \dot{C}_1 + \frac{\partial g}{\partial C_2} \dot{C}_2 + \dots + \frac{\partial g}{\partial C_n} \dot{C}_n \right) \quad (9.51)$$

By adopting the Cowper-Symonds model to establish the relationship between strain rate and DIF, the following equation is obtained.

$$\frac{\partial U_{sD}}{\partial C_i} = \left[ 1 + \left( \frac{\dot{\varepsilon}}{c} \right)^{1/p} \right] \frac{\partial U}{\partial C_i} \quad (9.52)$$

## 9.5 Results and Discussions

In this section, the FE model is adopted to simulate the axially-restrained SCS sandwich panel subjected to blast loading, and the results are compared with the predictions from analytical models. Since the maximum displacement instead of the displacement-time history is the most concern in the blast resistant design, the maximum displacements of SCS sandwich panels under blast load (a triangular blast pressure profile with zero rise time) are obtained using FE and analytical models and summarized in Table 9.3. The displacement of the SCS sandwich panel is given in Eq. (9.53) by employing combined deflection shape functions.

**Table 9.3** Maximum displacement comparison

$t_{s1}$	$t_{s2}$	$t_c$	$L$	$P_{\max}$	$t_d$	Max dis (mm)				Error (%)			
						FE	SDOF	LEM1	LEM2	SDOF	LEM1	LEM2	
3	3	70	1180	10	0.5	55.7	61.3	63.1	60.1	9.96	13.13	7.87	
					1	5	46.8	52.8	53.9	51.6	12.92	15.33	10.39
					0.5	5000	51.8	63.6	56.8	54.7	22.69	9.60	5.52
3	3	50	1180	10	0.5	66.8	71.2	76.9	73.5	6.56	18.09	10.07	
					1	5	55.5	61.3	63.8	61.6	10.36	18.85	10.93
					0.5	5000	56.6	66.2	61.4	58.9	16.97	13.04	4.07
1.5	3	50	1180	10	0.5	72.1	75.9	82.8	79.0	5.37	17.71	9.65	
					1	5	61.0	67.9	71.5	68.9	11.25	21.01	12.81
					0.5	5000	68.1	82.9	75.3	71.5	21.79	14.91	4.95
1.5	1.5	50	1180	5	0.5	53.8	54.2	57.3	54.1	0.68	8.77	0.39	
					0.5	5	46.7	50.0	50.5	47.9	7.08	10.92	2.68
					0.25	5000	56.3	64.4	58.5	56.1	14.31	8.44	-0.36

Note the unit of  $t_{s1}$ ,  $t_{s2}$ ,  $t_c$  and  $L$  is mm; the units of  $P_{\max}$  and  $t_d$  are MPa and ms; LEM1 and LEM2 stands for Lagrange Equation model with  $a = 1$ ,  $b = 2$  and  $a = 2$ ,  $b = 3$ , respectively

$$w(x, t) = C_1(t) \left[ \frac{4}{L^2} (Lx - x^2) \right]^a + C_2(t) \left[ \frac{4}{L^2} (Lx - x^2) \right]^b \quad (9.53)$$

where the term in the bracket is the deflection shape function defined in the SDOF model, and the parameters  $a$  and  $b$  are specified with different values to represent different deflection shape functions. It should be mentioned that any reasonable combination of deflection shape functions is acceptable, and more number of deflection shape functions may provide more accurate predictions.

Table 9.3 shows that the analytical-predicted maximum displacements of SCS sandwich panels match well with the FE predictions. However, the slightly larger values of maximum displacement are observed for the analytical-predictions, which may be caused by the underestimation of internal energy and neglect of energy dissipated through friction and damping in the analytical models. Another reason may be attributed to the different deflection shape functions between the FE and analytical models.

For the predictions from the SDOF model, they exhibit better match with the FE predictions in the impulsive loading range (i.e., short loading duration), with the differences of maximum displacement between the two models less than 10%. In addition, the separation between the front steel plate and concrete core during calculation can also be well captured by the SDOF model, as shown in Fig. 9.12. However, the SDOF model provides larger values of maximum displacement than that of FE model in the quasi-static loading range. This may be caused by the neglect of

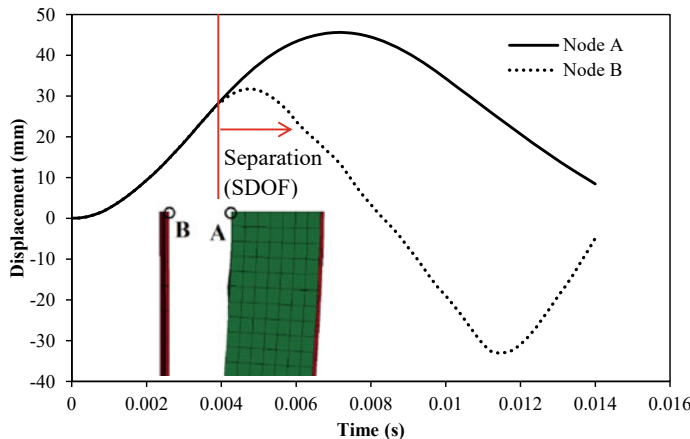


**Fig. 9.12** Comparison of the separation time between FE and SDOF analysis ( $t_s = 3 \text{ mm}$ ;  $t_c = 70 \text{ mm}$ ,  $P_{max} = 1 \text{ MPa}$ ;  $t_d = 5 \text{ ms}$ ), reprinted from Wang et al. (2015), copyright 2022, with permission from Elsevier

confinement effect on compressive strength of concrete when deriving the resistance–deflection function contributed by concrete core. This effect is more significant in quasi-static loading range since the separation is not observed during calculation.

For the Lagrange Equation model, it is found that the LEM2 provides closer predictions to the FE model as compared to LEM1. The deflection shape of the SCS sandwich panel obtained from FE analysis is compared with those from SDOF and LEM2 models, as presented in Fig. 9.13. The deflection shape from LEM2 is found to be closer to that from FE model. Since two combined deflection shape functions are employed for the Lagrange Equation model and a varying deflection shape can be achieved during calculation, it can provide more accurate predictions as compared to the SDOF model with single deflection shape function. It was observed by Baker et al. (1983) that the different deflection shape functions should be employed for

**Fig. 9.13** Comparison of the deflection shape between FE and analytical model ( $t_s = 3 \text{ mm}$ ;  $t_c = 70 \text{ mm}$ ,  $P_{max} = 1 \text{ MPa}$ ;  $t_d = 5 \text{ ms}$ ), reprinted from Wang et al. (2015), copyright 2022, with permission from Elsevier

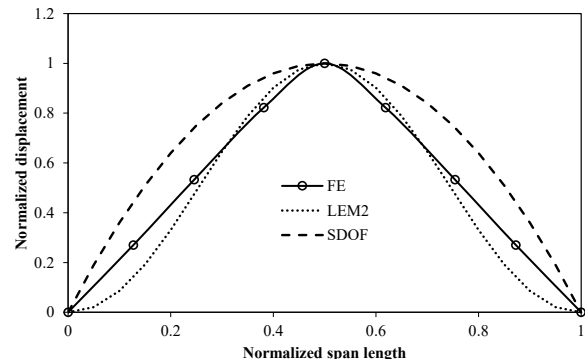
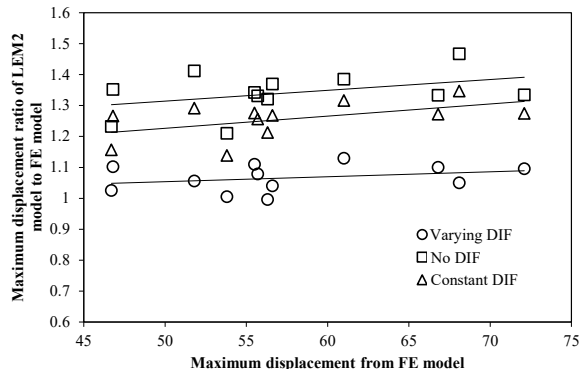


**Fig. 9.14** Varying DIF effect on the maximum displacement, reprinted from Wang et al. (2015), copyright 2022, with permission from Elsevier



the SDOF model to obtain the exact solutions of simply supported beams under impulsive and quasi-static loading ranges. Therefore, the SDOF model with single deflection shape function generally cannot provide accurate predictions in all the loading ranges (i.e., impulsive, dynamic and quasi-static loading ranges).

Both Lagrange Equation models and SDOF model provide better predictions with decreasing of the steel plate thickness, which indicates that the internal energy of steel plate is underestimated. This underestimation may be caused by the assumed deflection shape functions and the assumption that the strain is uniformly distributed along the span. The effect of varying DIF on the maximum displacement of the SCS sandwich panel is presented in Fig. 9.14. The LEM2 with varying DIF, constant DIF and without DIF was adopted to compare with the FE analyses. The constant DIF values of steel and concrete are adopted as 1.10 and 1.12, respectively (ASCE 2011). Figure 9.14 shows that the LEM2 with varying DIF provides better predictions than the LEM2 with constant DIF or without DIF. It is also observed from the fitting curves that the LEM2 with varying DIF provides approximately constant differences between the LEM2 and FE model, while the differences of LEM2 with constant DIF or without DIF exhibits increase with increasing maximum displacement. This demonstrates that the proposed varying DIF can more accurately capture the strain rate effect regardless of the maximum displacement, whereas the LEM2 with constant DIF or without DIF may overestimate the responses, especially for the large deflection.

For the axially-restrained non-composite SCS sandwich panels, the separation of front steel plate and concrete core generally occurs under impulsive loading range. Therefore, it is more efficient to improve the blast resistance by enhancing the back steel plate instead of front steel plate. Moreover, increasing the thickness of concrete core is also an important way, since it can reduce the obtained kinetic energy under blast loading.

## 9.6 Summary

Two analytical models were developed to predict the responses of axially-restrained SCS sandwich panels subjected to blast loading. The force equilibrium equation was employed to derive the resistance–deflection function of the SCS sandwich panel contributed by steel plates. The energy balance principle was adopted to obtain the resistance–deflection function contributed by concrete core. The varying DIF in terms of strain rate was included in the two analytical models, which could accurately capture the strain rate effect. The FE analyses were employed to validate the proposed two analytical models. Through the comparison of maximum displacements obtained from FE and analytical models, the analytical models were found to reasonably predict the responses of axially-restrained SCS sandwich panels under blast loading. It was observed from both FE and analytical models that the front steel plate was prone to separate from the concrete core owing to the absence of shear connectors. Hence, enhancing the back steel plate was preferred to improve blast resistance of the axially-restrained non-composite SCS sandwich panel.

## References

- ASCE/SEI 59-11 (2011) Blast protection of buildings. American Society of Civil Engineers, Reston, Virginia
- Bailey CG (2001) Membrane action of unrestrained lightly reinforced concrete slabs at large displacements. Eng Struct 23:470–483
- Baker WE, Cox PA, Westine PS et al (1983) Explosion and hazards and evaluation. Elsevier Scientific Publishing Compay, Amsterdam
- Biggs JM (1964) Introduction to structural dynamics. McGraw-Hill, New York
- Carta G, Stochino F (2013) Theoretical models to predict the flexural failure of reinforced concrete beams under blast loads. Eng Struct 49:306–315
- CEB-FIP (1993) CEB–FIP model code 1990. Redwood Books, Wiltshire
- Cowper GR, Symonds PS (1958) Strain hardening and strain rate effects in the impact loading of cantilever beams. Applied Mathematics Report, Brown University
- Donaldson BK (2006) Introduction to structural dynamics. Cambridge University Press, New York
- Eurocode 2 (2004) Design of concrete structures – Part 1–1: General rules and rules for buildings. BS EN 1992–1–1, London
- Federal Highway Administration (2007a) Evaluation of LS-DYNA concrete material model 159
- Federal Highway Administration (2007b) Users manual for LS-DYNA concrete material model 159
- Hallquist JO (2006) LS-DYNA theory manual. Livermore Software Technology Corporation (LSTC). Livermore, California
- Jones J, Wu C, Oehlers DJ et al (2009) Finite difference analysis of simply supported RC slabs for blast loadings. Eng Struct 31:2825–2832
- Jones N (1988) Structural impact. Cambridge University Press, New York
- Kang KW, Lee SC, Liew JYR (2013) Analysis of steel–concrete composite column subject to blast. P I Civil Eng–Str B 166:15–27
- Lan S, Lok TS, Heng L (2005) Composite structural panels subjected to explosive loading. Constr Build Mater 19:387–395

- Langdon GS, Schleyer GK (2005) Inelastic deformation and failure of profiled stainless steel blast wall panels. Part II: analytical modelling considerations. *Int J Impact Eng* 31:371–399
- Li GQ, Guo SX, Zhou HS (2007) Modeling of membrane action in floor slabs subjected to fire. *Eng Struct* 29:880–887
- Liew JYR, Sohel KMA (2009) Lightweight steel–concrete–steel sandwich system with J–hook connectors. *Eng Struct* 31(5):1166–1178
- Liew JYR, Sohel KMA, Koh et al (2009) Impact tests on steel–concrete–steel sandwich beams with lightweight concrete core. *Eng Struct* 31(9):2045–2059
- Liew JYR, Wang TY (2011) Novel steel–concrete–steel sandwich composite plates subjected to impact and blast load. *Adv Struct Eng* 14(4):673–686
- Nassr AA, Razaqpur AG, Tait MJ et al (2012) Single and multi-degree of freedom analysis of steel beams under blast loading. *Nucl Eng Des* 242:63–77
- Remennikov AM, Kong SY (2012) Numerical simulation and validation of impact response of axially-restrained steel–concrete–steel sandwich panels. *Compo Struct* 94:3546–3555
- Remennikov AM, Kong SY, Uy B (2013) The response of axially restrained non–composite steel–concrete–steel sandwich panels due to large impact loading. *Eng Struct* 49:806–818
- Schleyer GK, Hsu SS (2000) A modelling scheme for predicting the response of elastic–plastic structures to pulse pressure loading. *Int J Impact Eng* 24:759–777
- UFC 3–340–02 (2008) Structures to resist the effects of accidental explosions. US Department of Army, Navy and the Air Force, Washington, DC
- Wang Y, Liew JYR, Lee SC (2015) Theoretical models for axially restrained steel–concrete–steel sandwich panels under blast loading. *Int J Impact Eng* 76:221–231
- Wang Y, Xiong MX (2015) Analysis of axially restrained water storage tank under blast loading. *Int J Impact Eng* 86:167–178

# Chapter 10

## Curved Steel–Concrete–Steel Sandwich Shell Under Blast



### 10.1 Introduction

The impact and blast resistant performances of flat steel–concrete–steel (SCS) sandwich panels were extensively studied (Anandavalli et al. 2012; Wang et al. 2015; Liew and Wang 2011), and they showed high performance in resisting impact and blast loading owing to the high ductility, spalling protection, buckling resistance and energy absorption. Recently, the curved SCS sandwich shell was appealing in resisting blast loading, since the curved shell normally outperformed flat shell under blast loading via developing compressive force along the shell. Therefore, the curved SCS sandwich shell has high potential application as blast resistant wall, as illustrated in Fig. 10.1. Up to date, several studies on punching resistance of the curved SCS sandwich shell under concentrated load were conducted (Yan et al. 2016a, b; Huang and Liew 2015). However, minimal reported works on the curved SCS sandwich shell under blast loading were found in the open literature, and the blast resistant design method of such structure was also not available.

The equivalent single-degree-of-freedom (SDOF) method was widely used as a simple alternative to predict the dynamic response of continuous member subjected to blast loading (Biggs 1964; Wang and Xiong 2015; Rigby et al. 2014; Morison 2006; Carta and Stochino 2013). This method was also adopted by many design guidelines (UFC 2008; ASCE 2010, 2011) to evaluate the blast-induced damage level of a structure, since it could capture the global structural response with reasonable accuracy. Another simple method to predict the damage level of a structure under blast loading is Pressure-Impulse (P–I) diagram which is an iso-damage curve for a particular structural member loaded with a particular blast load history (Mays and Smith 1995). There are mainly two methods to establish P–I diagrams, i.e., SDOF method (Li and Meng 2002a, b; Fallah and Louca 2006; Krauthammer et al. 2008; Dragos and Wu 2013) and Finite Element (FE) method (Shi et al. 2008; Mutalib and Hao 2011). As for the SDOF method, the pressure and impulse asymptotes of a P–I diagram can be directly expressed as the formulae in terms of structural parameters, such as stiffness, mass, and allowable maximum displacement, etc. Support rotation

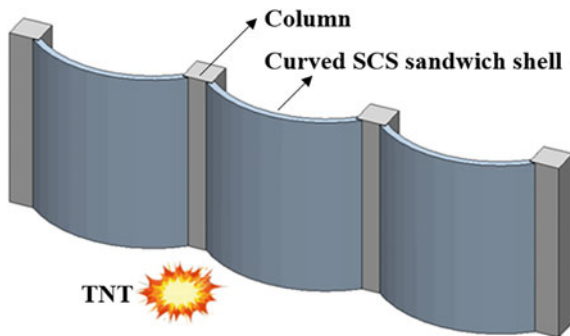


**Fig. 10.1** Curved SCS sandwich shell as blast resistant wall

or ductility ratio was generally adopted by the design guidelines to gauge the damage level of a structure (UFC 2008; ASCE 2010, 2011), and they could be directly obtained via employing the SDOF method. Hence, support rotation or ductility ratio was normally adopted as the damage level indicator for the P-I diagram generated via employing the SDOF method. This is reasonable for the structural members like beams and slabs, but not appropriate for the column whose failure is generally governed by its residual axial strength. Therefore, the FE method with easier output of residual axial strength is preferred for establishing the P-I diagram of the column. Shi et al. (2008) and Mutalib and Hao (2011) utilized the FE method to generate the P-I diagram for reinforced concrete (RC) columns and Fiber-Reinforced Polymer (FRP) strengthened RC columns, respectively. In their studies, the residual axial strength was applied as the damage level indicator, which was more representative as compared to support rotation or ductility ratio. Parametric studies and curve-fitting might be required to establish the relationship between pressure/impulse asymptotes and structural parameters.

In this chapter, The FE method was employed to study the responses of curved SCS sandwich shells under blast loading, and their failure modes under close- and far-field blast loading were also obtained. The effects of rise height (or rise to span ratio) and rear to front plate thickness ratio on the blast responses of curved SCS sandwich shells were studied. In addition to the numerical study, the SDOF model of the curved SCS sandwich shell subjected to uniformly distributed blast loading was developed, based on which the dimensionless P-I diagram was constructed. In addition, the pressure and impulse asymptotes were also formulated as the geometric and material properties of the curved SCS sandwich shell via applying the energy balance principle.

## 10.2 FE Model Establishment and Verification

The explicit code in LS-DYNA was adopted in this section to simulate the dynamic responses of curved SCS sandwich shells under blast loading, and the accuracies of the established FE models were verified with the available experimental results.

### 10.2.1 FE Model of Curved SCS Sandwich Shell

In this study, quarter FE model of the curved SCS sandwich shell was established in Fig. 10.2 owing to the symmetry of geometry and applied blast loading. The nodes on the end plate were restricted from translation to simulate the fixed boundary condition. The steel plates were meshed using S/R Hughes-Liu shell element, and eight-node solid element with reduced integration in combination with hourglass control was employed for the concrete core (Hallquist 2006).

Traditional FE modeling of the SCS sandwich shell was employing solid elements for steel plates, concrete core and shear connectors (Foundoukos and Chapman 2008; Clubley et al. 2003). This detailed FE modeling approach inevitably resulted in finer meshes at shear connectors as well as steel plates adjacent to shear connectors (Foundoukos and Chapman 2008), which leaded to smaller time step and longer computing time. Anandavalli et al. (2012) employed more uniform meshing approach, i.e., using shell and link elements for the steel plates and shear connectors, respectively. In this study, a simplified approach was employed, i.e., using Hughes-Liu beam elements for shear connectors and assuming the perfect bond between

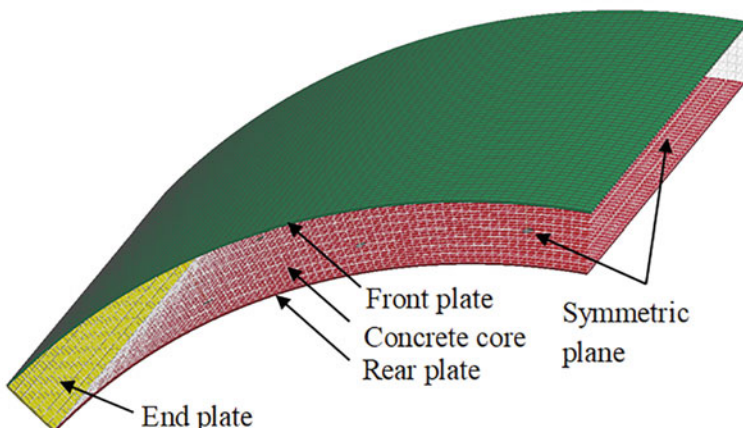


**Fig. 10.2** Quarter FE model of curved SCS sandwich shell, reprinted from Wang et al. (2016), copyright 2022, with permission from Elsevier

concrete core and shear connectors. This approach was also used to model RC structures against blast loading, and the predictions were proven to be acceptable (Li et al. 2015; Chen et al. 2015). Figure 10.3 illustrates the modeling of the connection between steel plates and shear connectors. The circular rigid panel (with same diameter of the shear connector) is attached to the shear connector through shared node, and meanwhile tied to the steel plate. This connection modeling approach can avoid stress concentration at the steel plate caused by directly sharing the node between the shear connector and steel plate. The geometry of the curved SCS sandwich shell in this study is given in Table 10.1. Blast load was generated using keyword \*LOAD\_BLAST\_ENHANCED (LBE) via the CONWEP feature in LS-DYNA (Hallquist 2013). The blast pressure was applied onto the front plate of the curved SCS sandwich shell and can be determined based on the amount of TNT charge, standoff distance and angle of incidence, as given below

$$P(t) = P_r \cos^2 \theta + P_i (1 + \cos^2 \theta - 2 \cos \theta) \quad (10.1)$$

where  $P_r$  is reflected pressure,  $P_i$  is incident pressure and  $\theta$  is angle of incidence.

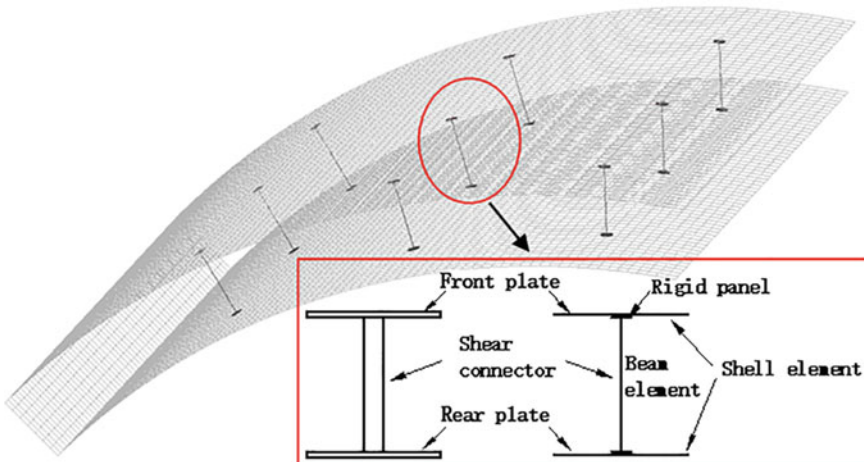


**Fig. 10.3** Simplified FE model of shear connectors, reprinted from Wang et al. (2016), copyright 2022, with permission from Elsevier

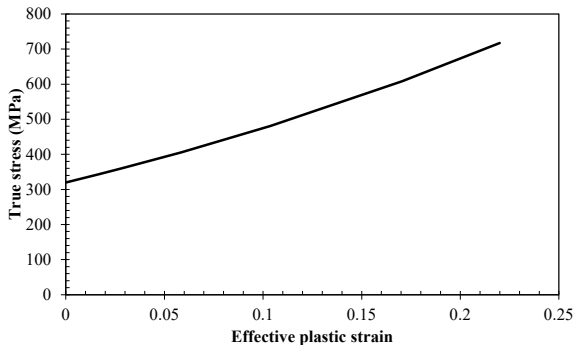
**Table 10.1** Geometry of curved SCS sandwich shell (Unit: mm)

Span	Width	Rise height	Steel plate thickness	Concrete depth	Shear connector diameter	Shear connector spacing
1200	1200	300	3	70	10	200

**Table 10.2** Material properties of concrete in FE analysis

Density (kg/m <sup>3</sup> )	Compressive strength (MPa)	Shear modulus (GPa)	Bulk modulus (GPa)
2310	35	12.06	13.21

**Fig. 10.4** True stress–effective plastic strain curve for mild steel, reprinted from Wang et al. (2016), copyright 2022, with permission from Elsevier



The Continuous Surface Cap (CSC) model in LS-DYNA (Hallquist 2006) was adopted to model the behavior of concrete. This material model was developed by US Federal Highway Administration to simulate the concrete-like material subjected to high rate loading, like impact and blast (FHWA 2007a, b). The main parameters of concrete used in this analysis are given in Table 10.2. As for the simulation of steel, the Piecewise Linear Plasticity material model in LS-DYNA was employed. The material properties of steel were obtained from the tensile coupon test, and the input true stress–effective plastic strain curve is shown in Fig. 10.4. In this material model, the Cowper-Symonds model (Cowper and Symonds 1958) is used to scale the yield stress, as defined in Eq. (1.8), and the strain rate parameters  $C$  and  $P$  were  $40.4 \text{ s}^{-1}$  and 5 for the mild steel (Jones 1988).

### 10.2.2 FE Model Verification

There is no available experimental data on curved SCS sandwich panel subjected to blast loading in the open literature. Hence, the field blast test on the flat SCS sandwich panel (Liew and Wang 2011; Kang et al. 2013), which has similar configuration of the curved SCS sandwich shell, was adopted to validate the established FE model, and the comparisons between the FE and test results were presented in Sect. 9.2. In order to calibrate the proposed FE modeling approach of shear connectors, the static test on SCS sandwich beams with shear connectors friction-welded to the steel plates (Xie et al. 2007) was employed. The same material models, element formulations and mesh size in Sect. 10.2.1 were used herein. The geometry of the SCS beam is shown in Fig. 10.5, and the material properties are given in Table 10.3. The load–displacement

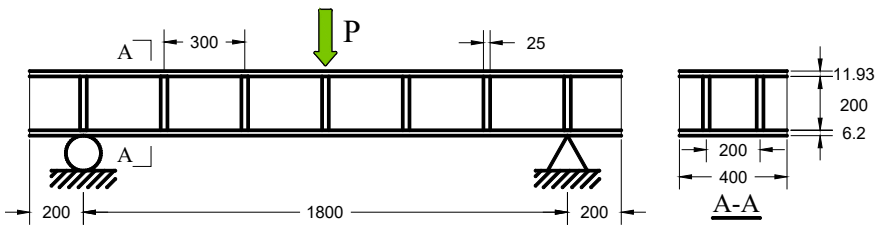


**Fig. 10.5** Details of SCS sandwich beam (Unit: mm)

**Table 10.3** Material properties of steel and concrete (Xie et al. 2007)

$f_{yP}$ (MPa)	$f_{uP}$ (MPa)	$f_{yB}$ (MPa)	$f_{uB}$ (MPa)	$f_{cu}$ (MPa)
384	507	541	566	58

response of the SCS sandwich beam under concentrated load from the test (Xie et al. 2007) is compared with the FE results with different modeling approaches of shear connectors, as shown in Fig. 10.6. All the three modeling approaches can yield similar ultimate strength. However, the discrepancy is observed at the initial loading stage, i.e., “solid elements modeling approach” by Foundoukos and Chapman (2008) shows stiffer response as compared to the test results, and “shell and link modeling approach” by Anandavalli et al. (2012) shows softer response. It is noted that the proposed “shell and beam modeling approach” shows better agreement with the test results, which validates the proposed FE modeling approach of shear connectors.

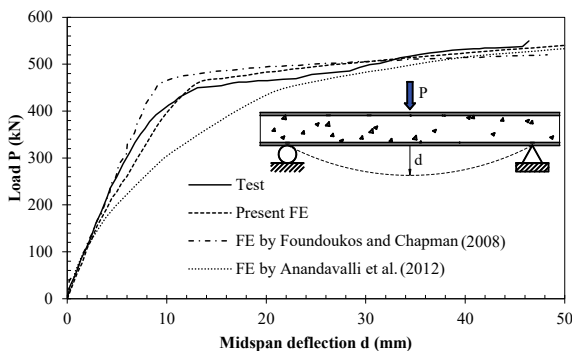


**Fig. 10.6** Load–displacement response of SCS sandwich beam

### 10.3 Curved SCS Sandwich Shell Without Shear Connectors

The responses of the curved SCS sandwich shell without shear connectors under blast loading were first examined to obtain the dynamic response characteristics and failure modes, which will be compared with those of the curved SCS sandwich shell with shear connectors in the next section. The blast load with TNT charge weight of 20 kg and standoff distance of 0.5 m was applied to the front plate of the curved SCS shell.

Figure 10.7 shows the deformation evolution of the curved SCS sandwich shell without shear connectors, and separation between faceplates and concrete core is observed owing to the absence of shear connectors. The blast load duration is very short (about 0.5 ms), which leads to an impulsive response regime of the shell (i.e., the shell only develops negligible deformation before the blast load decaying to zero). Hence, the blast energy is first transferred to the shell as kinetic energy, and the kinetic energy will be finally dissipated by the shell as internal energy. The resistance to mass ratio of the faceplate is initially higher than that of concrete core and the same to acceleration, which results in the front plate separating from concrete core after blast pressure decaying to zero. The separation between the rear plate and concrete core is also observed with relatively large deflection, which can be attributed to the reduced resistance of the rear plate after buckling. This is also demonstrated in Fig. 10.8, i.e., the increasing rate of internal energy of the rear plate slows down when the midpoint displacement exceeds 200 mm. Figure 10.8 also shows that the concrete core dissipates the majority of blast energy. In addition, the ultimate energy absorption capacity of the concrete core is reached, as shown in Fig. 10.9. The relatively smaller blast energy dissipated by faceplates can be attributed to (1) smaller volume of faceplates as compared to concrete core, (2) early separation of the front plate and (3) buckling of the rear plate for large deflection.

### 10.4 Curved SCS Sandwich Shell with Shear Connectors

The separation between faceplates and concrete core was observed for the curved SCS sandwich shell without shear connectors subjected to blast loading, which limited the blast resistant capacity of the curves SCS sandwich shell. Hence, shear connectors were introduced into the curved SCS sandwich shell to improve its blast resistant performance, and the effect of shear connectors on the blast response of the curved SCS sandwich shell was also discussed. Then, the failure modes of the curved SCS sandwich shell with shear connectors under close- and far-field blast loading were discussed. In addition, the effects of rise height (or rise to span ratio) and rear to front plate thickness ratio on the blast responses of curved SCS sandwich shells were also investigated.

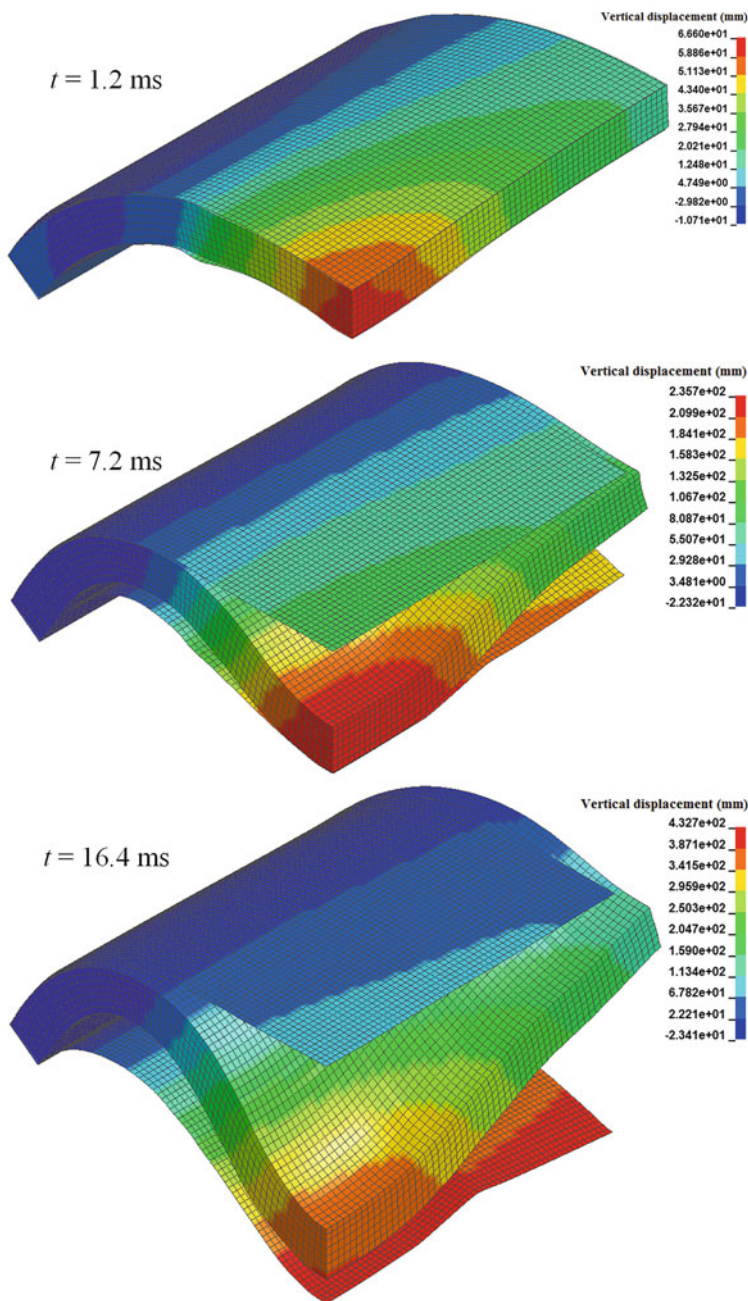


**Fig. 10.7** Deformation of curved SCS sandwich shell without shear connectors under blast loading, reprinted from Wang et al. (2016), copyright 2022, with permission from Elsevier

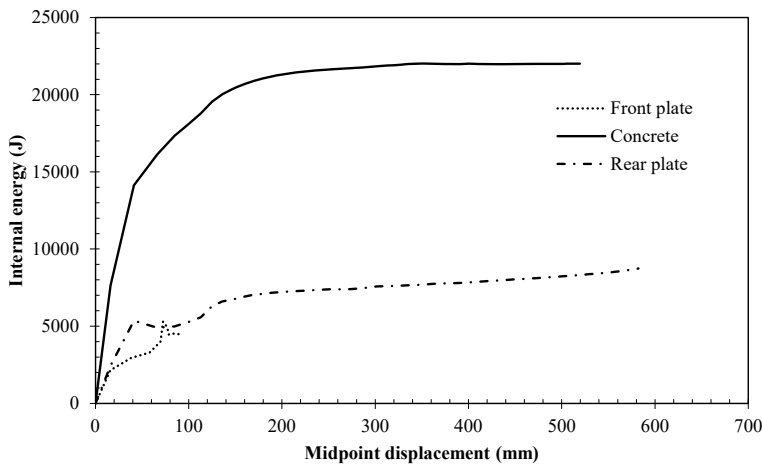


**Fig. 10.8** Internal energy–midpoint displacement curves, reprinted from Wang et al. (2016), copyright 2022, with permission from Elsevier

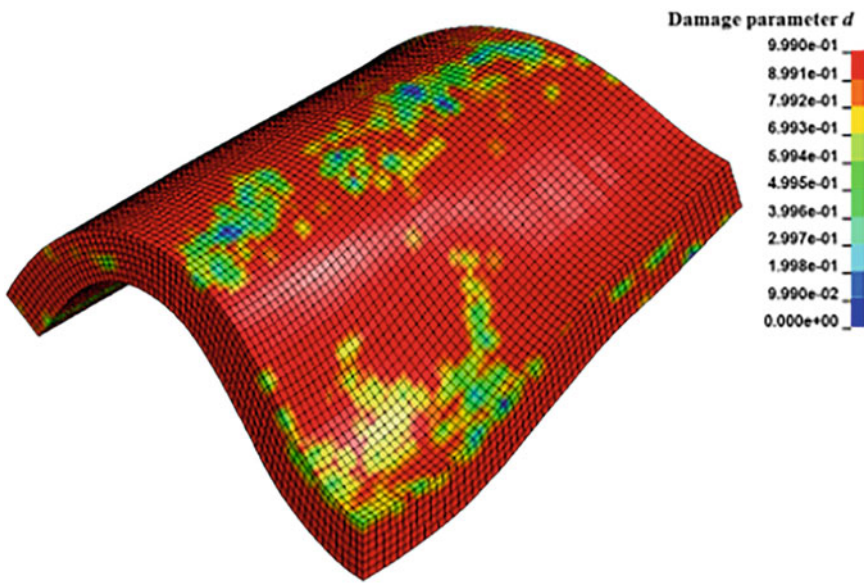


**Fig. 10.9** Contours of damage parameter of concrete core, reprinted from Wang et al. (2016), copyright 2022, with permission from Elsevier

### 10.4.1 Influence of Shear Connectors

The same blast load with 20 kg TNT charge detonated at 0.5 m away was applied to the curved SCS sandwich shell with shear connectors. Figure 10.10 presents the midpoint displacements of the front and rear plates for the two curved SCS shells. Significant reduction of displacement is observed for the curved SCS shell with shear connectors, especially for displacement of the rear plate. In addition, comparable displacement of the front and rear plate can be seen for the shell with shear connectors, which demonstrates that shear connectors can bond the faceplates to concrete core and improve blast resistance of the curved SCS sandwich shell. The amount of blast energy dissipated by the front plate, concrete core and rear plate for the two shells is presented in Fig. 10.11. The portion of blast energy dissipated by faceplates of the curved SCS shell with shear connectors is 35.5% higher than that of the shell without shear connectors. This is because shear connectors can prevent separation of faceplates from concrete core and enforce them deforming together to dissipate blast energy. In addition, higher blast energy dissipated by the rear plate as compared to the front plate is observed for both the two curved SCS shells, which is due to relatively larger deformation of the rear plate.

Unlike steel material, the strength of concrete under compression is much higher than that under tension, and the same to energy absorption capacity. In view of this, the curved SCS sandwich shell is superior to its flat counterpart through enforcing more portion of concrete core under compression. In CSC material model, a damage parameter,  $d$ , is employed to evaluate the damage level of concrete for single element. In this study, the average damage,  $d_a$ , defined in Eq. (10.2), is utilized to evaluate the global damage level of concrete core.

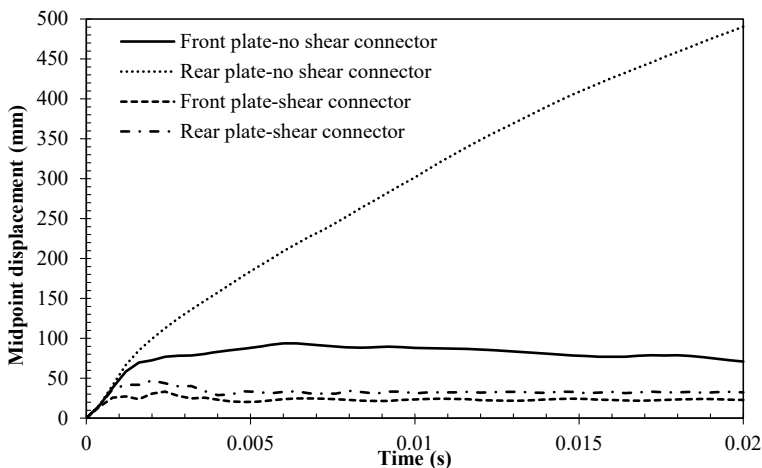


**Fig. 10.10** Displacement–time history of curved SCS sandwich panel, reprinted from Wang et al. (2016), copyright 2022, with permission from Elsevier

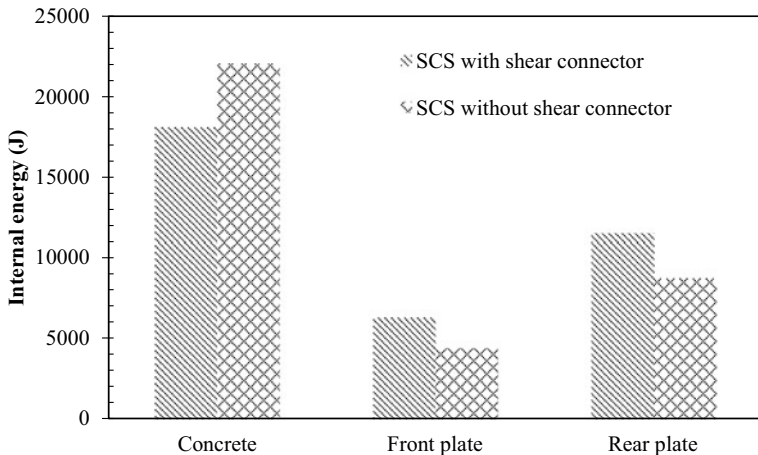


**Fig. 10.11** Comparison of internal energy of curved SCS sandwich shell with and without shear connectors, reprinted from Wang et al. (2016), copyright 2022, with permission from Elsevier

$$d_a = \frac{\sum_{i=1}^n d_i}{n} \quad (10.2)$$

where  $d_i$  is the damage parameter of element  $i$ , and  $n$  is the total number of concrete elements. Figure 10.12 shows the internal energy versus average damage curves of concrete core for the two curved SCS shells with and without shear connectors. The two curves are found to be close when the average damage value is small. However,

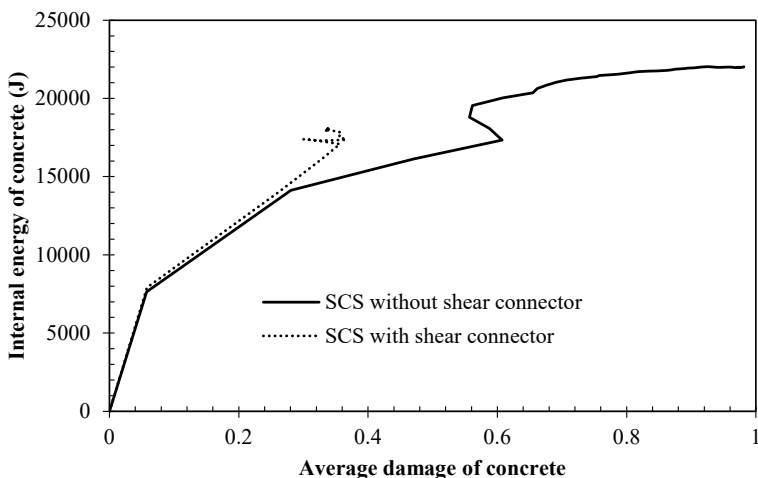


**Fig. 10.12** Internal energy–average damage curves of concrete core, reprinted from Wang et al. (2016), copyright 2022, with permission from Elsevier

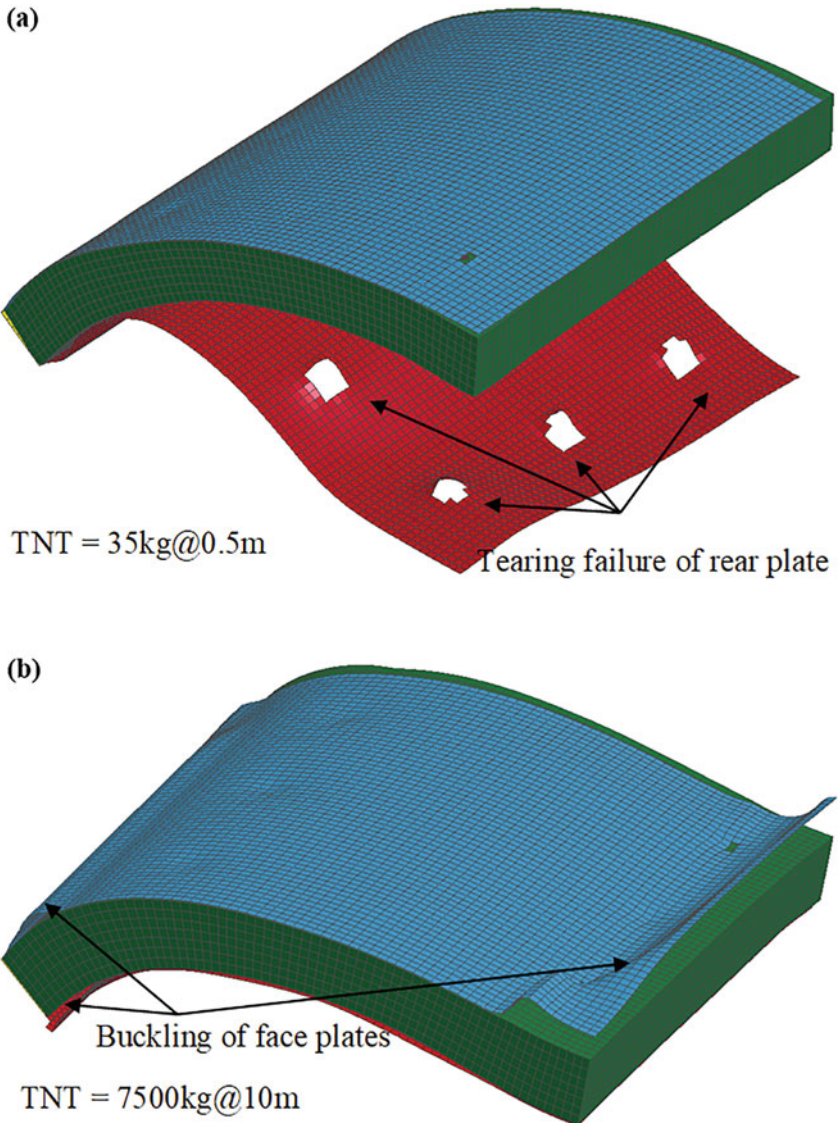
the concrete core of the curved SCS shell without shear connectors shows significant increase in global damage with only slight increase in internal energy, which is due to the increasing portion of concrete core under tension after separation between faceplates and concrete core. Hence, the utilization of shear connectors to increase the energy absorption capacity of concrete core is demonstrated.

#### **10.4.2 Influence of Blast Loading**

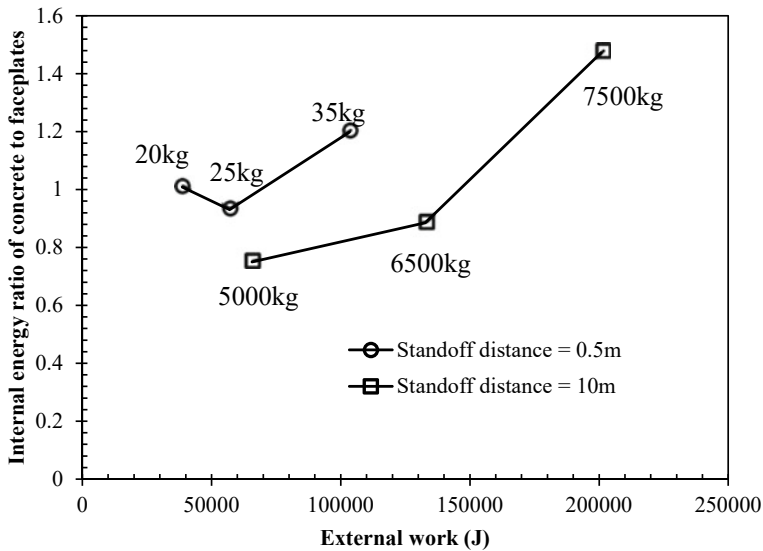
In order to obtain the failure modes of curved SCS sandwich shell with shear connectors under blast loading, the blast detonations with TNT charge weight of 20, 25 and 35 kg and standoff distance of 0.5 m were selected to represent close-field blast loading, and the blast detonations with TNT charge weight of 5000, 6500 and 7500 kg and standoff distance of 10 m were selected to represent far-field blast loading.

Figure 10.13a shows the failure mode of the curved SCS sandwich shell with shear connectors under close-field blast loading, and separation of the rear plate from concrete core can be observed after tearing failure of the rear plate. However, different failure mode is observed for the curved SCS sandwich shell under far-field blast loading, as shown in Fig. 10.13b, i.e., the buckling of faceplates appears at the end of the shell first, and the subsequent buckling of the front plate is observed at the mid-span. The loading duration of close-field blast loading is significantly shorter as compared to far-field blast loading and can be considered to act in an impulsive manner, the curved SCS sandwich shell under close-field blast loading generally experiences higher acceleration, which is prone to trigger a failure mode of separation between the rear plate and concrete core. As for the curved SCS sandwich shell under far-field blast loading, whose loading duration is longer and can be considered to act in a quasi-static or dynamic manner, the shell is prone to deform as that under quasi-static loading, showing buckling failure of faceplates.

Figure 10.14 presents the internal energy (or blast energy dissipation) ratios of concrete core to faceplates, and comparable amount of blast energy dissipated by concrete core and faceplates can be observed. For the close-field blast loading with standoff distance of 0.5 m, the blast energy dissipated by faceplates shows increase with increasing TNT charge weight before failure of the shell (from 20 to 25 kg TNT charge). However, more blast energy dissipated by concrete core is observed for the shell after failure (35 kg TNT charge), which can be attributed to the reduced blast energy dissipated by the rear plate after separating from concrete core. For the far-field blast loading with standoff distance of 10 m, the percentage of blast energy dissipated by concrete core shows increase with increasing TNT charge weight. Figure 10.14 also shows that the percentage of blast energy dissipated by faceplates of the shell under close-field blast loading is lower as compared to that under far-field blast loading at the same external work level, which can be attributed to the reduced blast energy absorption capacity of the rear plate after separation. As mentioned previously, the energy absorption capacity of concrete varies with loading path (e.g., compression or tension), and the average damage,  $d_a$ , is proposed to evaluate the



**Fig. 10.13** Failure modes of curved SCS sandwich shell with shear connectors: **a** close-field and **b** far-field blast loading, reprinted from Wang et al. (2016), copyright 2022, with permission from Elsevier



**Fig. 10.14** Internal energy ratio of concrete to faceplates versus external work, reprinted from Wang et al. (2016), copyright 2022, with permission from Elsevier

global damage level of concrete core. Herein, the ratio of internal energy per unit volume to average damage is used to evaluate the energy absorption efficiency of concrete core. It can be seen in Fig. 10.15 that the energy absorption efficiency of concrete core shows increase with increasing average damage. In addition, the energy

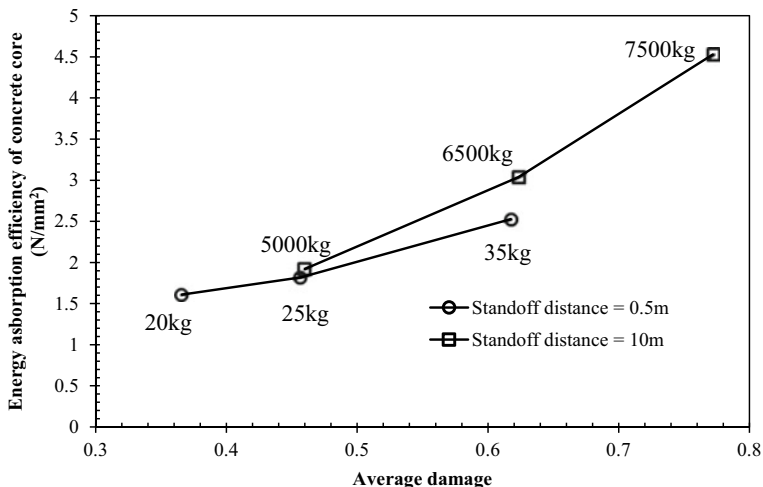


**Fig. 10.15** Energy absorption efficiency of concrete core versus average damage, reprinted from Wang et al. (2016), copyright 2022, with permission from Elsevier

absorption efficiency of concrete core for close-field blast loading case is lower as compared to far-field blast loading case at the same average damage level, which indicates that more portion of concrete core is under tension after occurrence of separation between the rear plate and concrete core.

### 10.4.3 Influence of Rise Height

The curved SCS sandwich shells with span of 1.2 m and four different rise heights (0, 0.3, 0.45 and 0.56 m) were subjected to close- (25 kg TNT charge with standoff distance of 0.5 m) and far-field (5000 kg TNT charge with standoff distance of 10 m) blast loading, and the external work, blast energy absorption and damage of the shell were discussed and presented as followings.

The effect of rise height on the dynamic responses of curved SCS sandwich shells under blast loading are illustrated in Table 10.4. The external work done by blast loading generally exhibits decrease with increasing rise height for both close- and far-field blast loading, i.e., the external work is reduced by 49.7% and 78.3% for close- and far-field blast loading, respectively, by increasing rise height from 0 m to 0.56 m. Since the external work done by blast loading will be dissipated by the shell as internal energy, the decrease in external work with increasing rise height also leads to the decrease in damage of concrete core and faceplates, as shown in Table 10.4. Herein, the average damage,  $d_a$ , defined in Eq. (10.2) is used to evaluate the global damage of concrete core, and the average effective plastic strain,  $\varepsilon_{ap}$ , defined in Eq. (10.3) (Wang and Liew 2015) is used to evaluate the global damage of faceplates.

$$\varepsilon_{ap} = \frac{\sum_{i=1}^n \varepsilon_{pi}}{n} \quad (10.3)$$

**Table 10.4** Summaries of FE results with varied rise heights

Rise height (m)	25 kg TNT@0.5 m				5000 kg TNT@10 m			
	$W_E$ (kJ)	$d_a$	$\varepsilon_{ap} (\times 10^{-2})$	$e_E$ (N/mm <sup>2</sup> )	$W_E$ (kJ)	$d_a$	$\varepsilon_{ap} (\times 10^{-2})$	$e_E$ (N/mm <sup>2</sup> )
0	96.4	0.59	4.01	1.06	237.6	0.74	5.53	1.34
0.3	57.0	0.46	1.88	1.82	65.6	0.46	2.20	1.92
0.45	50.0	0.33	1.05	2.41	50.7	0.36	1.25	2.14
0.56	48.5	0.34	1.02	1.82	51.7	0.35	1.15	1.87

Note  $W_E$ —External work;  $d_a$ —Average damage of concrete;  $\varepsilon_{ap}$ —Average effective plastic strain of face plate;  $e_E$ —Energy absorption efficiency of concrete core

where  $\varepsilon_{pi}$  is the effective plastic strain of element  $i$ , and  $n$  is the total number of face-plate elements. Table 10.4 shows that both the damages of concrete core and faceplates are reduced significantly by increasing rise height from 0 to 0.45 m. However, further increasing rise height from 0.45 to 0.56 m shows little effect on the damages of concrete core and faceplates. The effect of rise height on the energy absorption efficiency of concrete core is also illustrated in Table 10.4, and the highest energy absorption efficiency of concrete core is observed for the curved SCS sandwich shell with rise height of 0.45 m.

#### 10.4.4 Influence of Rear to Front Plate Thickness Ratio

The rear plate of the curved SCS sandwich shell experienced higher damage as compared to the front plate from previous FE simulations, and the effect of rear to front plate thickness ratio was discussed. The dynamic responses of curved SCS sandwich shells with three different combinations of rear and front plate thickness (i.e., rear/front plate thickness of 3/5, 4/4 and 5/3 mm), under close- (25 kg TNT charge with standoff distance of 0.5 m) and far-field (5000 kg TNT charge with standoff distance of 10 m) blast loading were studied, and the external work, blast energy absorption and damage of the shell were discussed.

The effect of rear to front plate thickness ratio on the dynamic responses of curved SCS sandwich shells is shown in Table 10.5. The increase in external work with increasing rear to front plate thickness ratio is observed for the shell under close-field blast loading, whereas the external work shows decrease with increasing rear to front plate thickness ratio for the shell under far-field blast loading. However, the variation in external work by increasing rear to front plate thickness ratio from 3/5 to 5/3 is not significant. Table 10.5 also shows that the damages of concrete core and faceplates generally decrease with increasing rear to front plate thickness ratio. This is because the rear plate experiences higher damage than that of front plate, and increasing rear plate thickness is more effective in improving blast resistance of the curved SCS sandwich shell. The effect of rear to front plate thickness ratio on the energy absorption efficiency of concrete core is also presented in Table 10.5, and slight increase in energy absorption efficiency is observed by increasing rear to front plate

**Table 10.5** Summaries of FE results with varied rear to front plate thickness ratios

Rear to front plate thickness ratio	25 kg TNT@0.5 m				5000 kg TNT@10 m			
	$W_E$ (kJ)	$d_a$	$\varepsilon_{ap} (\times 10^{-2})$	$e_E$ (N/mm <sup>2</sup> )	$W_E$ (kJ)	$d_a$	$\varepsilon_{ap} (\times 10^{-2})$	$e_E$ (N/mm <sup>2</sup> )
3/5	51.9	0.441	1.48	1.62	49.7	0.425	1.56	1.48
4/4	52.3	0.425	1.38	1.65	47.0	0.363	1.30	1.62
5/3	52.9	0.391	1.41	1.82	45.4	0.358	1.19	1.60

thickness ratio from 3/5 to 5/3 (i.e., 11.0% and 7.8% increase in energy absorption efficiency for close- and far-field blast loading, respectively). This demonstrates the improvement of blast resistance of the curved SCS sandwich shell by employing thicker rear plate.

## 10.5 SDOF Model for Curved SCS Sandwich Shell

The SDOF method was adopted to obtain the blast responses of curved SCS sandwich shells, and subsequently the dimensionless P–I diagram was constructed. The curved SCS sandwich shell under uniformly distributed blast loading can be equivalent to a SDOF system, and the procedures to establish the equation of motion (EOM) are described as follows: (a) assuming a reasonable deflection shape function, which can be obtained by applying an uniformly distributed loading on the shell in a static manner (Biggs 1964); (b) establishing the relationship between strain and mid-span displacement; (c) deriving the internal energy, kinetic energy of curved SCS sandwich shell in terms of mid-span displacement and velocity, respectively, and substituting them together with the potential energy of applied blast loading into the Lagrange's equation of motion.

### 10.5.1 Deflection Shape Function

For a one-way supported curved SCS sandwich shell under uniformly distributed loading shown in Fig. 10.16, it can be simplified as an arch, as the displacement in the radial direction is predominant and its value along the width direction is almost the same. Hence, the deflection shape function of the arch under uniform line load can be adopted to represent the deflection shape function of the curved SCS sandwich shell under uniformly distributed loading. As shown in Fig. 10.17 for the elastic arch under uniform line load,  $q$ , in the radial direction, the radial displacement (inwardly positive),  $w(\theta)$ , and tangential displacement,  $v(\theta)$ , are given as follows (Dym and Williams 2011):

$$w(\theta) = \frac{qR^4}{EI} \left\{ \left[ \left( \frac{1 + \bar{I}}{2} \right) \theta \sin \theta \right] C_1 - \bar{I}C_2 + (\bar{I} \cos \theta) C_3 + \bar{I} \right\} \quad (10.4)$$

$$v(\theta) = \frac{qR^4}{EI} \left\{ [(1 - \bar{I}) \sin \theta - (1 + \bar{I}) \theta \cos \theta] \frac{C_1}{2} - (\bar{I} \theta) C_2 + (\bar{I} \sin \theta) C_3 \right\} \quad (10.5)$$

where  $q$  is uniform line load,  $R$  is radius of arch,  $E$  is Young's modulus,  $I$  is second moment of area,  $\bar{I} = h^2 / 12R^2$  ( $h$  is thickness of arch),  $C_1$ ,  $C_2$  and  $C_3$  are unknown

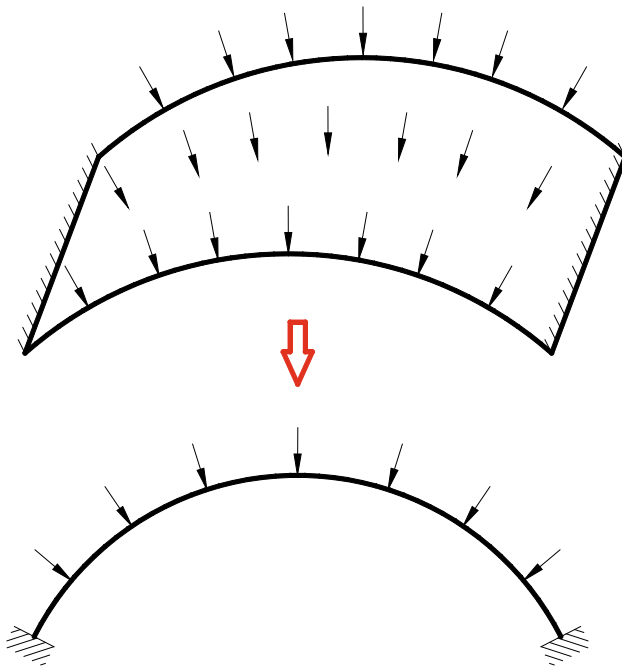


**Fig. 10.16** Simplification of curved shell to an arch

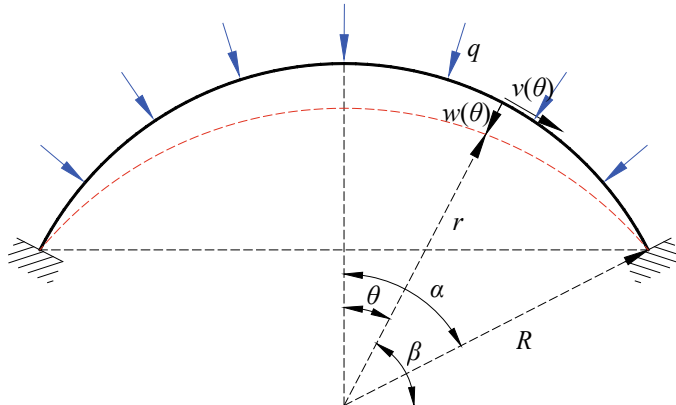


**Fig. 10.17** Geometry of arch

constants and can be determined by applying boundary conditions. For an arch with fixed ends, the following boundary conditions are applied:

$$w(\alpha) = 0, v(\alpha) = 0, \frac{dw}{d\theta} \Big|_{\theta=\alpha} = 0 \quad (10.6)$$

Then, the constants  $C_1$ ,  $C_2$  and  $C_3$  can be determined by substituting the boundary conditions in Eq. (10.6) into Eqs. (10.4) and (10.5) as follows:

$$C_1 = \frac{\bar{I}\alpha}{\sin \alpha - \frac{1+\bar{I}}{2}\alpha\left(\frac{\alpha}{\sin \alpha} + \cos \alpha\right)} \quad (10.7)$$

$$C_2 = \frac{\sin \alpha}{\sin \alpha - \frac{1+\bar{I}}{2}\alpha\left(\frac{\alpha}{\sin \alpha} + \cos \alpha\right)} \quad (10.8)$$

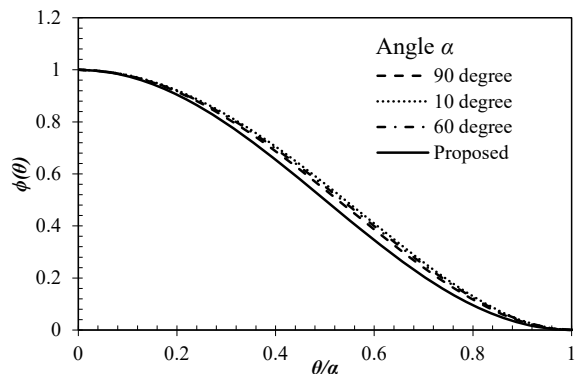
$$C_3 = \frac{\frac{1+\bar{I}}{2}\alpha(1 + \alpha \cot \alpha)}{\sin \alpha - \frac{1+\bar{I}}{2}\alpha\left(\frac{\alpha}{\sin \alpha} + \cos \alpha\right)} \quad (10.9)$$

The deflection shape function in the radial direction,  $\phi(\theta)$ , can be determined via dividing the radial displacement,  $w(\theta)$ , by the mid-span displacement of the arch,  $w(0)$ , i.e.,

$$\phi(\theta) = \frac{\sin \alpha \cdot \theta \cdot \sin \theta + (\sin \alpha + \alpha \cdot \cos \alpha) \cdot \cos \theta - \alpha - \sin \alpha \cdot \cos \alpha}{(1 - \cos \alpha)(\sin \alpha - \alpha)} \quad (10.10)$$

It is noted in Eq. (10.10) that the radial deflection shape function varies with angle  $\alpha$ , which is also illustrated in Fig. 10.18. In order to simplify the calculations of axial strain, internal energy, kinetic energy and potential energy in the following sections, a deflection shape function without the variable of angle  $\alpha$  in Eq. (10.11) is proposed, considering its minimal effect on the deflection shape function induced by the variation of angle  $\alpha$  from  $10^\circ$  to  $90^\circ$ . It was also noted by Baker et al. (1983) that the effect of deflection shape function on the structural response under blast loading was not significant if the adopted deflection shape functions were in accordance with the actual boundary condition. Hence, the simplified deflection shape function in Eq. (10.11), showing only minimal difference with the original ones, is adopted in the following calculations.

**Fig. 10.18** Deflection shape with varying angle  $\alpha$



$$\phi(\theta) = \frac{1}{2} \left[ 1 + \cos\left(\frac{\pi}{\alpha}\theta\right) \right] \quad (10.11)$$

### 10.5.2 Strain–Displacement Relationship

Establishing the relationship between strain and mid-span displacement is a primary to derive the internal energy in terms of mid-span displacement. In this study, the uniformly distributed compressive strain on the entire arch is assumed in order to provide a simple close-form solution of internal energy and arithmetic expression of dimensionless P-I diagram. In addition, the geometry requirements of arch are also presented in this section to bring down the errors induced by this assumption.

#### 10.5.2.1 Strain Calculation

By employing the simplified deflection shape function in Eq. (10.11), the radial displacement of an arch can be expressed as:

$$w(\theta) = \frac{1}{2} \left[ 1 + \cos\left(\frac{\pi}{\alpha}\theta\right) \right] w_m \quad (10.12)$$

where  $w_m$  is the mid-span displacement. According to Fig. 10.17, the developed length of arch can be determined as:

$$L_d = \int_{\pi/2-\alpha}^{\pi/2} \sqrt{r^2 + r'^2} d\beta \quad (10.13)$$

where  $r = R - \frac{1}{2} \left\{ 1 + \cos\left[\frac{\pi}{\alpha}\left(\frac{\pi}{2} - \beta\right)\right] \right\} w_m$  is radius of arch after deformation, and  $r' = \frac{dr}{d\beta}$ . Since it is difficult to obtain the close-form solution of the developed length,  $L_d$ , from Eq. (10.13), the following approximation is adopted to obtain the developed length of arch as:

$$L_d \approx \int_{\pi/2-\alpha}^{\pi/2} \left( \frac{r'^2}{2R} + r \right) d\beta = R\alpha \left( \frac{1}{4} B_1^2 B_2^2 + 1 - B_1 \right) \quad (10.14)$$

where  $B_1 = w_m / 2R$ ,  $B_2 = \pi^2 / 2\alpha$ . By adopting the assumption that compressive strain is uniformly distributed, the axial strain induced by shortening of arch,  $\varepsilon_c$ , can be determined as:

$$\varepsilon_c = \frac{L_o - L_d}{L_o} = \frac{w_m}{2R} - \frac{1}{16} \left( \frac{w_m \pi}{R\alpha} \right)^2 \text{ (Positive in compression)} \quad (10.15)$$

where  $L_o = R\alpha$  is original length of arch.

### 10.5.2.2 Geometry Requirements

In reality, the axial strain induced by shortening of arch,  $\varepsilon_c$ , is not uniformly distributed. Hence, the difference between the maximum and minimum axial strain along the arch needs to be limited to an acceptable value to bring down the errors induced by this assumption. The axial stress resultant of arch can be written as (Dym and Williams 2011):

$$N(\theta) = \frac{EA}{R} \left( \frac{dv(\theta)}{d\theta} - w(\theta) \right) \quad (10.16)$$

where  $A$  is cross-section area of arch. Then, substituting Eqs. (10.4) and (10.5) into Eq. (10.16) leads to

$$N(\theta) = -\frac{qR^3A\bar{I}}{I}(1 + C_1 \cos \theta) \quad (10.17)$$

Since the first term in Eq. (10.17) is only related to geometry of the arch and applied load, the axial strain,  $\varepsilon_c$ , can be written as:

$$\varepsilon_c(\theta) = \bar{\varepsilon}(1 + C_1 \cos \theta) \quad (10.18)$$

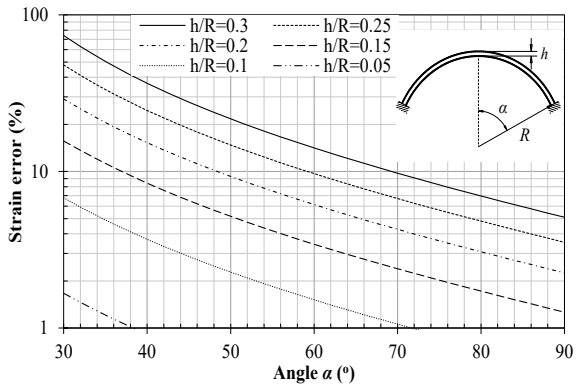
where  $\bar{\varepsilon}$  is a function of applied load, geometry and material properties of arch. It is noted that the axial strain varies along the arch, ranging from  $\bar{\varepsilon}(1 + C_1 \cos \alpha)$  at end to  $\bar{\varepsilon}(1 + C_1)$  at mid-span. Hence, the induced strain error,  $er_\varepsilon$ , can be determined as:

$$er_\varepsilon = \left| \frac{\varepsilon_{\max} - \varepsilon_{\min}}{\varepsilon_{\min}} \right| = \left| \frac{C_1(\cos \alpha - 1)}{1 + C_1} \right| \quad (10.19)$$

where  $\varepsilon_{\max}$  and  $\varepsilon_{\min}$  are the maximum and minimum axial strain along the arch, respectively. It is noted that  $er_\varepsilon$  is a function of  $\alpha$  and  $h/R$ , and therefore the  $er_\varepsilon$  in terms of  $\alpha$  and  $h/R$  are plotted in Fig. 10.19 to facilitate the selection of acceptable geometry of the arch (i.e., the arch with suitable  $\alpha$  and  $h/R$  satisfying the allowable strain error). Figure 10.19 shows that both increasing angle  $\alpha$  and decreasing  $h/R$  lead to the decrease of strain error.

Since the compressive strength of concrete is much higher than tensile strength, the continuous compression of arch subjected to blast loading is preferred. Therefore,

**Fig. 10.19** Effect of  $\alpha$  and  $h/R$  on the strain error



it is needed to ensure the monotonic increase of axial strain with increasing mid-span displacement before the arch reaching allowable maximum deformation, which leads to the following relationship:

$$\frac{w_{\max}}{R} \leq 4 \left( \frac{\alpha}{\pi} \right)^2 \quad (10.20)$$

where  $w_{\max}$  is the allowable maximum mid-span displacement of the arch.

In this calculation, only the axial strain induced by shortening of arch,  $\varepsilon_c$ , is considered, and the axial strain induced by bending,  $\varepsilon_b$ , is neglected. Similarly, a geometry limit needs to be provided to ensure the resultant axial stress of  $\varepsilon_c$  and  $\varepsilon_b$  is in compression on the entire arch. According to Fig. 10.17, the curvature of arch with thickness of  $h$  can be calculated as:

$$k_c(\beta) = \frac{|r^2 + 2r'^2 - rr'|}{(r^2 + r'^2)^{3/2}} = \frac{1}{R} f_1(w_m/R, \alpha, \beta) \quad (10.21)$$

where  $f_1(w_m/R, \alpha, \beta)$  is a function with  $w_m/R$ ,  $\alpha$  and  $\beta$  as independent variables. Then, the axial strain induced by bending at the outmost layer of arch is

$$\varepsilon_b = \frac{h}{2} \Delta k_c = \frac{h}{2R} f_2(w_m/R, \alpha, \beta) \quad (10.22)$$

It is noted that the maximum axial strain induced by bending,  $\varepsilon_{b,\max}$ , along the arch locates at the fixed end (i.e.,  $\beta = \pi/2 - \alpha$ ), and therefore  $\varepsilon_{b,\max}$  can be expressed as a function with  $w_m/R$  and  $\alpha$  as independent variables, i.e.,

$$\varepsilon_{b,\max} = \frac{h}{2} \Delta k_c = \frac{h}{2R} f_3(w_m/R, \alpha) \quad (10.23)$$

The requirement of no tensile axial strain on the arch leads to

$$\left| \frac{\varepsilon_{b,\max}}{\varepsilon_c} \right| = \frac{h}{2R} f_4(w_m/R, \alpha) \leq 1 \quad (10.24)$$

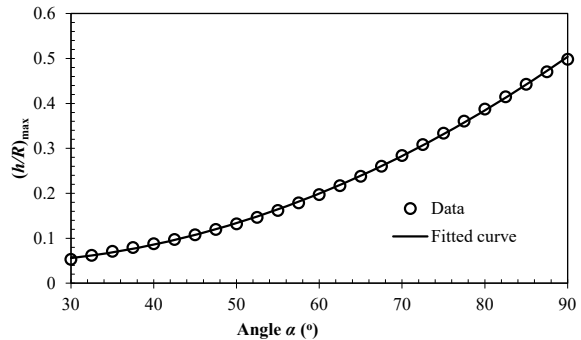
It is noted that  $f_4(w_m/R, \alpha)$  shows increase with increasing  $w_m/R$ . Hence, the allowable maximum mid-span displacement,  $w_{\max}$ , is used to replace  $w_m$  in Eq. (10.24), and this can ensure no tensile axial strain on the arch with mid-span displacement less than  $w_{\max}$ . For the curved SCS sandwich shell studied in this chapter, the ultimate strain of concrete,  $\varepsilon_u$ , can be chosen as a failure threshold of curved SCS sandwich shell under blast loading. From Eq. (10.15), the  $w_m/R$  corresponding to  $\varepsilon_u$  can be determined as:

$$\frac{w_{\max}}{R} = 4 \left( \frac{\alpha}{\pi} \right)^2 \left[ 1 - \sqrt{1 - \left( \frac{\pi}{\alpha} \right)^2 \varepsilon_u} \right] \quad (10.25)$$

Substituting Eq. (10.25) into Eq. (10.24) and setting  $\varepsilon_u = 0.0035$  (with concrete grade no higher than C50/60) (Eurocode 2004) leads to the allowable maximum ratio of thickness to radius,  $(h/R)_{\max}$ , with only  $\alpha$  as the independent variable. By utilizing curve fitting method, the expression of  $(h/R)_{\max}$  in terms of angle  $\alpha$  can be obtained in Eq. (10.26), and the fitted curve is shown in Fig. 10.20.

$$\frac{h}{R} \leq \left( \frac{h}{R} \right)_{\max} = (8.925\alpha^2 - 324.9\alpha + 7308) \times 10^{-5} \quad (\alpha \text{ in } {}^\circ) \quad (10.26)$$

**Fig. 10.20** Relationship between  $(h/R)_{\max}$  and angle  $\alpha$



### 10.5.3 Equation of Motion

As for the curved SCS sandwich shell with the geometry shown in Fig. 10.21 subjected to uniformly distributed blast loading, the equation of motion can be formulated in Eq. (10.27) by applying the Lagrange's equation.

$$\frac{d}{dt} \left( \frac{dK}{d\dot{w}_m} \right) + \frac{d(U + V)}{dw_m} = 0 \quad (10.27)$$

where  $K$  is kinetic energy,  $U$  is internal energy,  $V$  is potential energy, and  $w_m$  is mid-span displacement. The kinetic energy of the curved SCS sandwich shell can be calculated as:

$$K = \frac{1}{2} \int_0^{\alpha} m[\phi(\theta)\dot{w}_m]^2 d\theta \quad (10.28)$$

where  $m$  is mass per unit radian of the curved SCS sandwich shell and given in Eq. (10.29), and  $\dot{w}_m$  is the velocity at mid-span and can be obtained by differentiating the mid-span displacement,  $w_m$ , with respect to time,  $t$ .

$$m = \left[ \frac{1}{2} \rho_c (r_{out}^2 - r_{in}^2) + \rho_s (t_{in} r_{inm} + t_{out} r_{outm}) \right] W_d \quad (10.29)$$

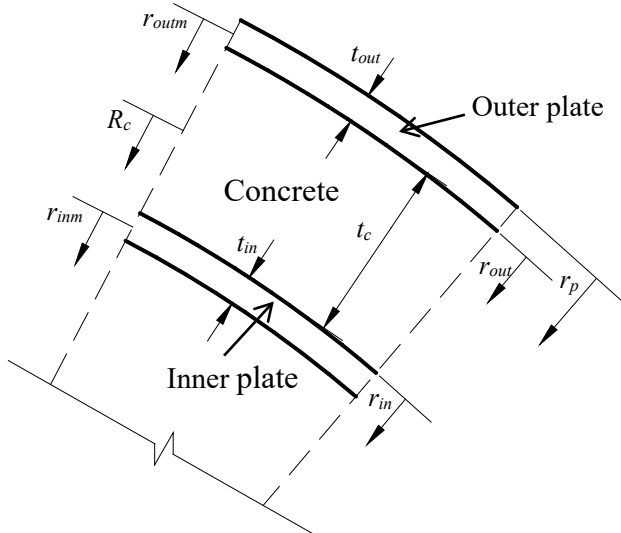


**Fig. 10.21** Geometry of curved SCS sandwich shell

where  $\rho_c$  and  $\rho_s$  are densities of concrete and steel, respectively,  $W_d$  is width of curved SCS sandwich shell, and other geometric parameters can be found in Fig. 10.21.

According to the assumption on axial strain in Sect. 10.5.2, i.e., the axial strain of concrete,  $\varepsilon_c$ , is uniformly distributed on the entire concrete core, the differential of internal energy of concrete core,  $U_c$ , with respect to mid-span displacement,  $w_m$ , can be formulated as:

$$\frac{dU_c}{dw_m} = V_c \frac{du_c}{d\varepsilon_c} \frac{d\varepsilon_c}{dw_m} \quad (10.30)$$

where  $V_c = 1/2(r_{out}^2 - r_{in}^2)W_d$  is volume of concrete core, and  $u_c$  is internal energy per unit volume of concrete core. The differential of  $u_c$  with respect to  $\varepsilon_c$  can be determined as:

$$\frac{du_c}{d\varepsilon_c} = \sigma_c(\varepsilon_c) \quad (10.31)$$

where  $\sigma_c(\varepsilon)$  specifies the relationship between compressive stress and strain of concrete and can be expressed in Eq. (10.32) according to Eurocode 2 (2004).

$$\sigma_c(\varepsilon_c) = \frac{k\varepsilon_c/\varepsilon_o - (\varepsilon_c/\varepsilon_o)^2}{1 + (k - 2)\varepsilon_c/\varepsilon_o} f_{cm} \text{ for } |\varepsilon| < |\varepsilon_u| \quad (10.32)$$

where  $k, f_{cm}, \varepsilon_o$  and  $\varepsilon_u$  are constants for specified concrete grade, and can be found in Eurocode 2. From Eq. (10.15), the differential of  $\varepsilon_c$  with respective to  $w_m$  can be obtained as:

$$\frac{d\varepsilon_c}{dw_m} = \frac{1}{2R_c} - \frac{w_m\pi^2}{8R_c^2\alpha^2} \quad (10.33)$$

where  $R_c$  is radius at the middle layer of concrete core, as shown in Fig. 10.21.

Similar to the calculation of  $dU_c/dw_m$ , the differential of internal energy of inner and outer steel plate with respect to mid-span displacement ( $dU_{si}/dw_m$  and  $dU_{so}/dw_m$ ) can be calculated as well. Herein, the elastic–plastic-hardening constitutive model in Eq. (10.34) is employed to determine the stress–strain relationship of steel.

$$\sigma_s(\varepsilon_s) = \begin{cases} E_s \varepsilon_s & \varepsilon_s \leq \varepsilon_y \\ E_s \varepsilon_y + \alpha_E E_s (\varepsilon_s - \varepsilon_y) & \varepsilon_s > \varepsilon_y \end{cases} \quad (10.34)$$

where  $E_s$ ,  $\varepsilon_y$ ,  $\alpha_E$  are Young's modulus, yield strain and hardening coefficient of steel. Hence, the differential of internal energy of the curved SCS sandwich shell with respect to mid-span displacement,  $dU/dw_m$ , can be obtained by summing the terms of concrete core, inner and outer steel plate as:

$$\frac{dU}{dw_m} = \frac{dU_c}{dw_m} + \frac{dU_{si}}{dw_m} + \frac{dU_{so}}{dw_m} \quad (10.35)$$

where  $U_c$ ,  $U_{si}$  and  $U_{so}$  are internal energy of concrete core, inner and outer steel plate, respectively.

The potential energy of blast loading can be calculated as:

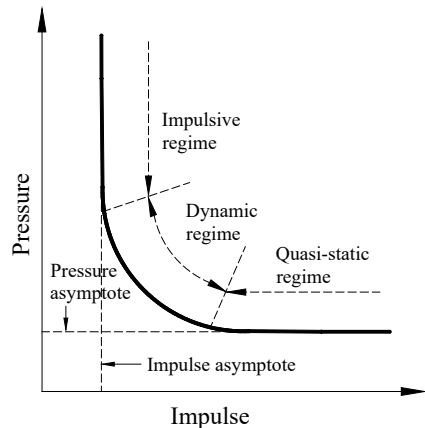
$$V = -W_d \int_0^\alpha P(t) r_p \phi(\theta) w_m(t) d\theta \quad (10.36)$$

where  $P(t)$  is applied blast pressure-time history, and  $r_p$  is the radius at outmost layer of the outer steel plate, as shown in Fig. 10.21. Then, the equation of motion of the curved SCS sandwich shell can be obtained by substituting Eqs. (10.28), (10.35) and (10.36) into Eq. (10.27). The fourth-order Runge–Kutta time stepping procedure was employed to solve the equation of motion and obtain the maximum mid-span displacement of the curved SCS sandwich shell under blast loading.

## 10.6 P–I Diagram for Curved SCS Sandwich Shell

Figure 10.22 shows a typical P–I diagram, and the pressure and impulse asymptotes are two vital parameters that define the limiting values for pressure and impulse, respectively. As seen in Fig. 10.22, the response behavior of a structure subjected to blast loading can be categorized into impulsive, dynamic and quasi-static response regimes in accordance with the ratio of blast load duration to the natural period of the structure. The pressure and impulse asymptotes (quasi-static and impulsive response

**Fig. 10.22** Typical P–I diagram



regimens) can be determined via employing the energy balance method, and the responses in the dynamic response regime can be obtained by employing the SDOF model presented in Sect. 10.5.

### 10.6.1 Internal Energy–Displacement Relationship

The internal energy per unit width of concrete core can be calculated as:

$$\bar{U}_c(w_m) = \bar{V}_c u_c \quad (10.37)$$

where  $\bar{V}_c = 1/2(r_{out}^2 - r_{in}^2)$  is the volume per unit width of concrete core, and  $u_c$  is the internal energy per unit volume of concrete core, which can be calculated as:

$$\begin{aligned} u_c(\varepsilon_c) &= \int_0^{\varepsilon_c} \sigma_c d\varepsilon \\ &= \varepsilon_o f_{cm} \left[ \frac{(k-1)^2 \varepsilon_c / \varepsilon_o}{(k-2)^2} - \frac{(\varepsilon_c / \varepsilon_o)^2}{2(k-2)} - \frac{(k-1)^2 \ln((k-2)\varepsilon_c / \varepsilon_o + 1)}{(k-2)^3} \right] \end{aligned} \quad (10.38)$$

Then, substituting  $\varepsilon_c = \frac{w_m}{2R_c} - \frac{w_m^2 \pi^2}{16R_c^2 \alpha^2}$  into Eq. (10.38) leads to the expression of internal energy per unit volume of concrete core in terms of mid-span displacement,  $u_c(w_m)$ . Similar to the calculation of internal energy per unit width of concrete core, the internal energy per unit width of inner and outer steel plate ( $\bar{U}_{si}(w_m)$  and  $\bar{U}_{so}(w_m)$ ) can be calculated as well. Herein, the relationship between internal energy per unit volume of steel plate and strain can be determined in Eq. (10.39) by employing the elastic–plastic-hardening constitutive model in Eq. (10.34).

$$u_s(\varepsilon_s) = \int_0^{\varepsilon_s} \sigma_s d\varepsilon' = \begin{cases} 0.5E\varepsilon_s^2 & \varepsilon_s \leq \varepsilon_y \\ 0.5\alpha_E E\varepsilon_s^2 + E(1-\alpha_E)(\varepsilon_y \varepsilon_s - 0.5\varepsilon_y^2) & \varepsilon_s > \varepsilon_y \end{cases} \quad (10.39)$$

Then, the internal energy per unit width of curved SCS sandwich shell can be obtained by summing the internal energy contributed by concrete core, inner and outer steel plate as:

$$\bar{U}(w_m) = \bar{U}_c(w_m) + \bar{U}_{si}(w_m) + \bar{U}_{so}(w_m) \quad (10.40)$$

where  $\bar{U}_c(w_m)$ ,  $\bar{U}_{si}(w_m)$  and  $\bar{U}_{so}(w_m)$  are internal energy per unit width of concrete core, inner steel plate and outer steel plate, respectively.

### 10.6.2 Dimensionless Pressure and Impulse

The blast pressure profile is required when constructing the dimensionless P-I diagram. In this study, a triangular blast pressure profile with zero rise time given in Eq. (10.41) was adopted.

$$P(t) = \begin{cases} P_{\max}(1 - t/t_d) & t < t_d \\ 0 & t \geq t_d \end{cases} \quad (10.41)$$

where  $P_{\max}$  is peak pressure and  $t_d$  is loading duration.

When loading duration is much longer than the natural period of the curved SCS sandwich shell, i.e.,  $t_d \gg T$ , the load can be considered to act in a quasi-static manner since the structure will reach its maximum displacement long before the load has diminished. Equating the external work done per unit width by blast loading with the internal energy per unit width of the curved SCS sandwich shell leads to

$$\overline{U}(w_m) = \frac{1}{2} P_{\max} r_p w_m \alpha \quad (10.42)$$

Then, rewriting Eq. (10.42) gives a modified pressure asymptote as

$$\frac{P_{\max}}{2\overline{U}(w_m)/r_p w_m \alpha} = 1 = \overline{P} \quad (10.43)$$

where  $\overline{P}$  can be treated as the dimensionless pressure with the dimensionless pressure asymptote to be one.

When loading duration is much shorter than the natural period of the curved SCS sandwich shell, i.e.,  $t_d \ll T$ , the load can be considered to act in an impulsive manner. The blast energy initially transfers to the structure as kinetic energy and is finally absorbed by the structure as internal energy. Applying Momentum Theorem leads to

$$\frac{1}{4} P_{\max} r_p \alpha t_d = \frac{3}{8} \alpha \overline{m} \dot{w}_m \quad (10.44)$$

where  $\overline{m} = m/W_d$ . The mid-span velocity of the curved SCS sandwich shell,  $\dot{w}_m$ , can be determined from Eq. (10.44), and the velocity of the curved SCS shell,  $\dot{w}(\theta)$ , can also be obtained by applying the deflection shape function,  $\phi(\theta)$ . Then, the kinetic energy per unit width of the curved SCS sandwich shell can be obtained as:

$$\overline{E}_k = \frac{\alpha r_p^2 I^2}{3\overline{m}} \quad (10.45)$$

where  $I = 0.5P_{\max}t_d$  is impulse. Equating  $\bar{E}_k$  with  $\bar{U}(w_m)$  gives the follow relationship:

$$\frac{\sqrt{\alpha}r_p I}{\sqrt{3m\bar{U}(w_m)}} = 1 = \bar{I} \quad (10.46)$$

where  $\bar{I}$  can be treated as the dimensionless impulse with the dimensionless impulse asymptote to be one.

### 10.6.3 Dimensionless P-I Diagram Establishment

With the SDOF model in Sect. 10.5 to obtain the maximum mid-span displacement of the curved SCS sandwich shell under blast loading, the procedures to construct the dimensionless P-I diagram are described as follows:

- (1) Select the curved SCS sandwich shells with varying parameters, including geometry (angle  $\alpha$ , radius, steel plate and concrete core thickness), material (steel and concrete grade) and blast loading (peak pressure and loading duration). It should be noted that the adopted geometry of the curved SCS sandwich shell must satisfy the geometry requirement specified in Sect. 10.5.
- (2) Obtain the maximum mid-span displacements of curved SCS sandwich shells with varying geometries, materials and blast loadings via employing the SDOF model and plot the pairs of dimensionless pressures,  $\bar{P}$ , and impulses,  $\bar{I}$ , in Fig. 10.23. (The dimensionless pressure and impulse are defined in Eqs. (10.43) and (10.46), respectively)
- (3) Fit the dimensionless pressure and impulse data in Fig. 10.23 and yield the formula of dimensionless P-I diagram in Eq. (10.47).

$$\ln(\bar{P} - 1) + 0.039 \ln^2(\bar{I} - 1) + 0.864 \ln(\bar{I} - 1) + 1.288 = 0 \quad (10.47)$$

**Fig. 10.23** Dimensionless P-I diagram from analytical model

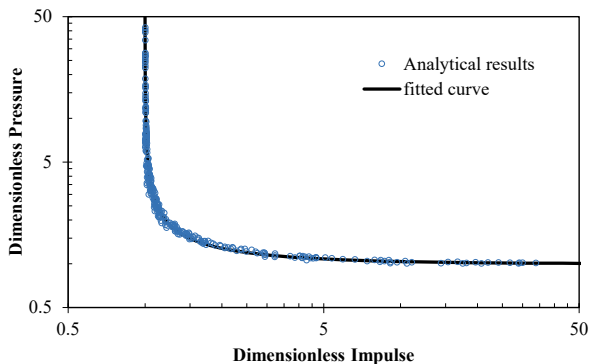
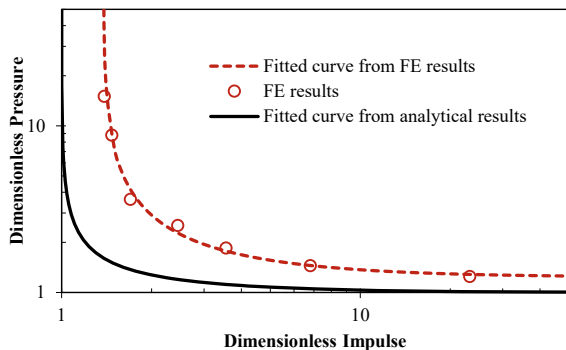


**Fig. 10.24** Modified dimensionless P-I diagram with FE analyses



Owing to the limitation of the established SDOF model, which cannot capture the strain rate effect, stress wave effect, confinement effect on concrete strength, etc., the FE model was adopted herein to improve the accuracy of the dimensionless P-I diagram constructed based on the SDOF method. Figure 10.24 plots the dimensionless pressures and impulses obtained from FE analyses. It is noted that the dimensionless P-I diagram constructed from SDOF method yields higher damage level as compared to that from the FE results. This is because the FE model can capture the strain rate effect, confinement effect on concrete strength, etc., and these contribute to the blast resistant improvement of the curved SCS sandwich shell. Hence, the new dimensionless P-I diagram given in Eq. (10.48) is generated by fitting the FE results to provide more accurate predictions on the damage level of the curved SCS sandwich shell under uniformly distributed blast loading.

$$\ln(\bar{P} - 1.24) + 0.04 \ln^2(\bar{I} - 1.38) + 0.9 \ln(\bar{I} - 1.38) - 0.1 = 0 \quad (10.48)$$

## 10.7 Blast Resistant Design Approach

The procedures of using the dimensionless P-I diagram to perform the blast resistant design for the curved SCS sandwich shell are presented as follows:

- (1) Determine the peak pressure and loading duration for a given blast loading;
- (2) Determine the maximum mid-span displacement based on the allowable damage level;
- (3) Choose the geometric and material properties of the curved SCS sandwich shell and the geometry has to satisfy the requirement specified in Sect. 10.5.
- (4) Calculate the dimensionless pressure and impulse from Eqs. (10.43) and (10.46), respectively, with the specified geometric and material properties, maximum mid-span displacement, peak pressure and loading duration from steps (1)–(3);

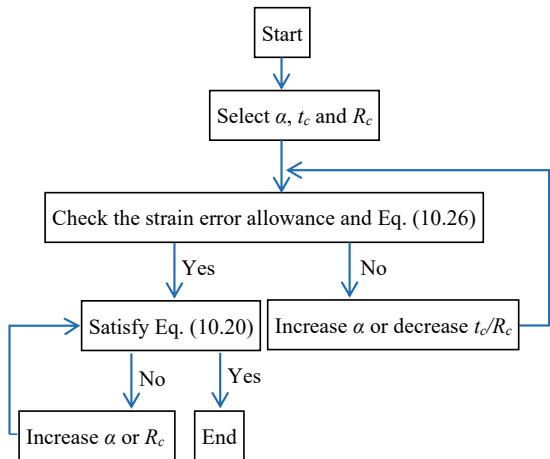
- (5) Check the location of dimensionless pressure and impulse with dimensionless P-I diagram plotted in Eq. (10.47). If the data point locates below the curve, the SCS sandwich shell experiences less damage than the allowable damage level. Otherwise, the curved SCS sandwich shell exceeds the allowable damage level, and it is necessary to change the material or geometric properties of the curved SCS sandwich shell and repeat the steps (3)–(5).

Since the ductility of concrete is much lower as compared to steel and the concrete core with larger volume is the main part for resisting blast load, two damage levels of the curved SCS sandwich shell subjected to blast loading are suggested based on the compressive strain of concrete, i.e.,  $\varepsilon_{\max} = \varepsilon_o$  (damage level I) and  $\varepsilon_u$  (damage level II), where  $\varepsilon_o$  and  $\varepsilon_u$  are the strain at peak stress and ultimate strain of concrete, respectively, and their values can be found from Eurocode 2 with specified concrete grade.

In order to simplify the calculation of internal energy as well as the formula of dimensionless P-I diagram, the assumption on axial strain is employed, and the corresponding geometry requirement on the curved SCS sandwich shell for bringing down the induced error is presented in Sect. 10.5. Herein, the procedures to select the suitable geometry of the curved SCS sandwich shell are illustrated in Fig. 10.25 and described as follows:

- (1) Determine the concrete core thickness,  $t_c$ , radius,  $R_c$  and angle  $\alpha$ .
- (2) Check the strain error allowance by utilizing Fig. 10.19 and check the ratio of thickness to radius,  $t_c/R_c$ , with the allowable value in Eq. (10.26). If any of them is not satisfied, it is needed to increase  $\alpha$  or decrease  $t_c/R_c$  and redo the checking.
- (3) Check the geometric parameters with Eq. (10.20). If not satisfied, it is needed to increase  $\alpha$  or  $R_c$  and redo the checking at current step.

**Fig. 10.25** Flow chart for determining the geometry of the curved SCS sandwich shell



## 10.8 Summary

In this chapter, the curved SCS sandwich shell was proposed to resist blast loading, and its blast response was numerically studied. In addition, a dimensionless P-I diagram of the curved SCS sandwich shell was constructed based on the SDOF model to facilitate the blast resistant design of such structure. The main findings from this chapter are summarized as follows:

- (1) The separation between faceplates and concrete core was observed for the curved SCS sandwich shell without shear connectors under close-field blast loading. With regard to the failure modes of the curved SCS sandwich shell with shear connectors, separation of the rear plate from concrete core was observed for the shell under close-field blast loading, whereas buckling of faceplates was observed for the shell under far-field blast loading.
- (2) The blast-induced deformation of the curved SCS sandwich shell with shear connectors could be significantly reduced as compared to the shell without shear connectors, which could be attributed to the improved bonding behavior between faceplates and concrete core.
- (3) The external work done by blast loading could be significantly reduced by increasing rise height. Both the damages of concrete core and faceplates could be reduced significantly by increasing rise height from 0 to 0.45 m, and further increasing rise height from 0.45 to 0.56 m showed little effect on their damages. Moreover, the highest energy absorption efficiency of concrete core was observed for the curved SCS sandwich shell with rise height of 0.45 m.
- (4) The damages of concrete core and faceplates generally showed decrease with increasing rear to front plate thickness ratio. The energy absorption efficiency of concrete core showed slight increase with increasing rear to front plate thickness ratio.
- (5) The constructed dimensionless P-I diagram using SDOF model yielded slightly higher damage as compared to the FE predictions, and therefore the FE model was employed to improve the accuracy of the dimensionless P-I diagram. In addition, the blast resistant design procedures were presented for the curved SCS sandwich shell by utilizing the dimensionless P-I diagram.

## References

- Anandavalli N, Lakshmanan N, Rajasankar J et al (2012) Numerical studies on blast loaded steel-concrete composite panels. *JCES* 1(3):102–108
- ASCE (2010) Design of blast-resistant buildings in petrochemical facilities. Am Soc Civ Eng
- ASCE (2011) Blast protection of buildings. ASCE/SEI 59–11. Am Soc Civ Eng
- Baker WE, Cox PA, Westine PS et al (1983) Explosion and hazards and evaluation. Elsevier Scientific Publishing Compay, Amsterdam
- Biggs JM (1964) Introduction to structural dynamics. McGraw-Hill, New York

- Carta G, Stochino F (2013) Theoretical models to predict the flexural failure of reinforced concrete beams under blast loads. *Eng Struct* 49:306–315
- Chen W, Hao H, Chen S (2015) Numerical analysis of prestressed reinforced concrete beam subjected to blast loading. *Mater Des* 65: 662–674
- Clubley SK, Moy SSJ, Xiao RY (2003) Shear strength of steel-concrete-steel composite panels. Part II—detailed numerical modelling of performance. *J Constr Steel Res* 59:795–808
- Cowper GR, Symonds PS (1958) Strain hardening and strain rate effects in the impact loading of cantilever beams. *Applied Mathematics Report*, Brown University
- Dragos J, Wu C (2013) A new general approach to derive normalised pressure impulse curves. *Int J Impact Eng* 62:1–12
- Dym CL, Williams HE (2011) Stress and displacement estimates for arches. *J Struct Eng* 137(1):49–58
- Eurocode 2 (2004) Design of concrete structures – Part 1–1: General rules and rules for buildings. BS EN 1992–1–1, London
- Fallah AS, Louca LA (2006) Pressure-impulse diagrams for elastic-plastic-hardening and softening single-degree-of-freedom models subjected to blast loading. *Int J Impact Eng* 34:823–842
- Federal Highway Administration (2007a) Evaluation of LS-DYNA concrete material model 159
- Federal Highway Administration (2007b) Users manual for LS-DYNA concrete material model 159
- Foundoukou N, Chapman JC (2008) Finite element analysis of steel-concrete-steel sandwich beams. *J Constr Steel Res* 64:947–961
- Hallquist JO (2006) LS-DYNA theory manual. Livermore Software Technology Corporation (LSTC). Livermore, California
- Hallquist JO (2013) LS-DYNA keyword user's manual. Livermore Software Technology Corporation (LSTC). Livermore, California
- Huang Z, Liew JYR (2015) Nonlinear finite element modeling and parametric study of curved steel-concrete-steel double skin composite panels infilled with ultra-lightweight cement composite. *Constr Build Mater* 95:922–938
- Jones N (1988) Structural impact, Cambridge University Press, Cambridge/New York
- Kang WK, Lee SC, Liew JYR (2013) Analysis of steel-concrete composite column subject to blast. *P I Civil Eng-Str B* 166:15–27
- Krauthammer T, Astarlioglu S, Blasko J et al (2008) Pressure-impulse diagrams for the behaviour assessment of structural components. *Int J Impact Eng* 35:771–783
- Liew JYR, Wang TY (2011) Novel steel-concrete-steel sandwich composite plates subjected to impact and blast load. *Adv Struct Eng* 14(4):673–686
- Li QM, Meng H (2002a) Pressure-impulse diagram for blast loads based on dimensional analysis and single-degree-of-freedom mode. *J Eng Mech* 1(87):87–92
- Li QM, Meng H (2002b) Pulse loading shape effects on pressure-impulse diagram of an elastic-plastic, single-degree-of-freedom structural model. *Int J Mech Sci* 44:1985–1998
- Li X, Chen JF, Lu Y et al (2015) Modelling static and dynamic FRP-concrete bond behaviour using a local concrete damage model. *Adv Struct Eng* 18(1):45–58
- Mays G, Smith PD (1995) Blast effects on buildings: Design of buildings to optimize resistance to blast loading. T. Telford, London
- Morison CM (2006) Dynamic response of walls and slabs by single-degree-of-freedom analysis—a critical review and revision. *Int J Impact Eng* 32:1214–1247
- Mutalib AA, Hao H (2011) Development of P-I diagrams for FRP strengthened RC columns. *Int J Impact Eng* 38:290–304
- Rigby SE, Tyas A, Bennett T (2014) Elastic-plastic response of plates subjected to cleared blast loads. *Int J Impact Eng* 66:37–47
- Shi Y, Hao H, Li ZX (2008) Numerical derivation of pressure-impulse diagrams for prediction of RC column damage to blast loads. *Int J Impact Eng* 35:1213–1227
- UFC 3–340–02 (2008) Structures to resist the effects of accidental explosions. US Department of Army, Navy and the Air Force, Washington, DC

- Wang Y, Liew JYR (2015) Blast performance of water tank with energy absorbing support. *Thin Wall Struct* 96:1–10
- Wang Y, Liew JYR, Lee SC (2015) Theoretical models for axially restrained steel-concrete-steel sandwich panels under blast loading. *Int J Impact Eng* 76:221–231
- Wang Y, Xiong MX (2015) Analysis of axially restrained water storage tank under blast loading. *Int J Impact Eng* 86:167–178
- Wang Y, Zhai X (2019) Development of dimensionless P-I diagram for curved SCS sandwich shell subjected to uniformly distributed blast pressure. *Front Struct Civ Eng* 13(6):1432–1445
- Wang Y, Zhai X, Lee SC et al (2016) Response of curved steel-concrete-steel shells subjected to blast loading. *Thin Wall Struct* 108:185–192
- Xie M, Foundoukos N, Chapman JC (2007) Static tests on steel-concrete-steel sandwich beams. *J Constr Steel Res* 63:735–750
- Yan JB, Liew JYR, Zhang MH et al (2016a) Punching shear resistance of steel-concrete-steel sandwich composite shell structure. *Eng Struct* 117:470–485
- Yan JB, Xiong MX, Qian X et al (2016b) Numerical and parametric study of curved steel-concrete-steel sandwich composite beams under concentrated loading. *Mater Struct* 49(10):3981–4001

# Chapter 11

## Steel-PU Foam-Steel-Concrete-Steel Panel Under Impact



### 11.1 Introduction

For recent decades, the extreme events or threats on buildings and infrastructures related to impact loading have shown an increasing trend. These have sparked intensive research works regarding the improvement of structural resistance against impact loading (Fu et al. 2020; Li et al. 2019a; Iqbal et al. 2019; Fan et al. 2019). The steel–concrete–steel (SCS) sandwich panel generally outperformed other panels (e.g., steel and reinforced concrete panels) in terms of high ductility, concrete spalling protection, buckling resistance and energy absorption capacity (Wang et al. 2016b). In addition, the foam materials (e.g., metallic foam, polymeric foam, cement-based foam and ceramic foam) were increasingly employed to enhance the structural resistance against impact or blast loading (Li et al. 2019b; Langdon et al. 2010; Zhou et al. 2015a, b), owing to their outperformances in weight and energy absorption capacity. The polyurethane (PU) foam with high specific energy absorption was attached to the front of SCS sandwich panel to form a new steel-PUF-steel–concrete–steel (SPUFSCS) panel. This new SPUFSCS panel is composed of “soft” and “stiff” layers with the aim of improving the impact resistance of the traditional SCS sandwich panel. The front steel plate and PUF belongs to the “soft” layer which is employed for dissipating impact energy and reducing peak force transmitted to the SCS panel, and the rear SCS panel is the “stiff” layer which is utilized for resisting the transmitted impact force from PUF.

The detailed review on the SCS sandwich structures under impact loading has been presented in Sect. 6.1. With regard to the foam material, it was widely employed to be filled into thin-walled metallic structures for dissipating impact and blast energy owing to its lightweight and high specific energy absorption. The foam-filled energy absorbers have shown extensive applications in aerospace, military, automotive engineering and civil engineering (Wang et al. 2020b). Up to date, the works on the applications of foam material in civil structures for impact load mitigation are still limited (Remennikov et al. 2011; Wang et al. 2019, 2020a; Schenker et al. 2005). Remennikov et al. (2011) conducted experimental and numerical studies on the foam- and

concrete-filled square steel tubes under low-velocity impact loading. The highest impact resistance and energy absorption were observed for the concrete-filled tubes, followed by rigid PUF-filled tubes and then the hollow tubes. Besides the foam-filled tubes, the PUF-filled energy absorption connectors were also proposed, which could be employed for attaching the façade or wall to the building and mitigating potential blast or impact energy (Wang et al. 2019, 2020a). The PUF filler was shown to significantly improve the energy absorption capacity of the connector. In addition, an analytical model considering strain rate effects of steel and PUF was also developed for evaluating the load-displacement response of the connector under dynamic crushing load (Wang et al. 2019, 2020a). With regard to the foam material as “soft” layer to mitigate impact loading, Schenker et al. (2005) conducted experimental and numerical studies on the impact response of reinforced concrete structures protected with aluminum foam, and the peak impact force was found to be reduced as compared to the counterpart without foam.

In this chapter, a new SPUFSCS panel was developed, and its impact response was experimentally studied via employing an instrumented drop-weight impact test system. Then, numerical studies on the SPUFSCS panel under impact loading were conducted to reveal its impact energy dissipation mechanism. As for the SPUFSCS panel under the impact of a cylindrical head, an analytical model was also proposed for predicting its displacement response.

## 11.2 SPUFSCS Panel Under the Impact of a Hemispherical Hammer

### 11.2.1 Experimental Study

#### 11.2.1.1 Specimens

The SPUFSCS panel consisted of a concrete core, a PUF layer, three steel plates, two end steel plates and shear connectors, as illustrated in Fig. 11.1a. Five SPUFSCS panels and one SCS panel were manufactured, and the geometric parameters of the specimens are listed in Table 11.1. The width ( $W$ ) and length ( $L$ ) of all the specimens were 900 and 1100 mm, respectively. The geometric parameters of the specimens were varied by varying the steel plate thickness (the nominal thicknesses are 3, 4, and 5 mm) and concrete core thickness (70, 85, and 100 mm). High-strength bolts were utilized as shear connectors to provide compaction and ensure the structural integrity of the SPUFSCS panel. All the bolts were 12 mm in diameter and had two types of lengths, including the long bolts connecting the top, middle, and bottom steel plates, and the short bolts connecting the middle and bottom steel plates. Figure 11.1b shows the detailed arrangement of the shear connectors.

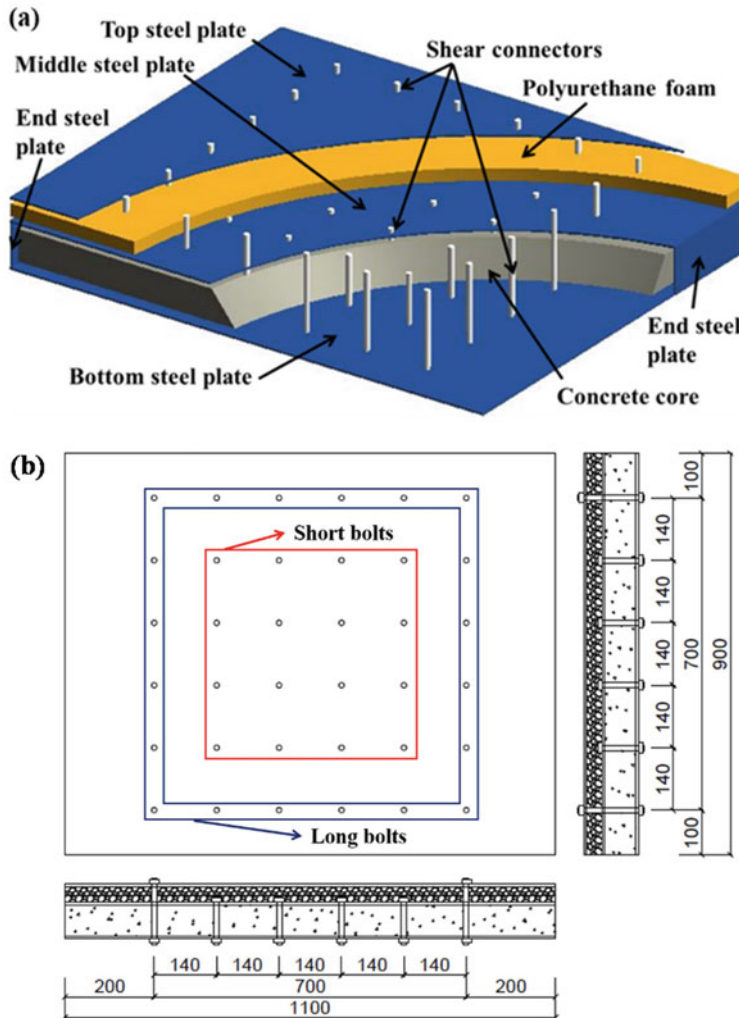


**Fig. 11.1** Detailed drawing of the SPUFSCS panel: **a** general illustration of the SPUFSCS panel and **b** arrangement of shear connectors, reprinted from Meng et al. (2021), copyright 2022, with permission from Elsevier

### 11.2.1.2 Materials

The steel plates used for the SPUFSCS panels were Q235 mild steel. The material properties of the steel faceplates with different thicknesses were obtained from tensile coupon tests according to GB/T 228.1–2010 (2010). The uniaxial compression tests of concrete were carried out on three cylindrical specimens with heights

**Table 11.1** Geometric parameters of SPUFSCS panels (hemispherical hammer)

Specimen	$t_{ls}$ (mm)	$t_{puf}$ (mm)	$t_{ms}$ (mm)	$t_c$ (mm)	$t_{bs}$ (mm)	$L$ (mm)	$W$ (mm)	$D$ (mm)	$S$ (mm)
SPUFSCS4-4	3.67	50	3.67	70	3.67	1100	900	12	140
SPUFSCS3-5	3.67	50	3.0	70	4.7	1100	900	12	140
SPUFSCS5-3	3.67	50	4.7	70	3.0	1100	900	12	140
SPUFSCS85	3.67	50	3.67	85	3.67	1100	900	12	140
SPUFSCS100	3.67	50	3.67	100	3.67	1100	900	12	140
SCS	0	0	3.67	70	3.67	1100	900	12	140

Note  $t_{ls}$ ,  $t_{ms}$  and  $t_{bs}$  represent top steel plate thickness, middle steel plate thickness and bottom steel plate thickness respectively,  $t_{puf}$  is PUJF layer thickness,  $t_c$  is concrete core thickness,  $L$  is length of panel,  $W$  is width of panel,  $D$  is diameter of connectors and  $S$  is spacing of connectors

**Table 11.2** Material properties

Concrete	Compressive strength (MPa)		Elastic modulus (GPa)	Poisson's ratio
45			29	0.211
	Yield strength (MPa)	Ultimate strength (MPa)	Elastic modulus (GPa)	Poisson's ratio
3 mm steel plate	283.3	419.1	208.8	0.27
4 mm steel plate	287.8	411.6	197.1	0.27
5 mm steel plate	286.2	424.1	205.5	0.27
bolt	640	800	200	0.27
PU foam	Density (kg/m <sup>3</sup> )		Elastic modulus (MPa)	Plateau stress (MPa)
	193.27		64.6	2.21

and diameters of 300 and 150 mm, respectively, and the average unconfined compressive strength of concrete was 45 MPa. PUF with a density of 193 kg/m<sup>3</sup> was used as the energy-absorbing layer. The stress–volumetric strain relationship of PUF was obtained by conducting a uniaxial compression test in accordance with GB/T 8813-2008 (2008). Grade 8.8 high strength bolts were employed as shear connectors of the SPUFSCS panels. The yield and ultimate strength of the high-strength bolt were 640 and 800 MPa, respectively. The main material parameters of the concrete, steel plates, bolts, and PUF used for the test specimens are listed in Table 11.2.

### 11.2.1.3 Test Setup and Instrumentation

The impact test was carried out by employing a drop-weight impact test system, as shown in Fig. 11.2. A hemispherical hammer with a diameter of 200 mm was chosen for this test, and the summed weight of the hammer head and counterweight was 620 kg for all specimens. The impact location of the drop hammer was at the center of the panel. In addition, the specimen was supported by only two steel bars welded on rigid supports with a clear span of 950 mm. The impact force–time curves of the panels were obtained using a 2000-kN dynamic load cell embedded in the hammer head. Three dynamic displacement transducers (i.e., potentiometers) were utilized to measure the displacements of the bottom steel plate, and their layouts are shown in Fig. 11.3. The impact force and displacements were recorded using a data logger with a sampling frequency of 10<sup>5</sup> Hz. A high-speed camera with a sampling frequency of 3000 frames per second was used to capture the deformation process of the SPUFSCS panel and the movement of the hammer head.

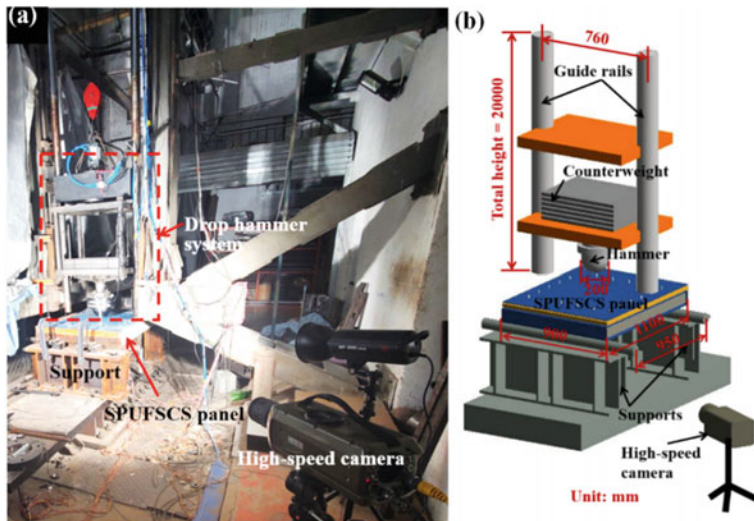


**Fig. 11.2** Setup and instrumentation for the impact test with a hemispherical hammer: **a** photo and **b** 3D view, reprinted from Meng et al. (2021), copyright 2022, with permission from Elsevier

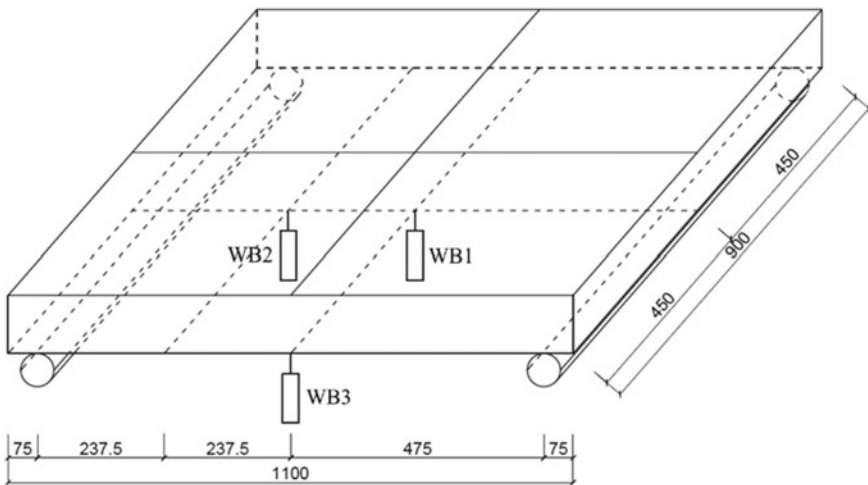


**Fig. 11.3** Layout of displacement transducers, reprinted from Meng et al. (2021), copyright 2022, with permission from Elsevier

#### 11.2.1.4 Test Results and Discussions

SPUFSCS4-4 was selected as the controlling specimen for the impact test, and the drop height was 3.68 m. Specimens SPUFSCS3-5, SPUFSCS5-3, and SPUFSCS4-4 were tested to investigate the influence of the ratio of the thickness of the middle

**Table 11.3** Experimental results of SPUFSCS panel under the impact of a hemispherical head

Specimen	$H$ (m)	$V_0$ (m/s)	$F_{\max}$ (kN)	$D_{b\max}$ (mm)	$D_{h\max}$ (mm)	$D_{bper}$ (mm)	$D_{tper}$ (mm)
SPUFSCS4-4	3.68	8.25	466.15	31.25	79.64	17.2	64.6
SPUFSCS3-5	3.75	8.48	497.92	30.52	75.03	17.7	63.5
SPUFSCS5-3	3.87	8.58	435.79	37.28	84.65	24.4	69.1
SPUFSCS85	3.28	7.76	—	27.16	67.73	15	51.3
SPUFSCS100	3.64	8.25	606.71	17.09	64.22	12.8	51.9
SCS	2.79	7.12	339.29	56.6	59.26	40	44.2

Note  $H$  represents the drop height,  $V_0$  represents the initial impact velocity of the drop hammer,  $F_{\max}$  represents the peak impact force,  $D_{b\max}$  and  $D_{h\max}$  are the maximum central displacements of the bottom steel plate and hammer, respectively,  $D_{bper}$  and  $D_{tper}$  are the central permanent displacements of the bottom steel plate and top steel plate, respectively

plate to that of the bottom plate (3/5, 1, and 5/3) on the impact resistance of the SPUFSCS panels. The concrete thicknesses of SPUFSCS85 and SPUFSCS100 were 85 and 100 mm, respectively, and the other parameters were the same as those of SPUFSCS4-4. In addition, an impact test on a traditional SCS panel without an SPUF layer was also carried out to study the effect of the PUF filler on the dynamic response of panels under impact loading. The impact velocities of the drop hammer ( $V_0$ ) obtained from the impact tests are listed in Table 11.3.

### Impact Process Analysis

The typical impact force and displacements over time histories of the SPUFSCS panel (SPUFSCS4-4) are shown in Fig. 11.4a.  $D_b$  and  $D_h$  represent the central displacement (displacement at the center point of the bottom steel plate) and hammer displacement, respectively.  $\Delta D$  ( $\Delta D = D_b - D_h$ ) is the displacement difference between the top and bottom steel plates of the panel at the impact point, which can be assumed to represent the local indentation depth of the SPUFSCS panel. The dynamic responses of the SPUFSCS panels under an impact load generated by dropping a hemispherical hammer on the panel can be divided into three stages: PUF crushing, loading, and unloading stages. The initial PUF crushing stage (OA: 0–7.1 ms in Fig. 11.4a) starts with the drop hammer making contact with the top steel plate. In this stage, the impact force exhibits a gradual and monotonic increase and its growth rate also rises with time. This can be attributed to the increased local contact stiffness of the SPUFSCS panel induced by more severe PUF densification and membrane stretching of the top steel plate with an increase in the local indentation depth. When the PUF reaches its densification strain, the SPUFSCS panel enters the next loading stage. According to Ref. (Li et al. 2006), the densification strain (or onset strain of densification) of PUF can be determined as the strain corresponding to the slope of the stress-strain curve reaching the elastic modulus. Thus, the initial PUF crushing stage ends when  $\Delta D$  reaches 38 mm (i.e., the densification strain of PUF is 0.76 based on the uniaxial compression test data). In addition, the deformation of the specimen is

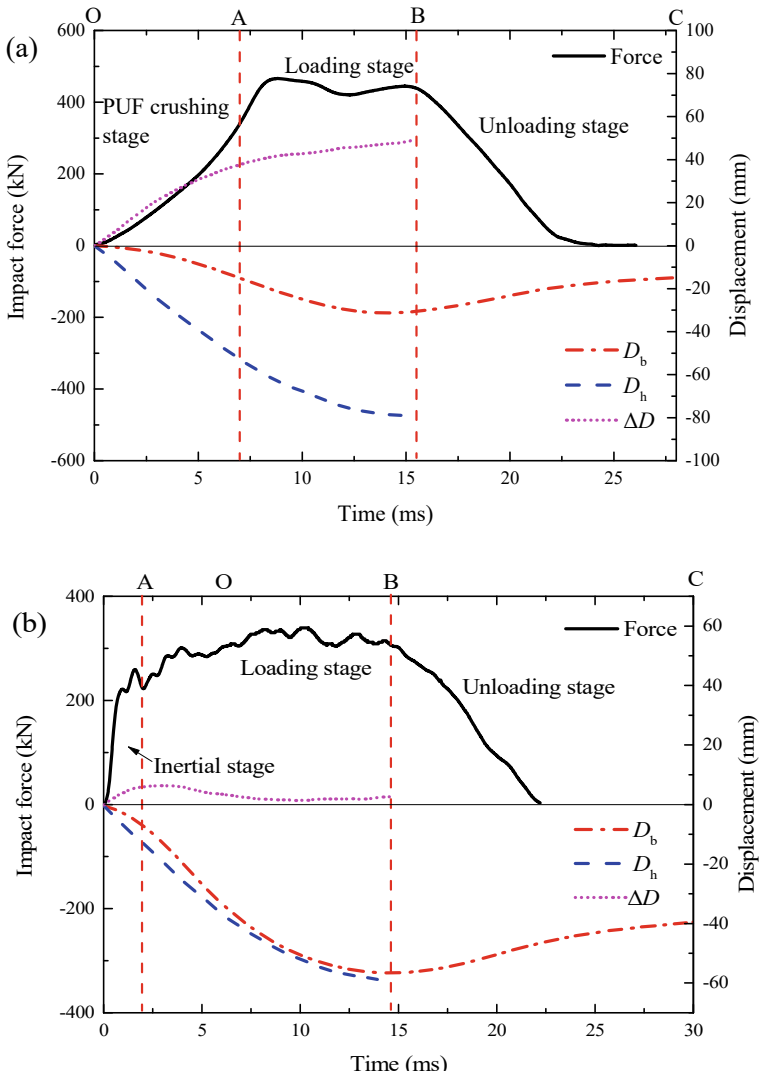


**Fig. 11.4** Typical impact force and displacement histories of **a** SPUFSCS panel and **b** SCS panel, reprinted from Meng et al. (2021), copyright 2022, with permission from Elsevier

dominated by local indentation at the initial stage, as shown in Fig. 11.4a, where the hammer displacement ( $D_h$ ) increases faster than the central displacement ( $D_b$ ). Subsequently, the SPUFSCS panel reaches the loading stage (AB: 7.1–15.6 ms). The impact force continuously increases and reaches its maximum value, which is called the peak impact force ( $F_{\max}$ ). Then, the force drops slightly until the beginning of the following unloading stage. At the loading stage, the increase in the displacement difference ( $\Delta D$ ) is less significant than that of the initial PUF crushing stage. Thus,

it can be inferred that, in the loading stage, more energy is transmitted to the SCS panel owing to the rapidly increasing global deformation of the specimen. When the displacement of the hammer reaches its maximum value and starts to decrease, the specimen enters the unloading stage (BC: 15.6–24 ms). In this stage, the impact force decreases gradually and reaches zero when the hammer is completely separated from the specimen. Elastic recovery occurs in this unloading stage, and the central displacement recovers to 55.02% of the maximum displacement.

Figure 11.4b illustrates the impact force and displacement over time histories of the SCS panel. The impact process includes the inertial, loading, and unloading stages. The SCS panel first experienced the inertial stage, in which the impact force rapidly increased. Compared with the slow increase in the impact force of the SPUFSCS panel in the initial stage (PUF crushing stage), a sharp increase in the impact force was observed for the SCS panel in the initial stage (inertial stage). This is because the particles of the panel below the hammer are instantaneously accelerated to the same speed as the hammer head when the hammer head strikes the SCS panel, and the impact force in the inertial stage cannot represent the actual load carried by the SCS panel. The inertial stage for SCS panels under impact loading has also been observed by other scholars. The loading and unloading stages of the SCS panels were the same as those of the SPUSCS panels. It can be seen from the  $\Delta D$ -time history in Fig. 11.4b that the displacement difference ( $\Delta D$ ) of the SCS panel is less than 7 mm during the impact, which indicates an insignificant local indentation of the SCS panel as compared to the SPUFSCS panel. The maximum central displacement ( $D_{b\max}$ ) of the specimen SPUFSCS4-4 was 31.25 mm, which is 55.2% of that of specimen SCS (56.6 mm) even though the SCS panel experiences less of the initial kinetic energy of hammer head (i.e., the initial impact velocities ( $V_0$ ) are 7.12 and 8.25 m/s, respectively, for specimen SCS and SPUFSCS4-4). Hence, attaching an SPUF layer to the front of the SCS panel can effectively reduce the deformation of SCS panels under impact loads.

#### Failure Mode and Permanent Deformation

Local indentation and global flexural deformation were observed for the SPUFSCS panels subjected to impact loading achieved by the dropping of a hemispherical hammer on the panels, as shown in Fig. 11.5. The top steel plate of the panel exhibited local indentation below the impact point, and the maximum contact surface between the hemispherical head and the panel was measured after the impact test. The results revealed that the contact surface was circular with a diameter of 100 mm. A local bulge was found at the center of the bottom steel plate of the SCS panel. However, no local bulge of the bottom steel plate was observed for the SPUFSCS panels, which could be attributed to the more uniformly distributed force applied to the middle steel plate in the presence of the SPUF layer. No separation between the PUF and SCS panel was observed during the impact test, which demonstrated that bolt connectors could effectively bond the PUF to the SCS panel and ensure the structural integrity of

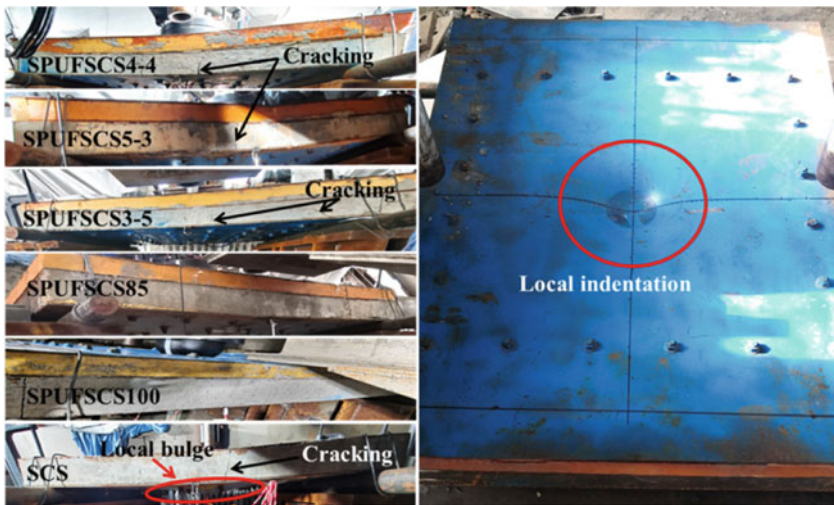


**Fig. 11.5** Failure modes of SPUFSCS panels under the impact of a hemispherical hammer, reprinted from Meng et al. (2021), copyright 2022, with permission from Elsevier

the SPUFSCS panel. Vertical cracks of the concrete core were observed at their mid-spans, as shown in Fig. 11.5, which further confirmed the global flexural deformation of the specimens.

The permanent deformation of the top and bottom steel plates of the specimens was measured using a laser ranging device after the impact test. The measuring points were distributed on the symmetric axis along the length and width of the specimen. The reading interval was determined as 10 mm near the impact point with local indentation, and a 50 mm reading interval was chosen for the rest of the locations. Figure 11.6 depicts the permanent deformation profiles of all the tested specimens. The deformation of the top steel plate was found to be dominated by a circular local indentation with a diameter of 250 mm. The values of the permanent displacement of the bottom steel plate were almost the same along the width direction, that is, the permanent displacement difference between the edge and center of the specimen was less than 9 mm. Thus, the failure mode of the SCS panel below the SPUF layer was dominated by the global flexural deformation. The central permanent displacements of the top steel plate ( $D_{tper}$ ) and bottom steel plate ( $D_{bper}$ ) are listed in Table 11.3. Furthermore, the central permanent displacement of the top steel plate of the SCS panel is less than that of the SPUFSCS panel, i.e., the  $D_{tper}$  of specimen SCS and SPUFSCS4-4 were 44.2 and 64.6 mm, respectively. This is because the SPUFSCS panel exhibits more significant local indentation than the SCS panel. However, the  $D_{bper}$  of the SCS panel was 40 mm, which was much larger than that of SPUFSCS4-4 (17.2 mm). This indicates that the SPUF layer can effectively dissipate the impact energy and reduce the local bulge of the bottom steel plate. By comparing the  $D_{tper}$  and  $D_{bper}$  of SPUFSCS4-4, SPUFSCS3-5 and SPUFSCS5-3, it can be concluded that the ratio of the middle to bottom steel plate thickness has little effect on the permanent

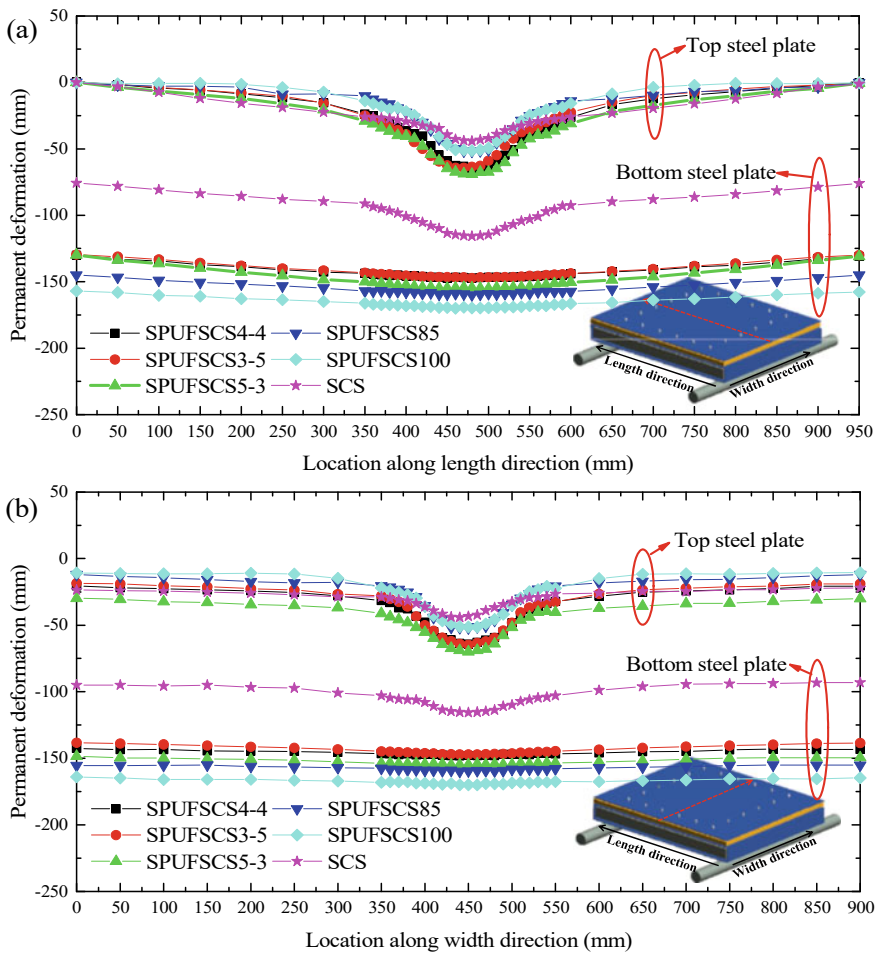


**Fig. 11.6** Permanent deformation curves along **a** length direction and **b** width direction, reprinted from Meng et al. (2021), copyright 2022, with permission from Elsevier

displacement of the specimen. In addition, by increasing the concrete thickness from 70 to 100 mm, the permanent displacement of the top steel plate decreases from 64.6 mm to 51.9 mm (reduced by 19.7%) while the permanent displacement of bottom steel plate decreases from 17.2 mm to 12.8 mm (reduced by 25.6%).

#### Impact Force and Displacement Histories

The impact force–time histories of all specimens are shown in Fig. 11.7. The impact force of SPUFSCS85 was not successfully recorded during the test. After the hammer head made contact with the specimen, the rising speed of the impact force of the

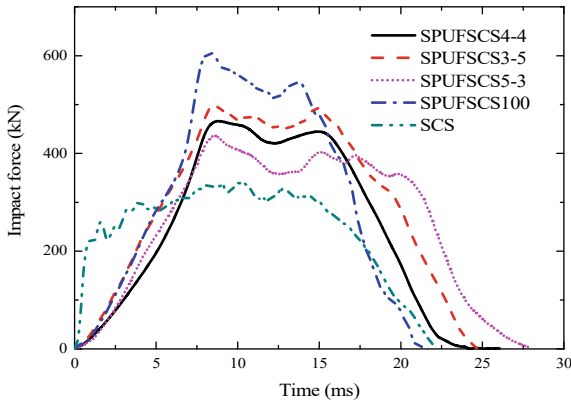


**Fig. 11.7** Comparison of impact force–time histories for specimens, reprinted from Meng et al. (2021), copyright 2022, with permission from Elsevier

SPUFSCS panel was evidently lower than that of the SCS panel. By increasing the concrete thickness from 70 to 100 mm, the  $F_{\max}$  of the panel increased from 466.15 kN to 606.71 kN (improved by 30.2%), as listed in Table 11.3. This is because the resistance of the SPUFSCS panel increases with an increase in concrete thickness. Comparing the peak impact forces of the specimens with different ratios of middle to bottom steel plate thickness, the peak impact forces of SPUFSCS4-4 and SPUFSCS5-3 were 93.6% and 87.5% of that of SPUFSCS3-5, respectively. This indicates that reducing the ratio of the middle to bottom steel plate thickness results in an increase in the peak impact force of the SPUFSCS panel, which can be attributed to the higher bending resistance of the SCS panel with a thicker bottom steel plate.

The impulse–time curves of the specimens, which were obtained by integrating the impact force–time curves, are shown in Fig. 11.8. Although the initial momentum of the hammer applied to the SCS panel was lower than that applied to SPUFSCS4-4, a more rapid rise in the impulse–time curve at the early impact stage is observed for the SCS panel, which indicates that the SPUF layer had an evident cushioning effect on the dynamic response of the SCS panel. When the initial PUF crushing stage of the SPUFSCS panel ended (i.e., the PUF reaches its densification strain), the slope of the impulse–time curve exhibited a significant increase because the impact force reached its peak value and maintained a high value at this stage. Moreover, the increasing rate of the impulse for SPUFSCS100 at the loading stage was greater than that for SPUFSCS4-4 because the SPUFSCS panel, which had a thicker concrete core, exhibited a higher impact force. The impulse curves ended when the hammer displacement reached its maximum value (i.e., the velocity of the hammer dropped to zero). By comparing the maximum value of the impulse–time curve with the initial momentum of the hammer, which is listed in Table 11.4, the conservation of momentum–impulse was verified.

Figure 11.9 shows the displacement–time histories of SPUFSCS panels with different concrete thicknesses and ratios of the middle to bottom steel plate thickness.

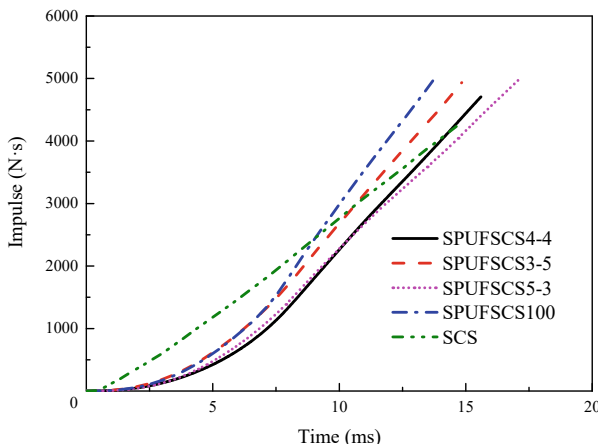


**Fig. 11.8** Comparison of impulse–time curves for specimens, reprinted from Meng et al. (2021), copyright 2022, with permission from Elsevier

**Table 11.4** The conservation of impulse-momentum obtained from tests

Specimen	Momentum (kg·m/s)	Impulse (kg·m/s)	Ratio of impulse to momentum
SPUFSCS4-4	5115	4707.3	0.92
SPUFSCS3-5	5257.6	4938.2	0.94
SPUFSCS5-3	5319.6	4988.2	0.94
SPUFSCS85	4811.2	—	—
SPUFSCS100	5115	5016.3	0.98
SCS	4414.4	4233.8	0.96

Initially, the displacement exhibits a monotonic increase with time. The displacement then decreases gradually when the hammer and specimen start to rebound and finally stabilizes to the permanent deformation of the specimen. The increase in concrete thickness significantly reduces the displacement of the SPUFSCS panel under the same impact loading. The maximum central displacements of the specimens ( $D_{b\max}$ ) are listed in Table 11.3. By increasing the concrete thickness from 70 to 100 mm, the maximum central displacement decreases from 31.25 mm to 17.09 mm (a reduction of 45.3%). Moreover, the maximum displacement of SPUFSCS3-5 ( $D_{b\max} = 30.52$  mm), which has a thicker bottom steel plate and thinner middle steel plate, is smaller than those of SPUFSCS4-4 ( $D_{b\max} = 31.25$  mm) and SPUFSCS5-3 ( $D_{b\max} = 37.28$  mm). This is due to the higher bending resistance of specimen SPUFSCS3-5, which has a thicker bottom steel plate. In addition, the maximum displacement of the SCS panel is greater than that of the SPUFSCS panel, which indicates that the presence of the top steel plate and PUF can improve the impact resistance of the traditional SCS panel.

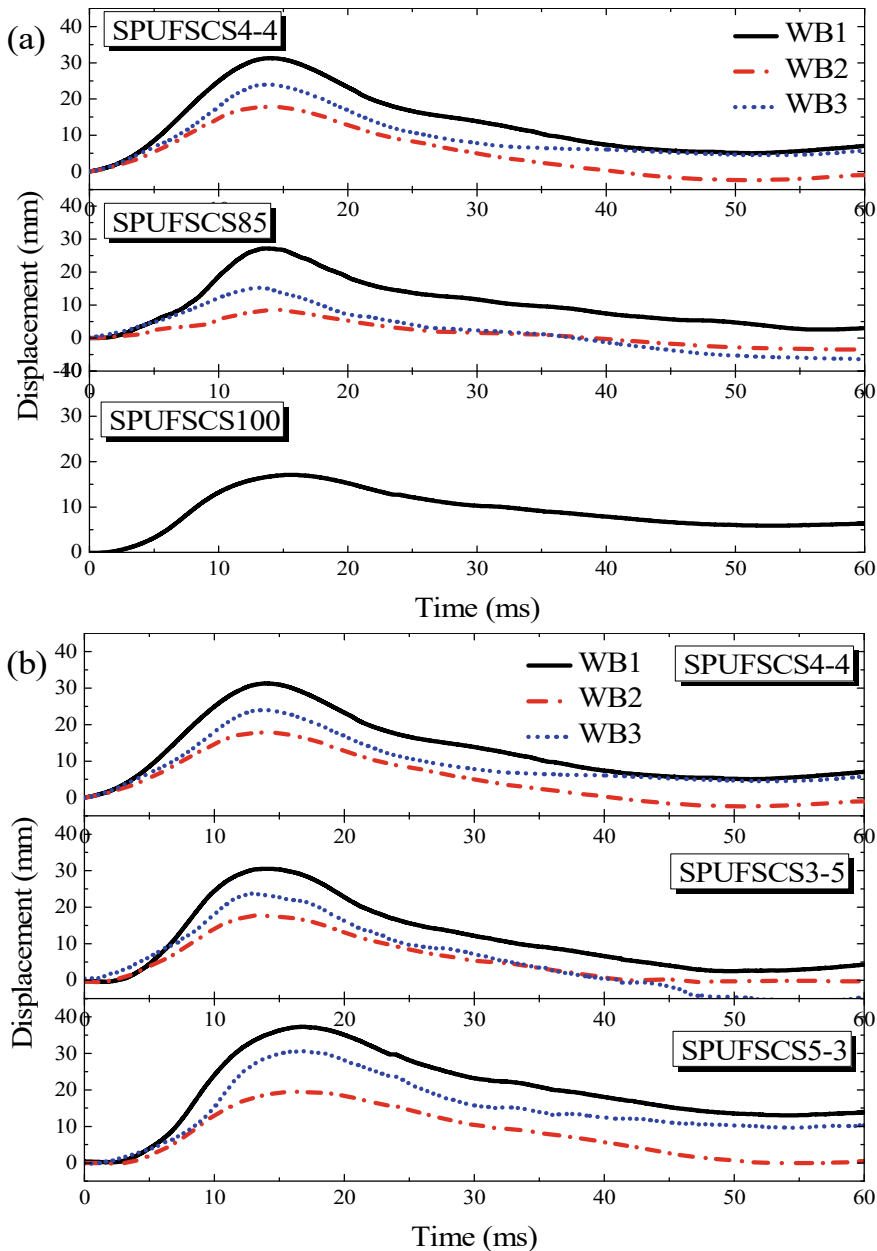


**Fig. 11.9** Displacement histories of the bottom steel plate for specimens: Effects of **a** concrete core thickness and **b** thickness ratio of middle to bottom steel plate, reprinted from Meng et al. (2021), copyright 2022, with permission from Elsevier

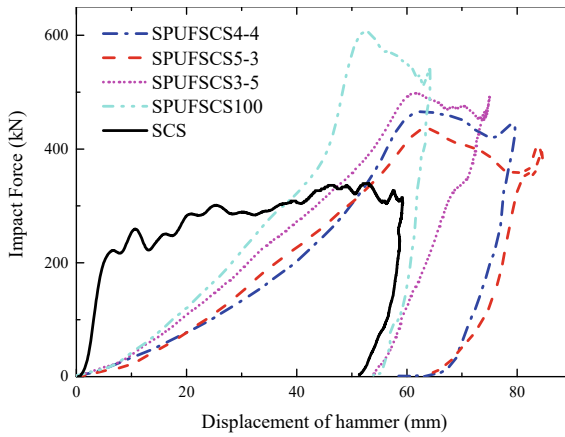


**Fig. 11.10** Impact force–displacement curves of SPUFSCS panels, reprinted from Meng et al. (2021), copyright 2022, with permission from Elsevier

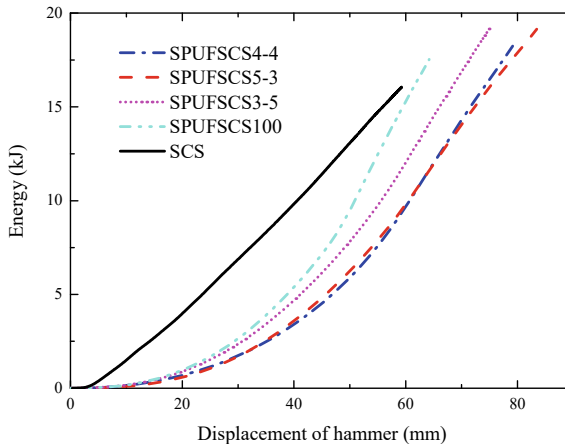


**Fig. 11.11** Energy–displacement curves of SPUFSCS panels under impact loading, reprinted from Meng et al. (2021), copyright 2022, with permission from Elsevier

The relationships between the impact force and displacement (displacement of the hammer head  $D_h$ ) of all specimens are shown in Fig. 11.10. All the impact forces of the SPUFCS panels with PUF exhibit a slower increase as compared to that of the SCS panel owing to the less significant inertial effect of the SPUFSCS panel, which has the SPUF layer. For the similar applied kinetic energy of the drop hammer, impact process, and failure mode, the SPUFSCS panel with a larger peak impact force shows a smaller maximum hammer displacement. Figure 11.11 is a plot of the energy–displacement curves of the specimens, which were obtained by integrating the impact force–displacement curves. At the initial stage, the impact

energy transmitted to the SPUFSCS panel increased more slowly than that of the SCS panel. However, the impact energy dissipation rate of the SPUFSCS panel exhibits a significant increase after the PUF is compacted (i.e., the panel reaches the end of the PUF crushing stage).

## 11.2.2 Numerical Study

### 11.2.2.1 FE Model Establishment

The explicit code in LS-DYNA was employed for the numerical simulation, and Fig. 11.12 presents the quarter FE model of the SPUFSCS panel subjected to drop hammer impact loading, considering the symmetry of the structure and computing efficiency. The drop hammer was simulated as a rigid mass in the FE model. A reduced integrated constant stress solid element was employed to model the PUF, concrete, drop hammer, and support. A Belytschko-Tsay shell element with five integration points along the thickness and a Hughes-Liu beam element were employed

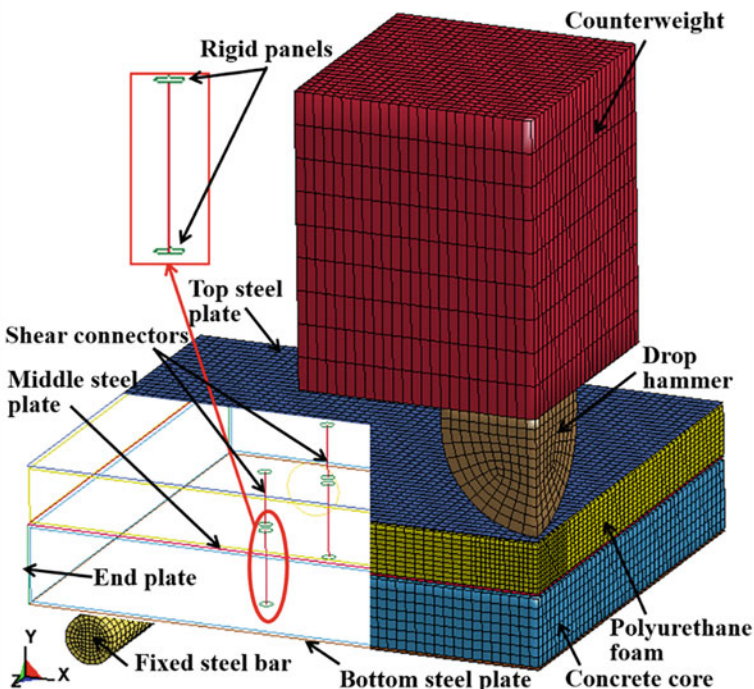
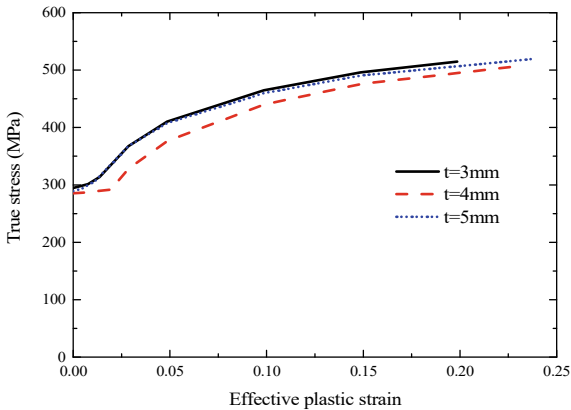


**Fig. 11.12** Quarter FE model of the SPUFSCS panel, reprinted from Meng et al. (2021), copyright 2022, with permission from Elsevier

**Fig. 11.13** True stress–effective strain curves for steel plates, reprinted from Meng et al. (2021), copyright 2022, with permission from Elsevier



to simulate steel plates and shear connectors, respectively. The mesh size of the shell element for the steel plate, the beam element for the connector, and the solid element for the concrete core were each 10 mm. The mesh size of the solid element for PUF was determined as  $10 \times 10 \times 5$  mm<sup>3</sup> at the edge and refined to  $5 \times 5 \times 5$  mm<sup>3</sup> near the local indentation zone with more severe deformation. The keyword \*INITIAL\_VELOCITY was used to define the initial impact velocity of the hammer.

A Piecewise Linear Plasticity model was employed to simulate the steel plates and bolt connectors in the FE model. The material properties of the steel plates and connectors used in the FE model are listed in Table 11.2. The true stress–effective plastic strain curves of the steel plates with different thicknesses were obtained from tensile coupon tests and are shown in Fig. 11.13. The failure behaviors of the steel plate and connector were neglected because no fracture occurred in the impact tests. The strain rate effect was also considered in the numerical simulation using the Cowper-Symonds constitutive equation, which describes the yield stress under different strain rates by scaling up the flow stress with the factor  $1 + (\dot{\varepsilon}_{eff}^P/C)^{1/P}$ , where  $\dot{\varepsilon}_{eff}^P$  denotes the effective plastic strain rate. C and P are the strain rate parameters, and were defined as  $40.4\text{ s}^{-1}$  and 5, respectively, for mild steel in this study (Jones 1988).

To accurately simulate the behavior of PUF subjected to impact loading, a modified crushable foam model was adopted. Users can define the stress–volumetric strain curves with different strain rates in this material model to consider the strain rate effect. Figure 11.14 shows the relationships between the stress and volumetric strain of the PUF used in this study. The reference curve with a strain rate of  $8E-4\text{ s}^{-1}$  was obtained by conducting an unconfined uniaxial compression loading test on PUF. The dynamic increase factor ( $DIF_f$ ) was applied to plot the other curves by scaling up the reference curve by a factor, as shown in Eq. (11.1).

$$DIF_f = 1 + (a_0 + b_0\varepsilon) \ln\left(\frac{\dot{\varepsilon}}{\dot{\varepsilon}_0}\right) \quad (11.1)$$

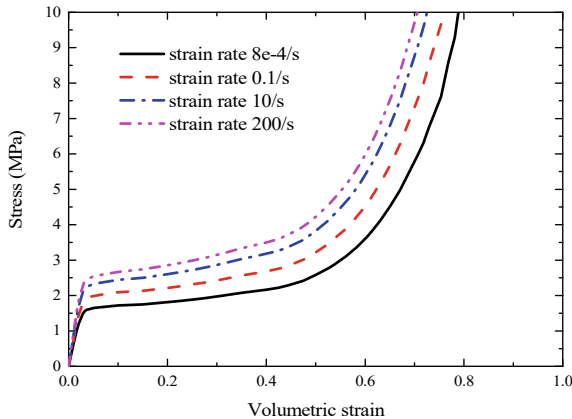


**Fig. 11.14** Stress–volumetric strain curves for PUF, reprinted from Meng et al. (2021), copyright 2022, with permission from Elsevier

where  $a_0$  and  $b_0$  are the strain rate parameters, and are defined as 0.0430 and 0.0165 (Jeong et al. 2012), respectively, and  $\dot{\varepsilon}_0 = 8 \times 10^{-4}$  is the reference strain rate.

With regard to the modeling of concrete, the Continuous Surface Cap (CSC) model developed by the US Federal Highway Administration was employed. This model has been widely used to simulate concrete-like (cement-based) materials under impact loading. The main parameters of the concrete are listed in Table 11.2.

A round rigid bar was established in the FE model to simulate a simply supported boundary condition. The translational and rotational displacements of the nodes on the steel bar were constrained, while the contact between the bottom steel plate and the round bar was simulated using the surface-to-surface contact option in LS-DYNA. The surface-to-surface contact option was also applied to define the contact between the steel plates and concrete, the contact between the steel plates and PUF, and the contact between the hammer head and top steel plate. The interface algorithm for the contact between the bottom steel plate and the support is based on the penalty method (Hallquist 2006). Using this interface algorithm, each slave node is checked for penetration through the master segment surface. When penetration occurs, an interface force is applied between the slave node and its contact point. The contact stiffness for brick elements and shell elements can be determined by the following formulae:

$$k = f_s K A^2 / V \quad (11.2)$$

$$k = f_s K A / \max(\text{shell diagonal}) \quad (11.3)$$

where  $f_s$  represents the scale factor of the interface stiffness, and its default value usually set as 1.0;  $K$  is the bulk modulus of the contact materials; and  $A$  and  $V$  are the

volume and contact area of the contact elements, respectively. This contact definition was also applied to simulate the contact between the drop hammer and top steel plate, and the contact between the steel plates and concrete. For the contact between the steel plates and PUF, a soft constraint penalty formulation was utilized because the soft materials may cause lower contact stiffness and excessive penetration. To eliminate excessive penetration, a formulation for the contact stiffness that is different from the traditional penalty formulation was employed as follows:

$$k(t) = 0.5 \cdot SOFSCL \cdot m^* \cdot (1/\Delta t_c(t)) \quad (11.4)$$

where  $SOFSCL$  is the scale factor for this soft constraint penalty formulation, and is set to the default value of 0.1, and  $m^*$  represents a function of the mass of the slave node and master nodes.  $\Delta t_c$  is set as the initial solution time step. Considering the possible stress concentration resulting from directly tying shear connectors to steel plates, circular rigid panels were set at both ends of the beam element, as shown in Fig. 11.12. The center of the circular panel was located at the end of the beam element, and its diameter was 12 mm, which is the same as the diameter of the bolt connector. The nodes on the circumference of the rigid panels were tied to the steel plate to simulate the connection between the shear connector and steel plate. A perfect bond between the shear connectors and concrete core was adopted by utilizing the method in which the brick element of the concrete and the beam element of the shear connector share common nodes. The same contact method was employed to simulate the connection between the shear connectors and the PUF.

### 11.2.2.2 FE Results and Discussions

Figure 11.15 shows a comparison of the failure modes of the SPUFSCS panel obtained from the impact test and numerical simulation. Both local and global flexural deformations were reasonably predicted by the established FE model. It is also worth noting that the FE model can indicate the damage-prone regions of concrete at mid-span induced by flexural deformation (i.e., the damage parameter  $d$  of the red part of the contour is close to 1). The impact force–time histories and displacement–time histories obtained from the experiments and FE analyses are shown in Figs. 11.16 and 11.17, respectively. The FE models can accurately predict the peak values and durations of the impact forces of the tested specimens. The peak values of the impact forces ( $F_{\max}$ ) obtained from the tests and FE models are listed in Table 11.5. The difference between the predicted peak impact force from the FE simulation and the measured values from the tests was less than 10.2%. The calculated average ratio of FE to test for peak impact force was 1.048, with a coefficient of variation (COV) of 0.045. Good agreement between the displacement and time histories obtained from the FE analyses and impact tests were observed for both the central displacement and hammer displacement, as presented in Fig. 11.17. Table 11.5 summarizes the numerical and experimental results for the maximum central displacement and hammer

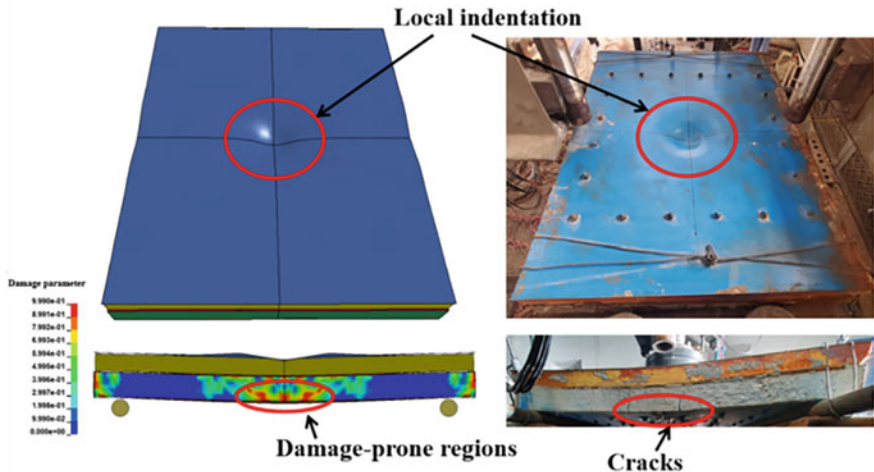


**Fig. 11.15** Comparison of failure mode between FE and experiment, reprinted from Meng et al. (2021), copyright 2022, with permission from Elsevier

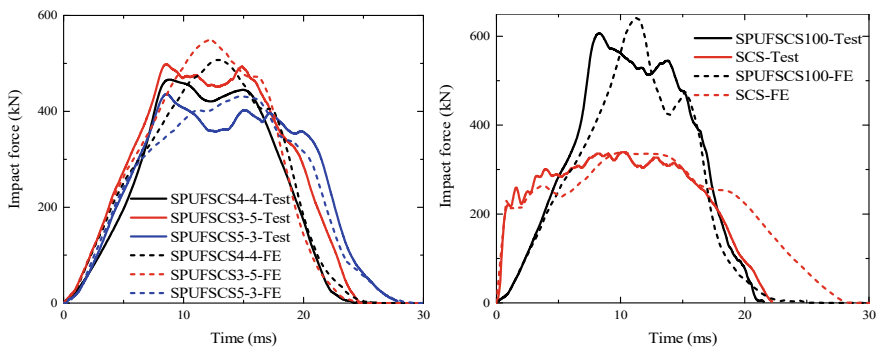


**Fig. 11.16** Comparison of impact force–time histories between tests and FE predictions, reprinted from Meng et al. (2021), copyright 2022, with permission from Elsevier

displacement. The average values of the ratios of FE prediction to test result were 1.033 and 1.078 for  $D_{b\max}$  and  $D_{h\max}$ , respectively, and the corresponding COVs were 0.117 and 0.044, respectively. Moreover, a comparison of the permanent deformation of the panel between the tests and FE results is shown in Fig. 11.18, and the work done (integral of the impact force–displacement curve from the beginning of the impact process to the moment when the panel starts to rebound, as shown in Fig. 11.19) and energy dissipation (the closed area under the loop of the displacement and impact force, as shown in Fig. 11.19) obtained from experimental and numerical studies is listed in Table 11.6. A reasonable agreement between the FE predictions and tests can be observed, which indicates that the FE modeling method can accurately predict the dynamic response of the SPUFSCS panel under impact loading.

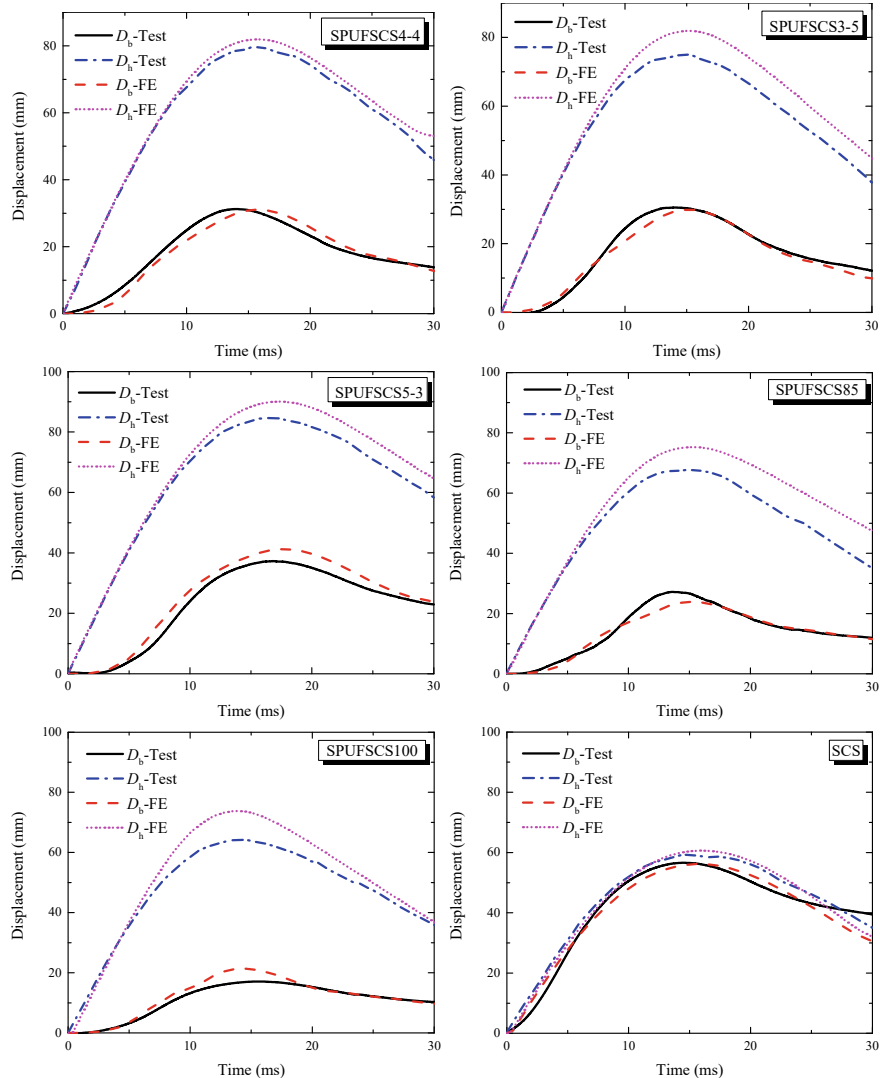


**Fig. 11.17** Comparison of displacement–time histories between tests and FE predictions, reprinted from Meng et al. (2021), copyright 2022, with permission from Elsevier

To investigate the influence of the thickness of the PUF and top steel plate on the dynamic response of the SPUFSCS panels under impact loading, a parametric study was carried out by employing the validated FE model. The thickness of PUF was taken as 20, 35, 50, and 65 mm, and for the top steel plate thicknesses, 3, 4, and 5 mm were adopted. An initial impact velocity of 8.25 m/s was employed for all specimens, and the geometric dimensions of the SCS layer of all specimens remained unchanged. Table 11.7 lists the results of the parametric study. Specimen PUF20

**Table 11.5** Comparison between test and numerical results

Specimen	$F_{\max}$ (kN)	$F_{\max\text{FE}}$ (kN)	$F_{\max\text{FE}}/F_{\max}$	$D_{\max}$ (mm)	$D_{\max\text{FE}}$ (mm)	$D_{\max\text{FE}}/D_{\max}$	$D_{\max}$ (mm)	$D_{\max\text{FE}}$ (mm)	$D_{\max\text{FE}}/D_{\max}$
SPUFSCS4-4	466.15	507.4	1.088	31.25	31.03	0.993	79.64	81.92	1.029
SPUFSCS3-5	497.92	548.51	1.102	30.52	29.87	0.979	75.03	81.89	1.091
SPUFSCS5-3	435.79	431.99	0.991	37.28	41.24	1.106	84.65	90.05	1.064
SPUFSCS8-5	—	545.31	—	27.16	23.89	0.88	67.73	75.24	1.111
SPUFSCS100	606.71	642.02	1.058	17.09	21.36	1.249	64.22	73.73	1.148
SCS	339.29	339.45	1.001	56.6	56.21	0.993	59.26	60.65	1.023
Average			1.048			1.033		1.078	
COV			0.045			0.117		0.044	

Note The parameters with FE as the subscript stand for the FE-predictions

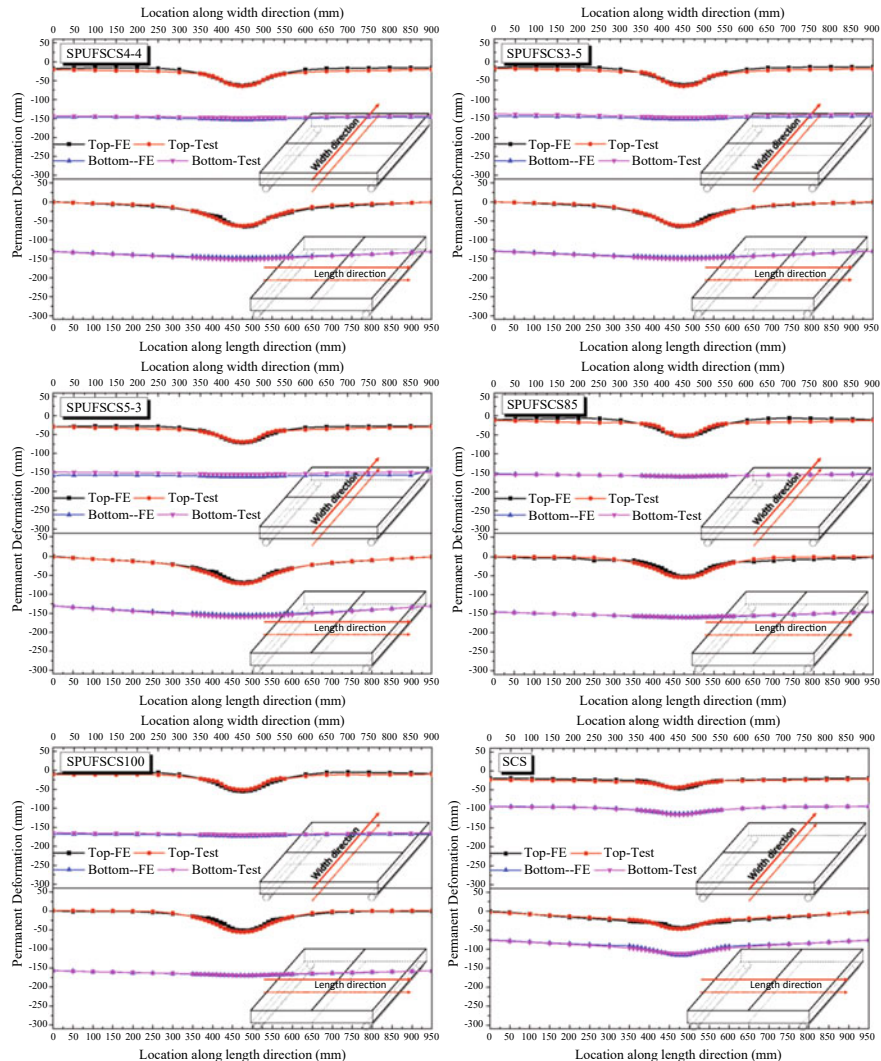


**Fig. 11.18** Comparison of permanent deformation between tests and FE predictions, reprinted from Meng et al. (2021), copyright 2022, with permission from Elsevier

represents the SPUFSCS panel with a PUF thickness of 20 mm, while specimen TOP3 is the SPUFSCS panel with a top steel plate thickness of 3 mm. As illustrated in Fig. 11.20a, similar impact force-time histories were obtained when the PUF thickness was in the range of 35–65 mm. When the thickness of the PUF was 20 mm, the cushioning effect of PUF was weakened because the PUF reached densification at the early impact stage when the displacement of the specimen was still small. The maximum and permanent displacements of the bottom steel plate ( $D_{b\max}$  and

**Fig. 11.19** Definition of work done and energy dissipation, reprinted from Meng et al. (2021), copyright 2022, with permission from Elsevier

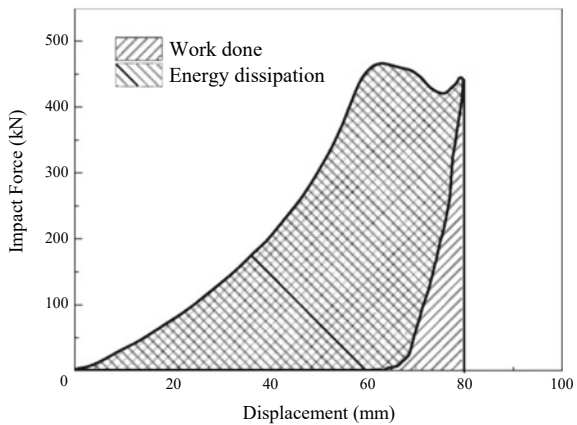


**Table 11.6** Work done and energy dissipation obtained from test and numerical results

Specimen	Test results		FE results		Ratio of FE results to test results	
	Work done (J)	Energy dissipation (J)	Work done (J)	Energy dissipation (J)	Work done	Energy dissipation
SPUFSCS4-4	18,459.7	16,347.4	20,458.6	18,640.0	1.108	1.140
SPUFSCS3-5	19,208.4	14,435.7	21,579.6	17,957.1	1.123	1.244
SPUFSCS5-3	19,627.4	16,353.6	22,234.0	19,945.1	1.133	1.220
SPUFSCS85	–	–	18,061.0	16,407.9	–	–
SPUFSCS100	17,533.5	15,758.7	20,258.3	18,018.7	1.155	1.143
SCS	16,058.4	15,296.5	15,349.2	12,343.4	0.956	0.807

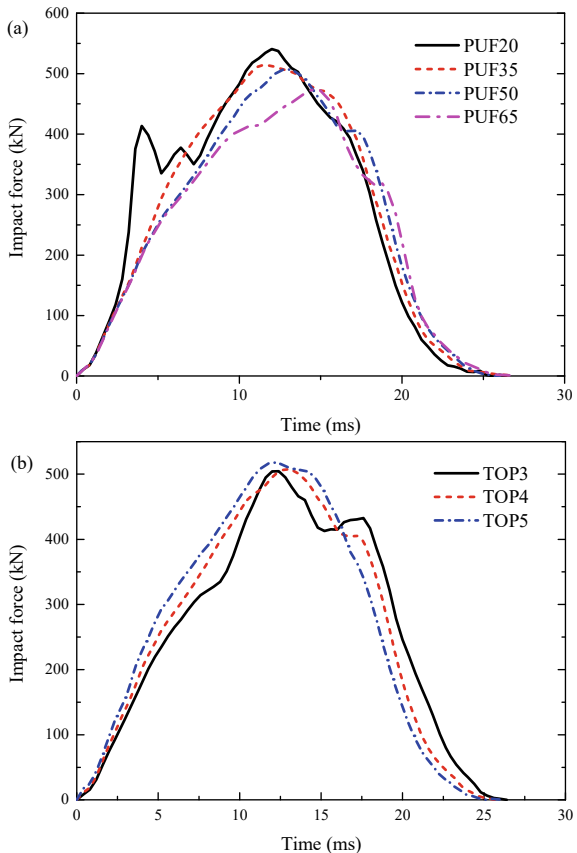
$D_{bper}$ ) were reduced by 46.5% and 43.5%, respectively, by increasing the thickness of PUF from 20 to 65 mm, which indicates that the SPUFSCS panel with a thicker PUF shows evident improvement in its impact resistance. However, the maximum and permanent displacements of the top steel plate ( $D_{hmax}$  and  $D_{tper}$ ) increased by 17.2% (from 71.97 mm to 84.35 mm) and 53.6% (from 46.05 mm to 70.75 mm), respectively, when the PUF thickness increased from 20 to 65 mm. This is because a thicker PUF exhibits a larger local indentation depth. Increasing the thickness of the top steel plate from 3 to 5 mm resulted in a decrease of  $D_{bmax}$  and  $D_{bper}$  by 10.1% and 18.1%, respectively, and the corresponding decreases in  $D_{hmax}$  and  $D_{tper}$  were 9.8% and 19.1%, respectively. The influence of the top steel plate thickness on the displacement of the panel was limited when the top steel plate thickness ranged from 3 to 5 mm. This is because the top steel plate is thin and contributes little to the overall stiffness and resistance of the SPUFSCS panel.

**Table 11.7** Results of parametric study

Specimen	$V_0$ (m/s)	$t_{\text{PUF}}$ (mm)	$t_{\text{TOP}}$ (mm)	$D_{\text{bmax}}$ (mm)	$D_{\text{hmax}}$ (mm)	$D_{\text{bper}}$ (mm)	$D_{\text{tper}}$ (mm)
PUF20	8.25	20	4	44.96	71.97	26.30	46.05
PUF35		35	4	40.20	77.87	23.80	55.71
PUF50(TOP4)	50	4	31.03	81.92	20.76	63.07	
PUF65	65	4	24.07	84.35	14.86	70.75	
TOP3	50	3	33.58	86.27	20.98	70.60	
TOP5	50	5	30.18	77.83	17.18	57.11	

Note  $t_{\text{PUF}}$  and  $t_{\text{TOP}}$  represent the thickness of PUF and the thickness of top steel plate, respectively

**Fig. 11.20** Comparison of impact force-time histories between various **a** PUF thickness and **b** top steel plate thickness, reprinted from Meng et al. (2021), copyright 2022, with permission from Elsevier



The energy dissipation capacity of the SPUFSCS panel during impact based on the numerical results is also discussed in detail after validating the FE model. Figure 11.21 depicts the vertical displacement contours of each part of the SPUFSCS panel obtained from the numerical simulation. It can be seen that only the global deformation of the middle steel plate of the SPUFSCS panel (top steel plate of SCS panel) is observed owing to a more uniformly distributed force in the presence of PUF, whereas evident local indentation of the top steel plate and PUF occurs below the impact point, which indicates that PUF plays a significant role in improving the impact resistance performance of the SCS panel and reducing its local indentation. The typical internal energy–time histories of each part of the SPUFSCS panel subjected to impact loading are shown in Fig. 11.22, and the internal energy was extracted from the FE results by summing the internal energy of the elements of each part in the FE method. At the initial PUF crushing stage (0–5 ms), the internal energies of the top steel plate and PUF exhibit a rapid increase with a decrease in the kinetic energy of the hammer, whereas the increase in the internal energy of the SCS panel is minimal at the initial stage. This indicates that the global flexural deformation of the SCS panel is small, and the majority of the impact energy is dissipated via

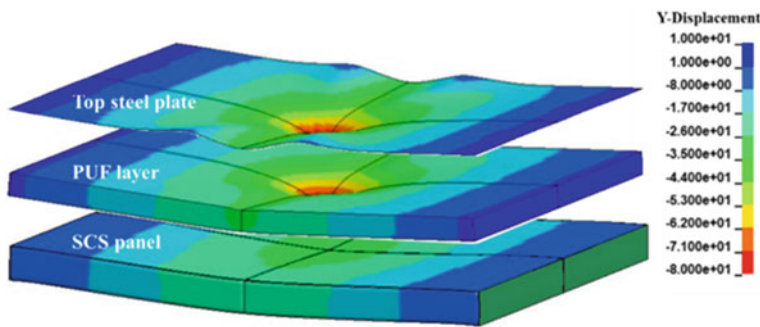
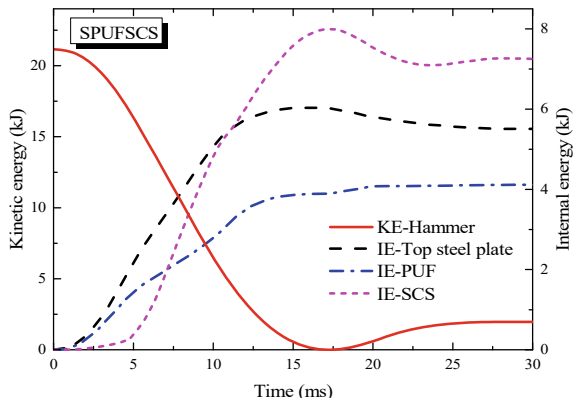


**Fig. 11.21** Deformation of each part of the SPUFSCS panel, reprinted from Meng et al. (2021), copyright 2022, with permission from Elsevier

**Fig. 11.22** Typical internal energy histories of SPUFSCS panels, reprinted from Meng et al. (2021), copyright 2022, with permission from Elsevier



local indentation of the top steel plate and PUF. Subsequently, the internal energy of the rear SCS panel increases rapidly, exceeding the internal energy of the PUF. This is because the deformation of the SPUFSCS panel at the loading stage is dominated by the global bending of the specimen after the densification of PUF. The internal energies of each part of the SPUFSCS panel reach their peak values when the kinetic energy of the hammer drops to zero. Subsequently, the kinetic energy of the hammer increases owing to the elastic recovery of the SPUFSCS panel, which also results in a decrease in the internal energy of the panel.

The peak values of the internal energy of the top steel plate, PUF, and SCS panel of SPUFSCS panels with various thicknesses of the concrete core, PUF, and top steel plate, and ratios of the middle to bottom plate thickness are shown in Fig. 11.23. These results were used to determine the influences of these parameters on the energy absorbing performance of the SPUFSCS panels. With an increasing ratio of the middle to bottom plate thickness from 3/5 to 5/3, the internal energy of the SCS panel increases by 6.3%, from 7.77 kJ to 8.26 kJ. This is because the bending resistance of the SPUFSCS panel with a thinner bottom plate and thicker

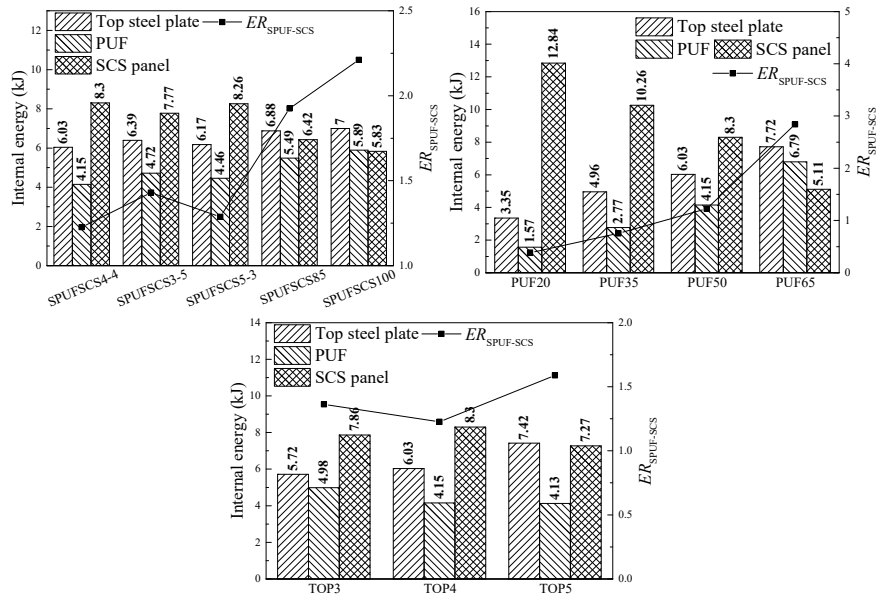


**Fig. 11.23** Peak values of internal energy of each part of SPUFSCS panels, reprinted from Meng et al. (2021), copyright 2022, with permission from Elsevier

middle plate is lower, thus leading to a larger global deformation of the panel and a higher proportion of the impact energy dissipated by the SCS layer. When the concrete thickness increases from 70 mm to 85 and 100 mm, the internal energy of the SCS panel decreases by 22.7% and 29.8%, respectively, while the internal energy of the PUF increases by 32.3% and 41.9%, respectively. This is because the thicker concrete layer improves the stiffness and resistance of the SPUFSCS panel, thus leading to a smaller deformation of the panel and a greater amount of impact energy is dissipated by the SPUF layer. The ratio of the summed internal energy of the top steel plate and PUF to the internal energy of the SCS panel ( $ER_{SPUF-SCS}$ ) was calculated and is presented in Fig. 11.23. The  $ER_{SPUF-SCS}$  ranges from 1.23 to 2.21 for all the tested SPUFSCS panels, which indicates that the impact energy dissipated by the top steel plate and PUF accounts for more than half of the total energy absorption. The internal energy of SPUF layer increases from 4.92 kJ to 14.51 kJ (by 195%) on increasing the PUF thickness from 20 to 65 mm. Meanwhile, the internal energy of SCS layer decreases from 11.84 kJ to 5.11 kJ (by 60.2%), which indicates that the SPUFSCS panel with a thicker PUF layer exhibits less damage of the SCS layer under impact loading. For a given impact load (the drop weight is 620 kg and initial impact velocity is 8.25 m/s), the impact energy dissipated by the SPUF layer is higher than that by the SCS layer ( $ER_{SPUF-SCS}$  is greater than 1.0) when the PUF thickness is more than 50 mm. As shown in Fig. 11.23, the influence of the top steel plate thickness on the internal energy of the SPUF layer and SCS layer is not significant, that is, the internal energy of the SPUF layer increases by 7.9% (from 10.7 kJ to

11.55 kJ) and the internal energy of the SCS layer decreases by 7.5% (from 7.86 kJ to 7.27 kJ) when the top steel plate thickness increases from 3 to 5 mm. This is because changing the top steel plate thickness from 3 to 5 mm has little effect on the deformation of the panel. In addition, the internal energy of top steel plate increases from 5.72 kJ to 7.42 kJ (by 29.7%) by increasing the top steel plate thickness from 3 to 5 mm owing to the increased volume of top steel plate. The  $ER_{SPUF-SCS}$  of the SPUFSCS panels with top steel plate thicknesses ranging from 3 to 5 mm are greater than 1.0. Moreover, the  $ER_{SPUF-SCS}$  is found to increase from 1.23 to 1.59 (by 29.3%) by increasing the top steel plate thickness from 4 to 5 mm (the increased mass of the SPUFSCS panel is 7.77 kg). A more significant increase of  $ER_{SPUF-SCS}$  by 130.9% (from 1.23 to 2.84) can be observed for the SPUFSCS panel when the PUF thickness is increased from 50 to 65 mm (the increased mass was only 2.87 kg). Hence, increasing the PUF thickness can be a more effective way of decreasing the energy dissipated by the SCS layer than increasing the top plate thickness.

## 11.3 SPUFSCS Panel Under the Impact of a Cylindrical Hammer

### 11.3.1 Experimental Study

#### 11.3.1.1 Specimens and Test Setup

Four SPUFSCS panels were designed for the drop-weight impact tests by dropping a hammer with cylindrical head, and their dimensions and material properties are some to those presented in Sect. 11.2.1.1. Table 11.8 presents the geometric parameters for the four specimens, and material properties of mild steel, PUF and concrete are given in Table 11.2. The impact test setup is shown in Fig. 11.24, which is similar to that presented in Sect. 11.2.1.3. Herein, the hammer with a cylindrical head (diameter of 200 mm and mass of 610 kg) was employed, and the drop height for all the four specimens was 5 m. Two dynamic displacement transducers were installed below the specimen at mid-span and quarter-span, respectively, to measure the deflections of the specimen. All the other instrumentations are consistent with those in Sect. 11.2.1.3.

**Table 11.8** Specimens for the impact tests (cylindrical hammer)

Specimen	$t_t$ (mm)	$t_p$ (mm)	$t_m$ (mm)	$t_c$ (mm)	$t_b$ (mm)
4-70-4	3.67	50	3.67	70	3.67
4-85-4	3.67	50	3.67	85	3.67
4-100-4	3.67	50	3.67	100	3.67
5-70-3	3.67	50	4.7	70	3.0

Note  $t_t$ ,  $t_p$ ,  $t_m$ ,  $t_c$  and  $t_b$ —Thicknesses of top plate, PUF, middle plate, concrete and bottom plate

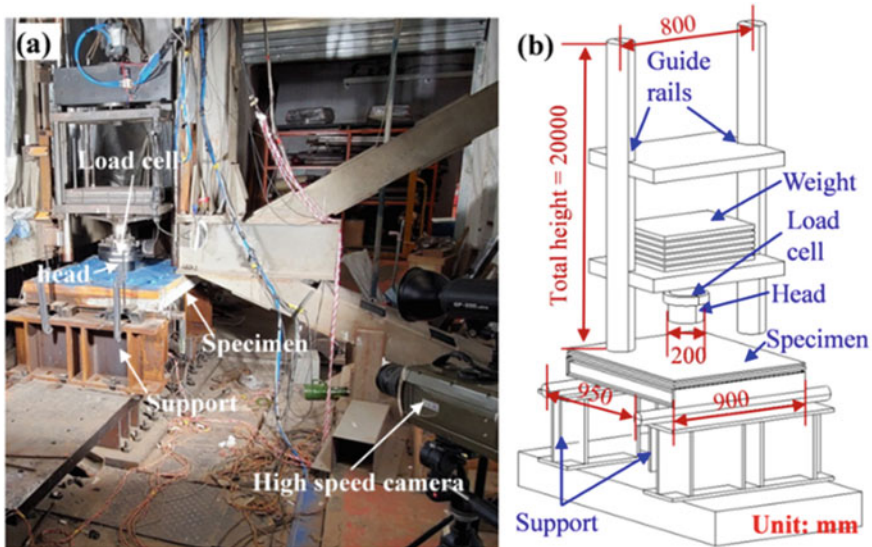


**Fig. 11.24** Setup and instrumentation for the impact with a cylindrical hammer: **a** photo and **b** schematic view, reprinted from Wang et al. (2021), copyright 2022, with permission from Elsevier

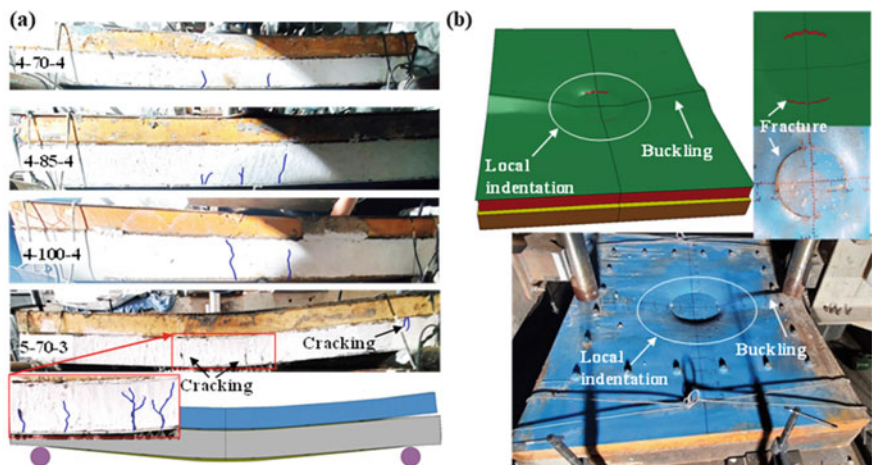


**Fig. 11.25** Failure modes of the SPUFSCS panel under the impact of a cylindrical hammer: **a** flexural deformation of SPUFSCS panel, **b** local indentation on plate and PUF, reprinted from Wang et al. (2021), copyright 2022, with permission from Elsevier

### 11.3.1.2 Test Results and Discussions

As illustrated in Fig. 11.25, all the SPUFSCS panels exhibit a combined failure modes of local and global deformations. Figure 11.25a shows evident flexural deformation

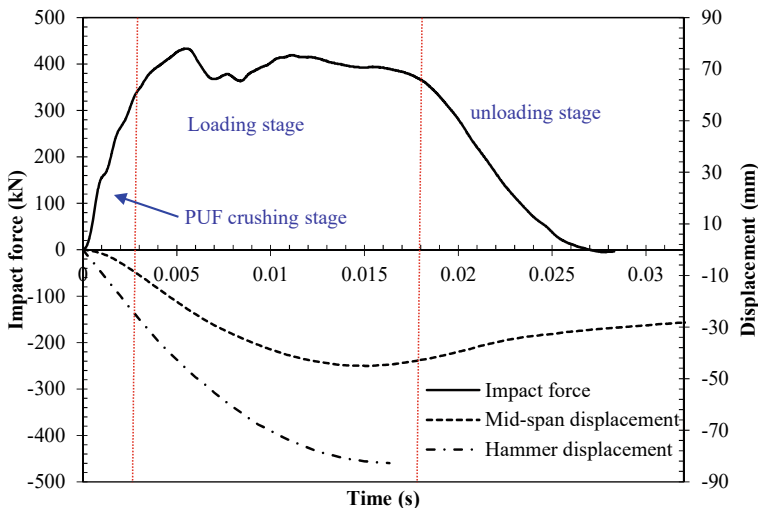


**Fig. 11.26** Typical impact force and displacement versus time histories of the SPUFSCS panel (cylindrical hammer), reprinted from Wang et al. (2021), copyright 2022, with permission from Elsevier

for all the test specimens with clear vertical cracks of concrete core near mid-span. The local indentation on the top plate and PUF is induced by the local large impact force and its shape is governed by the hammer head shape (i.e., cylinder head with the diameter of 200 mm). It is noted in Fig. 11.25b that the cylinder head causes a circular local indentation zone at the impact point, sharing same diameter to the hammer head. The indentation depth within this zone is uniform and exhibits gradual reduction towards the periphery of impact zone. In addition, the fracture of top plate along the periphery of impact zone is also observed. This may be caused by the sharp edge of the hammer head, which results in high value of local stress and fracture of the top plate. As shown in Fig. 11.25b, one side of the top plate near the mid-span also exhibits buckling due to the compression force induced by flexural deformation.

The typical impact force–time history of SPUFSCS panel (5-70-3) is plotted together with displacement responses (i.e., mid-span and hammer displacement–time histories) in Fig. 11.26. The impact process can be categorized into three stages, including PUF crushing stage, loading stage and unloading stage. The PUF experiences immediate crushing at the initial impact stage when the hammer reaches the top plate and starts to collide with the specimen. At this stage, the hammer displacement increases evidently faster than mid-span displacement (see Fig. 11.26), which results in the majority of the impact energy being dissipated by the top plate and PUF. Meanwhile, the impact force shows continuous increase with time. However, the inertial stage with initial large peak impact force for the colliding of two hard materials (Zhao and Guo 2018; Yan et al. 2020) is not observed for the SPUFSCS panel. This slow and smooth increase of impact force observed for the SPUFSCS panel can be attributed to low yield strength of PUF. When PUF reaches densification

and the impact force is large enough to cause evident deformation of the SCS panel, it enters loading stage. At this stage, both the hammer and mid-span displacements increase rapidly and the difference between them gradually approaches a constant value, which indicates a slow increase of indentation depth as well as impact energy dissipated by the top plate and PUF. Hence, the impact energy dissipated by the SCS panel climbs up. With regard to impact force at loading stage, it exhibits slight variation and the impact force can generally represent loading capacity of the SPUFSCS panel owing to the small inertial force. When the specimen reaches the maximum deformation and start to rebound, the unloading stage appears. The hammer and mid-span displacements as well as impact force start to reduce, and the impact force drops to zero when the hammer separates from the specimen. The above observations indicate that the hammer head shape exhibits little effect on impact response of the SPUFSCS panel.

The comparison of impact force-time histories of the four test specimens is presented in Fig. 11.27. The maximum peak impact force is observed for the specimen with thickest concrete (4-100-4), and the reduction of concrete thickness leads to the decrease in peak impact force. This can be attributed to the reduced resistance of the SPUFSCS panel with decreasing concrete thickness. As given in Table 11.9, the peak impact force is reduced by 17.0% and 24.0%, respectively, by reducing the concrete thickness from 100 mm to 85 and 70 mm. The peak impact force of specimen

**Fig. 11.27** Impact force-time histories of specimens, reprinted from Wang et al. (2021), copyright 2022, with permission from Elsevier

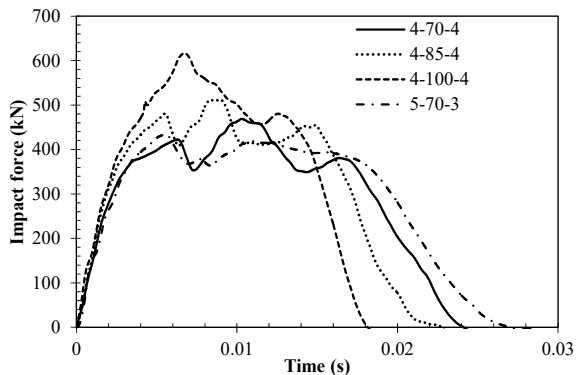
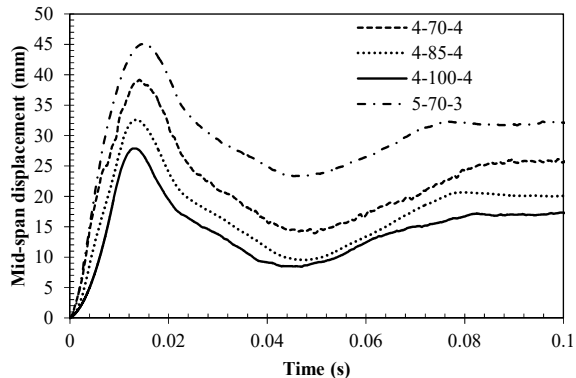


**Table 11.9** Summary of test results (cylindrical head)

Specimen	$V_0$ (m/s)	$F_{\max}$ (kN)	$D_{cm}$ (mm)	$D_{qm}$ (mm)	$D_{hm}$ (mm)	$D_{li}$
4-70-4	9.54	468.81	39.15	22.61	81.32	41.11
4-85-4	9.69	511.81	32.59	18.14	73.72	41.22
4-100-4	9.71	616.60	27.88	14.67	66.97	42.26
5-70-3	9.61	433.04	45.11	25.93	82.75	36.52

Note  $V_0$ ,  $F_{\max}$ —impact velocity and maximum impact force,  $D_{cm}$ ,  $D_{qm}$ ,  $D_{hm}$ ,  $D_{li}$ —maximum values of mid-span displacement, quarter-span displacement, hammer displacement and local indentation

**Fig. 11.28** Mid-span displacement–time histories of test specimens, reprinted from Wang et al. (2021), copyright 2022, with permission from Elsevier



5-70-3 with thinner bottom plate and thicker middle plate is 7.6% lower than that of specimen 4-70-4 although the two specimens share similar summed thickness of middle and bottom plates. This also can be attributed to the lower bending resistance of specimen 5-70-3. Figure 11.27 shows that the specimen with larger impact force exhibits smaller impact force duration, which is owing to the consistent impulse for all the test specimens who share the same drop weight and height.

The displacement–time histories of the test specimens are presented in Fig. 11.28. The mid-span displacements of all the specimens exhibit monotonic increase to their peak values after impact, and subsequently the gradual reduction of mid-span displacements is observed when the hammer starts to rebound. Finally, all the displacements approach their constant values (permanent displacements). The specimen with larger impact force shows smaller deformation (i.e., mid-span and quarter-span displacements) since the same impact energy is applied. Table 11.9 summaries the peak mid-span and quarter-span displacements. The peak mid-span displacement of SPUFSCS panel is reduced by 16.8% and 28.8%, respectively, by increasing the concrete thickness from 70 mm to 85 and 100 mm, which indicates that the deformation of the SPUFSCS panel can be evidently reduced by increasing the concrete thickness owing to the improvement in bending resistance. In addition, the mid-span displacement of specimen 5-70-3 is maximum among the four test specimens, which is also due to the low bending resistance of the SCS panel with thinner tension plate (bottom plate) and thicker compression plate (middle plate).

### 11.3.2 Numerical Study

#### 11.3.2.1 FE Model Establishment

The explicit code in LS-DYNA was also employed to carry out the FE simulation of the SPUFSCS panel under the impact of a cylindrical hammer. Figure 11.29 presents the established quarter FE model, which is consistent with the FE model presented

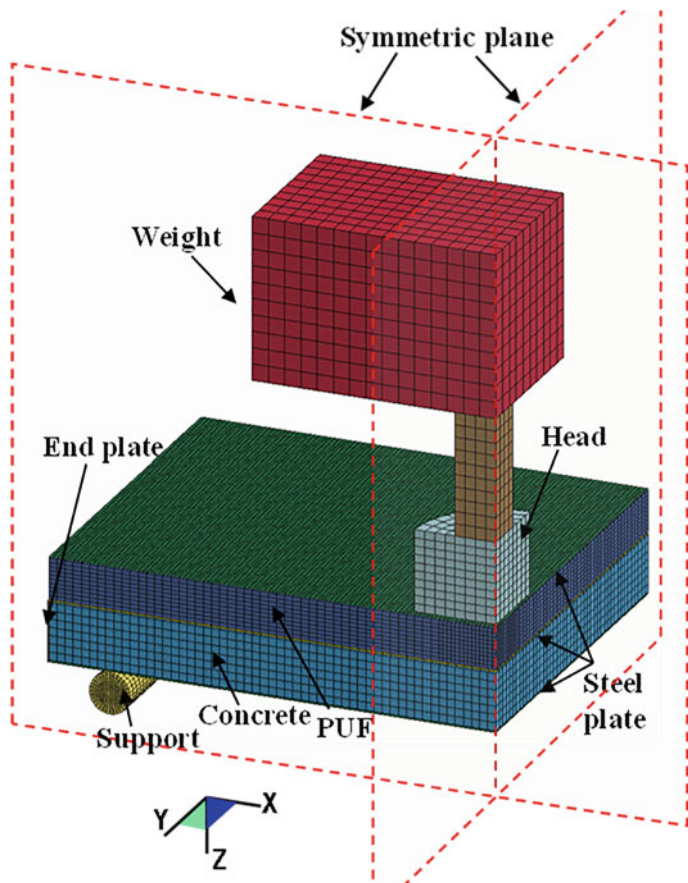


**Fig. 11.29** Quarter FE model of the SPUFSCS panel, reprinted from Wang et al. (2021), copyright 2022, with permission from Elsevier

in Sect. 11.2.2.1 in terms of element formulations, material models and material properties.

### 11.3.2.2 FE Results and Discussions

Figure 11.25 presents the comparison of failure modes of the SPUFSCS panels obtained from tests and FE predictions. The established FE models are shown to reasonably predict both the global and local deformations of the SPUFSCS panel. The flexural deformation mode of the panel can be found from the FE simulation, which is consistent with the test observation. In addition, the FE model can also capture the local indentation with fracture failure of top plate along the edge of hammer head, as observed from the tests. The FE-predicted maximum local indentation depths of the

four specimens are compared with those obtained from tests, as given in Table 11.10. The differences between them are found to be no more than 12%. The calculated average FE to test ratio for the maximum local indentation depth is 0.95 with COV to be 0.054. The buckling of the top plate at mid-span from FE prediction also matches with the test observations.

The FE-predicted impact force–time histories are compared with those from tests in Fig. 11.30, and good agreement between them in terms of both peak impact force and duration can be observed. Table 11.10 presents the comparison of peak impact forces between the FE predictions and test results, and their differences are found to be no more than 9%. The calculated average FE to test ratio for peak impact force is 1.036 with COV to be 0.054. The displacement–time histories obtained from FE analyses are compared with test results in Fig. 11.31. The established FE models can also provide good predictions on the displacement responses of the four test specimens. The peak values of mid-span and hammer displacements from FE predictions and tests are given in Table 11.10, and their differences are no more than 8% and 5% for the mid-span displacement and hammer displacement, respectively. The aforementioned comparisons indicate that the established FE models of SPUFSCS panels under impact loading are accurate in predicting the failure modes, impact force and displacement responses, and therefore can be employed for the following impact energy dissipation analysis.

The typical internal energy (or impact energy dissipation) versus time curves of top plate, PUF and SCS panel are plotted in Fig. 11.32 to reveal their impact energy dissipation evolutions. The internal energies of the top plate and PUF exhibit significantly higher rate of increase as compared to that of SCS panel at initial PUF crushing stage. This is because the top plate and PUF are first exposed to impact load, which leads to the dominating local indentation of the top plate and PUF and small global deformation of the SCS panel. Hence, the majority of impact energy is dissipated by the top plate and PUF at initial PUF crushing stage. In the loading stage, the internal energies of all the three parts show monotonic increase with time. However, the impact energy dissipated by the SCS panel rapidly climbs up and exceeds those of top plate and PUF. This is because the SPUFSCS panel almost reaches its maximum local indentation depth at loading stage, and therefore more impact energy is dissipated through global deformation of the SCS panel. The SCS panel and top plate exhibits evident elastic recovery at unloading stage when the hammer starts to rebound and separate from the SPUFSCS panel.

The internal energy of the SPUFSCS penal reaches its maximum value when the maximum deformation occurs. Figure 11.33 presents the internal energies of SPUFSCS panels at their maximum displacement moments. Generally, the impact energy dissipated by “soft” layer (top plate and PUF) is larger than that of “stiff” layer (SCS panel), and the internal energy ratio of “soft” layer to “stiff” layer varies from 1.35 to 2.52. A comparison of internal energies of SPUFSCS panels with different concrete thicknesses reveals that increasing concrete thickness leads to the increase in internal energies of the top plate and PUF, but decrease in internal energy of the SCS panel, i.e., the internal energy is increased by 19.7%, 36.4% and -29.7%, respectively, for the top plate, PUF and SCS panel when increasing concrete thickness

**Table 11.10** Comparison of FE and analytical predictions with test results (cylindrical head)

Specimen	$F_{\max\text{FE}}$ (kN)	$F_{\max\text{FE}}/F_{\max}$	$D_{cm\text{FE}}$ (mm)	$D_{cm\text{FE}}/D_{cm}$	$D_{cmA}$ (mm)	$D_{cmA}/D_{cm}$	$D_{hm\text{FE}}$ (mm)	$D_{hm}$	$D_{hm\text{FE}}/D_{hm}$	$D_{hmA}$ (mm)	$D_{hmA}/D_{hm}$	$D_{hf\text{FE}}$ (mm)	$D_{hf}$	$D_{hf\text{FE}}/D_{hf}$
4-70-4	448.31	0.96	42.37	1.08	43.30	1.11	78.96	0.97	77.50	0.95	36.07	0.88		
4-85-4	555.60	1.09	31.92	0.98	33.92	1.04	71.06	0.96	68.70	0.93	39.52	0.96		
4-100-4	645.10	1.05	26.98	0.97	26.11	0.94	66.47	0.99	61.85	0.92	41.56	0.98		
5-70-3	456.64	1.05	44.21	0.98	50.81	1.13	78.84	0.95	84.43	1.02	36.41	0.99		
Average	—	1.036	—	1.002	—	1.052	—	0.970	—	0.957	—	0.95	—	
COV	—	0.054	—	0.053	—	0.081	—	0.017	—	0.046	—	0.054	—	

Note The parameters with  $FE$  and  $A$  as the subscript stand for the FE and analytical predictions, respectively

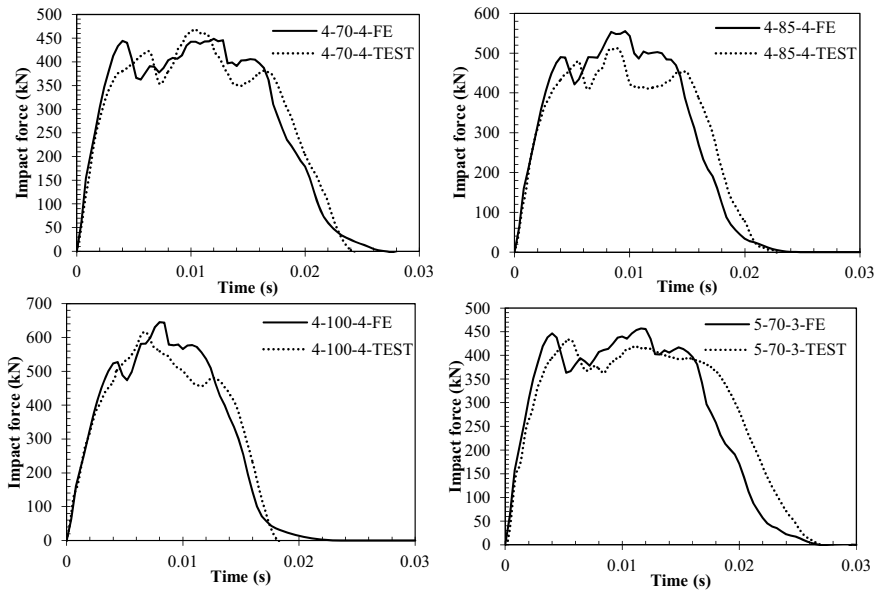


**Fig. 11.30** Comparison of impact force–time histories, reprinted from Wang et al. (2021), copyright 2022, with permission from Elsevier

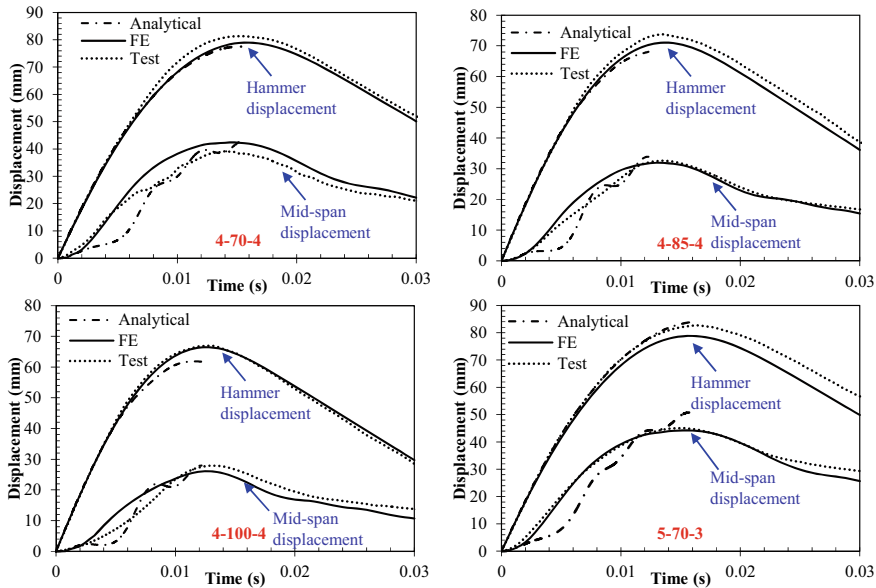


**Fig. 11.31** Comparison of displacement–time histories, reprinted from Wang et al. (2021), copyright 2022, with permission from Elsevier

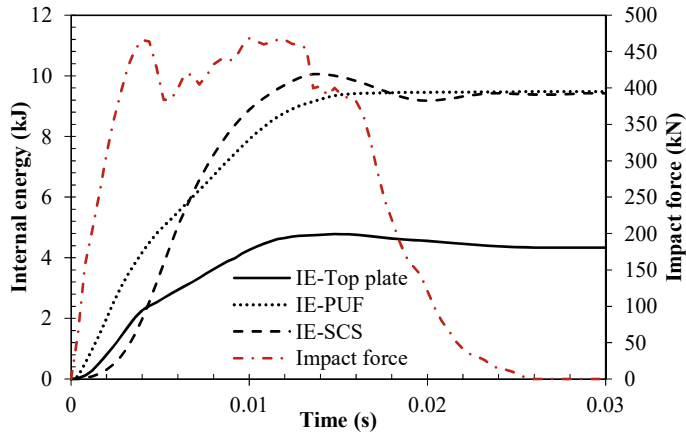
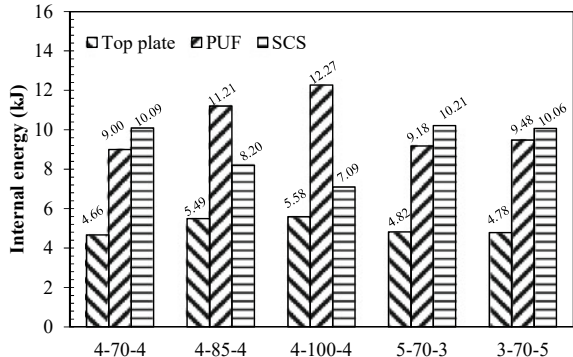


**Fig. 11.32** Typical internal energy–time histories of SPUFSCS panel, reprinted from Wang et al. (2021), copyright 2022, with permission from Elsevier

**Fig. 11.33** Internal energy of each part of SPUFSCS panel, reprinted from Wang et al. (2021), copyright 2022, with permission from Elsevier



from 70 to 100 mm. The thicker concrete leads to smaller global deformation and larger local indentation, which also causes the increase of impact energy dissipated by the top plate and PUF as well as the decrease of impact energy dissipated by the SCS panel. With regard to the influence of face steel plate thickness ratio of the SCS panel to the impact energy dissipation (i.e., specimen 5-70-3, 4-70-4, 3-70-5), the specimen with larger thickness ratio of tension plate (bottom plate) to compression plate (middle plate) generally leads to higher impact energy dissipation of the top plate and PUF, but lower impact energy dissipation of the SCS panel. However, this influence is negligible, i.e., the maximum differences of internal energies of the top plate, PUF and SCS panel among these three specimens are no more than 3.2%, 5.1% and 1.5%, respectively.

### 11.3.3 Analytical Study

The analytical model for predicting displacement response of the SPUFSCS panel under the impact of a hammer with cylindrical head is presented in this section, and the accuracy of the developed analytical model is validated against the test data.

#### 11.3.3.1 Analytical Formulation

It is assumed that the hammer and top plate move downwards together with the same velocity once the hammer strikes the top plate, and the SPUFSCS panel under impact loading can be equivalent to a two-degree-of-freedom (TDOF) system, as illustrated in Fig. 11.34. The equations of motion of the TDOF system can be formulated by employing the Lagrange's equation as follow:

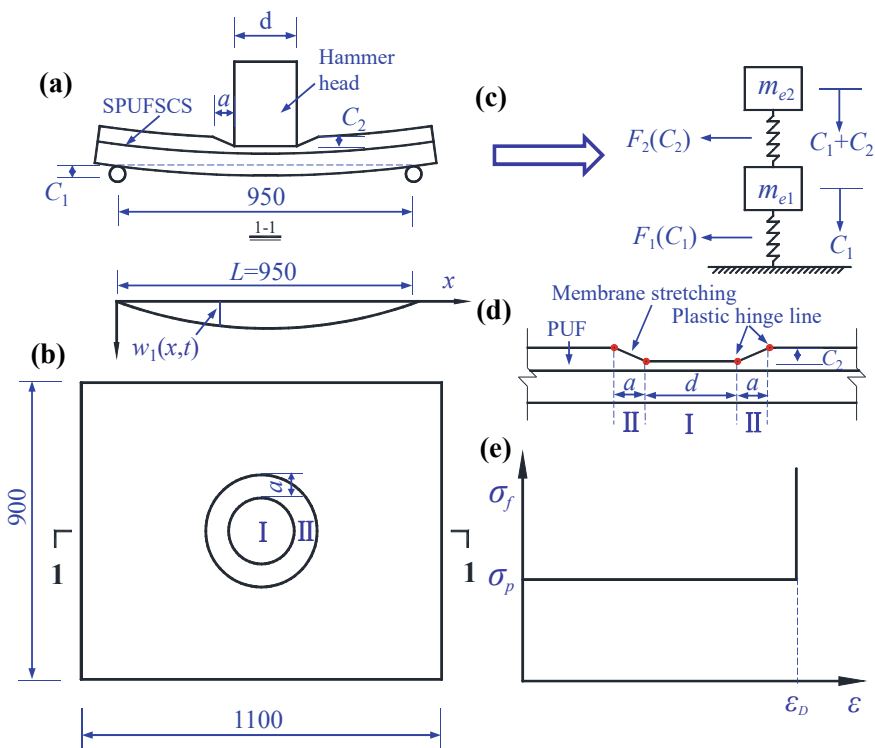


**Fig. 11.34** Analytical model for the SPUFSCS panel: **a** side view of deformed shape, **b** top view, **c** equivalent TDOF system, **d** local indentation and **e** idealized stress-strain curve of PUF, reprinted from Wang et al. (2021), copyright 2022, with permission from Elsevier

$$\frac{d}{dt} \left( \frac{\partial T}{\partial \dot{C}_i} \right) + \frac{\partial(U + V)}{\partial C_i} = 0, \quad i = 1, 2 \quad (11.5)$$

where  $T$ ,  $U$  and  $V$  are kinetic energy, strain energy and potential energy, respectively;  $C_1$  and  $C_2$  are mid-span displacement and local indentation, respectively. The calculation of strain energy and kinetic energy is presented in the following sections.

### Strain Energy

The partial differential of strain energy with respect to displacement ( $\partial U / \partial C_i$  in Eq. (11.5)) leads to the force–displacement function. Hence, the force–displacement relationships of local response,  $F_2(C_2)$ , and global response,  $F_1(C_1)$ , are calculated and presented in this subsection.

#### *Force–Local Indentation Relationship*

The local indentation of the SPUFSCS panel is observed in the test, and its profile can be assumed to be a truncated cone, i.e., a constant indentation depth below the hammer head (region I) and linearly varying indentation depth in the rest local indentation region (region II), as illustrated in Fig. 11.34d. The local indentation domain (parameter  $a$ ) has to be determined before the calculation of force–local indentation relationship,  $F_2(C_2)$ , and the following assumptions are employed to simplify the calculation of parameter  $a$  in Fig. 11.34d: (1) the mild steel used for the top plate follows rigid-perfectly plastic behavior (Jones 1988; Tran 2017) and (2) the stress–strain curve of PUF follows the relationship shown in Fig. 11.34e (Zhou et al. 2015b; Elahi et al. 2017).

According to the assumed stress–strain curve of PUF in Fig. 11.34e, its strain energy is determined as

$$U_f = \sigma_p \Delta \bar{V} \quad (11.6)$$

where  $U_f$ ,  $\sigma_p$  and  $\Delta \bar{V}$  are strain energy, plateau stress and volume change of PUF during crushing.  $\Delta \bar{V}$  can be calculated according to the assumed local indentation profile in Fig. 11.34d and being substituted into Eq. (11.6) leads to

$$U_f = \frac{1}{3}\pi C_2 \sigma_p \left( \frac{3}{4}d^2 + \frac{3}{2}da + a^2 \right) \quad (11.7)$$

where  $C_2$  is local indentation depth, and  $d$  is diameter of the hammer head. As illustrated in Fig. 11.34d, the strain energy of the top plate is caused by plastic hinge line and membrane stretching. The strain energy induced by two plastic hinge lines ( $U_{sp}$ ) can be approximated as

$$U_{sp} \approx 2M_p\pi \left( \frac{d}{a} + 1 \right) C_2 \quad (11.8)$$

where  $M_p = 0.25\sigma_0 t_t^2$  ( $\sigma_0 = \sqrt{\sigma_y \sigma_u}$  (Tran 2017) and  $t_t$  are flow stress and thickness of top plate) is plastic bending moment, and the strain energy of the top plate via membrane stretching ( $U_{ss}$ ) is obtained as

$$U_{ss} = \frac{1}{2}\sigma_0 t C_2^2 \left( \frac{d}{a} + 1 \right) \quad (11.9)$$

Then, the total strain energy induced by local indentation ( $U_{total}$ ) can be obtained as

$$U_{total} = U_f + U_{sp} + U_{ss} \quad (11.10)$$

The force can be obtained by differentiating total strain energy ( $U_{total}$ ) with respect to local indentation ( $C_2$ ) as

$$F_2 = \frac{dU_{total}}{dC_2} = \pi\sigma_p \left( \frac{d^2}{4} + \frac{da}{2} + \frac{a^2}{3} \right) + 2M_p\pi \left( \frac{d}{a} + 1 \right) + \sigma_0 t_t \left( \frac{d}{a} + 1 \right) C_2 \quad (11.11)$$

Then, minimizing the force  $F_2$  with respect to  $a$  (i.e.,  $\partial F_2 / \partial a = 0$ ) gives

$$\frac{2}{3}\pi\sigma_p a^3 + \frac{1}{2}\pi\sigma_p d a^2 - (\sigma_0 t_t C_2 + 2\pi M_p)d = 0 \quad (11.12)$$

The value of  $a$  can be determined by solving Eq. (11.12) and is found to be increasing with the increase of local indentation  $C_2$ .

It is noted in Fig. 11.34d that the compressive strain of PUF in region I is uniformly distributed and also exhibits larger value as compared to region II. This means that the PUF in region I is more likely to reach densification as compared to that in region II. Hence, more precise stress-strain curve of PUF is employed to calculate the force contributed by the compression of PUF in region I. Then, the force  $F_2$  can be modified as

$$F_2 = \pi\sigma_f \frac{d^2}{4} + \pi\sigma_p \left( \frac{da}{2} + \frac{a^2}{3} \right) + 2M_p\pi \left( \frac{d}{a} + 1 \right) + \sigma_0 t_t \left( \frac{d}{a} + 1 \right) C_2 \quad (11.13)$$

where  $\sigma_f$  is compressive stress of PUF and can be obtained in Eq. (11.14) by fitting the stress-strain curve of PUF in Fig. 11.14.

$$\sigma_f = 1.543 \left[ 1 - e^{-74.854\varepsilon_{fI}(1-\varepsilon_{fI})^{7.231}} + 1.421 \left( \frac{\varepsilon_{fI}}{1 - \varepsilon_{fI}} \right)^{1.149} \right] \quad (11.14)$$

where  $\varepsilon_{fI} = C_2/t_f$  is compressive strain of PUF in region I.

To consider the strain rate effects of mild steel and PUF on their strength enhancements, the Dynamic Increase Factor (DIF) is used herein to scale up the material strength. The DIF value of the top plate is taken as  $DIF_s = 1.1$  according to the design guideline for blast protection proposed by ASCE (2011) owing to the lack of design guideline for the impact-induced strain rate treatment of steel material. Moreover, the calculation of average strain rate of the top plate becomes impossible since the length of plastic hinge line and area of membrane stretching that affect strain energy of the top plate vary with the local indentation depth. With regard to the DIF value of PUF, the compressive strain rate of PUF in the local indentation region varies with time and space. Hence, a simplified method is proposed for evaluating the strain rate effect on the strength enhancement of PUF. The average compressive strain rate of PUF is defined and used to calculate the DIF value of PUF. It is noted that the compressive strain rate of PUF exhibits peak value at initial impact stage and gradually decreases to zero when the maximum indentation depth is reached. Hence, the average compressive strain rate of PUF ( $\dot{\varepsilon}_{\bar{f}}$ ) is taken to be the half value of the initial strain rate, as given in Eq. (11.15).

$$\dot{\varepsilon}_{\bar{f}} = \frac{\dot{C}_{20}}{2t_f} \quad (11.15)$$

where  $\dot{C}_{20}$  is initial velocity of local indentation and given in Eq. (11.49). Since the uniform compression of PUF in region I is observed, the assumed constant strain rate of PUF in region I is  $\dot{\varepsilon}_{\bar{f}}$ . With regard to strain rate of PUF in region II, the average compressive strain rate varies from zero at the periphery of local indentation to  $\dot{\varepsilon}_{\bar{f}}$  at the boundary between region I and II. Hence, it is reasonable to take  $\dot{\varepsilon}_{\bar{f}}/2$  as the average compressive strain rate of PUF in region II. Then, the DIF values of PUF in region I and II can be determined based on these two average compressive strain rates.

It is noted in Eq. (11.1) that the DIF value of PUF also varies with strain, and the DIF value employed for the analytical model is determined corresponding to the strain value of 0.3 which is the mean strain value of 0.2 to 0.4 employed for determining the plateau stress of PUF (ISO 2011). Hence, the DIF values of PUF in region I and II can be determined as

$$DIF_{fI} = 1 + (a_0 + 0.3b_0) \ln\left(\frac{\dot{\varepsilon}_{\bar{f}}}{\dot{\varepsilon}_0}\right), \text{ region I} \quad (11.16)$$

$$DIF_{fII} = 1 + (a_0 + 0.3b_0) \ln\left(\frac{\dot{\varepsilon}_{\bar{f}}}{2\dot{\varepsilon}_0}\right), \text{ region II} \quad (11.17)$$

Then, the force-local indentation relationship considering strain rate effects of mild steel and PUF can be determined as

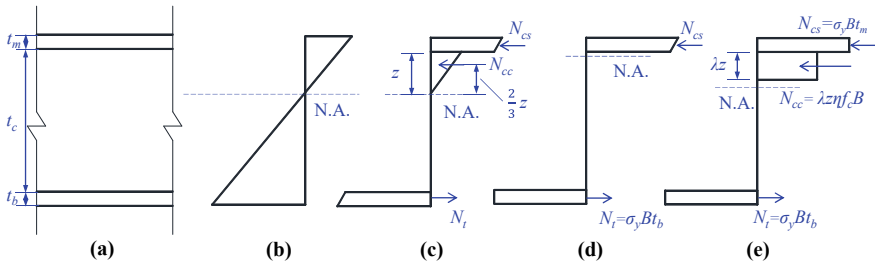


**Fig. 11.35** Strain and stress diagram for bending resistance calculation of SCS panel: **a** cross-section, **b** strain, **c** stress in elastic range, **d** stress for ultimate bending resistance ( $t_m > t_b$ ) and **e** stress for ultimate bending resistance ( $t_m < t_b$ ), reprinted from Wang et al. (2021), copyright 2022, with permission from Elsevier

$$F_2 = DIF_{fI}\pi\sigma_f \frac{d^2}{4} + DIF_{fII}\pi\sigma_p \left( \frac{da}{2} + \frac{a^2}{3} \right) + DIF_s \left[ 2M_p\pi \left( \frac{d}{a} + 1 \right) + \sigma_{0t} \left( \frac{d}{a} + 1 \right) C_2 \right] \quad (11.18)$$

#### Force–Global Displacement Relationship

The following assumptions are employed for simplifying the calculation of force–global displacement relationship of one-way supported SCS sandwich panel: (1) the mild steel employed for the middle and bottom plates follows the elastic-perfectly plastic material behavior, (2) plane section assumption is applicable for the SCS panel; (3) tension stress of concrete is negligible and (4) full composite action of the SCS panel can be achieved. Although the number of shear connectors of test specimens is not sufficient to achieve full composition action of the SCS panel, it was demonstrated that the two end plates could provide longitudinal shear resistance (Wang et al. 2016a), which could ensure the ultimate bending moment of the SCS panel equaling to that with full composited action (Wang et al. 2016a; Kang 2012). Hence, the full composite action assumption of the SCS panel is reasonable for calculating the ultimate bending moment of the SCS panel.

In the elastic range, the strain and stress are linearly distributed along the depth of the SCS panel based on plane section assumption, as shown in Figs. 11.35b, c. According to the force equilibrium in Fig. 11.35c, we have

$$N_t - N_{cc} - N_{cs} = 0 \quad (11.19)$$

where  $N_t$ ,  $N_{cc}$  and  $N_{cs}$  are resultant forces of tension plate, concrete and compression plate, respectively. Then, the position of neutral axis,  $z$ , can be determined as

$$z = [n^2(t_b + t_m)^2 + n(t_b^2 + 2t_b t_c - t_m^2)]^{1/2} - n(t_b + t_m) \quad (11.20)$$

where  $n = E_s/E_c$  is elastic modulus ratio of steel to concrete;  $t_b$ ,  $t_m$  and  $t_c$  are thicknesses of the bottom plate, middle plate and concrete. The yielding bending moment of the SCS panel can be obtained in Eq. (11.21) by taking moment about the action of compressive force of concrete.

$$M_y = N_t \left( t_c - \frac{z}{3} + \frac{t_b}{2} \right) + N_{cs} \left( \frac{z}{3} + \frac{t_m}{2} \right) \quad (11.21)$$

If the yielding curvature is defined as  $\phi_y$ , which corresponds to yielding of the SCS panel,  $N_t$  and  $N_{cs}$  can be calculated as

$$N_t = E_s B t_b \phi_y \left( t_c - z + \frac{t_b}{2} \right) \quad (11.22)$$

$$N_{cs} = E_s B t_m \phi_y \left( z + \frac{t_m}{2} \right) \quad (11.23)$$

where  $B$  is width of the SPUFSCS panel. It is noted that either yielding of bottom plate or compressive stress of concrete reaching  $0.4f_{cu}$  (Eurocode 2004) results in yielding of the SCS panel. Hence, the yielding curvature can be determined as

$$\phi_y = \min \left\{ \frac{2\varepsilon_y}{2t_c - 2z + t_b}, \frac{0.4f_{cu}}{E_c z} \right\} \quad (11.24)$$

where  $\varepsilon_y$  is yield strain of the steel plate. Then, the bending stiffness of the SCS panel in the elastic range can be obtained as

$$D_y = \frac{M_y}{\phi_y} \quad (11.25)$$

With regard to the analytical prediction of ultimate bending moment of the SCS panel, two different formulae are presented based on the different thickness ratios of middle plate (compression plate) to bottom plate (tension plate). For the case of middle plate thickness larger than bottom plate thickness, i.e.,  $t_m > t_b$ , the middle plate cannot yield when the ultimate bending moment is reached. The neutral axis continuously moves up with the increase of applied force, and the ultimate bending moment is reached when the neutral axis reaches the bottom of the middle plate (Liew and Sohel 2009). According to force distribution in Fig. 11.35d, taking moment about the action of compressive force of the middle plate gives the ultimate bending moment as

$$M_u = \sigma_y B t_b \left( t_c + \frac{t_b + t_m}{2} \right) \quad (11.26)$$

When the middle plate thickness is smaller than bottom plate thickness, i.e.,  $t_m < t_b$ , the ultimate bending moment is reached when the compressive strain of concrete below the middle plate reaches the ultimate compressive strain,  $\varepsilon_{cu}$ . Figure 11.35e shows the equivalent stress distribution along the depth of the SCS panel. According to the force equilibrium, we have

$$\sigma_y B t_m + \lambda z \eta f_c B - \sigma_y B t_b = 0 \quad (11.27)$$

where  $\lambda = 0.8$ ,  $\eta = 1.0$  and  $f_c$  is compressive strength of concrete (Eurocode 2004). Hence, the position of neutral axis,  $z$ , can be calculated as

$$z = \frac{\sigma_y(t_b - t_m)}{\lambda \eta f_c} \quad (11.28)$$

Then, by taking moment about the action of compressive force of concrete, the ultimate bending moment can be given as

$$M_u = \sigma_y B t_b \left( t_c - \frac{\lambda z}{2} + \frac{t_b}{2} \right) + \sigma_y B t_m \left( \frac{\lambda z}{2} + \frac{t_m}{2} \right) \quad (11.29)$$

It is noted that both Eqs. (11.26) and (11.29) yield same ultimate bending moment for the case of  $t_m = t_b$ . Previous studies demonstrated that the end plates could ensure the ultimate bending moment of the SCS panel without sufficient shear connectors equaling to the counterpart with full composite action (Wang et al. 2016a; Kang 2012). However, the bending stiffness is evidently smaller as compared to the fully-composited SCS panel owing to the slip between concrete and steel plates. This brings difficulties to the calculation of bending stiffness without knowing the slip value. Hence, a simplified force-displacement function of the SCS panel is proposed in Eq. (11.30), in which the stiffness gradually decreases with increasing displacement and only the initial elastic stiffness and ultimate loading capacity are kept.

$$F_1 = F_{1u} \tanh\left(\frac{k_y}{F_{1u}} C_1\right) \quad (11.30)$$

where  $F_{1u}$  and  $k_y$  are the ultimate loading capacity and elastic stiffness, and they are given as

$$F_{1u} = \frac{4M_u}{L}, k_y = \frac{48D_y}{L^3} \quad (11.31)$$

The DIF values of mild steel and concrete herein are taken to be 1.1 and 1.19, respectively, which are consistent with the DIF values for the flexural members specified in ASCE (2011), since the SCS panel also exhibits global flexural deformation mode under impact loading.

### Kinetic Energy from Global Deformation

For the equivalent TDOF system in Fig. 11.34c, the kinetic energy of the system can be calculated as

$$T = \frac{1}{2}m_{e1}\dot{C}_1^2 + \frac{1}{2}m_{e2}(\dot{C}_1 + \dot{C}_2)^2 = \frac{1}{2}(m_{e1} + m_{e2})\dot{C}_1^2 + m_{e2}\dot{C}_1\dot{C}_2 + \frac{1}{2}m_{e2}\dot{C}_2^2 \quad (11.32)$$

where  $m_{e1}, m_{e2}$  are equivalent masses of the TDOF system. The deformation of the SPUFSCS panel consists of two parts, i.e., global deformation and local indentation. In order to simplify the calculation of kinetic energy in Eq. (11.32), some of the kinetic energy from local indentation (i.e.,  $1/2m_{e2}\dot{C}_1^2$  in Eq. (11.32)) is included in the calculation of kinetic energy from global deformation.

The global displacement of the SPUFSCS panel can be given as

$$w_1(x, t) = \varphi(x)C_1(t) \quad (11.33)$$

where  $\varphi(x)$  is shape function and given in Eq. (11.34) for the left half span ( $x < L/2$ ) (Biggs 1964).

$$\varphi(x) = \begin{cases} \frac{x}{L^3}(3L^2 - 4x^2) & \text{elastic} \\ \frac{2x}{L} & \text{plastic} \end{cases} \quad (11.34)$$

Then, the kinetic energy caused by global deformation of the SPUFSCS panel can be determined as

$$T_1 = m_1 \int_0^{L/2} [\varphi(x)\dot{C}_1(t)]^2 dx = k_m m_1 L \dot{C}_1^2 \quad (11.35)$$

where  $m_1$  is mass per unit span length of the SPUFSCS panel,  $k_m$  is mass coefficient, and they are given as

$$m_1 = [\rho_s(t_t + t_m + t_b) + \rho_f t_f + \rho_c t_c]B \quad (11.36)$$

$$k_m = \begin{cases} 17/70 & \text{elastic} \\ 1/6 & \text{plastic} \end{cases} \quad (11.37)$$

where  $\rho_s$ ,  $\rho_f$  and  $\rho_c$  are densities of steel, PUF and concrete, respectively;  $t_t$ ,  $t_m$ ,  $t_b$  and  $t_f$  are thicknesses of the top, middle and bottom plates, and PUF, respectively.

### Kinetic Energy from Local Indentation

According to the assumed shape function in Eq. (11.34), the global deformation  $w_1$  of the SPUFSCS panel in local indentation region I is not uniform. In order to simplify the calculation of kinetic energy from local indentation, the uniform global deformation in region I ( $\bar{w}_{1I}$ ) is assumed and determined as

$$\bar{w}_{1I} = \gamma_1 C_1 \quad (11.38)$$

where  $\gamma_1$  is given as

$$\gamma_1 = \varphi \left( \frac{L}{2} - 0.202d \right) \quad (11.39)$$

It should be noted that the assumed uniform global deformation,  $\bar{w}_{1I}$ , in region I is the global displacement corresponding to  $x = L/2 - 0.202d$ , which divides the region I into two equal areas. Then, the local kinetic energy of the top plate in region I can be calculated as

$$T_2 = \frac{1}{2} m_2 (\dot{C}_2^2 + 2\gamma_1 \dot{C}_1 \dot{C}_2) \quad (11.40)$$

where  $m_2 = 0.25\rho_s\pi d^2 t_f$  is mass of the top plate in region I. Similarly, the local kinetic energy of PUF can be obtained as

$$T_3 = \frac{1}{2} m_3 \left( \frac{\dot{C}_2^2}{3} + \gamma_1 \dot{C}_1 \dot{C}_2 \right) \quad (11.41)$$

where  $m_3 = 0.25\rho_t\pi d^2 t_f$  is mass of PUF in region I.

Both uniform local indentation and global deformation of the SPUFSCS panel in region II are assumed to simplify the calculation of local kinetic energy of the top plate and PUF in this region. The uniform local indentation of the top plate in region II is assumed to be  $C_2/2$ , and the corresponding uniform global deformation is assumed to be

$$\bar{w}_{1II} = \gamma_2 C_1 \quad (11.42)$$

where  $\gamma_2$  is given as

$$\gamma_2 = \varphi \left( \frac{L - a}{2} - \frac{d}{4} \right) \quad (11.43)$$

Then, the local kinetic energy of the top plate in region II can be obtained as

$$T_4 = \frac{1}{2}m_4 \left( \frac{\dot{C}_2^2}{4} + \gamma_2 \dot{C}_1 \dot{C}_2 \right) \quad (11.44)$$

where  $m_4 = \rho_s \pi t_t (da + a^2)$  is mass of the top plate in region II. The local kinetic energy of PUF in region II can also be calculated as

$$T_5 = \frac{1}{2}m_5 \left( \frac{\dot{C}_2^2}{12} + \frac{1}{2}\gamma_2 \dot{C}_1 \dot{C}_2 \right) \quad (11.45)$$

where  $m_5 = \rho_s \pi t_f (da + a^2)$  is mass of the PUF in region II. The hammer head shares the same displacement with the top plate in region I, and the kinetic energy of the hammer can be given in Eq. (11.46) by employing the same assumption of uniform global deformation in region I.

$$T_h = \frac{1}{2}m_h (\dot{C}_2 + \gamma_1 \dot{C}_1)^2 \quad (11.46)$$

Then, the total kinetic energy of the SPUFSCS panel can be obtained in Eq. (11.47) by summing all the aforementioned kinetic energies.

$$T = T_1 + T_2 + T_3 + T_4 + T_5 + T_h \quad (11.47)$$

The Equations of motion of the TDOF system can be obtained by substituting the calculated kinetic energy and strain energy into Eq. (11.5) as

$$\begin{aligned} (k_m m_1 L + m_h \gamma_1^2) \ddot{C}_1 + \left( m_2 \gamma_1 + \frac{1}{2} m_3 \gamma_1 + \frac{1}{2} m_4 \gamma_2 + \frac{1}{4} m_5 \gamma_2 + m_h \gamma_1 \right) \ddot{C}_2 + F_1(C_1) &= 0 \\ \left( m_2 \gamma_1 + \frac{1}{2} m_3 \gamma_1 + \frac{1}{2} m_4 \gamma_2 + \frac{1}{4} m_5 \gamma_2 + m_h \gamma_1 \right) \ddot{C}_1 + \left( m_2 + \frac{1}{3} m_3 + \frac{1}{4} m_4 + \frac{1}{12} m_5 + m_h \right) \ddot{C}_2 + F_2(C_2) &= 0 \end{aligned} \quad (11.48)$$

For the equivalent TDOF system, the initial velocity of global deformation  $\dot{C}_{10}$  is zero, and the initial velocity of local indentation  $\dot{C}_{20}$  can be obtained by applying the conservation of momentum as

$$\dot{C}_{20} = \frac{m_h V_{h0}}{m_h + \hat{m}_1 + \hat{m}_2 + \hat{m}_3 + \hat{m}_4} \quad (11.49)$$

where  $V_{h0}$  and  $m_h$  is initial velocity and mass of the hammer;  $\hat{m}_1$ ,  $\hat{m}_2$ ,  $\hat{m}_3$  and  $\hat{m}_4$  are equivalent masses of the top plate in region I and II, and PUF in region I and II, respectively, and they can be obtained in Eq. (11.50) by ensuring the same momentum between the SPUFSCS panel and equivalent TDOF system.

$$\hat{m}_1 = \frac{1}{4} \rho_s \pi d^2 t_t$$

$$\begin{aligned}\hat{m}_2 &= \rho_s \pi t_t \left\{ \frac{(2a_0 + d)(d + a_0)}{2} - \frac{2}{3a_0} \left[ \left( \frac{d}{2} + a_0 \right)^3 - \left( \frac{d}{2} \right)^3 \right] \right\} \\ \hat{m}_3 &= \frac{1}{8} \rho_f \pi d^2 t_f \\ \hat{m}_4 &= \rho_f \pi t_f \left\{ \frac{(2a_0 + d)(d + a_0)}{4} - \frac{1}{3a_0} \left[ \left( \frac{d}{2} + a_0 \right)^3 - \left( \frac{d}{2} \right)^3 \right] \right\} \quad (11.50)\end{aligned}$$

where  $a_0$  is the value of  $a$  with local indentation to be zero. The numerical approach can be utilized to solve the equations of motion in Eq. (11.48) to obtain the displacement–time response of the SPUFSCS panel. Herein, the fourth-order Runge–Kutta time stepping procedure was employed.

### 11.3.3.2 Analytical Model Validation

The displacement–time histories obtained from the analytical models are compared with the test results in Fig. 11.31, and good agreement between them can be observed. The fluctuation of mid-span displacement–time histories observed from analytical models may be attributed to the absence of damping in the analytical model. The maximum values of mid-span and hammer displacements obtained from the analytical model are also compared with those from tests, as presented in Table 11.10, and the differences between the two results are no more than 13% and 8% for the mid-span displacement and hammer displacement, respectively. The calculated average analytical-prediction to test ratios for maximum mid-span and hammer displacements are 1.069 and 0.957 with COV to be 0.054 and 0.046, respectively. Hence, the developed analytical model is proven to be accurate and can be employed to predict displacement response of the SPUFSCS panel under impact loading. For the proposed SPUFSCS panel, the front “soft” layer (i.e., top plate and PUF) can be regarded as a sacrificial layer, and the damage level of the SPUFSCS panel is governed by the rear “stiff” layer (i.e., SCS panel) which exhibits global flexural deformation mode from the impact test observations. Hence, the damage level of the SPUFSCS panel under impact loading can be evaluated based on the maximum displacement of the SCS panel, similar to the damage level evaluation of the structural member under blast loading (ASCE 2011). Since the proposed analytical model can generally provide an accurate prediction on the impact-induced displacement response of the SPUFSCS panel, it can be employed as a simple alternative tool to quickly evaluate the damage level of the SPUFSCS panel under impact loading.

## 11.4 Summary

Drop-weight impact tests were carried out to investigate the impact responses of SPUFSCS panels. The FE model of the SPUFSCS panel under impact loading was established and verified against the test results. Finally, the analytical model was developed for predicting the displacement response of the SPUFSCS panel under the impact of a cylindrical hammer. The main findings from this study are summarized as follows:

- (1) The failure modes of the SPUFSCS panel subjected to drop-weight impact loading were identified, including local indentation and global deformation. The local bulge of the bottom steel plate was not observed in the SPUFSCS panel with the presence of the PUF layer.
- (2) Three stages of the dynamic response of the SPUFSCS panel under impact loading were identified, that is, PUF crushing, loading and unloading. Compared with the traditional SCS panel, the SPUFSCS panel exhibited a lower inertia-induced first peak impact force and damage level owing to the presence of the PUF layer.
- (3) The maximum displacement of the bottom steel plate of the SPUFSCS panel was found to be smaller than that of the SCS panel owing to the presence of PUF. With increasing concrete thickness, the peak impact force of the SPUFSCS panel was improved, and the maximum displacement was reduced. Moreover, the SPUFSCS panel with a thicker bottom steel plate exhibited a larger peak impact force and smaller global deformation.
- (4) The FE model of SPUFSCS panel was established and validated against test data. The FE results indicated that the majority of impact energy was dissipated by the “soft” layer (top plate and PUF) at initial PUF crushing stage, and the evident increase of impact energy dissipation rate was observed for the “stiff” layer (SCS panel) at loading stage. It was also found that more impact energy was dissipated by the “soft” layer as compared to the “stiff” layer.
- (5) The analytical model for predicting the displacement response of the SPUFSCS panel under impact loading was established via employing the equivalent TDOF system. In addition, the strain rate effects of mild steel, PUF and concrete on their strength enhancements were also included in the analytical model. The analytical-predicted displacement responses were found to be reasonable by comparing with the test results.

## References

- ASCE/SEI 59-11 (2011) Blast protection of buildings. American Society of Civil Engineers, Reston, Virginia
- Biggs JM (1964) Introduction to structural dynamics. McGraw-Hill, New York
- Elahi SA, Rouzegar J, Niknejad A et al (2017) Theoretical study of absorbed energy by empty and foam-filled composite tubes under lateral compression. *Thin Wall Struct* 114:1–10
- Eurocode 2 (2004) Design of concrete structures – Part 1–1: General rules and rules for buildings. BS EN 1992–1–1, London
- Fan W, Shen D, Yang T et al (2019) Experimental and numerical study on low-velocity lateral impact behaviors of RC, UHPFRC and UHPFRC-strengthened columns. *Eng Struct* 191:509–525
- Fu Y, Yu X, Dong X et al (2020) Investigating the failure behaviors of RC beams without stirrups under impact loading. *Int J Impact Eng* 137:103432
- GB/T 228.1–2010 (2010) Metallic materials – tensile testing – Part 1: Method of test at room temperature
- GB/T 8813-2008 (2008) Rigid cellular plastics-Determination of compression properties
- Hallquist JO (2006) LS-DYNA theory manual. Livermore Software Technology Corporation (LSTC). Livermore, California
- Iqbal MA, Kumar V, Mittal AK (2019) Experimental and numerical studies on the drop impact resistance of prestressed concrete plates. *Int J Impact Eng* 123:98–117
- ISO 13314 (2011) Mechanical testing of metal – Ductility testing – Compression test for porous and cellular metals
- Jeong KY, Cheon SS, Munshi MB (2012) A constitutive model for polyurethane foam with strain rate sensitivity. *J Mech Sci Technol* 26:2033–2038
- Jones N (1988) Structural impact. Cambridge University Press, New York
- Kang KW (2012) Blast resistance of steel-concrete composite structures. Dissertation, National University of Singapore
- Langdon GS, Karagiozova D, Theobald MD et al (2010) Fracture of aluminium foam core sacrificial cladding subjected to air-blast loading. *Int J Impact Eng* 37:638–651
- Li H, Chen W, Hao H (2019a) Dynamic response of precast concrete beam with wet connection subjected to impact loads. *Eng Struct* 191:247–263
- Li QM, Magkiriadis I, Harrigan JJ (2006) Compressive strain at the onset of densification of cellular solids. *J Cell Plast* 42:371–392
- Li Z, Chen W, Hao H (2019b) Numerical study of blast mitigation performance of folded structure with foam infill. *Structures* 20:581–593
- Liew JYR, Sohel KMA (2009) Lightweight steel-concrete-steel sandwich system with J-hook connectors. *Eng Struct* 31:1166–1178
- Meng L, Wang Y, Zhai X (2021) Experimental and numerical studies on steel-polyurethane foam-steel-concrete-steel panel under impact loading by a hemispherical head. *Eng Struct* 147:113201
- Remennikov AM, Kong SY, Uy B (2011) Response of foam- and concrete-filled square steel tubes under low-velocity impact loading. *J Perform Constr Fac* 25(5):373–381
- Schenker A, Antebi I, Nizri E et al (2005) Foam-protected reinforced concrete structures under impact: Experimental and numerical studies. *J Struct Eng* 131(8):1233–1242
- Tran TN (2017) Crushing and theoretical analysis of multi-cell thin-walled triangular tubes under lateral loading. *Thin Wall Struct* 115:205–214
- Wang Y, Chen J, Zhang R (2021) Impact response of steel-PU foam-steel-concrete-steel panel: Experimental, numerical and analytical studies. *Int J Impact Eng* 158:104007
- Wang Y, Liew JYR, Lee SC (2016a) Ultimate strength of steel-concrete-steel sandwich panels under lateral pressure loading. *Eng Struct* 115:96–106
- Wang Y, Lu J, Zhai X et al (2020a) Crushing of energy absorption connectors with polyurethane foam and asymmetric pleated plates. *J Constr Steel Res* 166:105902
- Wang Y, Lu J, Zhai X et al (2019) Response of energy absorbing connector with polyurethane foam and multiple pleated plates under impact loading. *Int J Impact Eng* 133:103356

- Wang Y, Zhai, X, Lee SC et al (2016b) Response of curved steel-concrete-steel sandwich shells subjected blast loading. *Thin Wall Struct* 108:185–192
- Wang Y, Zhang B, Lu J et al (2020b) Quasi-static crushing behaviour of the energy absorbing connectors with polyurethane foam and multiple pleated plates. *Eng Struct* 211:110404
- Yan C, Wang Y, Zhai X (2020) Low velocity impact performance of curved steel-concrete-steel sandwich shells with bolt connectors. *Thin Wall Struct* 150:106672
- Zhao W, Guo Q (2018) Experimental study on impact and post-impact behavior of steel-concrete composite panels. *Thin wall Struct* 130:405–413
- Zhou H, Ma G, Li J et al (2015a) Design of metal foam cladding subjected to close-range blast. *J Perform Constr Fac* 29(4):04014110
- Zhou H, Wang Y, Wang X (2015b) Energy absorption of graded foam subjected to blast: A theoretical approach. *Mater Design* 84:351–358